ERDC/EL TR-08-38

Environmental Laboratory

US Army Corps of Engineers®
Engineer Research and Development Center

*Environmental Quality and Installations Program*

# UXO Characterization: Comparing Cued Surveying to Standard Detection and Discrimination Approaches

Report 7 of 9
Marine Corps Base Camp Lejeune: UXO Characterization Using Ground Penetrating Radar

Kevin Kingdon and Stephen D. Billings

December 2008

Approved for public release; distribution is unlimited.

Environmental Quality and Installations Program

ERDC/EL TR-08-38
December 2008

# UXO Characterization: Comparing Cued Surveying to Standard Detection and Discrimination Approaches

Report 7 of 9
Marine Corps Base Camp Lejeune: UXO Characterization Using Ground Penetrating Radar

Kevin Kingdon and Stephen D. Billings

*Sky Research, Inc.*
*445 Dead Indian Memorial Road*
*Ashland, OR 97520-9706*

Report 7 of 9

Approved for public release; distribution is unlimited.

Prepared for Headquarters, U.S. Army Corps of Engineers
Washington, DC 20314-1000

Monitored by Environmental Laboratory
U.S. Army Engineer Research and Development Center
3909 Halls Ferry Road, Vicksburg, MS 39180-6199

**Abstract**: The detection and discrimination potential of GPR at the Marine Corps Base, Camp Lejeune are evaluated herein. Discrimination mode surveying data were collected over large areas by Witten Technologies CART imaging system and Applied Research Associates Nemesis Advanced Ordnance Detection. The Ohio State University multi-frequency, fully polarimetric system and a COTS GPR system were both deployed in a cued-interrogation surveying mode over previously identified targets. For all systems, saturated ground conditions at the time of the surveys resulted in significant attenuation of the GPR signal and degraded detection and characterization performance. The COTS GPR system provided accurate depths to targets and confirmed the presence of multi-object scenarios. While the inferred depths can be used to constrain inversions of EM data, detailed target information such as material properties, lengths, and aspect ratios are not attainable with a time domain (impulse), single-polarization COTS GPR system. A cued-interrogation approach incorporating OSU's fully polarimetric GPR system allowed for a more sophisticated classification of targets. An estimated linear factor could be calculated based on late time responses of the polarized data allowing targets to be classified as UXO-like or non-UXO.

**DISCLAIMER:** The contents of this report are not to be used for advertising, publication, or promotional purposes. Citation of trade names does not constitute an official endorsement or approval of the use of such commercial products. All product names and trademarks cited are the property of their respective owners. The findings of this report are not to be construed as an official Department of the Army position unless so designated by other authorized documents.

**DESTROY THIS REPORT WHEN NO LONGER NEEDED. DO NOT RETURN IT TO THE ORIGINATOR.**

# Contents

**Contents** ..... iii

**Figures and Tables** ..... v

**Preface** ..... xi

**Unit Conversion Factors** ..... xii

**Acronyms** ..... xiii

**1 Introduction** ..... 1

**2 Camp Lejeune Introduction and Preparation Field Work** ..... 4

2.1. Initial visit ..... 5

*2.1.1. Brown's Island* ..... 6

*2.1.2. G5 Gunnery Range* ..... 9

2.2. Geophysical site characterization ..... 10

*2.2.1. High frequency reflection GPR data* ..... 13

*2.2.2. Low frequency reflection GPR data* ..... 15

*2.2.3. CMP data* ..... 18

**3 Geophysical Surveys to Compare Cued Surveying to Standard Detection and Discrimination Approaches** ..... 21

3.1. Camp Lejeune EM and magnetometer surveys ..... 23

3.2. GPR surveys at Camp Lejeune ..... 23

**4 Sky Research GPR Data Acquisition and Results Obtained with COTS GPR System** ..... 30

4.1. Discussion of survey methods chosen ..... 31

4.2. Emplaced items ..... 35

*4.2.1. Data collected over emplaced items* ..... 35

*4.2.2. Types of items detectable with 250-MHz antenna* ..... 40

*4.2.3. High-frequency (1000-MHz) data* ..... 40

*4.2.4. Picked targets* ..... 46

*4.2.5. Challenging Scenarios* ..... 53

4.3 Conclusions from GPR data acquired with COTS GPR system ..... 56

**5 Conclusions** ..... 57

**Appendix A: Ohio State University ElectroScience Laboratory (OSU-ESL) Results for Camp Lejeune, NC** ..... 59

**Appendix B: Witten Technologies GPR Results for Camp LeJeune, NC** ..... 84

**Appendix C: ARA-Nemesis System Test Report for Camp Lejeune, NC** ..... 168

**Appendix D: COTS GPR Responses for Camp LeJeune, NC ..... 199**

**Report Documentation Page**

# Figures and Tables

## Figures

Figure 1. GPR system and bombing target on the beach of Brown's Island. ..... 6

Figure 2. The presence of salt water can preclude the use of GPR as an effective tool for subsurface imaging ..... 7

Figure 3. Potential UXO targets, a single target-like response occurs at a position of approximately 22 m and a cluster of targets appears near the far right of the data section. ..... 8

Figure 4. The majority of the interior of Brown's Island has significant vegetation, topography variations, and marsh areas, which will make effective ground-based geophysics difficult. ..... 8

Figure 5. Survey environment at the G5 Gunnery Range ..... 9

Figure 6. A typical GPR section from the G5 Gunnery Range site ..... 10

Figure 7. Site characterization grid at Camp Lejeune, NC ..... 11

Figure 8. Geophysical survey locations for the Camp Lejeune site characterization ..... 12

Figure 9. High-frequency GPR system acquiring reflection data ..... 13

Figure 10. High-frequency GPR reflection data acquired using the pulseEKKO 1000 system pictured in top image contains 450-MHz data; the middle, 900-MHz data; and the bottom two images display 1200-MHz data. ..... 14

Figure 11. Low-frequency GPR system acquiring CMP data. 100-MHz antennas are shown in use ..... 16

Figure 12. Low-frequency GPR reflection data acquired using the pulseEKKO 100 system pictured in Figure 11 and the Noggin 250-MHz Smart Cart shown in Figure 1 ..... 17

Figure 13. CMP profile and velocity analysis for 100-MHz data ..... 19

Figure 14. CMP data and velocity analysis for 900-MHz data ..... 20

Figure 15. EM61 towed array data from Grids D1, D2, E1, and E2 on the G6 Range, Camp Lejeune, NC ..... 24

Figure 16. Magnetometer array data from Grids D1, D2, E1 and E2 on the G6 Range, Camp Lejeune, NC ..... 25

Figure 17. EM63 cart data from Grids D1, D2, E1, and E2 on the G6 Range, Camp Lejeune, NC. ..... 26

Figure 18. The Ohio State University fully polarimetric GPR system acquiring data at Marine Corps Base Camp Lejeune. ..... 27

Figure 19. Applied Research Associates Nemesis Advanced Ordnance Detection System surveying at Camp Lejeune. ..... 28

Figure 20. Witten Technologies 400-MHz, 16-channel radar array system ready to begin collecting data at Camp Lejeune. ..... 29

Figure 21. Emplaced items and targets picked from EM surveys were marked with flags and a series of four GPR profiles were acquired over each target. ..... 30

Figure 22. Different types of data acquisition in the cued interrogation mode ..... 31

Figure 23. A photo of the target and a summary table are among the information compiled for each emplaced item. ..... 32
Figure 24. GPR profiles collected on four passes over the target indicated in Figure 23 ..... 33
Figure 25. GPR profiles collected on four passes over the target indicated in Figure 23 ..... 34
Figure 26. Average amplitude versus position for the time window indicated by the horizontal white lines in Figure 25. ..... 34
Figure 27. GPR profiles collected at 250 MHz over a 90-mm projectile buried in a vertical orientation at the 30-cm depth (on the left) and a 90-mm projectile with a dip of 45 deg at a depth of 60 cm (on the right) ..... 36
Figure 28. Average amplitude profiles for 10-ns time windows for the shallow and deep 90-mm targets shown in section views of Figure 27 ..... 37
Figure 29. Data collected over target G6A1_E19 with EM61 towed array, EM63 cart, and magnetometer array ..... 38
Figure 30. GPR profiles collected at 250 MHz over a 90-mm projectile buried at a 30-cm depth in a horizontal orientation and a vertical orientation ..... 39
Figure 31. Average amplitude profiles over the 10- to 20-ns time windows for the horizontal and vertical 90-mm targets shown in section view in Figure 30 ..... 39
Figure 32. Small items produce detectable responses in the GPR data even though the resolution is not sufficient to perform target discrimination. ..... 41
Figure 33. GPR profiles collected at 1000 MHz and 250 MHz collected over one of the smaller emplaced items, a Bomblet Dummy BDU-28/B buried at 15-cm depth in a horizontal orientation ..... 41
Figure 34. Average amplitude profiles for 5- to 10-ns time window for both 1000-MHz and 250-MHz sections collected over the Bomblet Dummy BDU-28/B ..... 42
Figure 35. Data volume for target G6A2_E21 with a horizontal slice at a depth of 60 cm and a vertical slice for X Position of 80 cm ..... 44
Figure 36 Data volume for target G6A2_E21 with a region cut out to reveal the target ..... 44
Figure 37. Individual frames from an animation of the 90-mm projectile, G6A2_E21 ..... 45
Figure 38. A typical adapter (left) and adapter end cap (right) target from the Camp Lejeune site. ..... 47
Figure 39. Section views and average amplitudes for G6B1_322 ..... 48
Figure 40. Section views for G6E1_P4 using both 250-MHz and 1000-MHz antennas ..... 49
Figure 41. Average amplitude plots for G6E1_P4 using both 250-MHz and 1000-MHz antennas ..... 49
Figure 42. Data volume for target G6E1_P4 displayed as a series of horizontal and vertical slices ..... 51
Figure 43. Data volume for target G6E1_P4 displayed as a cutout cube ..... 52
Figure 44. A cross section of items found during validation efforts at the Camp Lejeune G6 range. ..... 54
Figure 45. Target responses obtained on four passes over the target G6A1_E15, a 60-mm mortar body, using both 250-MHz and 1000-MHz antennas. ..... 55
Figure A1. The new OSU/ESL GPR system ..... 60
Figure A2. System set up at the Camp Lejeune test site. ..... 62
Figure A3. ROC curve of the GPR UXO classification performed at Camp Lejeune compared with ROC curves obtained from previous blind tests. ..... 66

Figure A4. Processed responses and photos for Item G6E1P8. ..... 67
Figure A5. Processed responses for a potential target beside Item G6E1P8. ..... 69
Figure A6. Scattering of a vertical UXO at offset position and trench effect. ..... 72
Figure A7. Processed data and extracted features of Item G6E3. ..... 73
Figure A8. Processed responses and extracted features of Item G6E3P2 ..... 76
Figure A9. Processed data of Item G6E1P1 ..... 79
Figure B1. Site overview map showing the access roads, survey control points, and survey grid. ..... 85
Figure B2. Photo of site illustrating the irregular surface, low-cut vegetation, and sediment soils. ..... 86
Figure B3. Close-up map of grid areas E1 and E2, showing the actual radar paths in more detail ..... 88
Figure B4. Close-up map of grid areas D1 and D2, showing the actual radar paths in more detail ..... 88
Figure B5. Close-up map of grid area D2 surveyed in North and South directions (D90), showing the actual radar paths in more detail ..... 89
Figure B6. Close-up map of grid areas A1, A2, and B2, showing the actual radar paths in more detail ..... 90
Figure B7. Robotic total station tracking the prism on top of a pole mounted in the center of the 400-MHz radar deck. ..... 90
Figure B8. Calculated change in measured elevation (in mm), due to a tilt of the 2-m prism pole for various tilt angles in the x and y direction. ..... 91
Figure B9. Change in measured x position (in mm), due to a tilt of prism pole in the x direction (X-Z plane) for various prism pole heights. ..... 92
Figure B10. Map indicating the location of all 269 individual radar profiles collected ..... 93
Figure B11. Relative depth errors in % of true RT picked pipe depth as a function of selected relative dielectric constant $\varepsilon_r$ assuming that $\varepsilon_r = 8$ is the correct relative dielectric constant ..... 96
Figure B12. Depth slice at 4 cm for area E using mfilt filtering. ..... 97
Figure B13. Depth slice at 23 cm for area E using mfilt filtering. ..... 98
Figure B14. Analysis plots for target G6A2E6 ..... 101
Figure B15. Analysis plots for target G6A2E7 ..... 102
Figure B16. Analysis plots for target G6A2E8 ..... 103
Figure B17. Analysis plots for target G6A2E9 ..... 104
Figure B18. Analysis plots for target G6A2E10 ..... 105
Figure B19. Migration results for G6A2E10 ..... 106
Figure B20. Analysis plots 1 m north of target G6A2E10 ..... 107
Figure B21. Migration results for anomaly 1 m North of G6A2E10. ..... 108
Figure B22. Analysis plots for target G6A2E15 ..... 109
Figure B23. Analysis plots for target G6A2E16 ..... 110
Figure B24. Analysis plots for target G6A2E17 ..... 111
Figure B25. Analysis plots for target G6A2E18 ..... 112
Figure B26. Analysis plots for target G6A2E20 ..... 113

Figure B27. Analysis plots for target G6A2E21 ..... 114
Figure B28. Analysis plots for target G6A2E22 ..... 115
Figure B29. Analysis plots for target G6A2E23 ..... 116
Figure B30. Analysis plots for target 2 m north of G6A2E23 ..... 117
Figure B31. Analysis plots for target G6A2E26 ..... 118
Figure B32. Analysis plots for target G6A2E27 ..... 119
Figure B33. Analysis plots for target G6A2E28 ..... 120
Figure B34. Analysis plots for target G6A2E29 ..... 121
Figure B35. Analysis plots for target G6A2E30. ..... 122
Figure B36. Analysis plots for target G6A2E31 ..... 123
Figure B37. Analysis plots for target G6A2E32 ..... 124
Figure B38. Analysis plots for target G6D2E33 using NS data. ..... 126
Figure B39. Analysis plots for target G6D2E33 using EW data ..... 127
Figure B40. Analysis plots for target G6D2E34 using NS data. ..... 128
Figure B41. Analysis plots for target G6D2E34 using EW data. ..... 129
Figure B42. Analysis plots for target G6D2E35 using NS data. ..... 130
Figure B43. Analysis plots for target G6D2E35 using EW data ..... 131
Figure B44. Analysis plots for target G6D2E36 using NS data. ..... 132
Figure B45. Analysis plots for target G6D2E36 using EW data ..... 133
Figure B46. Analysis plots for target G6D2E37 using NS data ..... 134
Figure B47. Analysis plots for target G6D2E37 using EW data ..... 135
Figure B48. Analysis plots for target G6D2E38 using NS data. ..... 136
Figure B49. Analysis plots for target G6D2E38 using EW data ..... 137
Figure B50. Analysis plots for target G6D2E39 using NS data ..... 138
Figure B51. Analysis plots for target G6D2E39 using EW data. ..... 139
Figure B52. Analysis plots for target G6D2E40 using NS data ..... 140
Figure B53. Analysis plots for target G6D2E40 using EW data ..... 141
Figure B54. Analysis plots for target G6D2E41 using NS data ..... 142
Figure B55. Analysis plots for target G6D2E41 using EW data. ..... 143
Figure B56. Analysis plots for target G6D2E42 using NS data ..... 144
Figure B57. Analysis plots for target G6D2E42 using EW data. ..... 145
Figure B58. Analysis plots for target G6D2E43 using NS data ..... 146
Figure B59. Analysis plots for target G6D2E43 using EW data ..... 147
Figure B60. Analysis plots for target G6D2E44 using NS data. ..... 148
Figure B61. Analysis plots for target G6D2E44 using EW data ..... 149
Figure B62. Analysis plots for target G6D2E45 using NS data. ..... 150
Figure B63. Analysis plots for target G6D2E45 using EW data ..... 151
Figure B64. Analysis plots for target G6D2E46 using NS data ..... 152
Figure B65. Analysis plots for target G6D2E46 using EW data ..... 153
Figure B66. Analysis plots for target G6D2E47 using NS data ..... 154

Figure B67. Analysis plots for target G6D2E47 using EW data. ..... 155
Figure B68. Analysis plots for target G6D2E48 using NS data ..... 156
Figure B69. Analysis plots for target G6D2E48 using EW data..... 157
Figure B70. Analysis plots for target G6D2E49 using NS data ..... 158
Figure B71. Analysis plots for target G6D2E49 using EW data ..... 159
Figure B72. Analysis plots for target 1 m south of G6D2E50 using NS data ..... 160
Figure B73. Analysis plots for target 1 m south of G6D2E50 using EW data. ..... 161
Figure B74. Photos of two versions of the CART imaging system housing the 17 radar antennas ..... 163
Figure B75. Twelve-inch depth slice of migrated radar data from Bronx survey. ..... 165
Figure B76. Partial view of migrated radar data slices from Bronx survey at depths of 18 in. and 24 in. ..... 166
Figure C1. Map of the test grid at G6 Gunnery Range. ..... 170
Figure C2. Practice UXO targets observed on the surface of the site ..... 170
Figure C3. The Nemesis preparing to traverse ponded water on the A grids ..... 171
Figure C4. GPSAR antenna array and antenna switch controllers enclosed in a custom radome enclosure ..... 172
Figure C5. STMR array and electronics ..... 173
Figure C6. Schematic diagram of the STMR system layout. ..... 173
Figure C7. Schematic diagram of the main components of the Nemesis data acquisition system. ..... 174
Figure C8. Nemesis prototype detection system mounted on the ASV RC-60-based robotic platform ..... 175
Figure C9. Teleoperated detection platform and Operator Control Station. ..... 176
Figure C10. Scaled profile drawing of the Nemesis platform and sensor arrays. ..... 178
Figure C11. Location of the survey grids at the Gunnery 6 site ..... 179
Figure C12. Map of the A grid data collection tracks. The majority of the northern part of the A2 grid was not passable due to standing water and mud. Acquisition on the A1 grid was limited to encounter runs over emplaced target locations because of impassable soft ground and standing water. ..... 180
Figure C13. Map of the D grid data collection tracks ..... 181
Figure C14. Map of the E grid data collection tracks ..... 182
Figure C15. Block diagram of a nominal processing chain for the Nemesis GPSAR data post-processing ..... 183
Figure C16. Example depth slice images for different stages of GPSAR data processing. ..... 185
Figure C17. Schematic diagram of the beam pattern effects during acquisition of GPSAR data ..... 185
Figure C18. Raw magnitude data over a metallic target ..... 186
Figure C19. Three-dimensional views of depth slice images over a 3.5-in.rocket. ..... 187
Figure C20. Three views of the 3.5-in. rocket also shown in Figure C19 ..... 187
Figure C21. Three-dimensional views of depth slice images over the 60-mm wax-filled UXO body rocket ..... 191
Figure C22. Depth slice and map detection views over the 60-mm wax-filled UXO body. ..... 191

Figure C23. Map view (A) and depth-slice images over a 40-mm projectile at 15-cm depth (ID: g6d2e48). ..... 192
Figure C24. GPS-referenced map view energy summed image over the 3.5-in. rocket emplaced in the D1 grid ..... 192
Figure C25. GPS-referenced map view image over a 12-oz. aluminum can in the D grid. ..... 193
Figure C26. GPS-referenced map view images for correlated EMI and GPSAR responses over a 40-mm target ..... 194
Figure C27. GPS-referenced map view images for correlated EMI and GPSAR responses over a 105-mm target. ..... 194
Figure C28. GPS-referenced map view images for correlated EMI and GPSAR responses over a 105-mm target ..... 195
Figure C29. GPS-referenced map view images of the raw integrated time-decay EMI data over emplaced targets in the D2 grid. ..... 196
Figure C30. GPS-referenced map view responses from raw integrated time-decay EMI data over the E1 and E2 grids ..... 197

## Tables

Table A1. GPR UXO Classification Performance (True UXO Criterion). ..... 63
Table A2. GPR UXO Classification Performance (UXO-like Criterion; L/D ratio > 2.5). ..... 64
Table A3. GPR Classification Results on the Buried UXOs (Lower pad). ..... 65
Table A4. GPR Classification Results on the actual UXOs (Upper pad). ..... 82
Table B1. Grid areas covered by radar survey. ..... 87
Table B2. Sizes of radar data files. ..... 94
Table B3. Technical Specifications: CART Imaging Systems. ..... 164

# Preface

This report was prepared as part of the Congressional Interest Environmental Quality and Installations Program, Unexploded Ordnance (UXO) Focus Area, Contract No. W912HZ-04-C-0039, Purchase Request No. W81EWF418-0425, titled, "UXO Characterization: Comparison of Cued Surveying to Standard Detection and Standard Discrimination Approaches." Research was conducted by Sky Research, Inc., for the Environmental Laboratory (EL), U.S. Army Engineer Research and Development Center (ERDC), Vicksburg, MS. The following Sky Research personnel contributed to this report:

- Dr. Stephen D. Billings was the project Principal Investigator and directed the field and data processing and analysis for this work;
- Kevin Kingdon was the project geophysicist, responsible for conducting the field work, data processing, and was the primary author for this report;
- Hyoung-sun Youn and Chi-Chih Chen of the Ohio State University ElectroSciences Laboratory conducted the work and prepared the report presented as Appendix A;
- Ralf Birken, Tuna Uluaydin, John Krause, and Carl Sellers of Witten Technologies conducted the Radar Tomography Survey and prepared the report presented a Appendix B;
- Dr. Gregory Shultz of Applied Research Associates was the Principal Investigator for the ARA-Nemesis System data collection and reporting presented as Appendix C;
- Terri Ayers was the copy editor for this report.

This project was performed under the general supervision of Dr. M. John Cullinane, Jr., Technical Director, Military Environmental Engineering and Sciences, EL; and John H. Ballard, Office of Technical Director and UXO Focus Area Manager, EL. Reviews were provided by Mr. Ballard and Dr. Dwain Butler, Alion Science and Technology Corporation. Dr. Elizabeth Fleming was Director, EL.

COL Gary E. Johnston was Commander and Executive Director of ERDC. Dr. James R. Houston was Director.

# Unit Conversion Factors

| Multiply | By | To Obtain |
|---|---|---|
| acres | 4,046.873 | square meters |
| degrees (angle) | 0.01745329 | radians |
| feet | 0.3048 | meters |
| inches | 0.0254 | meters |

# Acronyms

| | |
|---|---|
| ARA | Applied Research Associates |
| APDS | Armor Piercing Discarding Sabot |
| CART | Computer Assisted Radar Tomography |
| CLJ | Camp LeJeune |
| COTS | Commercial Off-the-Shelf |
| cm | centimeter(s) |
| CMP | Common Mid-Point |
| DoD | Department of Defense |
| DSB | Defense Science Board |
| EM | Electromagnetic |
| EMI | Electromagnetic Induction |
| EOD | Explosive Ordnance Disposal |
| ERDC | Engineer Research and Development Center |
| GHz | Gigahertz |
| GIS | Geographic Information System |
| GP*i*R | Ground Penetrating *imaging* Radar |
| GPR | Ground Penetrating Radar |
| GPS | Global Positioning System |
| HEAT | High Explosive Anti-Tank |
| IMU | Inertial Motion Unit |
| m | meter(s) |
| MHz | Megahertz |
| ns | nanosecond(s) |
| OSU | Ohio State University |
| RT | Radar Tomography |
| RTK GPS | Real-time Kinematic Global Positioning System |
| RTS | Robotic Total Station |
| SEC | Spherical and Exponential Compensation |
| SFCW | Stepped Frequency Continuous Wave |
| SUV | Sport Utility Vehicle |
| UXO | Unexploded Ordnance |
| USACE | U.S. Army Corps of Engineers |
| WTI | Witten Technologies, Inc. |

# 1 Introduction

The clearance of military facilities in the United States contaminated with unexploded ordnance (UXO) is one of the most significant environmental concerns facing the Department of Defense (DoD). A 2003 report by the Defense Science Board (DSB) on the topic estimated costs of remediation as tens of billions of dollars. The DSB recognized that development of effective discrimination strategies to distinguish UXO from non-hazardous material is one essential technology area where the greatest cost saving to the DoD can be achieved.

The objective of project W912HZ-04-C-0039 "UXO Characterization: Comparison of Cued-Surveying to Standard Detection and Standard Discrimination Approaches," was to research, develop, optimize, and evaluate the efficiencies of various modes of UXO characterization and remediation as a function of the density of UXO and associated clutter. Survey modes investigated in the research include:

1. Standard detection survey: All selected anomalies are excavated;
2. Advanced discrimination survey: Data collected in proximity to each identified anomaly are inverted for physics-based parameters and statistical or analytical classifiers are used to rank anomalies, from which a portion of the higher ranked anomalies are excavated;
3. Cued survey mode: Each selected anomaly is revisited with an interrogation platform, high-quality data are collected and analyzed, and a decision is made as to whether to excavate the item, or whether to leave it in the ground.

Specific technical objectives of the research were to:

- Determine the feasibility and effectiveness of various interrogation approaches based on the cued survey approach;
- Determine the feasibility and effectiveness of various interrogation sensors including magnetics, ground penetrating radar (GPR), and electromagnetic induction (EMI), and evaluate combinations of these sensors;
- Develop and evaluate the most promising interrogation platform designs;

- Develop optimal processing and inversion approaches for cued interrogation platform datasets;
- Evaluate the data requirements to execute accurate target parameterization and assess the technical issues of meeting these requirements using detection and interrogation survey techniques;
- Determine which survey mode is most effective as a function of geological interference, and UXO/clutter density;
- Investigate the feasibility and effectiveness of using detailed test-stand measurements on UXO and clutter to assist in the design of interrogation algorithms used in the cued-search mode.

The main areas of research involved in these coordinated activities include:

- Sensor phenomenology including GPR, EMI, and magnetometry;
- Data collection systems; platforms, field survey systems, field interrogation systems;
- Parameter estimation techniques; inversion techniques (single, cooperative, joint), forward-model parameterizations, processing strategies;
- Classification methods; thresholding, statistical models, information systems.

This report "UXO Characterization: Comparing Cued Surveying to Standard Detection and Discrimination Approaches: Report 7 of 9 – Marine Corps Base Camp Lejeune: UXO Characterization Using Ground Penetrating Radar" is one of a series of nine reports written as part of W912HZ-04-C-0039:

1. UXO Characterization: Comparing Cued Surveying to Standard Detection and Discrimination Approaches: Report 1 of 9 – Summary Report;
2. UXO Characterization: Comparing Cued Surveying to Standard Detection and Discrimination Approaches: Ground Penetrating Radar for Unexploded Ordnance Characterization: Report 2 of 9 – Fundamentals;
3. UXO Characterization: Comparing Cued Surveying to Standard Detection and Discrimination Approaches: Report 3 of 9 – Test Stand Magnetic and Electromagnetic Measurements of Unexploded Ordnance;
4. UXO Characterization: Comparing Cued Surveying to Standard Detection and Discrimination Approaches: Report 4 of 9 – UXO Characterization

Using Magnetic, Electromagnetic, and Ground Penetrating Radar Measurements at the Sky Research Test Plot;

5. UXO Characterization: Comparing Cued Surveying to Standard Detection and Discrimination Approaches: Report 5 of 9 – Optimized Data Collection Platforms and Deployment Modes for Unexploded Ordnance Characterization;
6. UXO Characterization: Comparing Cued Surveying to Standard Detection and Discrimination Approaches: Report 6 of 9 – Advanced Electromagnetic and Magnetic Methods for Discrimination of Unexploded Ordnance;
7. UXO Characterization: Comparing Cued Surveying to Standard Detection and Discrimination Approaches: Report 7 of 9 – Marine Corps Base Camp Lejeune: UXO Characterization Using Ground Penetrating Radar;
8. UXO Characterization: Comparing Cued Surveying to Standard Detection and Discrimination Approaches: Report 8 of 9 – Marine Corps Base Camp Lejeune: UXO Characterization Using Magnetic and Electromagnetic Data;
9. UXO Characterization: Comparing Cued Surveying to Standard Detection and Discrimination Approaches: Report 9 of 9 – Former Lowry Bombing and Gunnery Range: Comparison of UXO Characterization Performance Using Area and Cued-interrogation Survey Modes.

# 2 Camp Lejeune Introduction and Preparation Field Work

Marine Corps Base Camp Lejeune in North Carolina was investigated and subsequently chosen as a site for demonstration and validation of UXO remediation technologies. The main motivation behind the choice of Camp Lejeune was its suitability for GPR surveying. GPR signals are absorbed at different rates depending on the local survey environment, which results in finite, site-specific penetration depths. In general, sandy soils exhibit superior GPR performance over silty soils with significant clay content. It was anticipated that the soils at Camp Lejeune would provide an environment considered favorable for GPR surveying. The Ashland, Oregon test plot (see Report 4 0f 9, UXO Characterization: Comparing Cued Surveying to Standard Detection and Discrimination Approaches: Report 4 of 9 – UXO Characterization Using Magnetic, Electromagnetic, and Ground Penetrating Radar Measurements at the Sky Research Test Plot) is "unfriendly" to GPR and will serve to contrast performance with that on a GPR "friendly" site. Data collected by applying GPR technology at both "friendly" and "unfriendly" sites were used to gauge what could be achieved in the best-case surveying scenario as well as the limitations imposed by difficult surveying conditions.

At Camp Lejeune, four different GPR datasets were acquired using a variety of GPR systems. Data from the Witten Technologies CART imaging system and the Sensors and Software Inc. Smart Cart were collected using time domain (impulse) radars. These systems are described by the center frequency of the transmitter. The ratio of bandwidth to center frequency for these systems is typically 1. From this point on, the time domain (impulse) systems will be referred to by the center frequency of the antenna/system. Data were also acquired by both Applied Research Associates and Ohio State University using frequency domain GPR systems. Discrimination mode GPR surveying results in complete coverage of a given area. In cued interrogation mode GPR surveying, data in a small area directly surrounding individual targets were investigated. The surveying mode employed and system-specific details for the GPR data collected at Camp Lejeune are summarized below.

- A discrimination mode survey was conducted with the Applied Research Associates (ARA) "Nemesis Advanced Ordnance Detection system," deploys an array of magnetometers and an array of GPR antennas (GPSAR). The GPSAR array is a stepped frequency, continuous wave (SFCW) radar operating over the 400-megahertz (MHz) to 4-gigahertz (GHz) range.
- A discrimination mode survey was conducted with the Witten Technologies CART imaging system that operates an array of time domain (impulse) GPR antennas with a center frequency of 400 MHz.
- Cued interrogation was conducted with the Ohio State University, Ultra-wideband GPR system that collects fully-polarimetric data at multiple frequencies from 10 to 800 MHz.
- Cued interrogation was also conducted using a commercial, off-the-shelf (COTS) time domain (impulse) GPR system. The system deployed was a Sensors and Software Inc. Smart Cart using either a 250-MHz or a 1000-MHz antenna.

The Applied Research Associates, Witten, and Ohio State University data collection efforts and analysis reports are attached as appendices to this report.

## 2.1. Initial visit

A short reconnaissance visit to Camp Lejeune occurred on August 18-19, 2005. All indications were positive that the Camp Lejeune site would be conducive to GPR work. One factor that needed to be assessed was the potential presence of salt water at some of the intended sites. The determining factor in the success of most GPR surveys is the conductivity of the host soil. High conductivity soils limit GPR penetration. Salt water present in the pore space near coastal environments has the potential to severely limit the effectiveness of GPR surveying. Before committing to the mobilization and expense of a complete geophysical site assessment, it was thought prudent to confirm GPR performance via a set of profile lines collected in situ at the proposed sites.

This visit also permitted the chance to investigate the other desired characteristics for the site. An area between 10 and 20 acres in size was sought that was relatively flat and free of vegetation that would significantly hinder ground-geophysics. The site should be easily accessible and contain a fairly broad range of munitions.

The nature of the data required on the reconnaissance trip was such that a GPR system which could be quickly assembled and deployed at multiple locations was required. A COTS time domain system, a Noggin 250-MHz, cart-based GPR system, was chosen for its portability. The GPR system used at Camp Lejeune can be seen in Figure 1. Global positioning system (GPS) information could also be fed directly into the GPR's data logger, making it convenient to accurately assess GPR performance at a variety of locations.

### 2.1.1. Brown's Island

The first site selected for investigation was Brown's Island, which was accessible only by boat. The island consists of sandy beaches which transition into larger dunes that ring the interior of the island. Figure 1 is a photo of the GPR system on the beach taken on one of the dunes. Penetration was severely limited for any profiles collected near the water with signals attenuated within the top 0.5 meter (m). This includes areas that are clear of water at low tide but under water at high tide, as illustrated by the darker sand areas in Figure 1. The degradation in GPR performance that results from the presence of salt water is illustrated in Figure 2.

Figure 1. GPR system and bombing target on the beach of Brown's Island.

The data section on the top of Figure 2 was taken approximately 2 m in from the water line on the beach. Moving further inland, the data displayed at the bottom of Figure 2 are closer to the dunes that ring the interior of the island. No useful information from the subsurface can be extracted from the data collected in the presence of salt water, while the inland data show signal penetration down to at least the 3-m depth and excellent resolution of the internal structure of the sand dunes.

Although the main purpose of the data collection was the gauging of GPR performance rather than a detailed survey for target detection, some of the profiles collected inland near the dunes of Brown's Island did contain responses that would be typical for buried UXO targets. These areas were particularly clean of typical subsurface GPR clutter (e.g. tree roots, large rocks, or soil inhomogeneities). The hyperbolic responses indicated by the red circles in Figure 3 represent localized anomalies and are different from the internal structure and layering evident in the bottom data section of Figure 2.

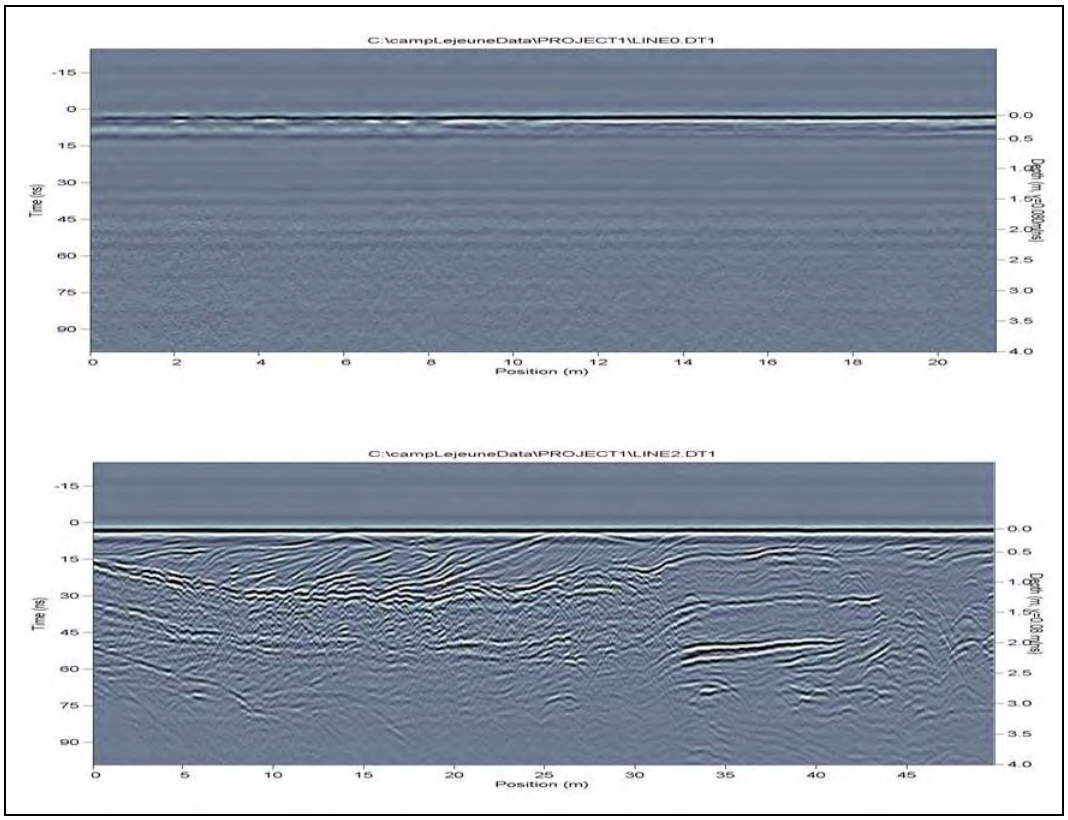


Figure 2. The presence of salt water can preclude the use of GPR as an effective tool for subsurface imaging. Top image was collected near the water's edge and bottom image was acquired approximately 50 m further inland.

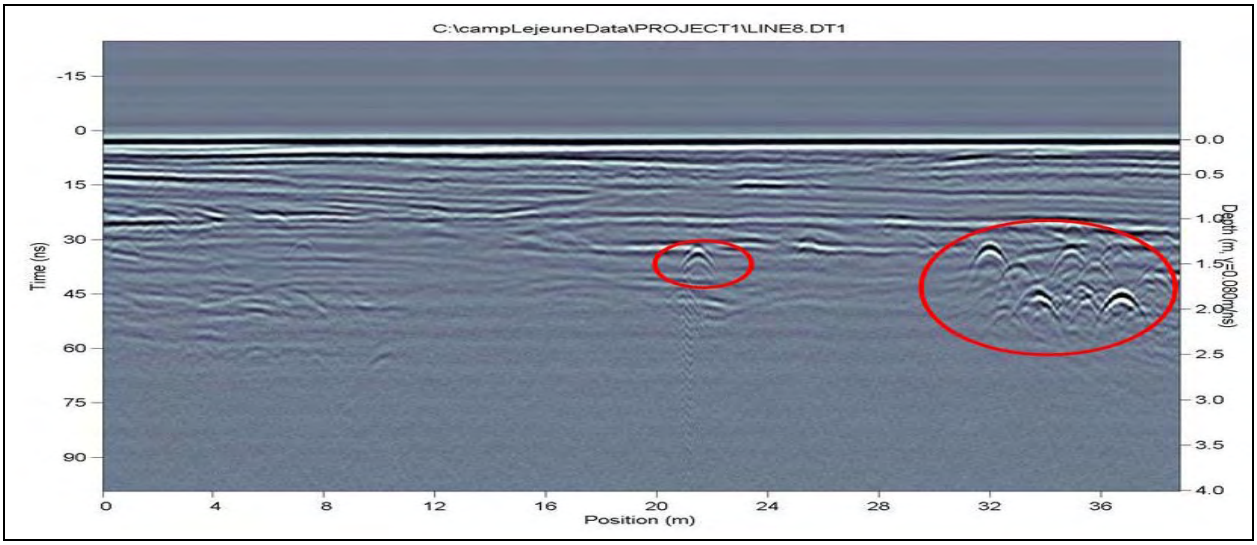


Figure 3. Potential UXO targets, a single target-like response occurs at a position of approximately 22 m and a cluster of targets appears near the far right of the data section.

While salt water limits the effectiveness of GPR measurements on the beach areas, improved GPR performance was observed at areas closer to the dunes and potential targets were identified (see Figure 3). However, this represents a rather minor portion of Brown's Island. The majority of the area with suitable soils is on sand dunes in the interior of the island. The terrain of this area is not conducive to effective ground-based geophysics. There are three main obstacles: dense vegetation, rolling topography, and marshy areas. One region of the interior of Brown's Island interior is shown in Figure 4.

Figure 4. The majority of the interior of Brown's Island has significant vegetation, topography variations, and marsh areas, which will make effective ground-based geophysics difficult.

Brown's Island was deemed inappropriate for GPR work, specifically as a GPR "friendly' site because of the saltwater issues and the rugged terrain. Accessibility to the site was also a concern as it would require a boat trip. In bringing these concerns to the Camp Lejeune personnel, they suggested a second site that was much flatter, had little vegetation and was readily accessible by vehicle.

### 2.1.2. G5 Gunnery Range

The second site recommended was chosen specifically to avoid the difficulties encountered at Brown's Island. The location selected was further inland so that saltwater effects would not be a concern. The topography was much flatter and the vegetation was minimal in most areas. According to Camp Lejeune representatives, types of ammunition used on the range included 106-mm recoilless rounds, 105-mm main tank rounds, 40-m linked Dragon rounds and possibly 2.75-in. rockets. Improvements in the survey environment for ground-based geophysics are evident in Figure 5.

Figure 5. Survey environment at the G5 Gunnery Range. Access road is visible in photo. The site ultimately chosen, the G6 Gunnery Range, is located in the distance, beyond the access road.

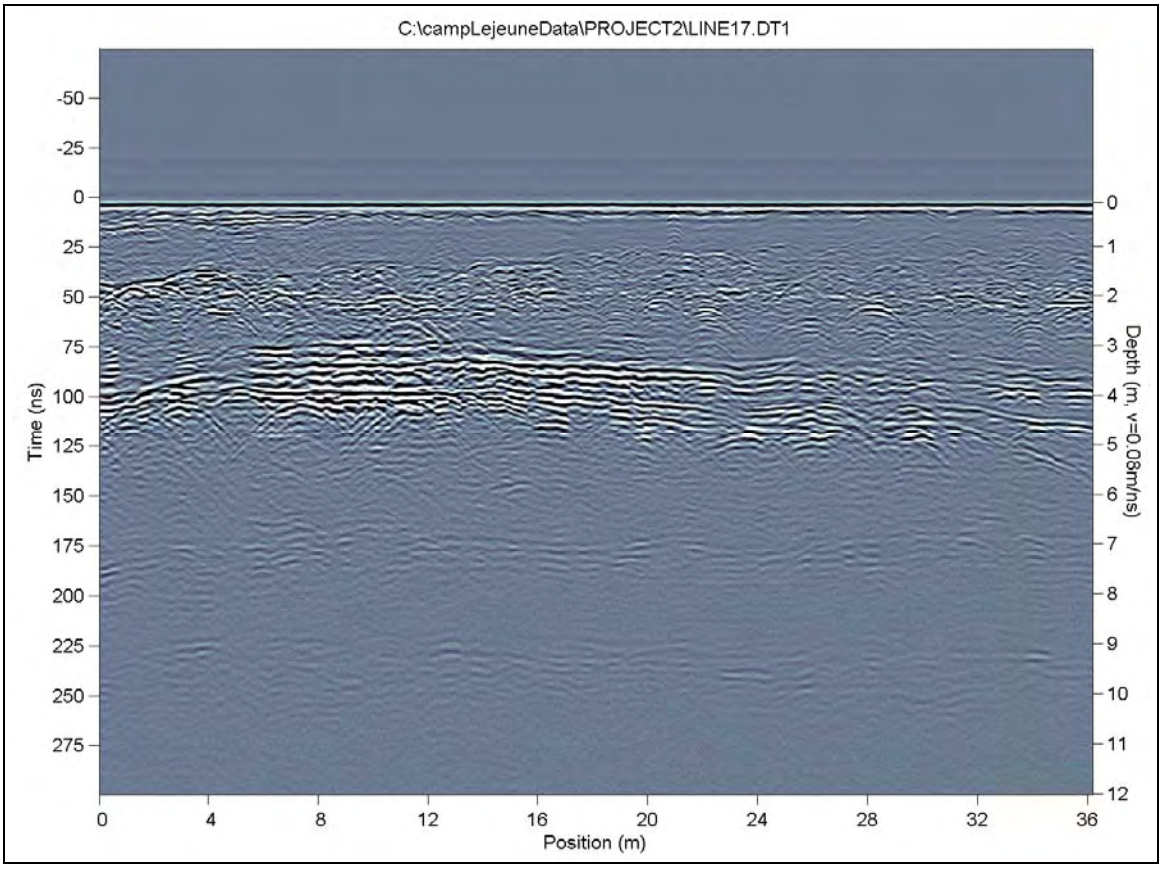


Figure 6. A typical GPR section from the G5 Gunnery Range site. Penetration was typically around 5 m.

The penetration at the G5 Gunnery Range was an improvement over the Brown's Island location, as 5-m penetration was typical in the areas surveyed. A sample data section is shown in Figure 6. The G5 range also exhibits increased scattering from smaller objects than was observed at the Brown's Island site, likely a consequence of a more complicated subsurface at G5 when compared with the sands of Brown's Island.

The reconnaissance visit proved to be essential for understanding the variation of GPR performance at the Camp Lejeune site. The ability to view a range of survey environments allowed for the selection of an optimal site for future geophysical surveys.

## 2.2. Geophysical site characterization

Having found favorable conditions for GPR data acquisition during the initial reconnaissance surveys at the Camp Lejeune site, a comprehensive geophysical site characterization was performed at the site September 21-26, 2005. The purpose was to understand the survey environment

and define a framework to interpret future geophysical datasets targeting UXO at the site. It was determined that the area of the G5 Gunnery Range previously selected did not contain a large enough area free of vegetation to encompass the entire 100-m by 400-m area required for the site characterization. As a result, the nearby G6 Range was chosen after confirming via a soils database that the area consisted of similar types of soils to the G5 Gunnery Range examined in the previous surveys. The site characterization grid is plotted on top of the soils information for the G6 Range in Figure 7. Sky Research personnel arrived on September 19 to finalize logistics and survey positions for the data acquisition to follow.

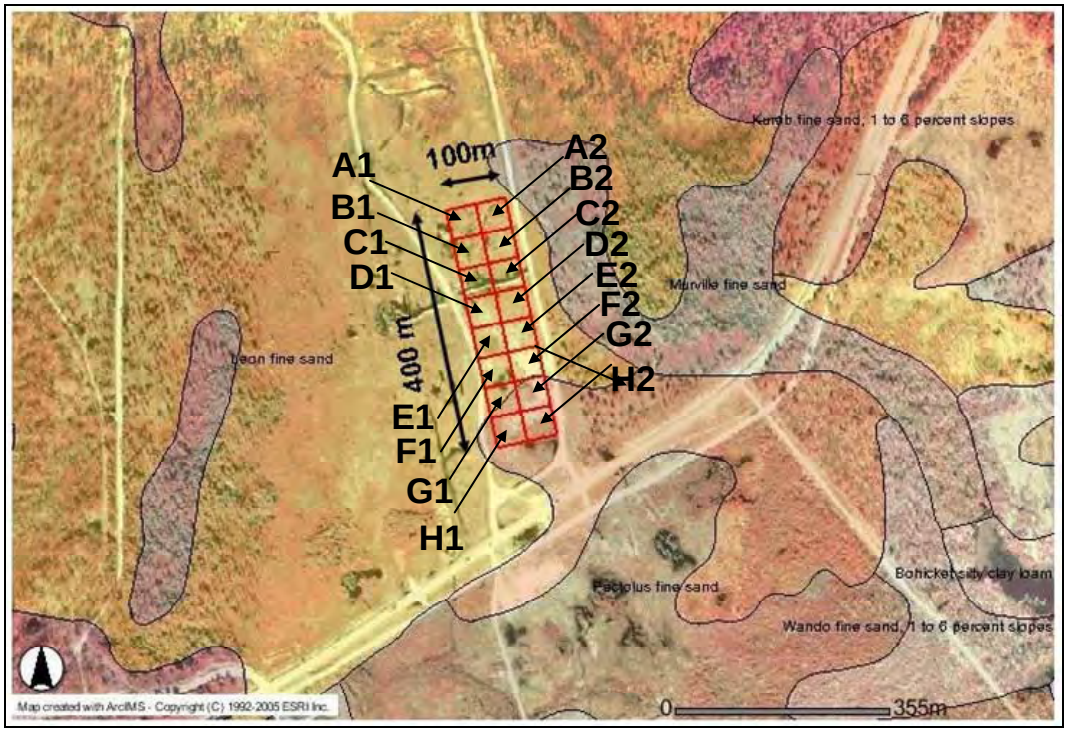


Figure 7. Site characterization grid at Camp Lejeune, NC. The area was bordered by roads on both sides, providing excellent accessibility for ground-based geophysical equipment. The area was divided up into a series of eight 50-m by 50-m grids.

The geophysical site characterization was planned and performed by the U.S. Army Corps of Engineers – Engineer Research and Development Center (USACE-ERDC). A comprehensive suite of geophysical methods was applied at the site. Data acquired by the ERDC team included magnetometer surveys, frequency domain EM31, electrical resistivity, magnetic susceptibility, and soil sampling for laboratory analysis.

GPR data acquisition was the most time-consuming portion of the site characterization, a consequence of the volume of data required. Because Camp Lejeune was selected specifically as a "friendly" site for GPR work, extensive measurements were acquired using both low-frequency (50, 100, 200/250 MHz) and high-frequency (450, 900, 1200 MHz) time domain GPR systems. Data were collected with each frequency antenna both in reflection and common mid-point (CMP) survey modes at multiple locations. The GPR data acquisition was completed by Sky Research personnel with support from the ERDC team. Resistivity, magnetic susceptibility, soil samples, and GPR data were collected at coincident locations as indicated in Figure 8.

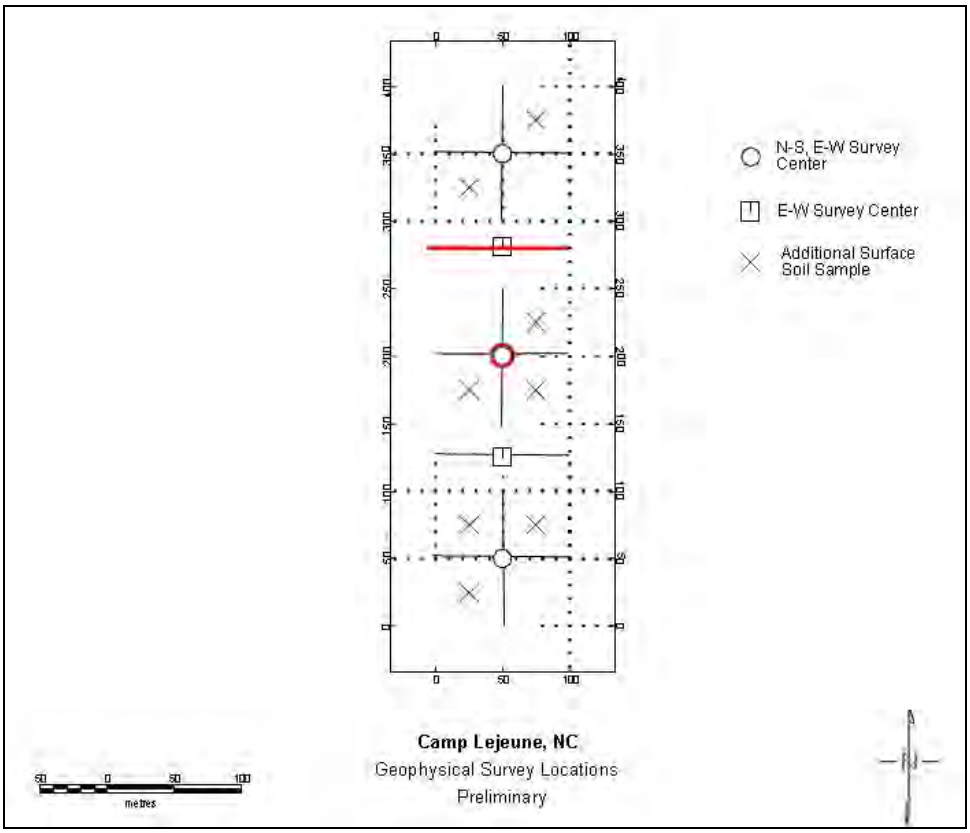


Figure 8. Geophysical survey locations for the Camp Lejeune site characterization. GPR reflection profiles are indicated by the solid red line and the center point for the CMP surveys discussed is represented by the red circle.

Reflection profiles were obtained using a cart to transport the antennas, electronics, and data logger. The high-frequency system is pictured collecting a line of reflection data in Figure 9. For each of the six GPR center frequencies used (50, 100, 200/250, 450, 900, 1200 MHz), eight reflection profile lines were collected as indicated by the N-S and E-W survey

lines of Figure 8. The E-W survey line, which extends from point (0, 280) to point (100, 280) and indicated by the solid red line in Figure 8 will be examined for all frequencies to illustrate the relative performance of the six GPR frequencies employed.

Figure 9. High-frequency GPR system acquiring reflection data. The front cart transports the GPR transducers and GPS antenna, while the rear cart contains all of the electronics, excess cabling, and data logger.

### 2.2.1. High-frequency reflection GPR data

The pulseEKKO 1000 GPR equipment used to collect high-frequency data is pictured in Figure 9 during reflection data acquisition. The pulseEKKO 1000 system consists of bi-static antennas. For all reflection data, the antennas were oriented in a parallel broadside configuration (both transmit and receive antennas aligned perpendicular to the survey line). The system is triggered to fire the transmitter using an odometer wheel. However, when problems were encountered with the triggering mechanism, the 450-MHz and 1200-MHz reflection data were acquired in a continuous mode. Fiducials were placed in the data at 10-m intervals as the cart was pulled at a near constant speed to sample at regular intervals. GPS information was also being recorded simultaneously to further constrain the cart location.

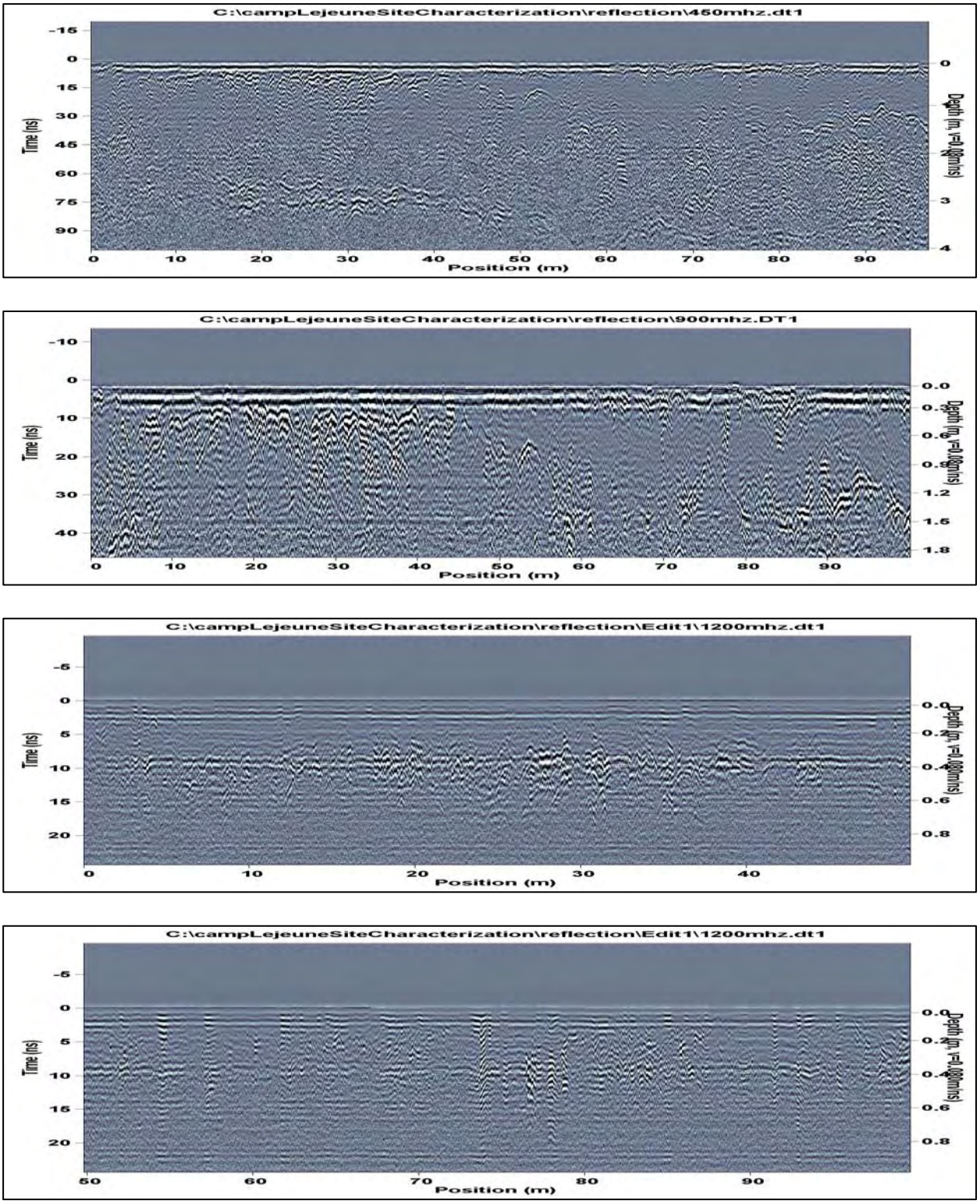


Figure 10. High-frequency GPR reflection data acquired using the pulseEKKO 1000 system pictured in top image contains 450-MHz data; the middle, 900-MHz data; and the bottom two images display 1200-MHz data.

Figure 10 shows the reflection profile responses for the three antenna frequencies deployed with the high-frequency GPR system over the E-W survey line noted with a solid red line in Figure 8. The lowest frequency used was 450 MHz and penetration to depths of up to 4 m was observed. There is a significant amount of shallow scattering evident up to the 2-m depth. These same scattering effects are captured at the higher frequency (900 MHz) data displayed in the middle image of Figure 10. There is also a weak horizontal reflector in the 450-MHz data located at approximately 3 m deep and starting at a position 15 m along the line. At approximately 50 m along the line, this reflector dips deeper and appears weaker from 60 m to 90 m along the line. This horizontal reflection is too deep to be captured in either of the other two high-frequency reflection profiles displayed in Figure 10. However, it is particularly clear in images collected with the lower frequency Noggin 250-MHz smart cart shown in Figure 12.

Nearly 2 m of penetration was observed in the 900-MHz data of Figure 10. The higher frequency antennas are capable of resolving smaller scale features. Comparing the 900-MHz data displayed in the middle image of Figure 10 with the first 2 m of depth of the 450-MHz data, similar features can be seen with an increasing amount of detail in the 900-MHz data. The 1200-MHz antennas generally should produce an even higher resolution image of shallow features observed in the 450-MHz and 900-MHz reflection profiles.

For display purposes, the 1200-MHz data are separated into two 50-m segments rather than a single 100-m profile. This avoids decimation of the closely spaced traces when generating the display. The 1200-MHz image displayed in the bottom two images of Figure 10 does not provide obvious improvements in resolution over the 900-MHz image, and penetration is limited to approximately 0.5 m. There is agreement between areas of increased scatter in the 1200-MHz images and the shallow depths of the 900-MHz data.

### 2.2.2. Low frequency reflection GPR data

The pulseEKKO IV/100 GPR equipment used to collect the 50-MHz and 100-MHz low-frequency data is pictured in Figure 11 during CMP data acquisition. The Smart Cart shown in Figure 1 was used to collect the 250-MHz data. Low-frequency data collection involves the use of longer wavelengths with the GPR signal being generated by physically larger

antennas. In the case of the lowest frequency, 50 MHz, the antennas are nearly 2 m in length. Like the high-frequency data, antennas were oriented in a parallel broadside configuration for all reflection data acquisition. All of the results for the low-frequency data were collected along the same survey line (see Figure 8) as the high-frequency data.

Figure 11. Low-frequency GPR system acquiring CMP data. 100-MHz antennas are shown in use. For reflection surveying, antennas were mounted to a cart not shown.

The top image of Figure 12 shows the results obtained with the 50-MHz antennas. These antennas proved to be too cumbersome for effective cart-based surveying, so only two portions of a single reflection profile were acquired. In the first portion, a strong signal is evident all the way down to the bottom of the time window. At approximately 49 m along the survey line, the antennas became dislodged from the cart and acquisition had to be restarted. At this point, the time window was increased so that the full penetration depth at 50 MHz could be assessed. Only 15 m of further data were acquired before similar problems halted 50-MHz reflection acquisition permanently. From that small portion of data with an extended time window, penetrations of up to 20 m were achieved. At this frequency, only broad scale features such as soil horizons are evident, as smaller scale items are not resolvable.

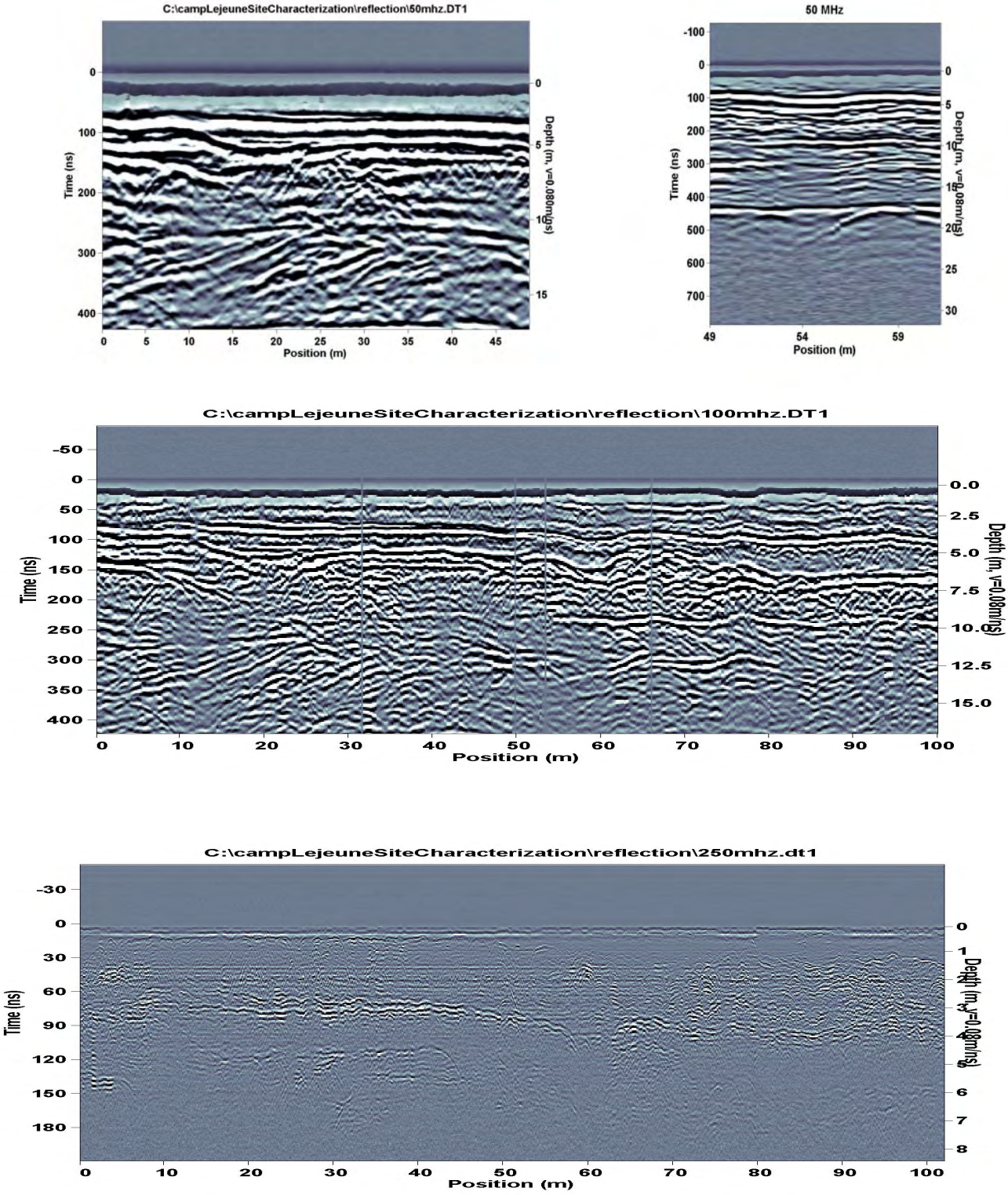


Figure 12. Low-frequency GPR reflection data acquired using the pulseEKKO 100 system pictured in Figure 11 and the Noggin 250-MHz Smart Cart shown in Figure 1. The 50-MHz data are shown in the top two images, 100 MHz in the middle, and 250 MHz in the bottom.

The middle image of Figure 12 illustrates the 100-MHz reflection profile. Penetration depth is comparable to the 50-MHz results. Once again there is strong signal down to the bottom of the time window, and the time window should have been extended longer. Penetrations of at least 17 m are observed and the major soil horizons and reflection events visible over comparable positions of the 50-MHz data can be identified. The transition to the higher 100-MHz frequency also results in additional structure and details being resolved that were not evident in the 50-MHz image.

The bottom image of Figure 12 was collected with the 250-MHz Noggin Smart Cart rather than the 200-MHz antennas and the pulseEKKO IV/100 system. The Smart Cart is more efficient and less cumbersome for surveying and the 250-MHz Noggin antenna would provide similar information as the 200-MHz antennas attached to the low-frequency system. The 250-MHz frequency bridges the gap between high-frequency and low-frequency signatures. The overlap with 450-MHz data was covered in the high-frequency discussion and some of the weaker, deeper responses in the 250-MHz data can also be seen in the 100-MHz data. For example, the strong response near the start of the 250-MHz line occurring just above 150 nanoseconds (ns) down the time window correlates well with a similar strong reflector in both the 100-MHz and 50-MHz images.

### 2.2.3. CMP data

In CMP surveying, an estimate of the GPR velocity variation with depth is obtained by varying the antenna separation about a fixed location and measuring the differences in recorded two-way travel times. A parallel broadside antenna configuration was used to obtain the widest angular coverage of subsurface reflectors. In CMP surveying, the antennas are placed at a minimal initial separation, then simultaneously moved apart at a constant increment. CMP surveying in progress is shown in Figure 11. Because the arrival times have a first order hyperbolic dependence on antenna separation, analysis of the moveout hyperbola of time versus separation permits an estimation of GPR propagation velocity. In CMP analysis, data traces are stacked at many different velocities. When traces are stacked at an incorrect velocity, they will destructively interfere and result in low amplitudes. Traces stacked at the correct velocity will constructively interfere and produce high amplitudes. Plotting the stacked data allows a velocity value to be chosen based on the highest amplitudes.

The CMP data collected with the low-frequency GPR system at a frequency of 100 MHz is shown in Figure 13. These data are from an E-W survey line about the point noted by the red circle in Figure 8. There is a strong air wave and ground wave event as well as a number of responses from deeper reflectors, with a strong reflector occurring just past the 400-ns mark. Performing a CMP analysis produces the image on the right of Figure 13. At early times, the presence of the airwave is indicated by the high-amplitude occurrence at a velocity of 0.3 m/ns, the propagation velocity of the GPR signal in air. The next strong amplitudes are observed just above the 100-ns point in the time window where the velocity is approximately 0.09 m/ns. At this point, the velocity gradually decreases with depth until just past the time window value of 200 ns, where the velocity is 0.07 m/ns. Deeper still, there are reflections in the profile around 300 ns and 400 ns, which both produce high amplitudes on the analysis image at a velocity of approximately 0.06 m/ns. These velocities seem low for a sandy soil environment, and may have been the result of a hurricane that passed through the area the previous week. The presence of water in the pore space can significantly alter the propagation velocity of the GPR signal.

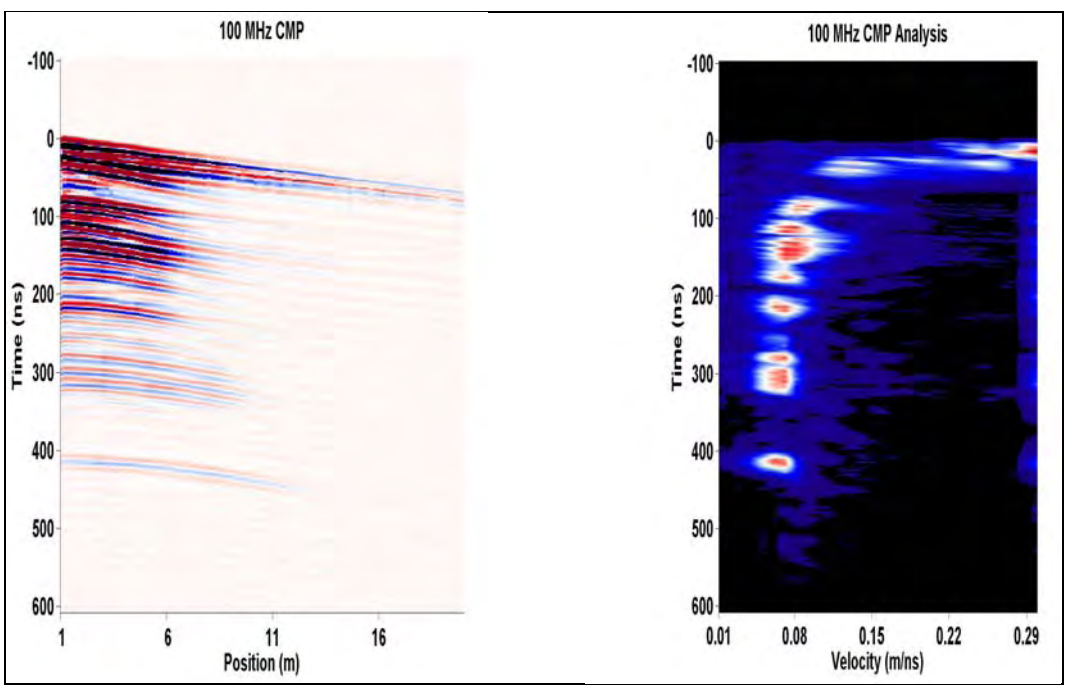


Figure 13. CMP profile and velocity analysis for 100-MHz data. Velocity exhibits a slight decrease with depth and ranges from a high value of 0.09m/ns to a low value of 0.06 m/ns.

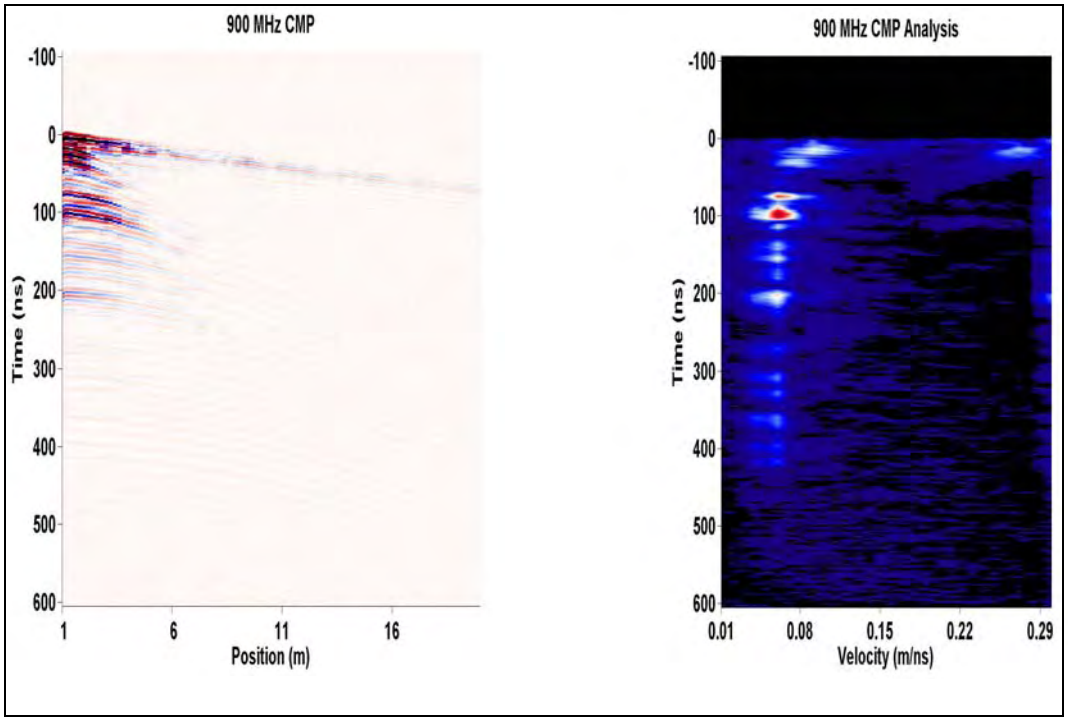


Figure 14. CMP data and velocity analysis for 900-MHz data. Velocity remains relatively constant with depth at a value of 0.06 m/ns. Heavy rains the night prior to the 900-Mhz measurements contributed to the low velocity measurements.

The CMP data collected over the same E-W survey line but using the high-frequency GPR system at a frequency of 900 MHz are shown in Figure 14. As with the reflection profiling results, the higher frequencies do not penetrate as deeply as the lower frequencies. In the 900-MHz CMP analysis, elevated amplitudes occur again at shallow depths, indicating the air wave and ground wave velocities. The velocity remains relatively constant with depth at a value of 0.06 m/ns. In addition to the hurricane of the previous week contributing water to the slow velocities, there were heavy rains on the evening between the CMP acquisition of the 100-MHz data and the 900-MHz data. This could explain the lower velocities observed for the 900-MHz data. If possible, future visits to the site should include CMP measurements at the same sites to compare variations in the velocity under different environmental conditions.

# 3 Geophysical Surveys to Compare Cued Surveying to Standard Detection and Discrimination Approaches

All of the geophysics at Camp Lejeune discussed thus far have focused on characterizing the site conditions to determine how conducive the site would be to evaluating different methodologies of UXO remediation. The next stage involved non-intrusive geophysical data collection using GPR and magnetic and electromagnetic sensors. Deployment modes included man-portable, cart-based, and towed array surveys. Anomalies identified during that survey work were selected for intrusive investigation, as anomalies were excavated to provide validation information. Validation information for targets that were interrogated at the G6 Range of Camp Lejeune was analyzed, merged, and archived. Photos were taken of items that were found. GPS information was collected and subsequently merged with descriptive notes taken by the explosive ordnance disposal (EOD) technician during the target investigations. These ground truth validations were passed on to the GPR contractors for use in interpretating the data that they acquired at the G6 site.

The geophysical surveys conducted at Marine Corps Base Camp Lejeune involved data collected on the G6 Gunnery Range using the following technologies:

- Full coverage with the five-element EM-61 towed array with Crossbow Inertial Motion Unit (IMU) for orientation and Leica Robotic Total Station (RTS) for positioning;
- Full coverage with the Sky quad-sensor magnetometer array with Crossbow IMU for orientation and RTS for positioning (optional, depending on schedule);
- Discrimination mode survey of selected sections with the EM-63 cart system;
- Cued interrogation of selected anomalies with the EM-63 cart system;
- Discrimination mode survey with the Applied Research Associates “Nemesis Advanced Ordnance Detection system,” which deploys an array of magnetometers and an array of stepped frequency continuous wave (SFCW) radar operating over the 400-MHz to 4-GHz range;

- Discrimination mode survey with the Witten Technologies CART imaging system, which operates an array of GPR antennas with 400-MHz center frequencies;
- Cued interrogation with the Ohio State University, Ultra-wideband GPR system, which collects fully polarimetric data at multiple frequencies from 10 to 800 MHz;
- Cued interrogation using a COTS GPR system. The system deployed was a Sensors and Software Inc. Smart Cart using either a 250-MHz or a 1000-MHz center frequency antenna.

The chronological sequence of events as they occurred during the Camp Lejeune mobilization is provided below. The grid locations (A1...H1 and A2...H2) are illustrated in Figure 7.

**February 21**: Emplace ordnance in grids A1 and A2.

**February 21-22**: Magnetometer array assembly, testing and full coverage survey over G6 Range.

**February 23-25**: EM-61 towed array assembly, testing and full coverage survey of the G6 Range.

**February 24 – March 10**: EM-63 assembly, testing and discrimination survey of six grids on the G6 Range, as well as cued interrogation of a number of anomalies.

**February 28 – March 28**: Validation of identified targets work progresses, starting from areas that will not be covered by the GPR systems.

**March 6-10**: GPR surveys in a cued interrogation mode using COTS GPR system. Data collected over anomalies picked from full coverage EM and magnetometer surveys.

**March 13-14**: Ohio State University collected data in a cued interrogation mode over a combination of picked and emplaced items using their fully polarimetric GPR system.

**March 13-17**: Witten Technologies GPR CART discrimination mode survey of selected areas. Assembly, testing, and full-coverage GPR surveys of G6 Ranges D and E 50-m by 50-m grids as well as covering some of the emplaced items in the A1 and A2 grids.

**March 20-26**: Applied Research Associates Nemesis Advanced Ordnance Detection System discrimination mode survey of selected areas. Assembly,

testing, and full-coverage GPR surveys of the G6 Range D1, D2, E1, E2 grids as well as covering some of the emplaced items in the A1 and A2 grids.

## 3.1. Camp Lejeune EM and magnetometer surveys

The entire selected portion of the G6 range site, which consisted of 16 grids (50-m by 50-m), was surveyed with the Sky Research, Inc. EM61 towed array and the magnetometer array. Six of the grids were surveyed with a Geonics EM63 mounted on a customized cart. During the EM61 and EM63 surveys, orientation data were recorded using a Crossbow Inertial Motion Unit; no orientation data were collected during the magnetic survey. The line spacing for each of the surveys was nominally 0.5 m. Figures 15, 16, and 17 provide a more detailed view of targets from Grids D1, D2, E1, and E2. The crosses on each of the plans indicate the location of validated targets. Eighteen UXO items were emplaced in Grid D2 prior to surveying with the EM63. The locations of these items are shown as triangles in Figure 17. The targets were not emplaced when the EM61 and magnetometer surveys were conducted; therefore, the locations are not plotted on the plans shown in Figures 15 and 16. The locations flagged for follow-up with GPR sensors were picked based on these magnetometer and EM surveys. Further details on the EM and magnetometer data collected at Camp Lejeune will follow in a separate report.

## 3.2. GPR surveys at Camp Lejeune

One of the main goals of the Camp Lejeune efforts was to evaluate the detection and discrimination potential of ground penetrating radar. Two different modes of surveying were employed:

1. Discrimination mode, where full-coverage data were collected over large areas. Two of the four systems were operated in this mode: (a) Witten Technologies CART imaging system, and (b) Applied Research Associates Nemesis Advanced Ordnance Detection.
2. Cued-interrogation mode, where targets previously identified in EM or magnetics data were flagged and resurveyed with a series of GPR profile passes over the marked area. The Ohio State fully polarimetric system and the commercial, off-the-shelf GPR system were both deployed in this mode.

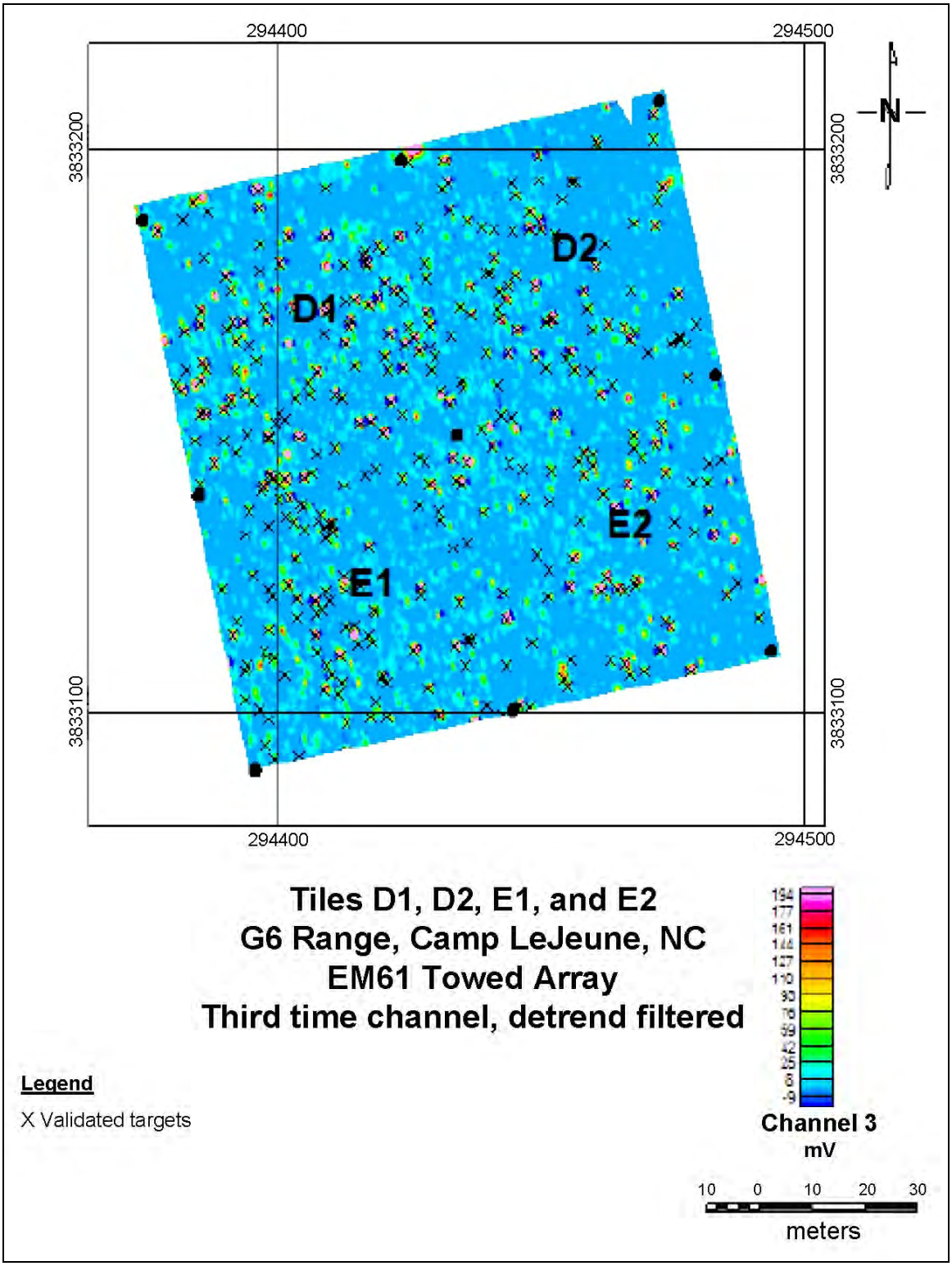


Figure 15. EM61 towed array data from Grids D1, D2, E1, and E2 on the G6 Range, Camp Lejeune, NC. The gridded image shown is the third time channel. The data have been detrend filtered. The black dots are the corners of the grids. The crosses indicate the location of validated targets. There were no emplaced rounds on Grid D2 when this survey was conducted. The text indicates the grid names.

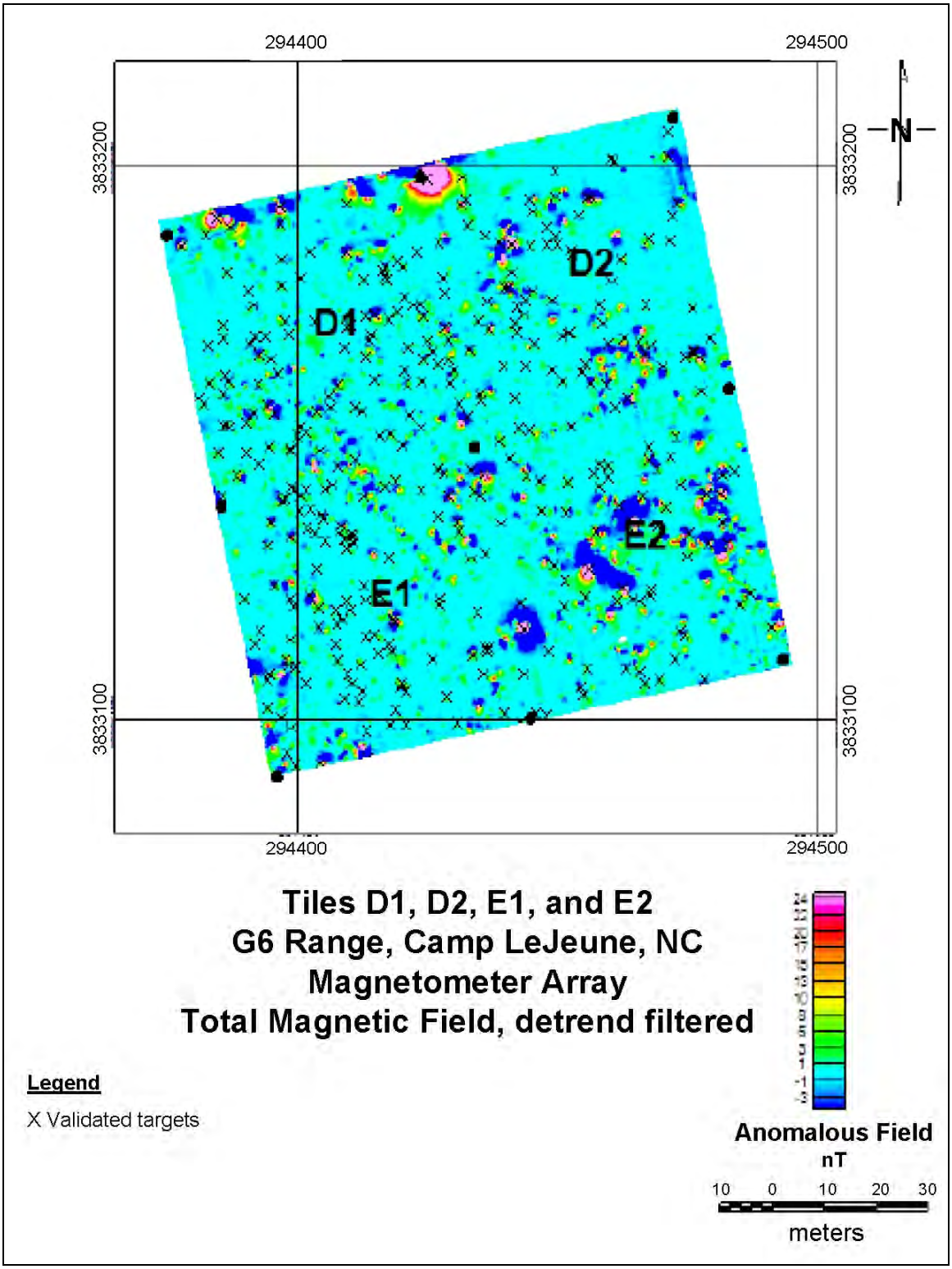


Figure 16. Magnetometer array data from Grids D1, D2, E1 and E2 on the G6 Range, Camp Lejeune, NC. The gridded image shown is the total magnetic field. The data have been detrend filtered. The black dots are the corners of the grids. The crosses indicate the location of validated targets. There were no emplaced rounds on Grid D2 when this survey was conducted. The text indicates the grid names.

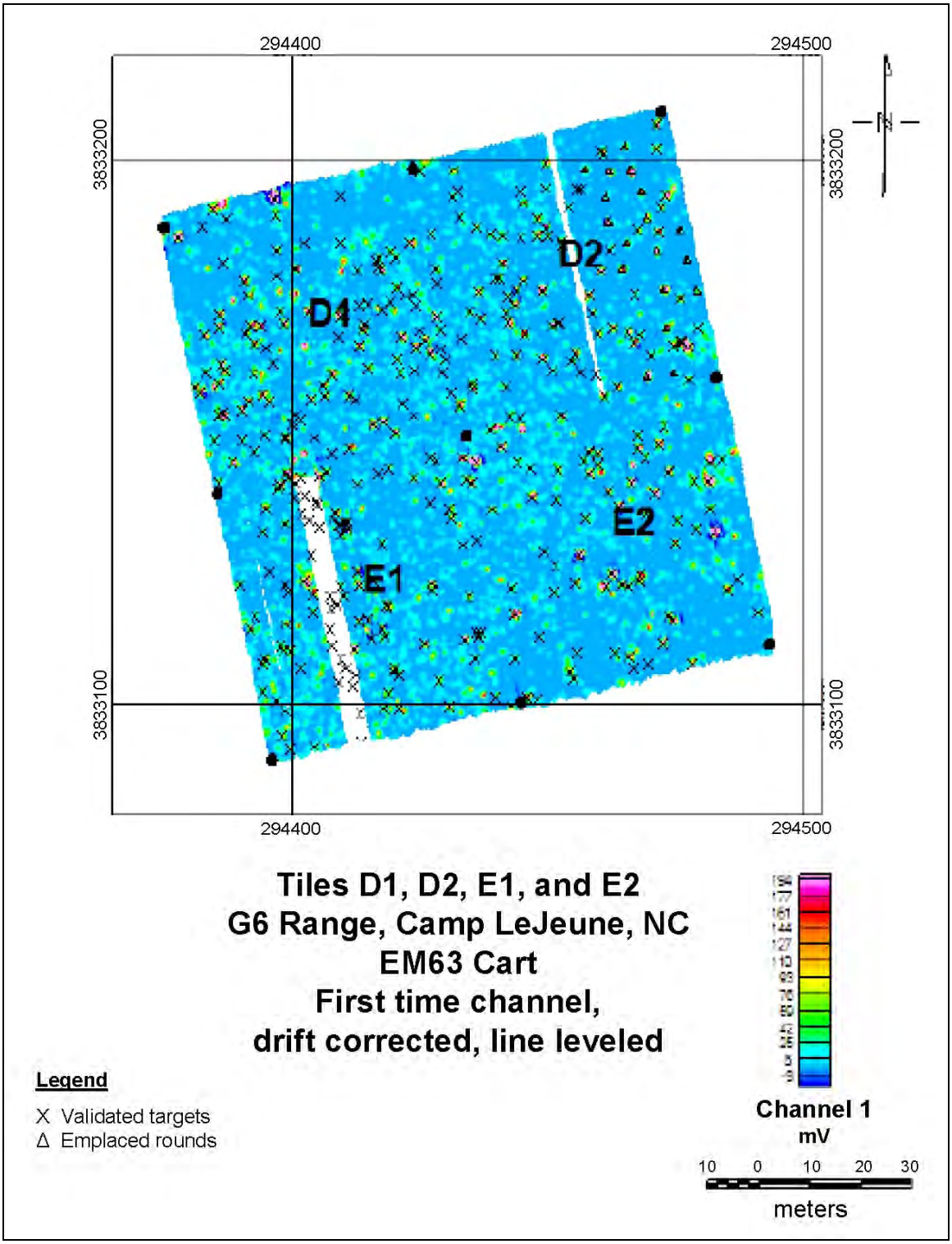


Figure 17. EM63 cart data from Grids D1, D2, E1, and E2 on the G6 Range, Camp Lejeune, NC. The gridded image shown is the first time channel. The data have been drift corrected and line leveled. The black dots are the corners of the grids. The crosses indicate the location of validated targets and the triangles indicate the location of emplaced rounds on Grid D2. The text indicates the grid names.

Summary reports were prepared by the various contractors and are included in this report as appendices. Brief descriptions of the systems deployed at Camp Lejeune follow below. Comprehensive discussions of the respective results are contained in the submitted reports found in the appendices.

***Ohio State University:*** Ohio State University collected data over a series of emplaced and picked targets with a fully polarimetric frequency domain system (Appendix A). This system produced encouraging results, and was able to correctly identify many of the picked targets as non-UXO like. It was more difficult to correctly discriminate small targets (i.e., 40-mm) and larger targets in vertical orientations. The main challenge in extracting features for vertical UXO was the presence of strong subsurface layering and saturated soils, which made it difficult to record scattering patterns indicative of vertical UXO.

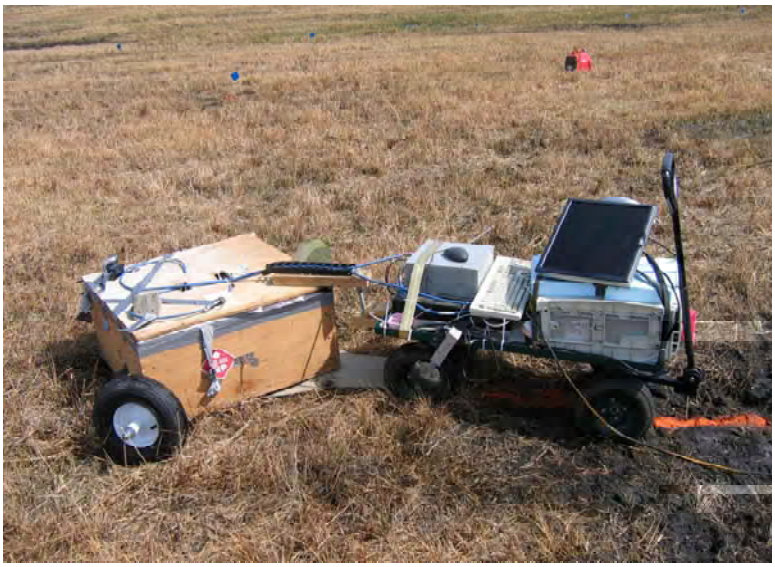

Figure 18. The Ohio State University fully polarimetric GPR system acquiring data at Marine Corps Base Camp Lejeune.

***Applied Research Associates (ARA)***: The ARA system was able to collect data over larger areas (Appendix C). Large amounts of data are generated in this type of surveying. Approximately 11 Gb of data were acquired over the A, D, and E grids. Nearly complete coverage of the E1 and E2 grids was accomplished using east-west trending passes. Selective coverage and encounter data were collected on the D1 and D2 grids. Multiple passes were made over the emplaced targets in the D1 grid. Initial results were provided for emplaced targets with known locations and

Figure 19. Applied Research Associates Nemesis Advanced Ordnance Detection System surveying at Camp Lejeune.

orientations. The GPSAR system operates at 0.4-4 GHz with a 2-m swath of coverage obtainable. This system made use of higher frequencies than any of the other systems and as a result, was able to image some of the smaller targets better. Part of the tradeoff with the use of those high frequencies was the shallower penetration depths of the GPR signals. Wet ground conditions and a strong ground reflection meant that it was difficult for ARA to image targets deeper than 35 centimeters (cm). The ARA Nemesis system also includes EMI sensors, which can be used to incorporate additional information in the interpretation process.

***Witten Technologies***: The Witten CART system collected data over larger areas of both emplaced UXO and pre-existing targets (Appendix B). The Witten system is also array-based, but unlike the Nemesis, its antennas operate in a time domain mode at a center frequency of 400 MHz. The sensor technology is similar to the Noggin Smart Cart deployed in a cued interrogation approach, but with a capacity to collect much larger volumes of data. The 16-channel radar array system covered a total of 13,360 $m^2$ (3.3 acres) during 5 days of surveying. Each data pass covers a swath about 123.75 cm wide with 16 channels spaced 8.25 cm apart. The lower frequency translated into a greater penetration but also meant that detection of the smallest targets was not likely. Data were collected on the D and E grids as well as over some of the emplaced items in the A grids (see Figure 5). On the D2 grid, an orthogonal set of lines was also collected to investigate whether or not that additional information would be beneficial in the processing of data.

Figure 20. Witten Technologies 400-MHz, 16-channel radar array system ready to begin collecting data at Camp Lejeune.

***Noggin Smart Cart***: Additional processing of commercial GPR data acquired over some of the validation targets and all of the emplaced items was completed by Sky Research personnel to act as a baseline of what is currently attainable via a commercial, off-the-shelf GPR system and to gauge the additional capabilities that more advanced GPR systems can provide. A discussion of the COTS GPR results follows in the next section and individual target responses are included in Appendix D.

# 4 Sky Research GPR Data Acquisition and Results Obtained with COTS GPR System

With two array-based systems for complete coverage of large areas (Witten and ARA), and a state-of-the-art cued interrogation system (OSU), Sky Research personnel focused on collection of cued-interrogation data with a commercial off-the-shelf system. The system chosen was Sensors and Software Inc.'s Noggin Smart Cart. It is a single-channel system with interchangeable antennas. Both 250-MHz and 1000-MHz data were collected at the Camp Lejeune site. The COTS GPR system is shown in Figure 21 with the 250-MHz antenna attached. The system contains both antenna elements and associated electronic components sealed in a single unit so the antenna separation and orientation are fixed. The cart-based system was chosen for its ability to quickly collect data in a robust manner. Fixed antenna separation meant that CMP surveys would not be possible, but the known depths to emplaced items could be used to estimate velocities.

Figure 21. Emplaced items and targets picked from EM surveys were marked with flags and a series of four GPR profiles were acquired over each target.

The GPR work at Camp Lejeune involved two different modes of operation. In the first method of operation, complete coverage over an area was sought. An alternate mode of operation for GPR acquisition was also considered, that of a cued interrogation approach. In this scenario, targets of concern are initially identified based on EMI and magnetics surveys. GPR data are then acquired in a controlled manner over a smaller region around the flagged area to further investigate the target of concern. In particular, GPR can be used to better determine the depth to the target in question and to differentiate closely spaced multiple targets that may cause a single, combined response in the EMI and magnetics data. Both the GPR data acquired by Sky Research personnel with the COTS GPR system and the data collected by Ohio State University's fully polarimetric GPR system utilized the cued interrogation approach.

## 4.1. Discussion of survey methods chosen

Two different approaches considered for the cued interrogation approach using the COTS GPR system are illustrated in Figure 22. The first case (a) used a series of four survey lines over each target. This approach represented a compromise between minimizing time over target and acquiring adequate target information. Each line passed directly over the flag marking the target location. The first line was oriented such that it ran approximately south to north. The second line was shifted by 45 deg counterclockwise and ran southwest to northeast. Another 45-deg counterclockwise shift meant that the third survey line ran from west to east. Finally, the fourth survey line ran in a northwest to southeast direction.

Figure 22. Different types of data acquisition in the cued interrogation mode. In the image on the left, (a) four survey lines were collected over each emplaced item. On the right, (b) a tightly spaced grid of survey lines was acquired.

The second approach, case (b), used a series of closely spaced orthogonal survey lines in a grid pattern over the target. The grid involves a larger volume of data acquisition per target but this additional information allows the generation of 3D volume images, which often makes interpretation and visualization of the data more intuitive. While the extra data acquired by collecting a grid of data over the target certainly aids in the interpretation process, it is significantly more time-consuming and involves substantially more processing.

For case (a), the series of four passes over each emplaced target are contained in their entirety in Appendix D. Each target is summarized as a single-page report. A photo of the target in question is accompanied by a table describing detailed position and orientation information recorded at the time of burial. A sample is shown in Figure 23 for one of the emplaced items, a 90-mm projectile.

| | |
|---|---|
| Target Name | G6A1E7 |
| Item Description | 90-mm projectile (blue AP) |
| Depth (cm) | 30 |
| Dip | 90 |
| Azimuth | n/a |
| Easting (m) | 294364.0337 |
| Northing (m) | 3833302.94 |

Figure 23. A photo of the target and a summary table are among the information compiled for each emplaced item.

The photo and summary table are followed by three different visualizations of the four survey lines collected over the emplaced item. In Figure 24, the GPR sections themselves are displayed. In the images shown, a dewow filter was applied to remove ground- and antenna-induced low-frequency transients from the raw data. A background subtraction process was also applied to remove flat-lying events such as the direct air and ground waves. Finally, spherical and exponential (SEC) gain was applied to the data in order to compensate for the attenuation of the GPR signal with depth and to present the clearest possible image for interpretation.

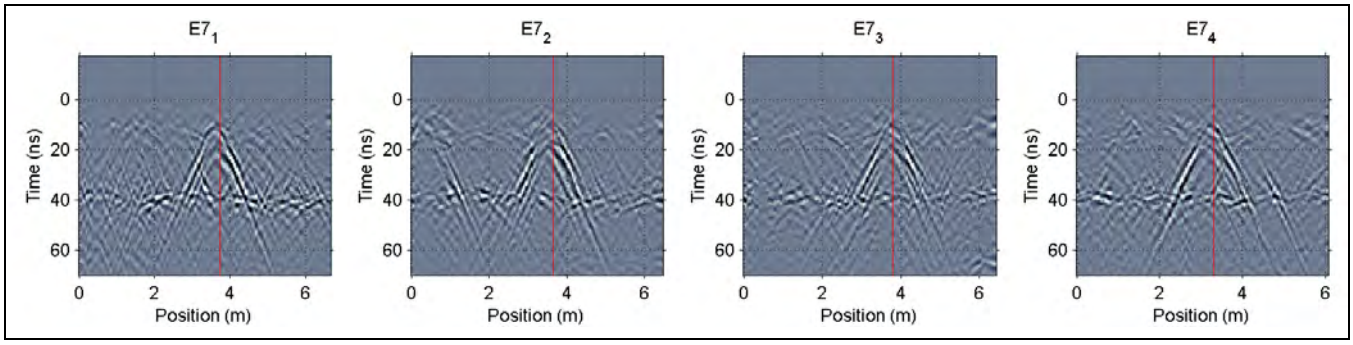


Figure 24. GPR profiles collected on four passes over the target indicated in Figure 23. Dewow filter, background subtraction, and an SEC gain were applied to produce the images displayed.

The vertical red line indicates a fiducial that was placed into the data stream when the sensor was directly over the flag previously placed in the ground to indicate the target position. In some cases a fiducial was accidentally not entered during data acquisition. In those cases, there will be no vertical red line.

The hyperbolic tails evident in Figure 24 characterize the typical target response. In general, localized targets generate scattering hyperbola as a consequence of the path length changing as the target is approached, then passed by the sensor. In order to concentrate the scattered energy into a localized area more representative of the target source, a migration process is applied. The migration used is a Kirchoff-style migration that assumes far-field wave propagation. For the shallowest targets, objects are within a fraction of a wavelength from the source. Despite this limitation, the migration routines work well back-projecting the scattered energy to the source position. Interpretation is also made more intuitive by considering the envelope of the oscillatory GPR signal. The GPR sections of Figure 24 are displayed after the data were migrated and enveloped via a Hilbert transform in Figure 25. No additional gain function was applied to the data. The data are left in an ungained state in order to compare average amplitudes for a range of target types, depths, and orientations. The vertical red line still marks the fiducial location entered directly over the target flag. The horizontal white lines indicate the region over which average amplitude versus position plots will be generated. The range considered is chosen to be the same for each plot, 10 ns in length. The particular starting and ending times for the window do, however, vary depending on the observed target response and are selected based on the section views of Figure 24 and migrated-enveloped section views of Figure 25.

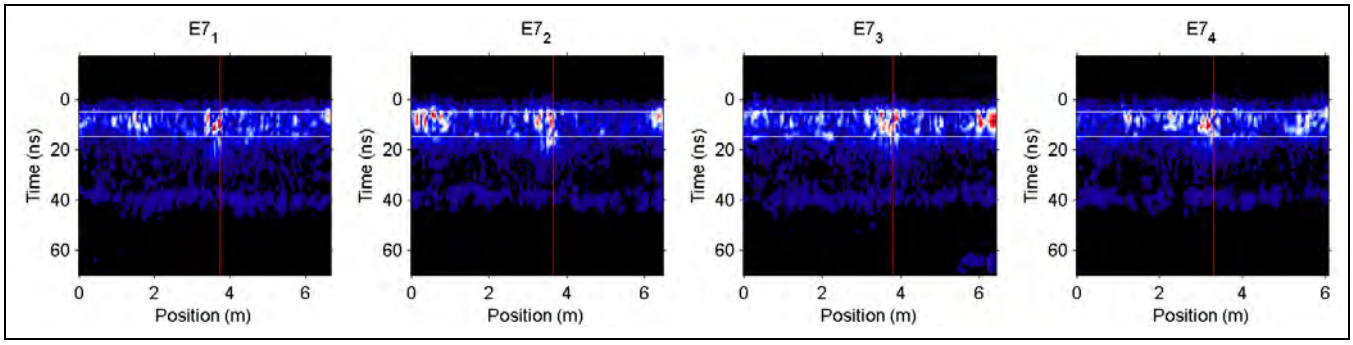


Figure 25. GPR profiles collected on four passes over the target indicated in Figure 23. Migration (v = 0.06 m/ns) and enveloping have been applied to the data of Figure 24, to which a dewow filter and background subtraction were previously applied.

It is often difficult to gauge the relative amplitudes from one GPR section to the next simply from the views displayed in Figures 24 and 25. Displaying the average amplitudes over a user-specified time window provides a more intuitive indication of where the strongest responses within a section occur. The time window chosen was always 10 ns in duration but the starting and ending points varied, depending on the target response observed in the profile images. The range to be covered by the time window was chosen based on the section views and the top of the observed target response. This display is also useful for comparing amplitudes from the four different passes over each emplaced item. Comparisons can also be made between relative amplitudes observed for unique targets or identical targets at different locations, orientations, and depths. An example of the average amplitude versus position plots is shown in Figure 26.

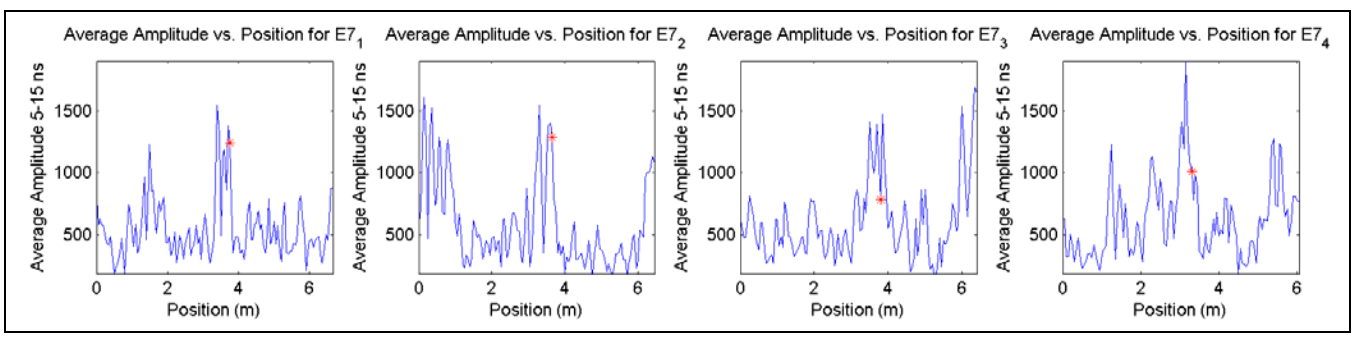


Figure 26. Average amplitude versus position for the time window indicated by the horizontal white lines in Figure 25.

Similar collections of photos, data plots, and emplacement details can be found for each of the emplaced targets in Appendix A.

## 4.2. Emplaced items

The first targets considered are the emplaced items. Because the exact range of targets that would be encountered at the Camp Lejeune site was uncertain, the decision was made to emplace a number of known items at the site. This set included a standard set of targets provided by Aberdeen Test Center, as well as some larger items recovered during work at a site in Montana. Fortunately, an adjacent range was undergoing active clearance simultaneously and a number of targets from the adjacent range were also buried in the site to be surveyed. A number of non-metallic clutter items (polystyrene foam, wood) were also emplaced on the survey site. These emplaced items would assist in the calibration of the instruments and provide targets where the position and orientation are known with a high degree of certainty. A range in the size of emplaced targets also allows for an understanding of those targets that produce distinct responses, which are not resolvable. Placing identical targets at differing depths and orientations allows the relative importance of those two factors to be considered. The emplaced items were buried at randomly chosen locations in the A and D grids. The intended location was first cleared by an EOD technician using a hand-held EMI detector. A hole of appropriate depth was then dug by the EOD technician. Consequently, there is evidence of disturbed soil in some of the GPR responses over the emplaced items. Directional drilling of emplaced items may have avoided some of the soil responses immediately above the emplaced targets; however, the presence of substantial water at Camp Lejeune during the time of emplacement meant access and burial were more efficient without heavy machinery.

### 4.2.1. Data collected over emplaced items

From the simple collection of four lines over individual emplaced items, some unique target characteristics can be obtained. Consider, for example, the two 90-mm projectiles, G6A1_E7 and G6A1_E8. The identical targets are located within 10 m of each other. The first target (G6A1_E7) was buried in a vertical orientation at a depth of 30 cm while the second target (G6A1_E8) was placed twice as deep at 60 cm and a dip of 45 degrees. In both cases, distinct responses are observed for each target as evidenced in Figure 27. A vertical orientation is usually more challenging because of the small cross-sectional area as the GPR sensor passes over the target. In the case of G6A1_E7 (vertical), a strong hyperbolic response is clear in the data. Even in the vertical orientation, the target is substantial enough and shallow enough that it is detected by the approaching and passing sensor

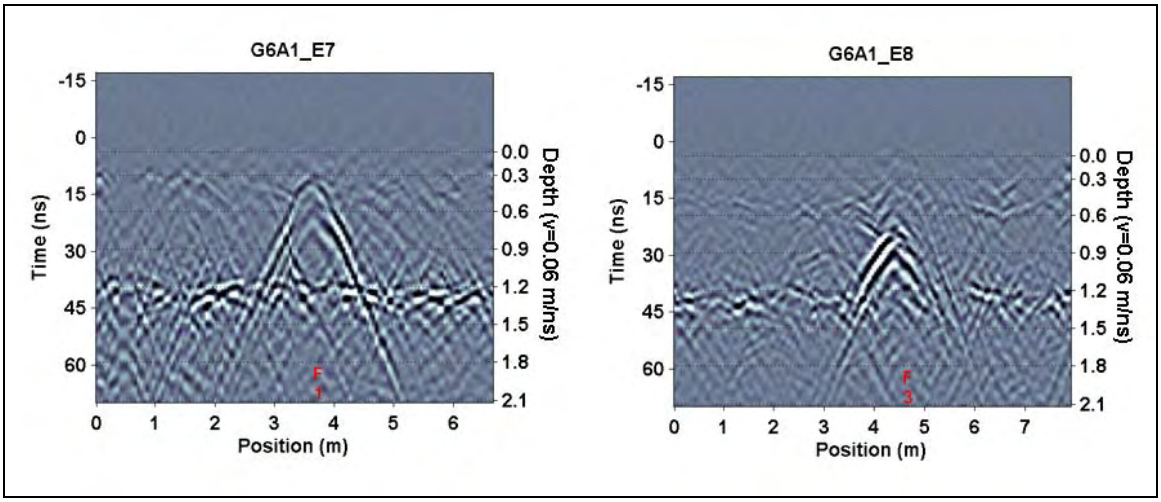


Figure 27. GPR profiles collected at 250 MHz over a 90-mm projectile buried in a vertical orientation at the 30-cm depth (on the left) and a 90-mm projectile with a dip of 45 degrees at a depth of 60 cm (on the right). Dewow filter, background subtraction and SEC gain applied.

and the varying path length of the moving sensor creates the hyperbolic response. The depth to the target as noted by the peak of the hyperbolic response is approximately 30 cm, agreeing well with the emplacement depth recorded. The target response for G6A1_E8 (45 degrees) appears deeper in Figure 27. The hyperbolic response is not as symmetric as for G6A1_E7, possibly an indication of the 45-degree dip of the target. The peak of the target response is at a greater depth than the vertical target and occurs at approximately 68 cm. The target depth inferred from the GPR response for G6A1_E8 is 8 cm deeper than the recorded emplacement depth, perhaps a result of ground settling after burial or a profile path slightly off the target center or the presence of water affecting the assumed wave speed velocity. The main point to be emphasized from Figure 27 is that GPR can be used to gain accurate information regarding the relative depths of targets and that this depth information can be valuable to the inversion of other geophysical data.

Both of the plots in Figure 27 are displayed using a gain function that compensated for attenuation losses as the GPR signal penetrates through the host soil. Gain functions were chosen to optimize the display of the image and assist in the interpretation of the profiles. Comparing the average amplitudes over a 10-ns window that encapsulates the target response is also informative. Because the targets are identical, the ungained average amplitudes of the deeper target would be expected to be significantly less as the GPR signal is attenuated more severely. The average amplitudes are weaker from the deeper target; however, the

response for the deeper target is actually a more distinct anomaly in the average amplitude plots of Figure 28. The shallower target still produces a distinct peak; however, the stronger signal at shallow depths also exhibits higher background values than the deeper target. The vertical orientation of the shallow target contributes to lowering the average amplitude of the target response, as identical targets at different orientations (see for example G6A2_E19 in Appendix A) at the same depth produced significantly higher average amplitude values.

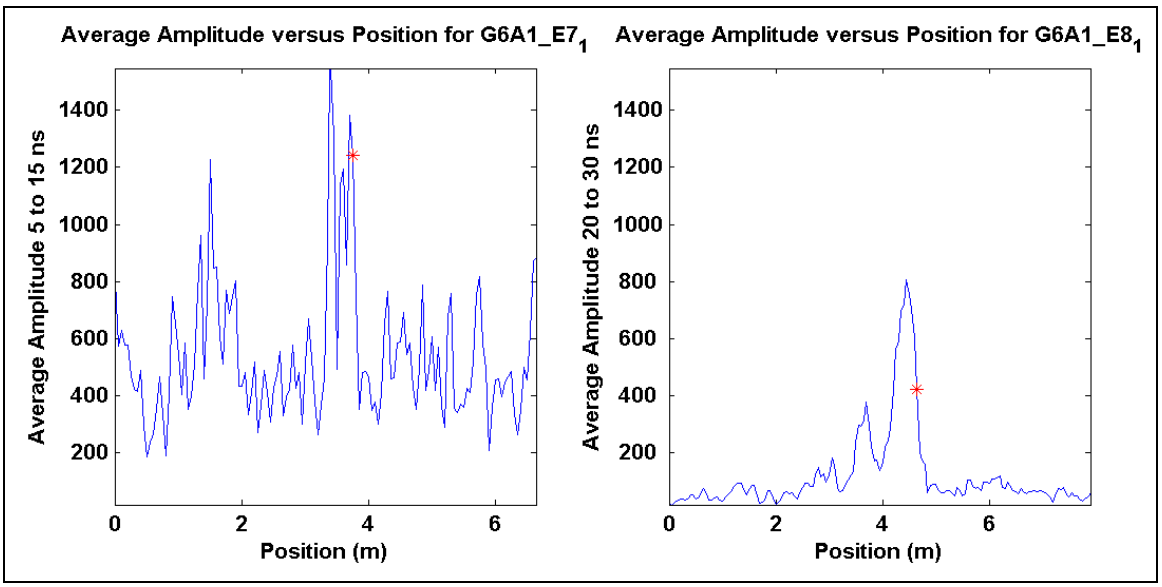


Figure 28. Average amplitude profiles for 10-ns time windows for the shallow (on left) and deep (on the right) 90-mm targets shown in section views of Figure 27. Dewow filter, background subtraction, migration (v = 0.06 m/ns), and enveloping were applied to the data prior to the calculation of the average amplitudes.

Beyond extracting depth information for targets, COTS GPR could also prove useful for cases of closely spaced targets, in particular determining when multiple targets are present that may be contributing to a combined EMI or magnetics response. Consider the EM and magnetometer data illustrated in Figure 29. The EM61 towed array data contains what appears to be two distinct target responses; however, the EM63 cart data and the magnetometer array data do not contain similar responses from distinct multiple targets. Incorporating information available from the GPR data acquired over the same target shown in Figure 29, confirmation of a second target is possible. Not only does the GPR information indicate the presence of a second target, it also illustrates that the second target is shallower than the primary target (G6A1_E19). It is possible that the second target was not evident in the EM63 cart data because the larger (1 m by 1 m) EM63 coil covered both targets simultaneously and recorded

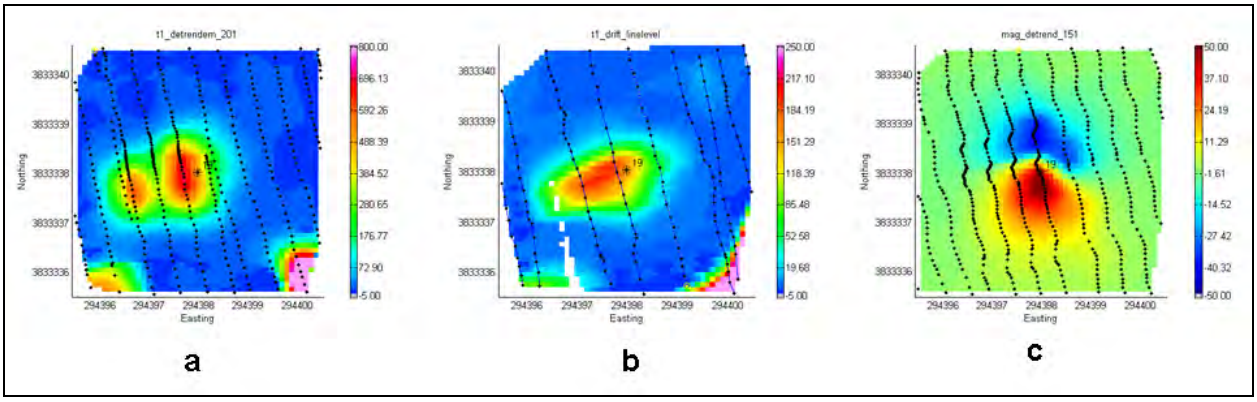


Figure 29. Data collected over target G6A1_E19 with (a) EM61 towed array, (b) EM63 cart, and (c) magnetometer array. Two targets appear possible in the EM61 towed array data, yet the data collected with the EM63 cart and the magnetometer array do not conclusively identify multiple targets.

a combined response while the EM61 array's smaller coils (0.5 m by 1 m) resulted in separate coils covering the two targets uniquely. It is also suspected that two targets were not obvious in the magnetometer array data because the second target was an Armor Piercing Discarding Sabot (APDS) adapter, which has a relatively weak magnetic signature. The presence of multiple targets and the respective depths to those targets extracted from COTS GPP data can be used as constraints in the inversion of EM data.

To further emphasize the importance of target orientation, consider two 90-mm targets, both buried at the same depth of 30 cm, but one placed in a horizontal orientation and the other a vertical orientation. Of the four passes collected over each target, the strongest response observed is displayed in Figure 30 for both horizontal and vertical 90-mm targets. On the left of Figure 30, the horizontal target creates a strong hyperbolic response centered at approximately 3 m along the position axis (a shallower, non-emplaced item is also evident in the data). A hyperbolic response is observed in the section view of the vertical target on the right in Figure 30 although not as prominent or as obvious at that observed for the horizontal case. The average amplitude plots of Figure 31 provide further indications that the vertical target orientation produces a weaker response in the GPR data. The same time window of 10 to 20 ns was applied to both data sections and the amplitudes for the vertical target are nearly five times less than those recorded for the horizontal target. This emphasizes one of the challenges in the application of GPR extending beyond known emplaced items to picked targets. Clearly the orientation of the picked targets will not be known. Some of the targets will be oriented such that they produce strong obvious returns in the GPR data, while others may be more subtle,

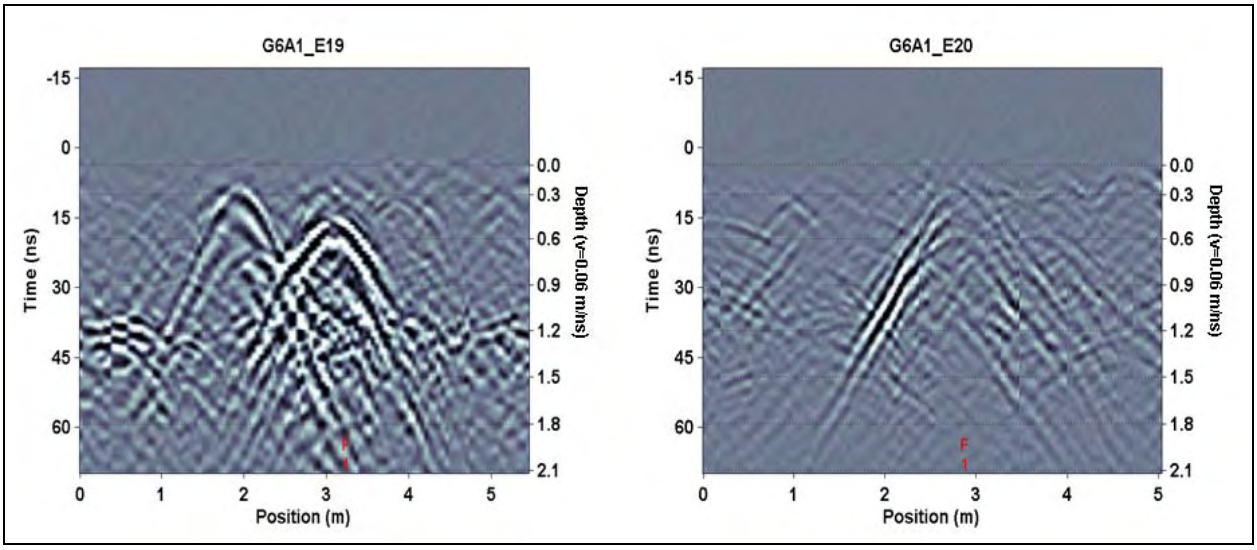


Figure 30. GPR profiles collected at 250 MHz over a 90-mm projectile buried at a 30-cm depth in a horizontal orientation (on the left) and a vertical orientation (on the right). Dewow filter, background subtraction, and SEC gain were applied to the data.

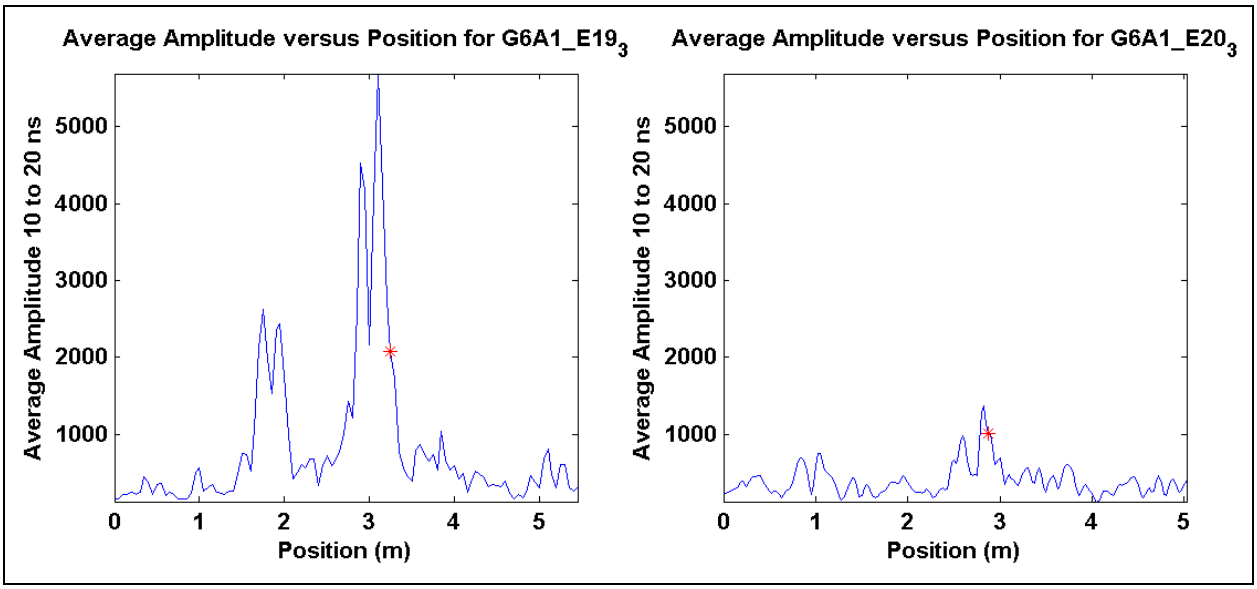


Figure 31. Average amplitude profiles over the 10- to 20-ns time windows for the horizontal and vertical 90-mm targets shown in section view in Figure 30. Dewow filter, background subtraction, migration (v = 0.06 m/ns), and enveloping were applied to the data prior to the calculation of the average amplitudes.

and in some cases, not detectable at all. This is yet another reason to consider GPR a confirmation tool that is most effectively used in conjunction with other sensors (EMI, magnetics) to extract the maximum amount of information concerning a target.

### 4.2.2. Types of items detectable with 250-MHz antenna

This decision to use the 250-MHz COTS GPR system was based, in part, on earlier work at the Ashland Test Plot, which found that the lower frequencies performed better. Earlier surveys, both as part of the initial site visit as well as the site characterization, indicated that the 250-MHz system would provide excellent penetration and still provide detectable target responses. The soils at Camp Lejeune were more conducive to GPR work than other sites. A small amount of data was also collected using a 1000-MHz antenna to investigate if the use of a higher frequency would allow more detailed information on targets to be extracted. For many of the smaller emplaced items, the wavelengths of the 250-MHz GPR signal are greater than the dimensions of the intended targets and consequently will produce low-resolution images. Resolution should not be confused with detection capability, as detectable responses can often be obtained from thin layers or small targets even though the critical dimensions of these same targets are not resolvable. Indications of important target details such as depth, possibly orientation, and the presence of closely spaced multiple targets may be inferred. Figure 32 shows three targets, all of which produce detectable responses from which, at a minimum, a depth estimate can be extracted.

### 4.2.3. High-frequency (1000-MHz) data

The majority of the data were collected using a 250-MHz antenna on the cart system as shown in Figure 21. Because the Camp Lejeune soils were relatively favorable for GPR penetration, data were also collected using a 1000-MHz antenna. The 1000-MHz data were primarily collected in the similar four profile lines per target as the 250-MHz data discussed earlier. A few tightly spaced grids (as shown in Figure 22) were also collected with the 1000-MHz antenna and will be discussed later. Most of these data were collected over the smaller sized emplaced items (G6A1_E13-G6A1_E18), as these smaller targets would be most likely to benefit from the increased resolution available at the higher frequencies. These same targets also tended to be buried shallow, which is advantageous due to the increased signal attenuation at the higher frequencies (the attenuation was particularly marked in those parts of the site that were saturated with water for the duration of the survey).

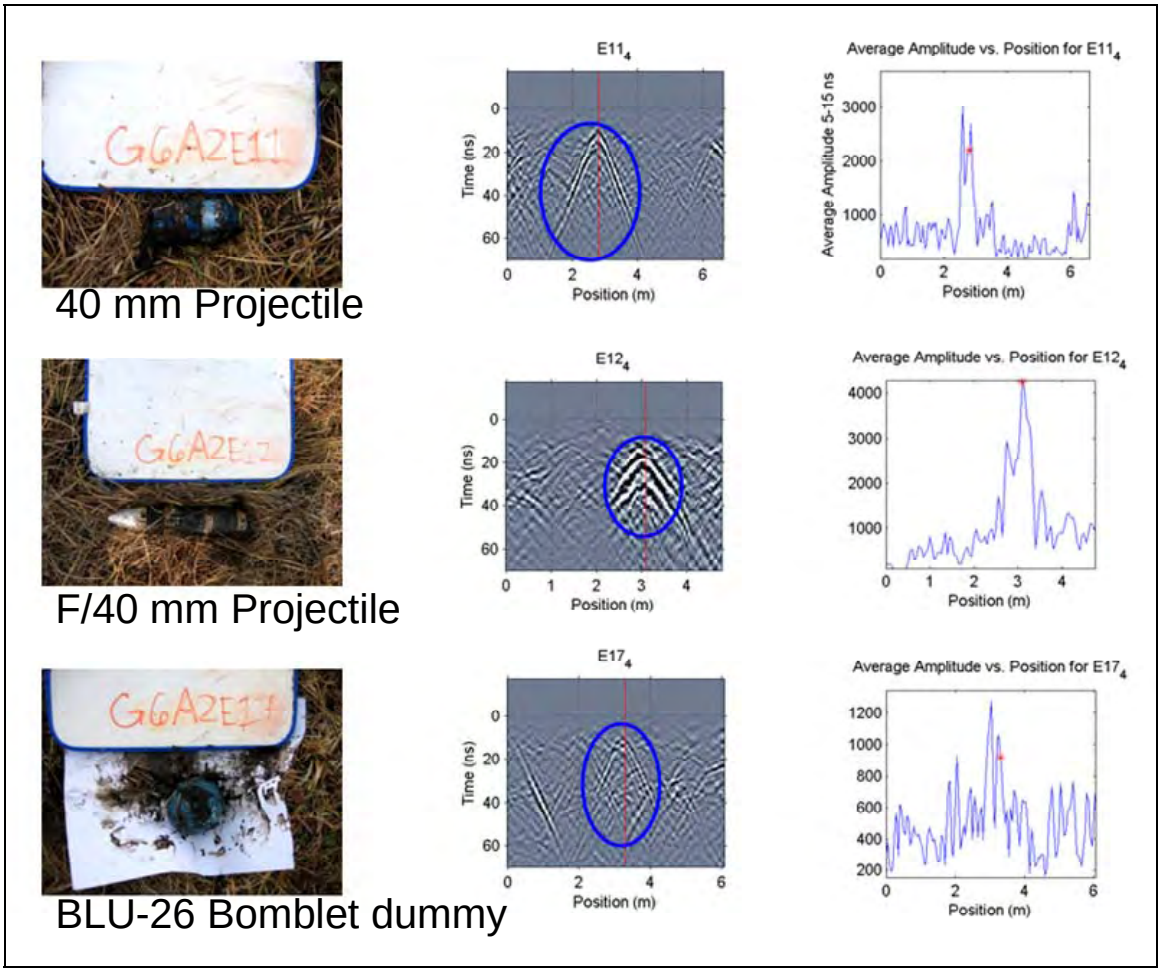


Figure 32. Small items produce detectable responses in the GPR data even though the resolution is not sufficient to perform target discrimination.

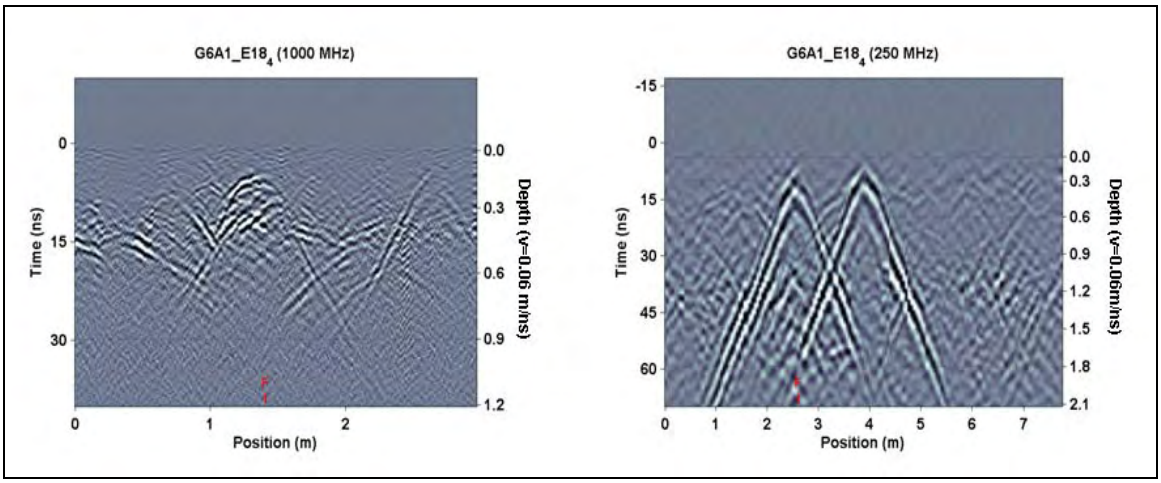


Figure 33. GPR profiles collected at 1000 MHz (on left) and 250 MHz (on right) collected over one of the smaller emplaced items, a Bomblet Dummy BDU-28/B buried at 15-cm depth in a horizontal orientation (note the different horizontal scales). Dewow filter, background subtraction, and SEC gain were applied to the data.

The small emplaced target that produced the strongest response in both the 250-MHz data and the 1000-MHz data was the Bomblet Dummy BDU-28/B. It produced strong, detectable responses on all four passes over the target at 250 MHz (one of the passes is shown in Figure 33). Although the responses were much weaker at 1000 MHz, the target was also detectable on all four passes at the higher frequency as well (Figure 33). The 250-MHz data show a strong hyperbolic response centered at approximately 2.5 m that corresponds with the emplaced item. There is an additional hyperbolic response about 1.5 m away, centered at approximately 4 m, that indicates a second in situ target at approximately the same depth. The second target was not excavated, but a likely candidate is an Armor Piercing Discarding Sabot (APDS) adapter, one of the most prevalent items at the site and often found at a similar depth. The 1000-MHz target response in Figure 33 is not as obvious. The signal attenuates more rapidly at higher frequencies and below 30 ns, the tails of the hyberbola are barely evident. Average amplitude plots of Figure 34 still indicate a strong single peak in the 1000-MHz data but the amplitudes are approximately six times less than the peak amplitude recorded using the 250-MHz antenna. Smaller scale scattering features are also more prevalent in the data at the higher frequency. The Bomblet Dummy BDU-28/B target is still detectable in the 1000-MHz data, as is the left-most tail of the second in situ target,

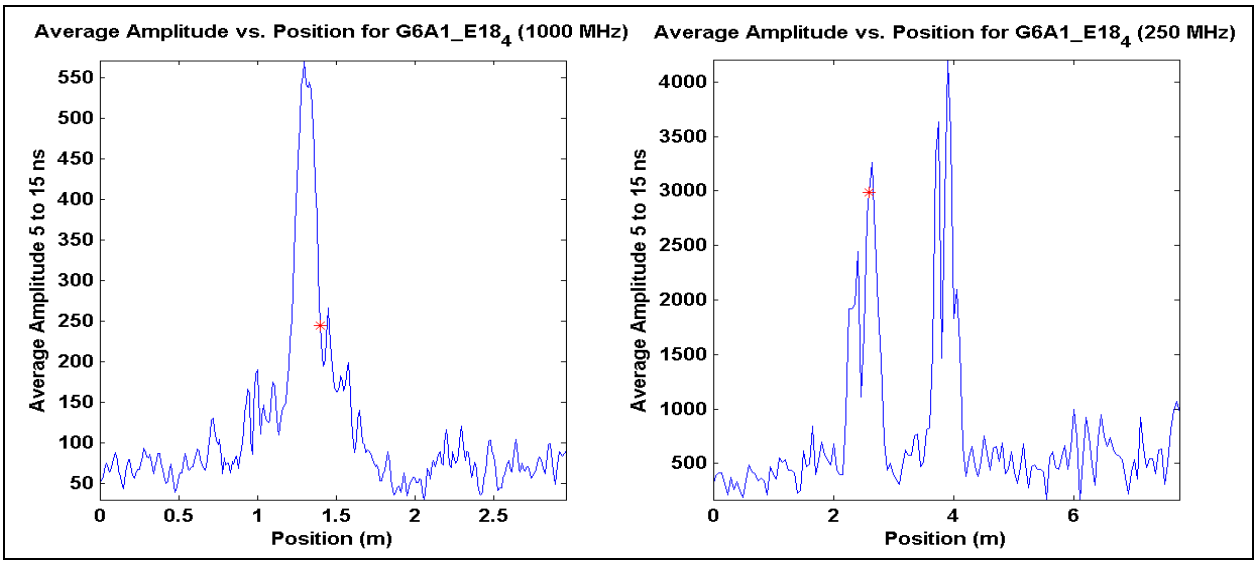


Figure 34. Average amplitude profiles for 5- to 10-ns time window for both 1000-MHz (on left) and 250-MHz (on right) sections collected over the Bomblet Dummy BDU-28/B. Dewow filter, background subtraction, migration (v = 0.06 m/ns), and enveloping were applied to the data prior to calculating the average amplitudes.

but the 250-MHz data result in a more definitive and interpretable image especially when noting that the extra resolution gained by using the higher frequency does not provide sufficient information for target discrimination.

The second approach considered for cued interrogation was the collection of a series of closely spaced orthogonal survey lines over a flagged area of interest as indicated in Figure 22. Two sets of 12 orthogonal survey lines were collected over the emplaced item G6A2_E21, a 90-mm projectile buried at a 60-cm depth with a dip of 45 degrees. The collection of this grid of denser data allows data volumes to be created. It is often helpful for interpretation to display a volume of data containing targets rather than a cross-sectional view of a single profile line. Target features that are large enough to span multiple lines in cross-sectional view will generate regions of high amplitudes in the volume plots. Once the volume has been generated, a variety of options are available for displaying the data. For example, Figure 35 shows a horizontal slice for a depth of 60 cm and an intersecting vertical slice that intersects the depth slice at the X position of 80 cm. The target location is clearly evident on both the vertical and horizontal slices. Generated images can be rotated in three dimensions to view the target from different angles. It is also possible to display the complete cube of data with a region cut out of that volume to expose the target. This type of display shows more of the surrounding volume than the slice view and can be useful for determining how the amplitude of the target compares with the rest of the volume. The same data set displayed as a series of slices in Figure 35 is shown as a volume cutout in Figure 36.

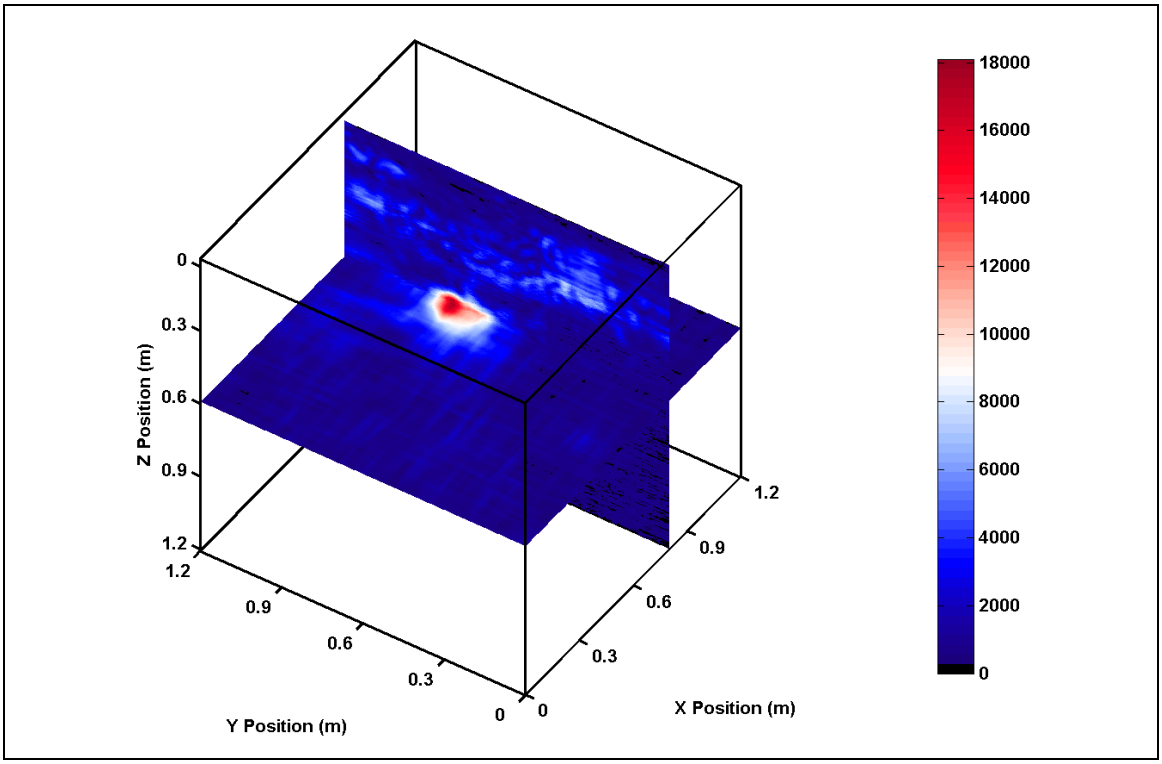


Figure 35. Data volume for target G6A2_E21 with a horizontal slice at a depth of 60 cm and a vertical slice for X Position of 80 cm. The high-amplitude area indicates the location of the 90-mm target.

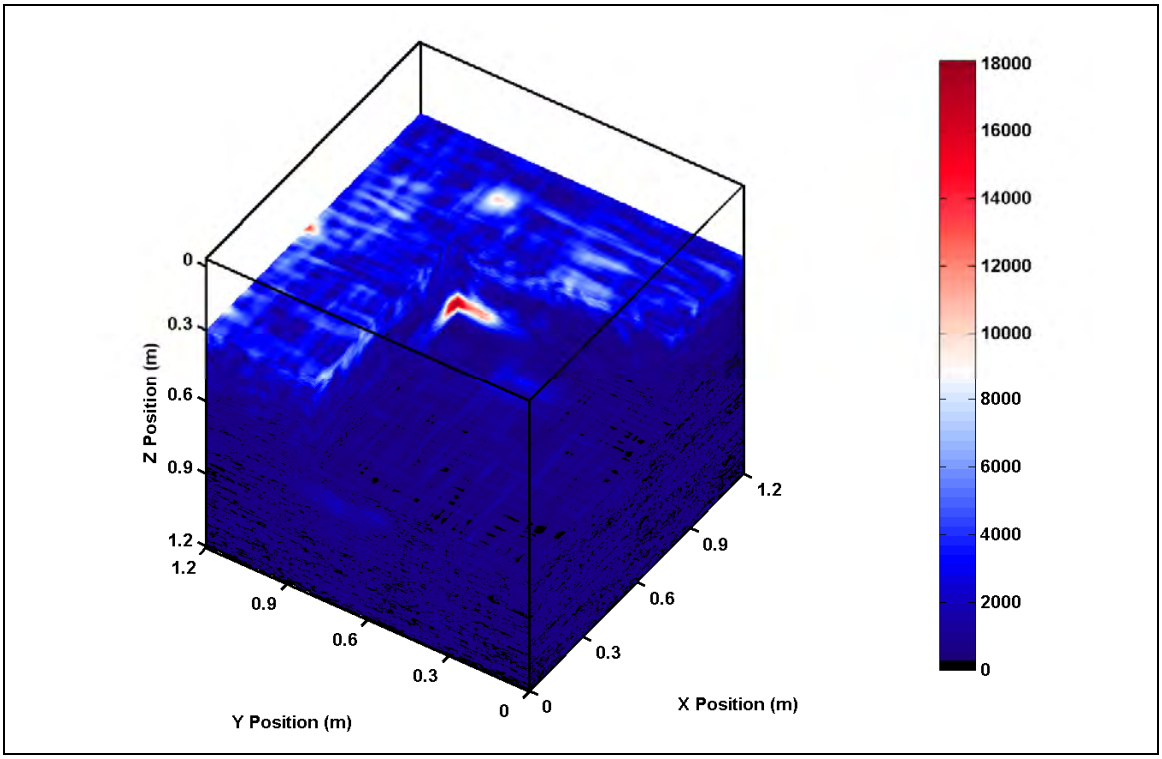


Figure 36 Data volume for target G6A2_E21 with a region cut out to reveal the target. The high-amplitude area indicates the location of the 90-mm target.

Sometimes it is useful to display only the higher amplitude values in the data volume; this is accomplished by plotting isosurfaces of the data volume. It is also possible to create animations of the volume, either slicing through in any of the three dimensions, rotating the cube about one of its axes, or fading into successively higher amplitude isosurfaces of the volume. While it is not possible to display an animation in this document, a series of frames from an animation are shown in Figure 37. In the animation shown, isosurfaces of progressively higher amplitude thresholds are displayed so that the strongest responses within a volume of data are gradually displayed as the weaker amplitudes are eliminated.

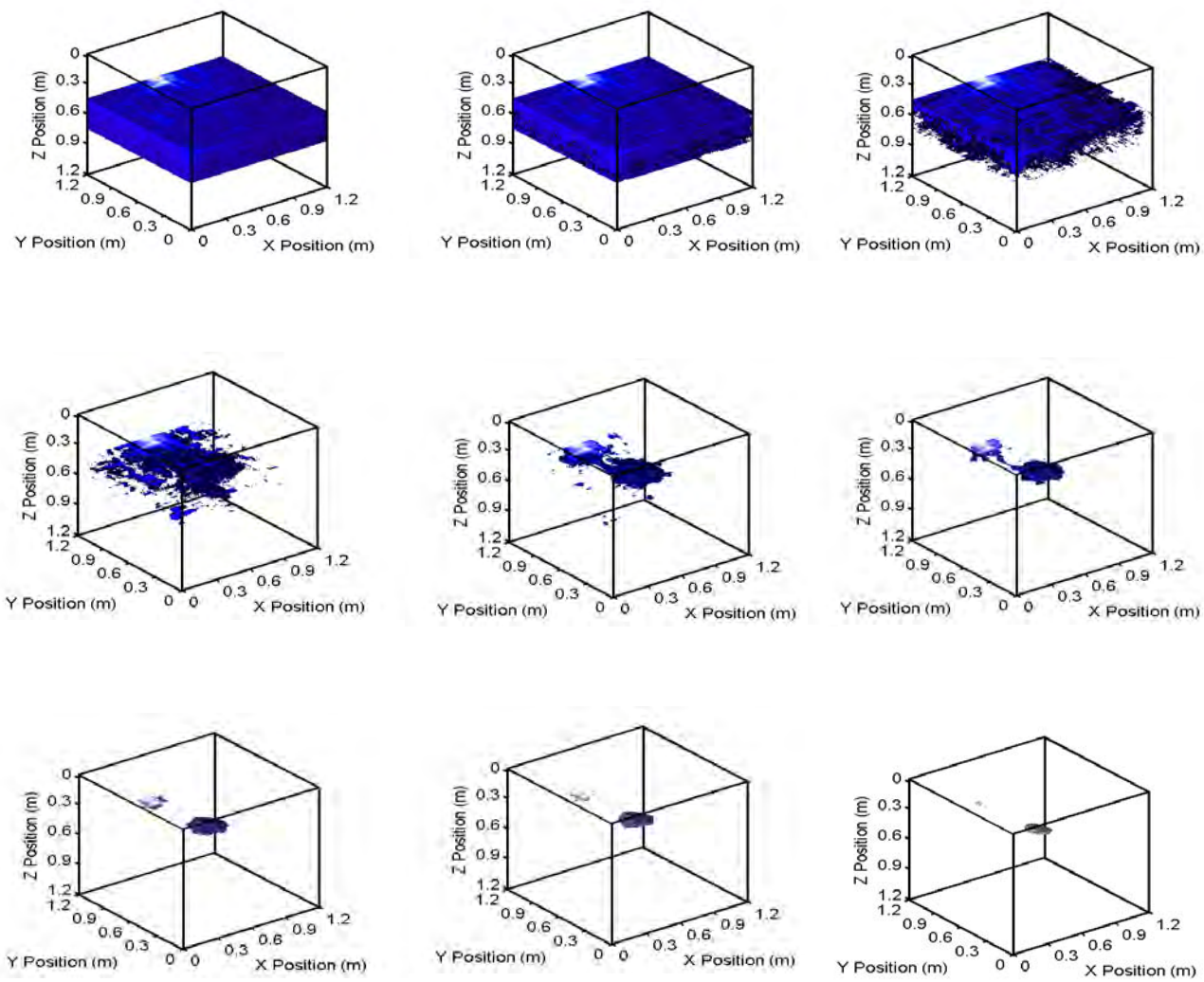


Figure 37. Individual frames from an animation of the 90-mm projectile, G6A2_E21. In this sequence of frames, lower amplitudes are progressively removed from the display to fade into an image that contains the highest amplitudes only on display.

### 4.2.4. Picked targets

The results obtained from the emplaced items provided a basis for understanding GPR performance at the Camp Lejeune site. Collecting data over targets where the respective locations and orientations were accurately known allowed an understanding of the site-specific target and clutter responses as well as providing an indication of the background response due to the local soil.

Focusing on the picked targets, the orientations and locations of the targets were no longer known. The picks were based on full coverage surveys using the Sky Research, Inc. towed array of EM61 sensors and EM 63 data acquired over specified 50-m by 50-m grid cells. A survey procedure similar to that utilized for the emplaced items was applied to the picked targets. Locations for the picked anomalies warranting further investigation were selected using a Trimble real-time kinematic (RTK) GPS system and a flag placed in the ground at the appropriate location.

Unlike the emplaced items, where an object was buried and a flag was placed directly on top of that target, there were some uncertainties with the positions of the picked targets as represented by the flags. The target positions were picked based on EMI towed array data. The uneven ground surface and the moving platform will both contribute to small errors in positioning (generally the item was within 30 cm of the interpreted location). Smaller errors in the positions' location could also occur when the picked target is relocated with the Trimble RTK GPS and a flag is placed in the ground. A fiducial was placed in the GPR data when the antenna was directly over the target flag. It was difficult to determine exactly when the sensor was directly over the target flag (as the flag was entirely underneath the sensor as the target was passed) and so it is not unreasonable that the fiducial placement in the GPR data could have been off by a few centimeters. Errors in the actual placement of the flag are of greater concern, particularly for the four-survey-line approach to data acquisition. Validation results indicated that it is not unusual for the target location to be found 20-30 cm away from the pin location. The concern here is that if the target is far enough away from the pin flag, it may fall outside the footprint of the GPR sensor. The four passes from different approaches may still pick up the intended target on some of the survey lines, but ideally the target should be immediately below the pin location so that it is covered by all four GPR survey lines. The best way to ensure this would have been to use the handheld EMI and magnetometry sensors to pinpoint a target

response prior to collecting the four GPR survey lines. The Ohio State representatives used this approach in their work as they attempted to determine the orientation of the magnetic dipole with a handheld differential magnetometer prior to collecting their GPR data. Unfortunately the handheld sensors were being used in the validation process and were not available to pinpoint targets prior to the collection of the COTS GPR data. Subsequent validation indicated that the picked targets were very close to the pin locations; hence, they will be focused on.

#### *4.2.4.1. Picked target type: APDS adapters*

The most prevalent in situ targets found on the G6 Range at the Camp Lejeune site were the adapters. They were found in two different types primarily, the cylindrical casing and the end cap as shown in Figure 38. Although these items are inert and are not munitions of concern, the properties of the target can be considered UXO-like from a GPR perspective in the sense that they are cylindrical and of a comparable diameter to actual UXO being sought.

Figure 38. A typical adapter (left) and adapter end cap (right) target from the Camp Lejeune site.

Consider the target response observed using the 250-MHz antenna over the target adapter G6B1_322, found during validation to be buried at a depth of 6 cm and 2 cm from the pin flag location. The section views and average amplitudes are shown for each of the four passes over the target in Figure 39. On all four survey lines collected, there is a strong response from the target. While it can be determined with confidence that there is a shallow target at the pin flag location, it is not possible to differentiate the adapter target from emplaced items or other targets based on the GPR data alone. All four GPR sections produce symmetric hyperbolas, and the average amplitudes are approximately equal.

Adding the high-frequency 1000-MHz antenna does not aid in target discrimination. Consider the data for a second adapter target, G6E1_4, that was collected using both 250-MHz and 1000-MHz data and is pictured in Figure 40. Validation indicated that the adapter was directly beneath the pin flag at a depth of 4 cm. The tails are much less pronounced on the hyperbolic responses in the 250-MHz data than they were in those sections displayed for adapter target G6B1_322 in Figure 39. There also appear to be responses from a nearby target in the 250-MHz data. The 1000-MHz signal is a weak response without any substantial signal deeper than 20 ns. Even though the data do not contain target signatures as obvious as those observed in Figure 39, there is nevertheless a distinct target response, albeit in a more challenging interpretation scenario.

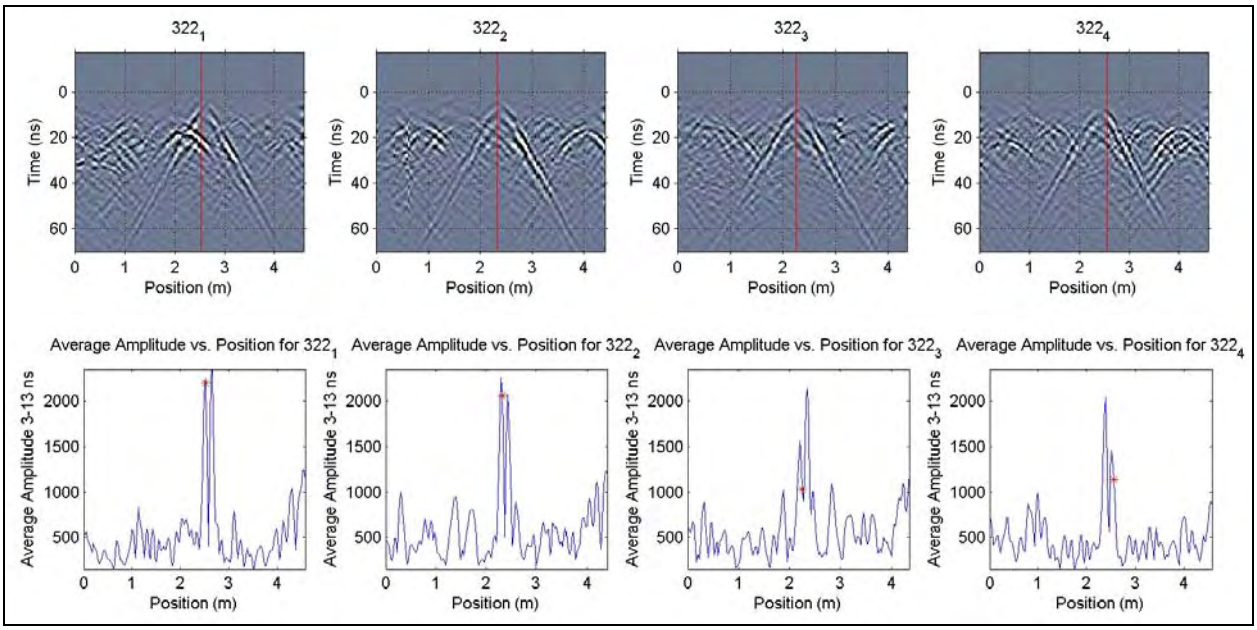


Figure 39. Section views and average amplitudes for G6B1_322. A strong and distinct response is observed for all four GPR survey lines over the target. Data acquired using the 250-MHz GPR antenna. Dewow filter, background subtraction, and SEC gain were applied to section views. Dewow, background subtraction, migration (v = 0.06 m/ns), and enveloping were applied to average amplitudes.

Because the section views contain relatively weak responses, the views available in the average amplitude plots shown in Figure 41 are considered. Even though the 250-MHz and the 1000-MHz profiles were collected at different starting and stopping points, they were all approximately centered over the pin flag representing the target. Data from both frequencies provide similar information. Even though the amplitude of the 250-MHz signal is much stronger, similar responses are observed.

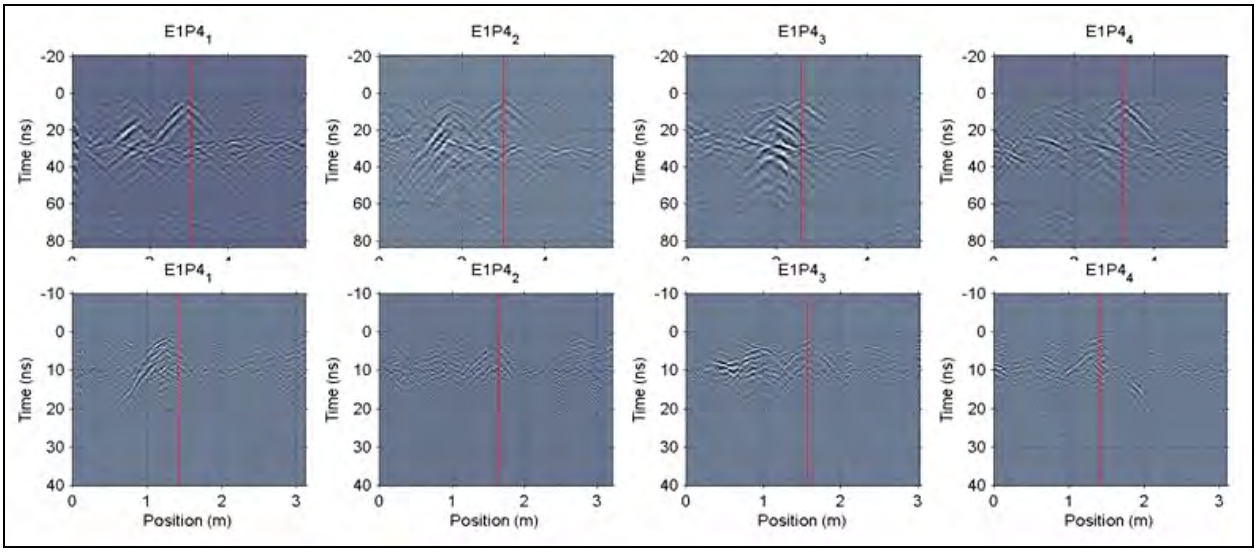


Figure 40. Section views for G6E1_P4 using both 250-MHz (top row) and 1000-MHz (bottom row) antennas. Dewow filter, background subtraction, and SEC gain were applied to section views.

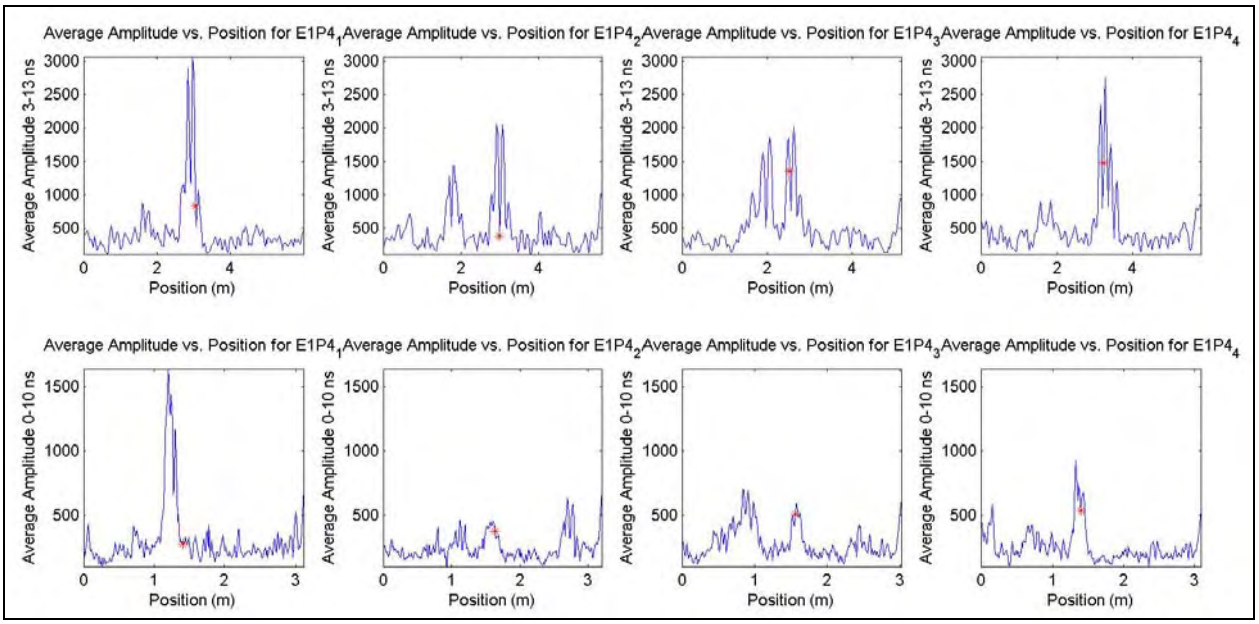


Figure 41. Average amplitude plots for G6E1_P4 using both 250-MHz (top row) and 1000-MHz (bottom row) antennas. Dewow filter, background subtraction, migration (v = 0.06 m/ns), and enveloping were applied to plots.

A prominent single peak occurs in the first and fourth average amplitude plots at both 250 MHz and 1000 MHz. On the second and third average amplitude plots, two peaks of similar magnitude are observed, one that corresponds to the adapter target, G6E1_4, and the second, which was also observed in the section views of Figure 40, but was not investigated during the validation process.

In addition to the four survey lines acquired over G6E1_P4 (Figures 40 and 41), multi-line grids were collected over the targets using both the 250-MHz and the 1000-MHz systems. As a result, three-dimensional images of the data volume surrounding the target can be prepared and investigated. For the 1000-MHz data, a set of perpendicular survey lines were collected at 10-cm line spacings, while the 250-MHz data involved a line spacing of 15 cm. Distance between traces in the along-track direction was 1 cm for the 1000-MHz data and 2.5 cm for the 250-MHz data. Figure 42 shows a series of slices taken throughout the data volume for the 250-MHz data and the 1000-MHz data. A high-amplitude area is evident in both images on the 10-cm depth slices; however, the higher frequency 1000-MHz data produce a more distinct response than the 250-MHz image, which appears more smeared in nature. The origins for both of the grids were not coincident and that is why the targets do not appear at the same location in both the 250-MHz and 1000-MHz images. The same data are displayed in Figure 43 but this time as a cube with a portion removed to show the target position embedded within the data volume. In this case, the near surface adapter target, G6E1_P4, can be seen in both images. Figure 43 also shows more detail on structure contained within the volume that is not evident in the slice views of Figure 42. In the 250-MHz data, there is a horizontal reflector below the target of interest occurring at approximately the 1-m depth. No such boundary is evident in the 1000-MHz data, as the signal at that frequency has dropped into the noise level before reaching a depth of 1 m.

The GPR responses generated by the adapter targets are quite similar to those observed for the emplaced items and it would not be possible to distinguish the two based on the COTS GPR data alone. While the collection of tightly spaced grids of data does enable the creation of data volumes, it takes approximately three times longer to cover the target than the four-survey-line approach. It is still not feasible to extract additional target characteristics (material properties, lengths, aspect ratios). Because time over target is a practical concern, the approach using four survey lines provides the most efficient means of extracting useful target information such as depths and the presence of nearby clutter items.

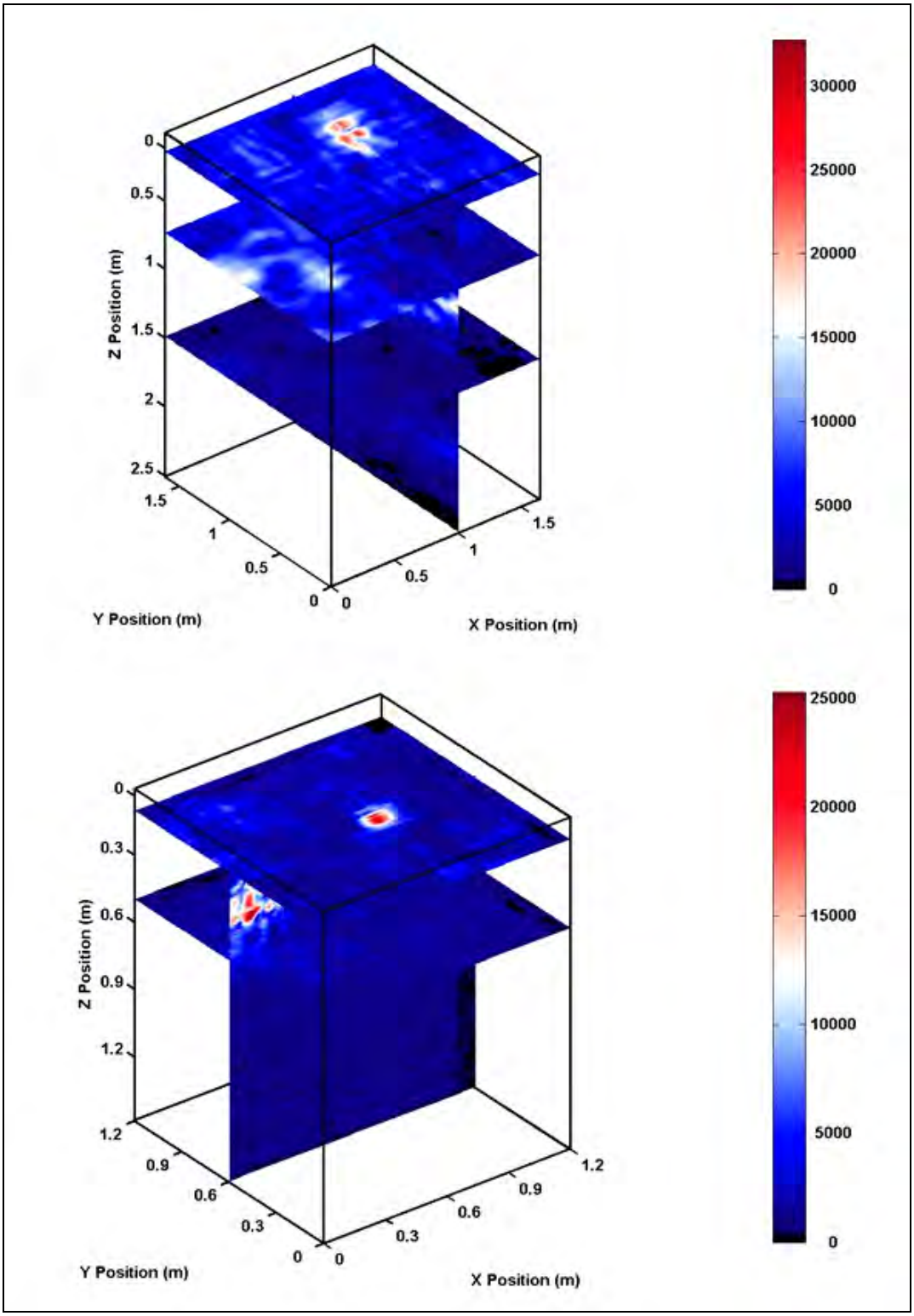


Figure 42. Data volume for target G6E1_P4 displayed as a series of horizontal and vertical slices. Results are shown for data acquired using the 250-MHz (top) and 1000-MHz (bottom) systems. Target response is evident as a high-amplitude area in the top depth slice of both images; however, the higher frequency data produce a more distinct anomaly.

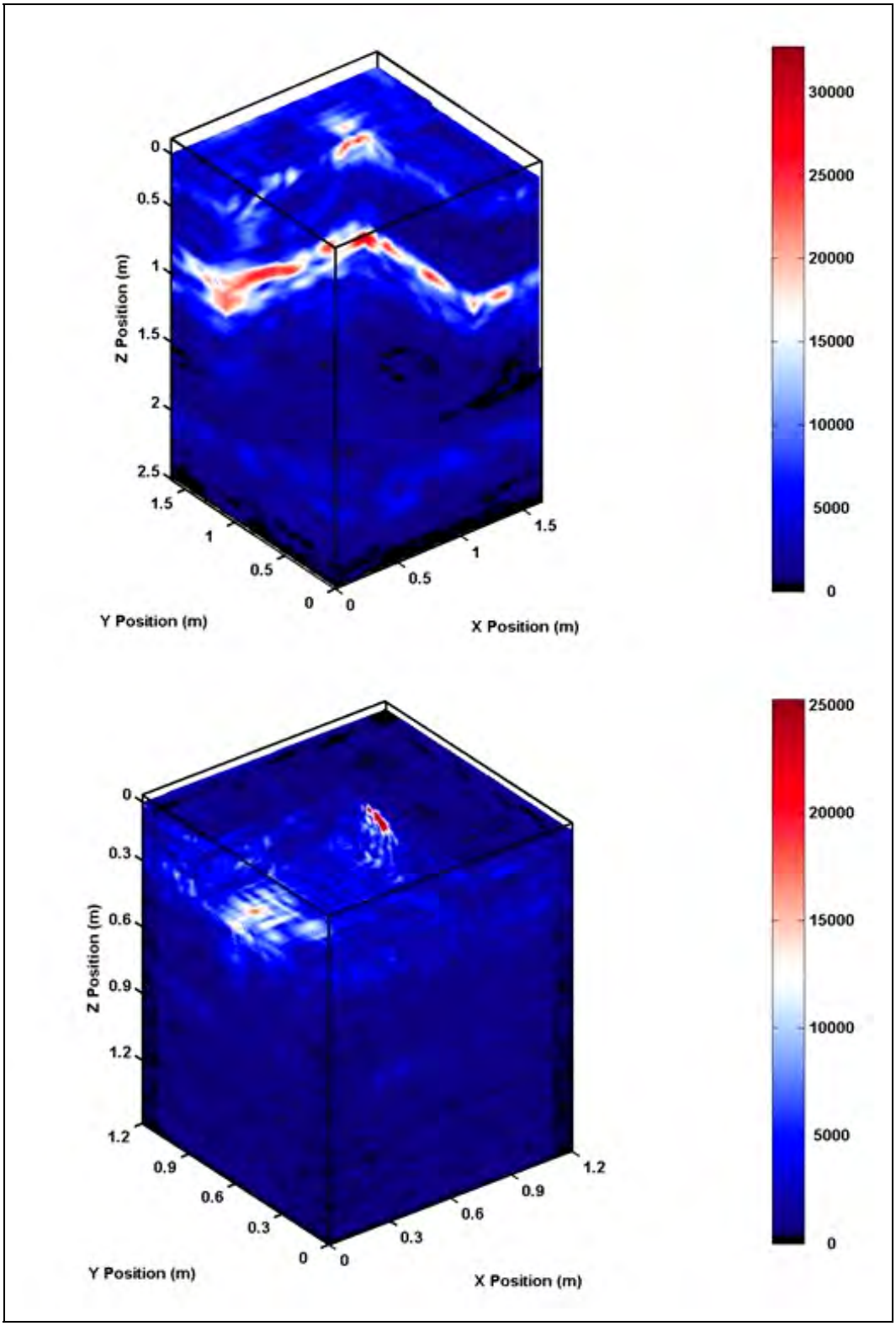


Figure 43. Data volume for target G6E1_P4 displayed as a cutout cube. Results are shown for data acquired using the 250-MHz (top) and 1000-MHz (bottom) systems. The high-amplitude area near the upper surface of both images corresponds to the adapter target.

#### *4.2.4.2. Other types of picked targets investigated*

In addition to the ubiquitous adapters, a wide range of items were found at the Camp Lejeune site during the validation process. Not all of these items were covered using the COTS GPR system. A sampling of some items that were covered as well as the corresponding target responses recorded over one of the four passes with the 250-MHz system are shown in Figure 44. Targets range from a 120-mm high-explosive anti-tank (HEAT) rocket, which was removed by Camp Lejeune EOD personnel, to large and small pieces of scrap and 40-mm grenade practice rounds. Responses ranged from obvious peaks over all four survey lines to no detectable responses in any of the four survey lines collected over the target. As mentioned earlier, GPR data were acquired over flags that were placed based on RTK GPS positions from targets picked based on EMI data. In some of these instances the actual target discovered during the validation process was not precisely beneath the flagged location and, in certain cases, the target might not have been illuminated by the footprint of the GPR signal.

### 4.2.5. Challenging scenarios

Results presented thus far indicated that identifiable target responses are obtainable with a COTS GPR system, even though discrimination between targets remains elusive. Although the plots shown in Figure 32 illustrated how some of the smaller targets were still capable of producing a detectable response in the 250-MHz data, some emplaced items did not produce conclusive target responses in the four survey lines collected. Considering the full set of target responses collected over emplaced items in Appendix A, it is also evident that some of the smaller items did not produce a distinct response at either 250 MHz or 1000 MHz. For example, the data obtained over the body of a 60-mm mortar shown in Figure 44 do not provide particularly convincing or conclusive evidence of a target of concern being present. In this case all of the 250-MHz data do appear to contain a hyperbolic response, but that response is largely obscured by additional scattering as evidenced by the lack of distinct strong peaks in the average amplitude plots of Figure 45.

Most of the larger emplaced items result in strong hyperbolic responses in the data section images, which correspond to definitive peaks in the average amplitudes. These peaks often occur in all four of the passes over the target increasing the confidence that a target of interest lies below.

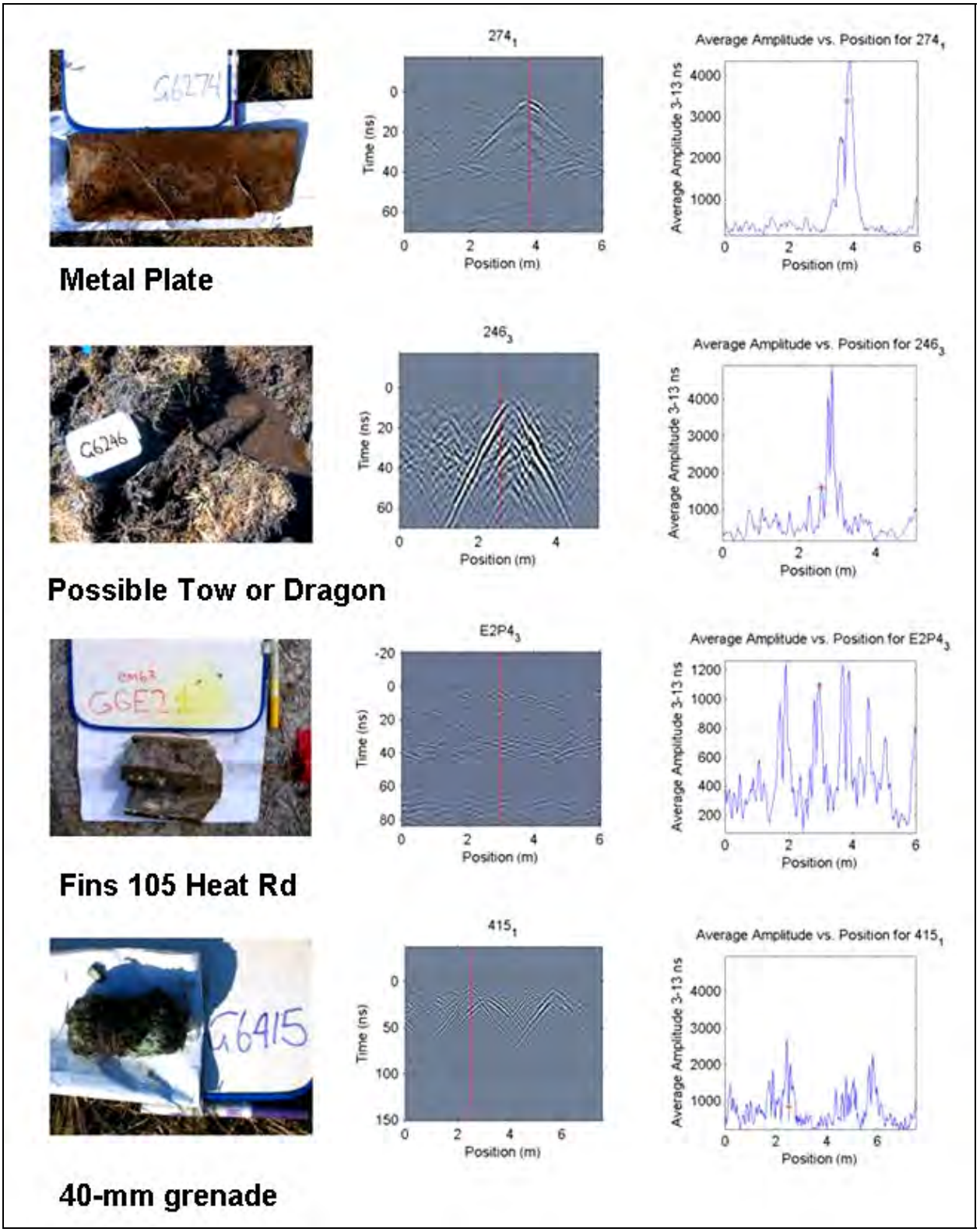


Figure 44. A cross section of items found during validation efforts at the Camp Lejeune G6 range.

Examining the target responses contained in Appendix A, there is one target, G6A2_E22 (81-mm mortar, 30-cm depth, horizontal), which does not produce a detectable response on any of the four passes. The lack of response for this target is troubling in that a nearby identical deeper target, G6A2_E24 (81-mm mortar, 60-cm depth, horizontal), and another identical target at a more difficult orientation G6A2_E23 (81-mm mortar, 30-cm depth, vertical), both produced detectable responses. Based on the GPR responses observed, no further information could be provided on target G6A2_E22. It is difficult to understand why there is no response for this target; the soil was similar for all three targets as they were relatively close to each other.

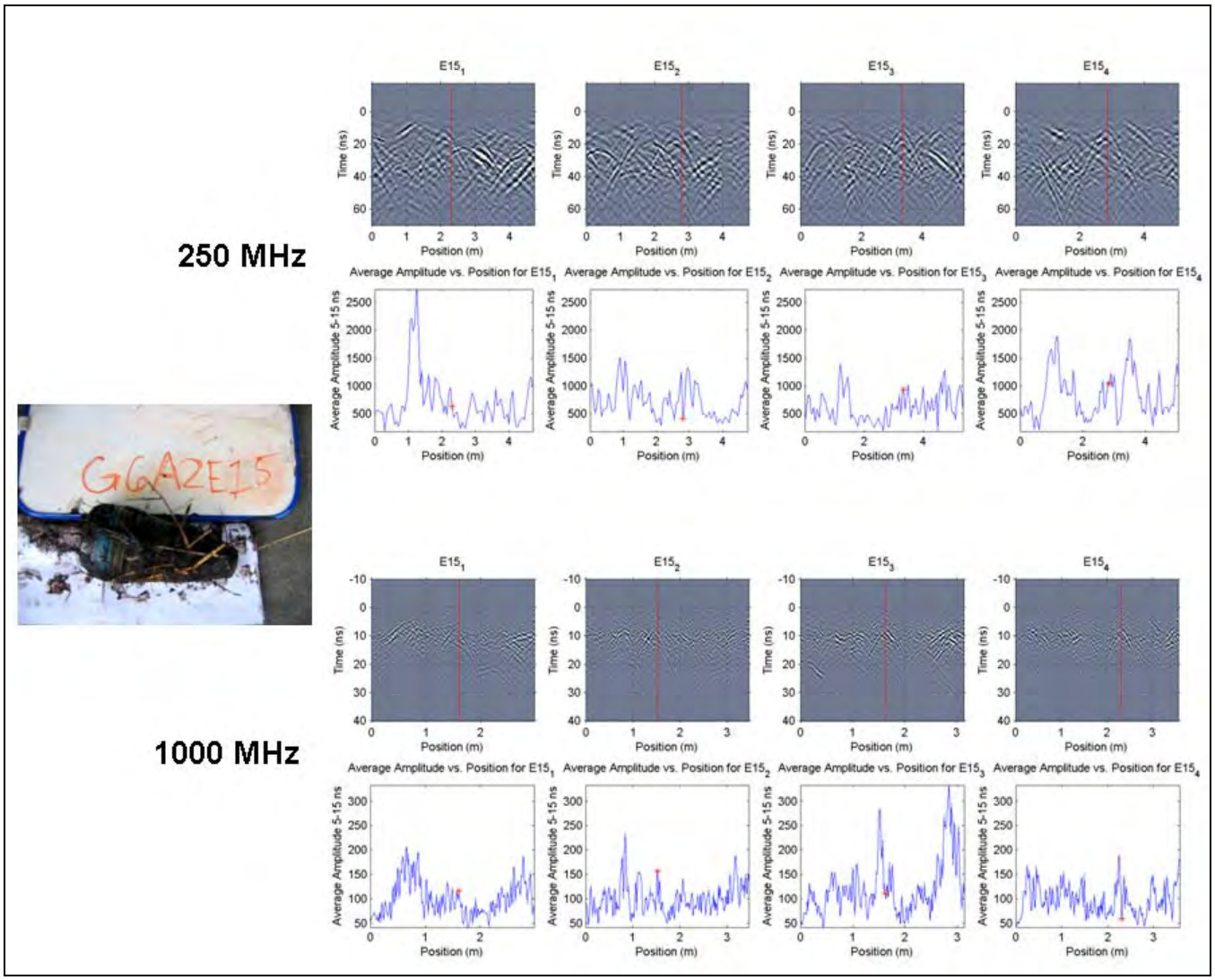


Figure 45. Target responses obtained on four passes over the target G6A1_E15, a 60-mm mortar body, using both 250-MHz (top 2 rows) and 1000-MHz (bottom two rows) antennas.

## 4.3 Conclusions from GPR data acquired with COTS GPR system

A COTS GPR system, operating at either 250 or 1000 MHz, was deployed in a cued-interrogation mode at Camp Lejeune. As regards the UXO discrimination ability of such a COTS sensor at a “GPR favorable” site, the following conclusions are drawn:

- Information that can be extracted from a series of GPR profiles is mostly limited to the location and depth of an item and the presence of any nearby clutter items. It may on occasion be possible to estimate the orientation of the item and to estimate a characteristic length.
- The 1000-MHz data provided higher resolution images of the smaller, shallower emplaced items. However, the increased resolution did not contribute to improved interpretation. The higher frequency signal was also more rapidly attenuated and more readily scattered by small geologic and anthropogenic heterogeneities than the 250-MHz data, which limited interpretability.
- Cued interrogation using a COTS GPR system is most efficiently deployed by collecting four survey lines over the identified area of concern rather than collecting a tightly spaced grid.

# 5 Conclusions

One of the main goals of the Camp Lejeune efforts was to evaluate the detection and discrimination potential of ground penetrating radar. Two different modes of surveying were employed. In discrimination mode surveying, data were collected over large areas by a Witten Technologies CART imaging system and Applied Research Associates Nemesis Advanced Ordnance Detection. In the cued-interrogation surveying mode, targets previously identified in EMI or Magnetics data were flagged and resurveyed with a series of GPR profile passes over the marked area. The Ohio State fully polarimetric system and a commercial off-the-shelf GPR system were both deployed for cued interrogation.

Regarding the UXO discrimination ability of GPR sensors at a "GPR favorable" site, the following conclusions are drawn:

- A commercial off-the-shelf GPR system can provide valuable information in a cued interrogation approach. Depths to targets can be extracted, as can the presence of nearby clutter or multi-object scenarios. Knowledge gained from the COTS GPR data can be used to constrain inversions of EM data. Detailed target information such as material properties, lengths, and aspect ratios are not readily attainable with a time domain (impulse) commercial off-the-shelf GPR system.
- Heavy rains in the weeks prior to the GPR surveys at the Camp Lejeune site created saturated ground conditions, particularly in the grids at the northern end of the survey area. This produced two unique challenges. Accessibility became an issue, particularly in the grids of the northern region in the survey areas where standing water was present. Attenuation of the GPR signal also limited the penetration in some areas of the site that were saturated.
- A cued-interrogation approach incorporating Ohio State University's fully polarimetric GPR system allowed for a more sophisticated classification of targets than the COTS cued-interrogation approach. An estimate linear factor could be calculated based on late-time response of the polarized data allowing targets to be deemed as UXO-like or non-UXO items.
- Array-based GPR systems are able to provide complete coverage over substantial areas (Witten Technologies CART imaging system covered

over 3 acres during 5 days of surveying). The volume of data generated is substantial, as full coverage with GPR requires smaller line spacings than EMI or magnetometer surveys. It remains a challenge to locate and extract these often weak GPR responses from the large volumes of acquired data, particularly when all GPR systems are also susceptible to scattering from small geologic and anthropogenic heterogeneities, which will often produce target responses indistinguishable from target responses generated by UXO targets.

- Full coverage GPR may prove most valuable as a confirmation of EMI and magnetometer selected targets. The Applied Research Associates Nemesis system also incorporates EMI sensors and correlating the EMI information with their GPSAR data produced encouraging results for the detection and discrimination of shallow UXO targets. A number of shallow emplaced items (up to 35-cm depths) were also detected.

# Appendix A: Ohio State University Electro-Science Laboratory (OSU-ESL) Results for Camp Lejeune, NC[1]

## A.1. OSU-ESL GSR system description

The new OSU/ESL GPR system used at Camp Lejeune, NC during March 13 – 14, 2006, is a swept-frequency radar operating from 10 to 1000 MHz. The objective is to perform target classification such that UXO and non-UXO items can be discriminated. Late-time radar features such as natural resonance and polarization were utilized to separate false alarm objects from UXO-like items that have elongated bodies with length-to-diameter (L/D) ratios greater than two (Higgins and Chen 2000). Additional features such as length, depth, and orientation were also extracted from the data. Various UXO types could be further classified based on their lengths estimated from the electromagnetic resonance. Such a technology has been applied previously at the Tyndall AFB site, Blossom Point Site, Jefferson Proving Ground, and Fort Ord (Higgins and Chen 2000, 2001a, 2001b; Chen 2002; Chen and Peters 2002).

These measurements show that the overall GPR system needs to be improved in mobility, measurement speed, and spatial resolution. Therefore, a new OSU-ESL GPR system and miniaturized antenna were subsequently developed. The new GPR system, shown in Figure A1, adopts advanced digital transceiver technology that includes a direct digital synthesizer (DDS), dual-RF channels for fully polarimetric measurements, and a direct digital receiver (DDR) with digital down converter (DDC). These digital components allow for faster frequency sweep and smaller size, so that the survey can be conducted by a single operator at a walking speed.

The typical frequency range for UXO classification is from 10 MHz to 810 MHz at 4-MHz increments. The OSU-ESL GPR collects swept-frequency fully polarimetric data, including co-polarized (S11 and S22)

---

[1] Chi-Chih Chen, TEL: (614) 292-3403, email: chen.118@osu.edu; The Ohio State University ElectroScience Laboratory, Department of Electrical Engineering, 1320 Kinnear Road, Columbus, OH 43212.

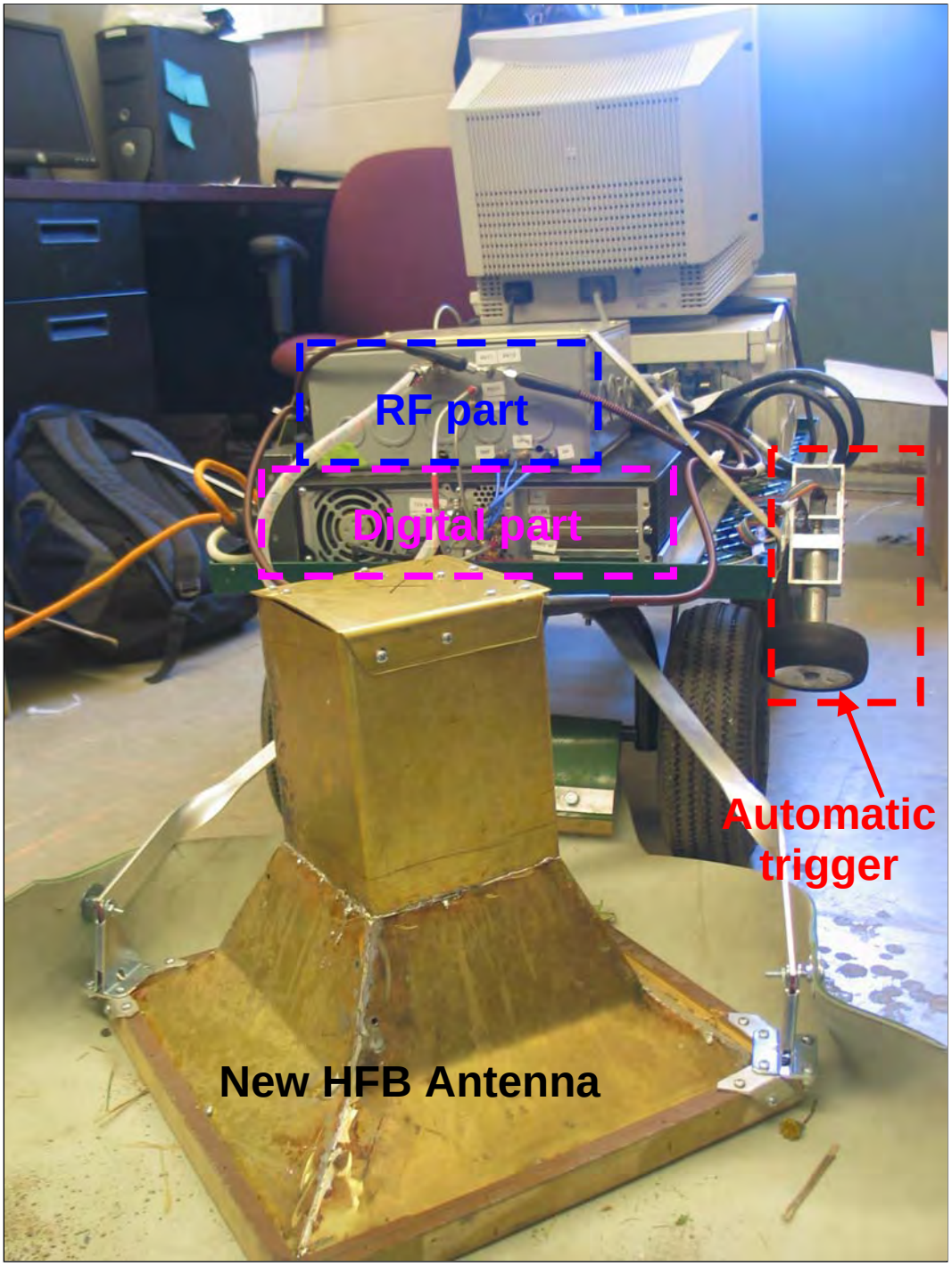


Figure A1. The new OSU/ESL GPR system (A swept-frequency radar operating from 10 to 1000 MHz).

and cross-polarized (S21) reflections with +7 dBm of output power. Three measurements (S11, S21, and S22) are performed every 3 in. along a survey line approximately 10 ft in length, controlled by an encoder installed on a wheel. A portable generator was used as the power source.

The OSU-ESL GPR system operates with a novel UWB fully-polarimetric zigzag bowtie (ZZB) antenna, newly developed to improve the spatial resolution by reducing antenna size. The ZZB antenna has two perpendicular linearly polarized antenna elements. Polarization “1” was designated as the one parallel to direction of travel. The transverse element was designated as polarization “2.” A personal computer was used for radar operation, data acquisition, and display.

A typical GPR survey includes one to three linear scans along straight lines centered at each flagged “hot spot.” Each GPR survey line was usually 10 ft in length, with data taken at 3-in. increments. Preferably, the magnetic dipole orientation (if any) would have been selected from magnetic surveys and was chosen as the orientation of the initial GPR pass. However, such information was not available and a hand-held magnetometer was used to survey each site prior to the GPR survey to locate strong magnetic dipole orientation. If no magnetic dipole orientation was detected, an arbitrary direction was chosen for the initial pass. Post-processing then extracted orientation information for anomalies that showed linear scattering features. In this case, the second pass was chosen to be orthogonal to the dipole direction. For items that didn’t show a clear linear feature, an additional pass transverse to the first pass was performed.

The soil type of the Camp Lejeune site appeared to be a mixture of clay and sea sand. The two adjacent survey areas are referred as “lower pad” and “upper pad” herein due to different elevation. The lower pad was completely saturated with water at the time of the survey. The upper pad appeared to be dry on the surface. The high moisture content increased soil absorption of electromagnetic and enhanced subsurface heterogeneity such as layers, wells, and trenches, causing higher radar clutter level. The surface of the test site was covered with dried vegetation as shown in Figure A2.

## A.2. Classification results

This section discusses blind UXO classification results. The features (length, depth, and azimuth orientation) for correctly classified UXOs were found to be reasonably accurate. Most false alarms were found to be from sites containing so-called “adapters.” Missed UXO items were found to be either small (40-mm cartridges) or vertically inclined UXOs.

(a) system in the field

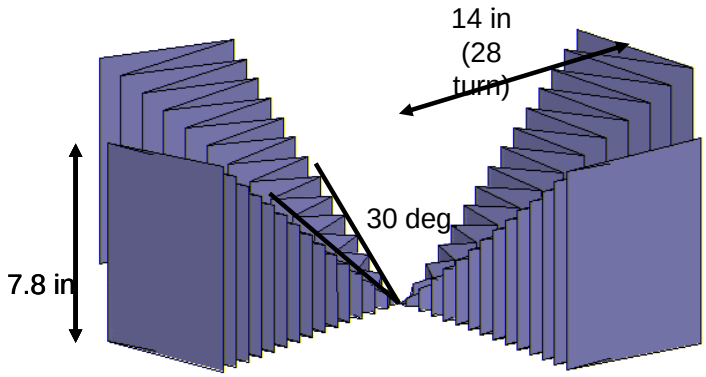

(b) miniature UWV antenna design

Figure A2. System set up at the Camp Lejeune test site.

Note that all the GPR data examples presented in this document were plotted with background removal and gain slope applied. The gain slope is commonly used in displaying GPR data to compensate the soil attenuation with increased depth and provide a better viewing dynamic range. Such a gain slope is applied only when data are displayed and does not affect the target features. Both S11 and S22 data will also be plotted using the same scale in the same figure. However, S21 data will be plotted using a twice-

emphasized scale, since S21 response is too weak compared to the co-polarization signals (S11 and S21). All targets were classified by OSU-ESL personnel based on extracted features from radar data without the knowledge of ground truth, which was provided after classification results were submitted to Mr. Stephen Billings at Sky Research, Inc.

### A.2.1. Blind target classification results

Ideally, one would like to separate a true UXO from any non-UXO object even if the geometries are similar. Such designation is not practical to achieve from radar data derived from external scattering. A UXO-like designation is adopted based on the length-to-diameter (L/D) ratio. A target is classified as UXO-like if its L/D ratio is greater than 2.5; otherwise, it is a clutter. Evidently, such classification will pick up false alarms from fragments (such as G6E1P1) that have L/D ratios greater than 2.5. The frequency range of the current radar system is too low to classify surface-laid 40-mm projectiles, which have small L/D ratios. Tables A1 and A2 summarize the classification statistics based on two different criteria for UXO designations. Note that these tables use the minimal UXO-like threshold. That is, all UXO-like objects with HIGH, MEDIUM, and LOW confidence levels are included as UXO-like objects. All objects that are not UXO-like are classified as clutter. The ground truth containing target features and UXO classification of the blind targets were provided by Sky Research, Inc. and are summarized in Table A3.

Table A1. GPR UXO Classification Performance (True UXO Criterion).

| | |
|---|---|
| Total Number of True UXO | 20 |
| Total Number of Empty Sites | 1 |
| Total Number Fragments (Including one magnetic rock) | 23 |
| Total Number of UXO Classified as UXO | 13 |
| Total Number of Clutter Classified as UXO | 5 |
| Total Number Missed True UXO | 7 |
| Correctly Classified UXO Rate: $\frac{Number\ of\ UXO\ Classified\ as\ UXO}{Total\ Number\ of\ UXO}$ | 65.0% |
| False Classification Rate: $\frac{Number\ of\ Clutter\ Classified\ as\ UXO}{Total\ Number\ of\ Clutter}$ | 21.7% |

Table A2. GPR UXO Classification Performance (UXO-like Criterion; L/D ratio > 2.5).

| | |
|---|---|
| Total Number of UXO-like | 17 |
| Total Number of Empty Sites | 1 |
| Total Number Fragments (Including one magnetic rock) | 26 |
| Total Number of UXO Classified as UXO | 13 |
| Total Number of Clutter Classified as UXO | 5 |
| Total Number Missed UXO-Like | 4 |
| Correctly Classified UXO Rate: $\frac{Number\ of\ UXO\ Classified\ as\ UXO}{Total\ Number\ of\ UXO}$ | 76.5% |
| False Classification Rate: $\frac{Number\ of\ Clutter\ Classified\ as\ UXO}{Total\ Number\ of\ Clutter}$ | 18.5% |

The ROC curve generated based on the following five thresholds (Chen and Peters 2002) is plotted in Figure A3.

1. UXO with HIGH confidence.
2. UXO with MEDIUM confidence.
3. UXO with LOW confidence.
4. CLUTTER with LOW confidence.
5. CLUTTER with MEDIUM confidence.

During the process of blind classification, a confidence level was assigned to each target. There are “high,” “medium,” and “low” confidence levels, which are determined subjectively based on the guide shown below.

1. HIGH - good SCR, clear scattering patterns, clear ETO.
2. MEDIUM - medium SCR, acceptable scattering patterns, acceptable ETO.
3. LOW - low SCR, ambiguous/insufficient/new scattering patterns, unstable/ambiguous ETO.

It is interesting to compare the blind classification performance from the current site with previously published results from the JPG (IN) and Fort Ord (CA) sites. Note that the new curve may not be statistically correct due to the relative small number of items surveyed. Still, the ROC curve shows slightly improved performance.

Table A3. GPR Classification Results on the Buried UXOs (Lower pad).

| Target ID | Description | GPR ID | True ID | Conf. | Time ELF | Freq ELF | Early ELF | ETO | CNR (MHz) | Dep. (nsec) | Depth (cm) | Dip | Azimuth | Mag | Mag. Dip |
|---|---|---|---|---|---|---|---|---|---|---|---|---|---|---|---|
| G6E2 | 105-mm projectile | 1 | 1 | H | 0.55 | 0.7 | 0.36 | 70 | 80 | 26 | 50 | 45 | 94 | S | S |
| G6E4 | 2.75-in. rocket | 1 | 1 | H | 0.9 | 0.8 | 0.7 | 0 | 80 | 20.8 | 30 | 0 | 240 | S | S |
| G6E5 | 76-mm projectile | 1 | 1 | H | 0.95 | 0.95 | 0.9 | 110 | 95 | 23.9 | 30 | 45 | 320 | S | W |
| G6E8 | 90-mm projectile | 1 | 1 | H | 0.75 | 0.95 | 0.7 | 100 | 90 | 36.7 | 60 | 45 | 120 | S | N |
| G6E10 | 81-mm mortar | 1 | 1 | H | 0.9 | 0.9 | 0.95 | 110 | 70 | 37.2 | 60 | 45 | 120 | S | N |
| G6E13 | MK118 – | 1 | 1 | H | 0.85 | 0.85 | 0.8 | 75 | 100 | 18.8 | 15 | 0 | 40 | S | S |
| G6E19 | 90-mm projectile | 1 | 1 | H | 0.8 | 0.95 | | 60 | 60 | 24.2 | 30 | 0 | 180 | S | S |
| G6E22 | 81-mm mortar | 1 | 1 | H | 0.8 | 0.85 | 0.8 | 75 | 85 | 22.4 | 30 | 0 | 95 | S | N |
| G6E24 | 81-mm mortar | 1 | 1 | H | 0.7 | 0.8 | 0.6 | 75 | 100 | 30.1 | 60 | 0 | 70 | M | N |
| 37K1 | UNKNOWN | 1 | 1 | H | 0.8 | 0.9 | 0.86 | 160 | 170 | 21.3 | | | | S | S |
| G6E16 | 57-mm projectile | 1 | 1 | L | 0.7 | 0.7 | 0.6 | 60 | 110 | 12.3 | 25 | 45 | 270 | | |
| G6E18 | Bomblet dummy | 1 | 0 | L | 0.85 | 0.8 | 0.75 | 120 | 105 | 7.2 | 15 | 0 | 45 | S | N |
| X0Y30 | UNKNOWN | 1 | 1 | L | 0.5 | 0.8 | 0.9 | 140 | 140 | 10.2 | | | | S | S |
| G6E9 | 81-mm mortar | 0 | 1 | L | | | | | | | 30 | 90 | n/a | N | N |
| G6E14 | Body assembly | 0 | 0 | L | | | | | | | 15 | 45 | 180 | S | N |
| G6EMP26 | GPR clutter | 0 | 0 | L | | | | | | | 26 | | 110 | | |
| G6EMP30 | GPR clutter | 0 | 0 | L | 0.2 | 0.3 | 0.4 | 80 | NR | 2.4 | 8 | | 360 | N | N |
| G6E15 | Body 60 mm | 0 | 0 | M | 0.15 | 0.1 | 0.15 | 100 | 50 | | 25 | 45 | 0 | S | N |
| G6E17 | Bomblet dummy | 0 | 0 | M | | | | | | | 15 | 0 | n/a | S | N |
| G6EMP29 | GPR clutter | 0 | 0 | M | 0.6 | 0.6 | | 80 | NR | | 18 | | 350 | N | N |
| G6E3 | 81-mm projectile | 0 | 1 | H | 0.15 | 0.11 | 0.09 | 72 | 280 | 1.64 | 30 | 90 | n/a | | |
| G6E6 | 4.2-in. projectile | 0 | 1 | H | 0.2 | 0.35 | 0.2 | 120 | 400 | 3.1 | 50 | 90 | n/a | S | N |
| G6E11 | 40-mm projectile | 0 | 1 | H | 0.2 | 0.2 | 0.15 | 30 | 600 | 2.5 | 15 | 0 | 200 | N | N |
| G6E7 | 90-mm projectile | 0 | 1 | H | 0.15 | 0.2 | 0.1 | 90 | 105 | 2.53 | 30 | 90 | n/a | S | N |

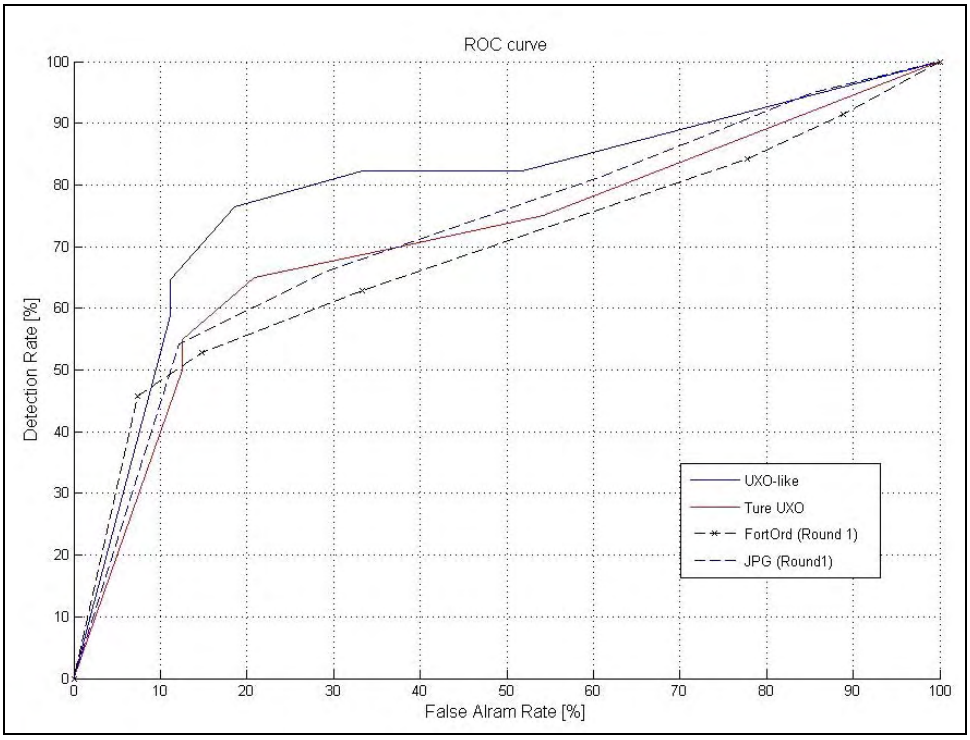


Figure A3. ROC curve of the GPR UXO classification performed at Camp Lejeune compared with ROC curves obtained from previous blind tests.

### *A.2.1.1. Investigation on false alarm items*

Three false alarms occurred at the upper pad and were related to sites containing UXO adaptors, capped metal cylinders with L/D ratios around 1.5. Two of them (G6E1P4 and G6D1P4) were located near the surface (<4 cm). Investigations revealed that the features selected for classification were actually associated with another deeper and offset item near the intended adapter. If the ground truth (not available) of this unknown item is indeed a UXO-like object, this classification would be correct. Since these classifications have a high confidence level, they would improve the ROC curve near the low false alarm region (left of Figure A3).

Figure A4 shows the processed data and pictures of Item G6E1P8, a metal cylinder cavity buried 2 cm under the ground. Target responses indicated by arrows in the co-polarization channels are observed at -5 nsec in the time axis and 40 in. in the x axis, while the cross-polarization channel (S21) shows the late-time response from -10 nsec in the time domain. This false alarm is suspected to be caused by strong coupling between the antenna and the target.

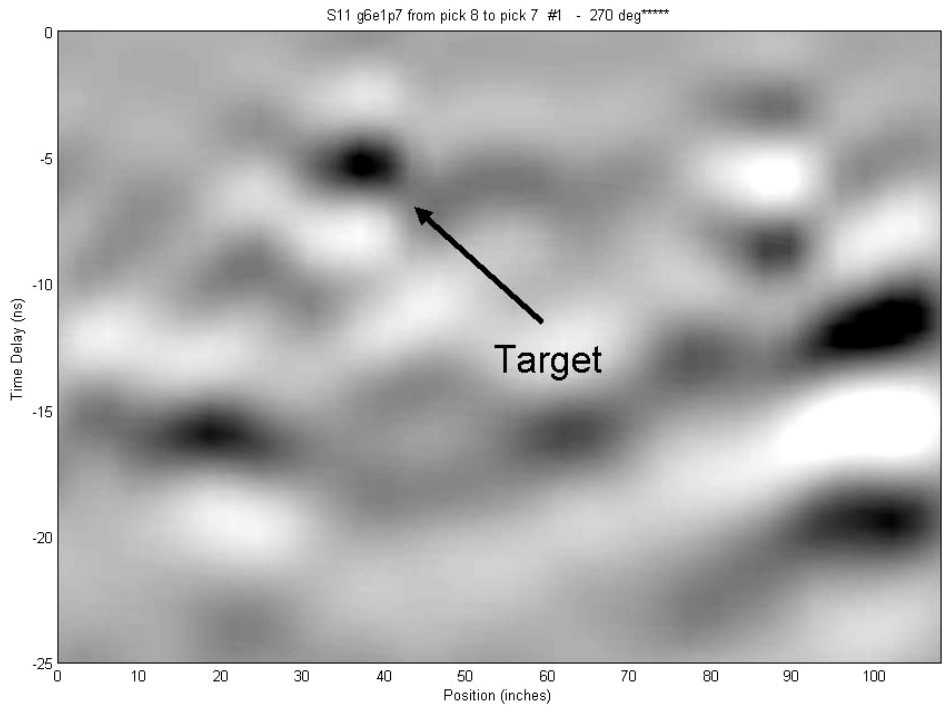


(a) S11 responses.

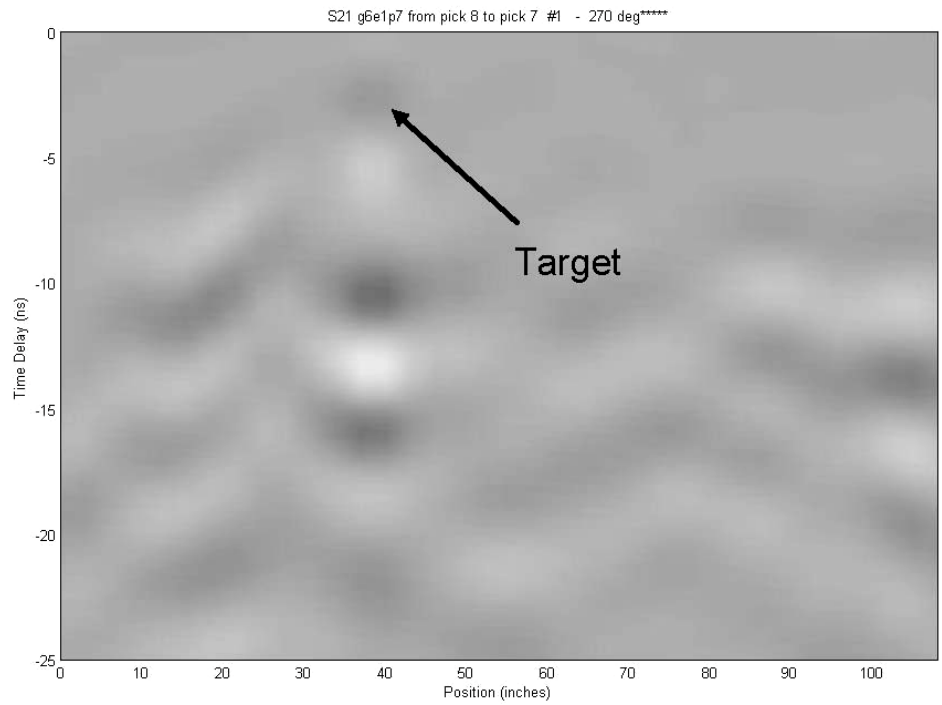


(b) S21 responses.

Figure A4. Processed responses and photos for Item G6E1P8 (Continued).

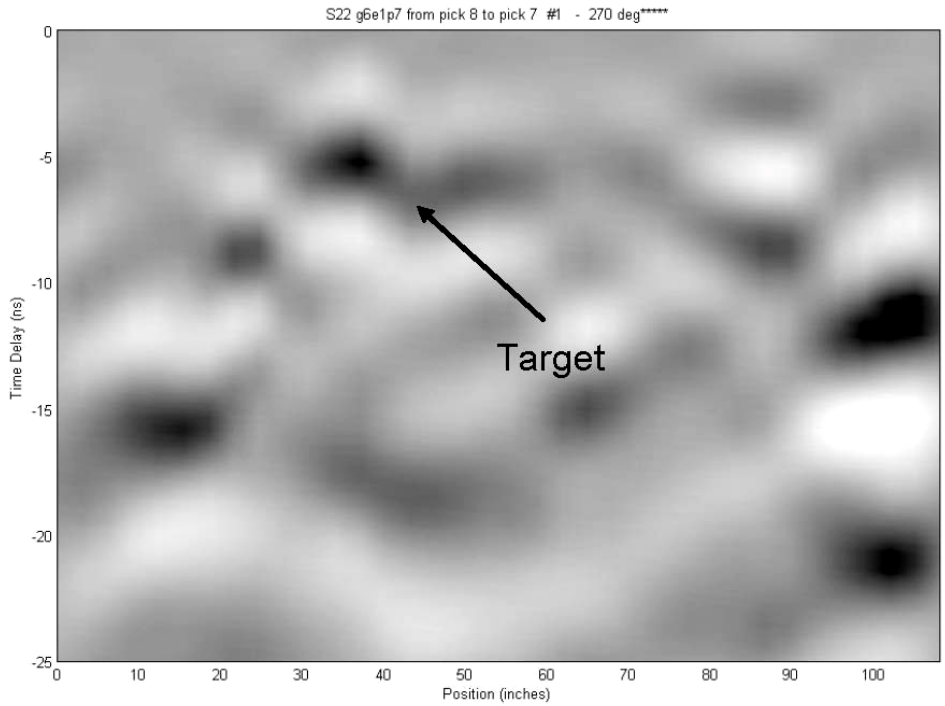


(c) S22 responses.

(d) Metallic cylinder cavity (Item G6E1P1).

Figure A4. (Concluded).

Items G6E1P4 and G6D1P4 are also part of the near-surface metallic cylinder cavity. However, strong target responses with pronounced resonance were found at an offset position and different depth. These items were classified based on the features extracted from these potential linear targets. Further excavations for these items are required to verify the classification result. Figure A5 shows the processed data and extracted features of the potential UXO-like target, which is located 30 in. away from Item G6E1P4.

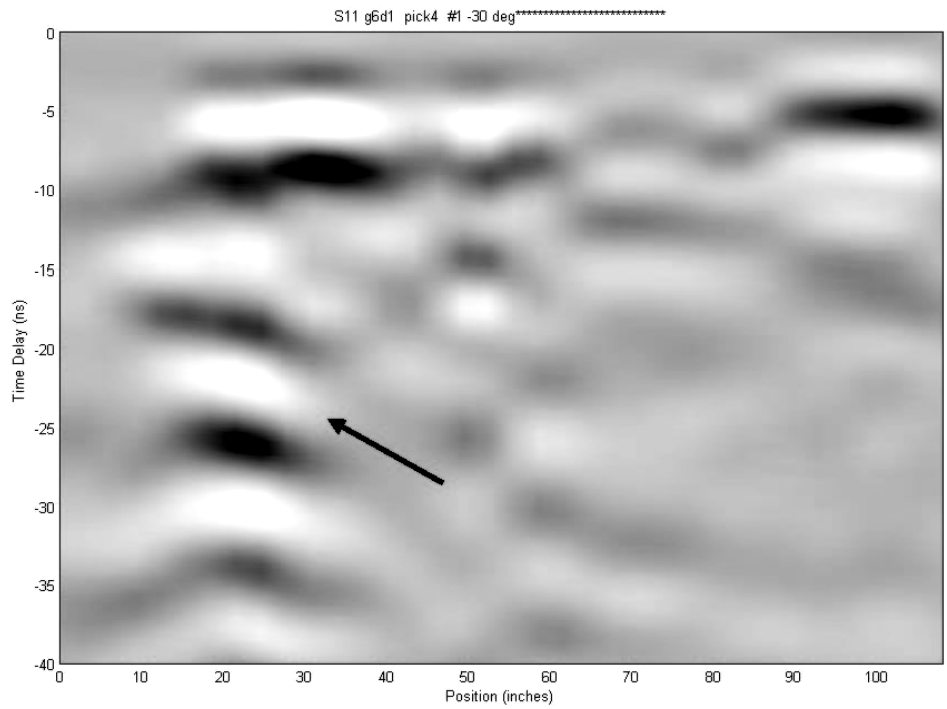


(a) S11 responses.

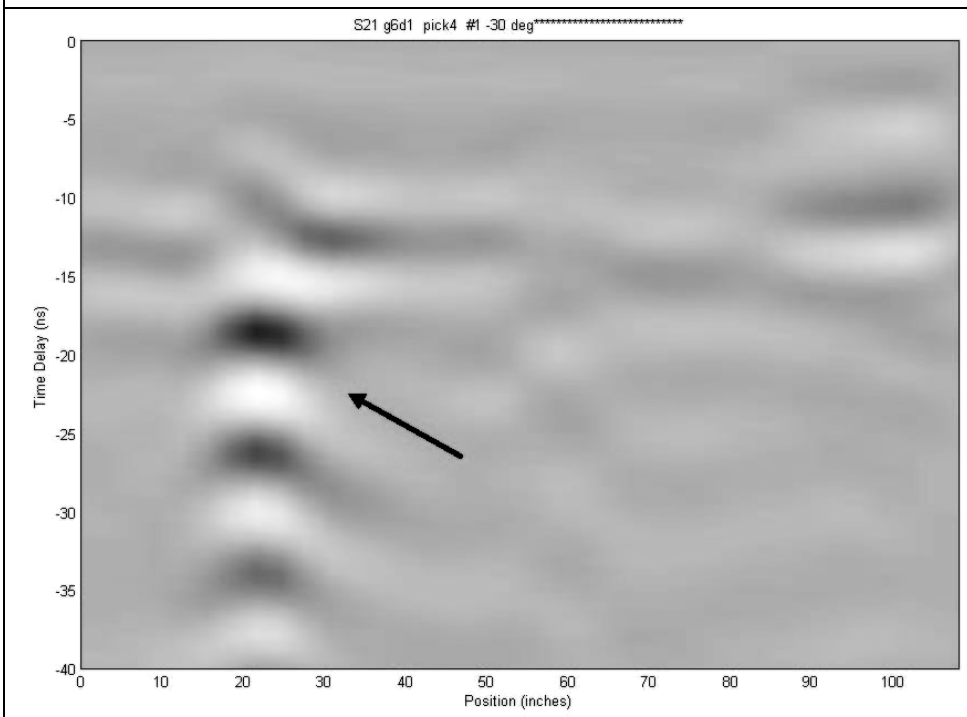


(b) S21 responses.

Figure A5. Processed responses for a potential target beside Item G6E1P8 (Sheet 1 of 3).

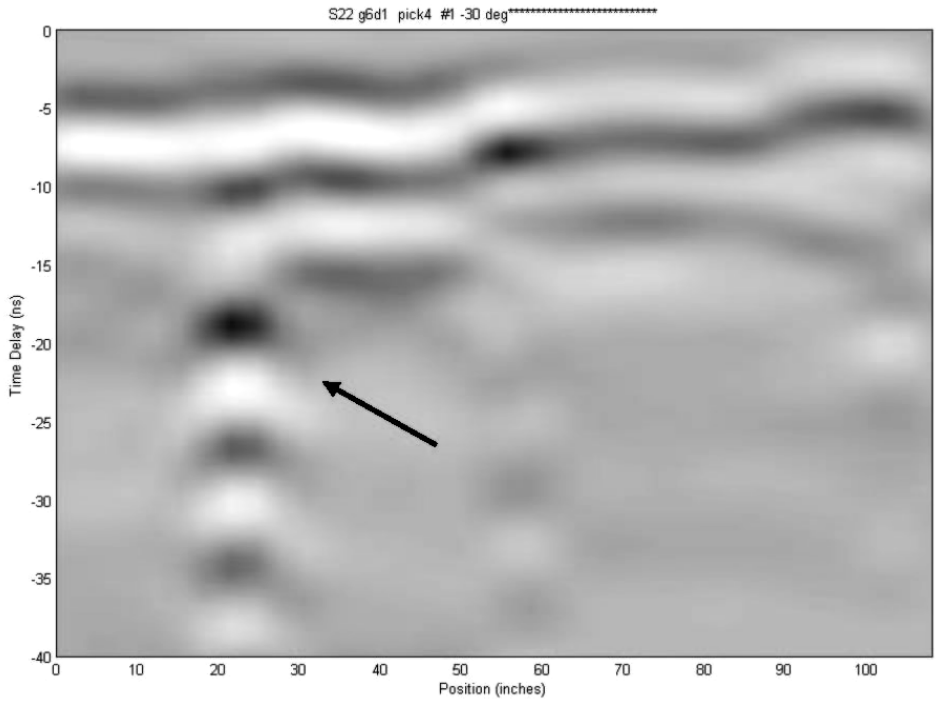


(c) S22 responses.

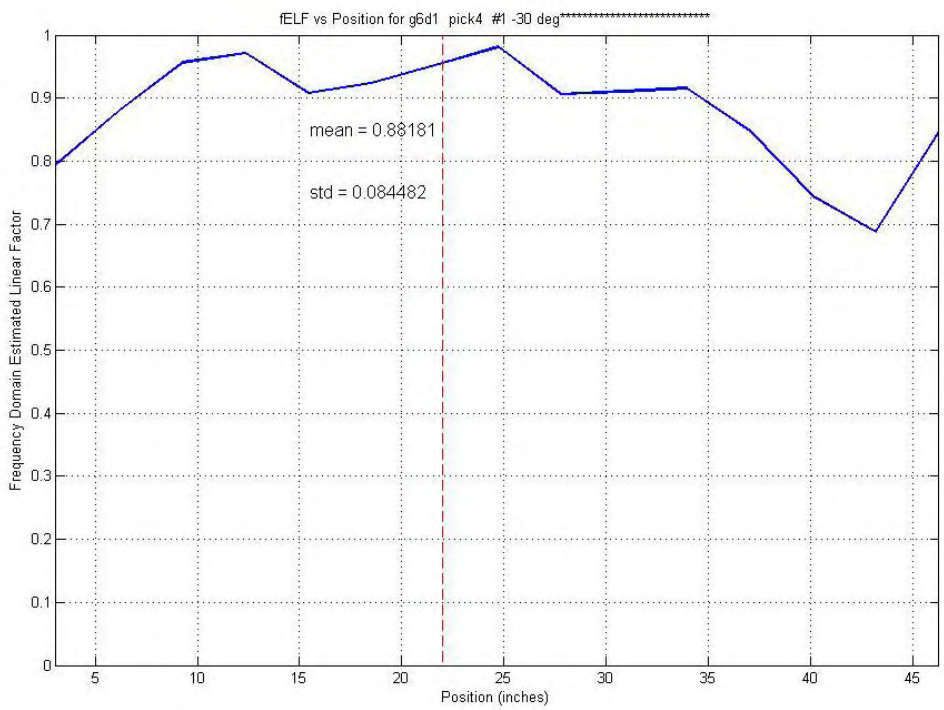


(d) Extracted Estimated Linear Factor (ELF).

Figure A5. (Sheet 2 of 3).

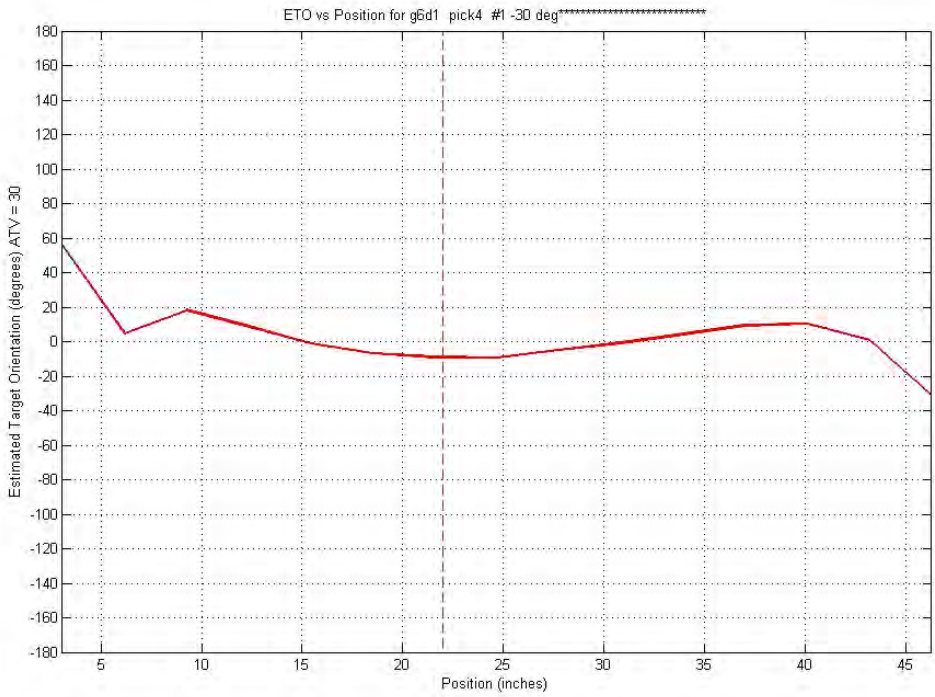


(e) Extracted Estimated Target Orientation (ETO).

Figure A5. (Sheet 3 of 3).

All three channels show strong resonance response. The extracted features (ELF, ETO) indicate with high confidence the presence of UXO-like objects. The authors suspect that they are indeed undiscovered UXO-like objects.

### *A.2.1.2. Investigation on Missed UXO-like Items*

Most missing UXO-like items were vertical UXOs, with processed estimated depths much shallower than the true depths. The classification appeared to be associated with surface anomalies due to the weak response from the intended UXO item. In general, a vertical UXO item is difficult to detect and classify due to its small cross section area when radar is directly above. However, classification of this kind of target is achievable from an offset position if the target depth is not too deep and the surrounding medium is relatively homogeneous (Chen 2002). At offset position, natural resonance can be excited from oblique incident fields. Such resonance is best excited from the plane transverse to the UXO axis. At the Camp Lejeune site, scattering from artificial trenches (walls and corners) and water tables not only increased the clutter level but also prevented proper excitation of vertical UXO as illustrated in Figures A6 and A7. Figure A7 shows an example of the vertical UXO (G6E3 – vertical

81-mm projectile) response and extracted features. A solid box in the co-polarization channels indicates a response from accumulated water in the trench, which is much stronger than the vertical UXO response. Response from the vertical UXO is weakened by the trench and it has poor signal-to-clutter ratio. Thus, responses indicated by the dotted box in the co-polarization channels (S11 and S22) were mistakenly selected. These responses came from a surface anomaly as a potential target and were processed to extract the linear features. The extracted features of course indicated a non-UXO anomaly. Notice the other two strong scatterings from water accumulated near the man-made trench.

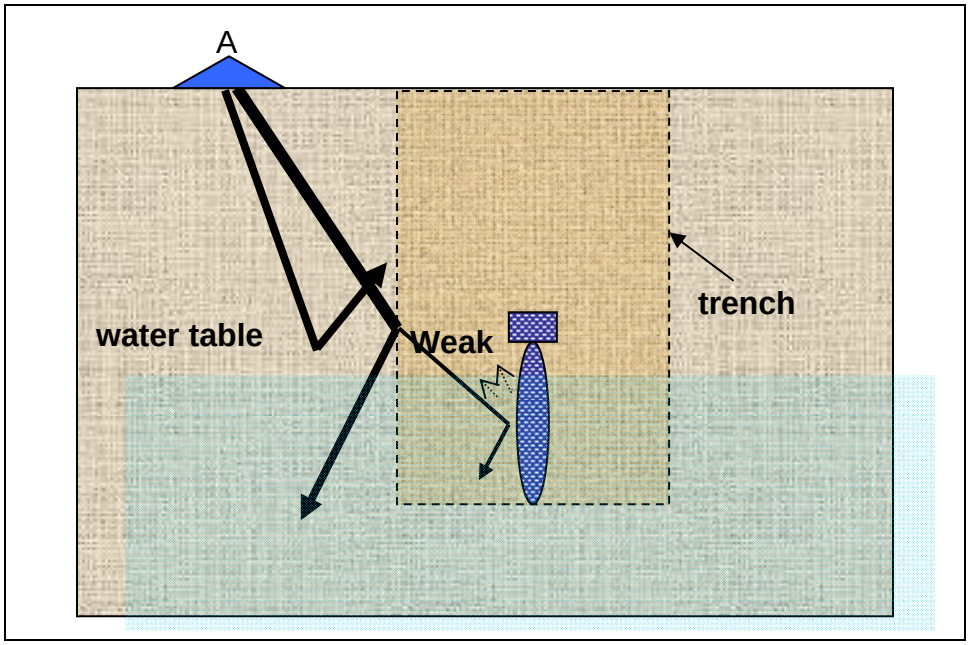


Figure A6. Scattering of a vertical UXO at offset position and trench effect.

Another missed UXO-like item was an elongated nonferrous metal fragment (G6E11), which is located very close to the surface (depth = 1 cm). Figure A6 shows the processed data and picture of Item G6E11. As one can see, strong responses are observed in all three channels, indicated by the dotted box. These responses were misled by a weak magnetic response, were treated as a strong coupling between trench and antenna, and were intentionally removed by the local background subtraction method. After local background subtraction, target response was mistakenly selected. Had EMI data been used, this situation could have been avoided.

(a) Vertical 81-mm projectile in the trench saturated by water.

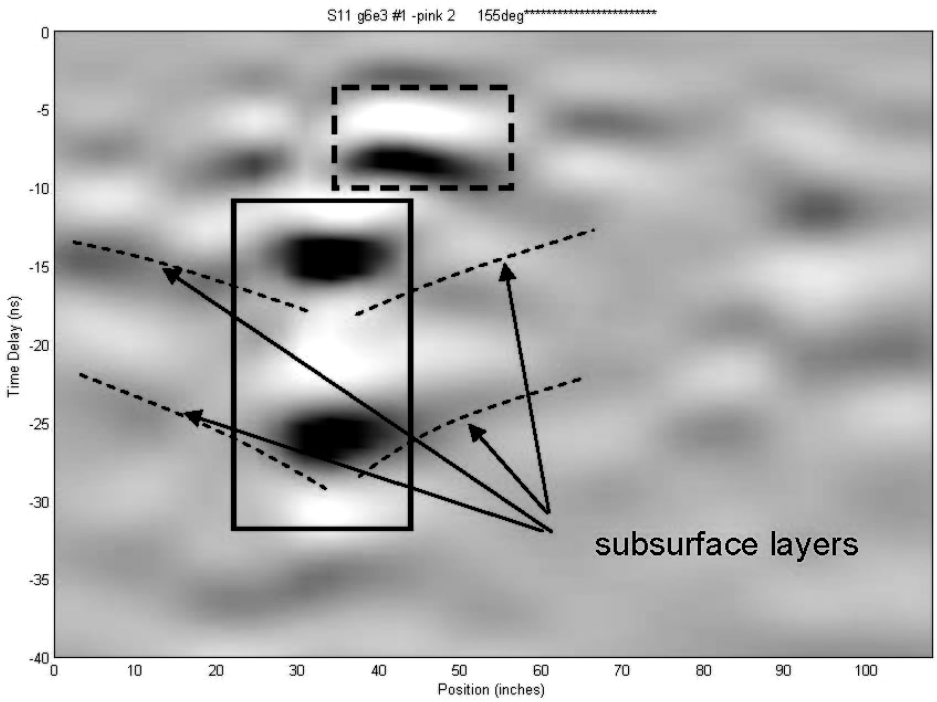


(b) S11 responses.

Figure A7. Processed data and extracted features of Item G6E3 (vertical 81-mm projectile) (Sheet 1 of 3).

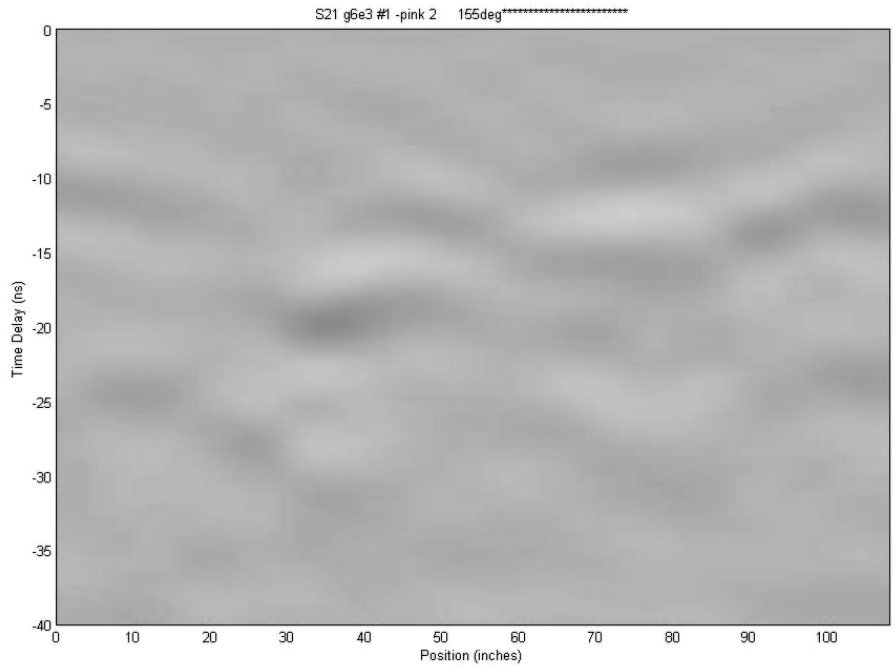


(c) S21 responses.

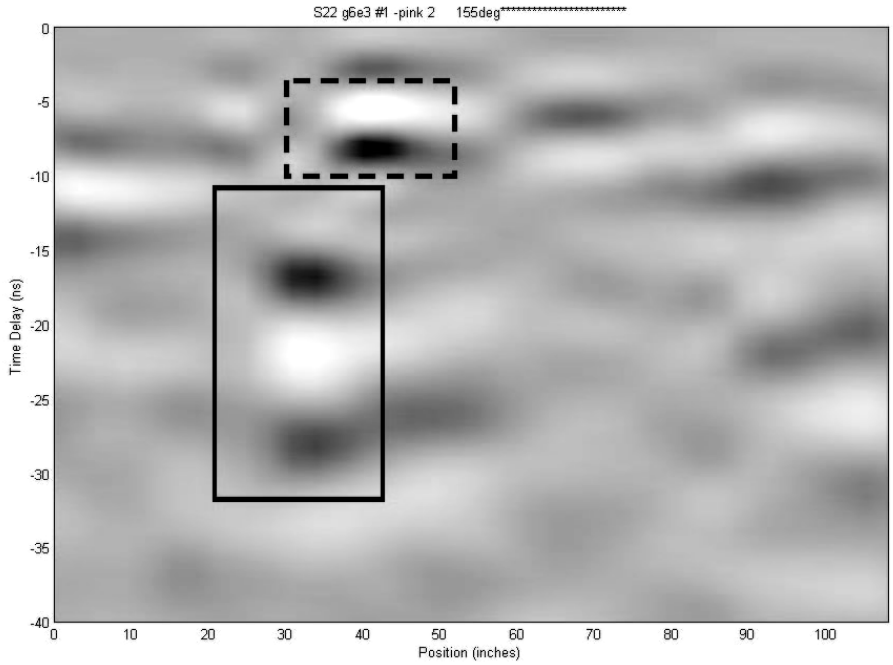


(d) S22 responses.

Figure A7. (Sheet 2 of 3).

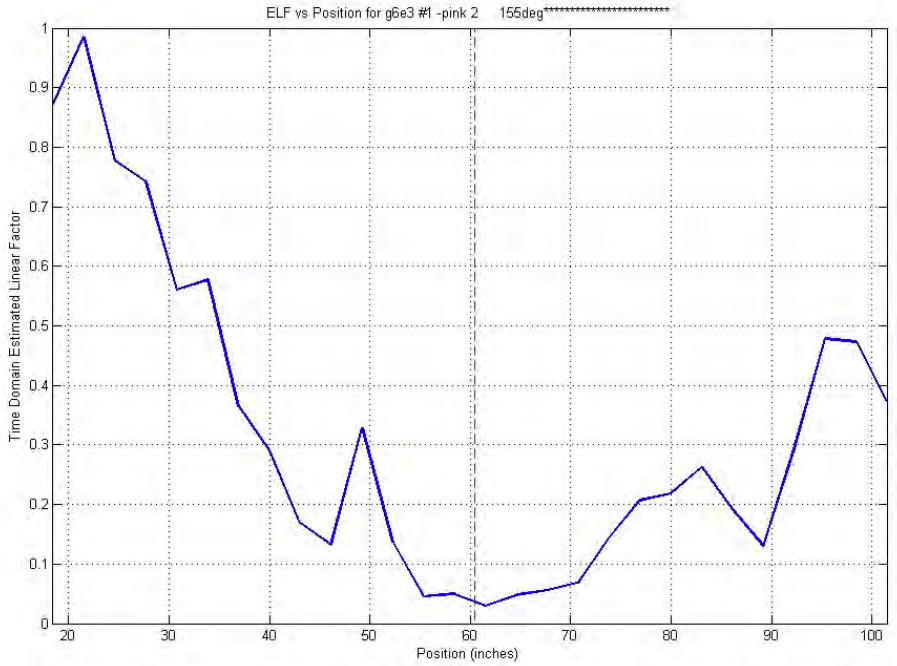


(e) Estimated linear factor extracted from late-time time-domain response.

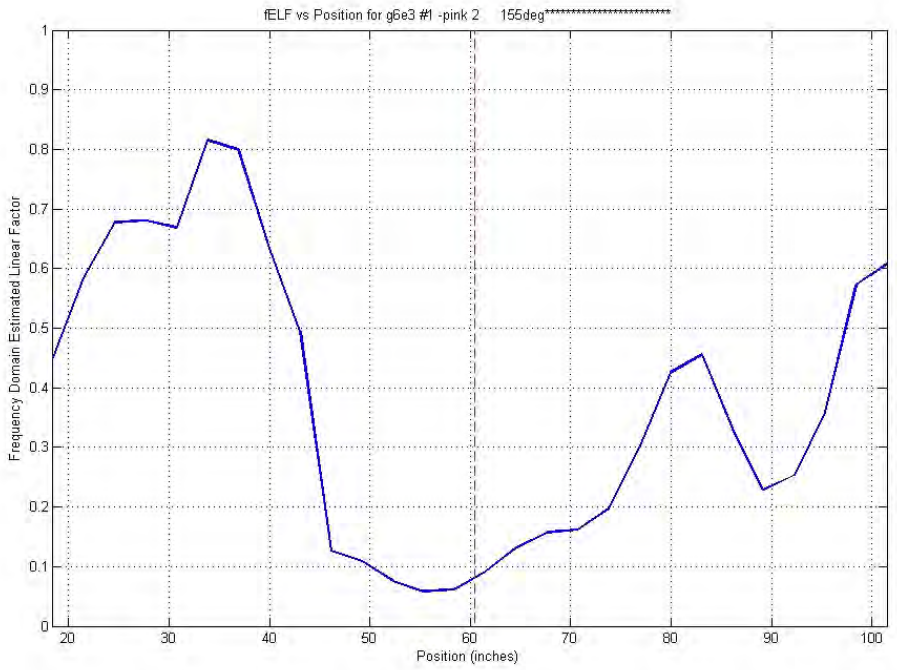


(f) Estimated linear factor extracted from late-time frequency spectrum.

Figure A7. (Sheet 3 of 3).

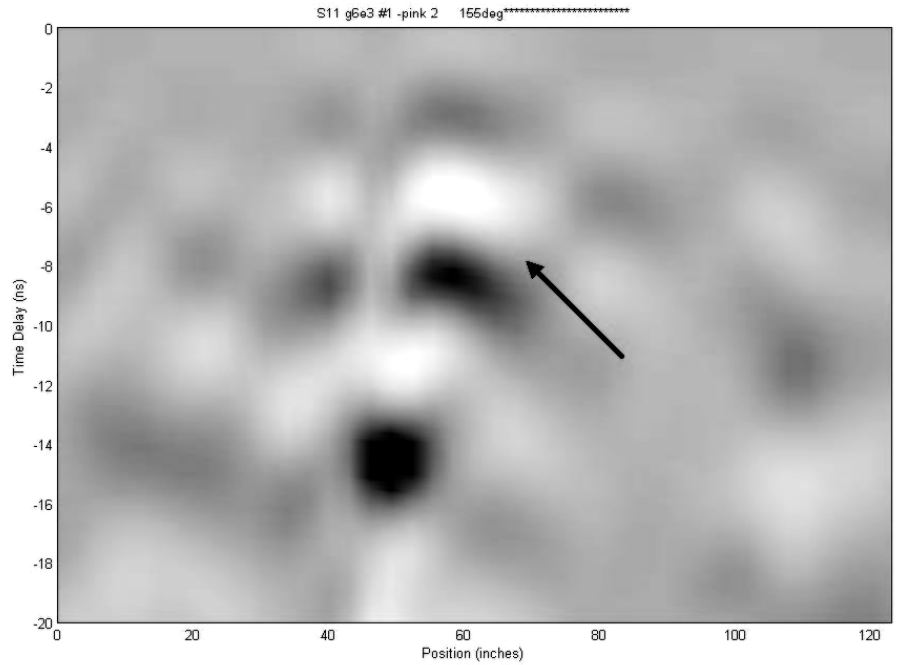


(a) S11 responses.

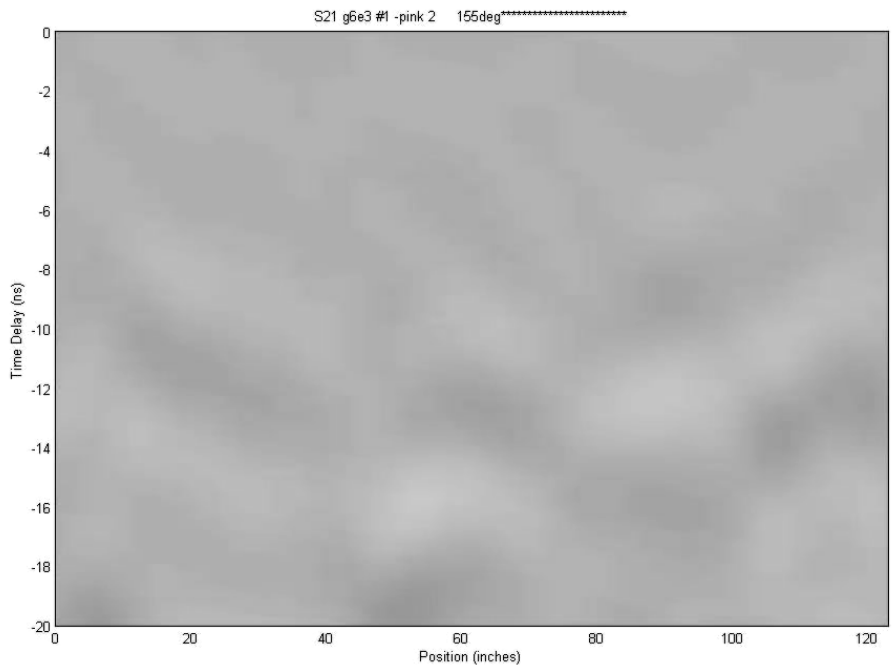


(b) S21 responses.

Figure A8. Processed responses and extracted features of Item G6E3P2 (40-mm projectile) (Sheet 1 of 3).

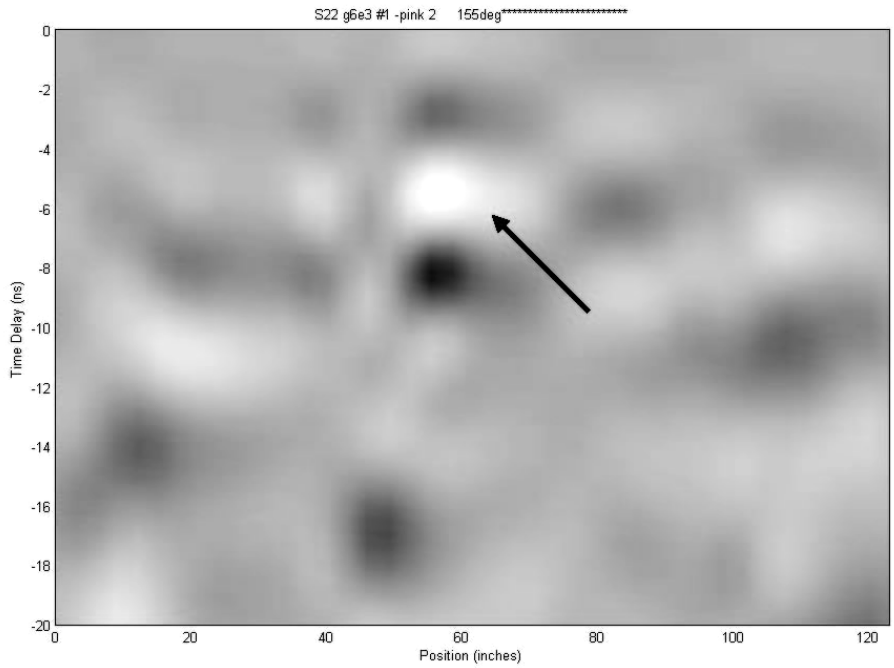


(c) S22 responses.

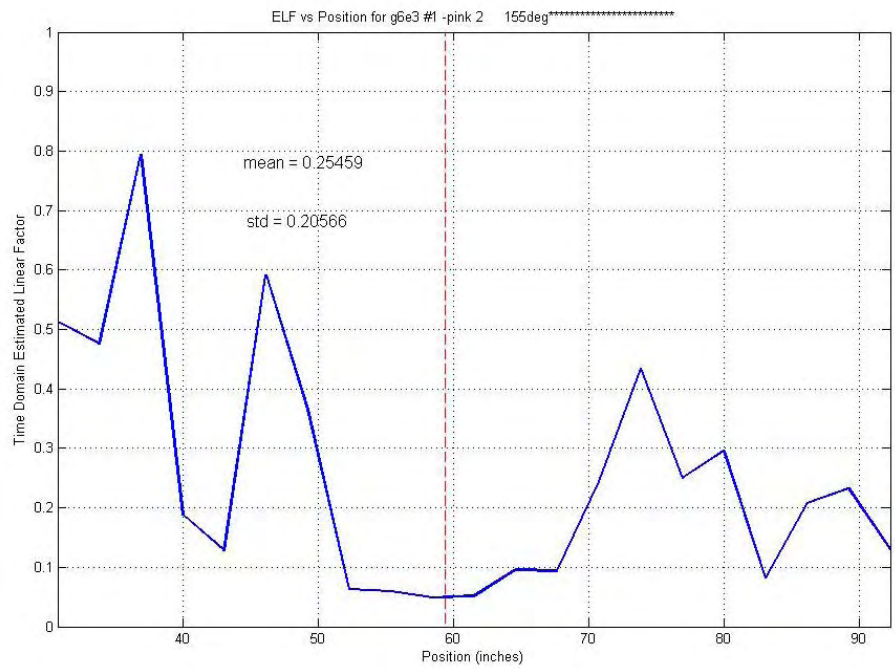


(d) Estimated linear factor extracted from late-time time-domain response.

Figure A8. (Sheet 2 of 3).

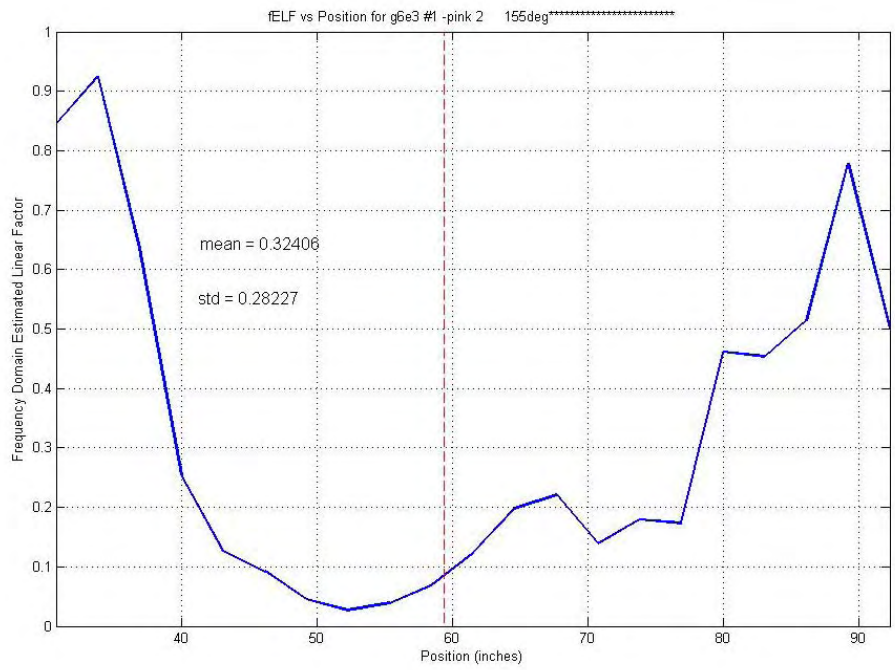


(e) Estimated linear factor extracted from late-time frequency spectrum.

Figure A8. (Sheet 3 of 3).

## A.3. Conclusions

The blind UXO classification conducted at Camp Lejeune, NC during March 13–14, 2006 showed consistent and improved UXO classification capability of technology based on a UWB fully polarimetric radar prototype. A length-to-diameter (L/D) ratio greater than 2.5 has been used as a criterion to designate UXO-like and non-UXO items in assessing the UXO classification performance of the GPR systems. The incorporation of magnetometer response was adopted from the lessons learned in the previous field test. Classification performance of the GPR system in this test site was estimated by ROC curve. A detection rate of 76.5 percent was achieved, while the false alarm rate was 18.5 percent. False alarms and missed UXOs are described in the text that follows.

(a) Non-ferrous metallic fragment (G6E1P1).

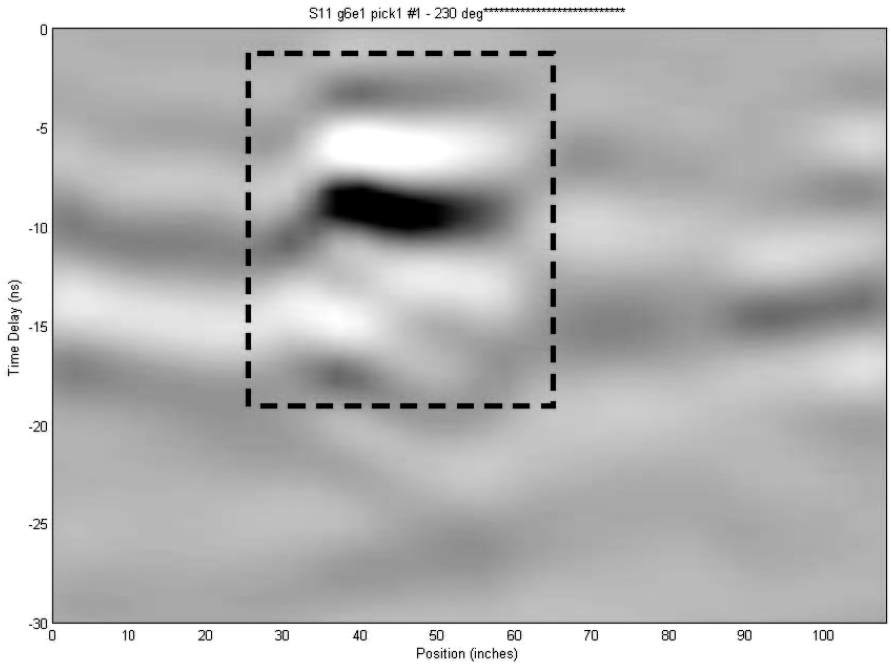


(b) S11 responses.

Figure A9. Processed data of Item G6E1P1 (non-ferrous metallic fragment) (Continued).

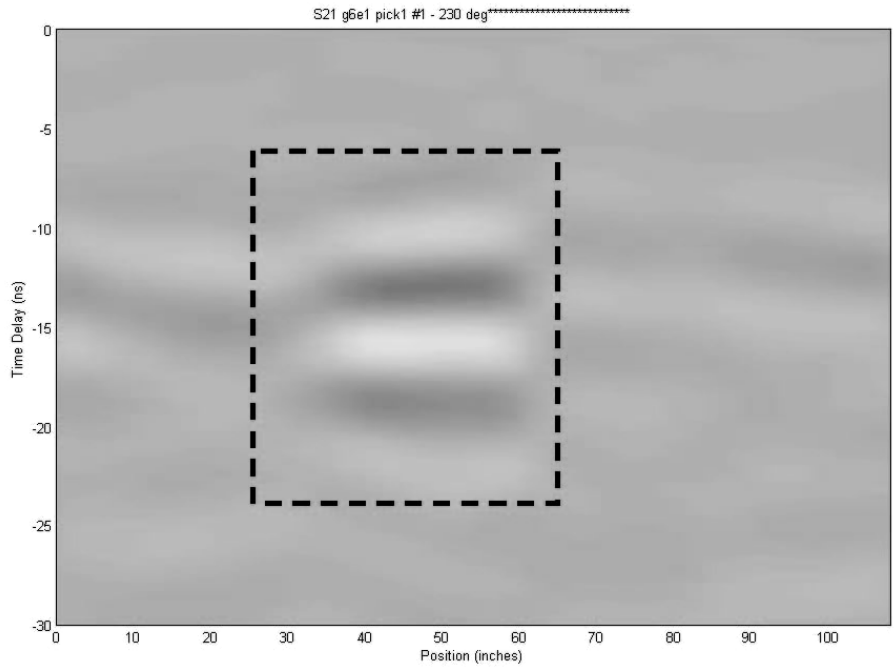


(c) S21 responses.

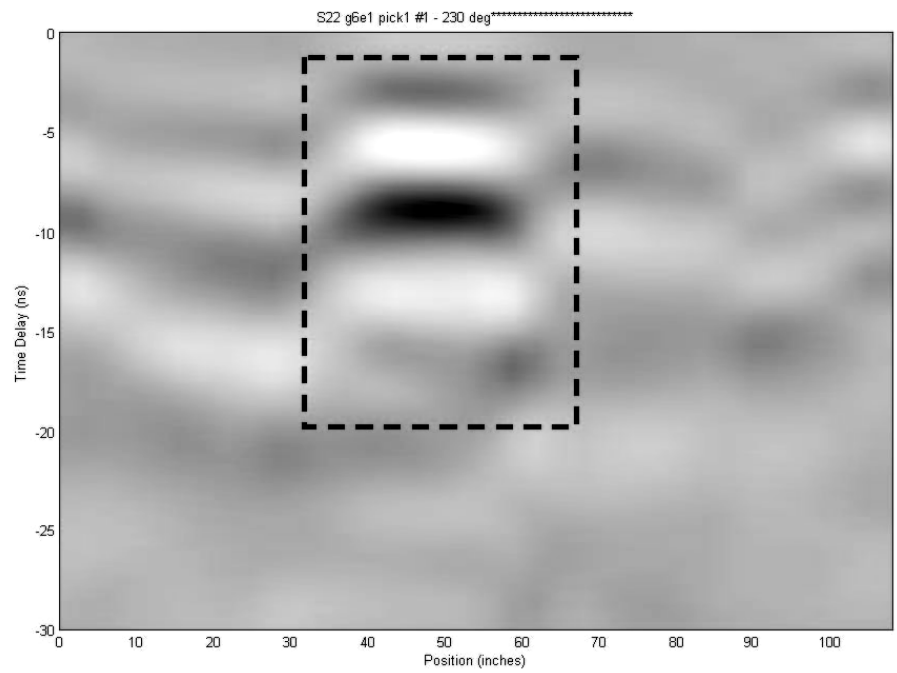


(d) S22 responses.

Figure A9. (Concluded).

Based on the data observed, this site appeared to have a high clutter level at the time of the survey due to a saturated water condition. Classification results could be greatly improved if all EMI, magnetometer, and radar data are effectively utilized instead of relying on radar signature alone. The proposed fusion procedure would analyze magnetometer and EMI data for magnetic dipole quality (strong or weak, ...) and property (orientation, ...). This information would then be used to guide the GPR survey and to modify the final classification (Chen and Peters 2002; Sun et al. 2005).

Tables A3 and A4 show the processed results and the orientation, length, and depth features for buried targets measured at Camp Lejeune. Table A3 contains classification results for the known target sets which were buried at the lower pad, while Table A4 includes results for the actual target sets located at the upper pad. The first column indicates the item number designated by the site preparation team. The UXO-like items, which are classified based on GPR features, are indicated by the number "1" in the third column. The Confidence Level associated with each classification is listed in the fifth column. This level is entered subjectively by the operator based on the signal level and the clarity of the features according to the criteria. Three estimate-linear-factors (ELF) are listed in the sixth, seventh, and eighth columns. The estimated orientation is listed in the ninth column with an ambiguity of +-180$^{o}$. The tenth column lists the extracted complex natural resonance (CNR) feature.

Tables A3 and A4 include the following fields:

- **Target ID** – Target number designated for Camp Lejeune test site.
- **Description** – Target description.
- **GPR ID** – UXO-like(1) /non-UXO(0) designation based on GPR features.
- **True ID** – UXO-like(1) /non-UXO(0) designation based on ground truth.
- **Confidence Level** – (H) high confidence (M) moderate confidence (L) low confidence.
- **Time ELF** – Estimated linear factor extracted from late-time time-domain response.
- **Freq. ELF** –Estimated linear factor extracted from late-time spectrum.
- **Early ELF** – Estimated linear factor extracted form early-time response.

- **ETO** – Estimated target orientation (azimuth).
- **CNR (MHz)** – Resonant frequency of the complex natural resonance.
- **DEP(nsec)** – Estimated target depth in nanoseconds.
- **Depth (cm), Dip, Azimuth** – known depth and orientation of buried targets.

Table A4. GPR Classification Results on the actual UXOs (Upper pad).

| Target ID | Description | GPR ID | True ID | Conf. | Time ELF | Freq ELF | Early ELF | ETO | CNR (MHz) | Dep. (nsec) | Depth (cm) | Mag | Mag. Dipole |
|---|---|---|---|---|---|---|---|---|---|---|---|---|---|
| G6D1 | Adapter | 1 | 0 | H | 0.85 | 0.65 | 0.75 | 145 | 150 | 13.6 | 0 | S | S |
| G6E1 | Adapter | 1 | 0 | H | 0.9 | 0.95 | 0.85 | 100 | 71 | 17.8 | 4 | S | S |
| G6E1 | Adapter | 1 | 0 | H | 0.8 | 0.8 | 0.4 | 30 | 220 | 2.8 | 2 | M | N |
| G6E2 | 25-mm cartridge | 1 | 1 | M | 0.6 | 0.9 | 0.7 | 60 | 160 | 5.8 | 10 | S | S |
| G6E1 | 5.56-mm brass and links | 1 | 0 | L | 0.8 | 0.8 | 0.75 | 32 | 400 | 8.5 | 0 | S | N |
| G6E1 | Adapter | 0 | 0 | L | 0.15 | 0.2 | 0.17 | 20 | 500 | 3.8 | 0 | M | S |
| G6D1 | 40 mm | 0 | 1 | M | 0.4 | 0.15 | 0.4 | 140 | 100 | | 0 | S | S |
| G6E2 | Adapter | 0 | 0 | M | 0.08 | 0.03 | 0.6 | 80 | 50 | | 5 | W | N |
| G6D1 | Nothing found | 0 | 0 | H | 0.3 | 0.25 | 0.08 | 120 | 130 | 2.6 | | S | S |
| G6D1 | Adapter | 0 | 0 | H | 0.5 | 0.3 | 0.2 | | 120 | | 0 | | N |
| G6D1 | Sabot half | 0 | 0 | H | 0.5 | 0.65 | 0.3 | 0 | 260 | | 0 | | |
| G6D2 | Metal washer | 0 | 0 | H | 0.15 | 0.25 | 0.35 | | 110 | | 6 | S | D |
| G6D2 | 0.5-cal bullet | 0 | 0 | H | 0.2 | | 0.5 | | | | 0 | M | N |
| G6E1 | Slap Flare | 0 | 1 | H | 0.55 | 0.15 | 0.19 | 150 | 550 | 1.89 | 2 | M | M |
| G6E1 | 40 mm | 0 | 1 | H | 0.17 | 0.18 | 0.2 | 82 | 430 | | 7 | | |
| G6E1 | 40 mm | 0 | 1 | H | 0.1 | 0.74 | 0.13 | 75 | 400 | 1.9 | 10 | S | N |
| G6E1 | Frag | 0 | 0 | H | 0.35 | 0.2 | 0.13 | 10 | 60 | 13 | 10 | M | N |
| G6E2 | Fins 105 heat | 0 | 0 | H | | | | | | | 0 | M | N |
| G6E2 | Link from track | 0 | 0 | H | | | | | | | 10 | S | N |
| G6E2 | Adapter | 0 | 0 | H | 0.1 | 0.08 | 0.06 | | 110 | | 3 | W | N |

## A.4. References

Chen, C.-C. 2002. *Fort Ord site UXO classification demonstration using fully polarimetric GPR*. The Ohio State University ElectroScience Laboratory Technical Report 737990-9.

Chen, C.-C., and L. Peters, Jr. 2002. *Application of fully polarimetric ground penetrating radar for subsurface UXO classification*. The Ohio State University ElectroScience Laboratory Technical Report 737990-final.

Higgins, M., and C.-C. Chen. 2000. *Data processing results for UXO classification using UWB Full-Polarization GPR System*. The Ohio State University ElectroScience Laboratory Technical Report 737990-1.

_____. 2001a. *GPR UXO classification results of the Blossom Point Site*. The Ohio State University ElectroScience Laboratory Technical Report 737990-6.

_____. 2001b. *GPR UXO classification results for Jefferson Proving Ground V*. The Ohio State University ElectroScience Laboratory Technical Report 737990-8.

Sun, K., K. O'Neill, F. Shubitidze, I. Shamatava, K. D. Paulsen, C.-C. Chen, and H. S. Youn. 2005. Highly contaminated UXO sites: Combination of GPR and EMI for discrimination of clustered scatterers. In *Symposium on the Application of Geophysics to Engineering and Environmental Problems, April 2005, Atlanta, GA*, 1156–1165.

# Appendix B: Witten Technologies GPR Results for Camp LeJeune, NC[1]

A ground penetrating radar survey was conducted from March 13 to 17, 2006 on a former shooting range at the Camp LeJeune U.S. military facility in North Carolina. The goal was to map the locations of unexploded ordnance designated for cleanup.

A 400-MHz, 16-channel radar array system was used to assess a total of 13,360 $m^2$ during 5 days of surveying. Radar traces were collected with 256 time samples in a 62-ns-long time window. The areas were covered on a 0.05-cm (trigger or station spacing) by 0.08-cm (channel spacing) grid.

The data were filtered, merged with the precise geometry data, and parts were migrated. Depth slice movies were created for each area and preliminary analyses of the emplaced targets were conducted in some of the areas.

The preliminary data analyses performed for this report were only able to scratch the surface of what may be possible with this data set. Further, more detailed analysis of the data is required to make any conclusions about the true value of single-polarity, dense 3D radar data to detect and/or classify UXO targets alone or in conjunction with other data sets, such as electromagnetic induction.

## B.1. Field survey

The ground penetrating radar (GPR) survey was conducted from March 13-17, 2006. This chapter discusses the survey location, data coverage, and radar array system used.

### B.1.1. Location and site description

The GPR survey was conducted on the Camp LeJeune U.S. military facility. The goal was to map the locations of unexploded ordnance (UXO) on the former shooting range (Figure B1) designated for cleanup.

[1] Witten Technologies, Inc., 1365 Windsor Harbor Drive, Jacksonville, FL 32225.

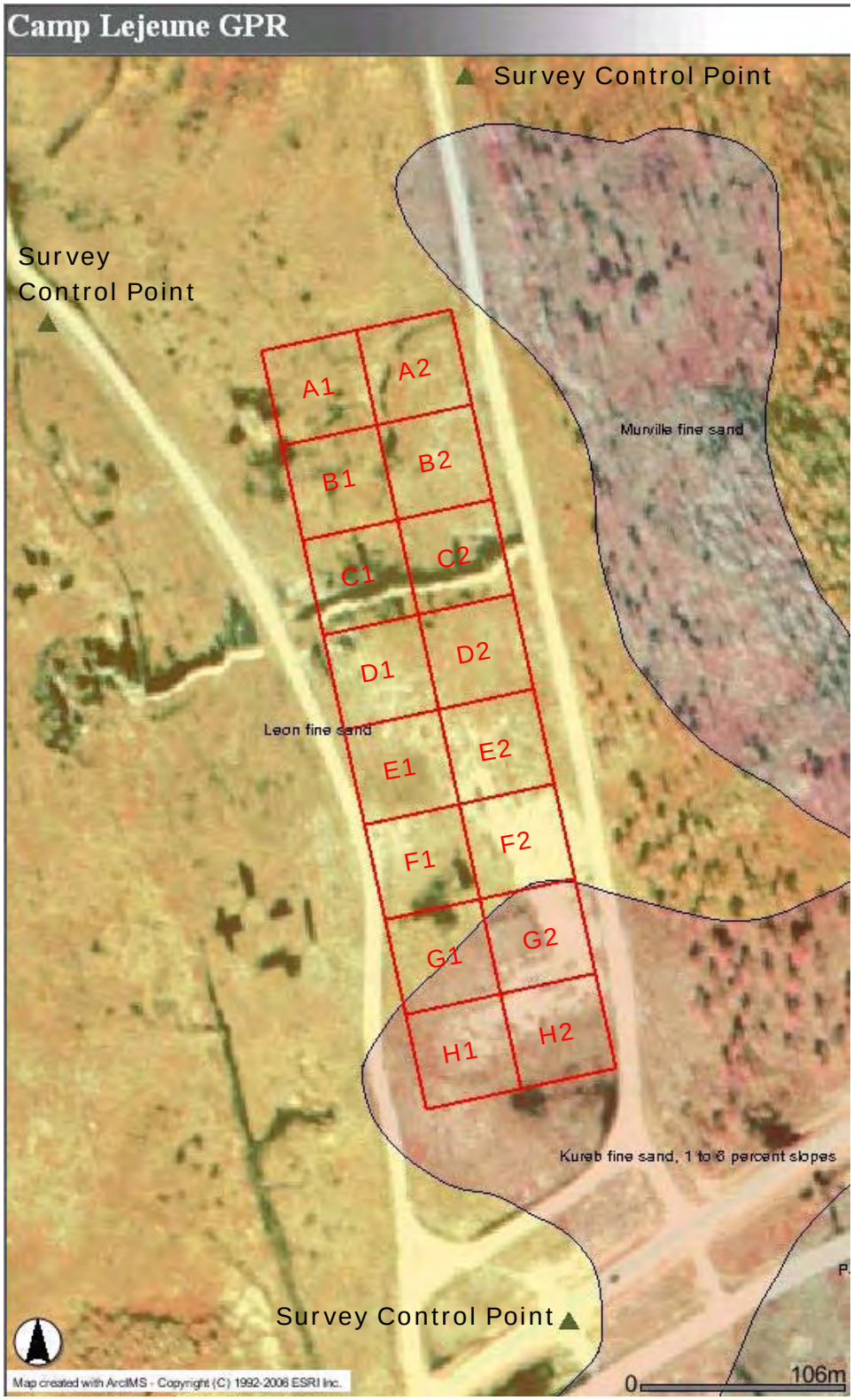


Figure B1. Site overview map showing the access roads, survey control points, and survey grid.

The site subsurface is made up of fine sand, which is covered by low-cut grass-like vegetation (Figure B2). The overall elevation changes throughout the site are small, but the surface is rather irregular at the order of feet. Numerous small hills and valleys cause a challenge for the positioning system (see details in Section B.1.3.1). During the survey, only a small amount of night precipitation occurred and most of the D and E grids were rather dry. However, local topographic lows in grid cells A and B had some exposed wet areas, making it impossible to access certain areas with the positioning system or an SUV.

Figure B2. Photo of site illustrating the irregular surface, low-cut vegetation, and sediment soils.

### B.1.2. Coverage

A total of 13,360 $m^2$ were covered uniquely with the 400-MHz CART imaging system during 5 days of surveying (for a detailed breakdown by area, see Table B1). Each CART path is about 123.75 cm wide with 16 channels spaced 8.25 cm apart. Trigger spacing is 5 cm. This leads to about 250 radar traces per square meter.

Table B1. Grid areas covered by radar survey.

| Areas | Survey Direction | Coverage [m$^2$] | Coverage [ft$^2$] | Profile Numbers |
|---|---|---|---|---|
| E1 and E2 | EW | 5,178 | 55,736 | 1-100 |
| D1 and D2 | EW | 5,489 | 59,083 | 99-207 |
| D2 | NS | 2,442 | 26,285 | 208-261 |
| A1, A2 and B2 | Mixed | 251 | 2,702 | 262-267, 900-901 |
| | **Totals:** | **13,360** | **143,806** | |

### B.1.3. System and acquisition procedures

The 400-MHz CART imaging system described in Section B6 was used with the following data acquisition parameters:

- Number of time samples: 256
- Sampling frequency: 4129.433105 MHz
- Trigger spacing: 0.05 m
- Channel spacing: 0.0825 m
- Timewindow: 61.993982 ns
- Stacks: 1

For areas E and D, the CART system would drive east to west the full width of the site (approximately 100 m), collecting radar profiles approximately 50 m long (compare to Figures B3 and B4). After that the system turned around and drove west to east parallel to the initial paths, aiming for an overlap of 30 to 60 cm. Grid area D2 was also surveyed with profiles oriented north and south; this surveyed area is also referred to as the D90 area (Figure B5). In grid areas A1, A2, and B2, only a few individual profiles were surveyed to cover as many known targets as possible in the time remaining to complete the survey (Figure B6). To determine the survey direction of a particular profile, the starting point was marked with a circle that had an X in it and was the same color as the survey path outline.

#### *B.1.3.1. Laser positioning system*

Positioning information was collected with a survey-grade robotic total station that locks on to a prism located in the center of the radar deck (Figure B7). The station tied into the three existing survey control points shown in Figure B1, so all coordinates should correspond to client maps. On flat surfaces this usually provides centimeter-accuracy positioning data.

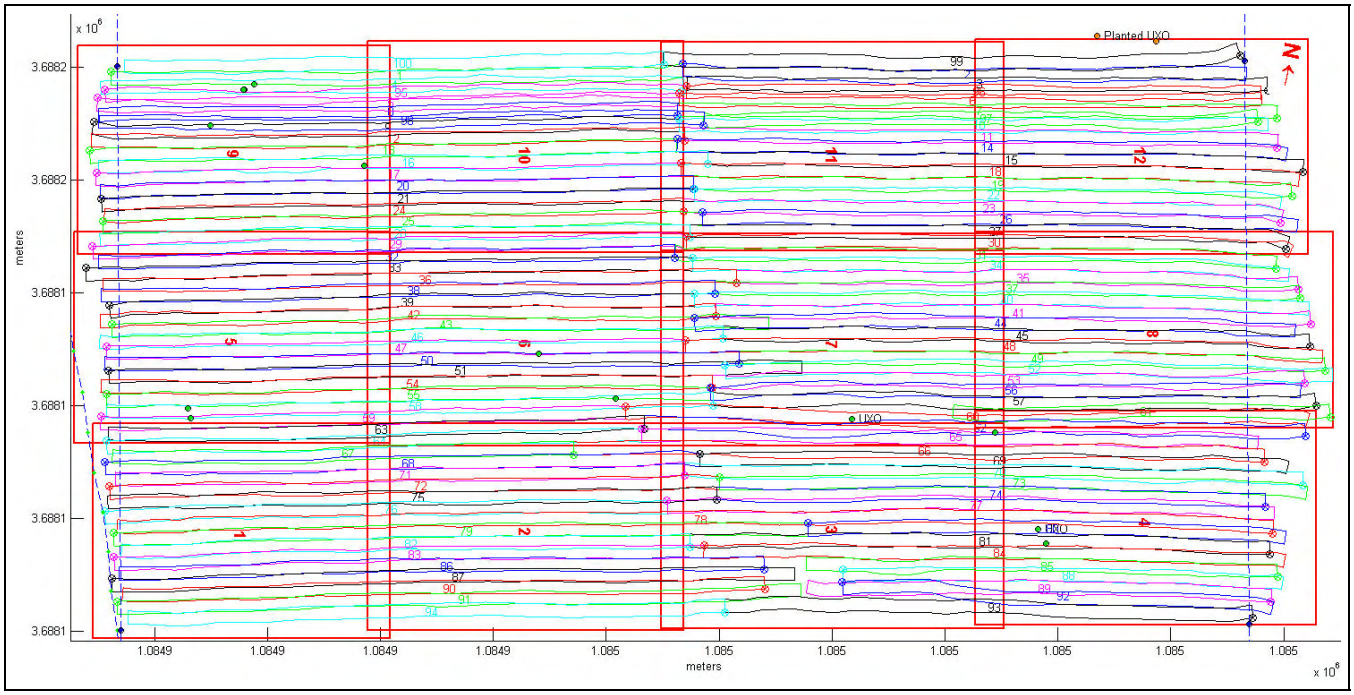


Figure B3. Close-up map of grid areas E1 and E2, showing the actual radar paths in more detail. Red rectangles are processing subdivisions called "chunks" (see text for details).

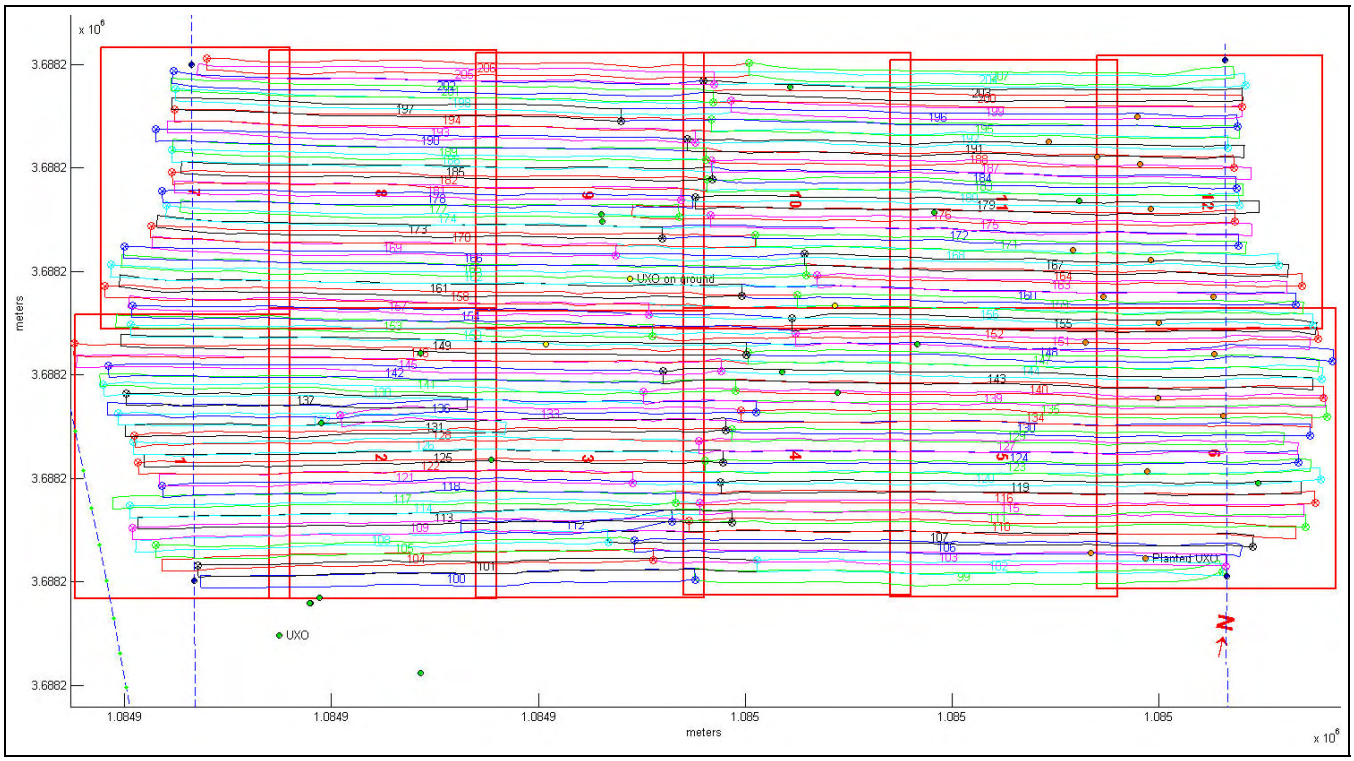


Figure B4. Close-up map of grid areas D1 and D2, showing the actual radar paths in more detail. Red rectangles are processing subdivisions called "chunks" (see text for details).

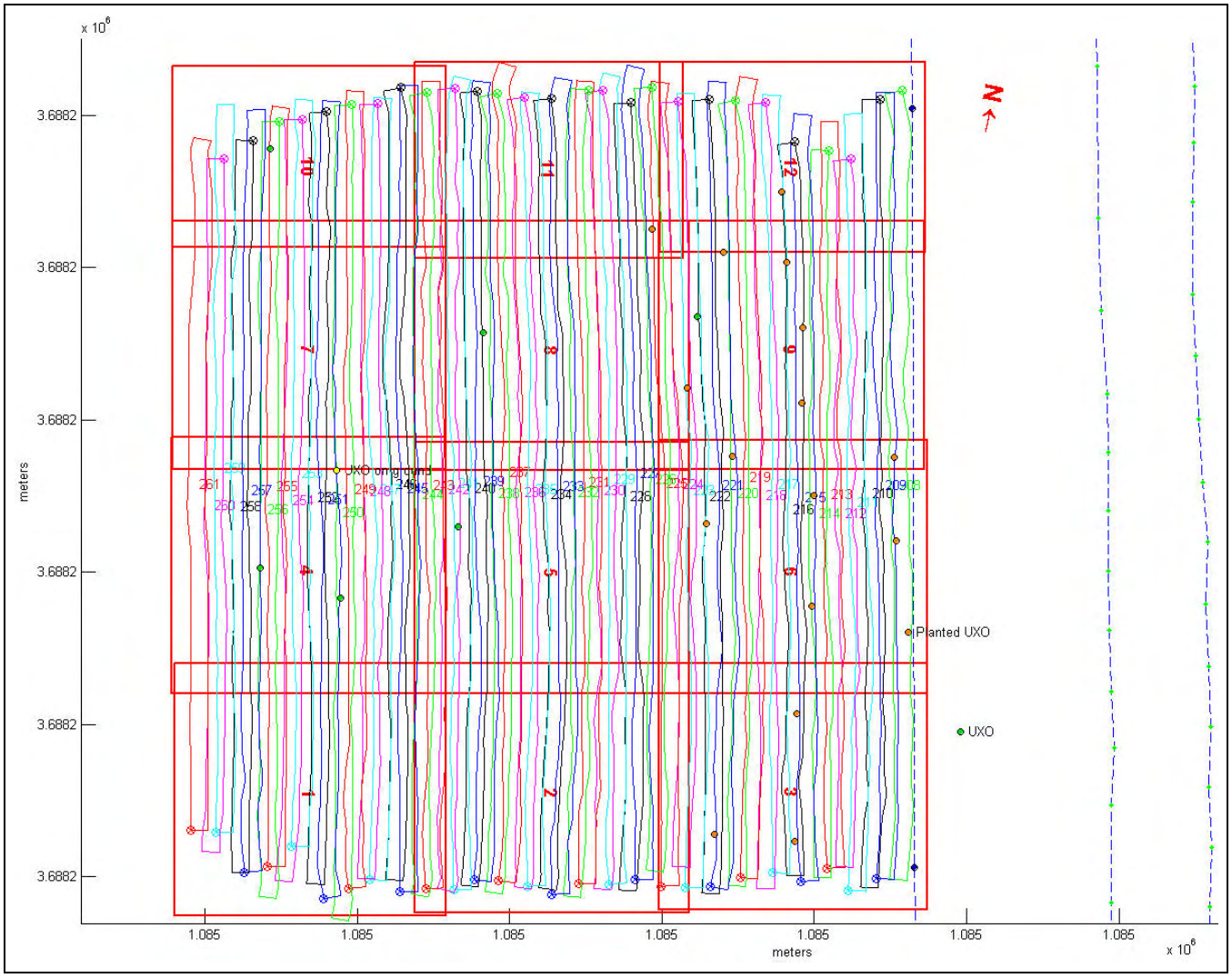


Figure B5. Close-up map of grid area D2 surveyed in North and South directions (D90), showing the actual radar paths in more detail. Red rectangles are processing subdivisions called "chunks" (see text for details).

However, due to the rough topography (Figure B2) the assumption that the pole is vertical to the ground is violated. The following plots (Figures B8 and B9) illustrate the theoretical deviations a tilted 2-m-tall prism pole would have on the measured depth and horizontal position and can be used to estimate positioning errors. Figure B8 illustrates the kinds of deviations from the correct elevation (in millimeters) one can expect for a tilted 2-m prism pole. Figure B9 shows the deviation (in millimeters) from the correct x coordinate value considering a tilted pole in the x-z plane for various prism pole heights. Only positive x tilt values from 0 to 15 degrees are shown because negative values are mirror images of those values. Obviously, any tilt in the y direction does not impact the x coordinate.

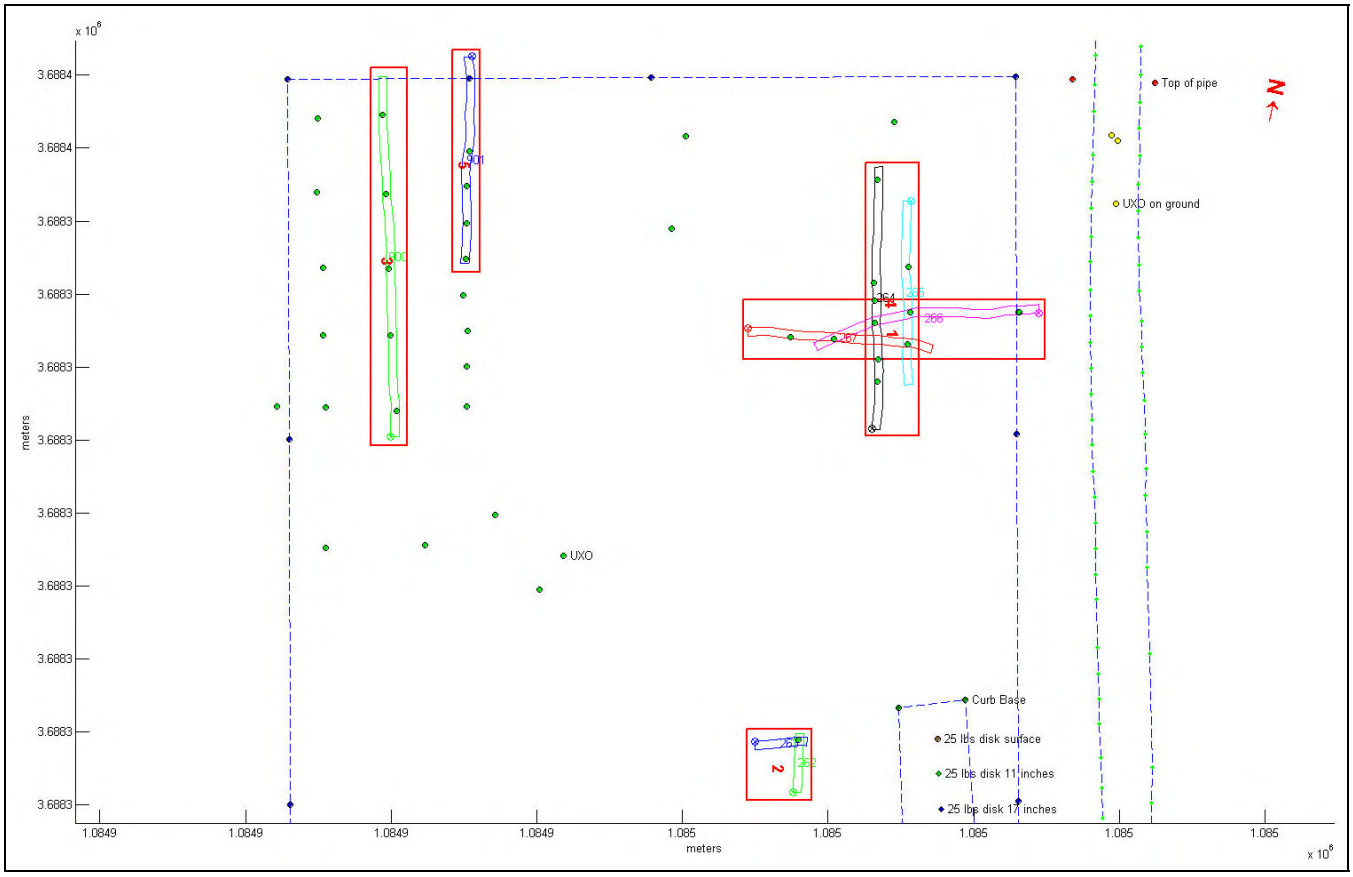


Figure B6. Close-up map of grid areas A1, A2, and B2, showing the actual radar paths in more detail. Red rectangles are processing subdivisions called "chunks" (see text for details).

Figure B7. Robotic total station tracking the prism on top of a pole mounted in the center of the 400-MHz radar deck.

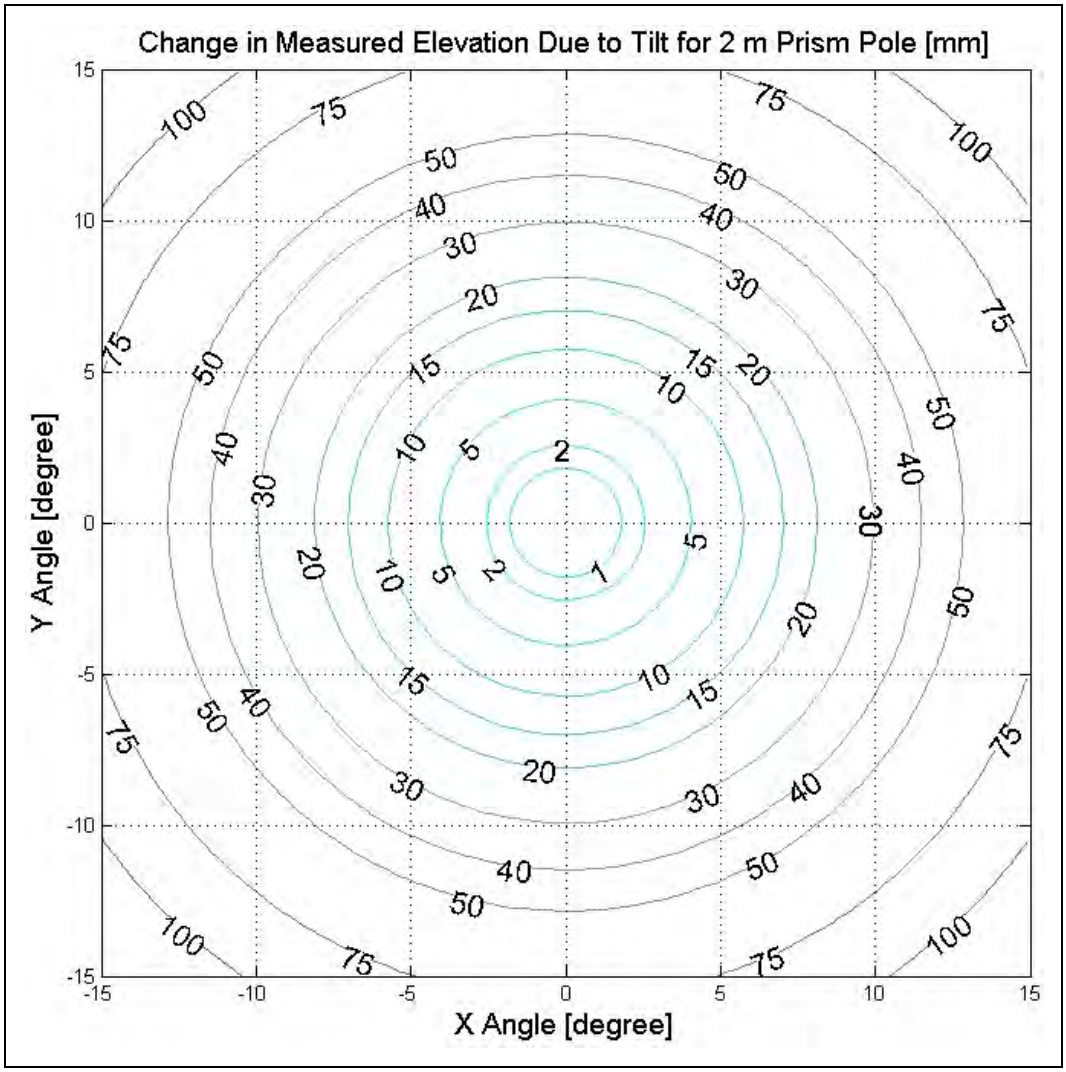


Figure B8. Calculated change in measured elevation (in mm), due to a tilt of the 2-m prism pole for various tilt angles in the x and y direction.

The location correction increases with increasing pole height. Elevation changes are smaller than the changes of the horizontal coordinate for a given tilt angle and pole heights above 0.25 m. This is particularly true for a pole height of 2 m, which was used for most of the RT surveys in this project. Witten Technologies, Inc. (WTI) is in the process of developing a tilt sensor system to measure the prism pole tilt during RT surveys to correct for this problem in the near future.

## B.2. Radar processing and visualization

Raw radar data are recorded in standard Mala file format, i.e. *.rad ASCII header files and corresponding binary *.rd3 data files. The positioning data are recorded in *.raw files, a common land surveying format.

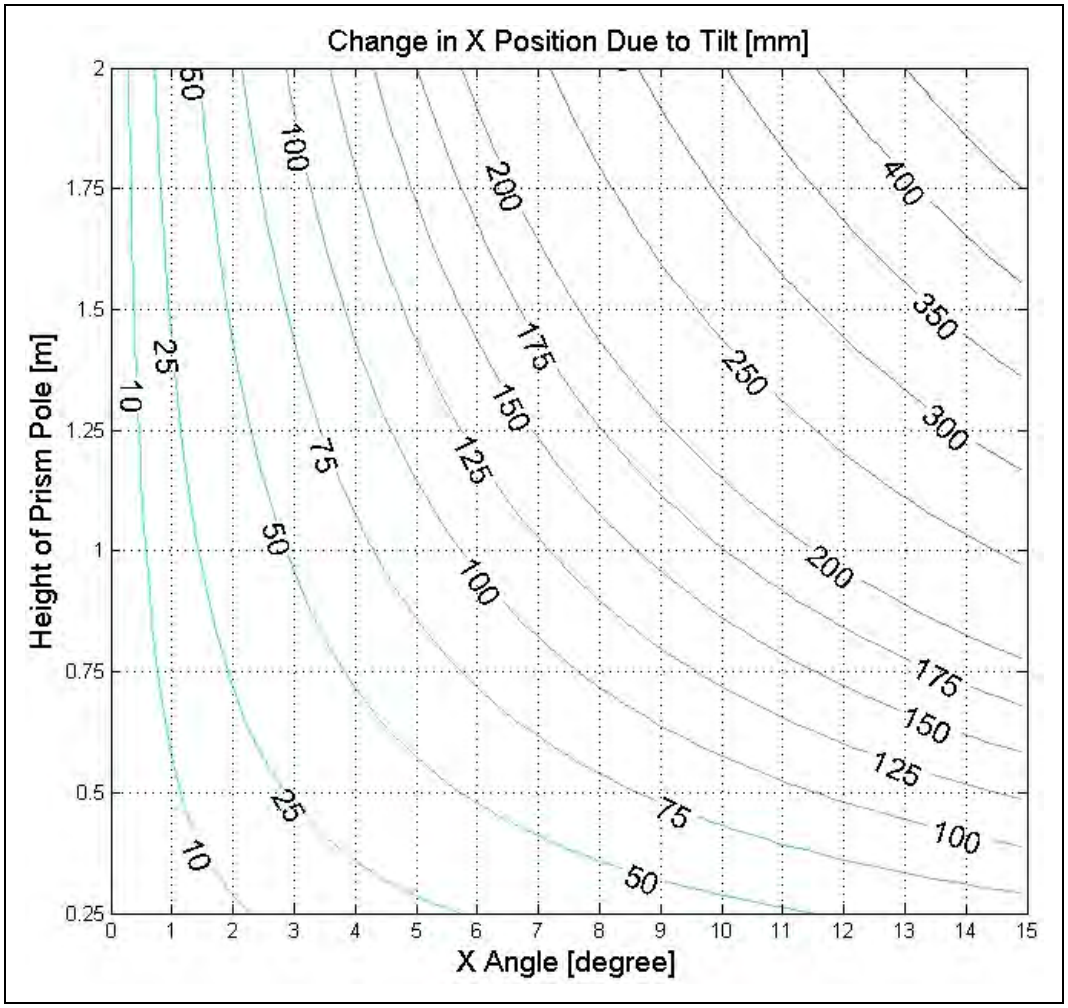


Figure B9. Change in measured x position (in mm), due to a tilt of prism pole in the x direction (X-Z plane) for various prism pole heights.

Initially the positioning data (survey paths and additional features such as roads, grid corner points, UXO locations, etc.) are plotted as shown in Figure B10 and corrected if necessary. For this survey, the actual survey paths showed more than usual horizontal deviations, which are due to the rough topography of the field as discussed in Section B.1.3.1. Since it is known that the system didn't move significantly left and right along its path (rather the prism pole is tilted due to different local topography, e.g., different elevation under each system wheel), it was justified to smooth those paths slightly. The resulting radar profile paths are plotted in Figures B3 to B6. Note the north arrows on those maps, because the maps are rotated by 12 degrees out of north for plotting purposes only.

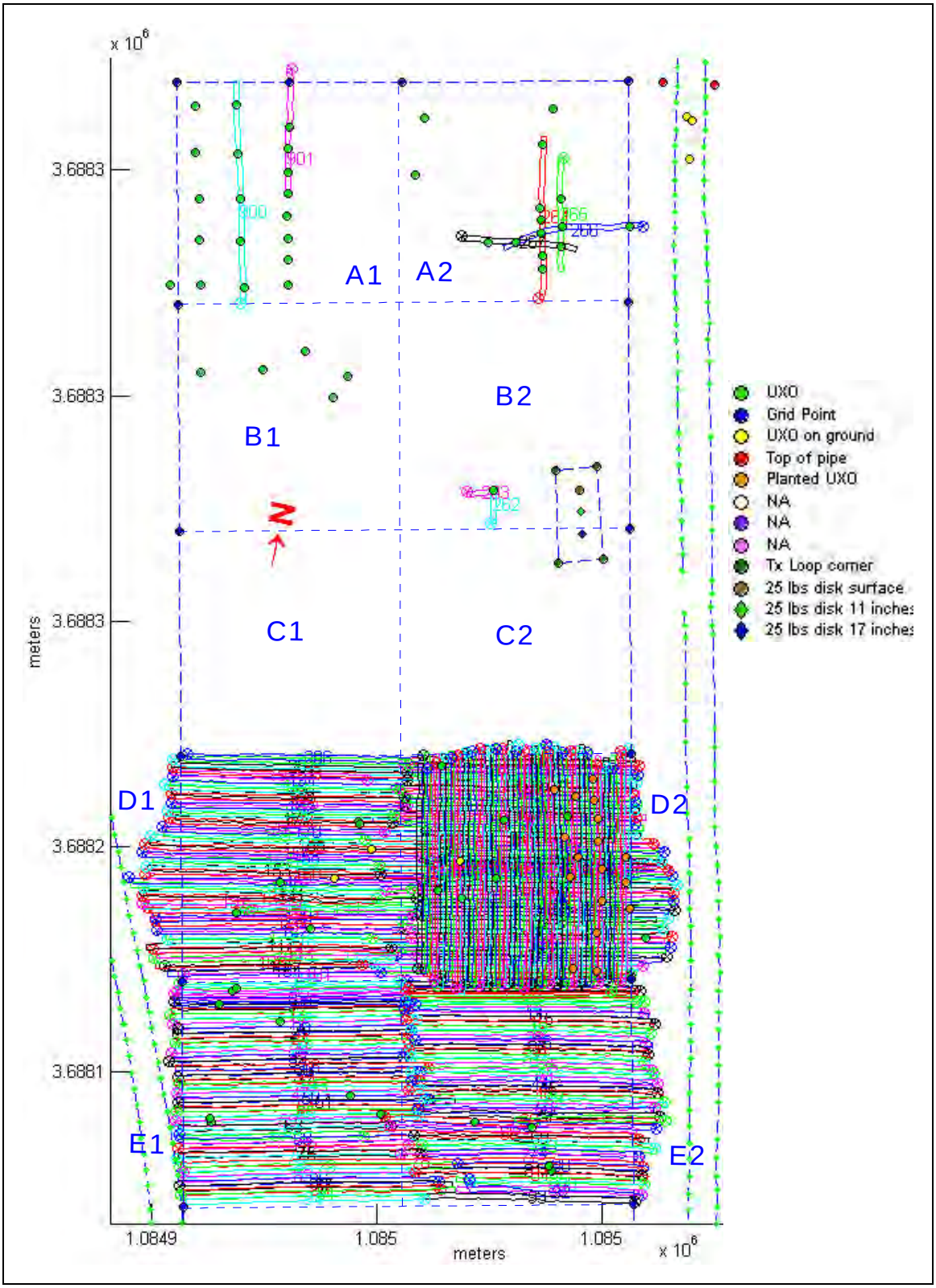


Figure B10. Map indicating the location of all 269 individual radar profiles collected. Blue dashed lines indicate survey grid locations (also labeled in blue and see Figure B1). Blue-dashed lines with green symbols are the edges of the dirt roads on either side of the survey area. All other symbols are indicators for subsurface objects according to the legend on the right.

The next step is to accumulate all radar profiles for each of the four areas (Figures B3–B6) into one file and associate each trace with its proper coordinates. At this point the data are on an irregular grid due to the nature of the paths, but each trace is located properly. Those combined irregularly gridded radar data files have the following approximate file sizes (Table B2):

Table B2. Sizes of radar data files.

| Areas | Survey Direction | Coverage [$m^2$] | Coverage [$ft^2$] | Profile Numbers |
|---|---|---|---|---|
| E1 and E2 | EW | 5,178 | 55,736 | 1-100 |
| D1 and D2 | EW | 5,489 | 59,083 | 99-207 |
| D2 | NS | 2,442 | 26,285 | 208-261 |
| A1, A2 and B2 | Mixed | 251 | 2,702 | 262-267, 900-901 |
| | **Totals:** | **13,360** | **143,806** | |

- Area E: 875 MB
- Area D: 980 MB
- Area D90: 460 MB
- Area AB: 45 MB

At least three versions of those files were created for each area, depending on their stage of pre-processing. Files are named as follows:

- prep_shift*
  a. raw radar traces as recorded except that the first breaks are properly aligned
- prep_mfilt*
  b. prep_shift* files filtered with a matchfilter to equalize the difference in channels
- prep_mfilt_custom*
  c. prep_shift* files filtered with a different matchfilter to equalize the difference in channels

Those files are not practical for further processing due to their large size; they are typically just used to assess the data quality, the effectiveness of the pre-processing, to determine the wavespeed of the site, and to set up the migration. The pre-processed files are reduced to a manageable file size by dividing the survey areas into rectangular *chunks* (red rectangles in Figures B3–B6). In preparation for the migration the irregularly gridded data in the prep* files, data are resampled onto a regular 10-cm grid for

each chunk (file size typically < 20 MB). A 5-cm grid was decided against due to positioning issues. The file size was kept smaller for faster processing and visualization. Typically only the best looking pre-processed data set is resampled into the regular grids; however, for this survey, all three prep* files mentioned above were gridded.

Each chunk can then be migrated individually. Note that the chunks have certain overlap to make the migration results match and to create seamless-looking migrated 3D radar images of the whole area. The current migration algorithm is a single wavespeed algorithm. The wavespeed $v$ is expressed in terms of the relative dielectric constant $\varepsilon_r$, which is related to $v$ via $c$ = 2.9979e08 m/s being the speed of light in vacuum:

$$v = \frac{c}{\sqrt{\varepsilon_r}}$$

During the velocity analysis, large spreads of $\varepsilon_r$ were found throughout each area.

- Area E: $\varepsilon_r$ from 7 to 10.5, with 14.5 at greater depth
- Area D: : $\varepsilon_r$ from 4 to 11
- Area AB: $\varepsilon_r$ from 4 to 22

Variations of $\varepsilon_r$ are probably due to differences in moisture content, in different areas and at different depths. One limitation of this project was that one average $\varepsilon_r$ had to be determined for the whole survey area for migration. For the E and D grids, the value for $\varepsilon_r$ was consistently found to be 4 to 5 in the top 0.5 m and 8 to 12 below that level. Therefore, a two-layer velocity model would have been better for these grids. There is no quick way to overcome this shortcoming; therefore, the E and D areas were migrated with an average $\varepsilon_r$ = 8. For eastern profiles collected in grid A2, $\varepsilon_r$ = 22 was used, appropriate for wet ground conditions.

Consulting Figure B11, it is fair to say that the UXO depths could be overestimated by about 40 percent if the true local $\varepsilon_r$ is as low as 4 and underestimated by about 25 percent if the local $\varepsilon_r$ is as high as 14.5, not considering a multi-velocity scenario or the wet areas.

Most plots will indicate the $\varepsilon_r$ used to calculate the shown depth. All figures in Section B4 show the corresponding time, depth, and relative

dielectric constant. In general, $\varepsilon_r$ = 22 was used for the figures in Section B4, $\varepsilon_r$ = 4 or 5 for the shallower targets and $\varepsilon_r$ = 9 for the deeper targets investigated in the figures in Section B5. The two $\varepsilon_r$ values used clearly correlate with the target depth; shallow targets are in a rather dry top layer and deeper targets are found in a layer with increased moisture content.

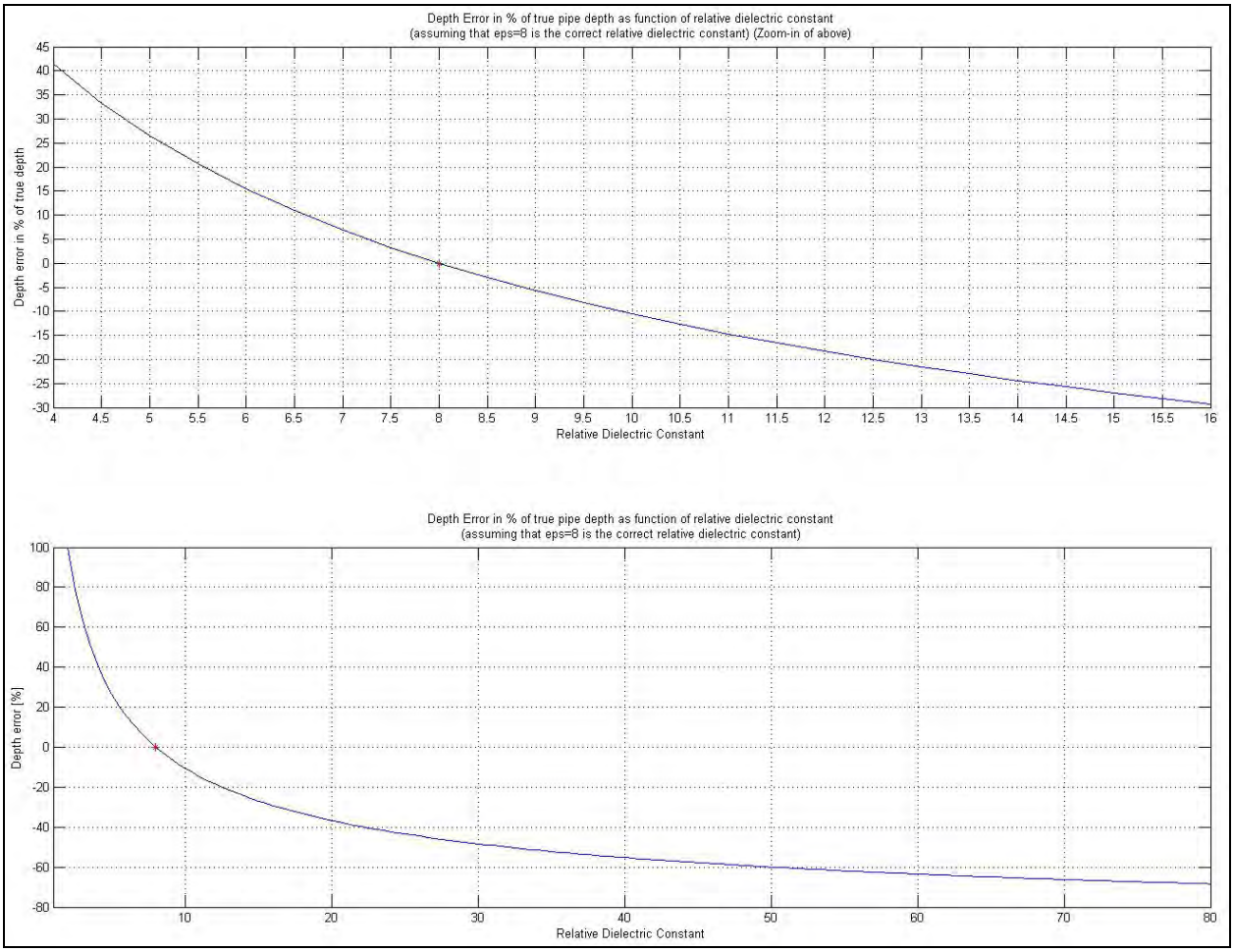


Figure B11. Relative depth errors in % of true RT picked pipe depth as a function of selected relative dielectric constant $\varepsilon_r$ assuming that $\varepsilon_r$ = 8 is the correct relative dielectric constant. (Bottom) $\varepsilon_r$ ranges from 1 to 80. (Top) Zoomed-in version of (Bottom), $\varepsilon_r$ ranges from 4 to 16.

## B.3. Example data visualizations

The gridded or migrated data can be visualized in many ways: vertical or horizontal sections, or 3D plots. Typically the most useful way to visualize those large-scale radar images is in depth slice movies. One Quicktime movie was created for each area for each of the regularly gridded pre-processed data files (Section B2).

Since it is not possible to visualize the 3D nature of the data set in this document, what the movies show is summarized with two selected depth slices (Figures B12 and B13). Each area is sliced horizontally in 1-cm increments. At the shallow depth, the images show a striped or checkerboard pattern, due to combining the irregular topography with the back and due to acquisition directions (i.e., the up-and-down of the radar antenna deck over small hills and valleys are reversed for adjacent profiles).

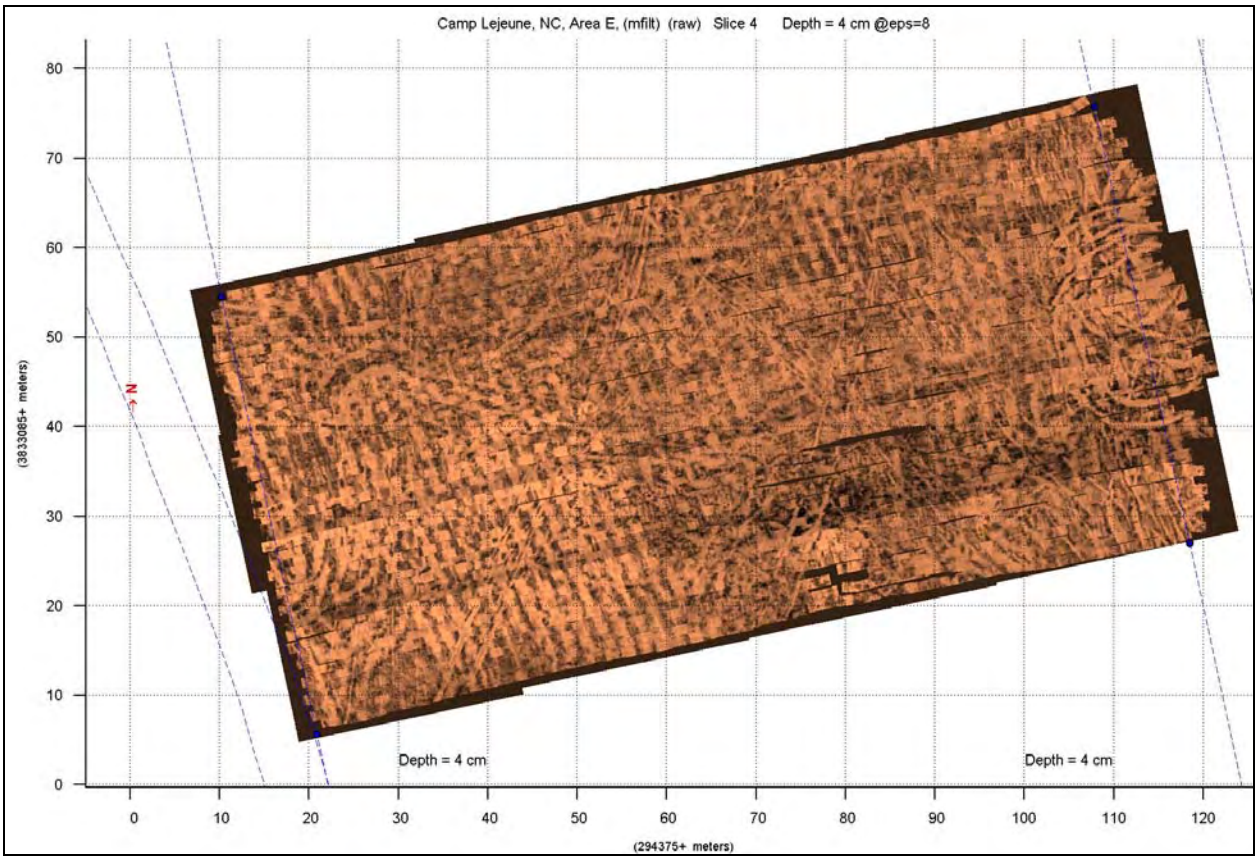


Figure B12. Depth slice at 4 cm for area E using mfilt filtering.

At around the 20-cm depth, the movies become more focused and show geological detail, vehicle tracks, and point objects. Some of those point objects correspond to flagged UXO locations, while others do not, which makes them candidates for further evaluation. This further analysis needs to develop criteria to distinguish between UXO and geological "clutter." The depth slice movies show that in order to analyze individual UXO locations or suspect locations one has to zoom in significantly. To address this issue, a feature was added to the software that creates the plots shown in Sections B4 and B5. The ground truth information, provided by Sky Research, was loaded into the software as an additional layer. Users can

now zoom in to known locations and analyze them in detail by identifying a suitable depth slice and location to plot two perpendicular vertical sections.

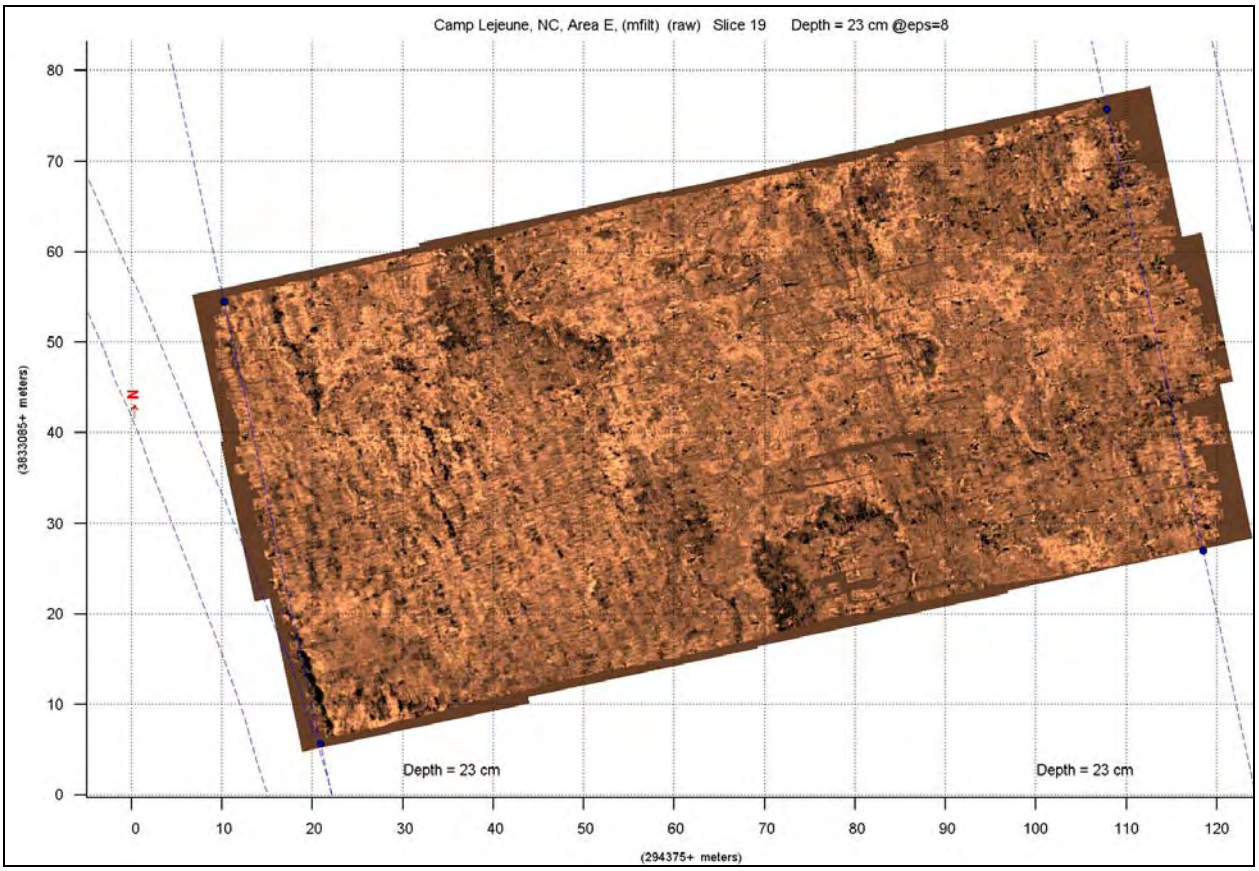


Figure B13. Depth slice at 23 cm for area E using mfilt filtering.

The process was followed for the known UXO surveyed in areas A1, A2, and B2 (green symbols in Figure B6) and for the planted UXO in D2 (orange symbols in Figure B5). The resulting plots are shown in Sections B4 and B5. As an example, the data for target G6A2E10, located in a wet area of area A2, is discussed in more detail in Section B.3.1.

Looking at all the figures in Sections B.4 (Figures B14–B37) and B.5 (Figures B38–B73) one will find that certain targets show a clear anomaly in the radar data, others are hardly distinguishable from the clutter of the host material.

The preliminary data analysis performed for this report was only able to scratch the surface of what may be possible with this data set. Further, more detailed analysis is required to reach any conclusions about the true

value of single-polarity dense, 3D radar data to detect and/or classify UXO targets alone or in conjunction with other data sets, such as electromagnetic induction.

### B.3.1. Example – Target G6A2E10

Target G6A2E10 is an 81-mm mortar that was excavated at a depth of 60 cm at the coordinates shown in parentheses in Figure B18. The unmigrated data clearly show an anomaly. Both vertical sections show hyperbola at the center of the sections. The plan view depth slice at 61.7 cm also shows a circular/oval anomaly typically seen for UXO. It is very interesting to observe the hint of two hyperbola in the vertical profile along the Y-axis, which could be an indication of the dip (measured to be 45 deg), or the top and bottom of the mortar.

Figure B19 shows a plan view (left) and two vertical sections crossing at the target location. The data were migrated with an $\varepsilon_r = 22$ and the brightest anomaly appears at 83.82 cm. Both vertical sections show the top and bottom of the mortar. In addition one can see a horizontal layer at a depth of 1.5 m. In the longer vertical section, a second shallower anomaly is visible at about 2.5 m. This unknown anomaly, which is located approximately 1 m north of target G6A2E10, was further investigated in Figures B20 and B21.

The plan view in Figure B20 again indicates the typical circular anomaly at a depth of 34.1 cm, but the two vertical sections only show partial hyperbola. The corresponding migrated data plots (Figure B21) show a bright anomaly in that location at a depth of 33.02 cm. The vertical sections show anomalies that are significantly different from the ones in Figure B19, but until excavated and checked, what the anomalies in the radar data have identified will not be known.

## B.4. Example data plots – Area AB

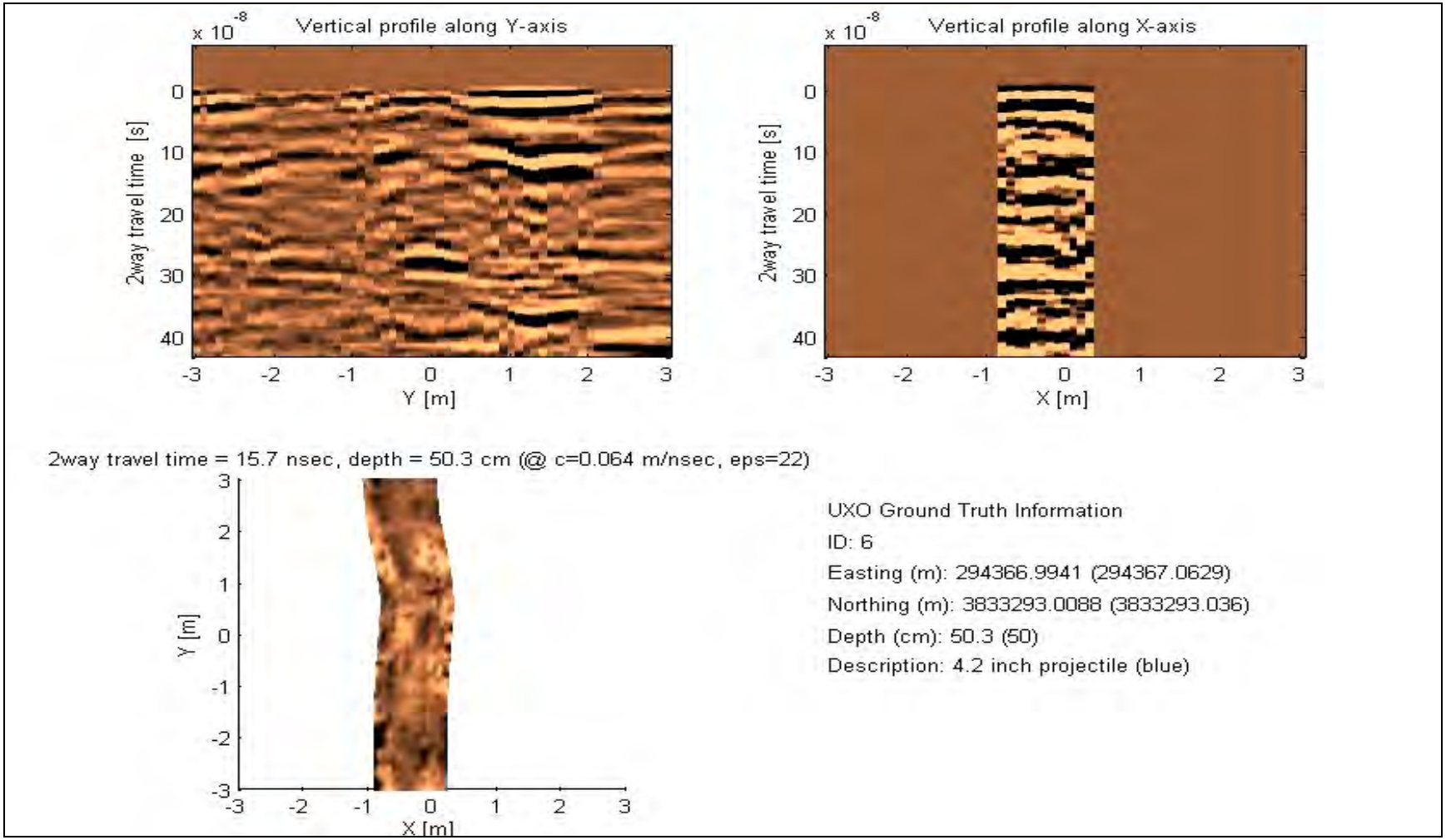


Figure B14. Analysis plots for target G6A2E6. Coordinates of center plot point are followed by ground truth coordinates in parenthesis.

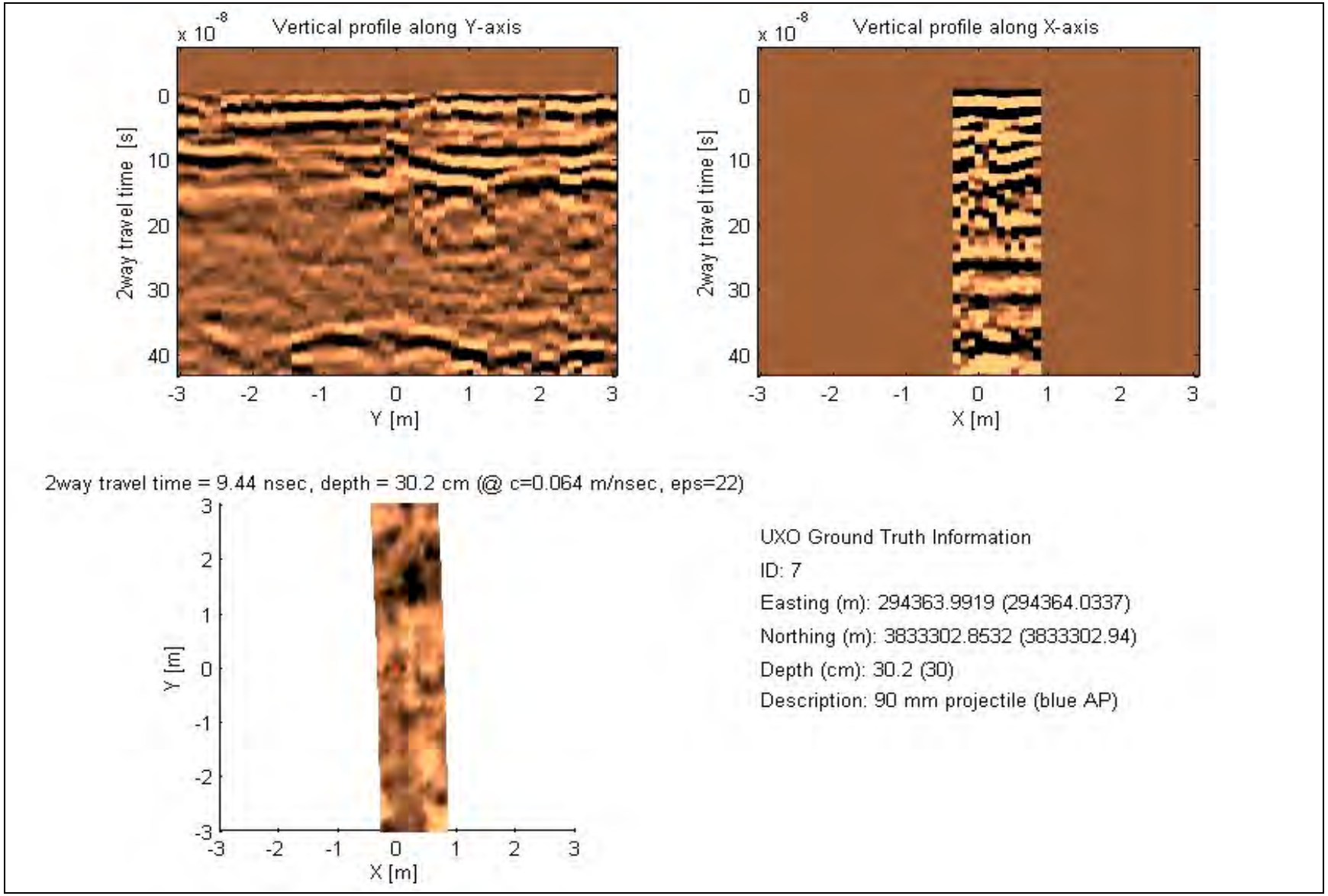


Figure B15. Analysis plots for target G6A2E7. Coordinates of center plot point are followed by ground truth coordinates in parenthesis.

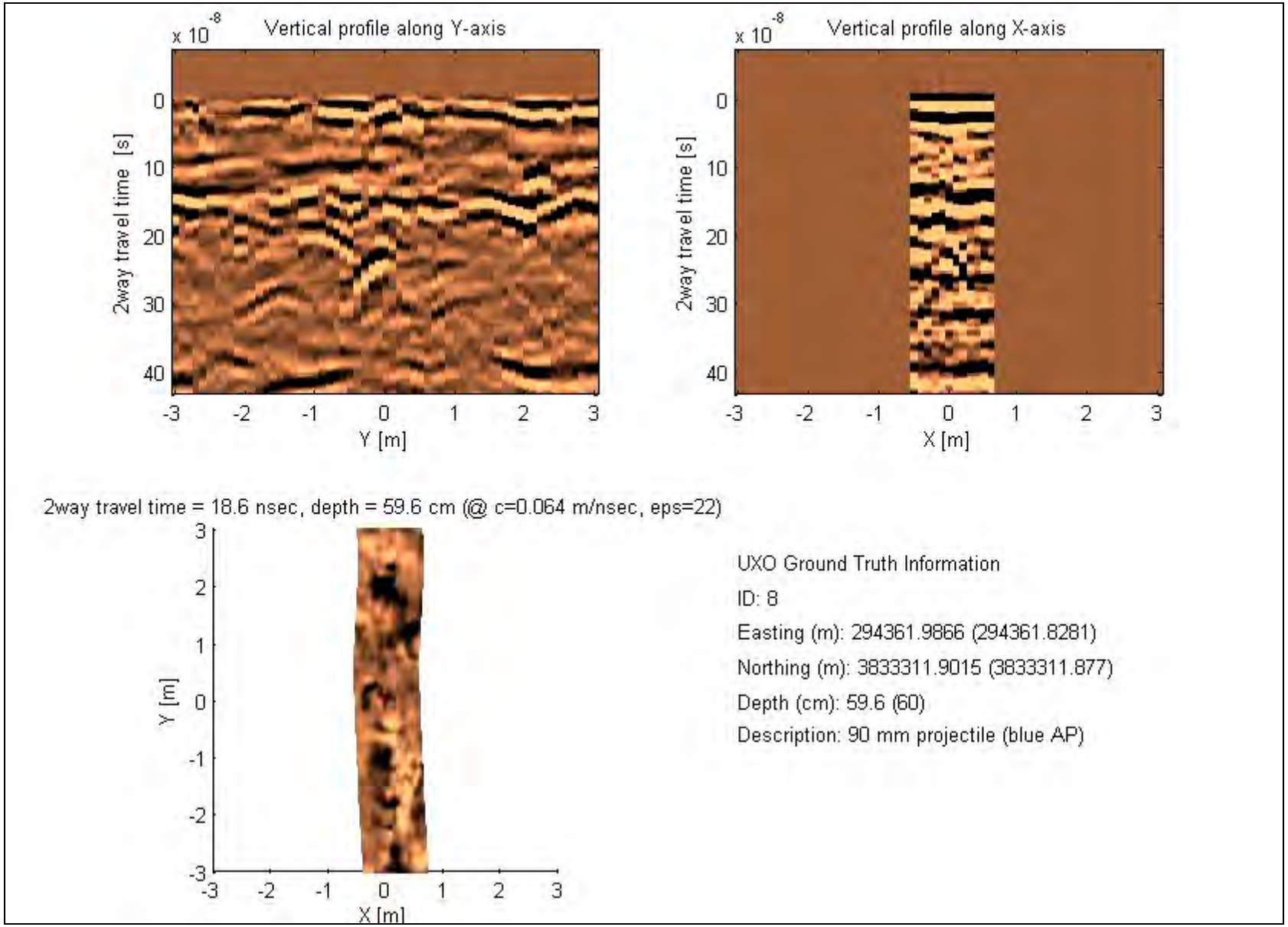


Figure B16. Analysis plots for target G6A2E8. Coordinates of center plot point are followed by ground truth coordinates in parenthesis.

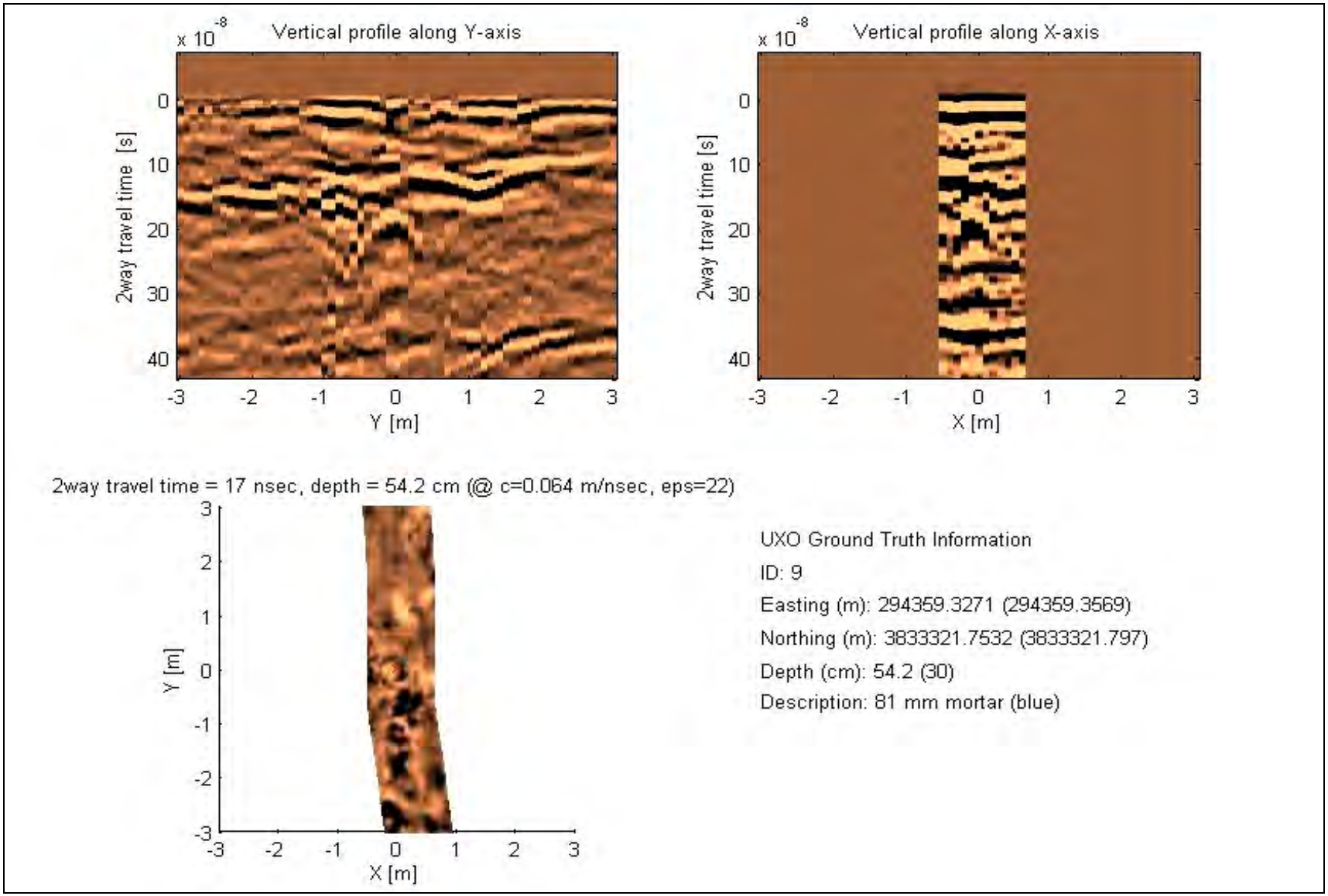


Figure B17. Analysis plots for target G6A2E9. Coordinates of center plot point are followed by ground truth coordinates in parenthesis.

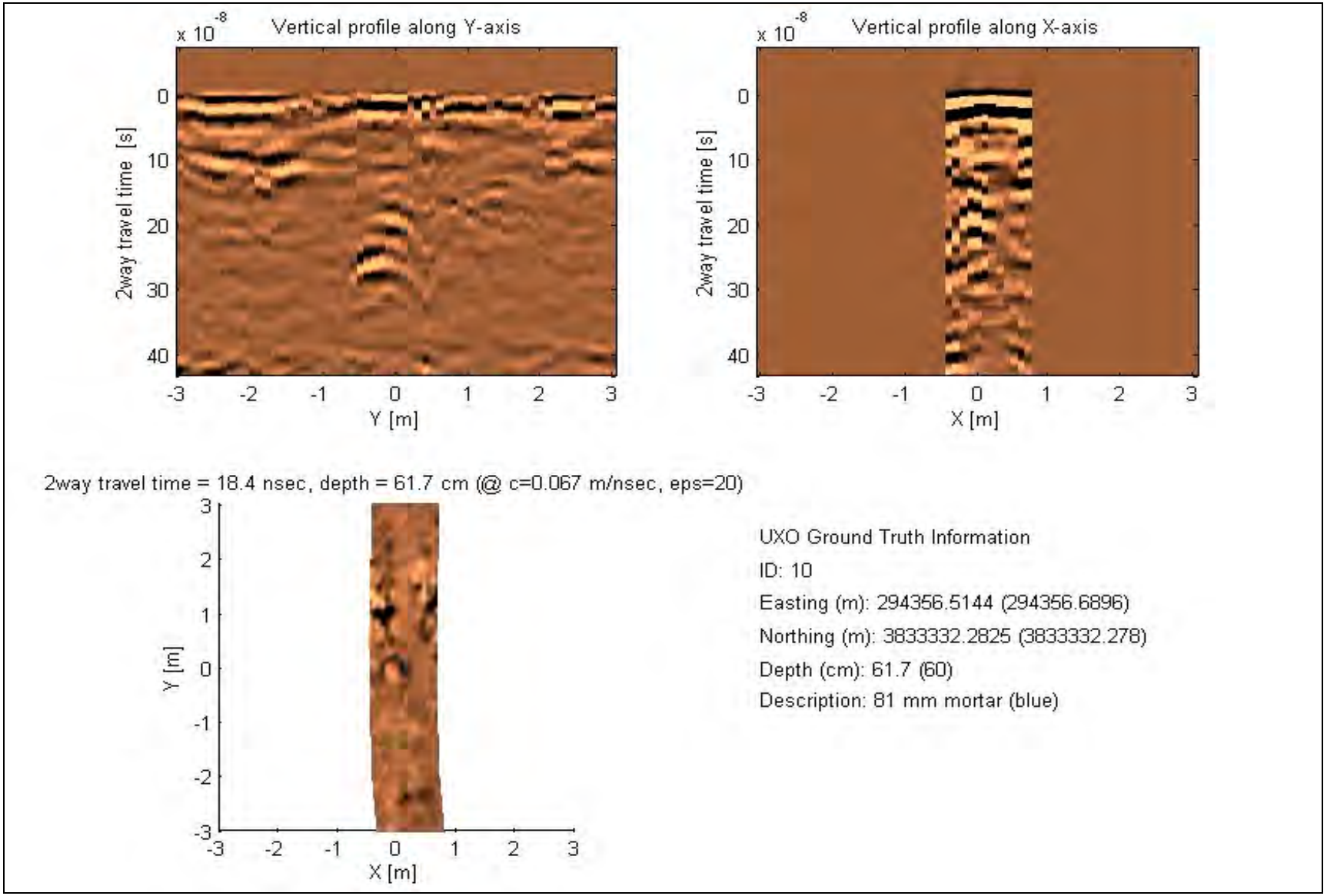


Figure B18. Analysis plots for target G6A2E10. Coordinates of center plot point are followed by ground truth coordinates in parenthesis.

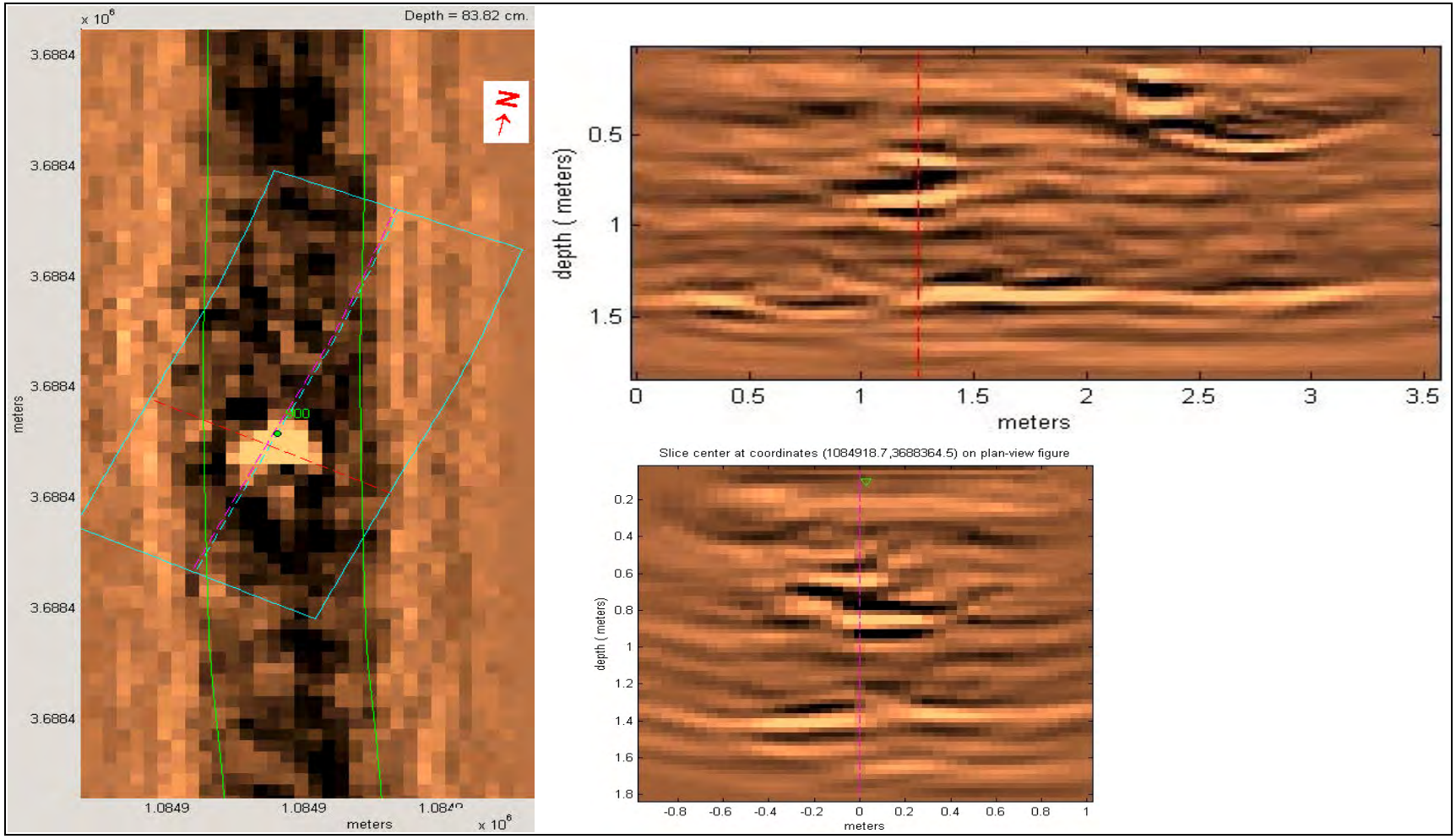


Figure B19. Migration results for G6A2E10. (Left) Plan view at 83.82 cm depth of migrated radar data of profile 900 outlined in green in grid A2 (Figure B6) rotated by -12 degrees. The blue rectangle is a cut out 3D data volume that is sliced vertically along the red (Bottom right) and purple (Top right) lines. Note the shallower anomaly visible in the Top Right plot at about 2.5 m, which corresponds to the anomaly described in Figures B20 and B21. The two vertical profiles on the right intersect at (1084918.7; 3688364.5) in the rotated coordinate system, which corresponds to (294356.5; 383333.2) in the original coordinate system.

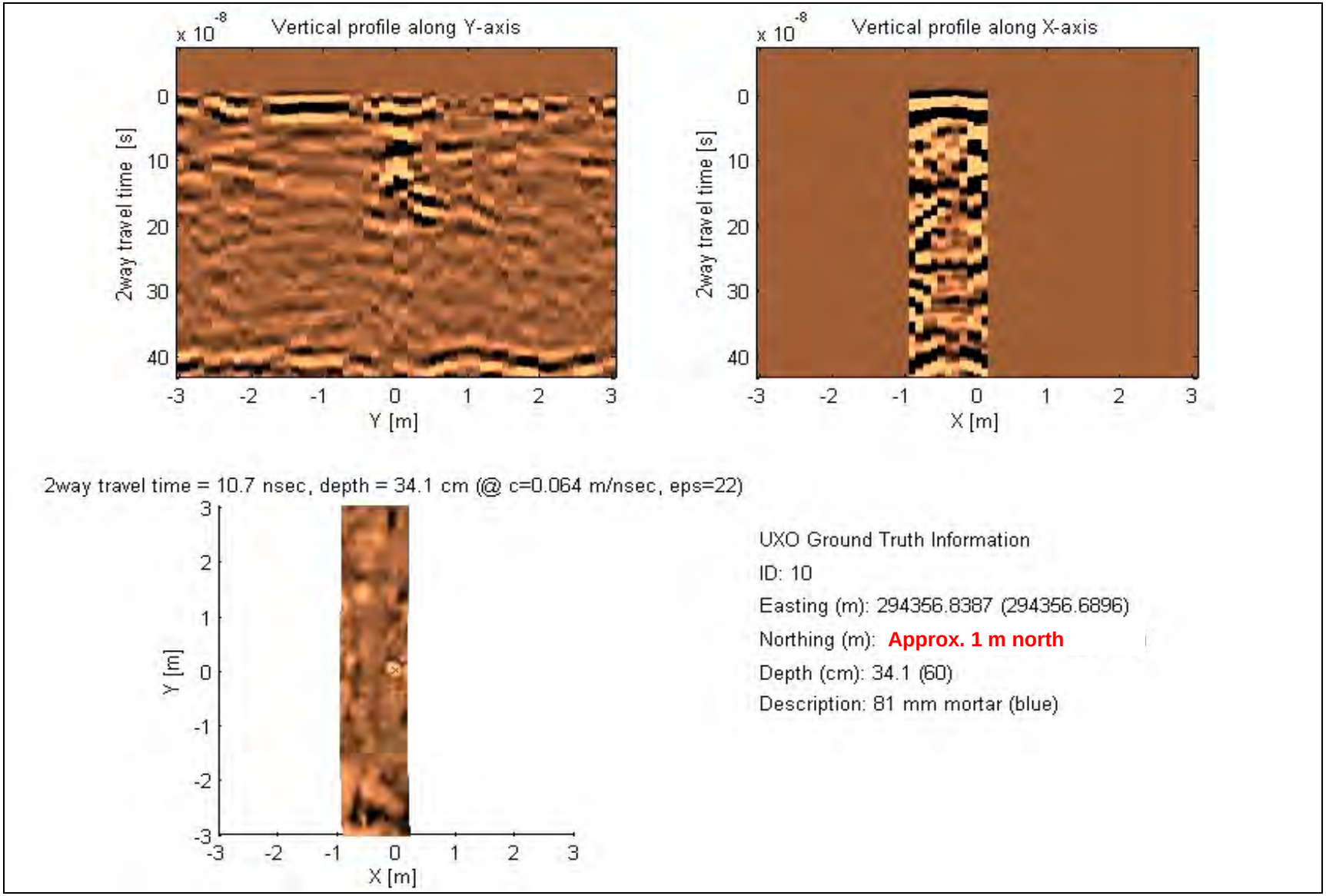


Figure B20. Analysis plots 1 m north of target G6A2E10. Coordinates of center plot point are followed by ground truth coordinates in parenthesis.

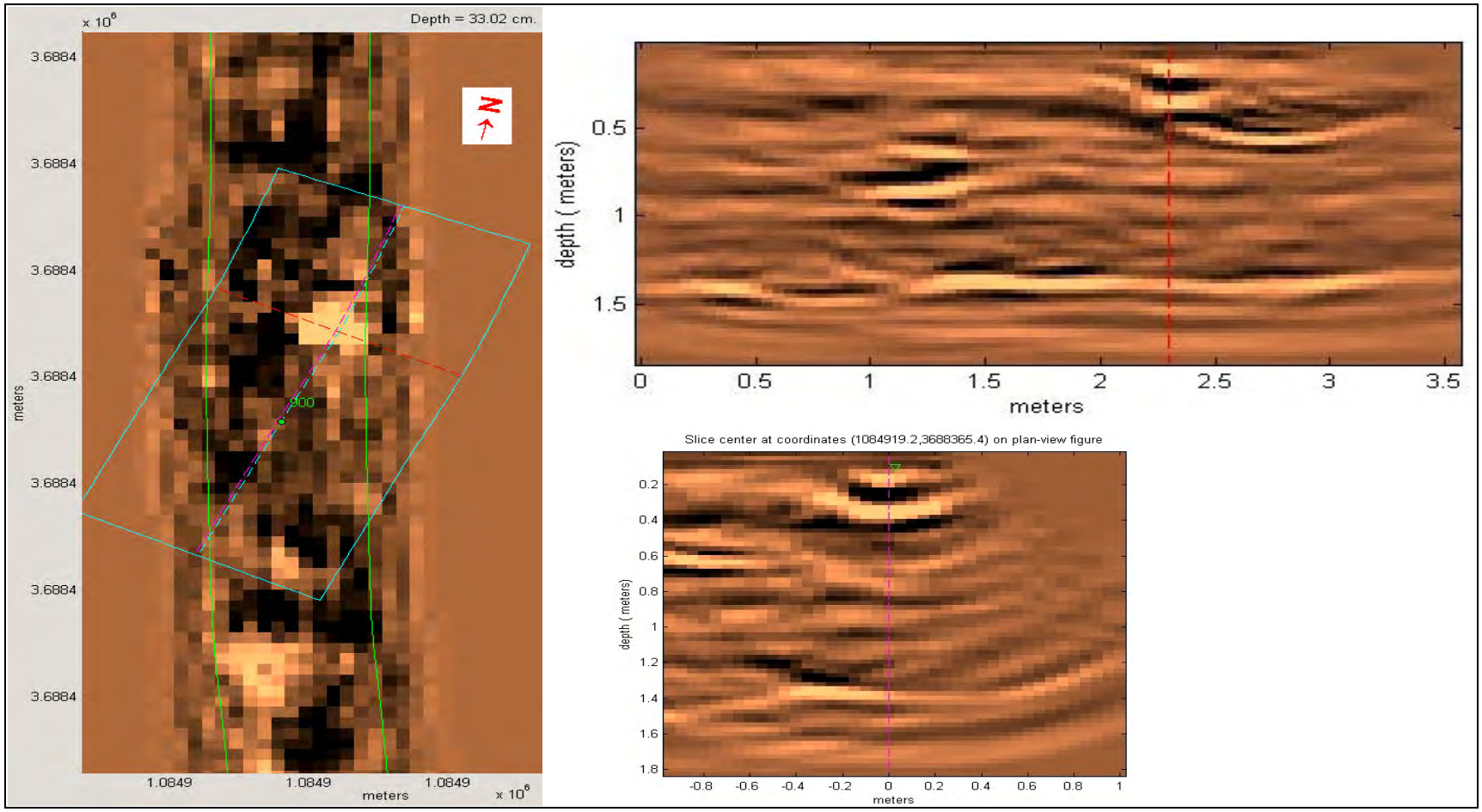


Figure B21. Migration results for anomaly 1 m North of G6A2E10. (Left) Plan view at 33.02 cm depth of migrated radar data of profile 900 outlined in green in grid A2 (Figure B6) rotated by -12 degrees. The blue rectangle is a cut out 3D data volume that is sliced vertically along the red (bottom right) and purple (top right) lines. Note the deeper anomaly visible in the top right plot at about 1.25 m, which corresponds to the anomaly described in Figures B18 and B19. The two vertical profiles on the right intersect at (1084919.2; 3688365.4) in the rotated coordinate system, which corresponds to (294356.8; 383333.3) in the original coordinate system.

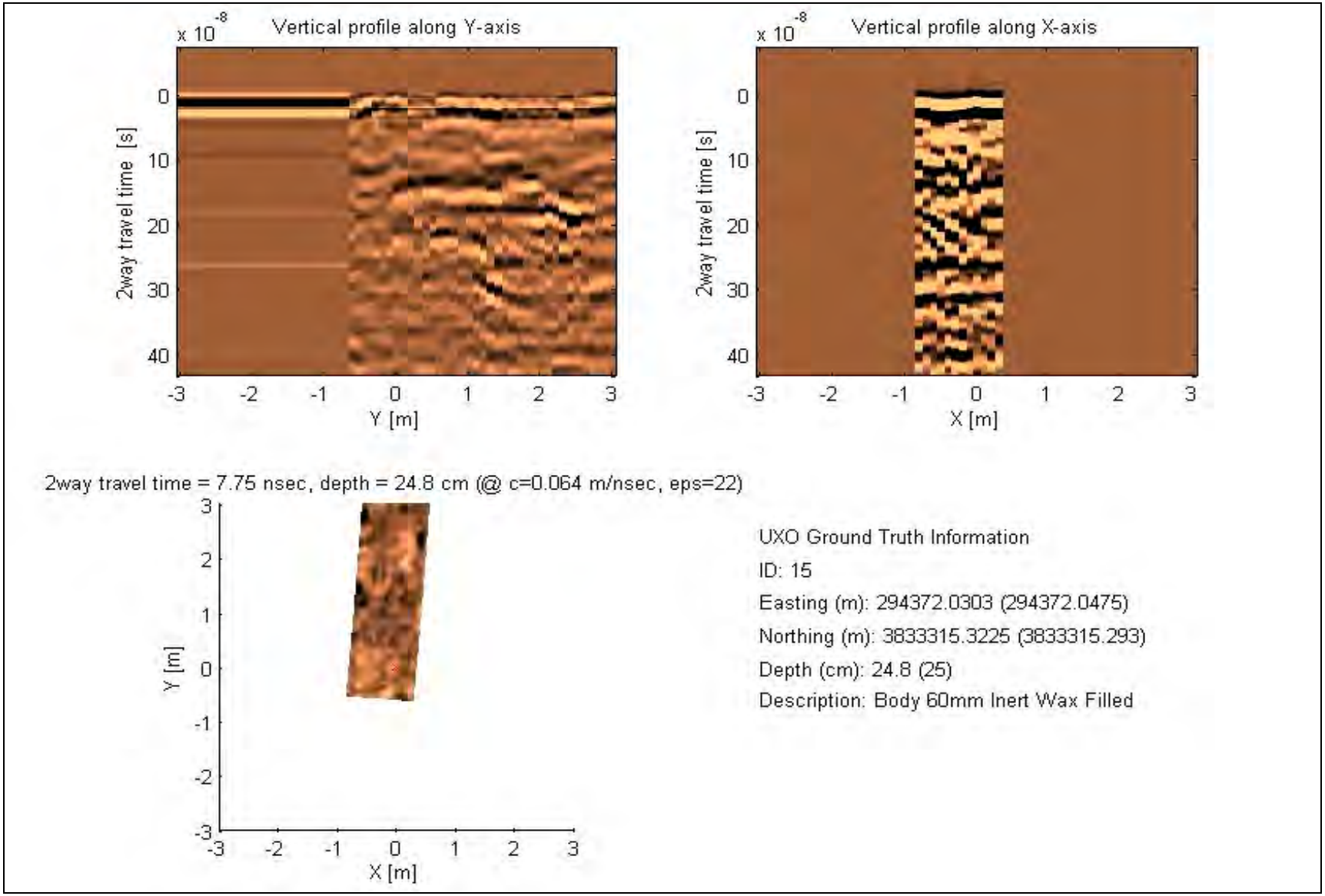


Figure B22. Analysis plots for target G6A2E15. Coordinates of center plot point are followed by ground truth coordinates in parenthesis.

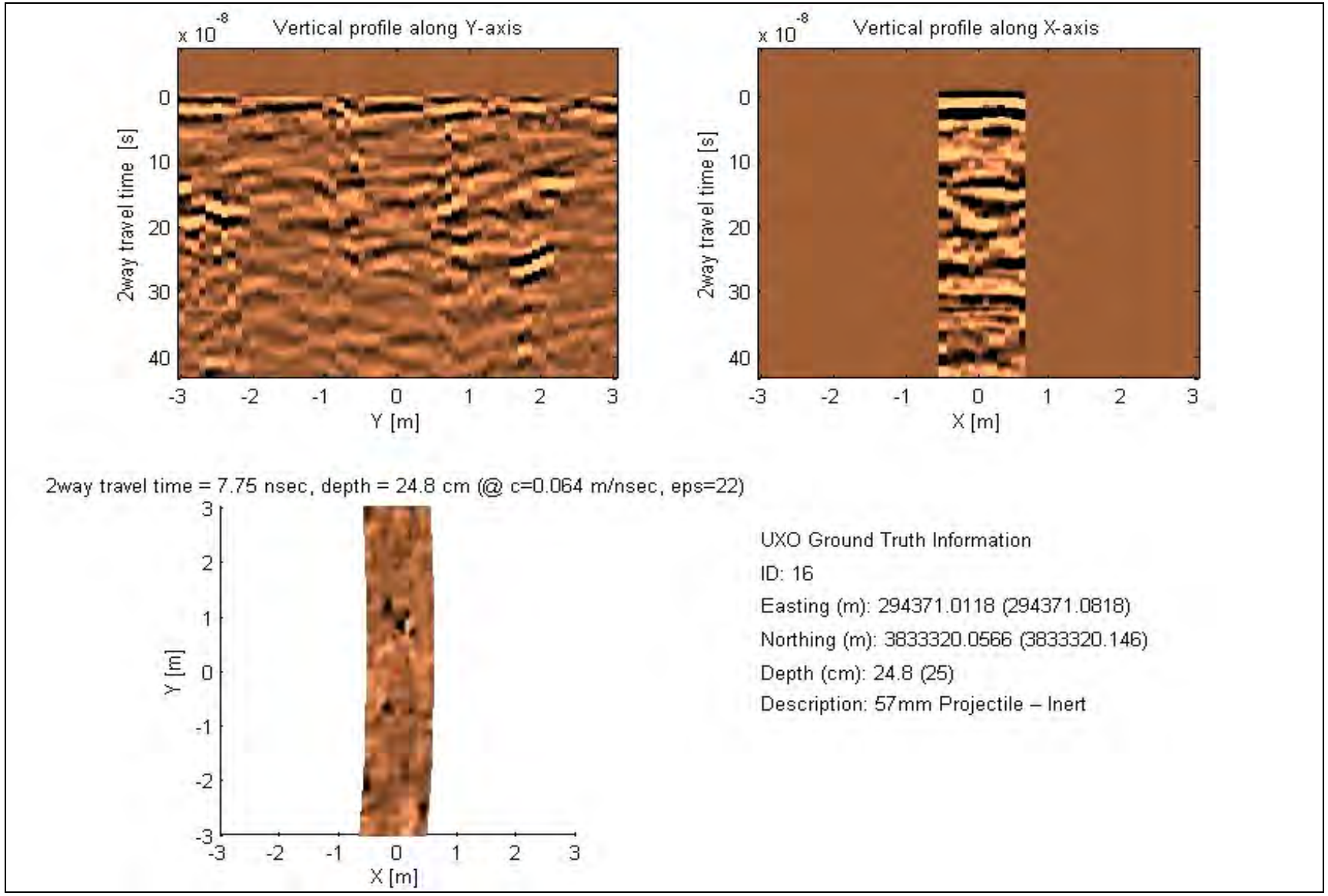


Figure B23. Analysis plots for target G6A2E16. Coordinates of center plot point are followed by ground truth coordinates in parenthesis.

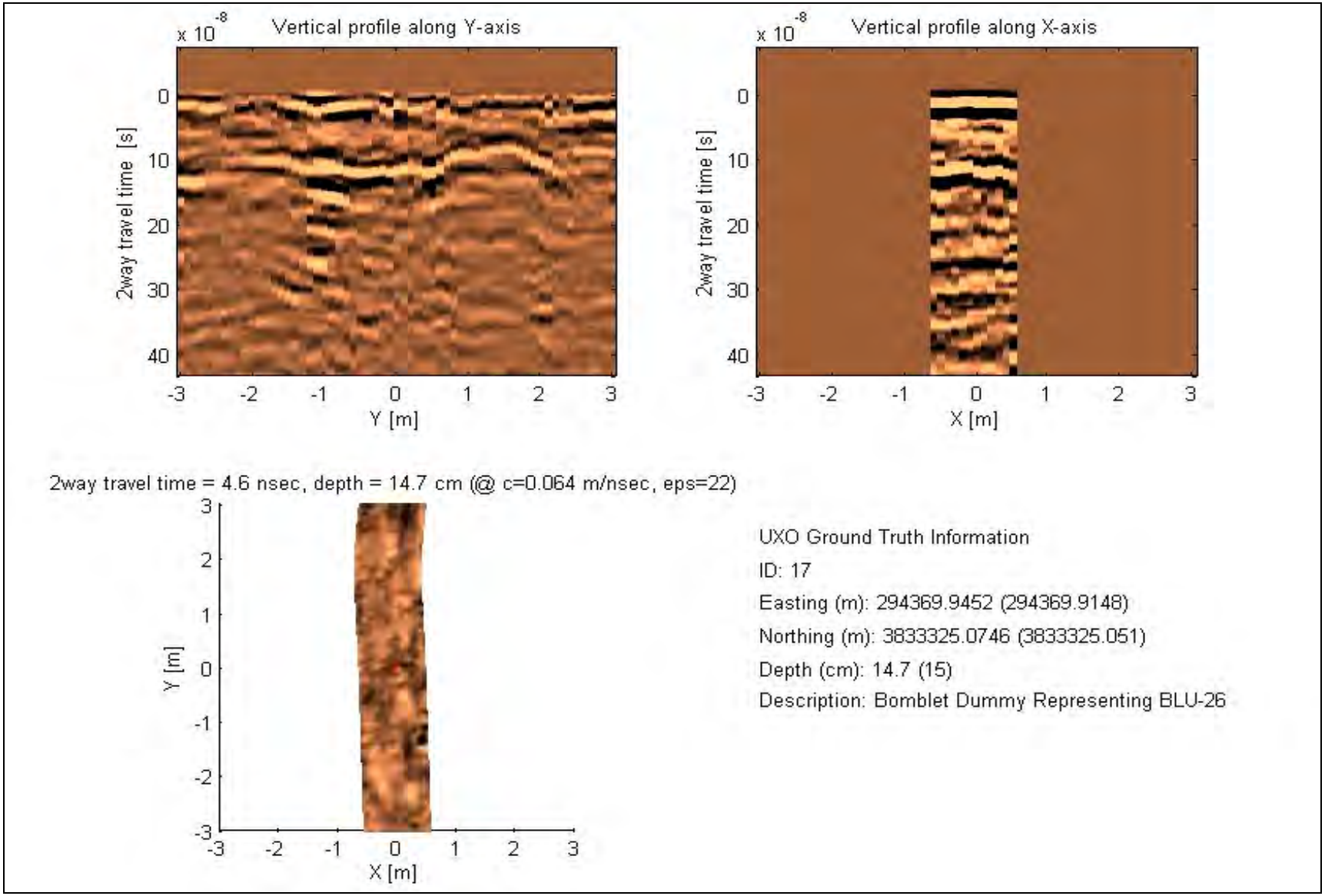


Figure B24. Analysis plots for target G6A2E17. Coordinates of center plot point are followed by ground truth coordinates in parenthesis.

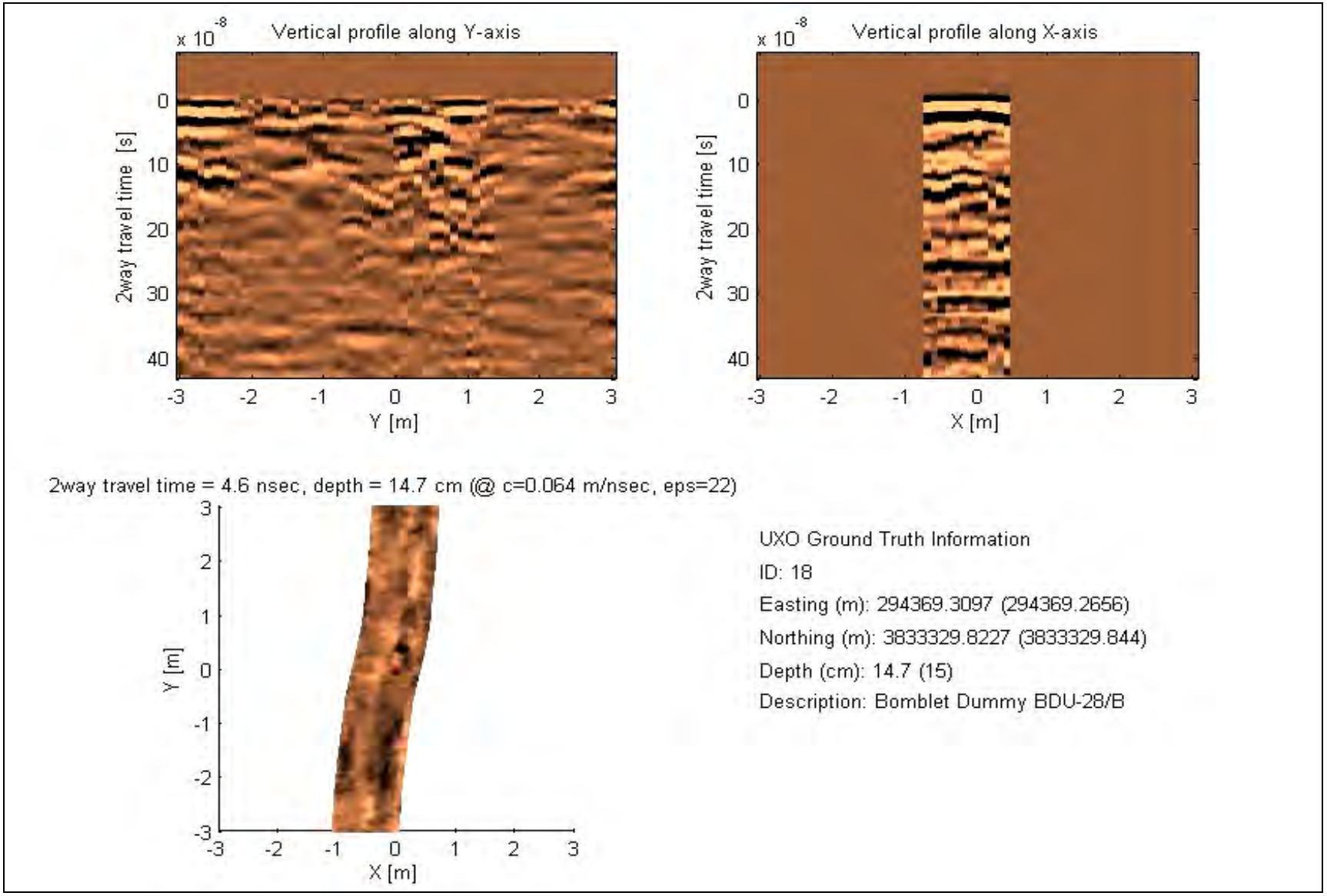


Figure B25. Analysis plots for target G6A2E18. Coordinates of center plot point are followed by ground truth coordinates in parenthesis.

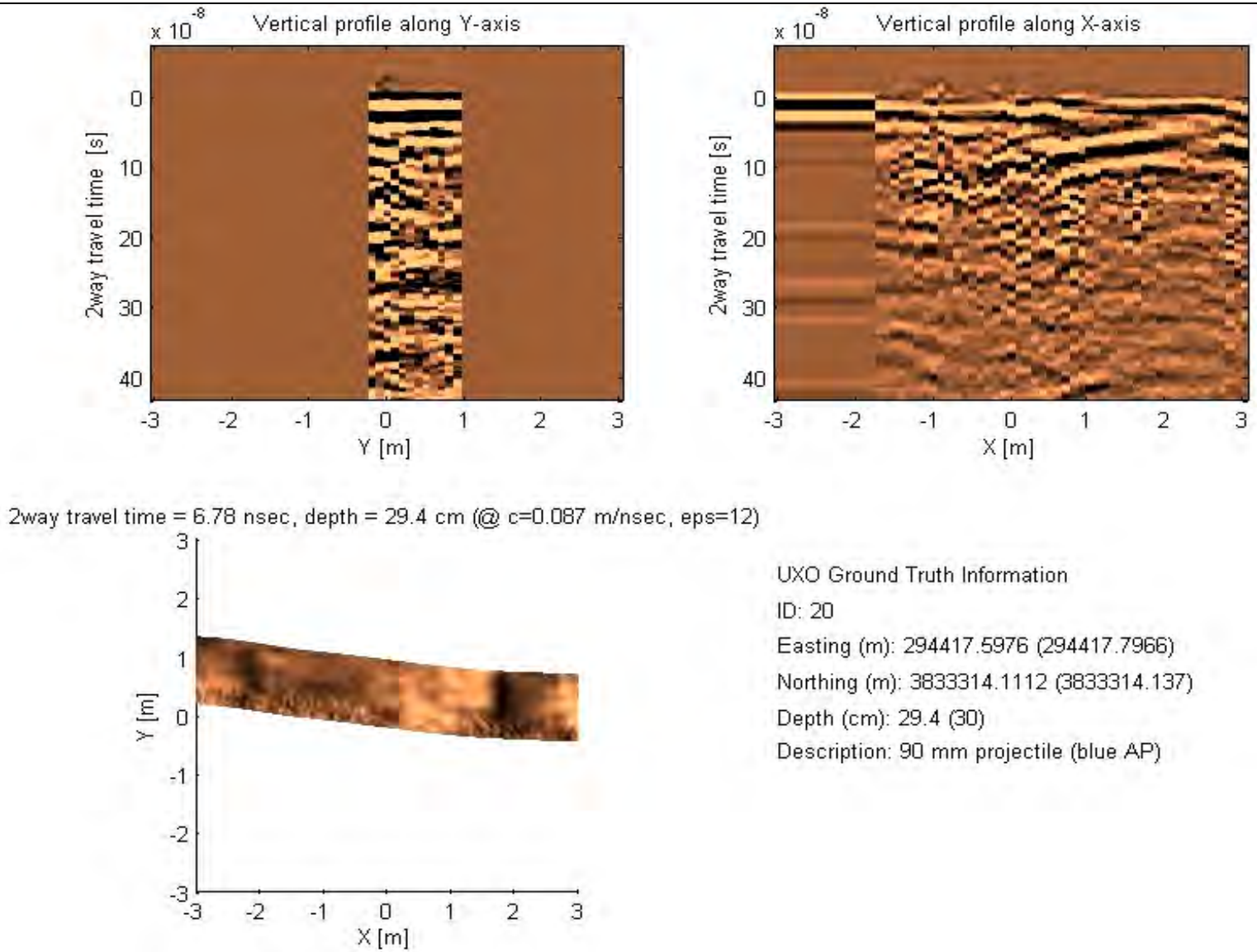


Figure B26. Analysis plots for target G6A2E20. Coordinates of center plot point are followed by ground truth coordinates in parenthesis.

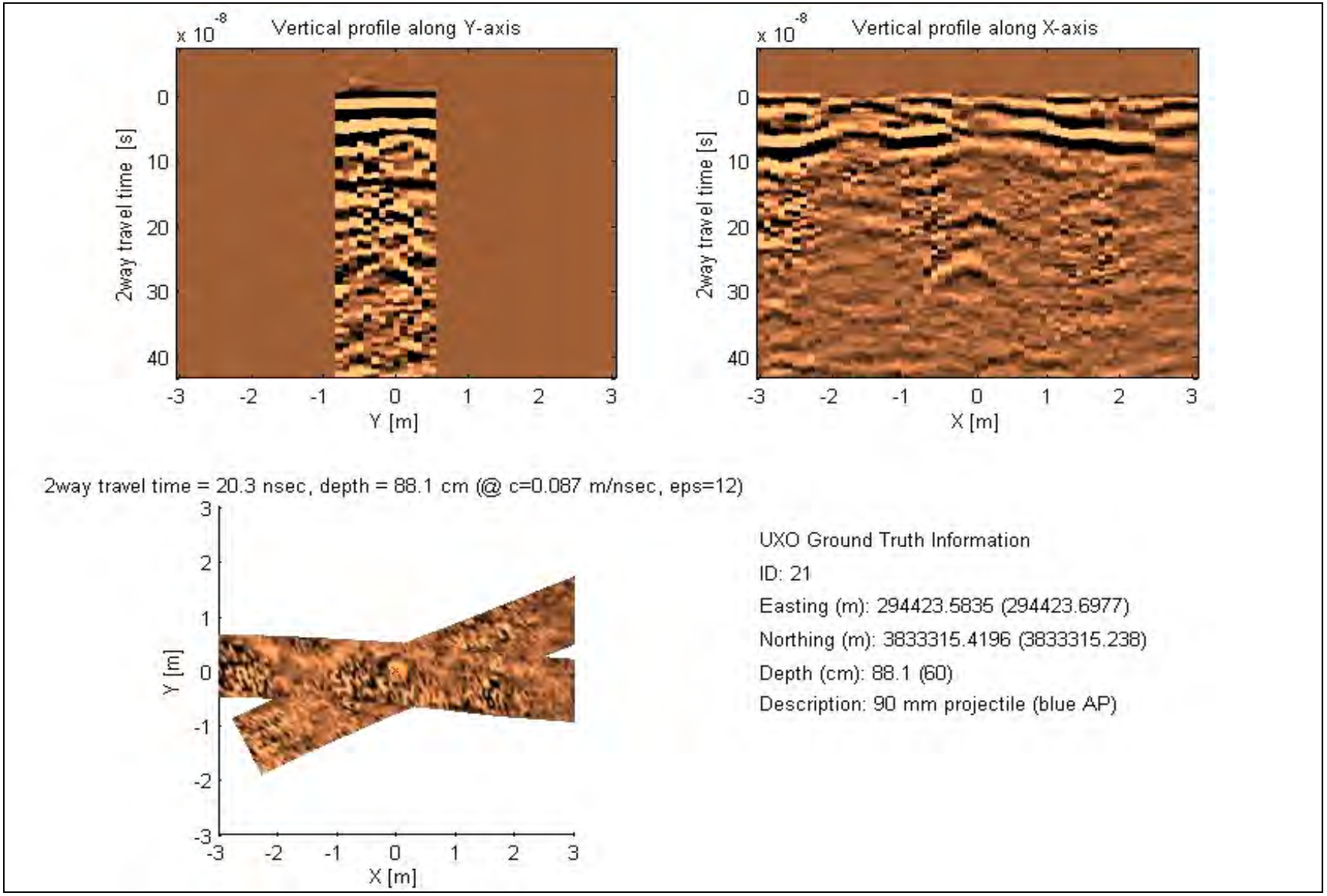


Figure B27. Analysis plots for target G6A2E21. Coordinates of center plot point are followed by ground truth coordinates in parenthesis.

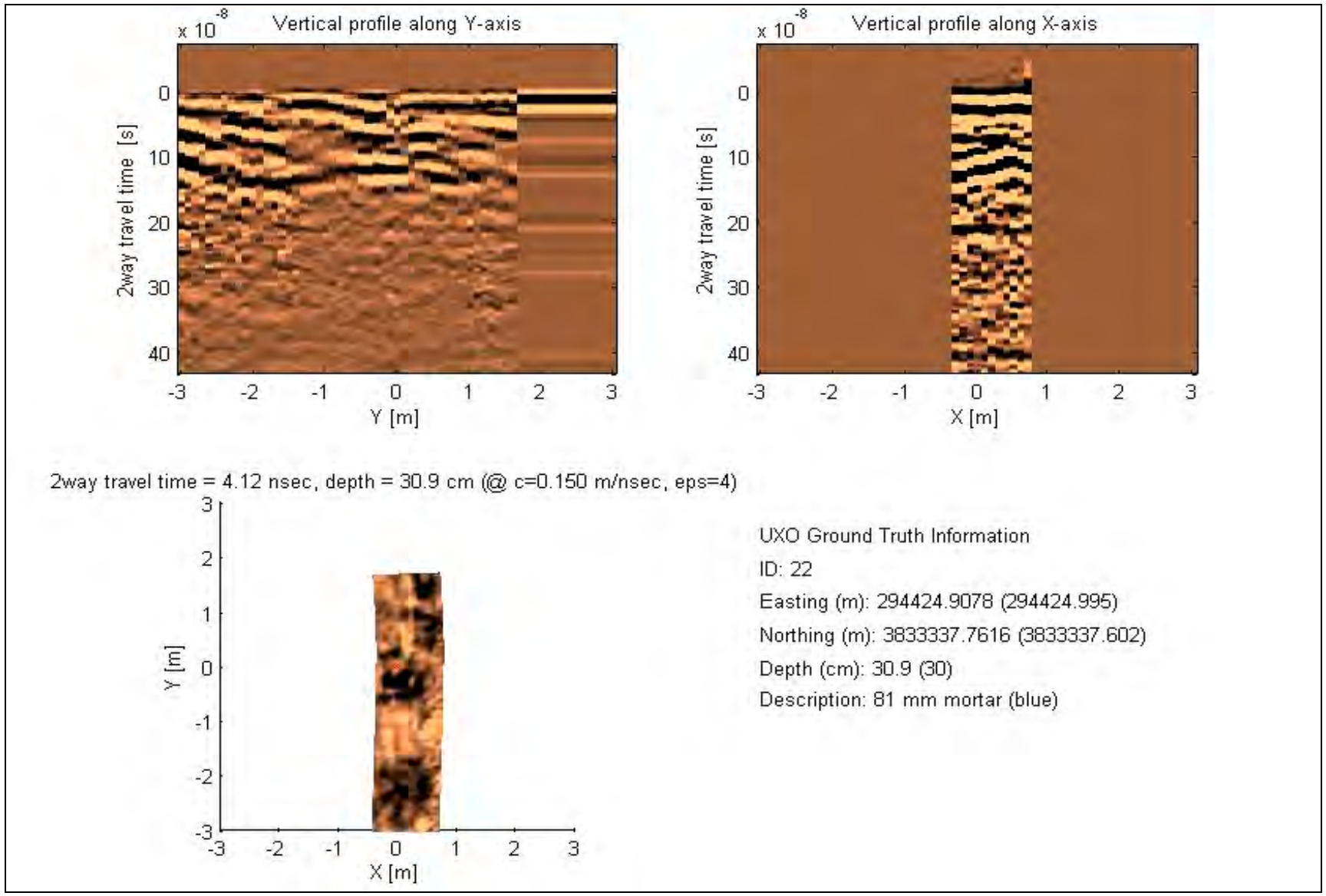


Figure B28. Analysis plots for target G6A2E22. Coordinates of center plot point are followed by ground truth coordinates in parenthesis.

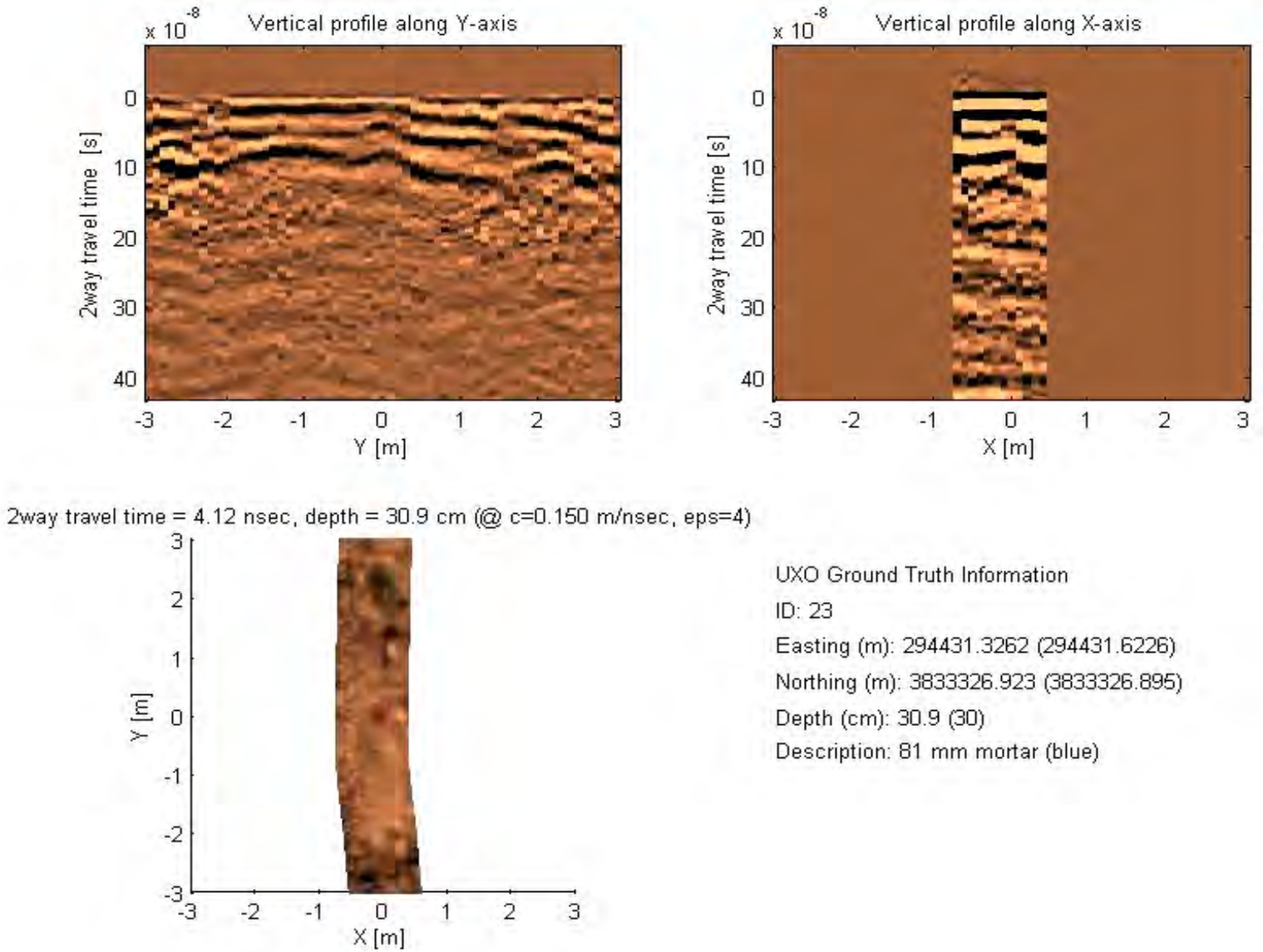


Figure B29. Analysis plots for target G6A2E23. Coordinates of center plot point are followed by ground truth coordinates in parenthesis.

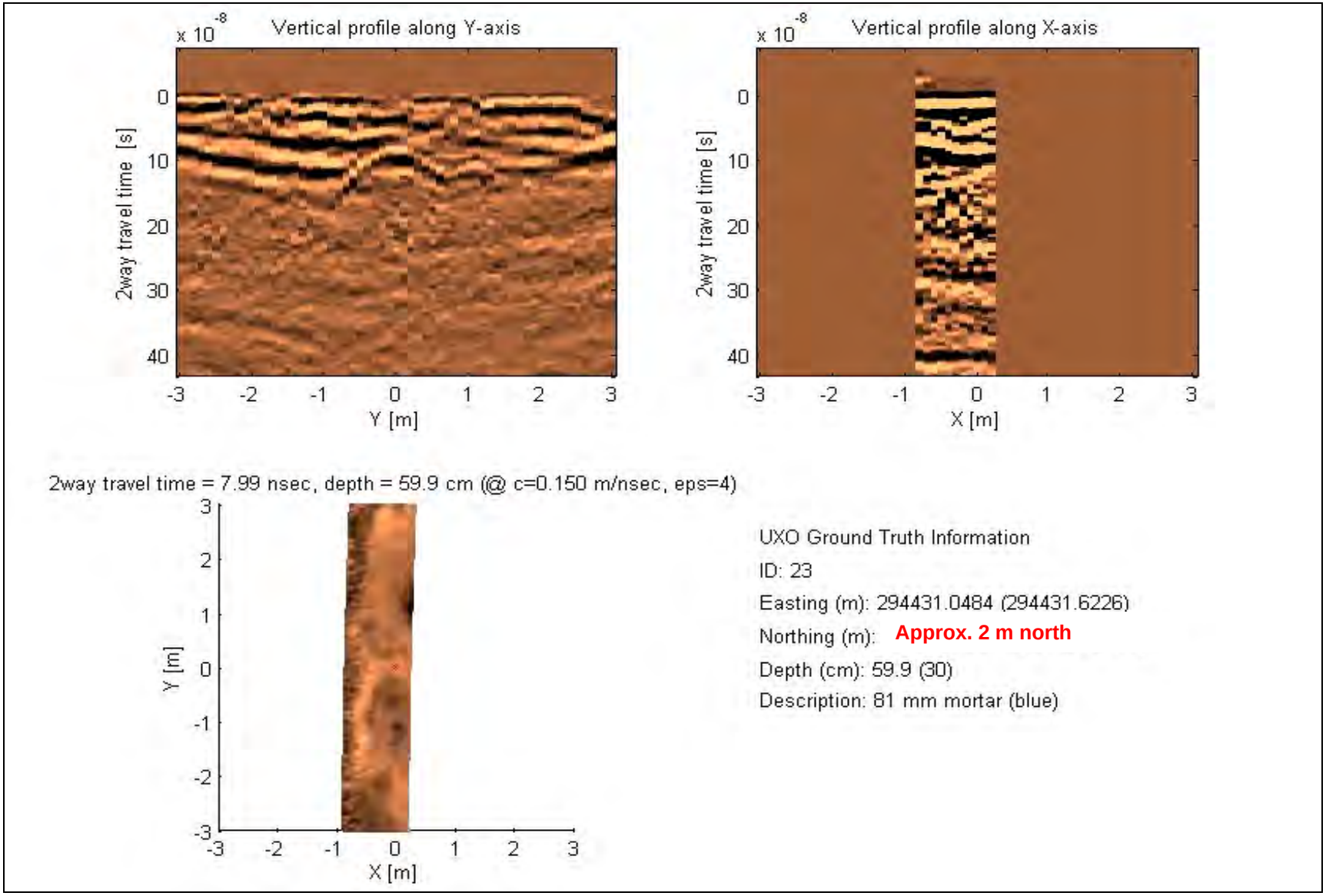


Figure B30. Analysis plots for target 2 m north of G6A2E23. Coordinates of center plot point are followed by ground truth coordinates in parenthesis.

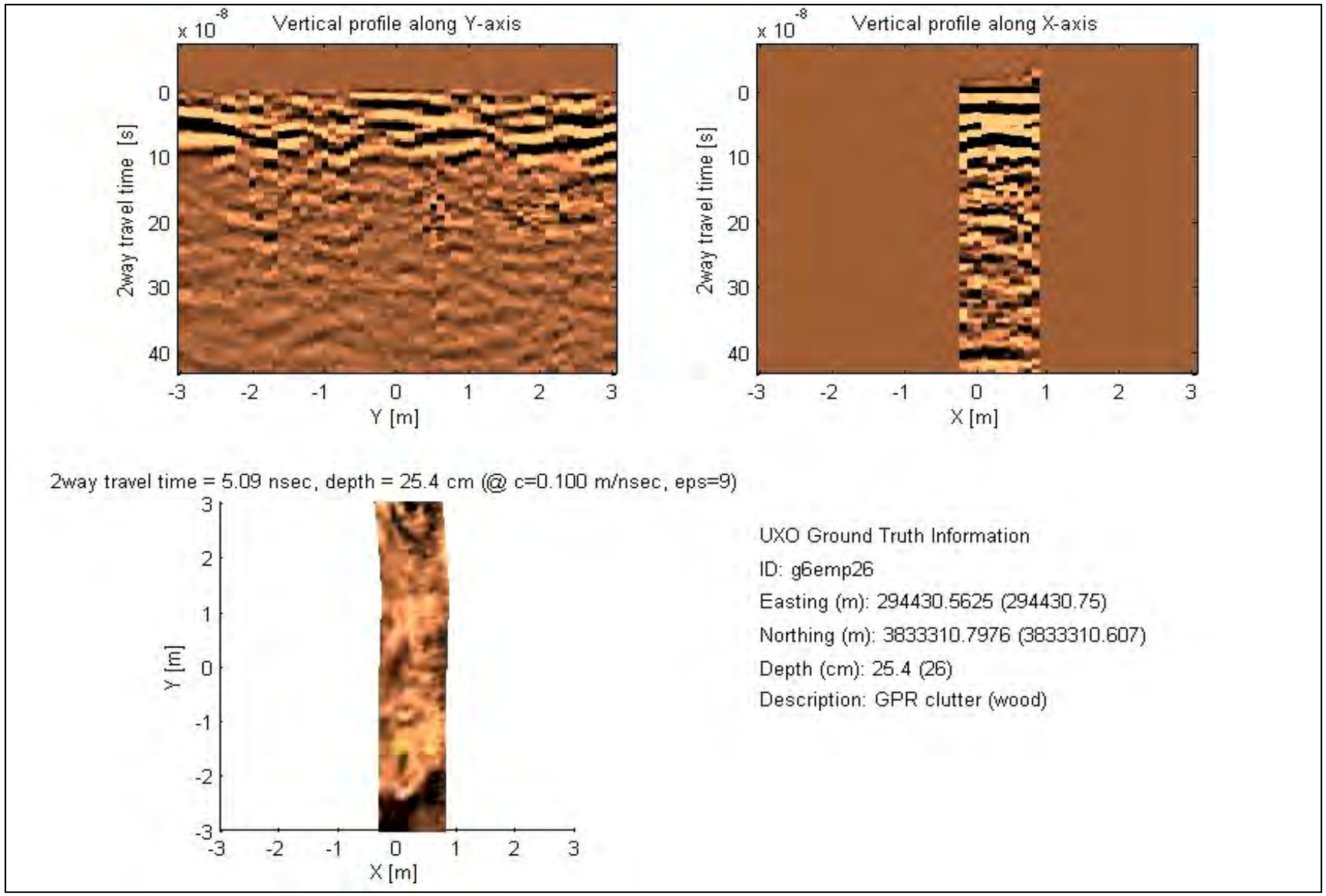


Figure B31. Analysis plots for target G6A2E26. Coordinates of center plot point are followed by ground truth coordinates in parenthesis.

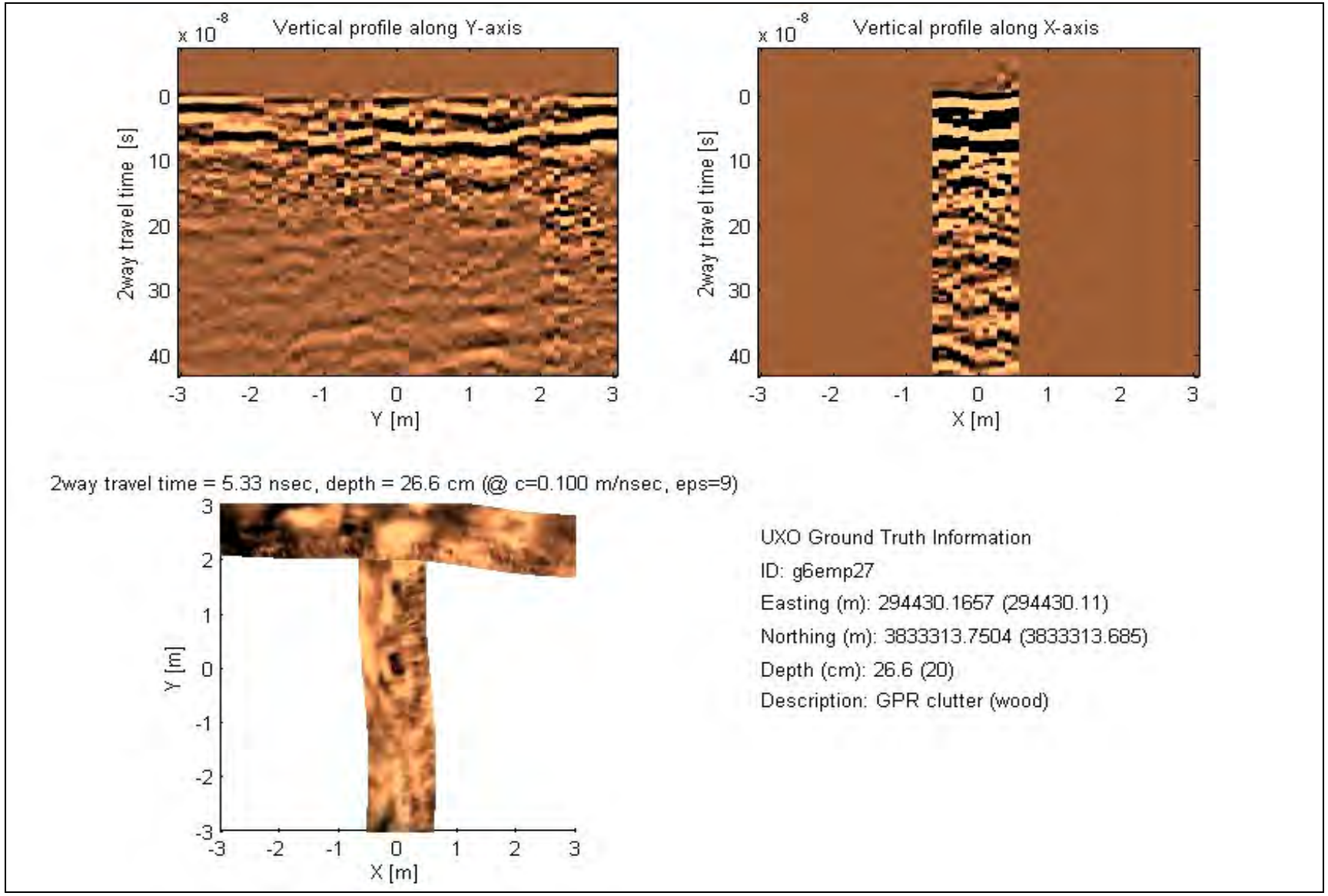


Figure B32. Analysis plots for target G6A2E27. Coordinates of center plot point are followed by ground truth coordinates in parenthesis.

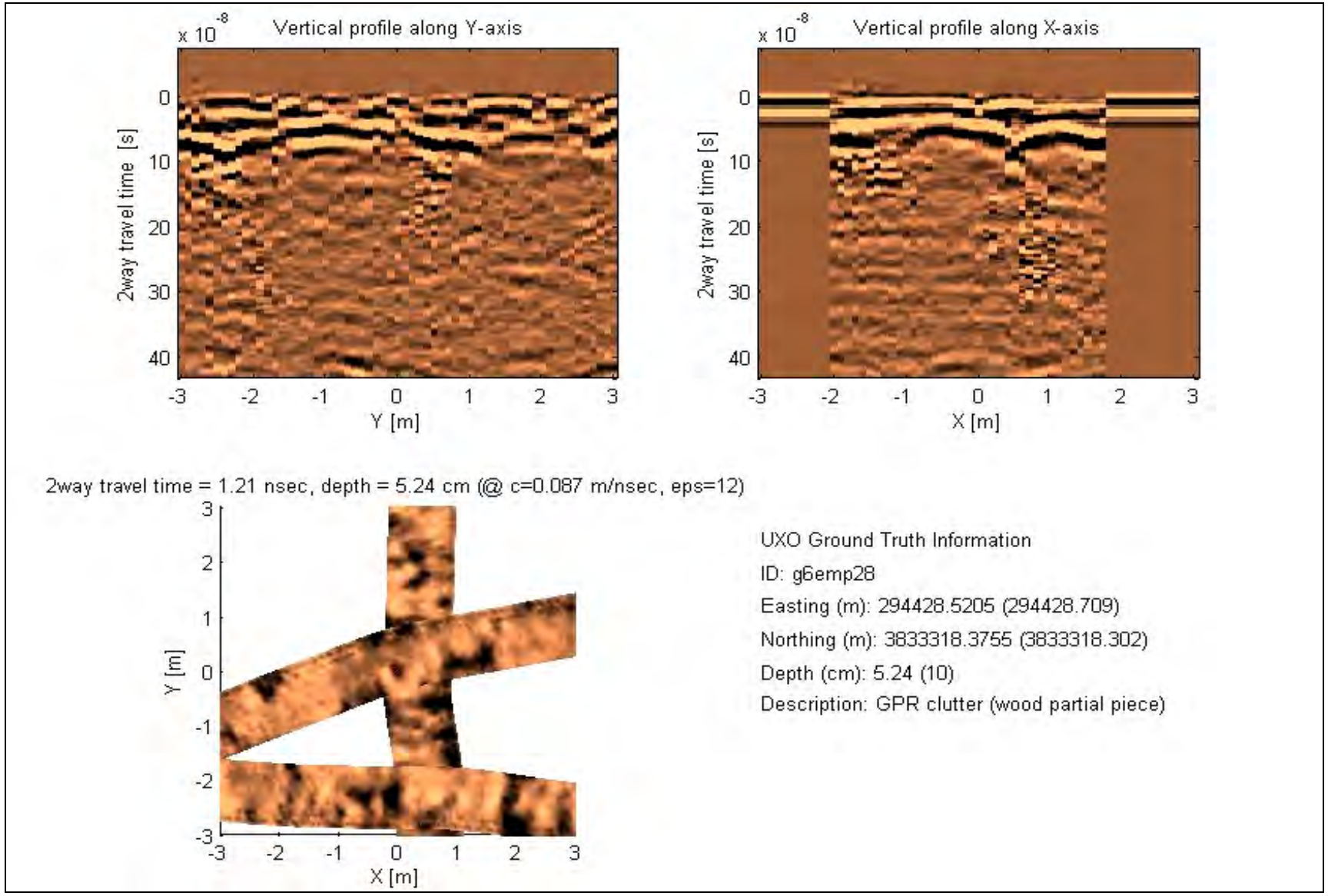


Figure B33. Analysis plots for target G6A2E28. Coordinates of center plot point are followed by ground truth coordinates in parenthesis.

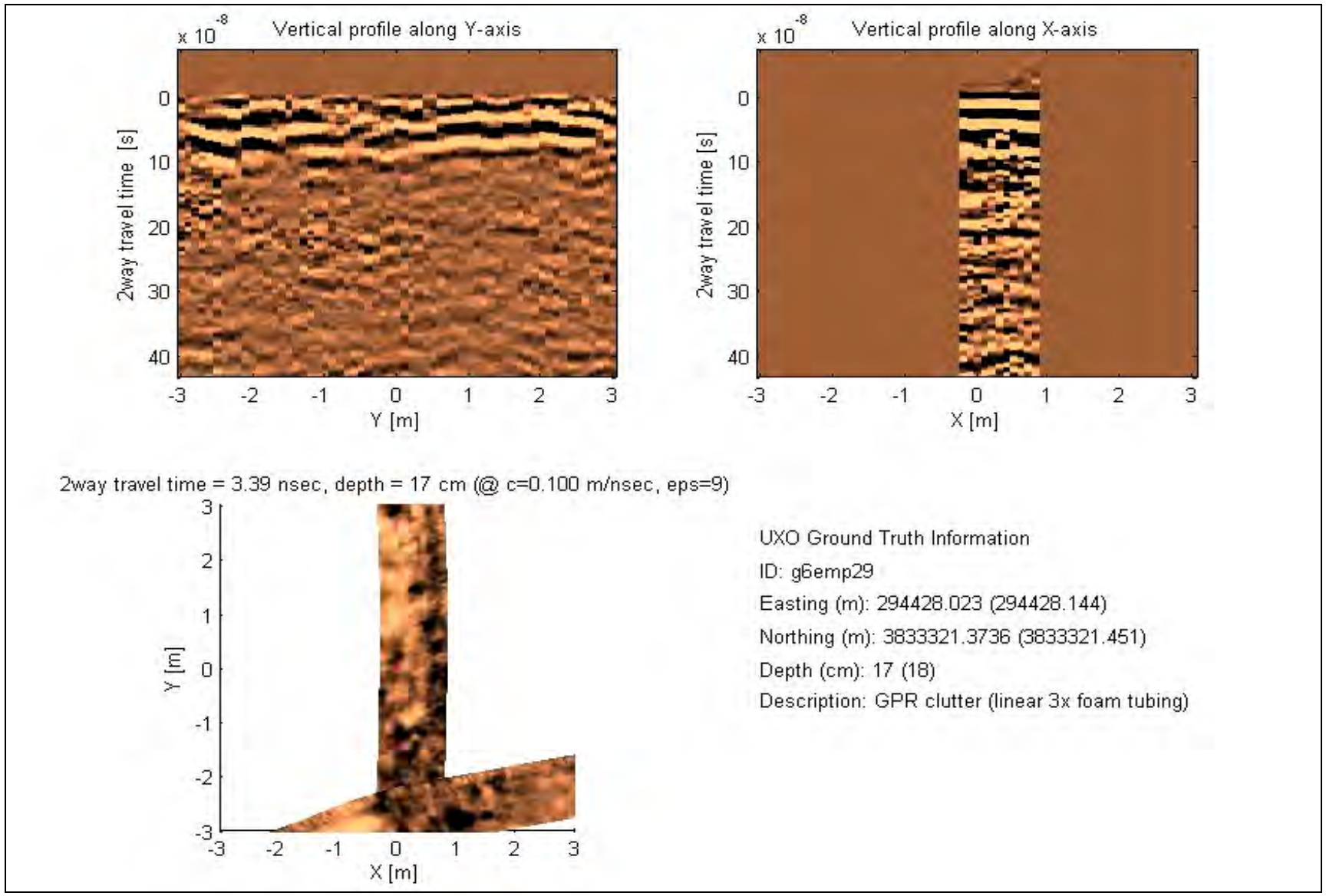


Figure B34. Analysis plots for target G6A2E29. Coordinates of center plot point are followed by ground truth coordinates in parenthesis.

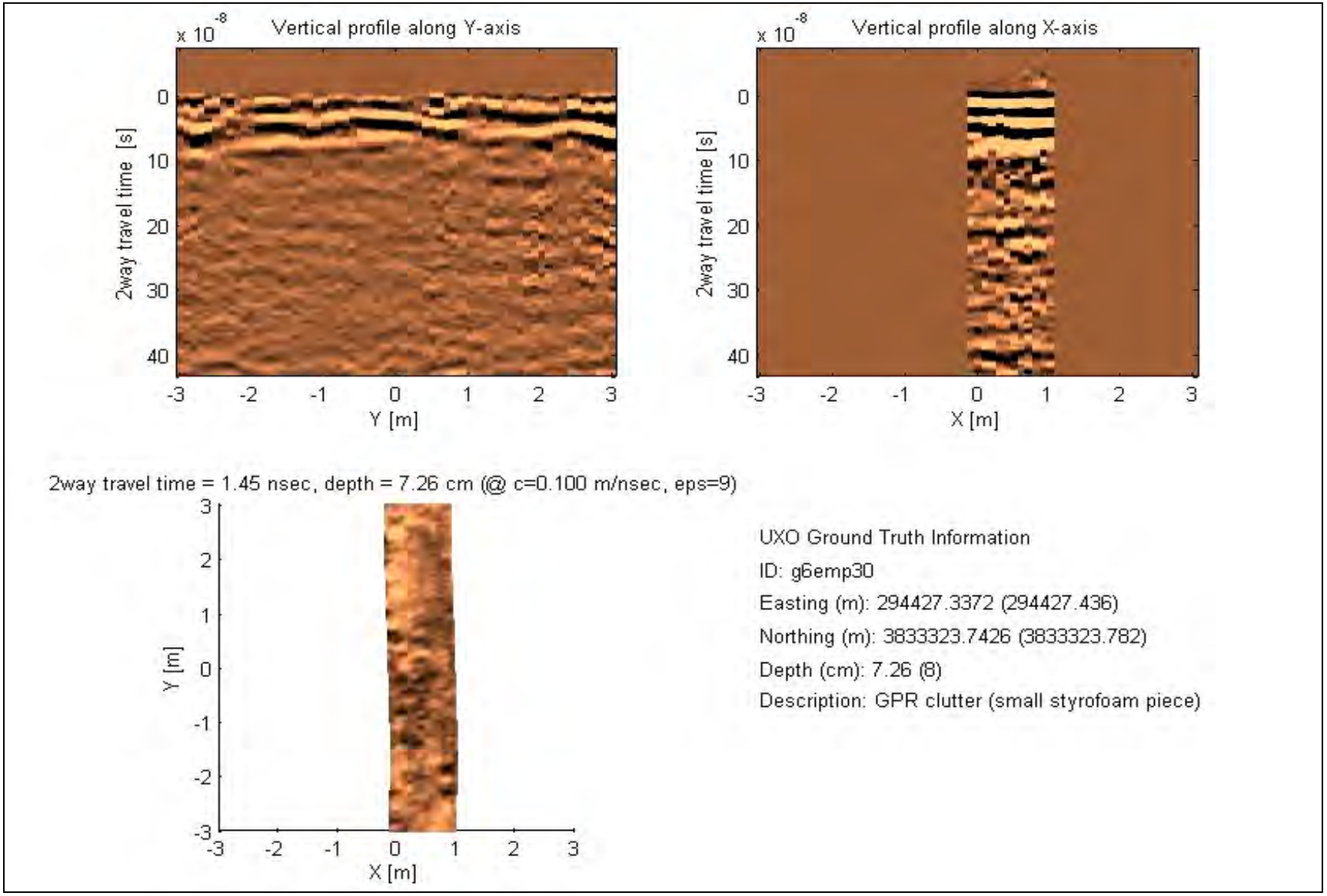


Figure B35. Analysis plots for target G6A2E30. Coordinates of center plot point are followed by ground truth coordinates in parenthesis.

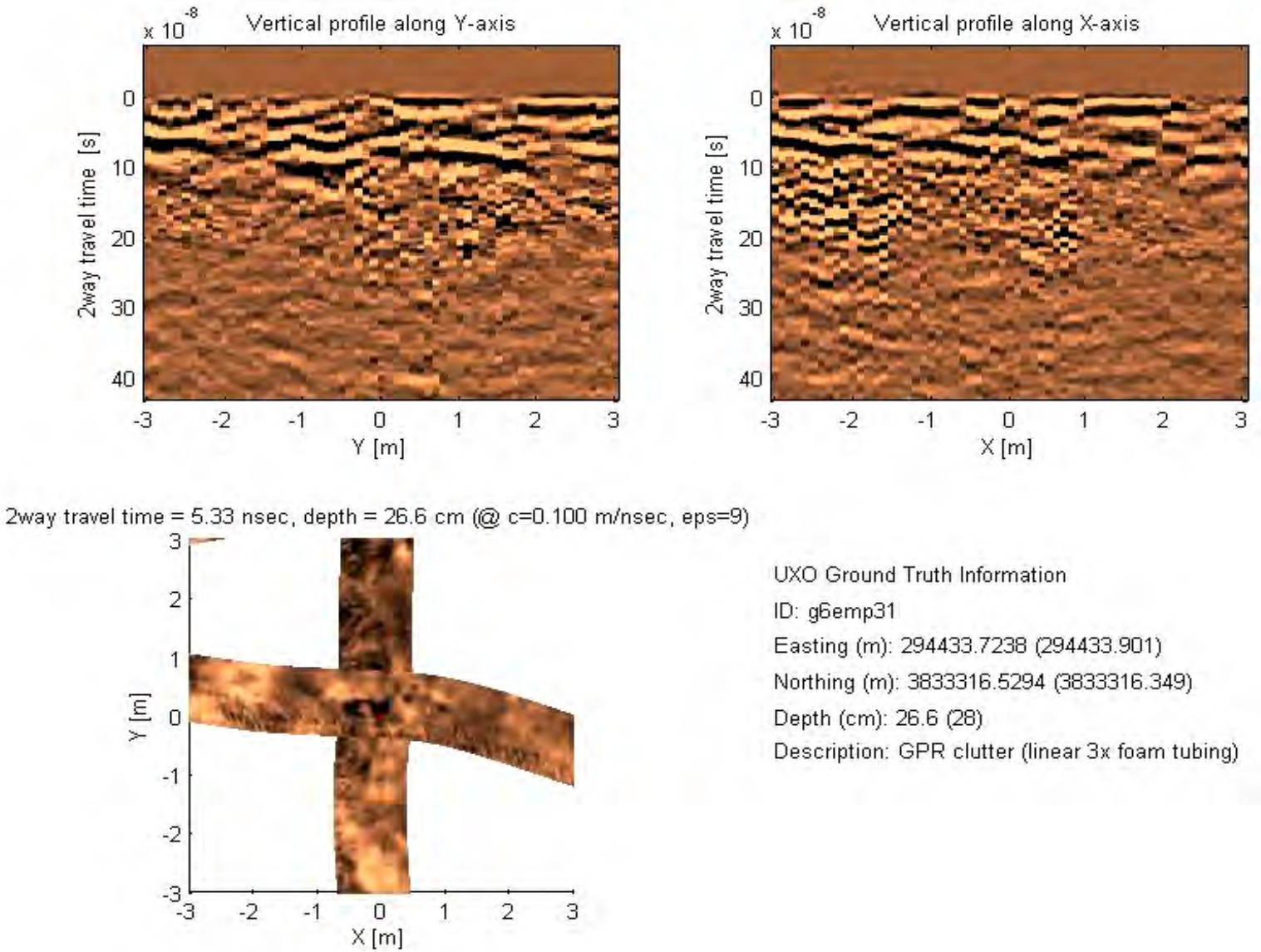


Figure B36. Analysis plots for target G6A2E31. Coordinates of center plot point are followed by ground truth coordinates in parenthesis.

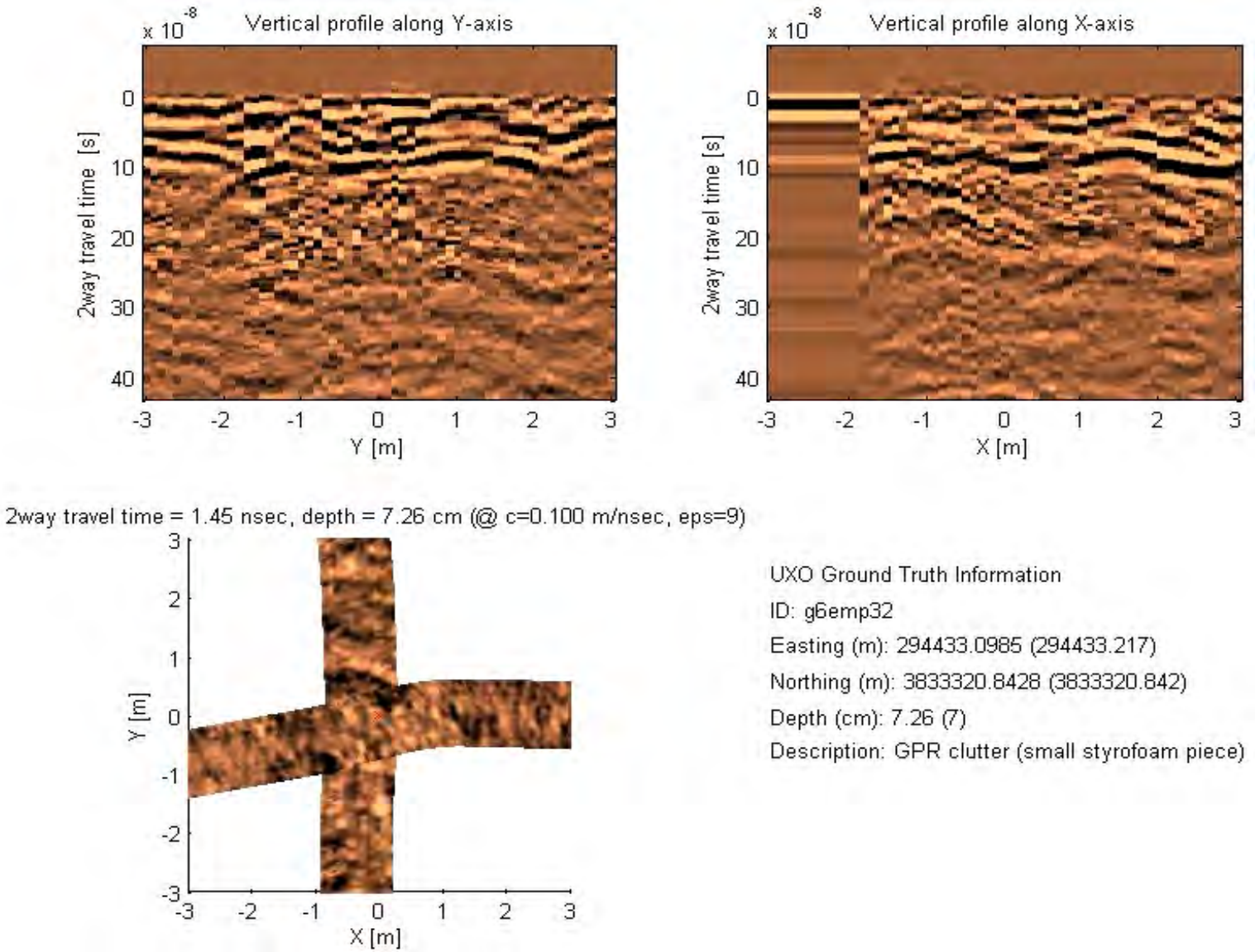


Figure B37. Analysis plots for target G6A2E32. Coordinates of center plot point are followed by ground truth coordinates in parenthesis.

## B.5. Example data plots - Area D2

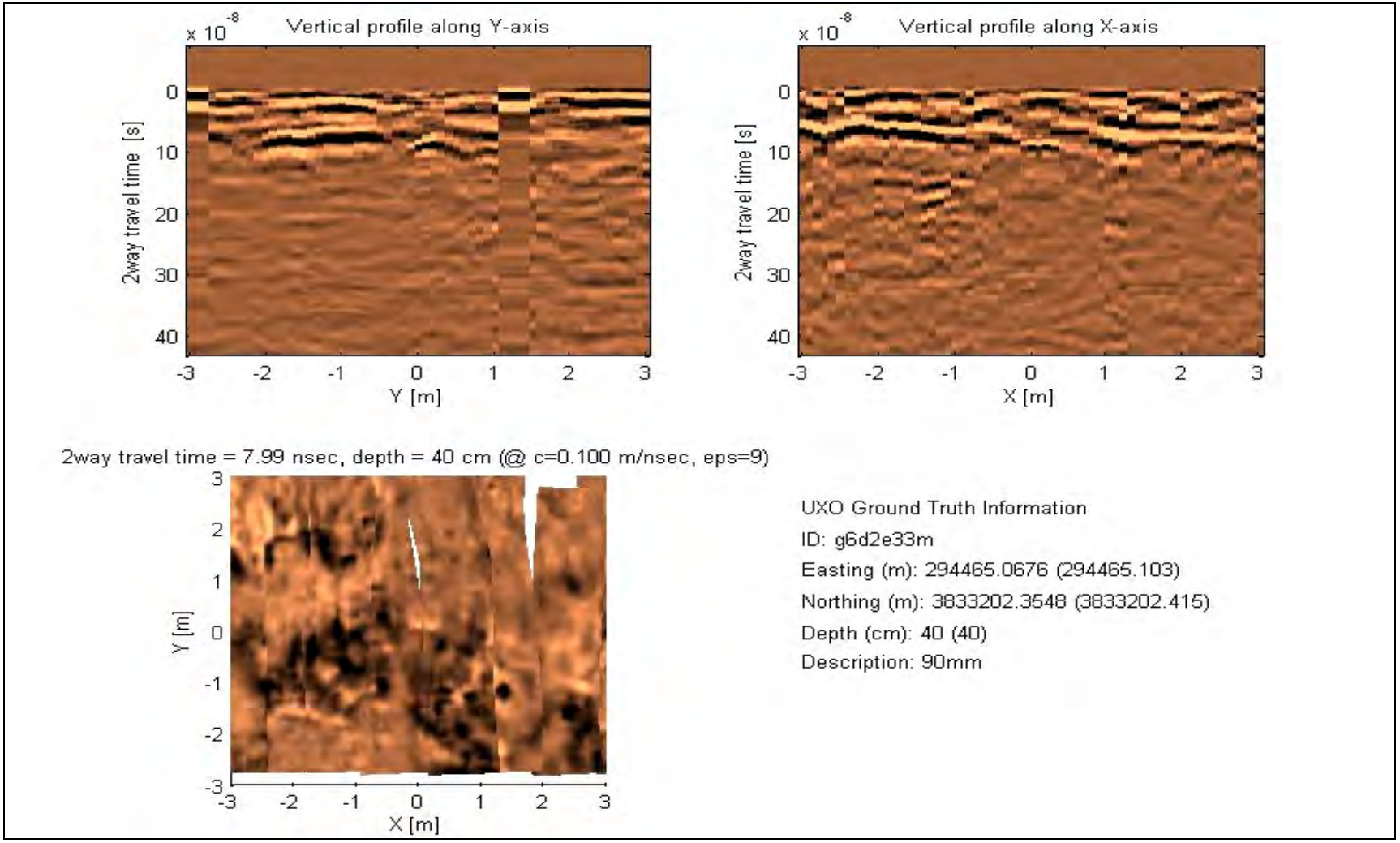


Figure B38. Analysis plots for target G6D2E33 using NS data. Coordinates of center plot point are followed by ground truth coordinates in parenthesis.

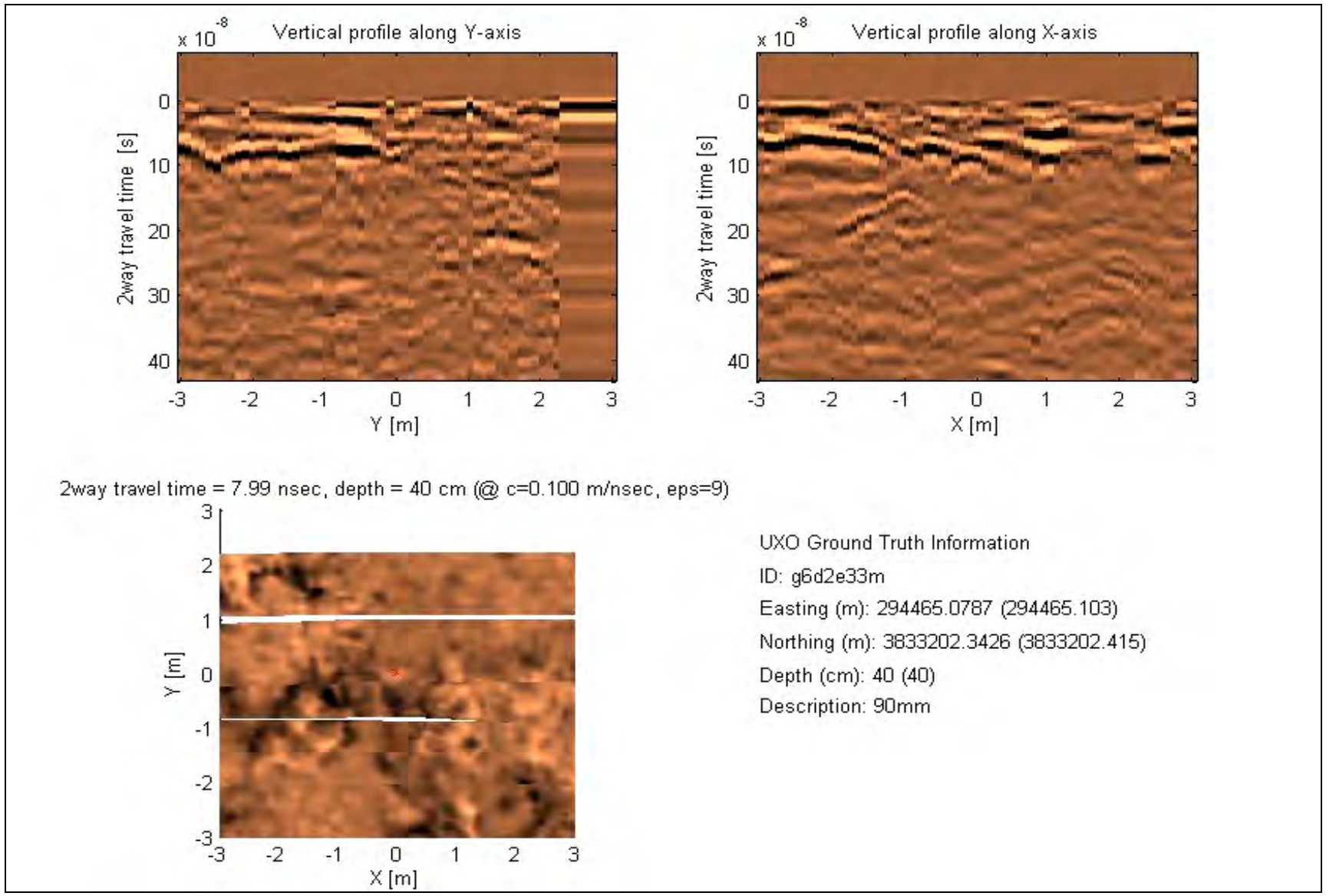


Figure B39. Analysis plots for target G6D2E33 using EW data. Coordinates of center plot point are followed by ground truth coordinates in parenthesis.

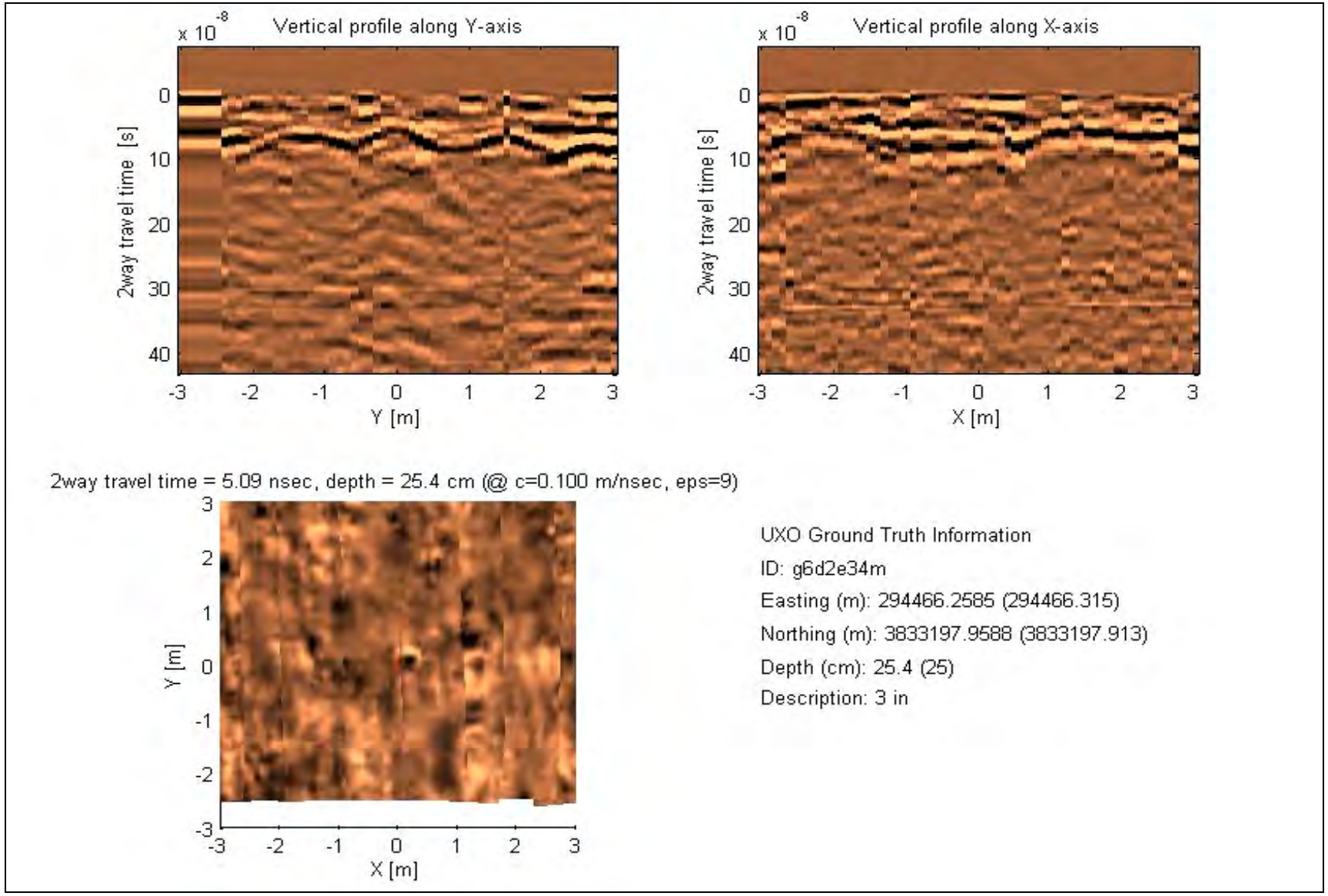


Figure B40. Analysis plots for target G6D2E34 using NS data. Coordinates of center plot point are followed by ground truth coordinates in parenthesis.

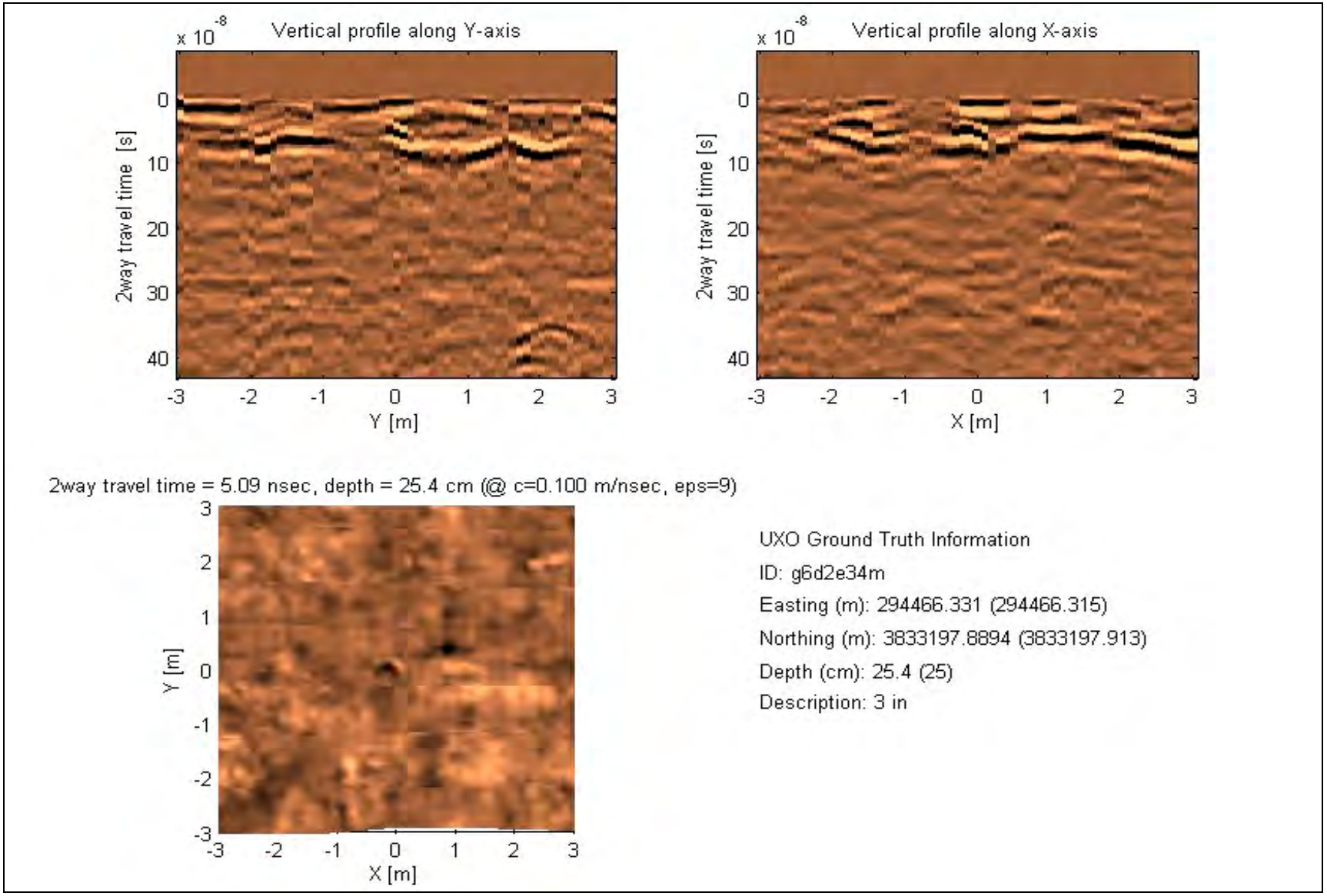


Figure B41. Analysis plots for target G6D2E34 using EW data. Coordinates of center plot point are followed by ground truth coordinates in parenthesis.

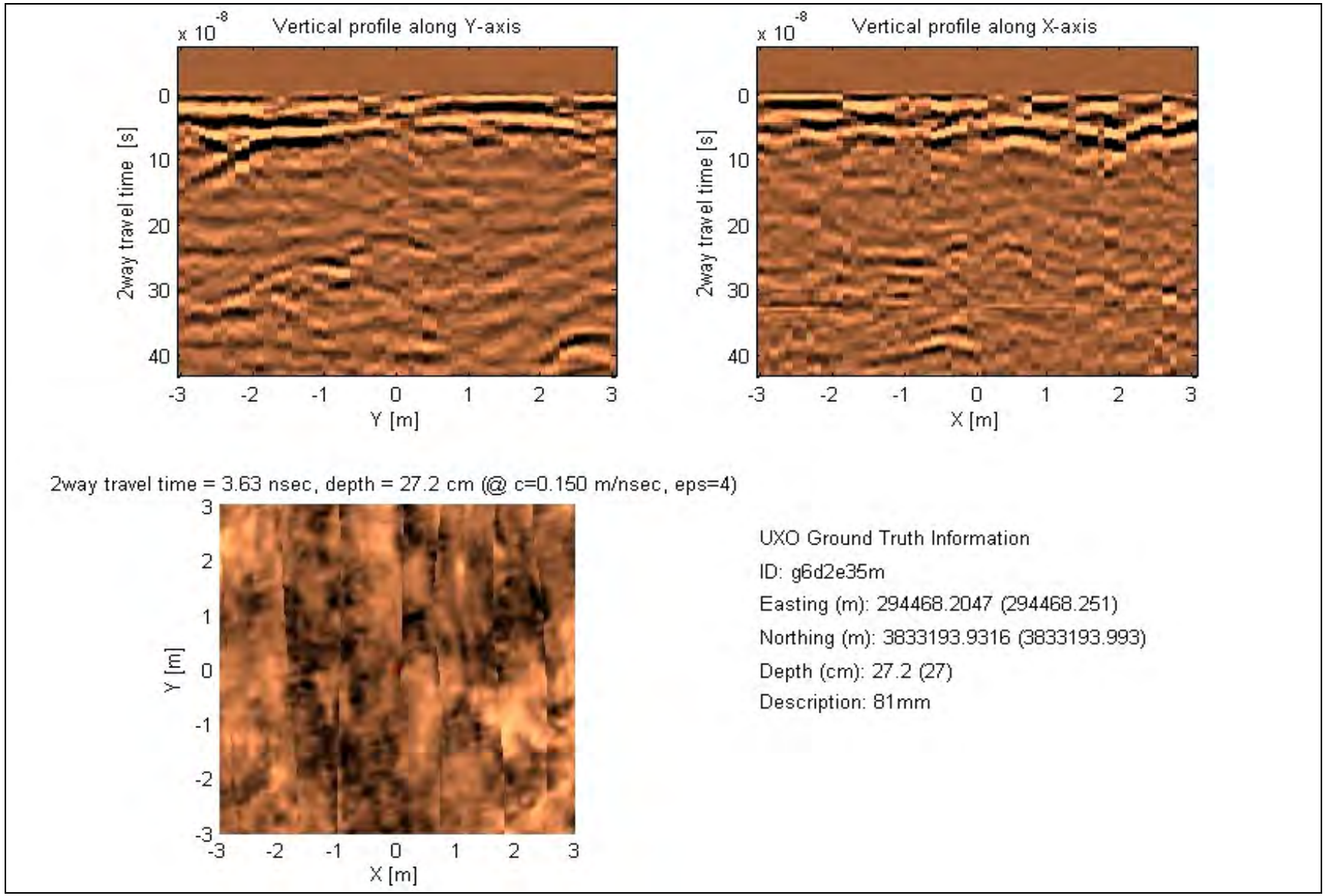


Figure B42. Analysis plots for target G6D2E35 using NS data. Coordinates of center plot point are followed by ground truth coordinates in parenthesis.

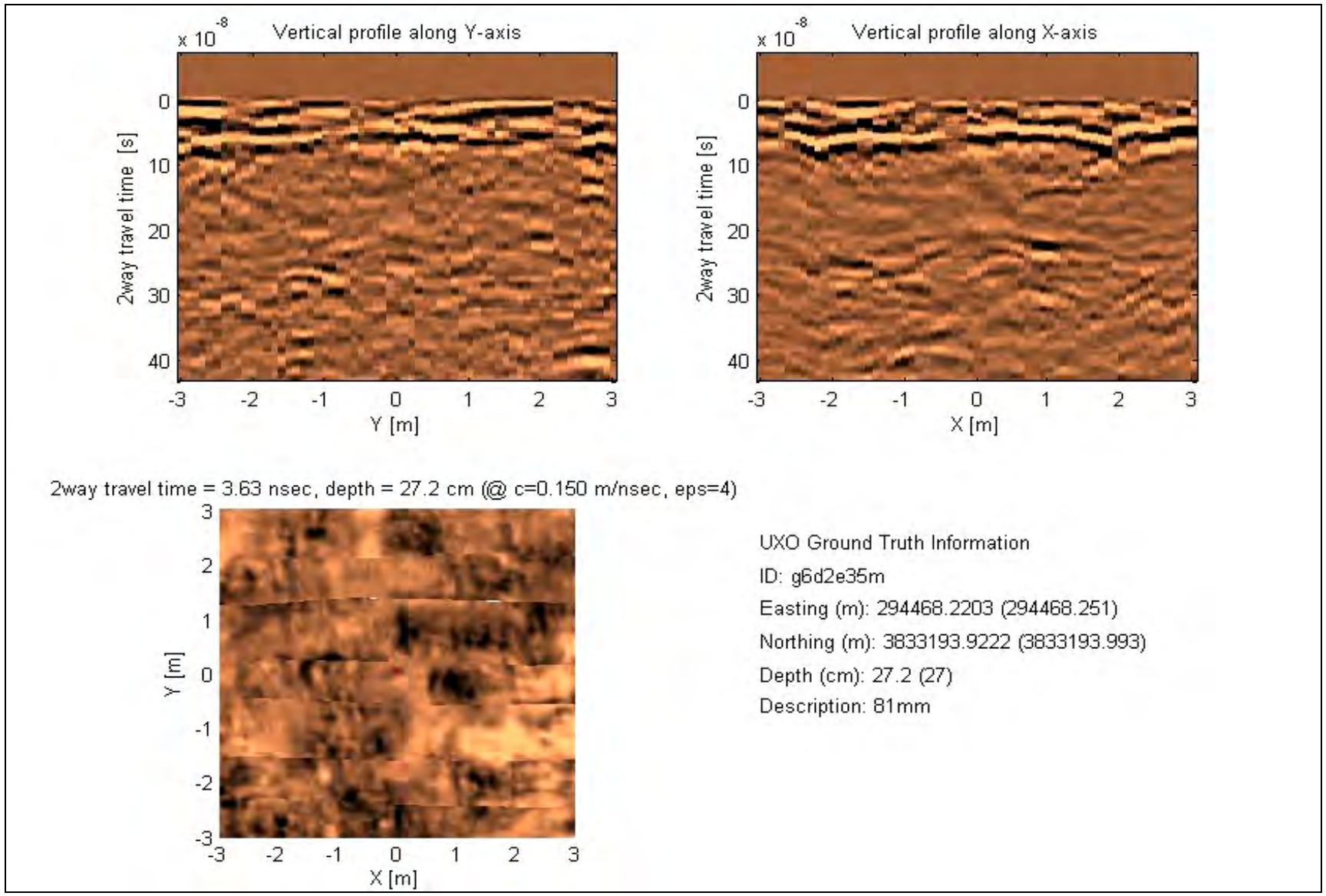


Figure B43. Analysis plots for target G6D2E35 using EW data. Coordinates of center plot point are followed by ground truth coordinates in parenthesis.

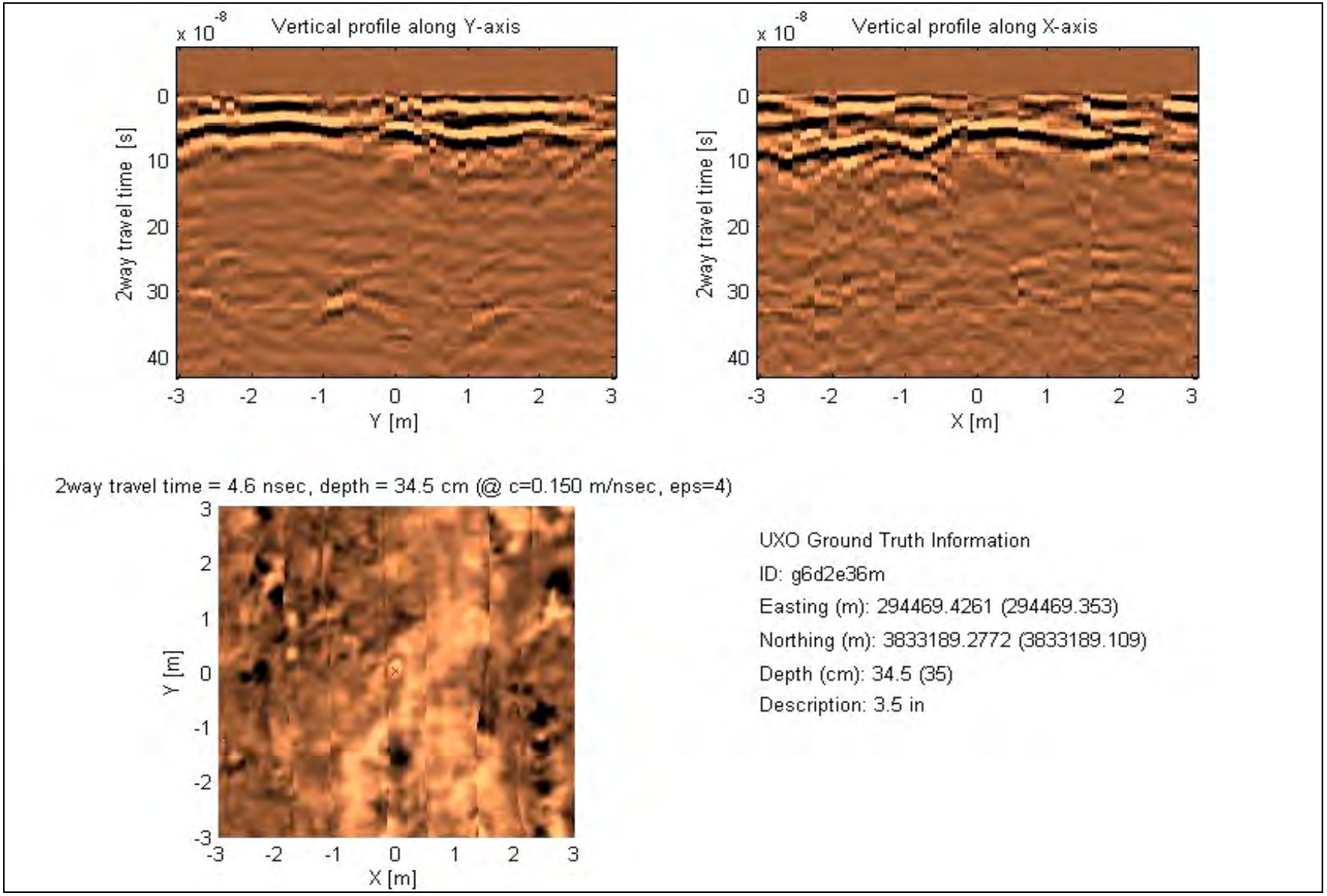


Figure B44. Analysis plots for target G6D2E36 using NS data. Coordinates of center plot point are followed by ground truth coordinates in parenthesis.

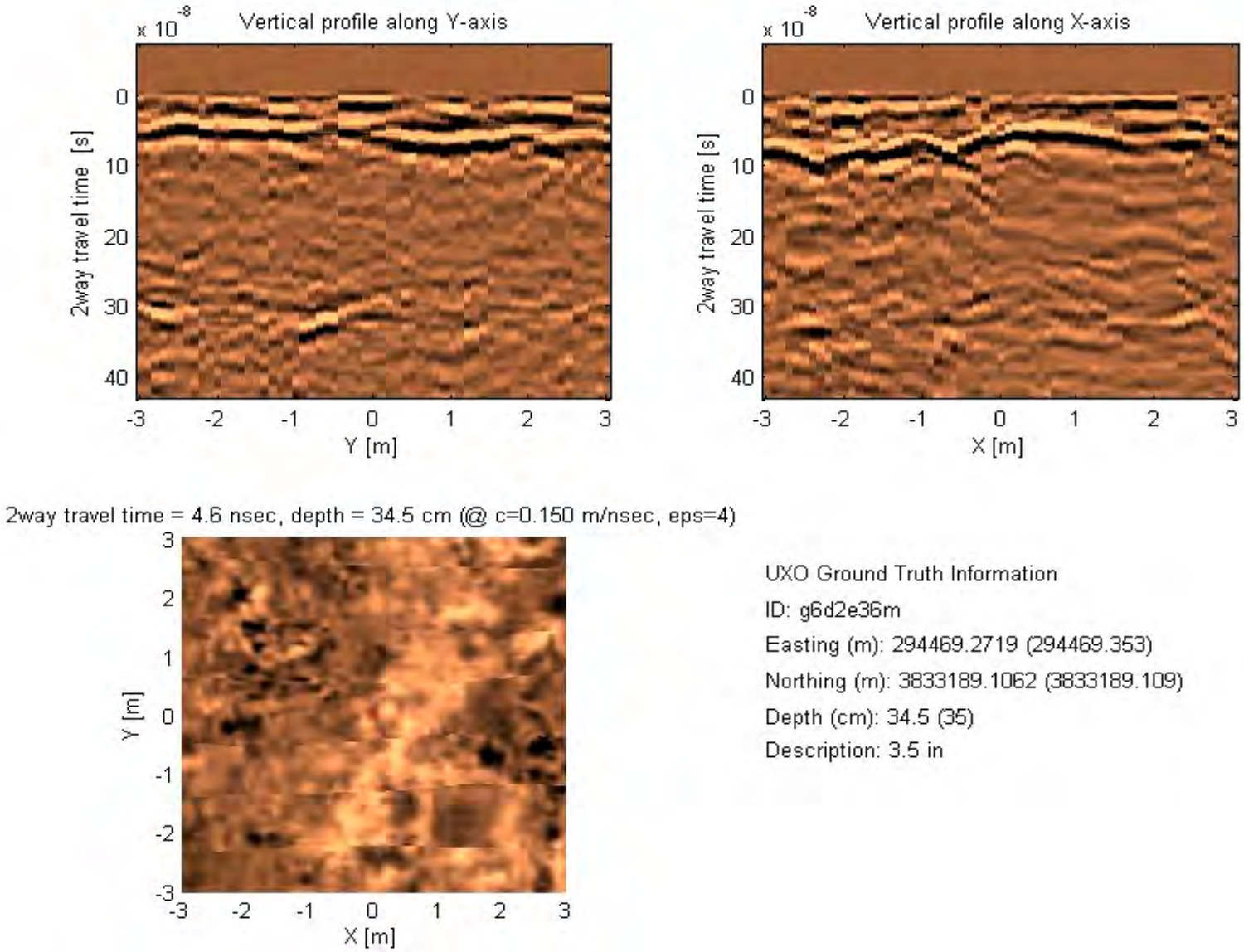


Figure B45. Analysis plots for target G6D2E36 using EW data. Coordinates of center plot point are followed by ground truth coordinates in parenthesis.

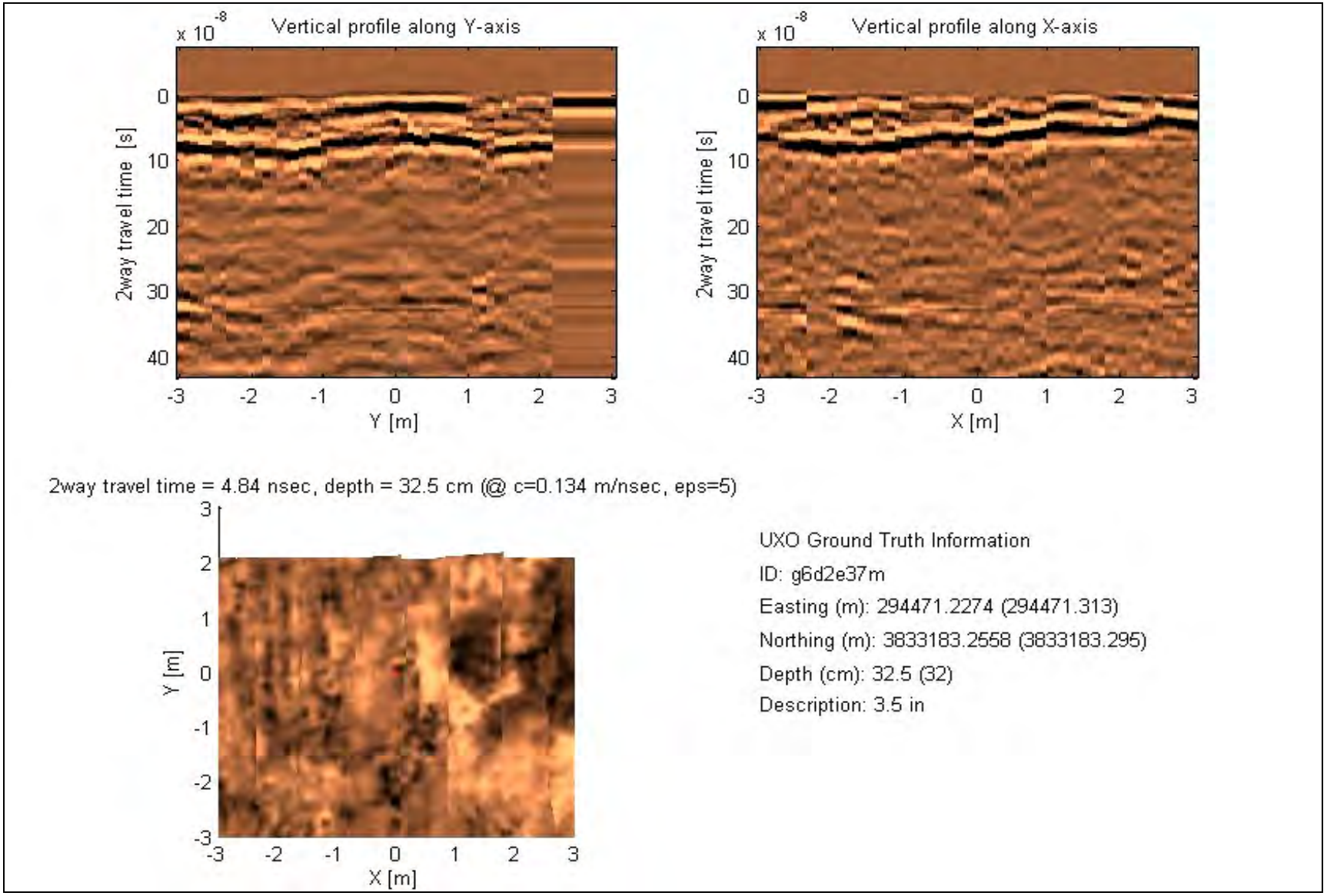


Figure B46. Analysis plots for target G6D2E37 using NS data. Coordinates of center plot point are followed by ground truth coordinates in parenthesis.

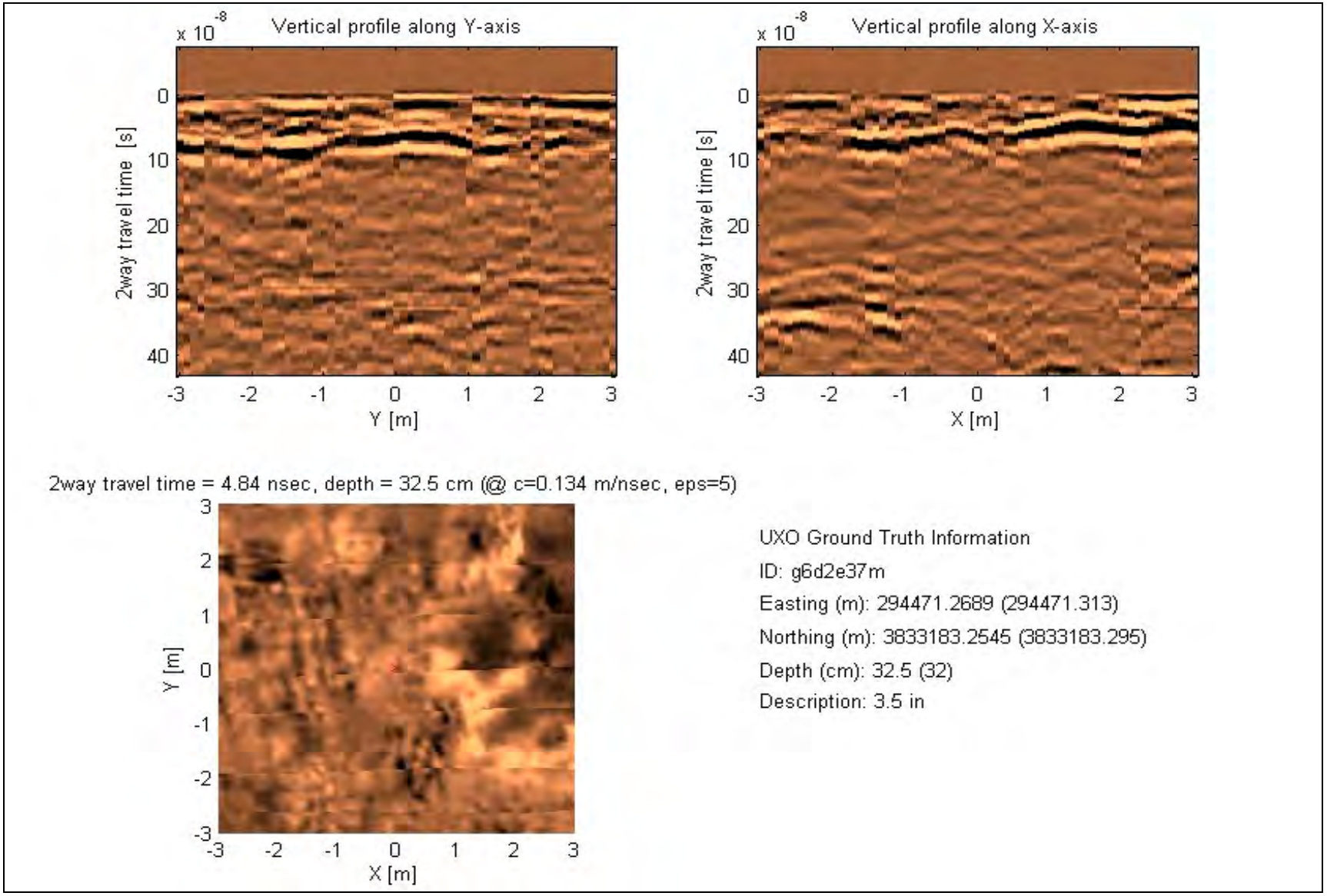


Figure B47. Analysis plots for target G6D2E37 using EW data. Coordinates of center plot point are followed by ground truth coordinates in parenthesis.

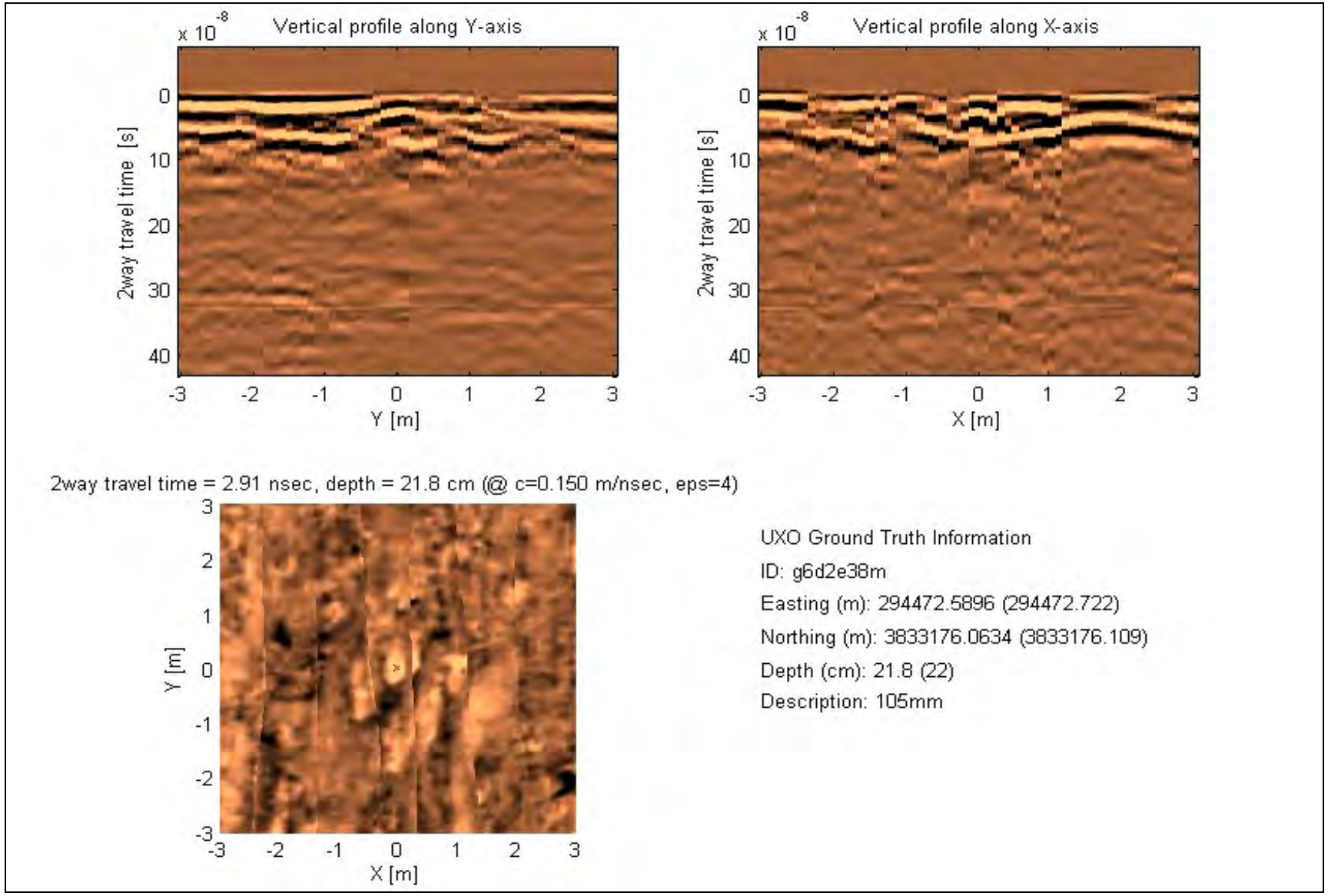


Figure B48. Analysis plots for target G6D2E38 using NS data. Coordinates of center plot point are followed by ground truth coordinates in parenthesis.

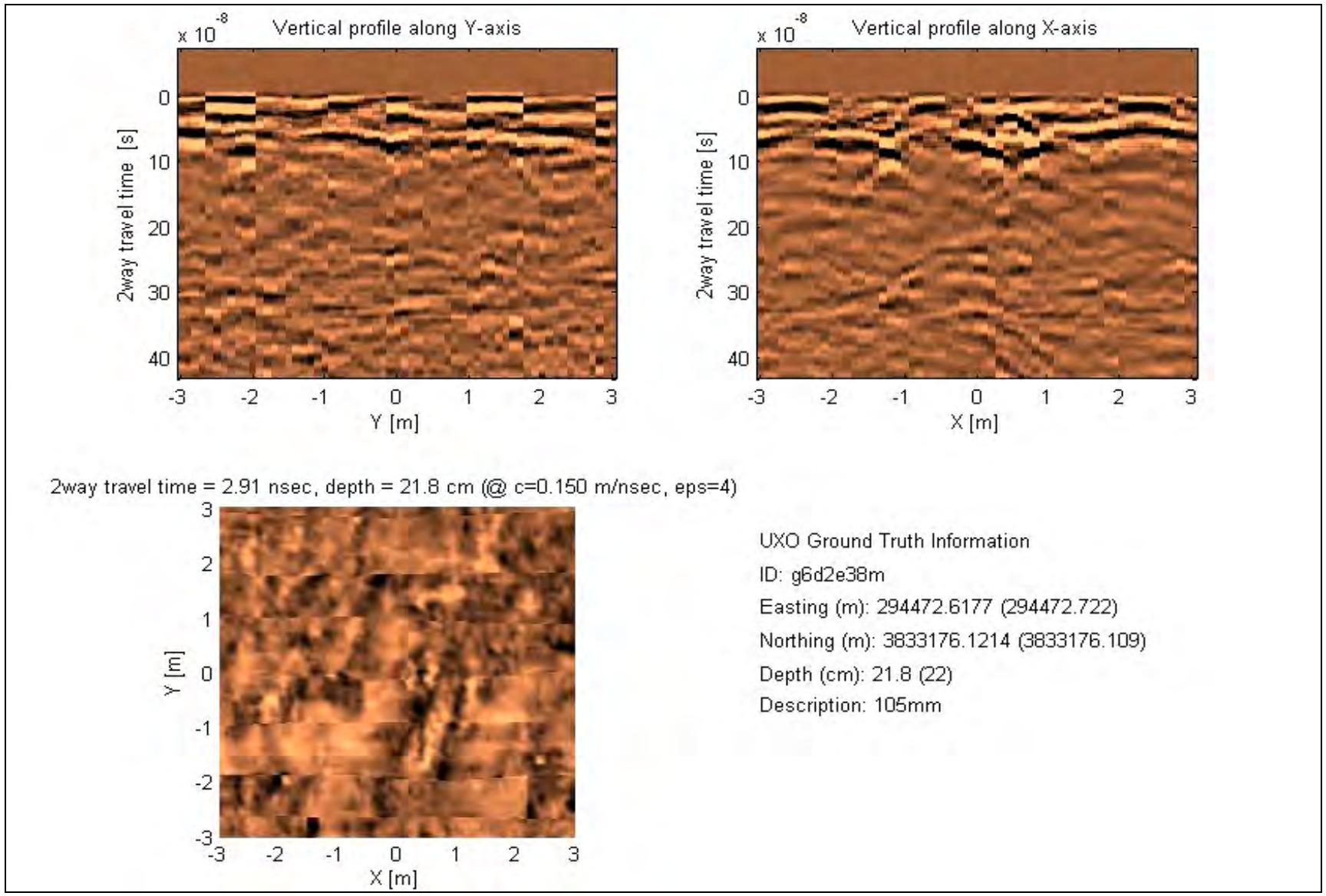


Figure B49. Analysis plots for target G6D2E38 using EW data. Coordinates of center plot point are followed by ground truth coordinates in parenthesis.

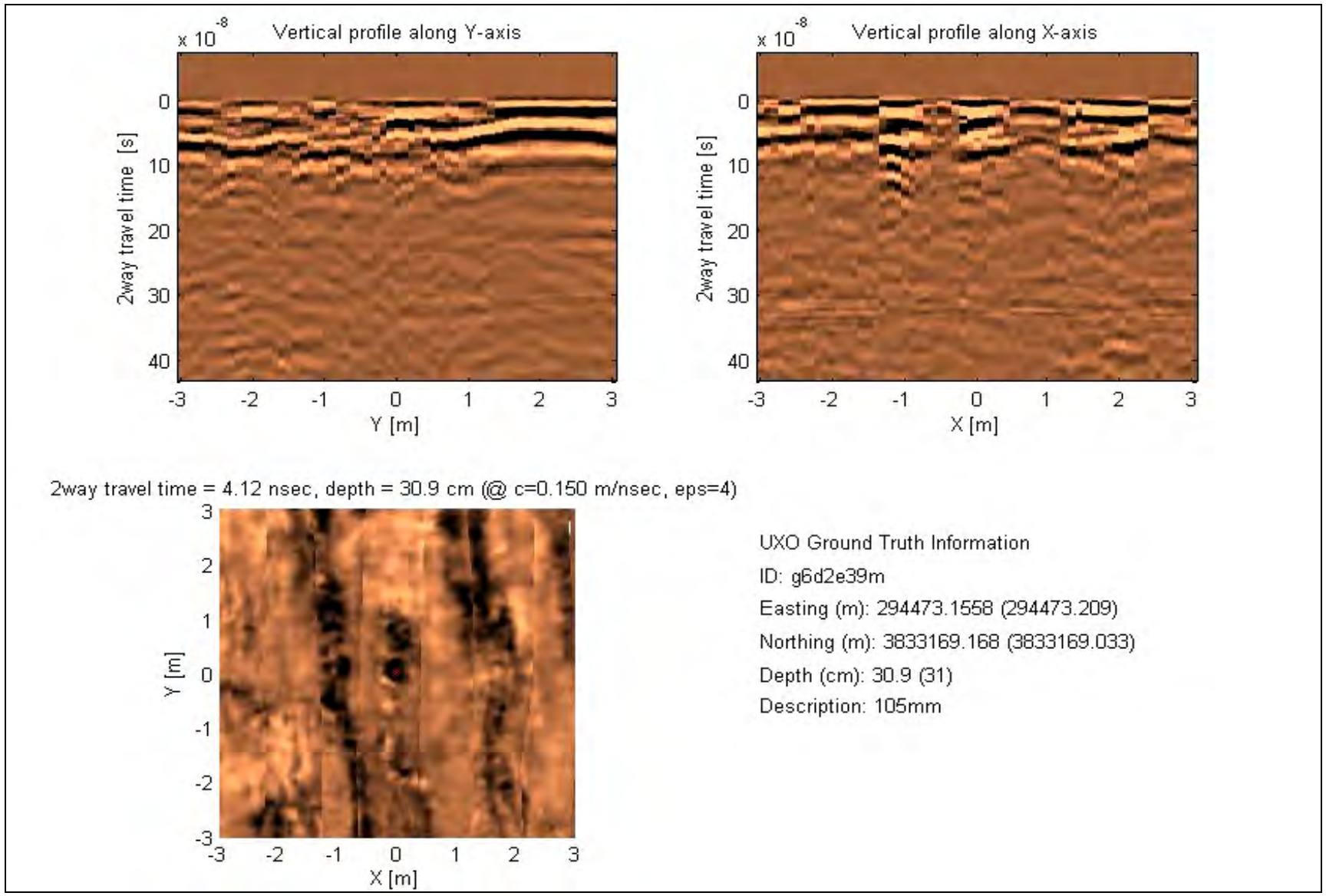


Figure B50. Analysis plots for target G6D2E39 using NS data. Coordinates of center plot point are followed by ground truth coordinates in parenthesis.

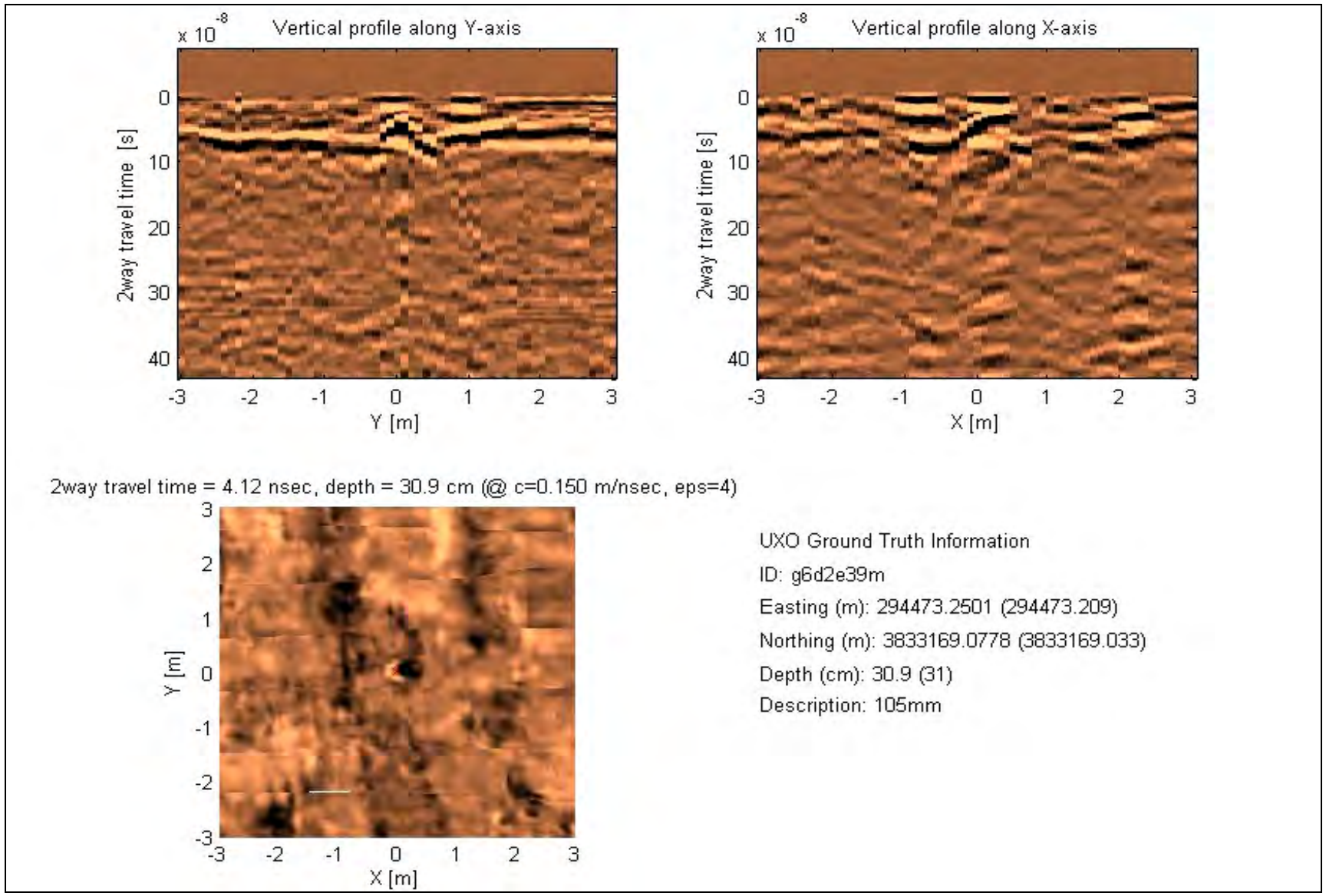


Figure B51. Analysis plots for target G6D2E39 using EW data. Coordinates of center plot point are followed by ground truth coordinates in parenthesis.

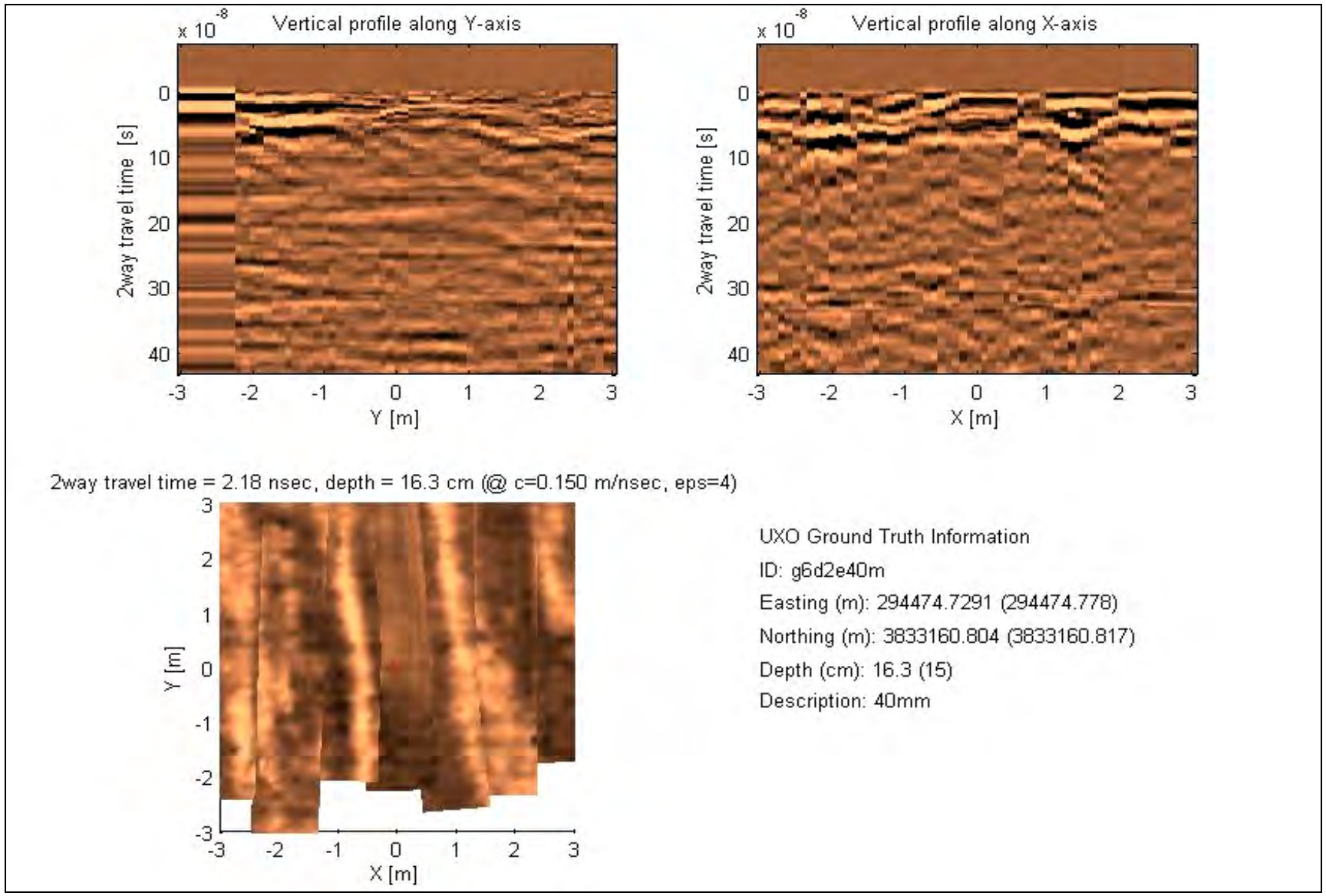


Figure B52. Analysis plots for target G6D2E40 using NS data. Coordinates of center plot point are followed by ground truth coordinates in parenthesis.

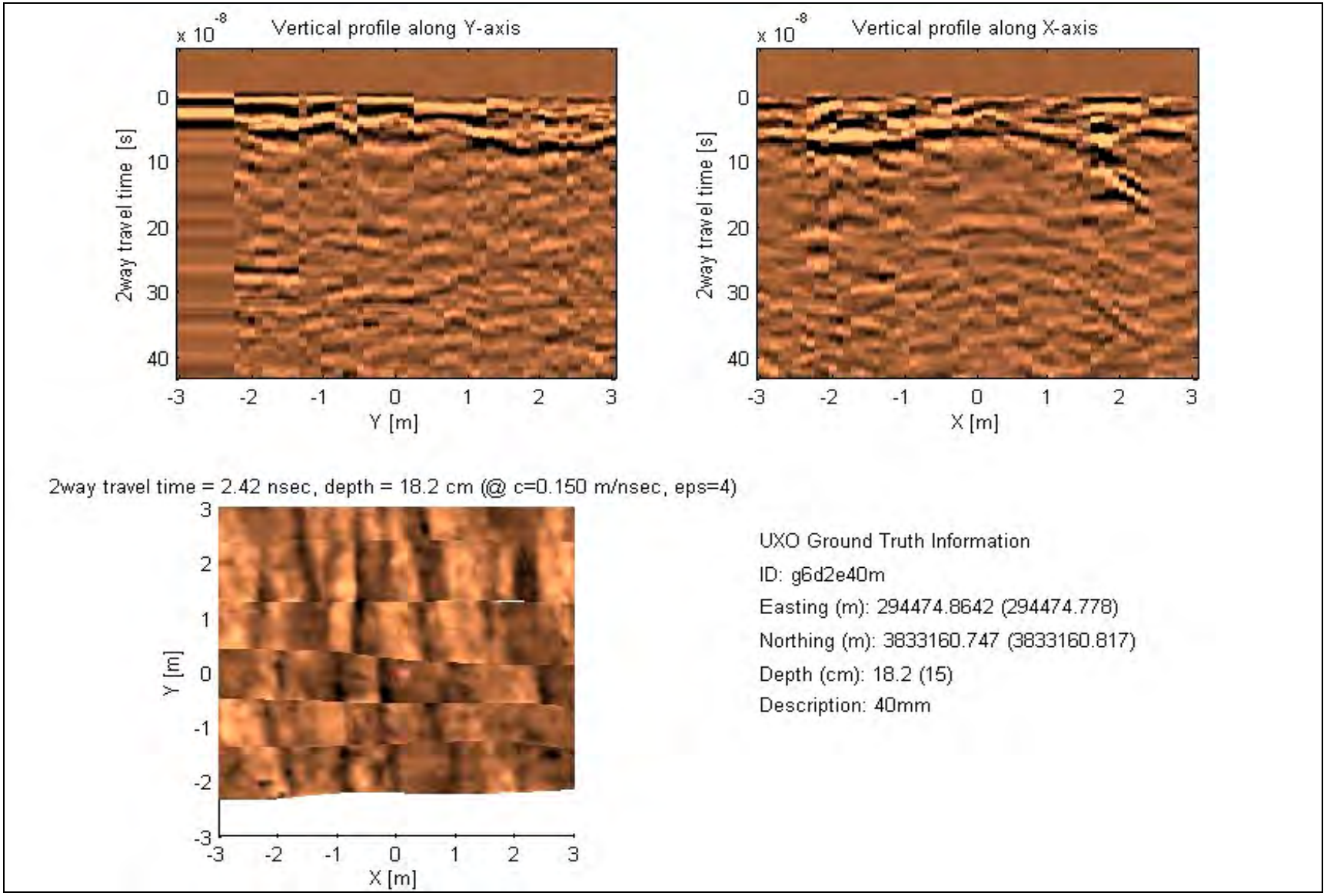


Figure B53. Analysis plots for target G6D2E40 using EW data. Coordinates of center plot point are followed by ground truth coordinates in parenthesis.

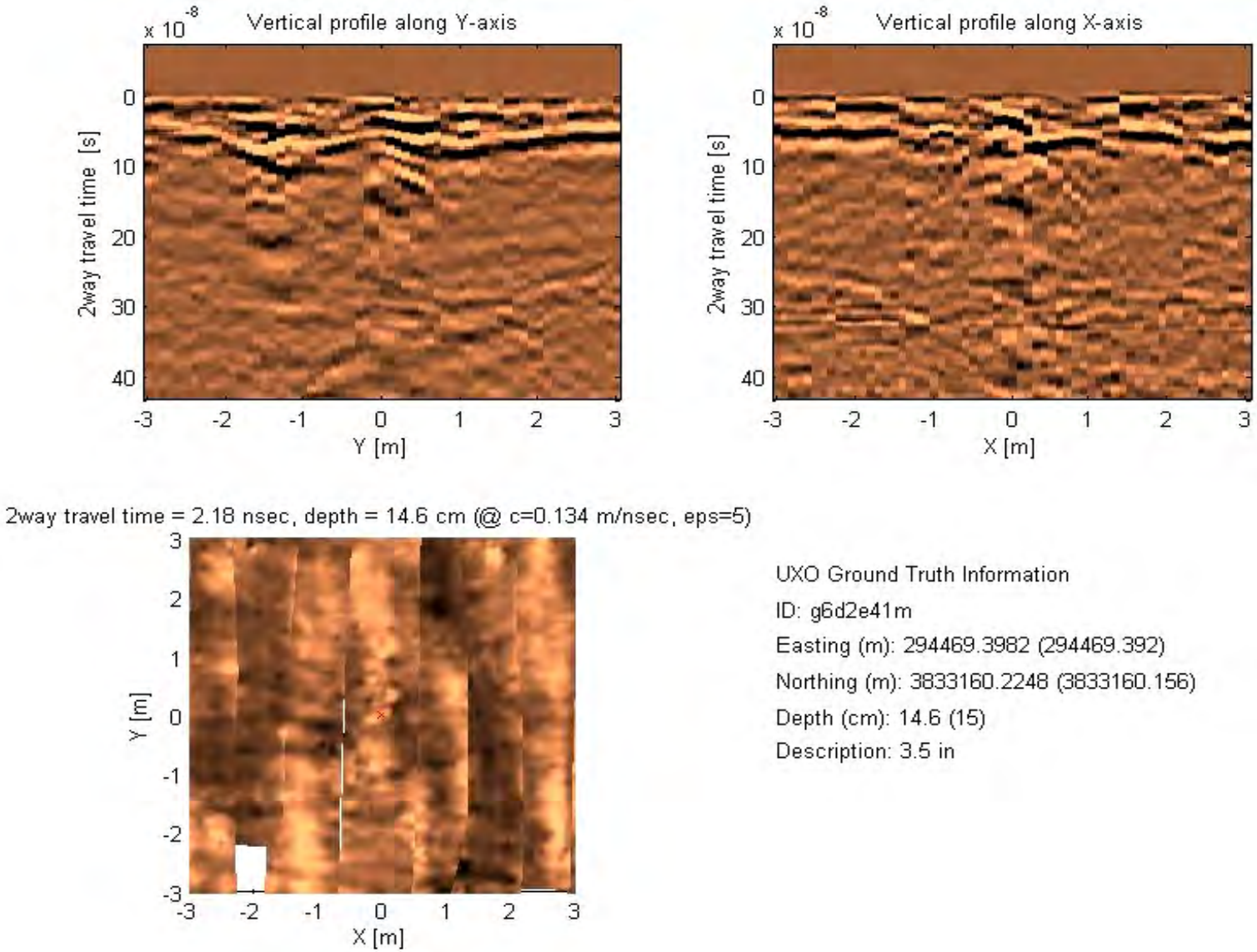


Figure B54. Analysis plots for target G6D2E41 using NS data. Coordinates of center plot point are followed by ground truth coordinates in parenthesis.

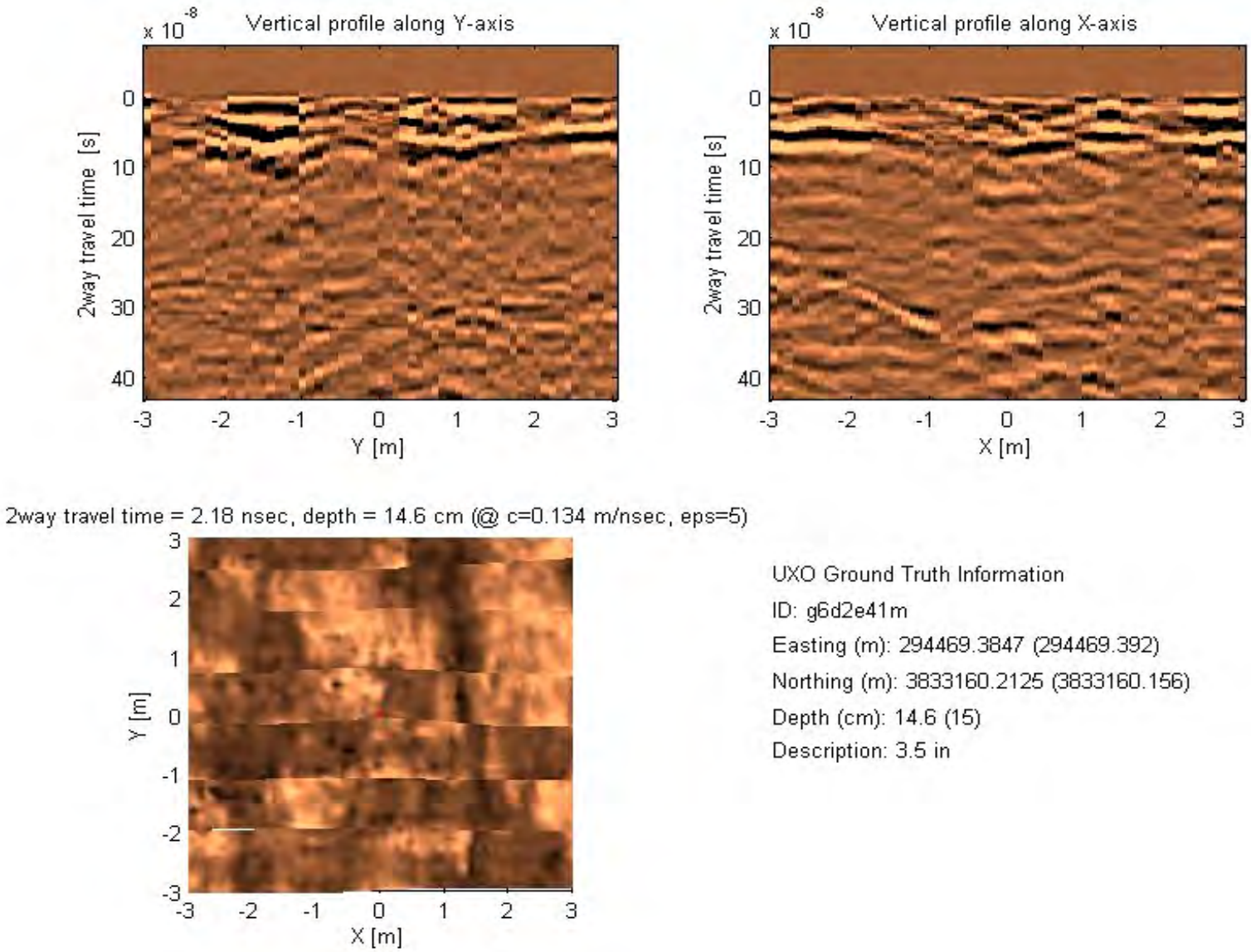


Figure B55. Analysis plots for target G6D2E41 using EW data. Coordinates of center plot point are followed by ground truth coordinates in parenthesis.

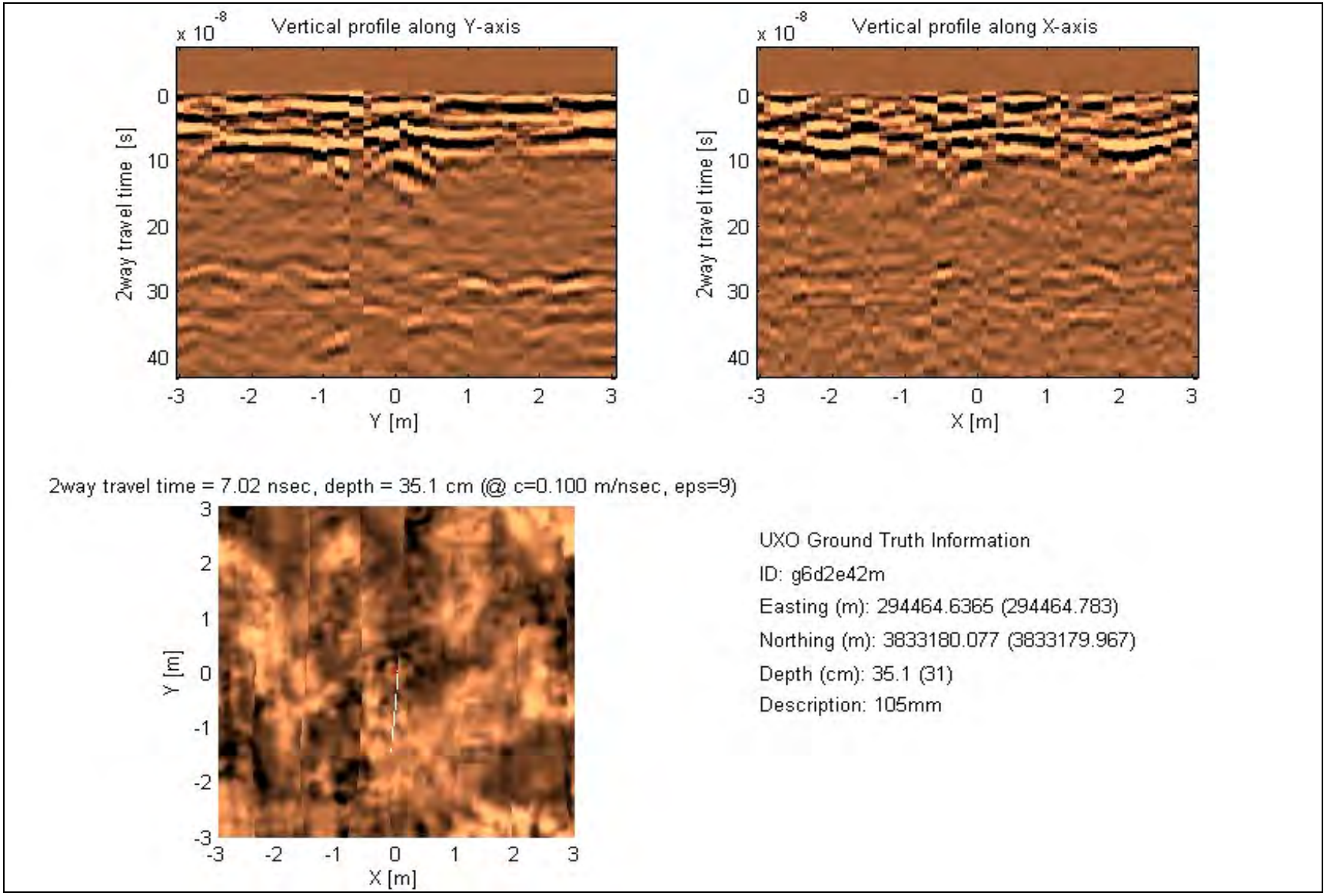


Figure B56. Analysis plots for target G6D2E42 using NS data. Coordinates of center plot point are followed by ground truth coordinates in parenthesis.

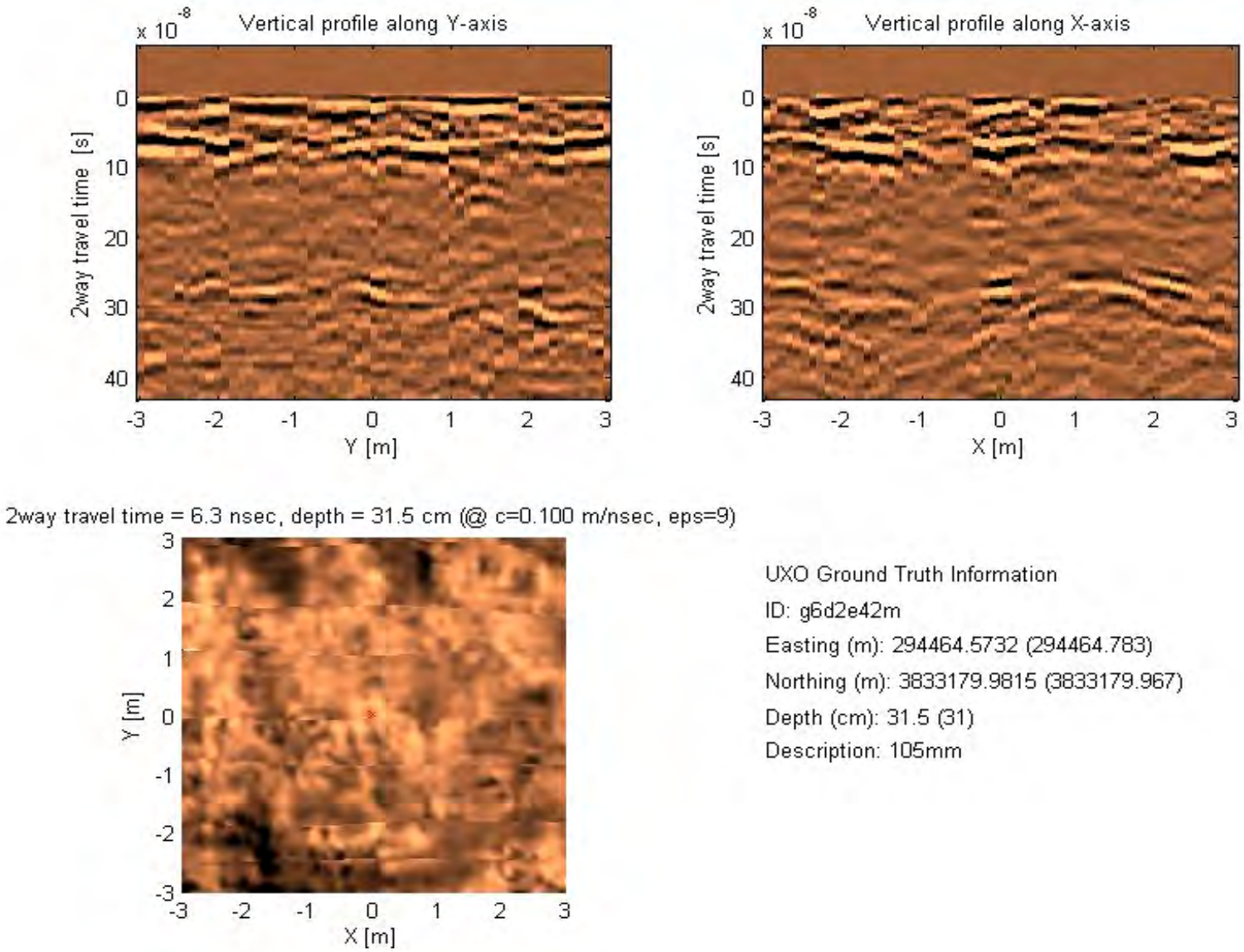


Figure B57. Analysis plots for target G6D2E42 using EW data. Coordinates of center plot point are followed by ground truth coordinates in parenthesis.

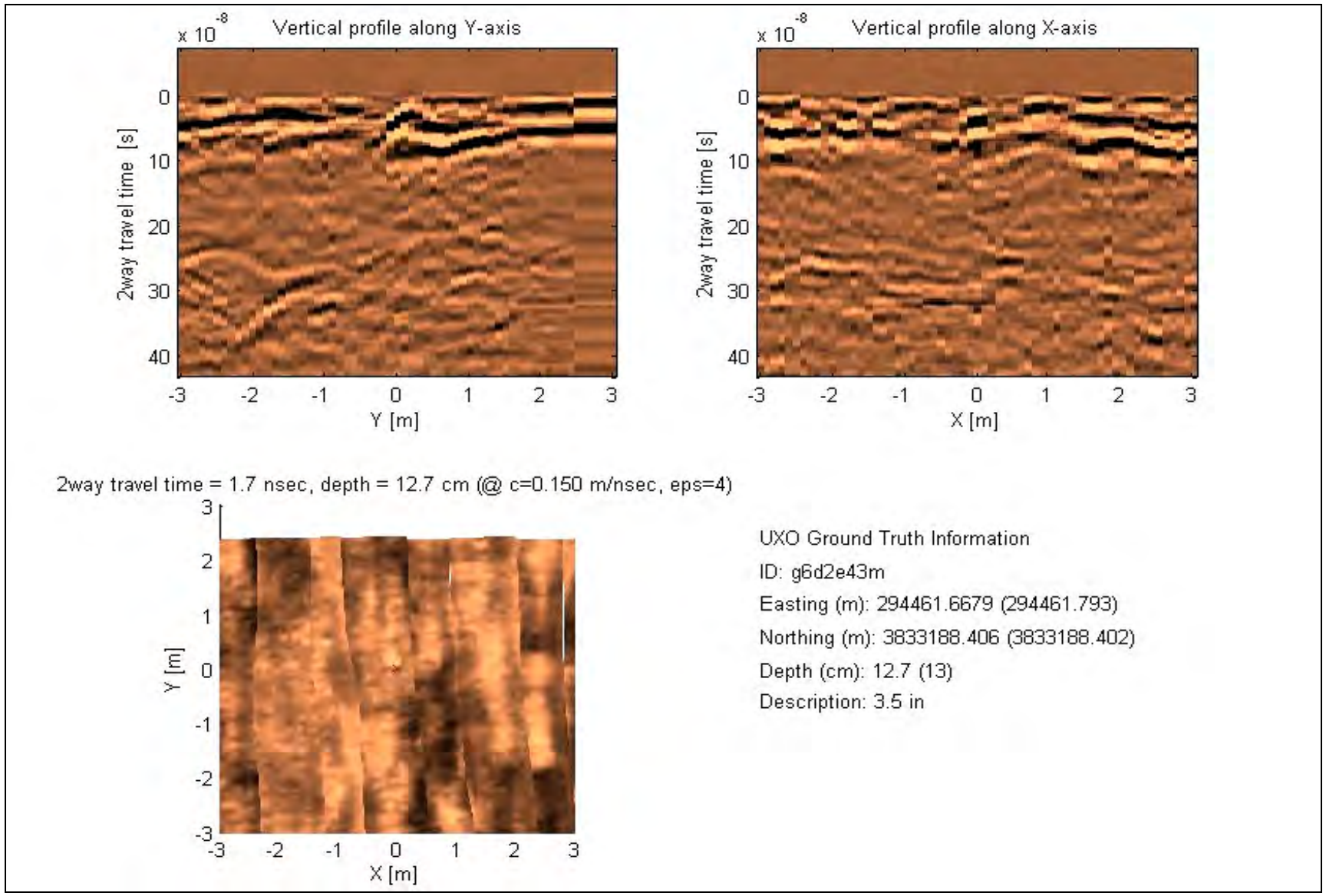


Figure B58. Analysis plots for target G6D2E43 using NS data. Coordinates of center plot point are followed by ground truth coordinates in parenthesis.

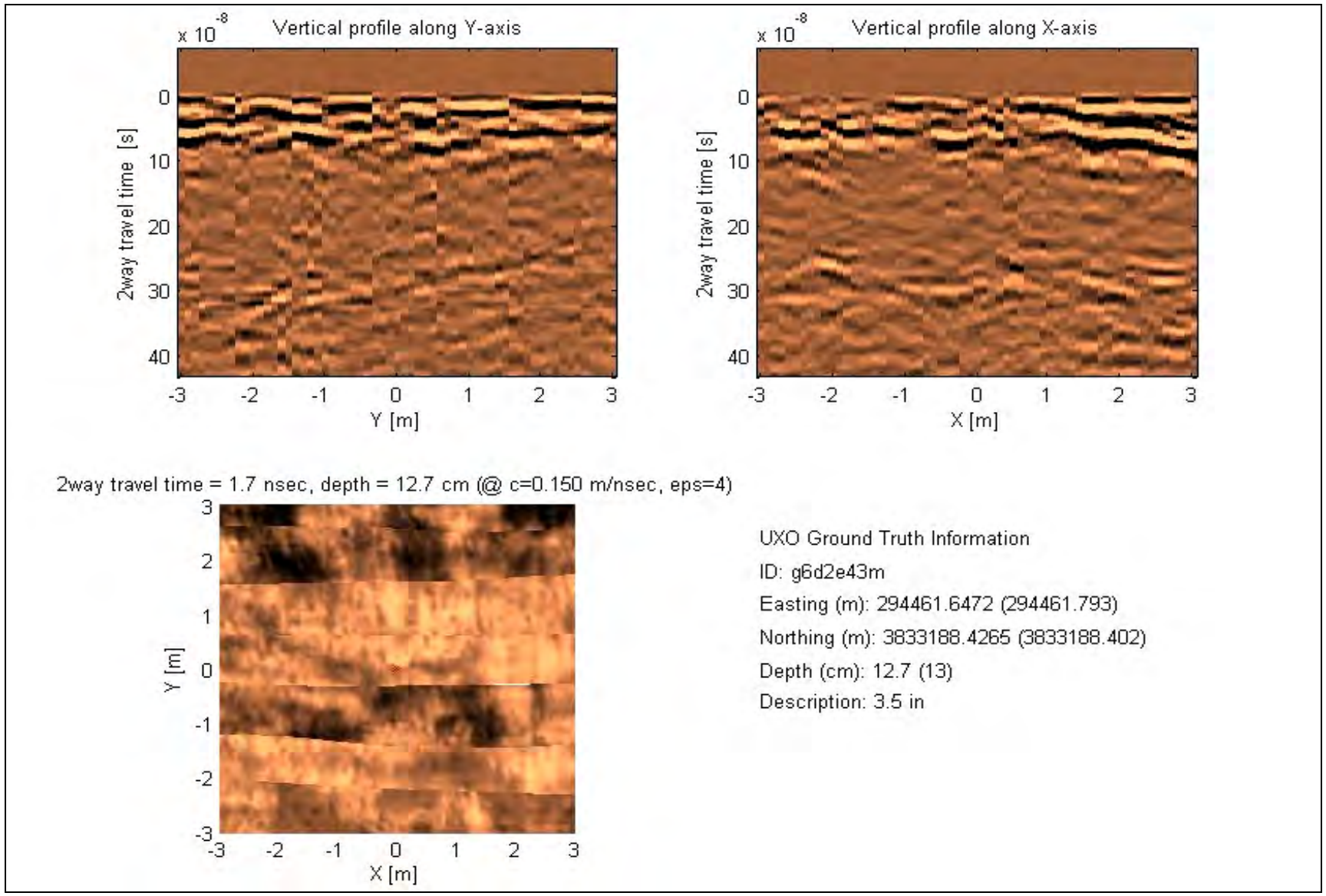


Figure B59. Analysis plots for target G6D2E43 using EW data. Coordinates of center plot point are followed by ground truth coordinates in parenthesis.

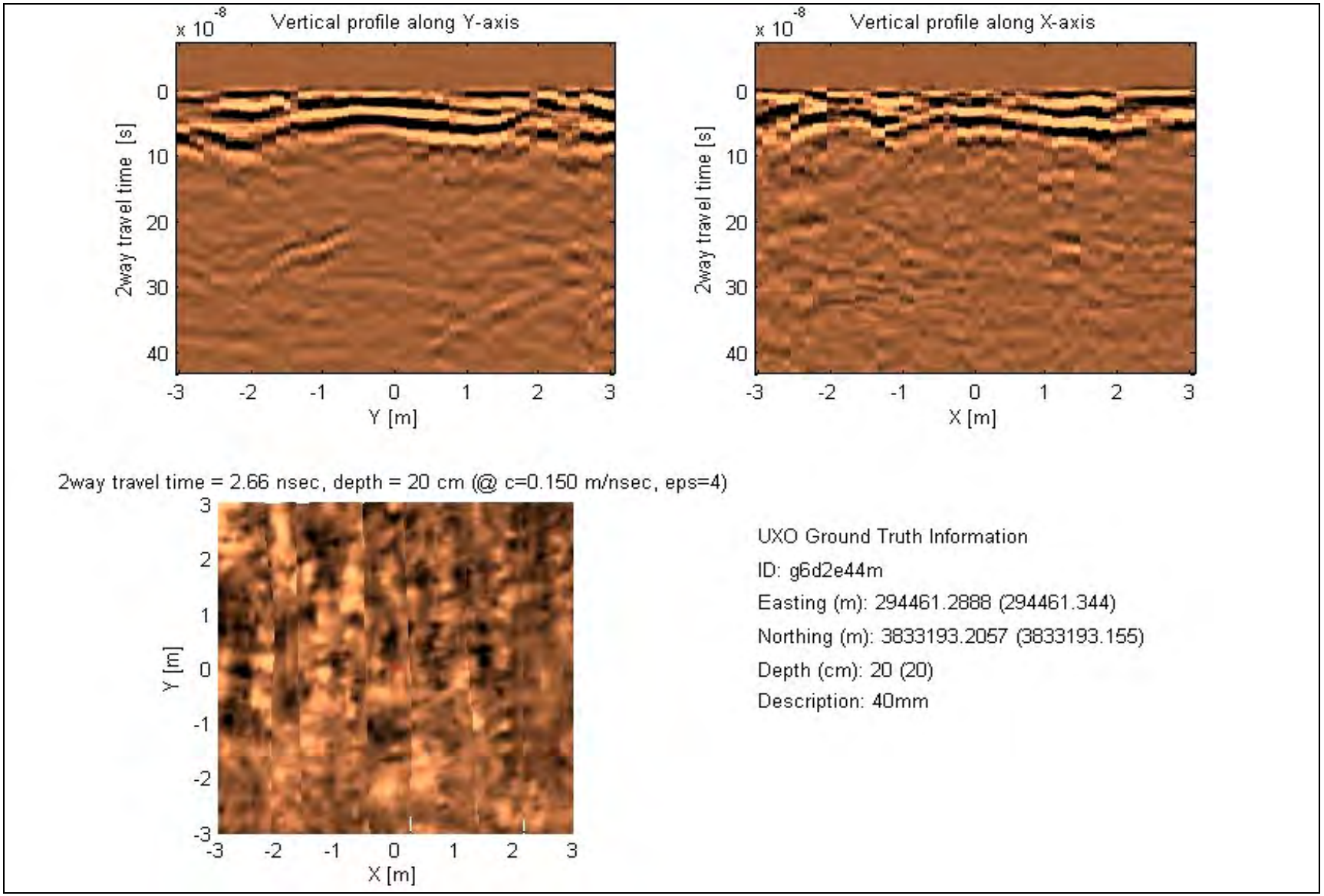


Figure B60. Analysis plots for target G6D2E44 using NS data. Coordinates of center plot point are followed by ground truth coordinates in parenthesis.

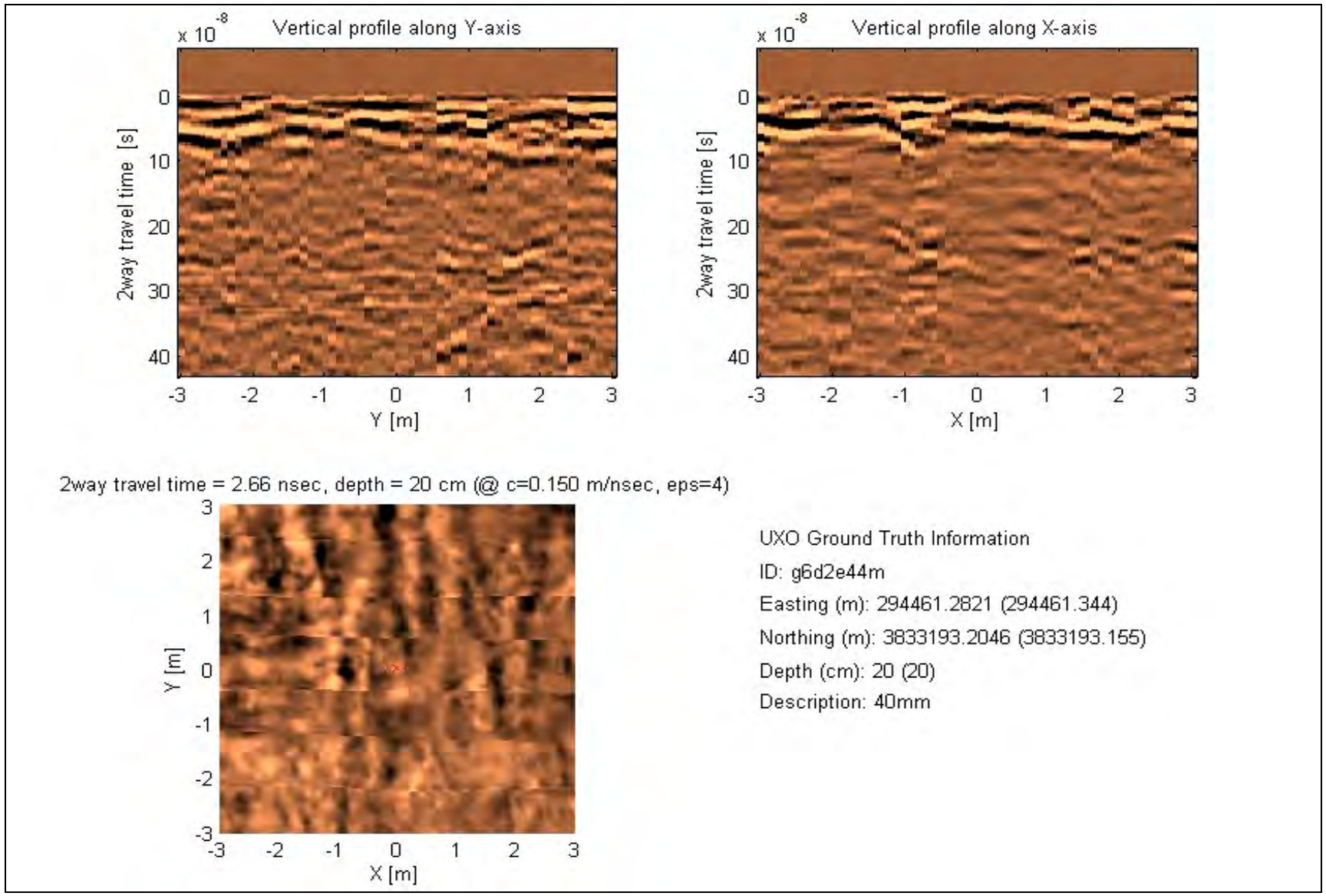


Figure B61. Analysis plots for target G6D2E44 using EW data. Coordinates of center plot point are followed by ground truth coordinates in parenthesis.

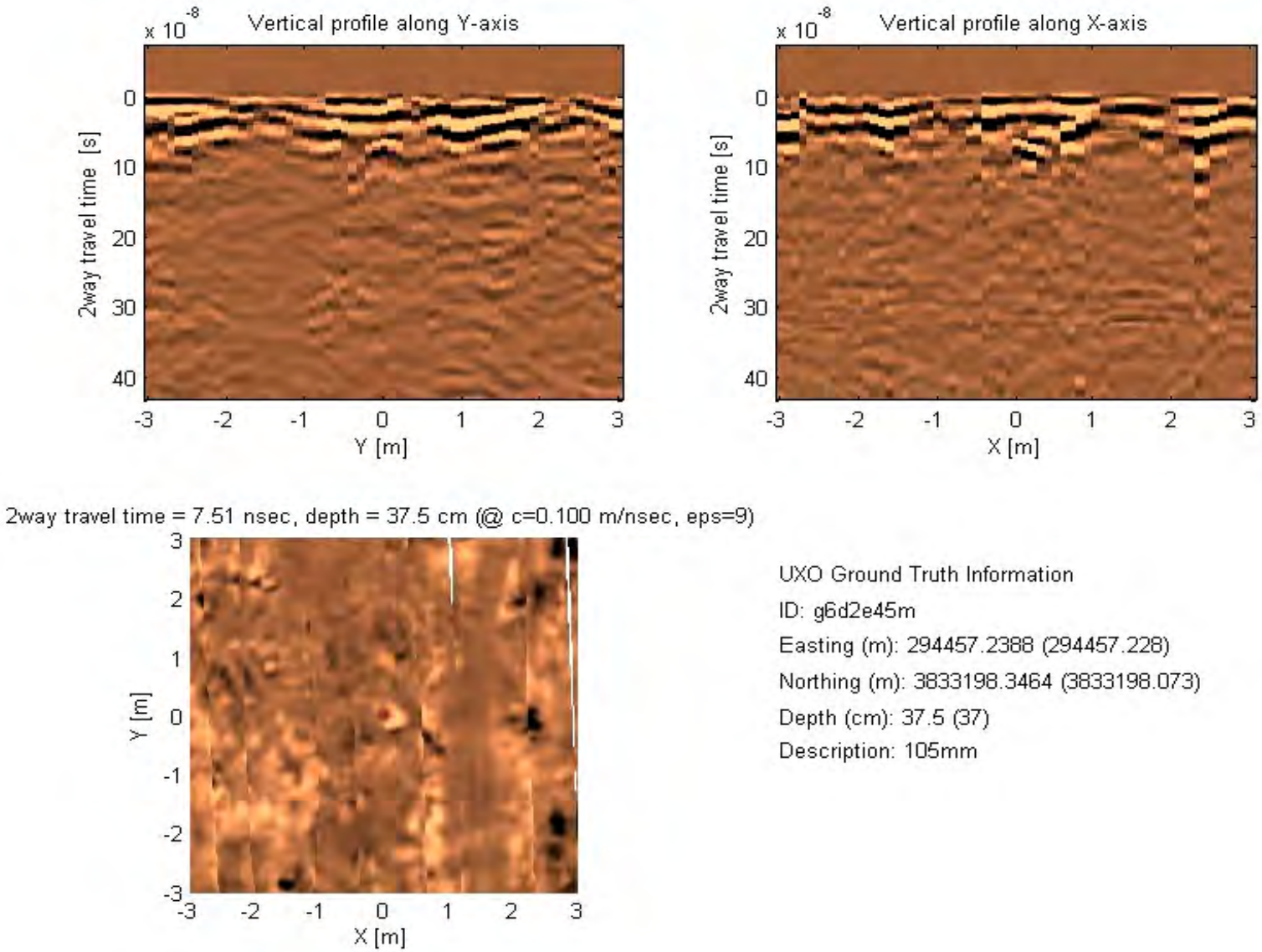


Figure B62. Analysis plots for target G6D2E45 using NS data. Coordinates of center plot point are followed by ground truth coordinates in parenthesis.

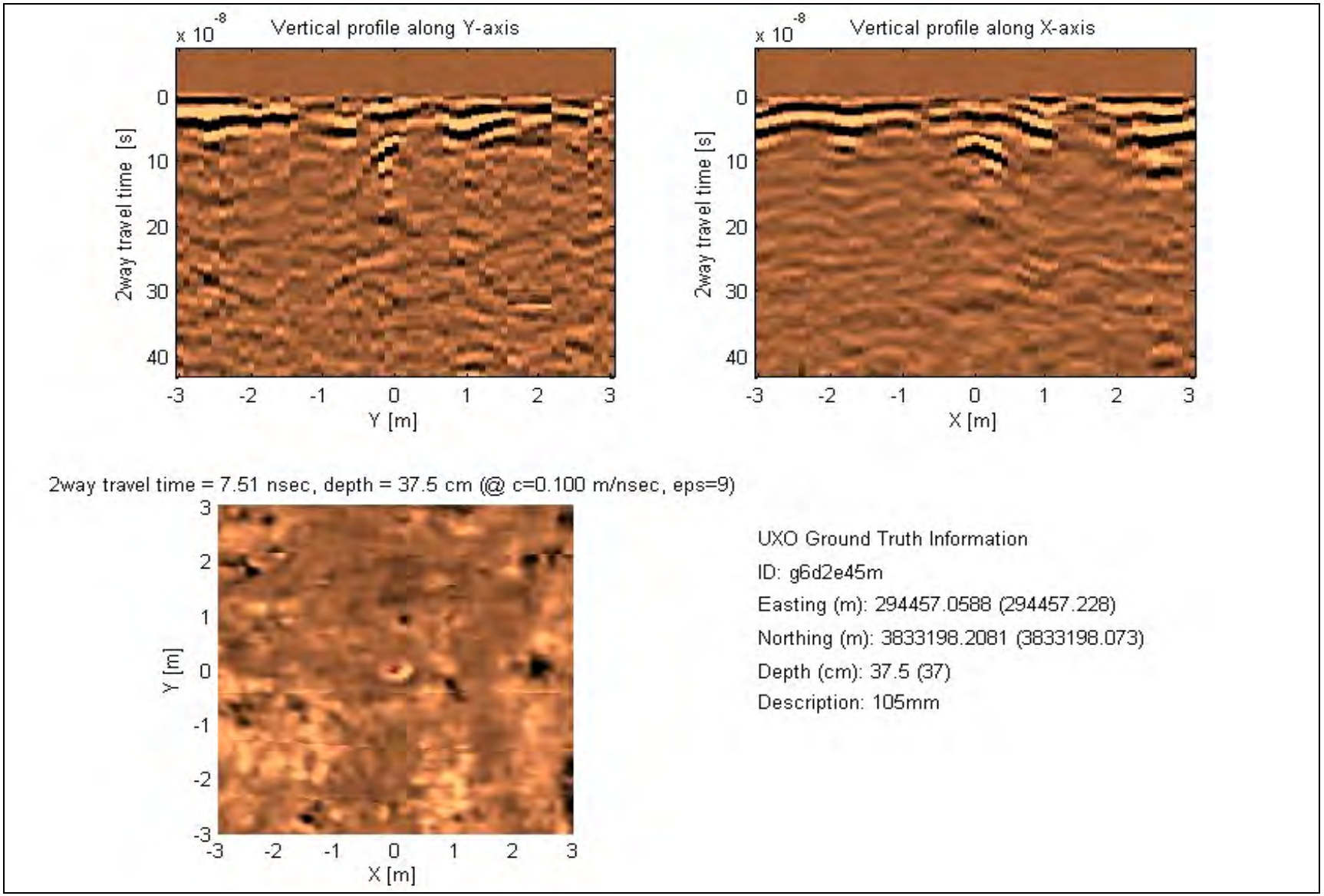


Figure B63. Analysis plots for target G6D2E45 using EW data. Coordinates of center plot point are followed by ground truth coordinates in parenthesis.

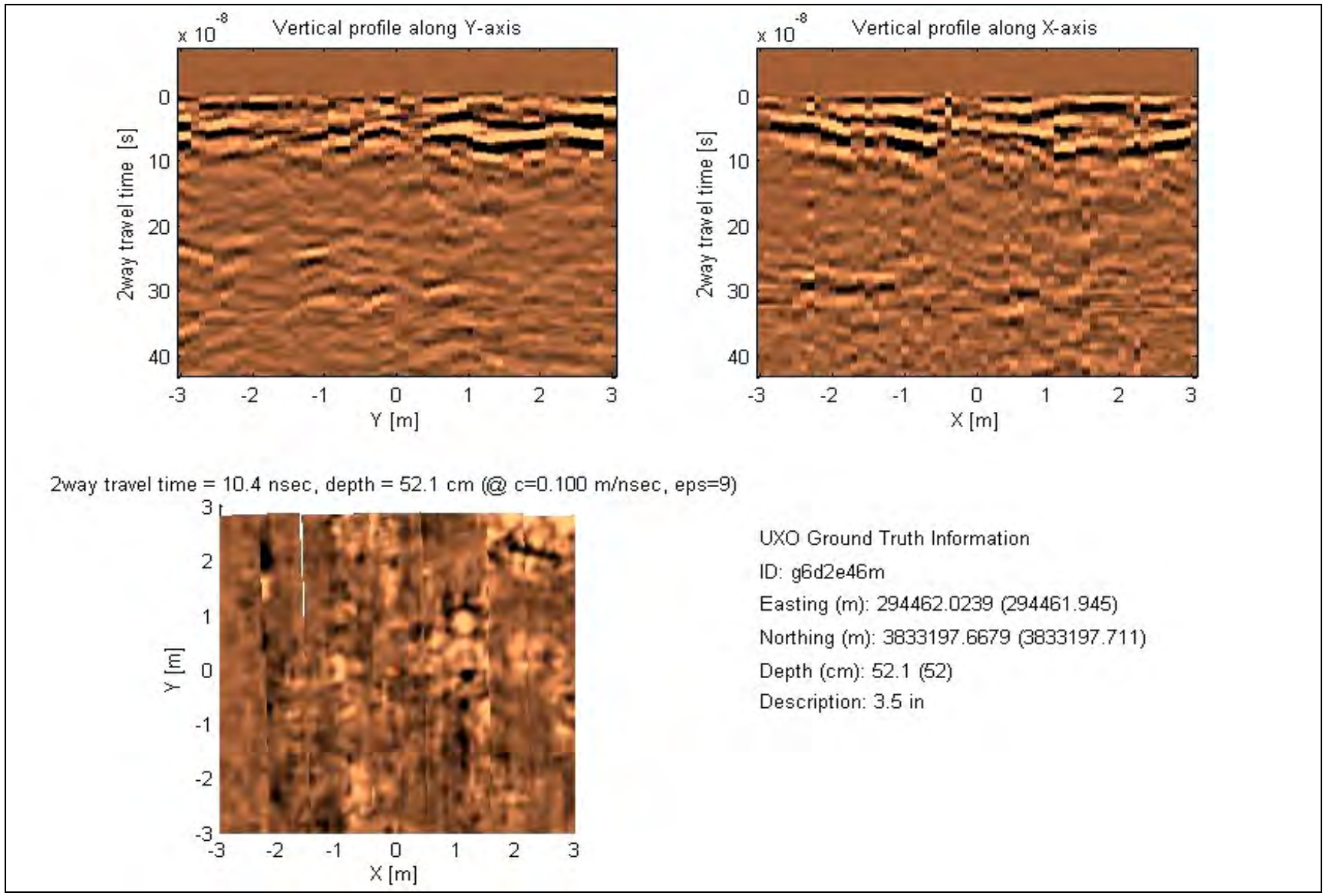


Figure B64. Analysis plots for target G6D2E46 using NS data. Coordinates of center plot point are followed by ground truth coordinates in parenthesis.

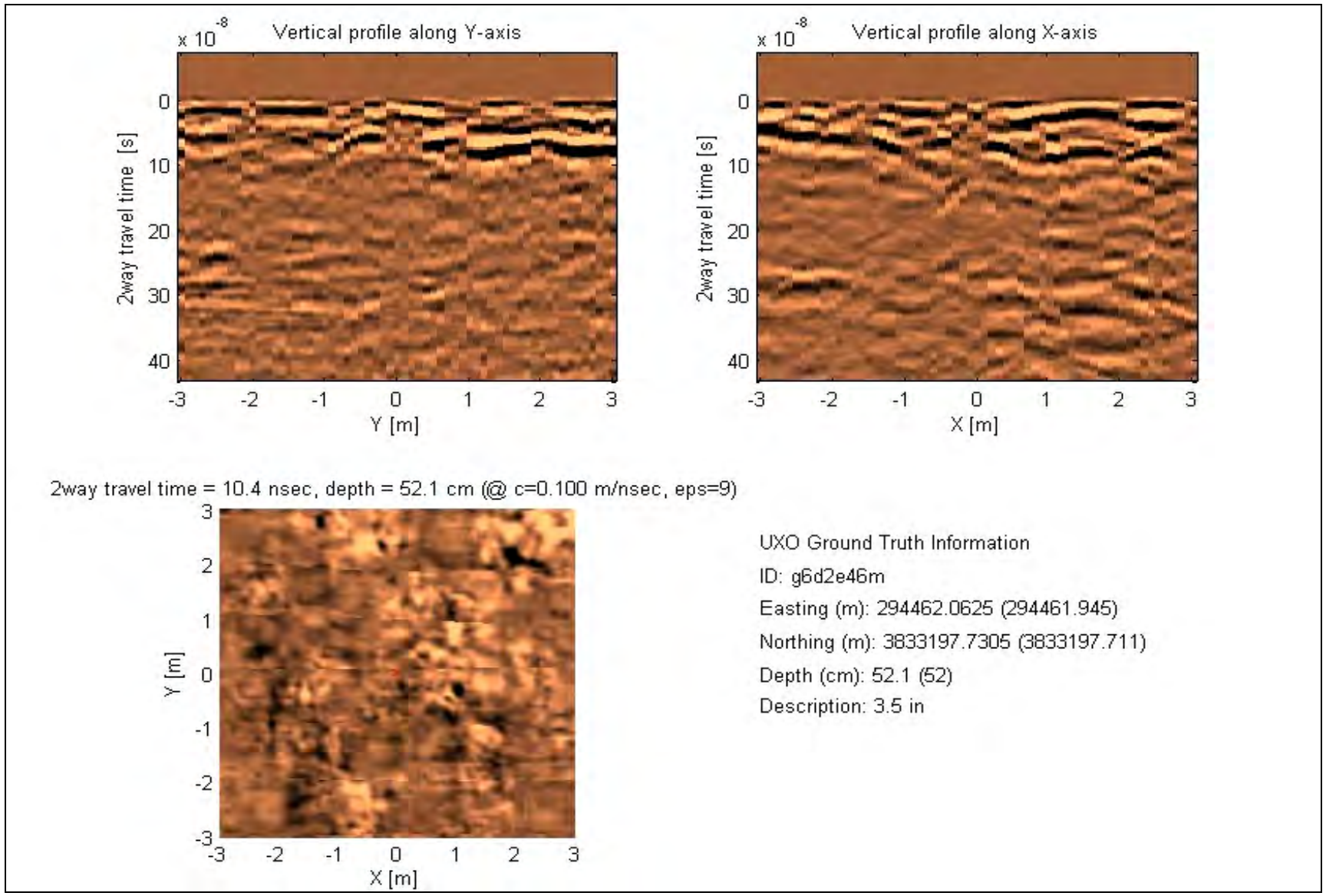


Figure B65. Analysis plots for target G6D2E46 using EW data. Coordinates of center plot point are followed by ground truth coordinates in parenthesis.

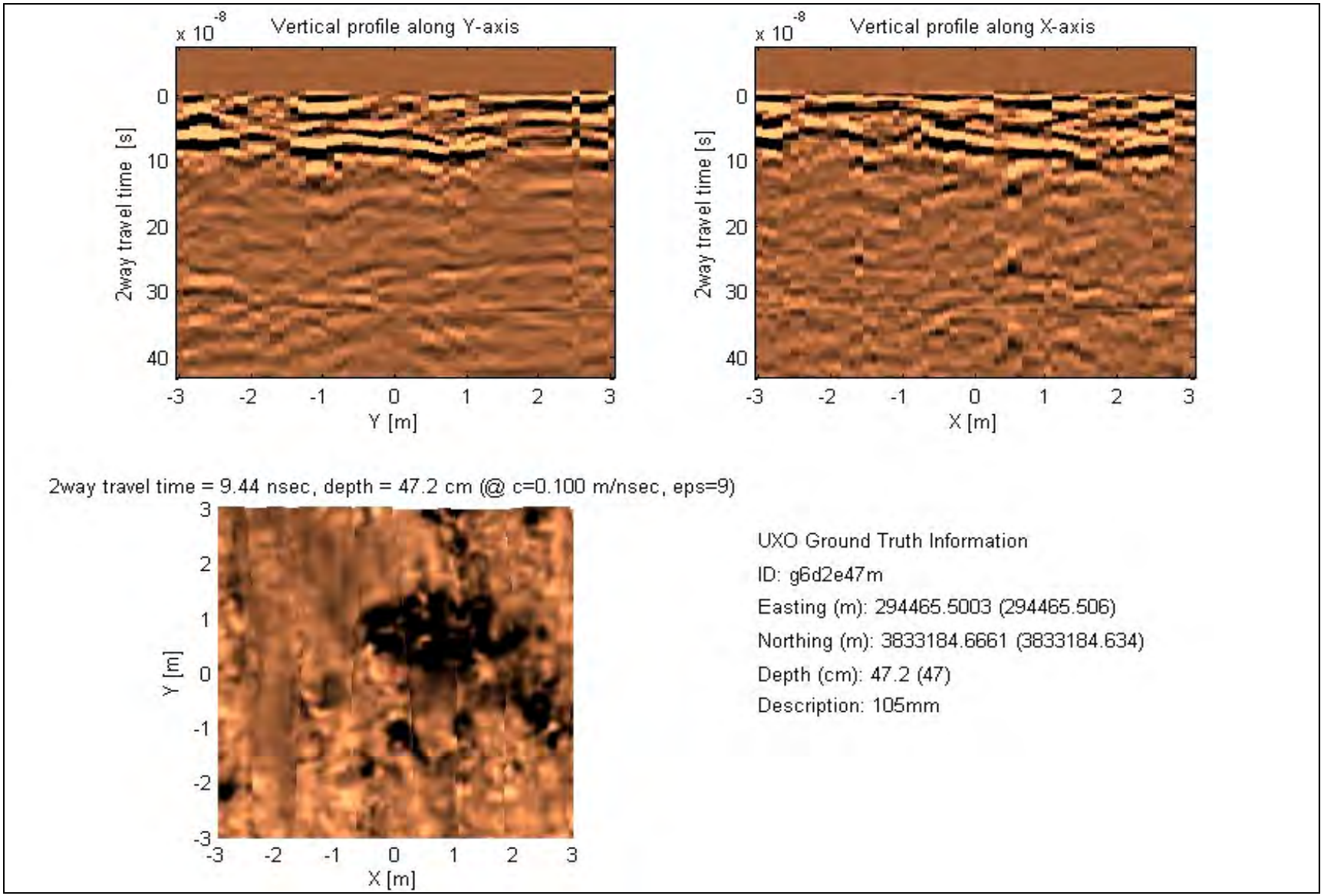


Figure B66. Analysis plots for target G6D2E47 using NS data. Coordinates of center plot point are followed by ground truth coordinates in parenthesis.

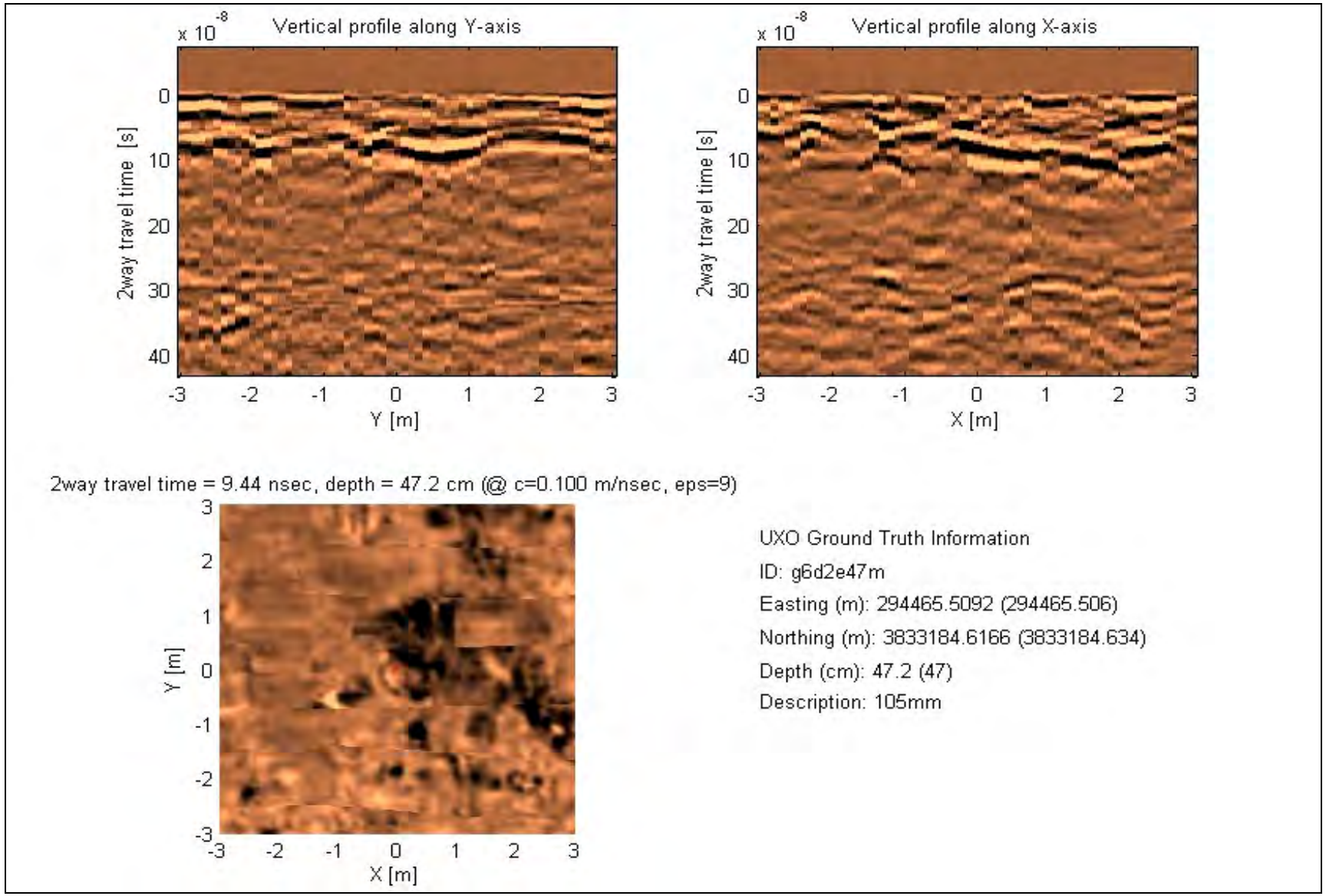


Figure B67. Analysis plots for target G6D2E47 using EW data. Coordinates of center plot point are followed by ground truth coordinates in parenthesis.

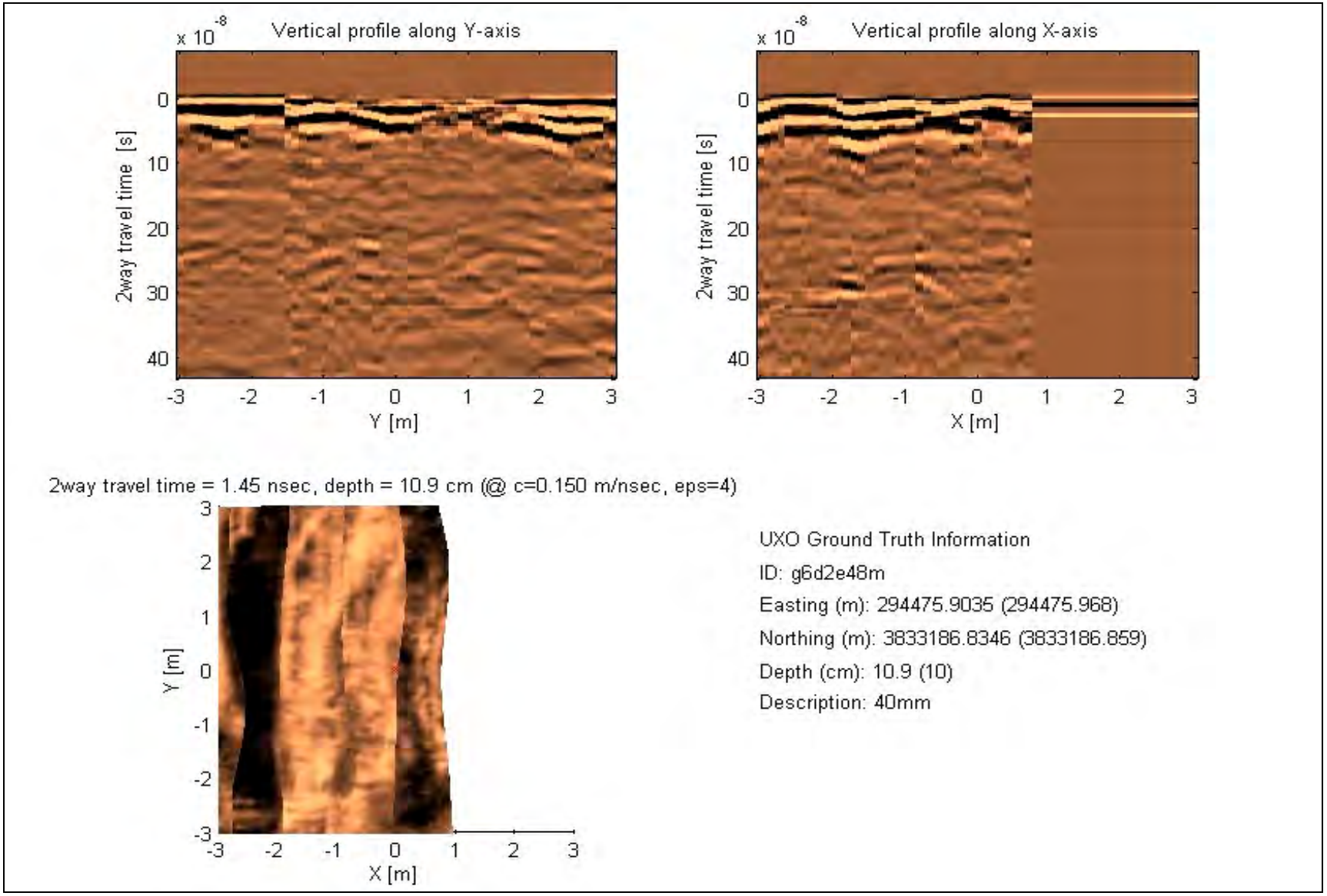


Figure B68. Analysis plots for target G6D2E48 using NS data. Coordinates of center plot point are followed by ground truth coordinates in parenthesis.

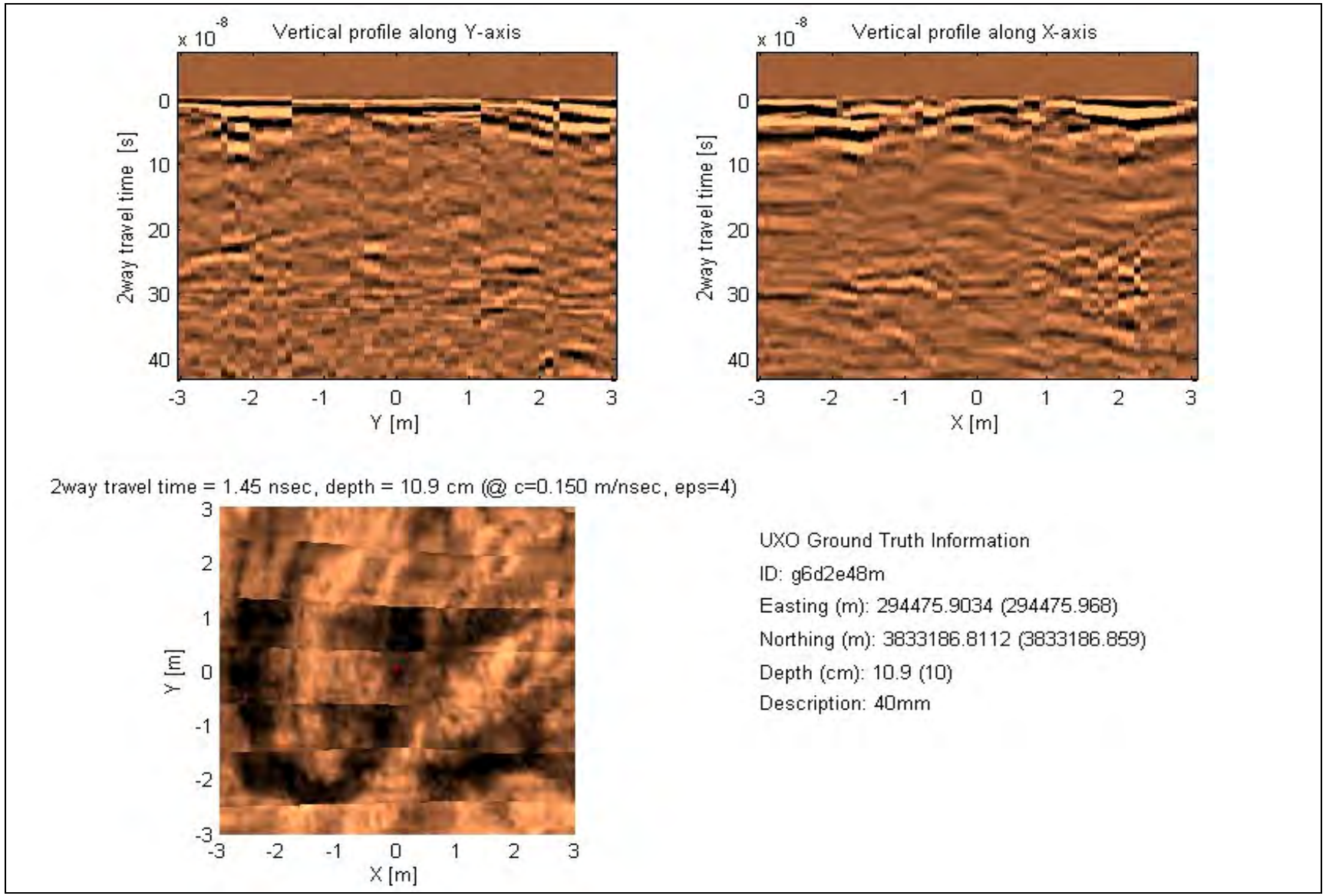


Figure B69. Analysis plots for target G6D2E48 using EW data. Coordinates of center plot point are followed by ground truth coordinates in parenthesis.

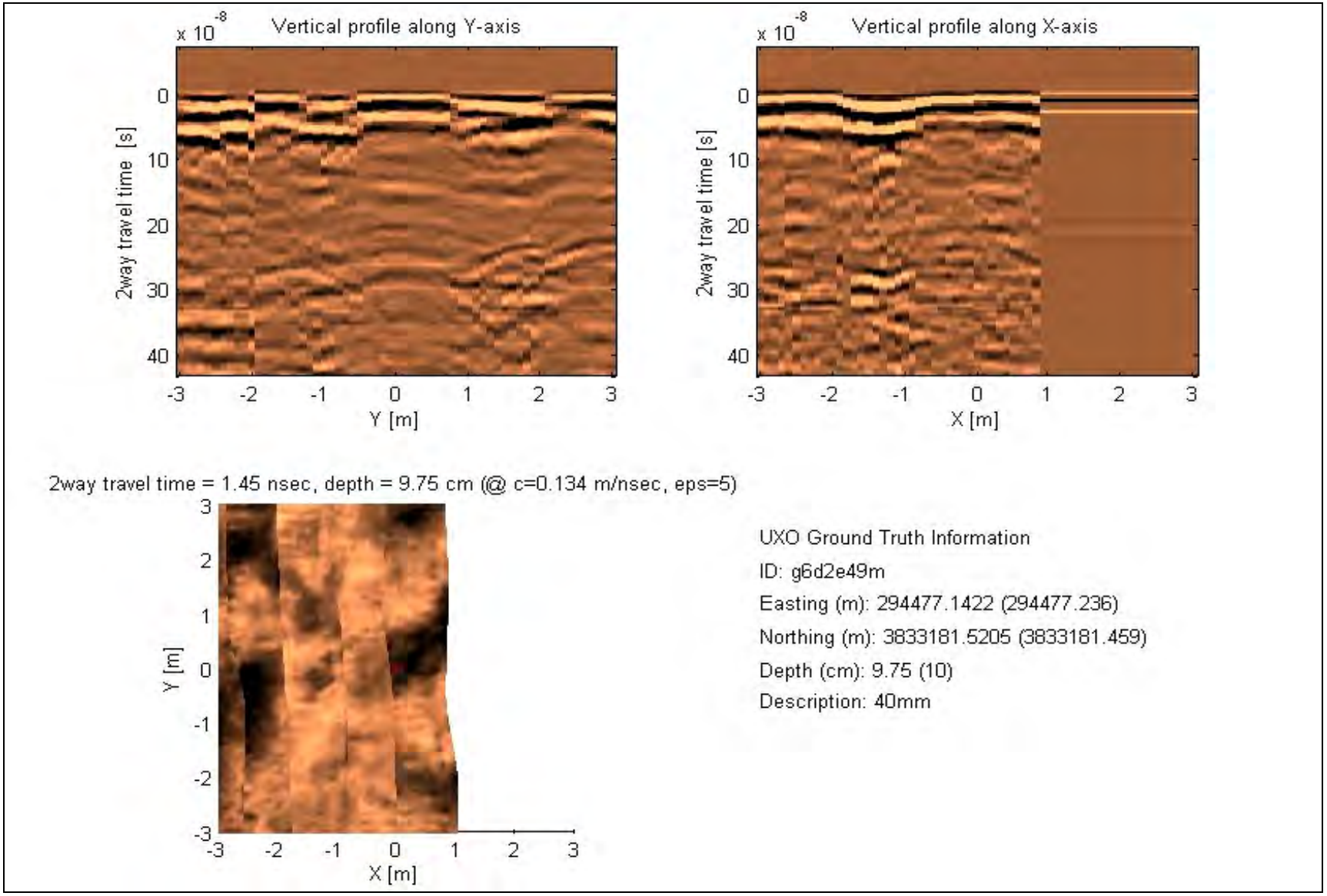


Figure B70. Analysis plots for target G6D2E49 using NS data. Coordinates of center plot point are followed by ground truth coordinates in parenthesis.

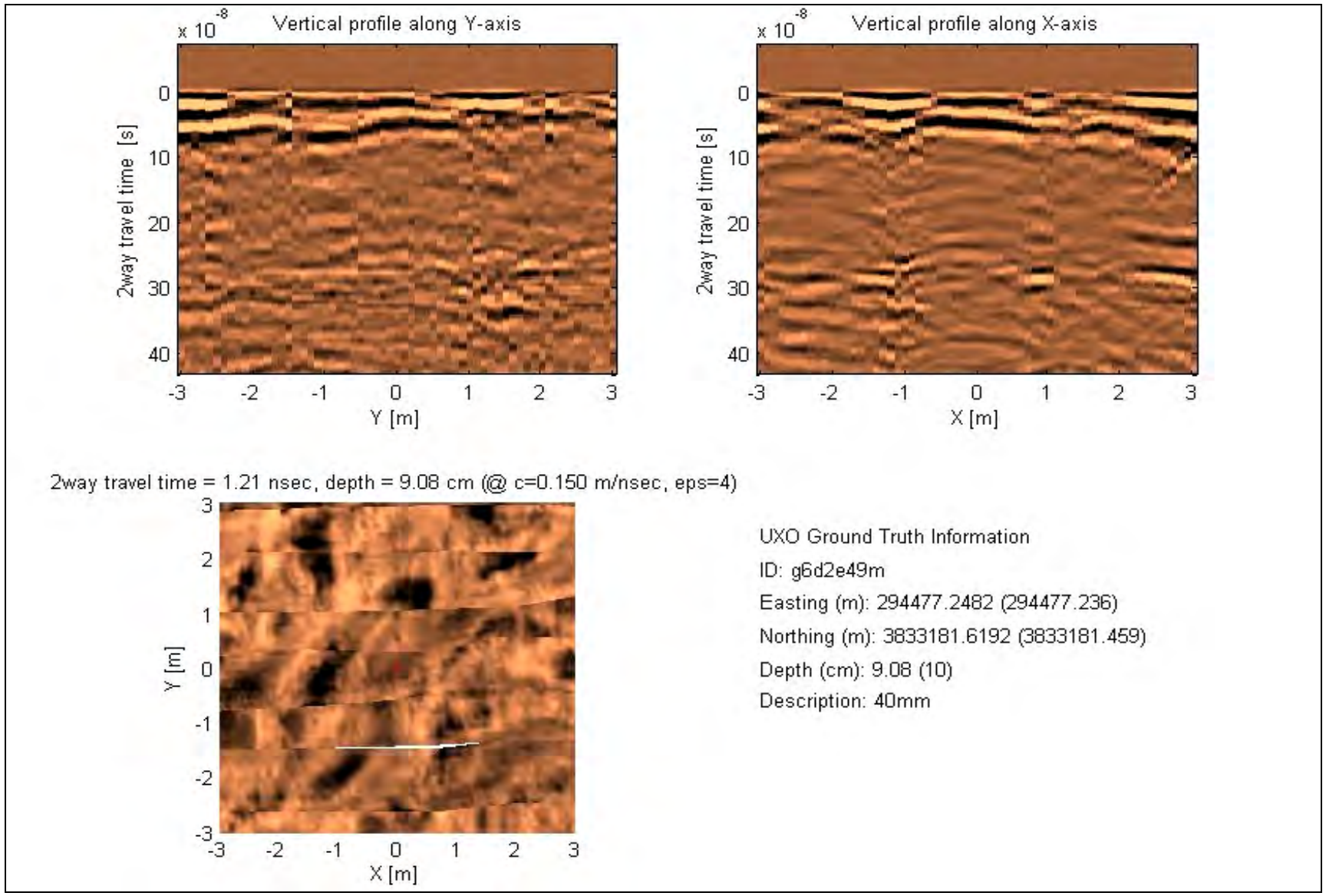


Figure B71. Analysis plots for target G6D2E49 using EW data. Coordinates of center plot point are followed by ground truth coordinates in parenthesis.

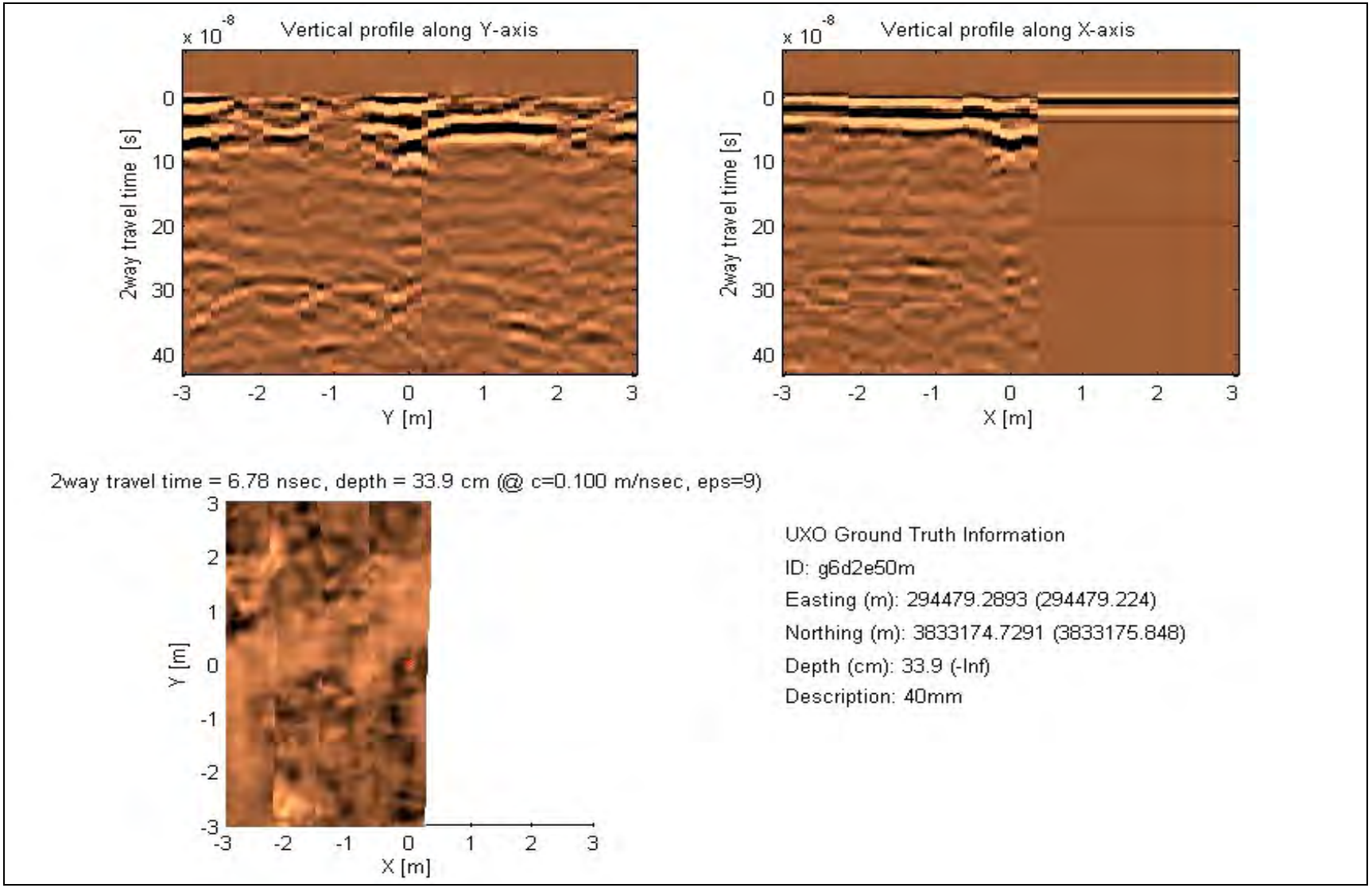


Figure B72. Analysis plots for target 1 m south of G6D2E50 using NS data. Coordinates of center plot point are followed by ground truth coordinates in parenthesis.

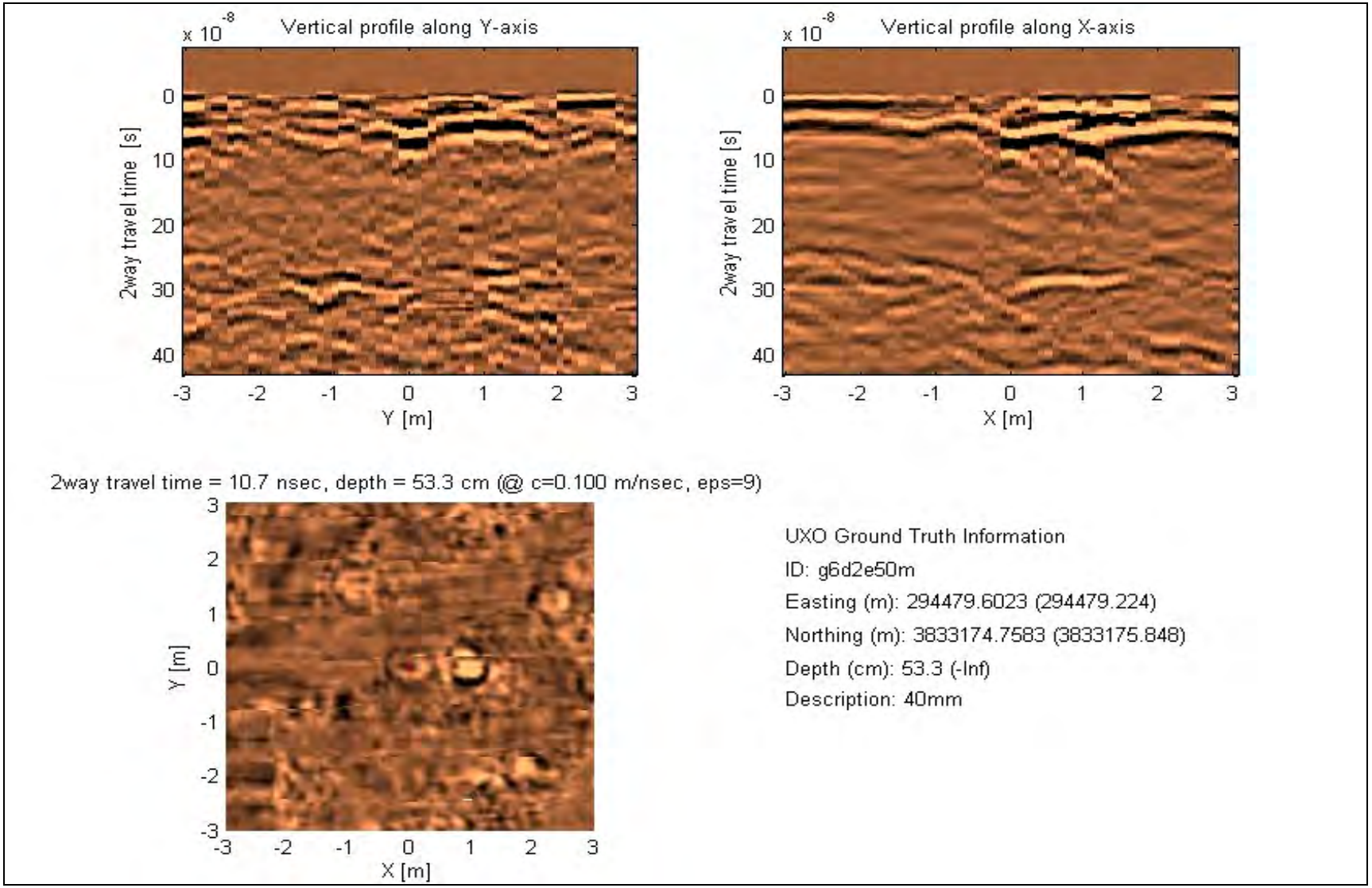


Figure B73. Analysis plots for target 1 m south of G6D2E50 using EW data. Coordinates of center plot point are followed by ground truth coordinates in parenthesis.

## B.6. The CART Imaging System: A multi-channel ground penetrating radar system for efficient large-scale utility mapping

Ground penetrating *imaging* radar (GP*i*R), also referred to as Radar Tomography (RT), is a technology that combines multiple standard GPR antennas in an array configuration with accurate positioning and advanced signal processing to create high-resolution three-dimensional (3D) images of the shallow subsurface. The continuous images show buried objects (UXO, pipes, cables, conduits, and valves) of most types and compositions (plastic, metal, ceramic and cement) and changes in soil conditions (such as boulders and backfill in a trench) down to depths of about 2 to 3 m (in typical organic soils) with a resolution of centimeters. These images are used to create 3D underground utility maps from scratch or to correct existing maps.

A commercial GP*i*R called the CART Imaging System (Figure B74 left), developed by WTI and manufactured by Malå Geoscience (Johansson 2002), uses a radar array consisting of nine transmitters and eight receivers in two parallel rows. Typically it covers approximately an acre per day with dense spatial coverage of one radar trace on every grid point of approximately a 10-cm grid. During operation, a laser theodolite automatically tracks the position of the array at all times, which typically moves at speeds of about 3 km/hr. CART mapping services have been available since 2001.

Two systems are available that broadcast an impulse with a peak frequency of about 200 or 400 MHz. All antennae are ultra-wideband bow-ties with a bandwidth from about 50 MHz to 400 MHz or 100 MHz to 650 MHz, respectively. Control electronics with special timing circuits fire the transmitters and control the receivers in sequence to create 16 GPR channels covering a 2-m swath on the ground (Figure B74 right). In this standard “bi-static” mode of operation, each transmitter fires twice in sequence, with each firing being recorded by an adjacent receiver. A multi-static mode, in which each transmitter fires once in sequence and is recorded by all the receivers, is also possible. More technical details can be found in Table B3.

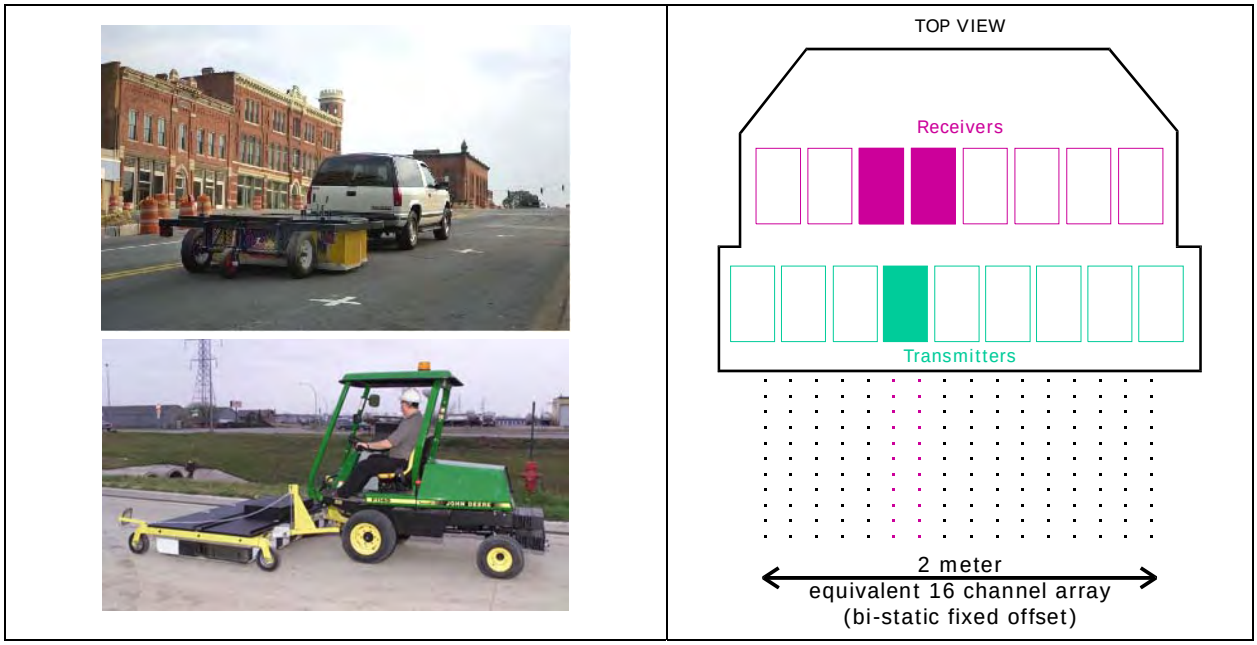


Figure B74. (Left) Photos of two versions of the CART imaging system housing the 17 radar antennas. (Right) Schematic top view of CART 200-MHz antenna array, which distributes 16 standard GPR channels over a 2-m swath considering a bi-static fixed offset data acquisition mode.

The system collects enough data in a single pass over the ground to form a high-resolution 3D image beneath its track; side-by-side passes are stitched together—using the accurate positioning information provided by the theodolite, signal processing, and synthetic aperture imaging—to create a seamless image of the subsurface (Burns et al. 2004; Birken et al. 2002).

Processing the raw radar data into images involves several steps. Data are filtered with pre-processing algorithms that align traces in each channel and balance channels with filters that remove static shifts and match the mean (or median) response across channels (based on reasonable assumptions about the response in certain areas of the survey). Radar data are then merged with geometry data, gridded, and migrated to produce 3D radar images of the subsurface (Oristaglio et al. 2001; Hansen and Johansen 2000).

Table B3. Technical Specifications: *CART* Imaging Systems.

| | | | | |
|---|---|---|---|---|
| Type of radar | Ultra-wideband impulse (“stepped-time” data recording) | | | |
| Antennas | Broadband shielded bow-tie: 9 Tx, 8 Rx | | | |
| Tx-Rx channels (zero-offset) | 16 | | | |
| Tx-Rx channels (multi-offset) | 72 | | | |
| Timing resolution | 0.05 ns | | | |
| Source firing rate | 100 kHz | | | |
| Data acquisition rate | 16 radargrams, 256 samples each, in approx. 40 ms | | | |
| Linear coverage rate (maximum) | 8.3 ft/s (5.7 mi per hr) with 4 in sampling in profile direction<br>Maximum linear coverage rate is speed at which array moves the profile sampling distance (e.g., 4 inches) in the time to acquire one array frame (16 channels, 256 samples each) | | | |
| Tracking accuracy | +/- (0.01 ft + 2 ppm) up to 656 ft; +/- (3 mm + 3 ppm) up to 200 m<br>+/- (0.016 ft + 3 ppm) beyond 656 ft; +/- (5 mm + 3ppm) beyond 200 m | | | |
| Dynamic range | 60 dB (theoretical)<br>44 dB (maximum signal/system noise level) | | | |
| Power supply | 12V DC | | | |
| Output power | Approx. 20 mW average | | | |
| | 200 MHz CART | | 400 MHz CART | |
| Frequency bandwidth | 50 MHz to 400 MHz | | 100 to 650 MHz | |
| Channel spacing (cross-line) | 5.25 in. (13.4. cm) | | 3.25 in (8.25 cm) | |
| Depth of penetration [1] | About 6 ft (1.6 m) | | About 4 ft (1.2 m) | |
| Resolution (image voxel size) | *Horizontal:*<br>*Vertical:* | 3 in. (7.6 cm)<br>1 in. (2.54 cm) | *Horizontal:*<br>*Vertical:* | 2 in. (4.0 cm)<br>1 in. (2.54 cm) |
| Location accuracy [2]<br>(of an imaged feature) | +/- 5% in depth<br>+/- 2% in horizontal position | | +/- 5% in depth<br>+/- 2% in horizontal position | |

[1] Depth of penetration depends on soil resistivity and dielectric. Figure given is for sandy-clay soil with resistivity of 50 ohm-m and relative dielectric of 9.

[2] Depths are normally provided with respect to ground surface; absolute depths relative to a base station can be provided with 3D geometry control and special processing. Accuracy quoted for horizontal locations applies within 25 ft of a mapped surface feature, such as a manhole cover or street sign.

Positions of surface features, such as curbs, street signs, valves, light posts, hydrants, and manhole covers, were also surveyed with the theodolite to provide a local reference map for the final 3D radar images of the underground. The final processed 3D images are visualized with large-scale maps and electronic movies that scroll through the 3D data volume in 1-in. depth slices going down from the surface to the maximum depths of penetration and show the enormous complexity of the subsurface in large cities (Birken et al. 2002). Figures B75 and B76 show some large-scale depth slice examples, taken from a 120,000-ft$^2$ survey conducted in December 2000. Notice the large amount of detail present in the images and the changes with depths.

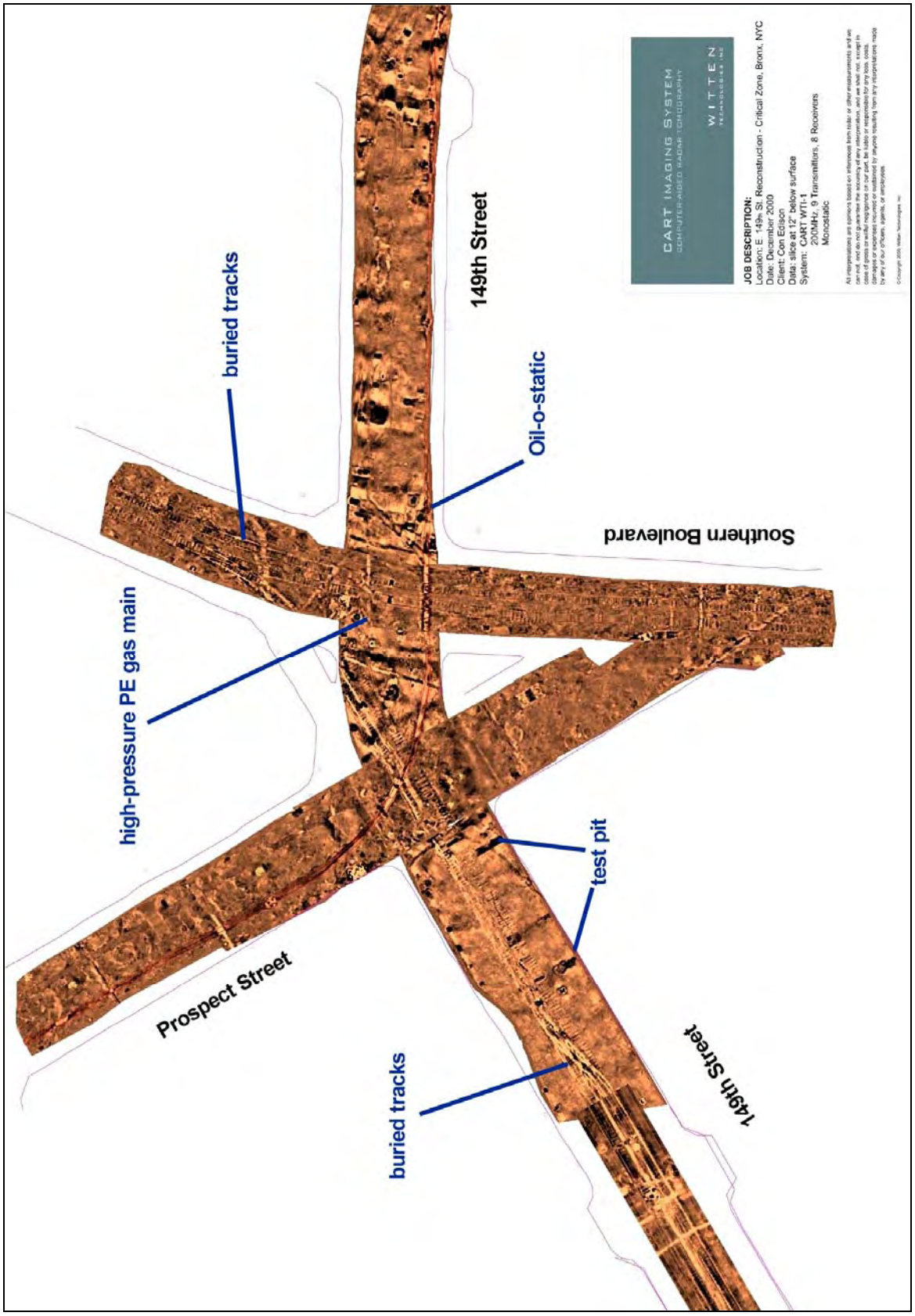


Figure B75. Twelve-inch depth slice of migrated radar data from Bronx survey.

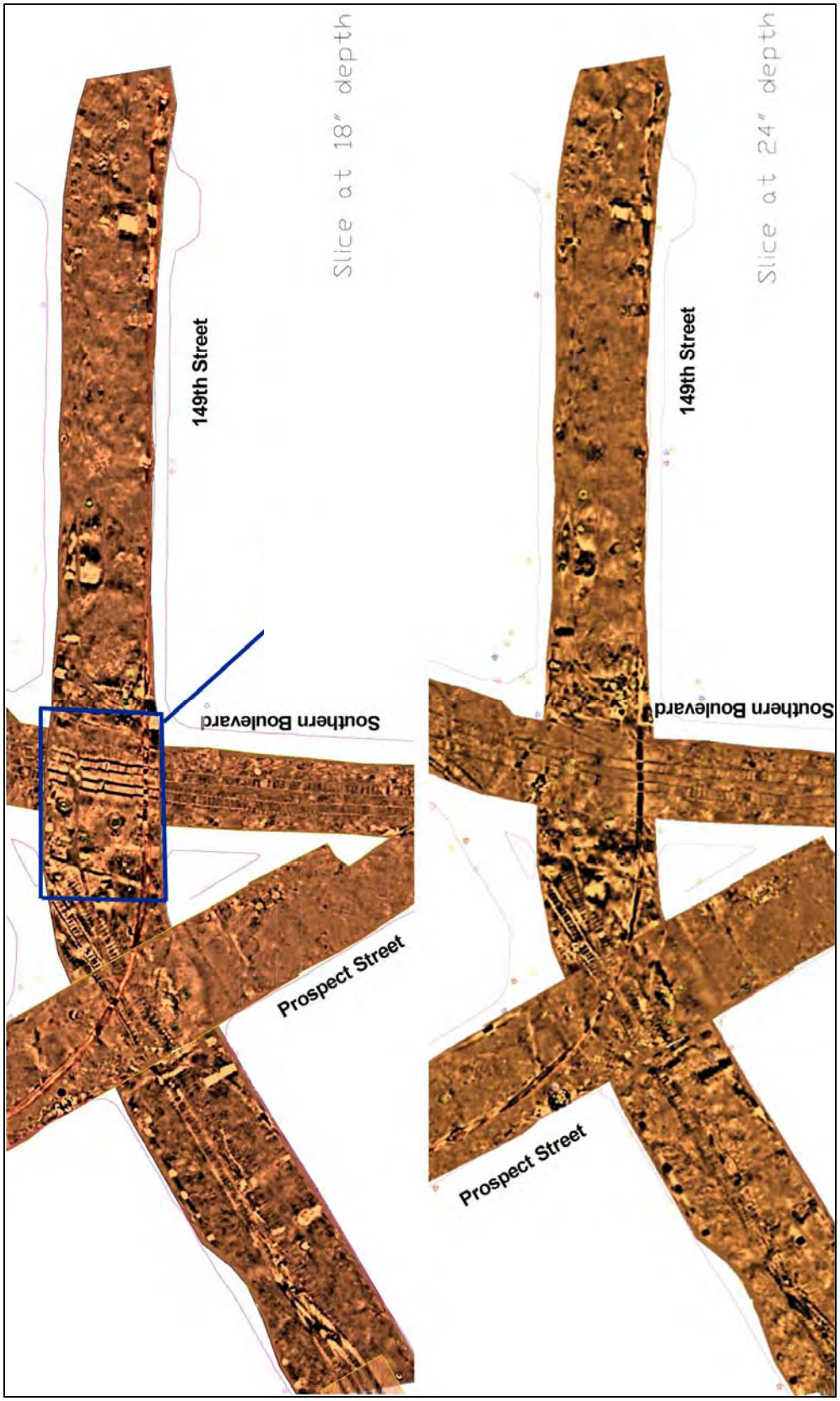


Figure B76. Partial view of migrated radar data slices from Bronx survey at depths of 18 in. and 24 in.

## B.7 References

Birken, R., D. Miller, M. Burns, P. Albats, R. Casadonte, R. Deming, T. Derubeis, T. Hansen, and M. Oristaglio. 2002. Efficient large-scale underground utility mapping in New York City using a multi-channel ground-penetrating imaging radar system. In *Proceedings of the SPIE* 4758:186–191.

Burns, M., T. Derubeis, P. Albats, R. Casadonte, R. Birken, R. Deming, J. Haldorsen, T. Hansen, D. E. Miller, and M. L. Oristaglio. 2004. Method for merging position information with measurements and filtering to obtain high-quality images that are positioned accurately with respect to global coordinates: United States patent 6,766,253.

Hansen, T., and P. M. Johansen. 2000. Inversion scheme for ground penetrating radar that takes into account the planar air-soil interface. *IEEE Geoscience and Remote Sensing* 38(1):496–506.

Johansson, B. 2002. Ground-penetrating radar array and timing circuits: U.S. patent 6,496,137.

MacIntosh, S., R. Birken, and Q. Zhu. 2006. Correcting 3D position measurement for geophysical surveys using a tilt sensor system. In *Proceedings of SAGEEP 2006, Seattle, Washington*. CD-ROM, 327–337.

Oristaglio, M., D. E. Miller, and J. Haldorsen. 2001. Ground probing radar. In *Scattering*, ed. P. Sabatier and E. R. Pike, 1, Chapter 1.6.4. London: Academic Press.

# Appendix C: ARA-Nemesis System Test Report for Camp Lejeune, NC[1]

## C.1. Introduction

In support of work conducted by Sky Research, Inc. (Sky), Applied Research Associates, Inc. (ARA) acquired data with the U.S. Army Nemesis ordnance detection system at the Gunnery 6 (G6) site within the Camp Lejeune Marine Corps Base, North Carolina in March 2006. This report summarizes the data acquisition, analysis, and results of UXO detection work. The results of this work also support ongoing development of the Nemesis system by ARA under contract to the US Army Night Vision Electronic Sensors Directorate Humanitarian Demining group.

## C.2. Background

The Nemesis system, currently under development for the US Army, seeks to provide an efficient and reliable, tele-operated detection platform to eradicate explosive ordnance. The primary goal of the program is to develop a cost-effective system that will address humanitarian demining (HD) and force protection mine clearance needs. The integration of detection and neutralization technologies on a robotic platform provides an integrated end-to-end landmine eradication system. Specifically, the Nemesis will support operations to detect and clear mined areas in an effort to safely release the areas for reoccupation by local inhabitants.

During the development phase of the Nemesis program, ARA has led the design, integration, and testing of prototype detection arrays. The detection subsystem is comprised of pulsed induction electromagnetic (EMI) and ground penetrating synthetic aperture radar (GPSAR) array systems. It can be operated in single or dual mode and is integrated on a remotely operated tracked vehicle. Evaluations of the detection arrays were conducted at a U.S Army Engineer Cold Regions Research and Engineering Laboratory (CRREL) test facility in winter 2004 and at an eastern temperate U.S. Government test site in spring 2004. Subsequently, ARA made several recommendations to the array manufacturers for improvements in the sensor design and data acquisition. These changes were

[1] Applied Research Associates, Inc.

incorporated into a set of modified arrays, which were delivered to ARA in winter 2004/2005. Testing and evaluation of the revised arrays was conducted at the ARA test facilities during spring and summer of 2005. Additional evaluations of the revised detection system were performed at U.S. Government test sites in May and September 2005 and January 2006. During testing over landmines at select test sites, limited testing over UXO calibration areas was also preformed.

### C.2.1. Testing objectives

The main focus of this work was the acquisition of ground penetrating radar (GPR) data over suspected UXO sites to test the ability of the Nemesis GPR system in the detection and discrimination of the available targets. Preliminary testing and GPR data collected at the site in August and September 2005 by Sky indicated that the transmission frequencies employed by the Nemesis GPR system may be able to penetrate the sub-surface and elucidate UXO responses. Sky's preliminary data revealed that propagation of EM energy at frequencies lower than 1 GHz yielded the best penetration. It is important to note that the Nemesis GPR system has not been designed for deep penetrating UXO detection, and optimal performance was not expected with the current system. Nonetheless, the main goal was to gauge the performance of the current Nemesis GPR sensor and analysis algorithms to determine potential system modifications that would lead to an effective UXO detection platform.

### C.2.2. Site description and targets

During Sky's reconnaissance visit to the site in September 2005, a 100-m by 400-m survey grid was established and characterized (Figure C1). Portions of this grid were the focus of testing.

Emplaced targets at the site included a number of items from 105-mm projectiles to 40-mm practice grenades, 3.5-in. to 81-mm rockets, bomblets and other ordnance, as well as GPR-specific clutter such as wood and styrofoam. Other targets observed or detected at the site included 40-mm practice launch grenades, a suspected single 120-mm HEAT round, numerous small arms (20-, 38-, and 50-caliber) rounds, and associated UXO clutter (APDS adapters, shell casings, sabot pedals) as shown in Figure C2.

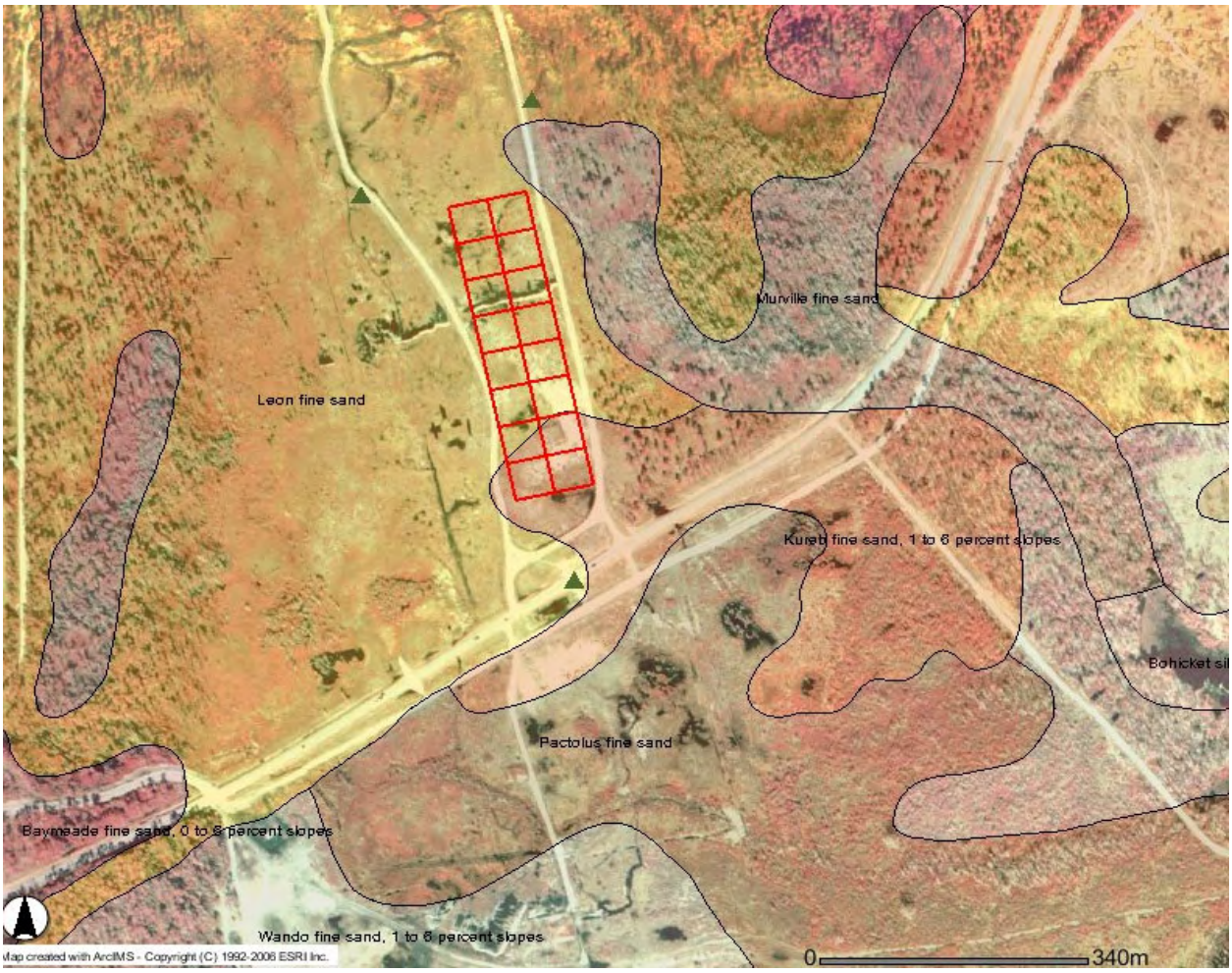


Figure C1. Map of the test grid at G6 Gunnery Range (from Sky Research).

Figure C2. Practice UXO targets observed on the surface of the site. Numerous APDS adapters, small caliber rounds and casings, as well as 40-mm practice grenades littered the site.

During testing, portions of the site were completely inundated with water from recent rainfall. Ponded water persisted throughout the testing on the northern parts of the site (A grids). The photos in Figure C3 show some examples of soft mud and ponded water that made testing on the A grids difficult.

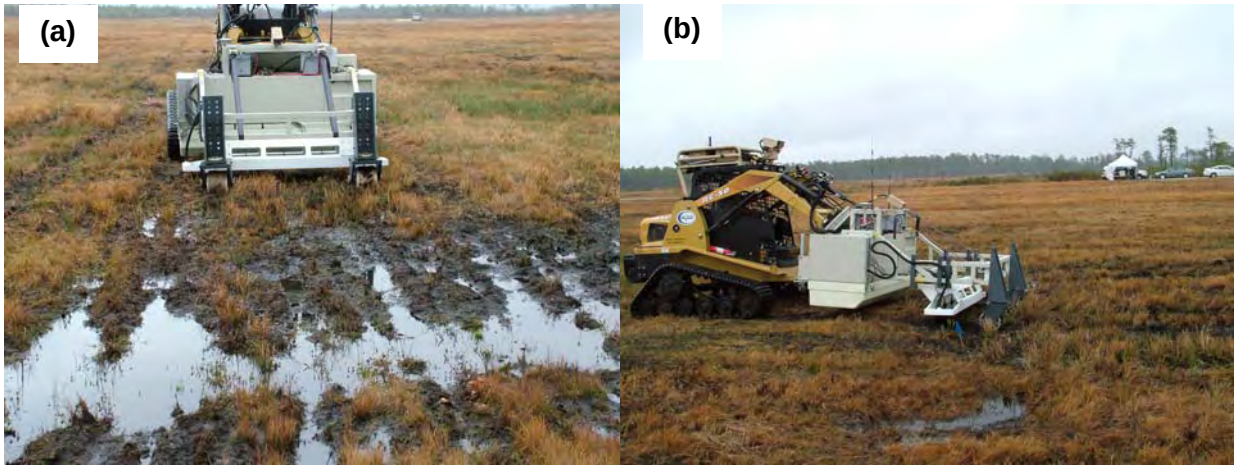


Figure C3. (a) The Nemesis preparing to traverse ponded water on the A grids. (b) Standing water persisted on the A grids for the duration of the data collection.

### C.2.3. Detection sensors

The detection sensor systems were selected for their ability to detect anti-personnel and anti-tank landmines for the Nemesis Program. Both systems are configured as an array of sensors leading to improved ground coverage and performance over handheld versions of these technologies. These arrays are capable of high spatial resolution (3 cm or less) and overlapping detections, thus increasing both the precision and accuracy of the overall system. During a single scan, the system collects data from each of the sensing elements, effectively imaging an areal portion of the subsurface.

#### *C.2.3.1. Ground penetrating synthetic aperture radar array*

The GPSAR array (Figure C4) is a stepped frequency continuous wave (SFCW) radar operating over the 400-MHz to 4-GHz range. Because stepped frequency systems transmit continuously in time, they can transfer more energy into the ground than time domain impulse radar systems that have an extremely low duty cycle. An additional advantage of this stepped frequency system over comparable systems is the versatility of designing the frequency spectrum to adjust for soil conditions or clutter.

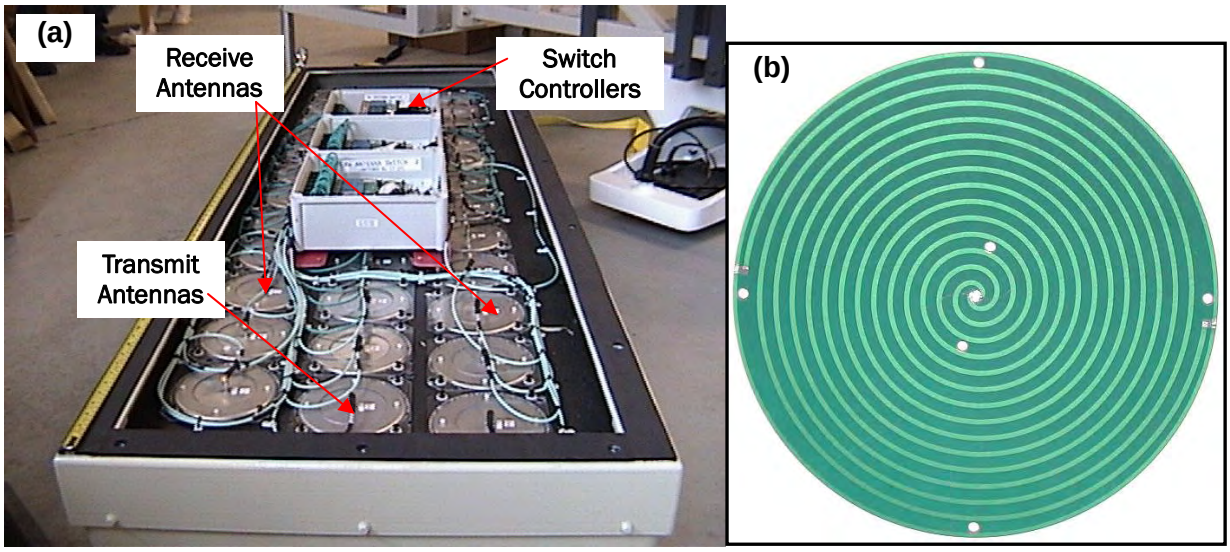


Figure C4. (a) GPSAR antenna array and antenna switch controllers enclosed in a custom radome enclosure. (b) The radiating element of the antenna is a terminated two-arm Archimedean spiral embedded in a printed circuit board.

Multiple Archimedean spiral transmit and receive antennas are used to acquire 46 independent real-aperture data points across the 1.8-m array (Figure C4). This design results in real-aperture across-track ground sampling of 4.0 cm with over 120 dB of dynamic range. Along-track resolution is dependent on the rate of advance. The GPSAR system utilizes a custom 400-MHz digital high-frequency data acquisition system that permits 3.0-cm ground sampling resolution at nominal speeds (~1.5 km/h) and 6.0-cm resolution at speeds >10 km/h. Depth resolution in relatively dry soils ($k_r$ ~ 3-7) is approximately 1-2 cm. It should be noted that the antennas, applied frequency range, and corresponding bandwidth have all been optimized for detection of small shallowly buried landmine targets and depth penetration may be limited for deeper (>50 cm) UXO detection. Future antenna modifications could extend penetration depths to more than 2 m.

### *C.2.3.2. Pulsed induction EMI array*

The EMI sensor is a single transmit, multiple receive (STMR) pulsed induction metal detector array that is capable of detecting low-metal content ordnance to depths of ~60 cm or more. The STMR (Figures C5 and C6) array uses a multi-period sensing technology to account for variability in soil conductivity, including highly mineralized soils. The system also incorporates bipolar transmission from a single transmitter coil and an array of receiver coils to reduce the effect of mutual coupling.

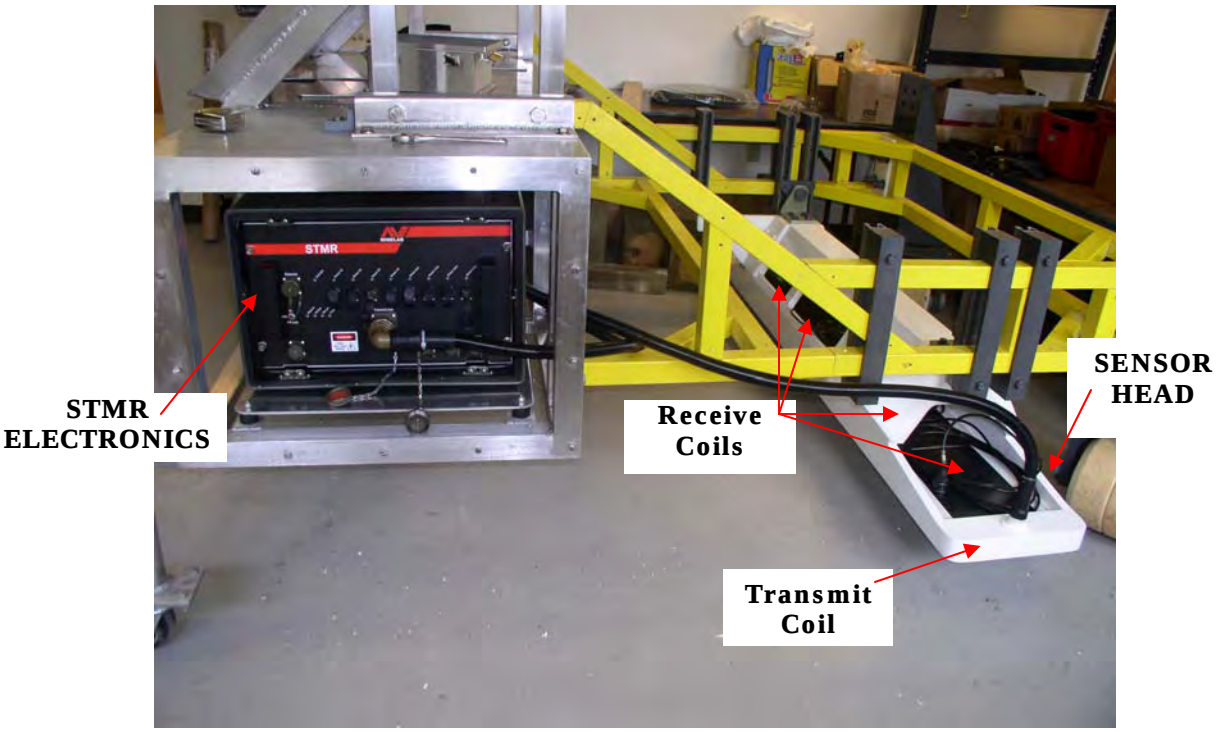


Figure C5. STMR array and electronics

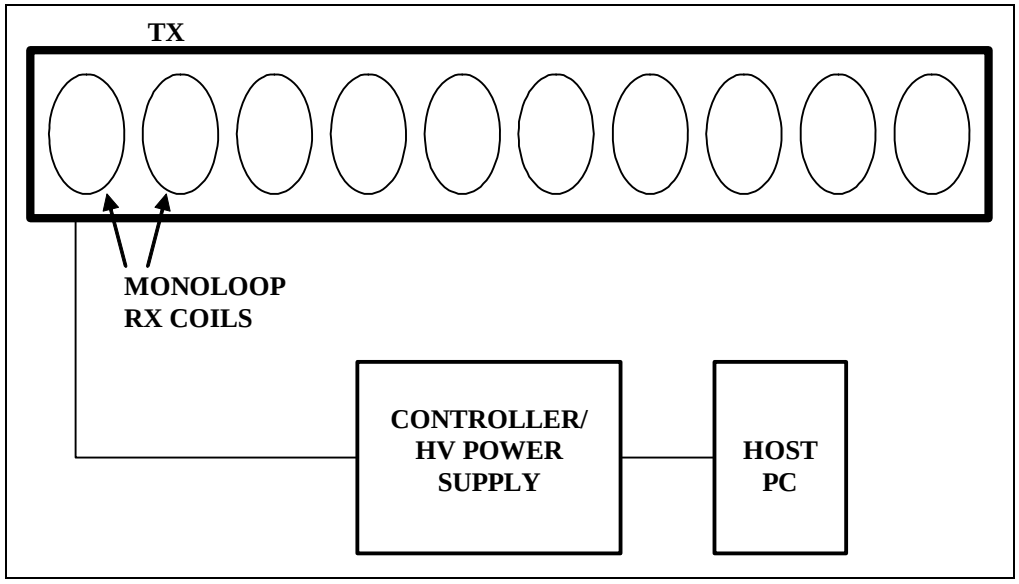


Figure C6. Schematic diagram of the STMR system layout.

A major innovation of the STMR array is its ability to compensate for variability in soil properties without loss of sensitivity.

The STMR array employs multiple receive coils to acquire data over scan widths of 1.8 m and lengths up to 0.4 m simultaneously. The 10 receive coils are mounted as induction-balanced (see Figure C6) monocoils inside a single rectangular transmit coil. Raw data manipulation and post-processing such as filtering, ground balancing, and DC offset removal are performed within the STMR microprocessors. The system is currently configured for selectable sampling rates and is capable of acquiring a full set of array data every 1.5 cm along track at speeds up to 3.2 km/h (estimated maximum speed is 15 km/h).

*C.2.3.3. Data acquisition system*

Simultaneous acquisition and correlation of GPSAR and EMI data are provided by the embedded data acquisition and analysis (DAS) system computer mounted in the electronics enclosure. The DAS is a power-PC platform with a LINUX-based real-time operating system for command/control of sensor and navigation systems and on-board processing and archival of data. Detection and discrimination-level data processing is currently handled off-line (off-board), but near-term development implementations utilize the real-time environment under which the DAS software has been developed. The schematic diagram in Figure C7 provides an overview of the components of the data acquisition system.

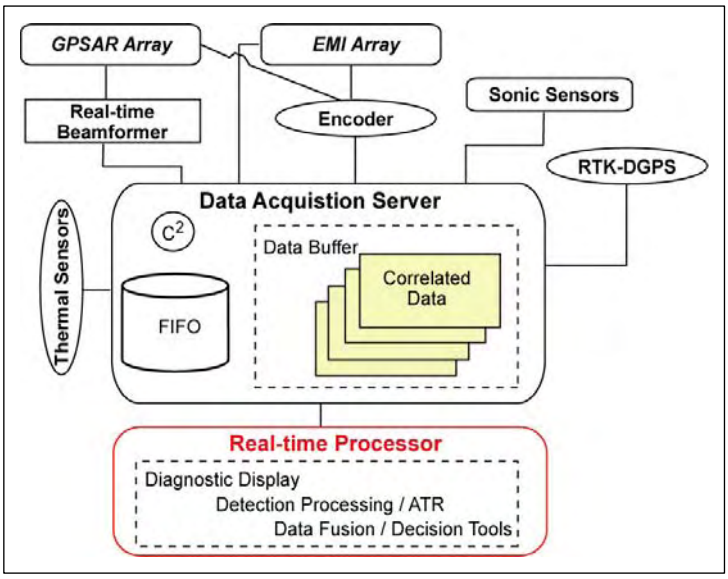


Figure C7. Schematic diagram of the main components of the Nemesis data acquisition system.

### C.2.4. Mobile platform components

The vehicle test platform is the All-Season Vehicle (ASV) RC-50, rubber tracked, skid-steer loader with ARA's integrated modular robotic control system (MRCS). This vehicle has hydraulic pilot-valve control, an advanced suspension, and the ASV proprietary engine management system, providing an excellent base to conduct mine or unexploded ordnance (UXO) detection operations. In particular, the low-ground pressure rubber-tracked system is well suited for operation in multi-faceted terrains. Approximate average ground pressure on the tracks is 3.1 psi. The sensor arrays are mounted on a nonmetallic test frame (Figure C8) connected to the loader arms on the front of the vehicle. This test frame allows for both vertical and horizontal adjustment of the position of the sensor arrays.

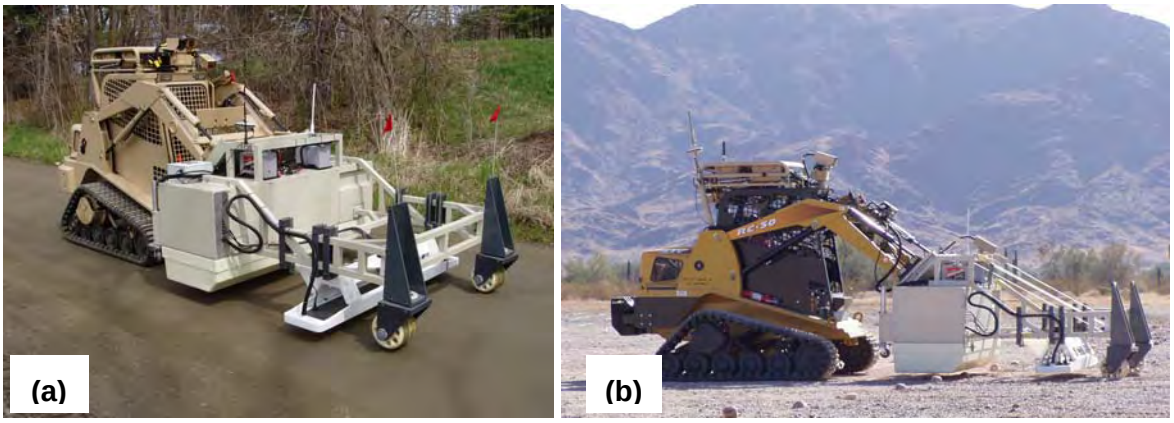


Figure C8. (a) Nemesis prototype detection system mounted on the ASV RC-60-based robotic platform. (b) Nemesis detection system mounted the ASV RC-50 tracked vehicle with integrated robotic control during testing on the Yuma Proving Ground UXO calibration grid.

#### *C.2.4.1. Robotic control*

ARA's Modular Robotic Control System (MRCS) is integrated on the roof of the light utility tracked vehicle. The MRCS architecture consists of three main elements: 1) a man-portable Operator Control Station (OCS); 2) Platform Control Components (PCCs); and 3) a wireless data and video link. The OCS provides the remote operator with command, control, and communication with the PCCs located on the vehicle. The PCCs consist of control nodes linked by high speed Ethernet. The wireless data and video link incorporates radios and antennas to transmit video and send commands between the OCS and the platform PCC. The MRCS is designed to be compliant with the Joint Architecture for Unmanned Systems (JAUS). Closed-loop speed control of the vehicle platform was developed to

provide the required slow speed operation for the ordnance detection subsystem.

Figure C9 shows both the platform with the Modular Robotic Control System (MRCS) and the Operator Control Station (OCS). In addition to added safety, teleoperation of the detection platform provides improved visibility. The location of several cameras on the platform and frame-mount enables the operator to switch through a variety of views to ensure safe and accurate control of the detection system. The OCS allows speed, throttle, and directional control as well as standoff and tilt control of the detection arrays. Both split-screen and full-screen camera views are possible on one display, while a second touch-screen display provides platform feedback (e.g., speed, throttle, fuel level, etc.).

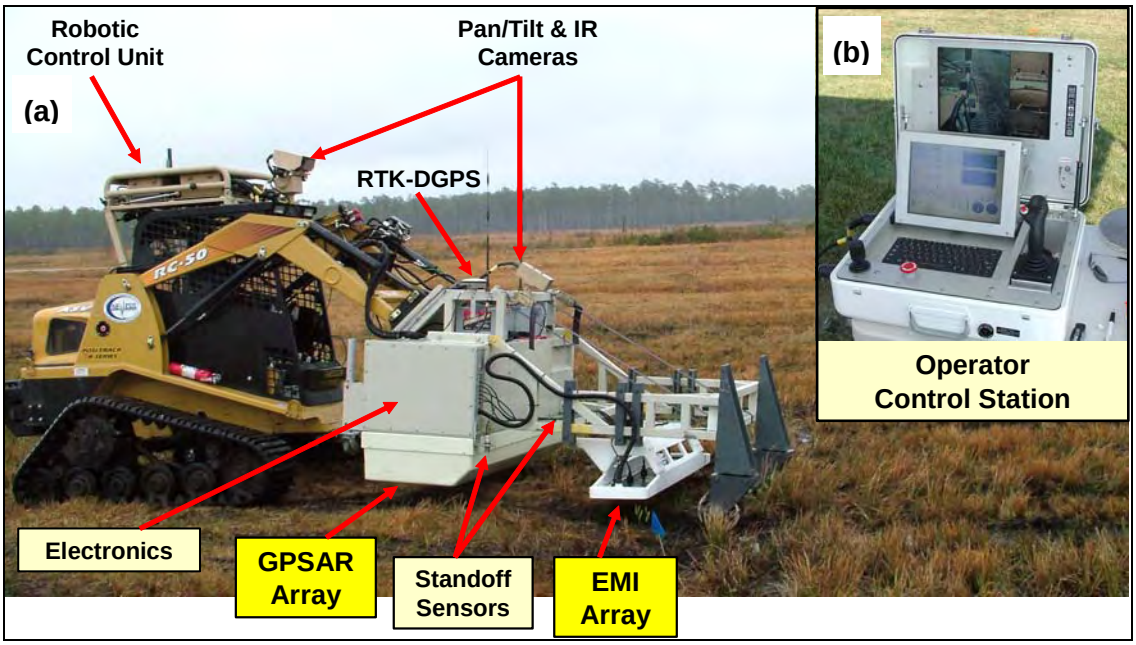


Figure C9. (A) Teleoperated detection platform and (B) Operator Control Station (OCS).

*C.2.4.2. Navigation and positioning subsystem*

The navigation and positioning module uses a real-time kinematic (RTK), differential global positioning system (DGPS) coupled with a local optical encoder-based positioning system to accurately provide position information correlated to each data scan. The DGPS system consists of a reference base station and a roving differential station located on the Nemesis vehicle. Sensor positions are measured in semi-real-time (20 Hz) with +/-1 cm static accuracy in the horizontal direction (i.e., locally tangential to the geoid) and +/- 2 cm static accuracy in the vertical direction. All

navigation and sensor data are time-stamped with UTC reported from GPS satellite clocks and recorded by the DAS. In addition to the positioning information derived from DGPS measurements, the DAS also records local positioning information input from two optical encoders mounted on vehicle road wheels. If satellite links are lost, local positioning will be used to determine the position of the recorded data.

## C.3. Data acquisition

### C.3.1. Data collection parameters

Setup and calibration of the integrated Nemesis system was conducted before acquiring data at the G6 site. Setup of the Modular Robotic Control System (MRCS) and vehicle platform as well as detection system components was conducted to ensure system functionality and account for site-specific parameters such as the local or global position reference frame for registration of spatial data, electromagnetic ground conditions, and clutter environment for setting detection noise floors, and to assess terrain and obstacles for setting safe and effective operating speeds and control gains. During operation, the Nemesis requires a base station including operator control station for the mobile platform and MRCS communications antenna mast.

Before data acquisition, a GPS reference base station was also set up, all system elements were confirmed to be functioning properly, the data acquisition computer system was initialized by performing built-in tests, and verification datasets were collected. The sensor locations on the vehicle during data collection at Camp Lejeune are shown in Figure C10. The reference point for all locally positioned data collection is the frame-mount front-center position. The vast majority of the testing at Camp Lejeune was based on GPS-based spatial referencing. The GPS base station was located directly over the “skycp3” reference point set up by Sky Research. GPS data were collected using the WGS-84 datum and associated geoid parameters.

Calibration procedures for the detection system include in-air data acquisition and standard target tests to ensure functionality and performance. Site-specific calibration was conducted through a ground standoff test in a clutter-free area of the site, otherwise known as an “air shot.” Periodically during testing, background data and data over a metal plate were acquired for use as a calibration target.

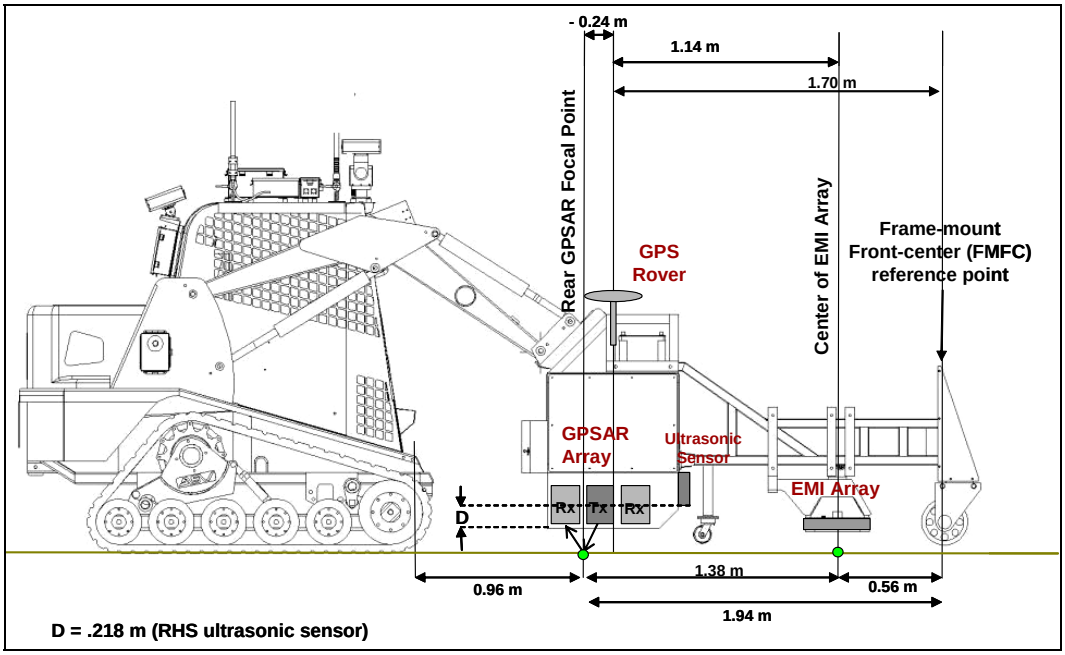


Figure C10. Scaled profile drawing of the Nemesis platform and sensor arrays.

### C.3.2. Site coverage

Data collection was focused on designated areas in the 50- by 50-m grids at the G6 site. Encounter data acquisition was performed on the A and D grid targets. Encounter data collection involves single-pass scans over known target locations. Additional encounter data collection runs were conducted by approaching emplaced targets from multiple orientations or by implementing variable sensor standoff distances. Due to weather-related downtime and persistent standing water, only limited data were collected over calibration (i.e., emplaced) targets on the A1 and A2 grids. Limited data passes and short encounter data runs were acquired on the D1 and D2 grids. Due to the availability of emplaced targets, encounter data acquisition focused on the D2 grid targets. Limited data collection was also conducted over anomalies previously identified by Sky Research during EM surveying.

Coverage data collection was performed on the E grids. Coverage data requires multiple passes and is intended to cover larger areas of suspected targets. Standard operating speeds of 0.5 to 1 km/hr were used. Nearly full coverage was attempted on the E grids using passes that were oriented approximately parallel with the east-west trend of the grid. Remote operation with closed-loop speed control set to 0.6 km/hr produced acquisition over most of the E grids in less than 6 hr including downtime related to data downloads system setup and routine functionality checks. This

corresponds to an approximate coverage rate of 1666 $m^2$/hr (1/6 hectare/hr) or approximately 1 hectare/day (~2.5 acres). Figure C11 provides an overview of coverage of the G-6 site overlaid on an image acquired from Google Earth (www.earth.google.com/).

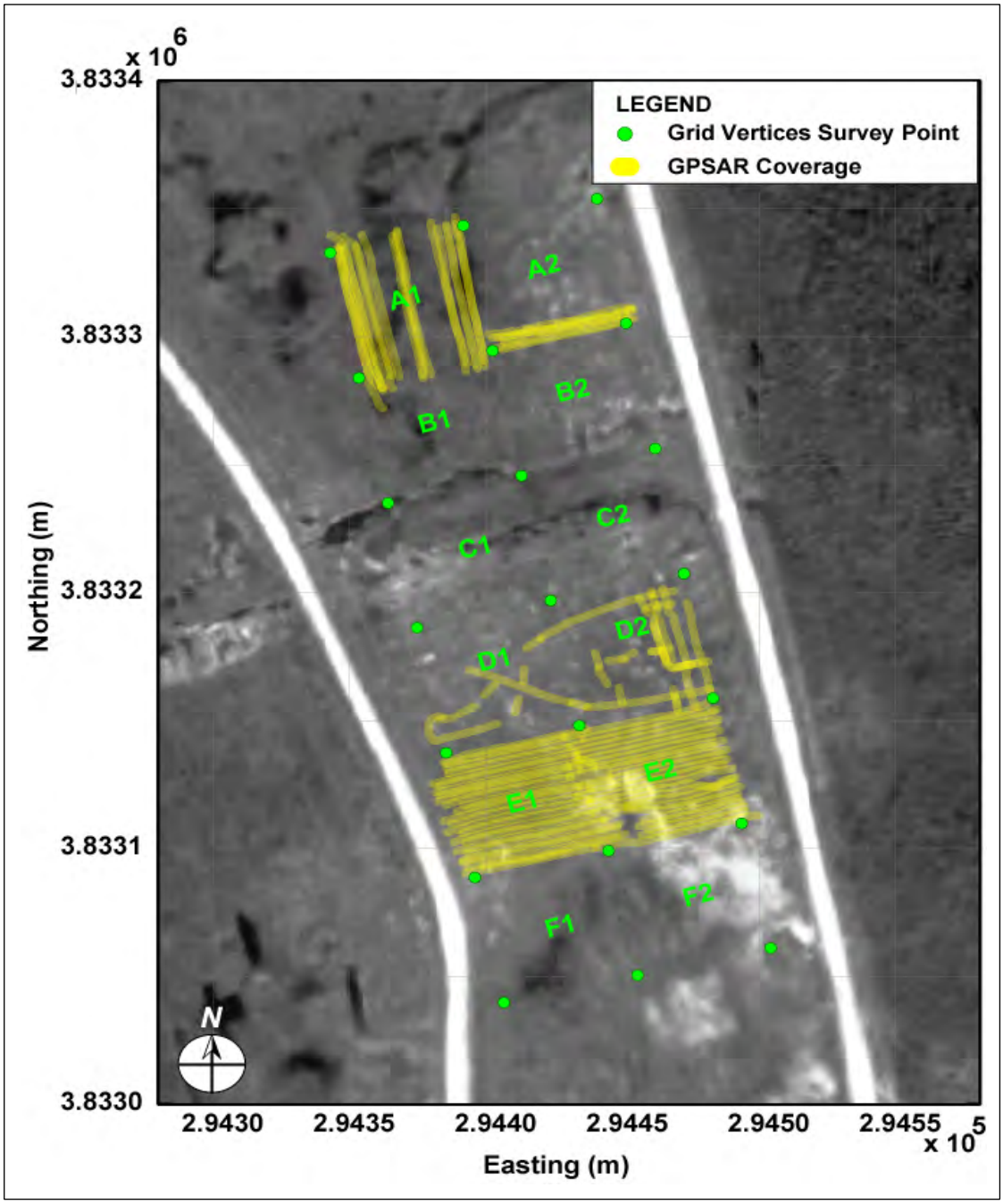


Figure C11. Location of the survey grids at the Gunnery 6 site. Grids G and H extend south of this map, although data were not collected by the Nemesis in those areas. The grid vertices were plotted based on survey points provided by Sky Research. Coverage tracks show the spatial coverage of data acquisition during the week of 20 March 2006 overlaid on a composite aerial image extracted from Google Earth (www.earth.google.com).

During testing, the vast majority of the A2 grid and large parts of the A1 grid were highly saturated or inundated with standing water that was not safely passable with the Nemesis. Data acquisition over emplaced targets in the A1 grid began on Monday 20 March 2006. Diagnostic testing revealed that a DB9 connector in one of the antenna switch enclosures had become disconnected during shipping and was subsequently reattached. The system was tested again over a metal calibration target (14-cm by 14-cm by 1-cm steel plate). Constant and periodically heavy rain impeded testing on Tuesday 21 March. Despite areas of standing water and poor testing conditions, some additional data runs were acquired over emplaced targets in the A1 grid. Maps of transects and grid coverage are shown in Figures C12–C14 along with ground-truth information provided by Sky Research.

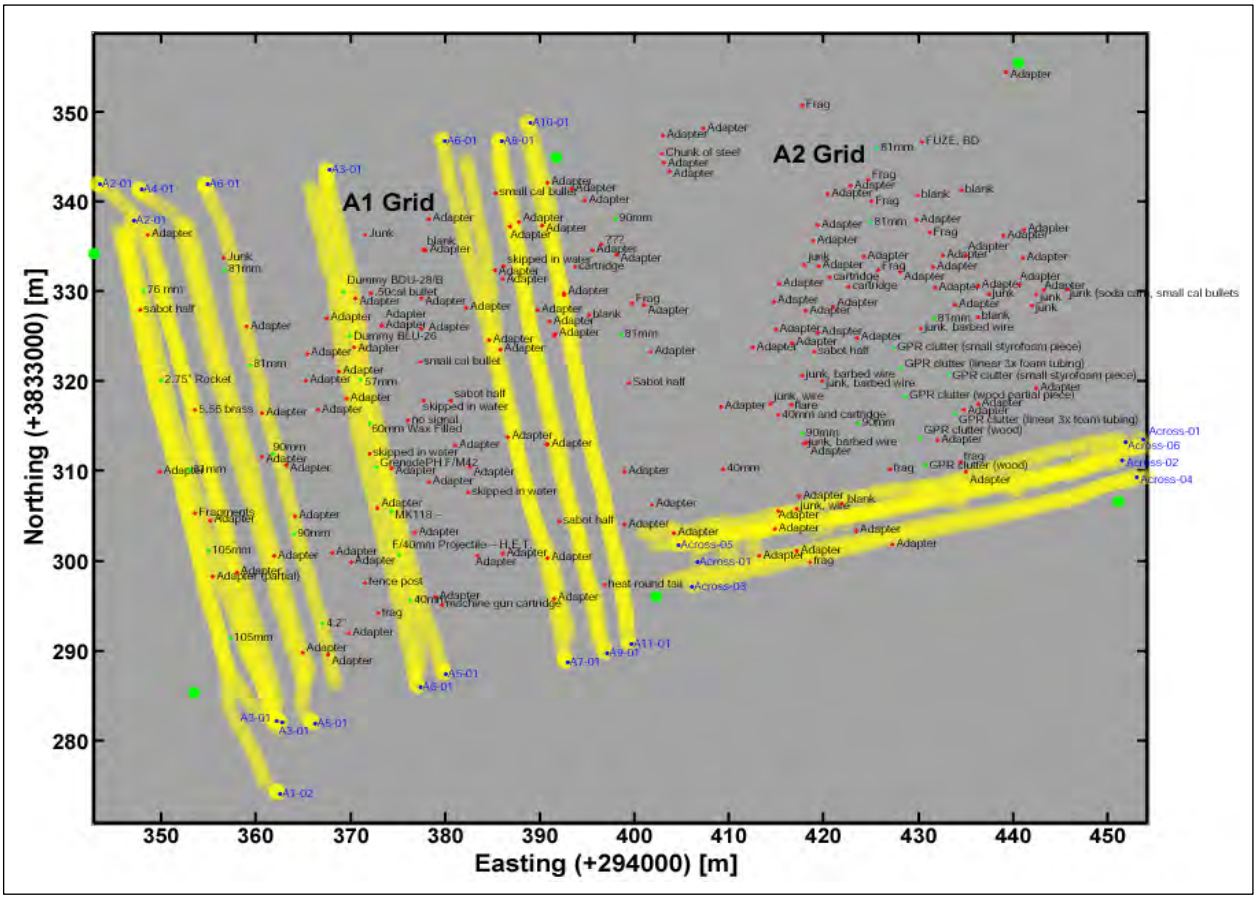


Figure C12. Map of the A grid data collection tracks. The majority of the northern part of the A2 grid was not passable due to standing water and mud. Acquisition on the A1 grid was limited to encounter runs over emplaced target locations because of impassable soft ground and standing water.

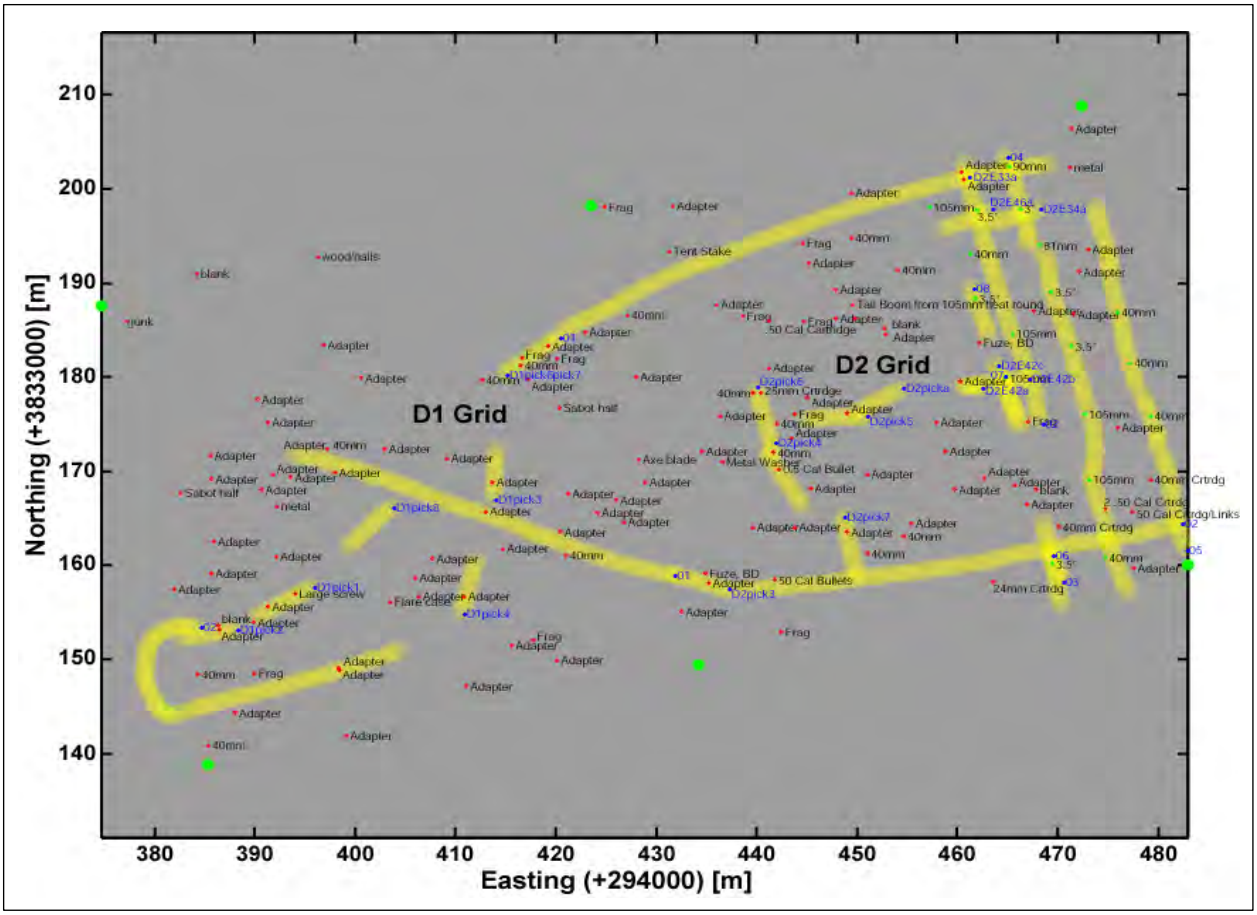


Figure C13. Map of the D grid data collection tracks. Data collected on the D2 grid focused on encounter data over emplaced targets. Longer runs over the D1 grid covered "pick" targets and were focused on flagged target picks specified by Sky Research. Numerous APDS adapters were observed on or just below the surface in these grids.

Standing water persisted on the A1 and A2 grids on Wednesday 22 March. Very limited data were collected on the A2 grid on 21 and 22 March because the majority of the grid was covered with standing water or soft ground. On Thursday 23 March, coverage on the E1 and E2 grids with parallel east-west transects was begun and completed. Data could not be acquired over two areas that had rapid elevation drops (i.e., depressions) in the E2 grid.

Encounter data collection involves single-pass scans over known target locations. Additional encounter data collection runs were conducted by approaching emplaced targets from the multiple orientations or by implementing variable sensor standoff distances. Encounter data were performed on the A and D grid targets. Due to weather-related downtime, only limited data were collected over calibration (i.e., emplaced) targets on the A1 and A2 grids. During testing in March 2006, the vast majority of

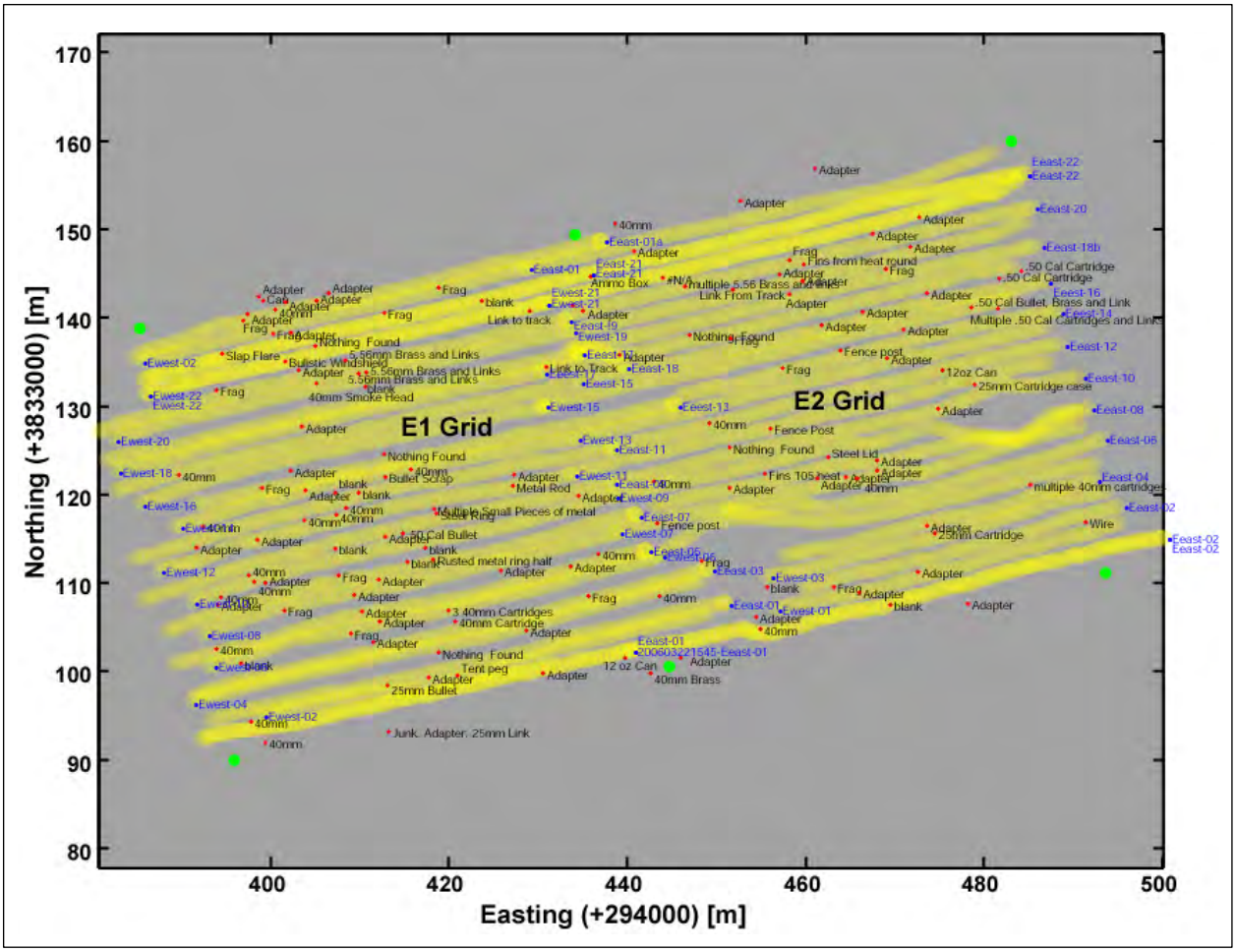


Figure C14. Map of the E grid data collection tracks. An attempt was made to completely cover the E grids with the exception of two areas that were not safely passable by the Nemesis. These two areas were approximately centered around 294455 m east, 38333109 m north and 294488 m east, 38333130 m north.

the A2 grid and large parts of the A1 grid were highly saturated or inundated with standing water that was not safely passable with the Nemisis system. Limited data pass and short encounter data runs were acquired on the D1 and D2 grids. Due to the availability of emplaced targets, acquisition was focused on the D2 grid targets. Select data collection was also conducted over areas that contained anomalies previously identified by Sky Research (i.e., “picks”).

## C.4. Data analysis

Data processing and analysis were implemented in three main stages: 1) post-processing, 2) image formation, and 3) automatic target detection. The primary objective of data post-processing is to enhance the signal-to-noise ratio while preserving the useful signal bandwidth associated with the raw data at all stages in the analysis. Common to both the GPSAR and

EMI sensors are processing steps that remove system and process noise from the responses. These steps include channel balancing across the respective array elements, spatial and predictive filtering, and processing to form coherent images of target responses for detection. The image formation and detection stages are intended to segment data collected over areas free of targets from regions of interest that contain target-like anomalies.

### C.4.1. GPSAR array data processing

#### *C.4.1.1. Filtering and 3D SAR processing*

The key post-processing steps applied to the GPSAR data are channel balancing, spatial filtering, synthetic aperture beamforming, and gain control (Figure C15). However, before any of these steps are applied, system-related delays (i.e., channel and frequency switch delays, delays related to variable cable lengths, antenna phase correction) are removed by frequency-domain processing. Scaled gains and two-dimensional filters are applied to the individual receiver channels to normalize array channel responses and reduce the influence of noise and clutter. The resulting quadrature and in-phase data arrays or data cubes ({along-track or scan} by {across-track or channel} by {frequency}) are used in the target cueing stage or passed to the beamforming client for further processing.

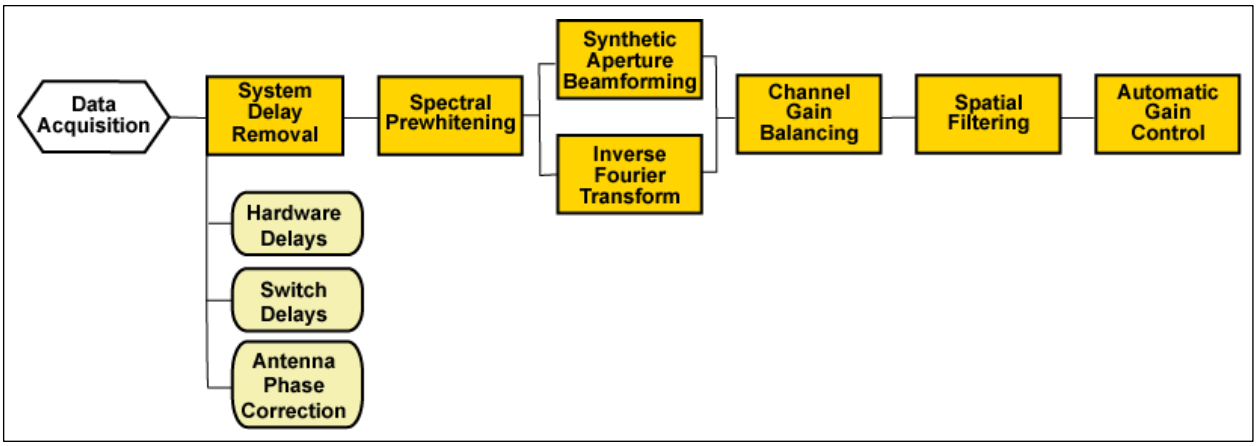


Figure C15. Block diagram of a nominal processing chain for the Nemesis GPSAR data post-processing. All data reported in Section C.5 were beamformed as opposed to inverse fast Fourier transformed. The beamforming process is described in Section C.4.1.2.

Beamforming is a two-dimensional imaging process that is used to eliminate distortions caused by the wide beam generated by the radar antennas. The process is repeated over all focal points and depths specified. The

result of the beamforming process is a focused, interpolated, and inverse Fourier-transformed (time-domain) complex image of the subsurface. More detailed descriptions of the beamforming and 3D analysis are given in the next section. The final processing step applies gain control in the time domain. Gain control is used to reduce the effects of geometric spreading and attenuation losses. Various versions of programmed gain control are utilized, such as instantaneous gain control and RMS amplitude gain control to enhance the detection of deep targets. Gain control does, however, remove the ability to directly compare the amplitude of different responses. To retain the relative amplitudes over depth regions, a depth-binned normalization was implemented.

#### *C.4.1.2. Beamforming and image formation*

The DAS incorporates a real-time synthetic aperture radar (SAR) beamforming algorithm. Beamforming is a two-dimensional imaging process that is used to reduce distortions caused by the radar antenna's wide beam. Figures C16a and C16b illustrate a target response spreading effect caused by the unfocused antenna beam. Beamforming effectively focuses energy spread over characteristic radar reflection hyperbolas to a point. As the antenna passes over a subsurface target, off-axis reflections appear as deeper targets. This results in a hyperbolic spreading of the target signature (Figure C17). Beamforming algorithms focus the wide antenna beam by accounting for a time delay in the reflected signal as the antenna moves past a target. Thus, a synthetic aperture is created by using the focal points generated along track to increase the effective aperture of the array. Additionally, beamforming uses the real aperture focal points generated by the across-track spacing of the antennas in the array. This two-dimensional beamforming results in an optimal focusing of the radar antenna beam to maximize the target signal-to-noise ratio.

The beamforming process is repeated over all focal points and depths specified. This processing step improves both signal-to-noise ratio (SNR) and resolution of a target. Figure C18 shows depth views of a target using both raw and beamformed data.

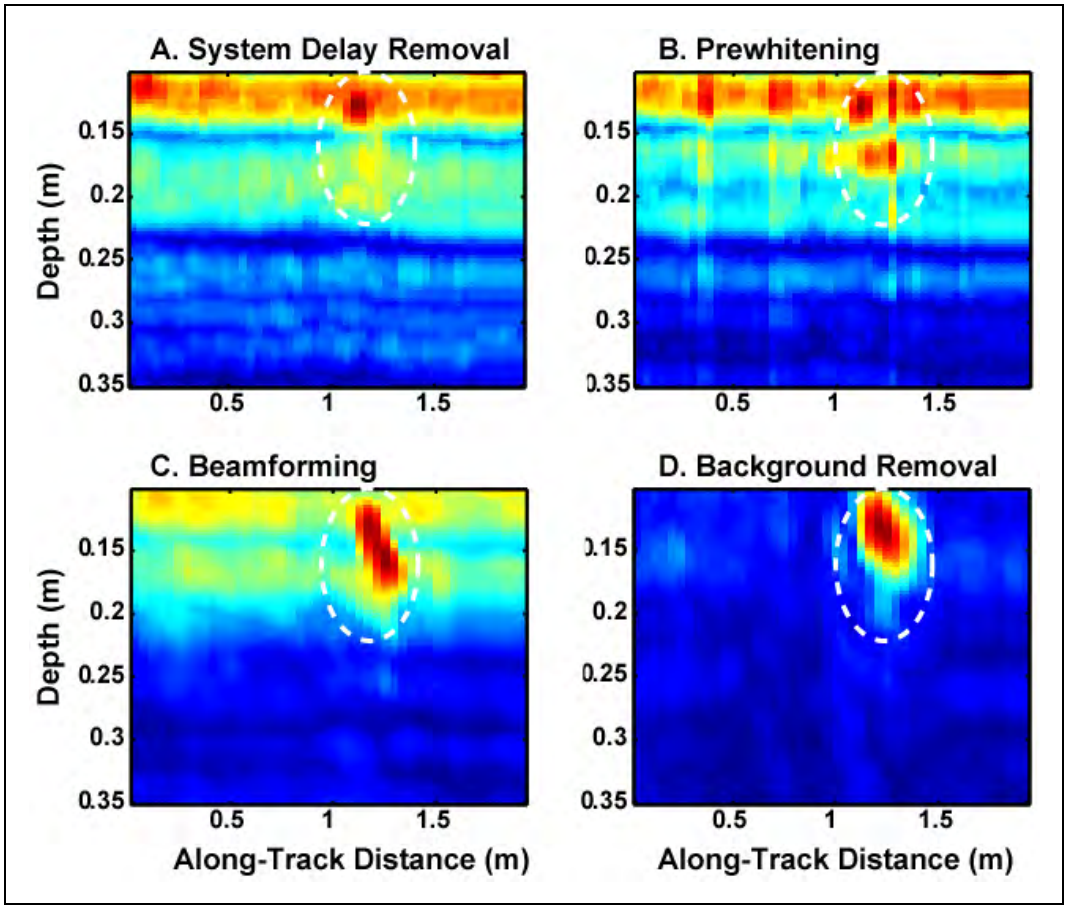


Figure C16. Example depth slice images for different stages of GPSAR data processing.

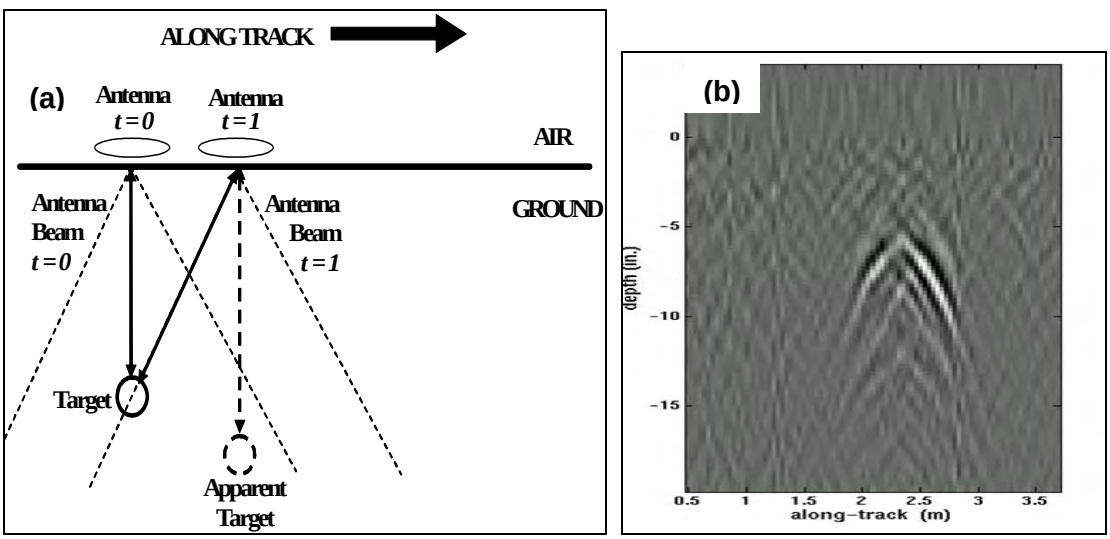


Figure C17. (a) Schematic diagram of the beam pattern effects during acquisition of GPSAR data. As the antenna moves along track during the time interval from $t$ = 0 to $t$ = 1, the antenna beam causes weaker reflections to appear as deeper targets. (b) Imaginary component of GPSAR inverse Fourier transformed data over a target. The hyperbolic nature of the amplitude response is evident in this depth slice image. Beamforming tends to focus these hyperbolas into points.

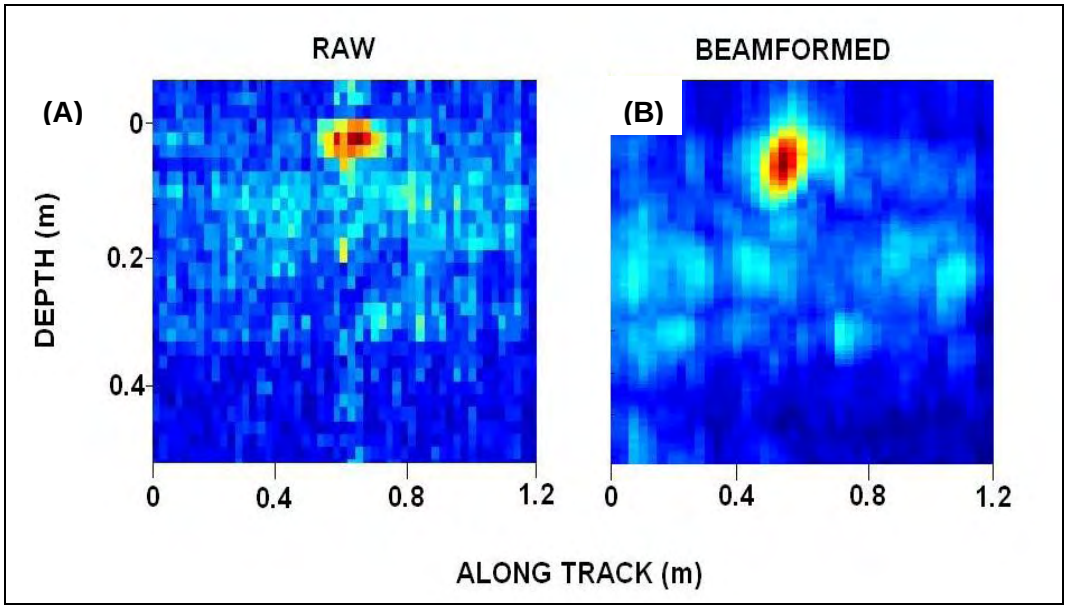


Figure C18. (A) Raw (unfocused) magnitude data over a metallic target. (B) The resulting beamformed image of the same target.

*C.4.1.3. Target detection and 3D image analysis*

Automated detection of GPSAR anomalies is performed by adaptive thresholding in the three primary mappings of the data: 1) along track by depth maximum energy, 2) across track by depth maximum energy, and 3) along track by across track (i.e., map view) summed energy. To cue GPSAR regions of interest, a constant false alarm detector (CFAR) is applied. The cell-averaging CFAR energy detector provides detection of zero-mean Gaussian noise by constraining the probability of false alarm and maximizing the probability of detection under a binary hypothesis. The CFAR algorithm is based on the estimate of the mean amplitude and standard deviation of the background region surrounding a set of test pixels.

Prior to application of the CFAR algorithm in the along- and across-track depth slices, the average background response is subtracted from the data volume. Next, a CFAR filter is applied to the maximum energy for the respective projection of the data, resulting in a thresholded image. The detected anomalies from both the along- and across-track projections are then checked to see if they were derived from coherent responses in 3D. If detected regions are coherent in 3D, then their projection in the along-across track view is mapped using the detection area mask. An example of this process is shown for detection of the emplaced 3.5-in. rocket target in the D2 grid in Figures C19 and C20. Figure C19 shows the along- and

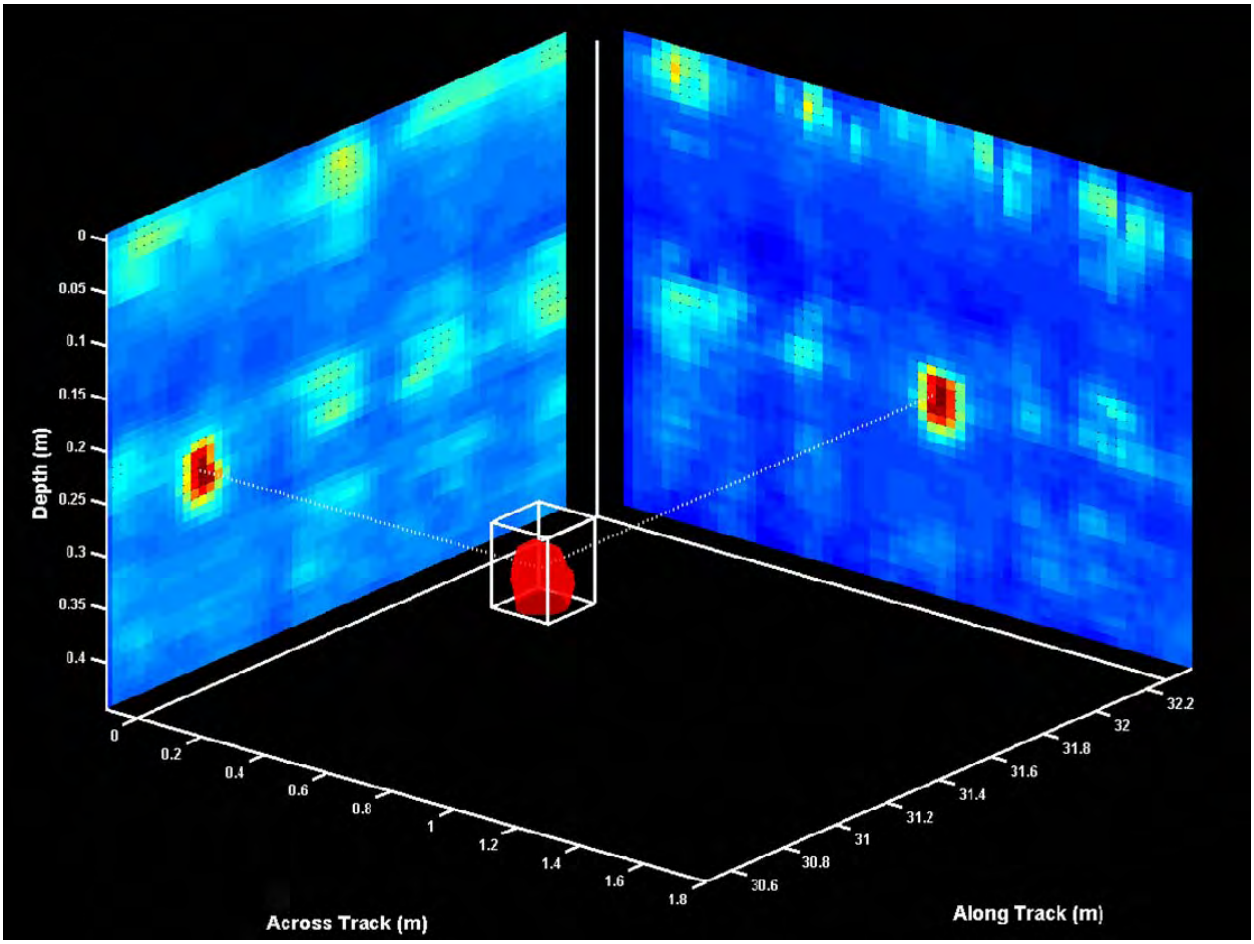


Figure C19. Three-dimensional views of depth slice images over a 3.5-in.rocket. Detection-level processing invokes constraints on the 3D coherence of targets such that along-track by depth and across-track by depth anomalies produce matched volumes as represented by the red isosurface projected into the data volume.

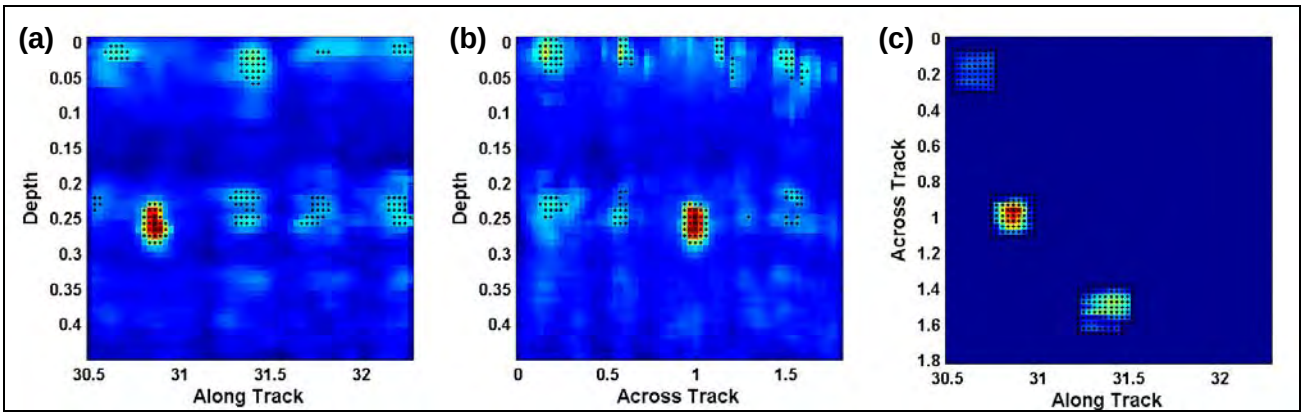


Figure C20. Three views of the 3.5-in. rocket also shown in Figure C19. The along-track by depth (a) maximum energy and across-track by depth (b) maximum energy data are overlaid by stippled detection regions determined by a cell-averaging CFAR detector. The matched and projected map view (c) from depth-binned slice responses are masked by regions of interest that form coherent volumes in 3D.

across-track maximum energy projections of a subvolume of data over the target. Figures C20a–C20c show the data with overlaid CFAR detections for the three views of the data described above. A ground radar velocity of 0.85 by $10^8$ m/s produces an image at the expected depth of the target. This corresponds to an approximate real relative dielectric permittivity of ~12.5. The final masked detection regions are shown in the map view figure in Figure C20c.

## C.4.2. EMI array data processing

### *C.4.2.1. Filtering and ground compensation*

One of the key features of the Nemesis EMI array is the noise reduction capability of the on-board low-pass filters. The STMR system includes three digital low-pass filters as part of the embedded software executing on each receiver sensor card. Their main roles are to eliminate as much broadband noise and interference as possible (filtering) and to permit a reduction of the sample rate (decimation). The digital filters process the output of the analog-to-digital converter, which is preceded by the synchronous demodulators and analog low-pass filters. These filters have a -3-dB cut-off frequency of approximately 20 Hz and eliminate most of the transmitter-related signals and some of the noise. However, the analog filter pass-band is wide enough to include some external noise interference. The frequency spectrum of the target response is such that a narrow pass-band can be implemented without losing valuable target information. The digital low-pass filters provide this narrower pass-band to reduce noise while maintaining target response frequency characteristics. Thus, the overall response is dominated by the digital low-pass instead of the analog filters. The input data rate for the digital low-pass filters is 400 samples/sec and there are three possible selections for the output rate: 100 samples/sec, 50 samples/sec, or 25 samples/sec.

Vibration of the detection platform contributes to background noise. As the sensor head vibrates, varying sensitivity to nearby metallic components is evident. Applying the fast filter, which has the broadest pass-band, allows corruption by higher frequencies and results in the greatest noise levels. Applying the slow filter, which has the narrowest pass-band, filters some of these higher frequencies and results in a significant reduction in background noise.

Unlike similar time-domain EMI systems, the STMR array incorporates Minelab's patented cross-channel correlation technology (US Patents 4894618 and 5576624), which reduces false alarms due to highly mineralized or conducting soils. The method relies on various pulse lengths to differentiate the response of a metal target from the background ferrite response. Linear combinations of different time-integration windows are used such that the background ferrite responses sum to zero, thus removing the effect of soil variability from target responses. This method produces the two soil-compensated data types (S and C types). The three types of data are then normalized to balance the responses for the different coils and remove static offsets due to variability in the receiver electronics. In general, a two-dimensional spatial filter is then applied to reduce the effects of high-frequency noise and clutter. These post-processed data are subsequently used for cueing targets in the response detection stage.

#### *C.4.2.2. Image formation and target cueing*

Before applying an adaptive thresholding method to the EMI data, the ground balanced data arrays, S and C, were combined using a pixel level fusion algorithm. The ground channel (G) and the fused ground-balanced data types (S+C) were evaluated independently using a combination of the adaptive thresholding method of Otsu and two-dimensional matched filters with region growing to generate anomalous regions of interest. The algorithm used in this work uses the gray-level histogram to select an optimal threshold and correlated peak detection. If one or both of the G and combined S&C data types exceed the threshold, then all coherent regions exceeding the threshold are passed onto a discrimination stage processor. Because the focus of this work was on the assessment of GPSAR data, the EMI data have not been processed beyond the target detection stage.

## C.5. Results

### C.5.1. GPSAR performance

Overall, the performance of the Nemesis GPSAR was likely limited by the very wet conditions experienced during testing. Inundation of water in the soil and ponding of water on the ground surface significantly detract from the ability of EM waves to propagate into the subsurface and reflect off of dielectric targets. The addition of water in the soil leads to an increase in the bulk dielectric permittivity of the subsurface and yields a lower

dielectric contrast with respect to UXO targets. In addition, the increase in the dielectric permittivity influences the loss tangent, which controls the attenuation of EM energy away from the transmitter. Therefore, less energy was arriving at the target. This effect is especially severe over the frequency range (450–2400 MHz) at which the GPSAR operates. Cropping of the frequencies processed by limiting the upper frequencies to ~2 GHz generated some improvement in SNR without comprising depth resolution significantly.

*C.5.1.1. Emplaced targets*

Despite limitations due to the highly saturated conditions, images were formed of a subset of the targets over which data was collected. Detection of emplaced targets in the A1 grid was found to be very difficult. Under less challenging environmental conditions at a Western arid test site, the Nemesis GPSAR system had elucidated coherent responses from similar targets to those placed in the A1 grid (i.e., 105-mm projectile, 90-mm projectile, 81-mm projectile, and MK118). However, coherent images from data collected over any of these targets could not be generated with the exception of the 60-mm wax-filled UXO body buried 25 cm BGS at $0^{o}$ dip and $40^{o}$ azimuth. Projections of the data volume and isosurface from the detected regions associated with this target are shown in Figure C21.

Although a number of relatively strong radar returns are visible in the projections of the data volume, only those associated with the 60-mm target are coherent in all three dimensions. The detected regions in the depth slices are shown in Figures C22a and C22b, while only the coherent detections, that is, those paired detections that are matched to a coherent three-dimensional region, are projected to the map view in Figure C22c. This particular target generated multiple responses in depth (represented by the four isosurfaces in Figure C21), an attribute that is common to other UXO targets that have been imaged. This example illustrates the value of the three-dimensional nature of the data to distinguish targets from non-coherent scatter or clutter returns.

Targets placed in the D2 grid could be images and detected to a greater extent than those in the A1 grid. For example, coherent images of the 40-mm UXO buried at 10 cm BGS (ID: g6d2e48) were generated in both the along-track by depth maximum energy and across-track summed energy map view projections. The locally referenced images for this target are shown in Figure C23.

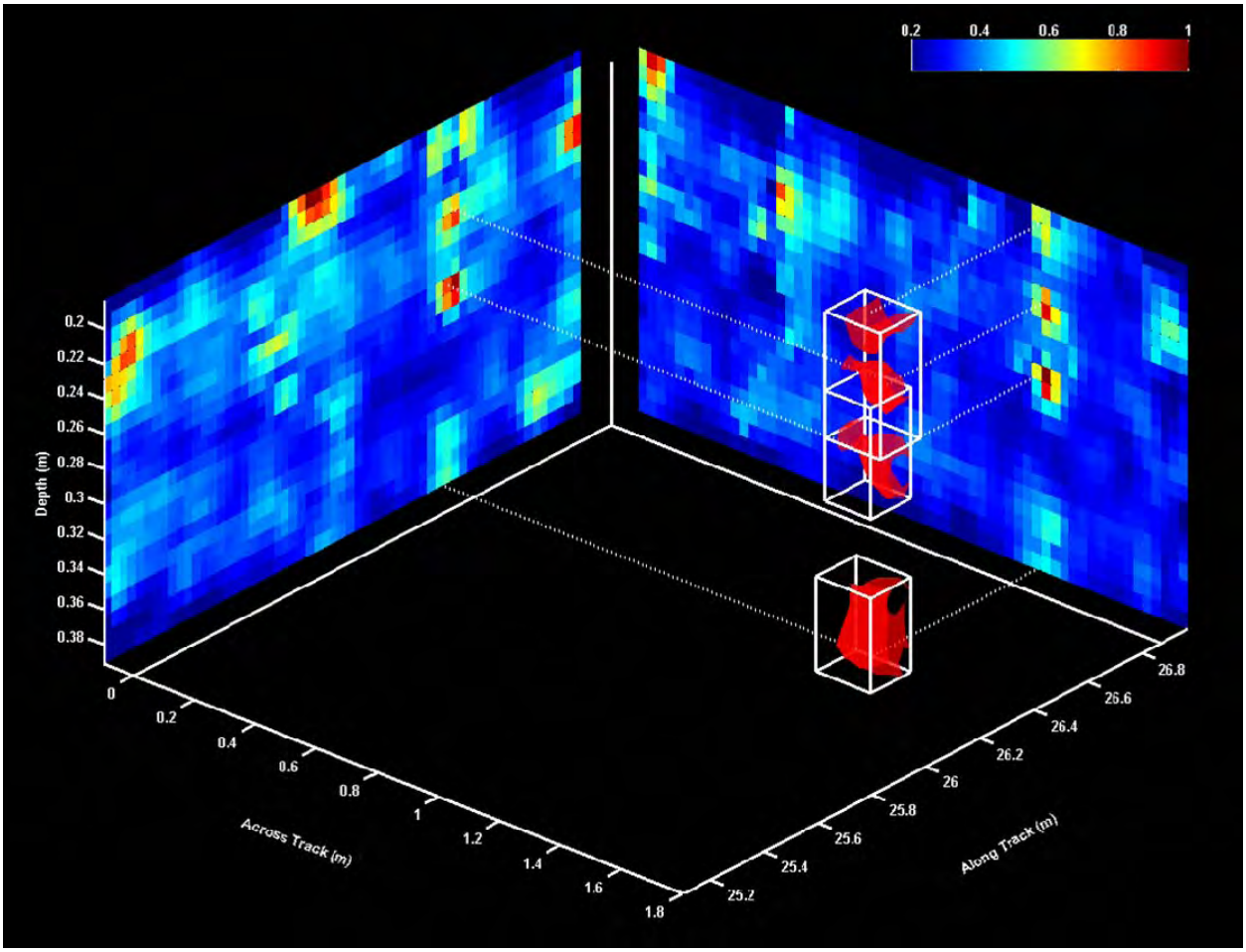


Figure C21. Three-dimensional views of depth slice images over the 60-mm wax-filled UXO body rocket. Multiple detections in depth under the reported location for the target (26.3 m along track, 1.55 m across track) form coherent volumes. The reverberating nature represented by the multiple responses is a common feature of detected targets.

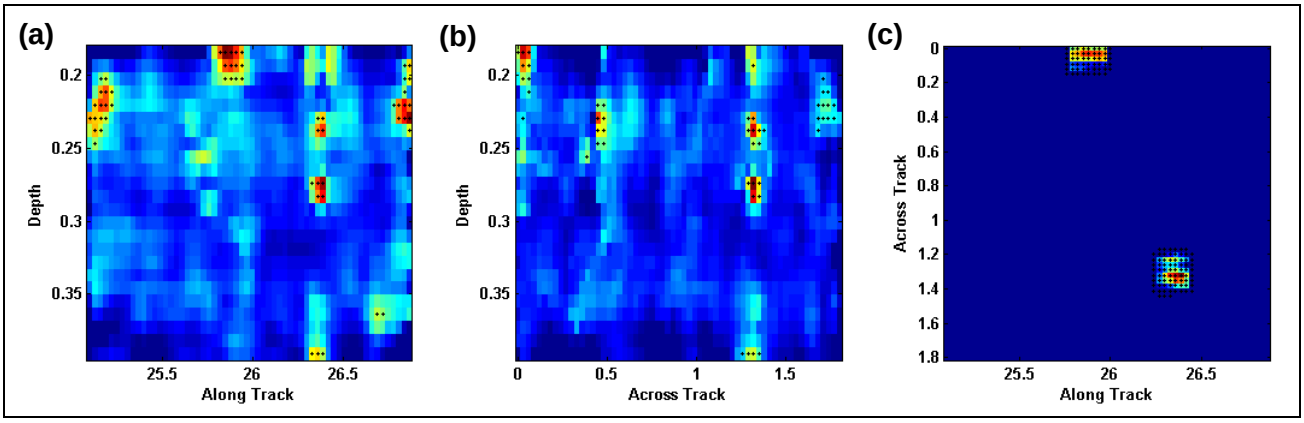


Figure C22. Depth slice and map detection views over the 60-mm wax-filled UXO body. Although a number of strong radar responses are observed in the depth slice images, only two form matched coherent response volumes when analyzed in 3D. The map view detection at ~26.3 m along track, 1.4 m across track is associated with the 60-mm target.

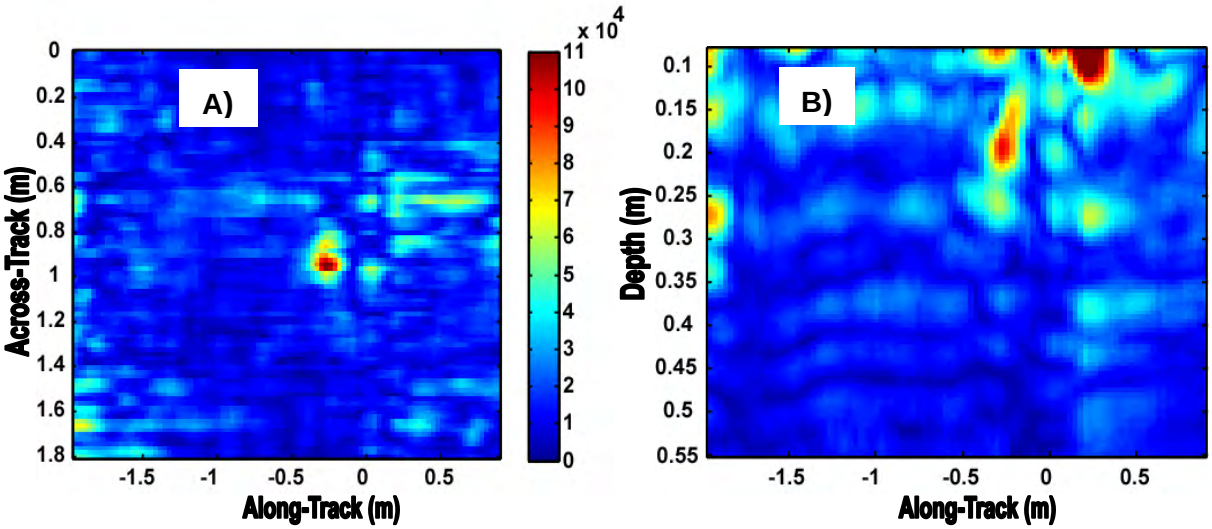


Figure C23. Map view (A) and depth-slice images over a 40-mm projectile at 15-cm depth (ID: g6d2e48).

The highest signal-to-noise image was produced for the 3.5-in. rocket buried at 15 cm BGS (ID: g6d2e41). The globally referenced, depth-segmented, summed energy map view of this target is shown in Figure C24. The projected map view image shows two coherent responses with maxima oriented along the reported azimuth for the target. The radar return from the tail of this target is expected to generate a strong response after the data are beamformed. However it appears that the body and the tail generate distinct responses with the body return having a higher signal-to-noise ratio.

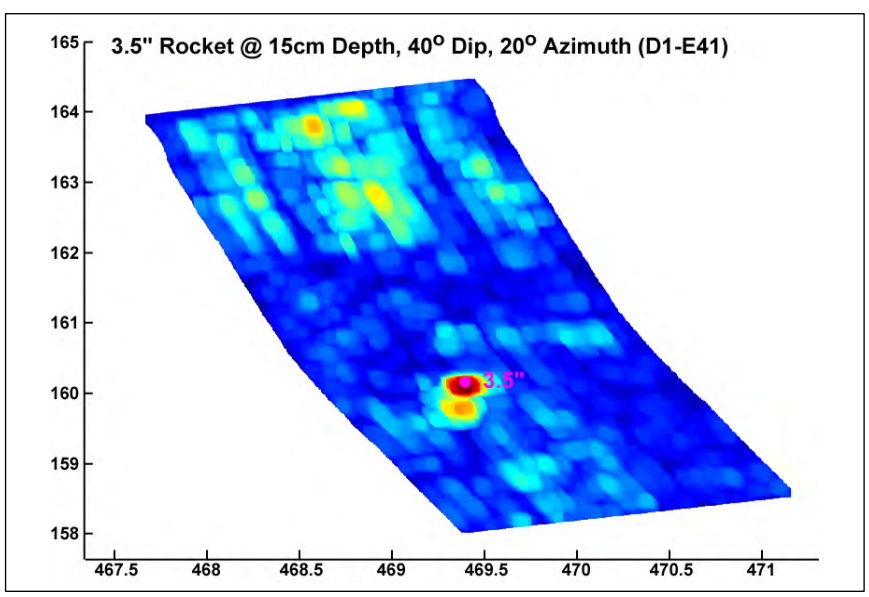


Figure C24. GPS-referenced map view energy summed image over the 3.5-in. rocket emplaced in the D1 grid. Easting values are relative to 294000 m East and Northing values are relative to 38333000 m North.

The high frequencies employed by the GPSAR provided the ability to image small targets like the 40-mm projectile as well as small clutter objects like the 12-oz. aluminum can shown in the globally referenced, depth-segmented, summed energy map view in Figure C25. This target was cued and tagged by previous EM surveying by Sky Research. Upon visible inspection, the image of this target does not yield any discriminative information, although a quantitative statistical analysis of computed features would give a more complete description of the potential of such an image to aid in the discrimination process.

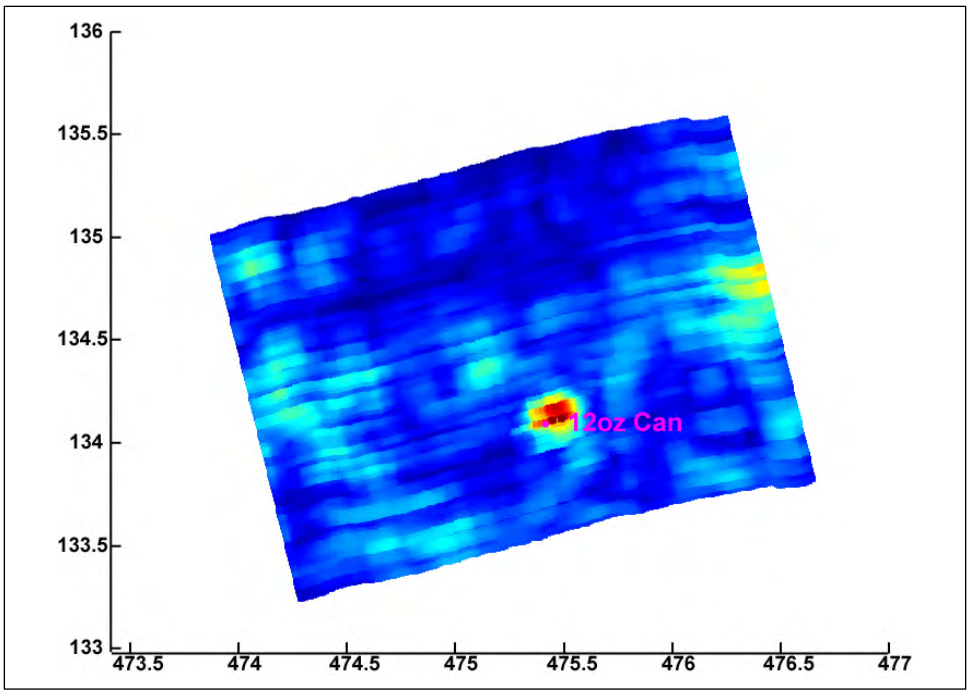


Figure C25. GPS-referenced map view image over a 12-oz. aluminum can in the D grid.

### *C.5.1.2. Targets cued by EMI anomalies*

This analysis also investigated select anomalies that were cued by EM detections. Both "picks" from surveying with a Geonics EM-61 provided by Sky Research as well as anomalies identified from the Nemesis EMI array were used to focus GPSAR processing. The examples reported here have been limited to those over known/placed targets: 1) 40 mm at 15 cm BGS (ID: g6d2e40), 2) 105 mm at 31 cm BGS (ID: g6d2e39), and 3) 105 mm at 22 cm BGS (ID: g6d2e38) (Figures C26–C28).

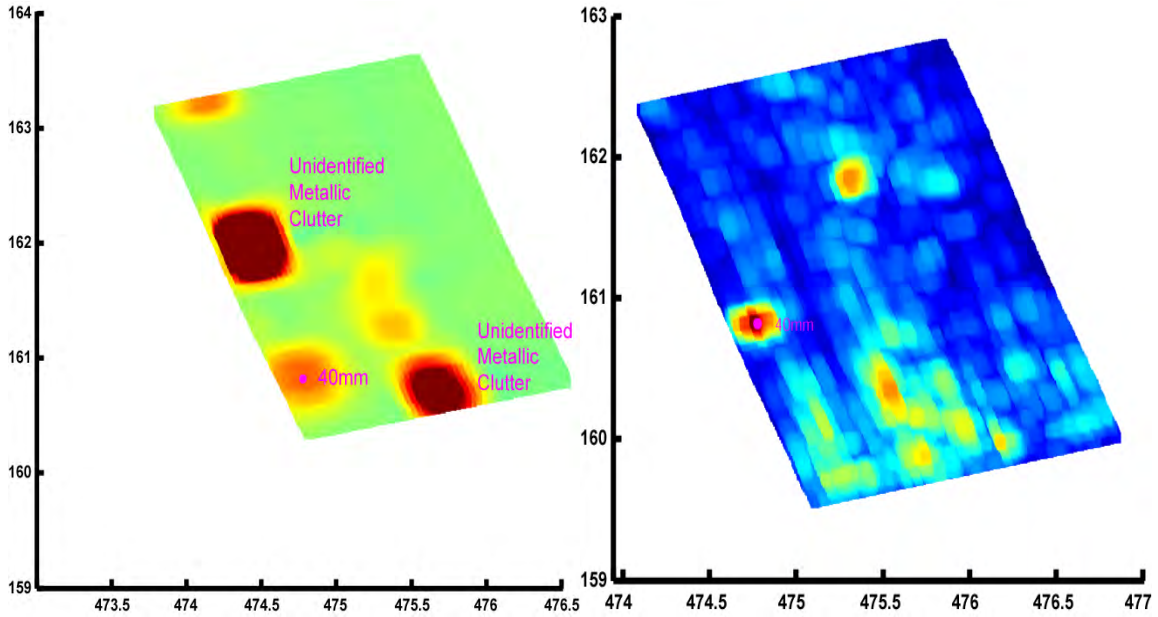


Figure C26. GPS-referenced map view images for correlated EMI and GPSAR responses over a 40-mm target. Only the target response is matched for both data.

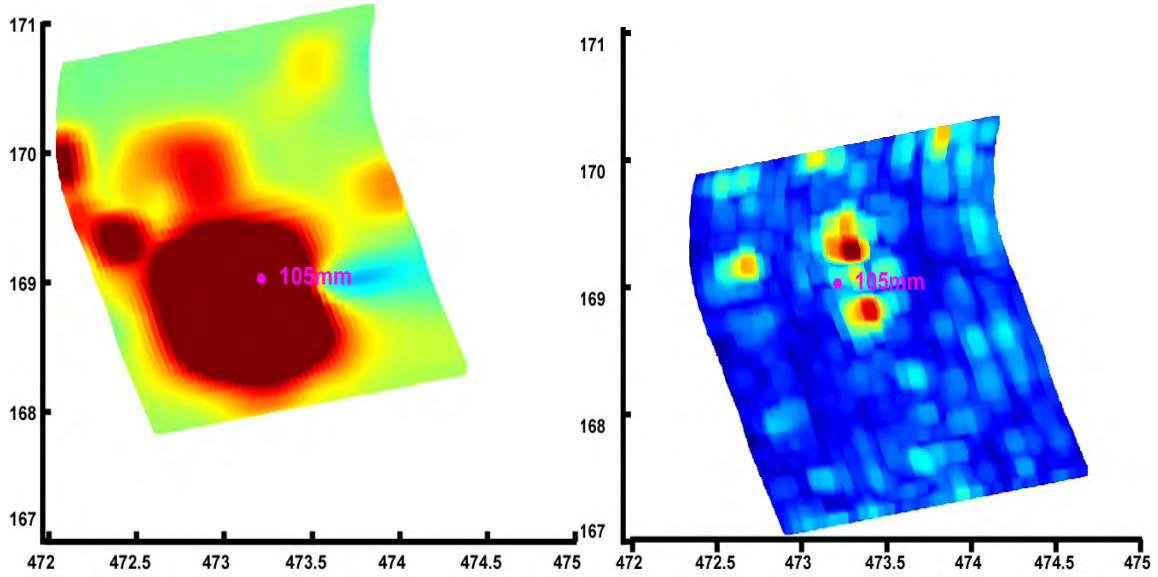


Figure C27. GPS-referenced map view images for correlated EMI and GPSAR responses over a 105-mm target.

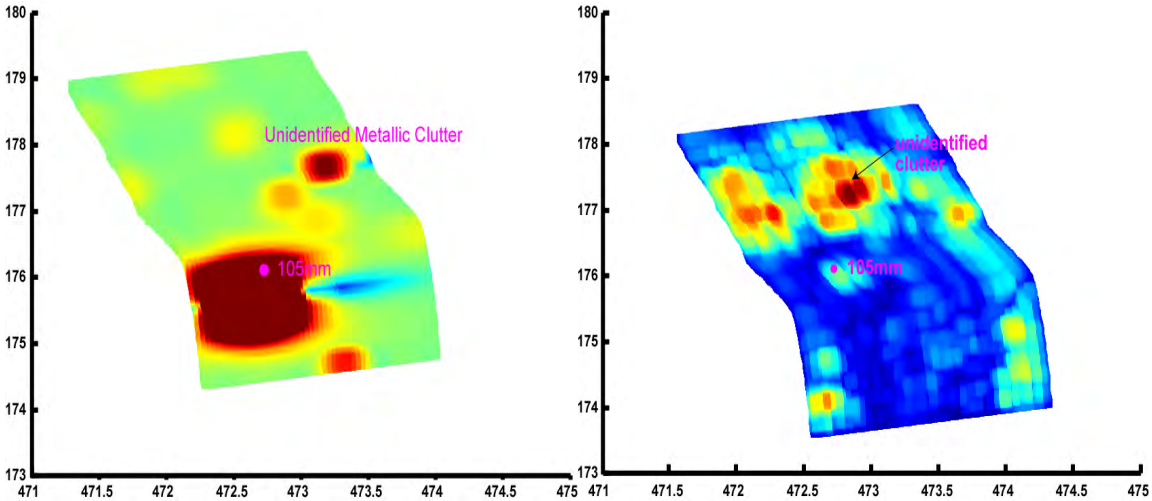


Figure C28. GPS-referenced map view images for correlated EMI and GPSAR responses over a 105-mm target. Note the same clutter object yields response in both GPSAR and EMI images.

### C.5.2. EMI performance

A preliminary analysis of the Nemesis EMI array data revealed well-defined spatial responses over all placed UXO targets in the D2 grid and numerous responses in the E grids. To date, only the raw integrated ground channel (G data type) has been processed. Raw, integrated time-decay data plots over select emplaced targets in the D2 grid are shown in Figure C29.

The spatial responses are indicative of strong axi-symmetric dipoles. The characteristic hourglass-shaped positive portion of the response and corresponding negative lobes are observed on most of the larger UXO targets. It is important to note that at close distances to the receiver coils, maximums in the spatial response may not occur directly over the target and are dependent on the depth, orientation, aspect ratio (for prolate spheroid targets), and material properties.

The distribution of EMI anomalies is also shown for the E grid coverage in Figure C30 with ground-truth information overlay. The data also show the relative accuracy of the GPS positions correlated with the ground-truth information. Inconsistencies between overlapping runs are likely due to variable DC offsets set upon initiation of each run.

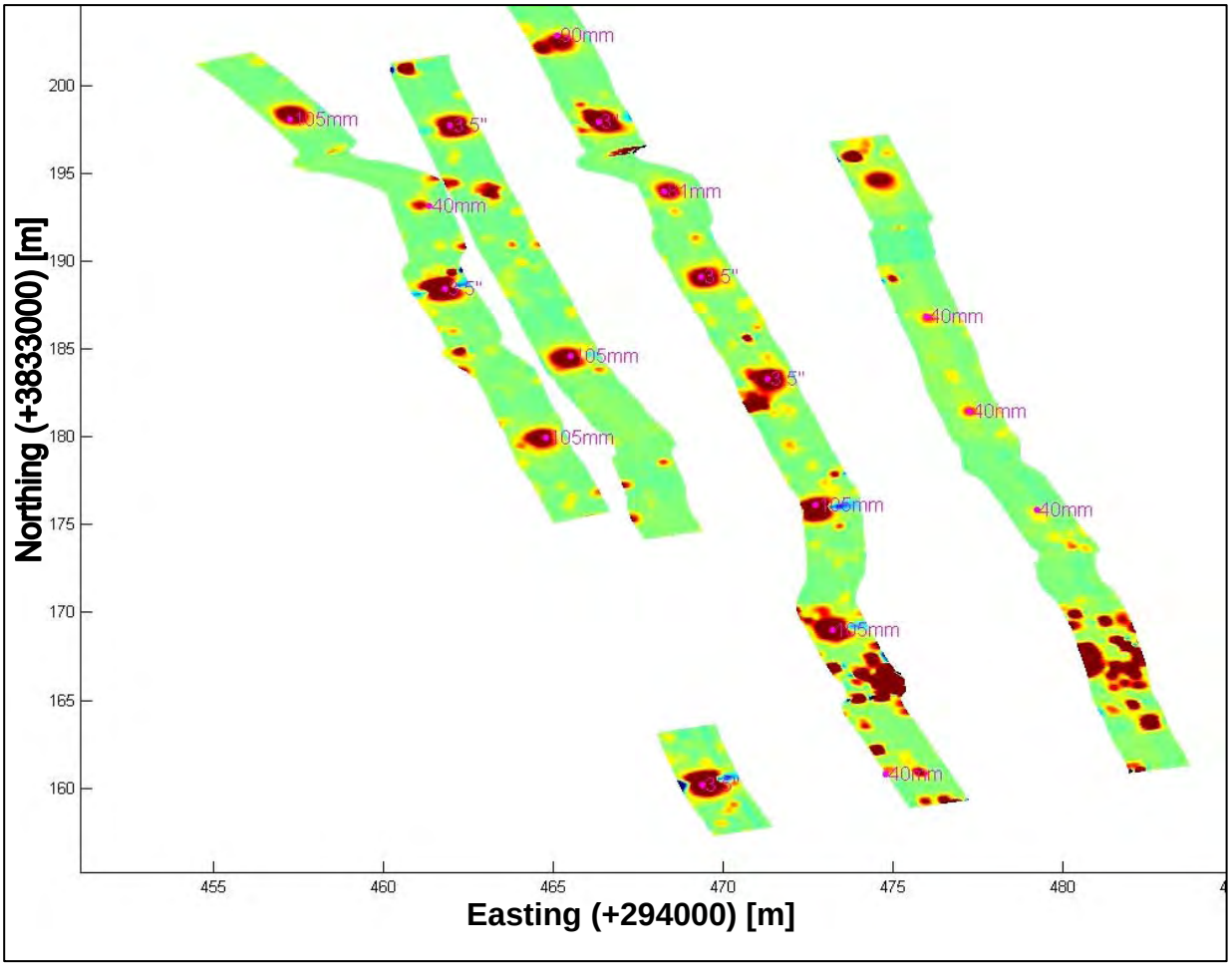


Figure C29. GPS-referenced map view images of the raw integrated time-decay EMI data over emplaced targets in the D2 grid.

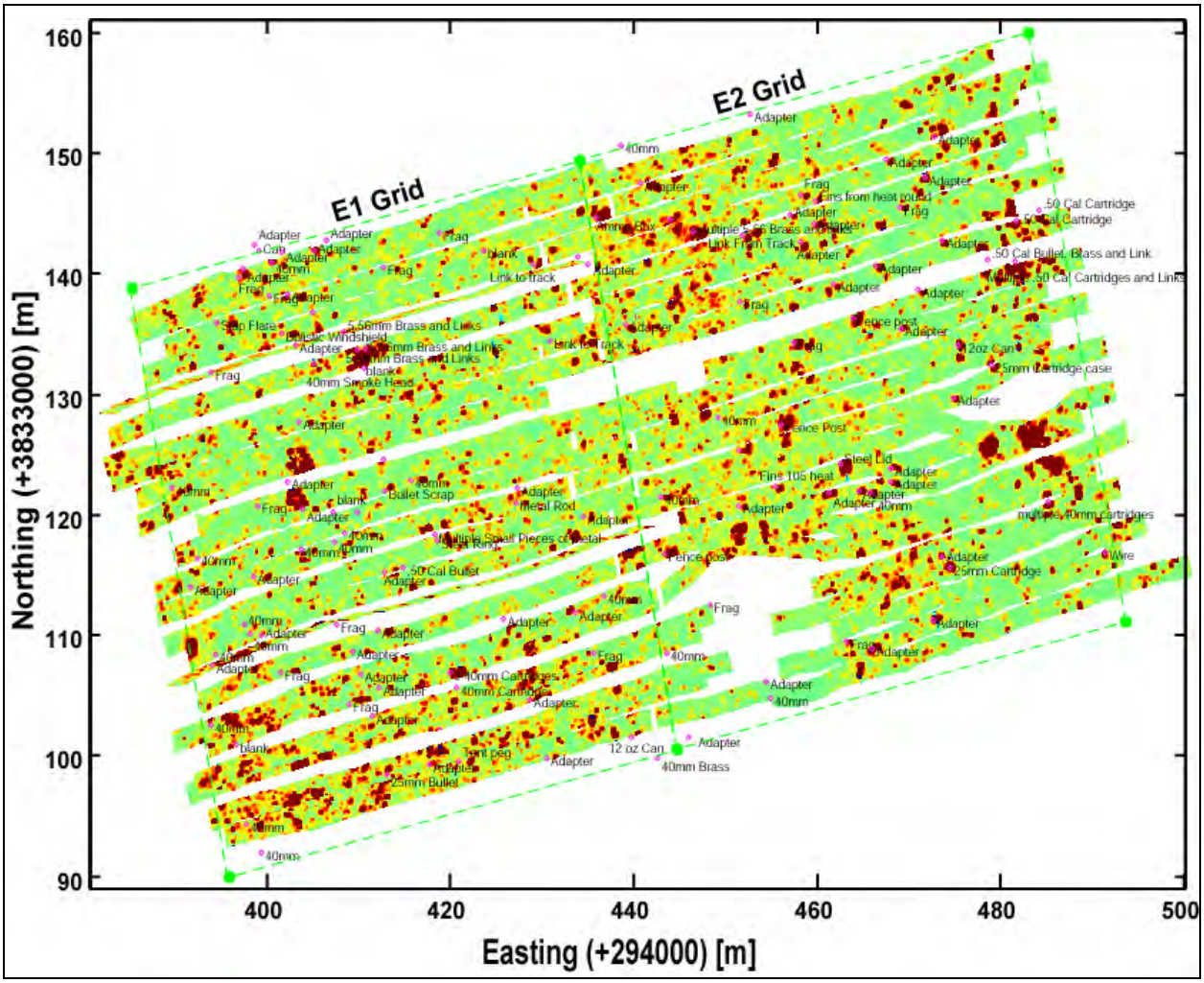


Figure C30. GPS-referenced map view responses from raw integrated time-decay EMI data over the E1 and E2 grids. Adapter responses align with the overlaid ground-truth information as surveyed and supplied by Sky Research. Some anomalies indicating target-like spatial response were not associated with ground-truth information such as those at Northing (+38333000), Easting (+294000) pairs [99, 419], [102,438], [117,439], [116,464] meters.

## C.6. Conclusions

Data collection by the Nemesis system at the Camp Lejeune site focused on six of the 16- to 50-m by 50-m grids surveyed by Sky Research. Despite weather-related downtime, ~11 GB of data (~140 datafiles) were collected on the A, D, and E grids. Standing water and mud-filled ditches in grids A1 and A2 prevented full coverage by Nemesis. Nearly complete coverage of the E1 and E2 grids was accomplished using east-west trending passes. Selective coverage and encounter data were collected on the D1 and D2 grids. Multiple passes were made over the emplaced targets in the D1 grid.

Analysis of GPR data detected emplaced targets (105-mm rockets, 3.5-in. rockets, and 90-mm projectile) at depths of up to 0.35 m; however, further analysis is required to determine the maximum penetration depth of the radar system given the soil conditions at the site. Site conditions for the week of 20 March were not favorable for GPR data acquisition. Periods of moderate to heavy rain throughout the week left the ground saturated with areas of standing water for each day of testing. Soil moisture content likely had a significant impact on the effective penetration range of the GPR. Despite these limitations, coherent two- and three-dimensional images of GPR radar returns were produced.

A joint analysis with correlated EMI data yielded some confidence in the ability of the Nemesis GPSAR to aid in the detection and discrimination of UXO targets, although transmission frequencies were not appropriate for deeper targets. Significant improvements from extending the lower frequency of the system to 180 MHz (preliminary analyses indicate an optimal frequency range between 180 and 1800 MHz) are anticipated. This can be accomplished by implementing a “drop-in” lower-frequency radar module and antenna array with slightly larger antennas. In addition, a digital frequency synthesizer to optimize frequency sampling (wider effective bandwidth) will be implemented under the U.S. Army Nemesis program. This should lower phase noise and increase stacking ability for signal-to-noise improvement.

# Appendix D: COTS GPR Responses for Camp LeJeune, NC

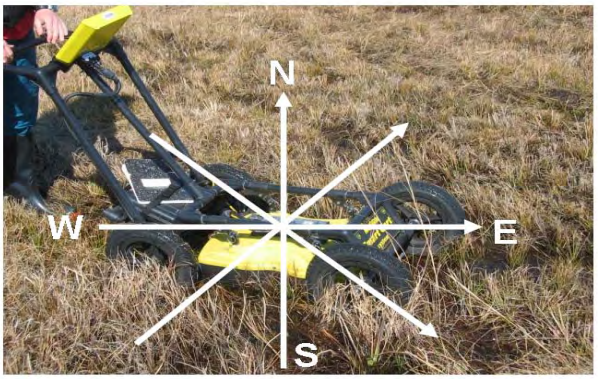

A series of four survey lines were collected over each target. Each line passed directly over the flag marking the target location. The first line was oriented such that it ran approximately south to north. The second line was shifted by 45 degrees counterclockwise and ran southwest to northeast. Another 45-degree counterclockwise shift meant that the third survey line ran from west to east. Finally, the fourth survey line ran in a northwest to southeast direction. The four survey lines collected for each target are depicted above.

Each target is summarized in this appendix as a single-page report. A photo of the target in question is accompanied by a table describing detailed position and orientation information recorded at the time of burial. These are followed by three different visualizations of the four survey lines collected over the emplaced item. In the first row of plots, the GPR sections themselves are displayed. The second row of plots displays the data after it has been migrated and enveloped. Finally, a row of average amplitude versus position plots over a user-specified time window is shown. Further details of the processing applied to generate these plots can be found in the body of the report.

## D.1. 250 MHz emplaced items

| | |
|---|---|
| Target Name | G6A1E1 |
| Item Description | 105-mm Projectile – Inert |
| Depth (cm) | 45 |
| Dip | 0 |
| Azimuth | 5 |
| Easting (m) | 294357.2598 |
| Northing(m) | 3833291.355 |

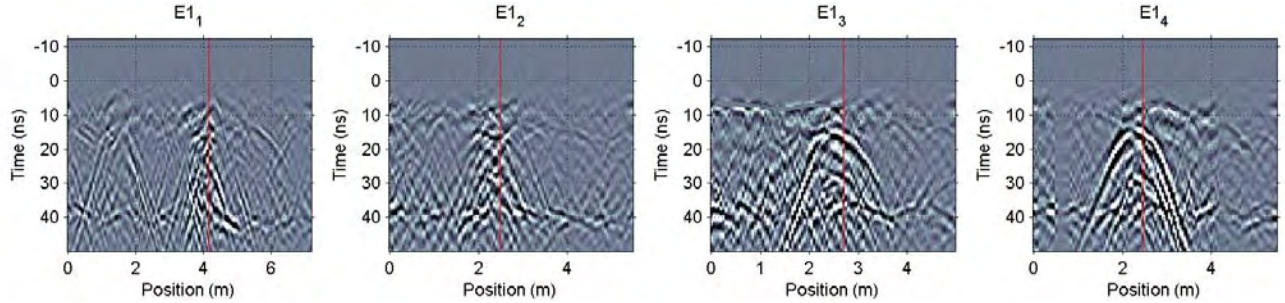


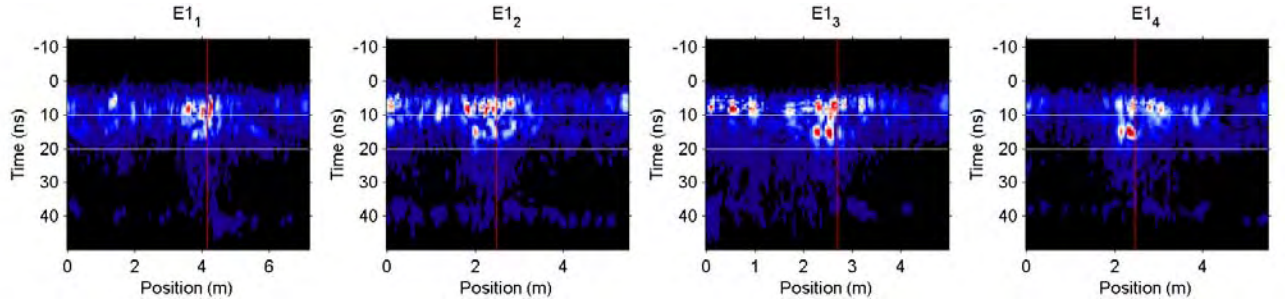


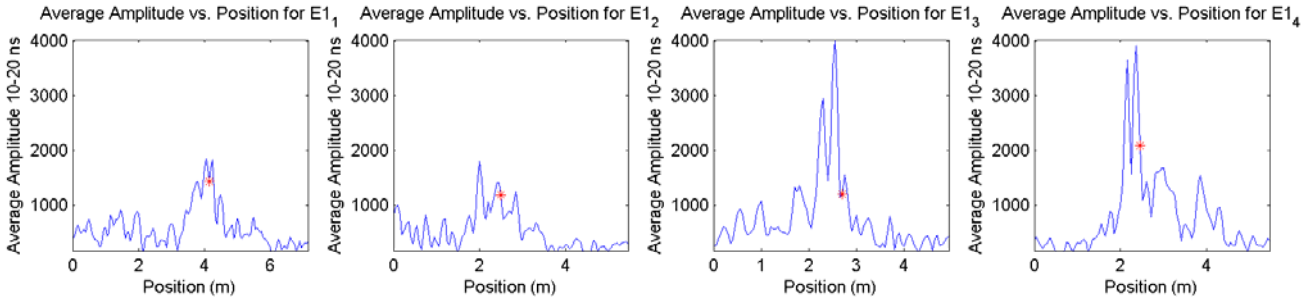

| | |
|---|---|
| Target Name | G6A1E2 |
| Item Description | 105-mm Projectile – Heat Empty |
| Depth (cm) | 50 |
| Dip | 45 |
| Azimuth | 94 |
| Easting (m) | 294354.9188 |
| Northing(m) | 3833301.11 |

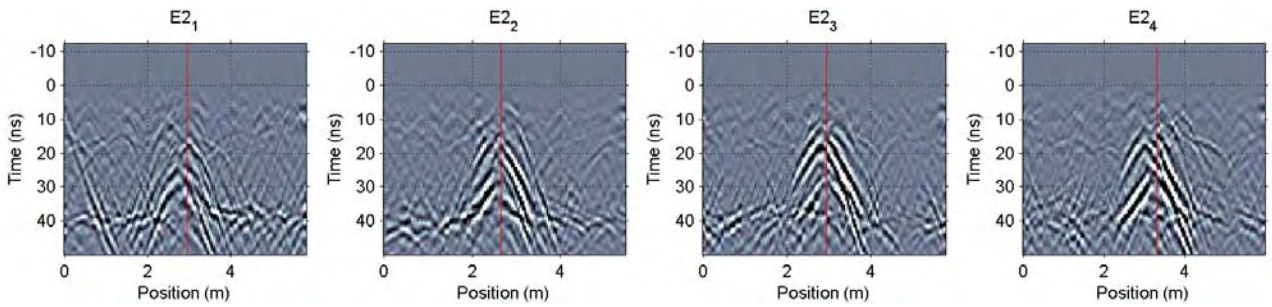


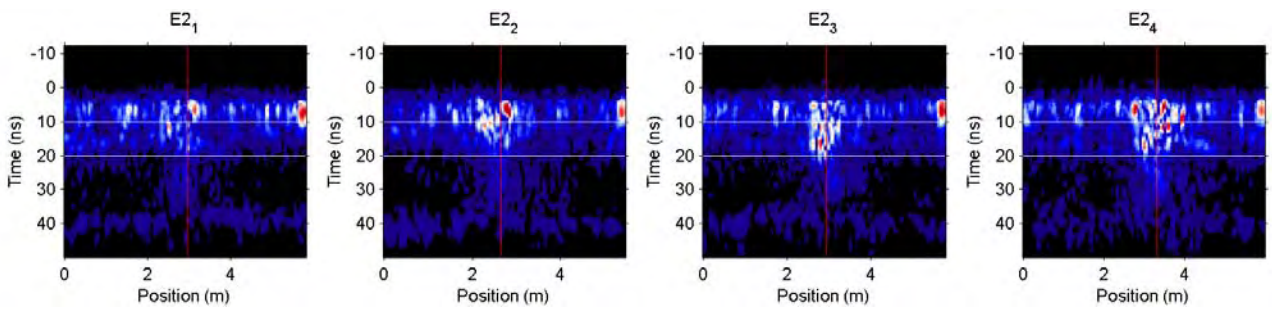


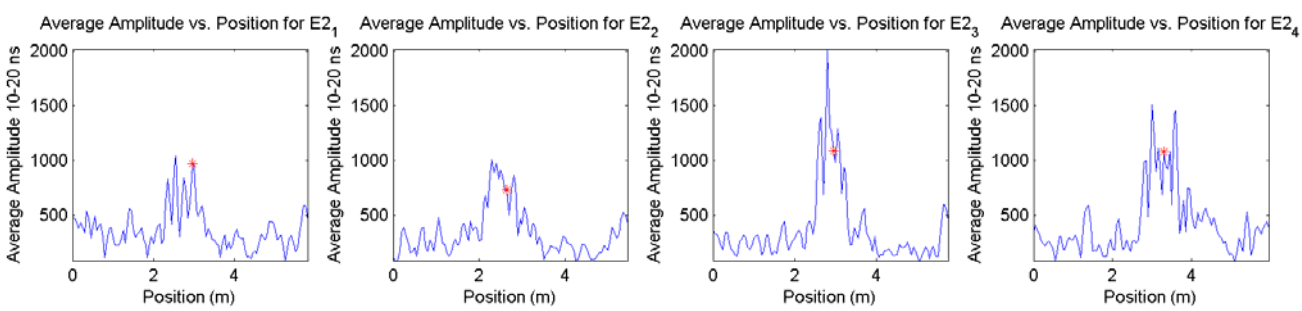

| | |
|---|---|
| Target Name | G6A1E3 |
| Item Description | 81-mm Projectile M821A1/M889A1 – Empty |
| Depth (cm) | 30 |
| Dip | 90 |
| Azimuth | n/a |
| Easting (m) | 294353.0052 |
| Northing(m) | 3833310.054 |

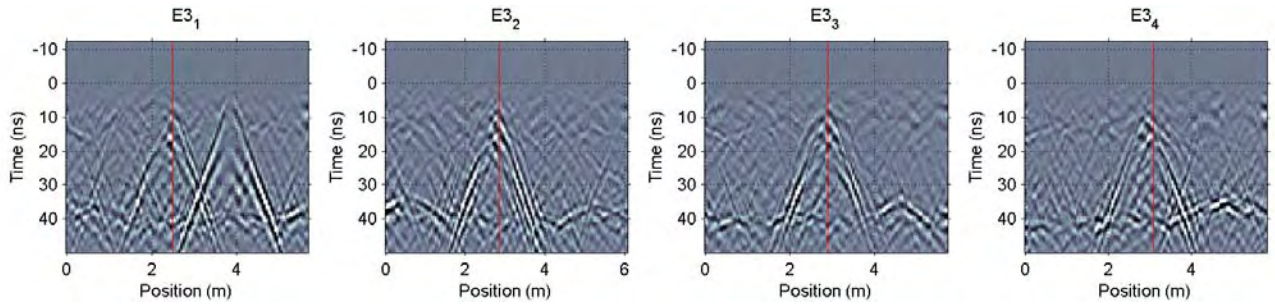


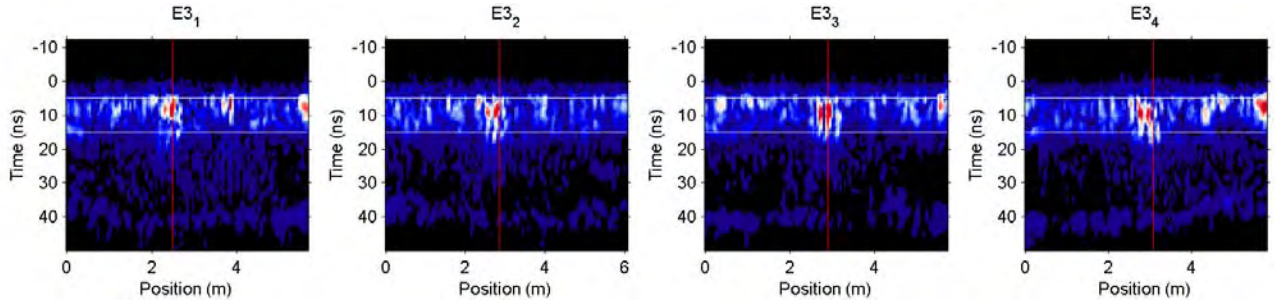


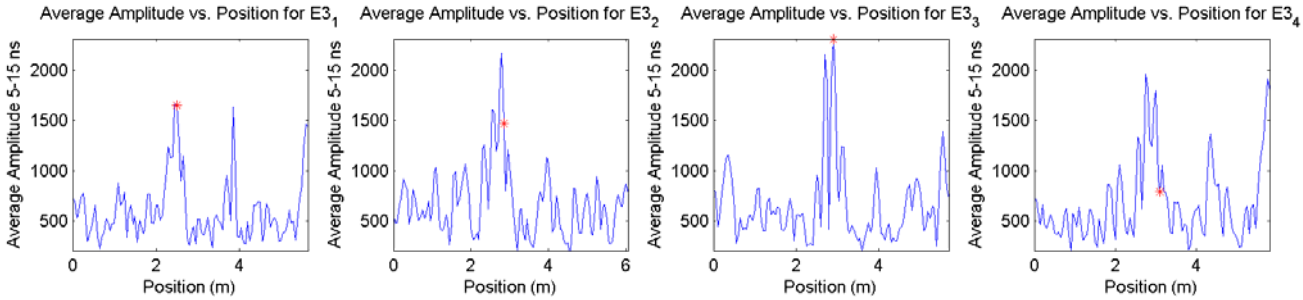

| | |
|---|---|
| Target Name | G6A1E4 |
| Item Description | 2.75-in. Warhead Rocket – Empty |
| Depth (cm) | 30 |
| Dip | 0 |
| Azimuth | 240 |
| Easting (m) | 294350.0119 |
| Northing(m) | 3833319.968 |

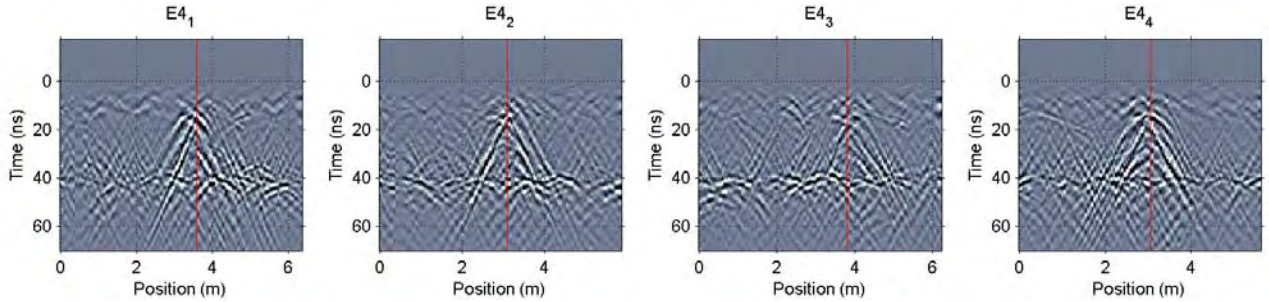


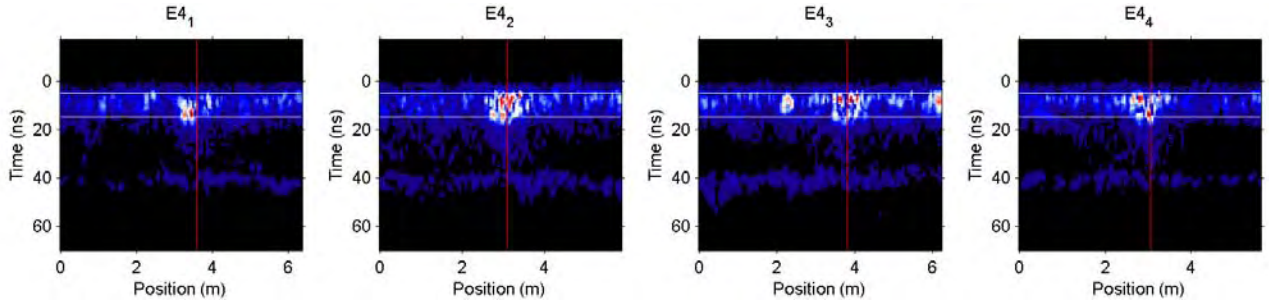


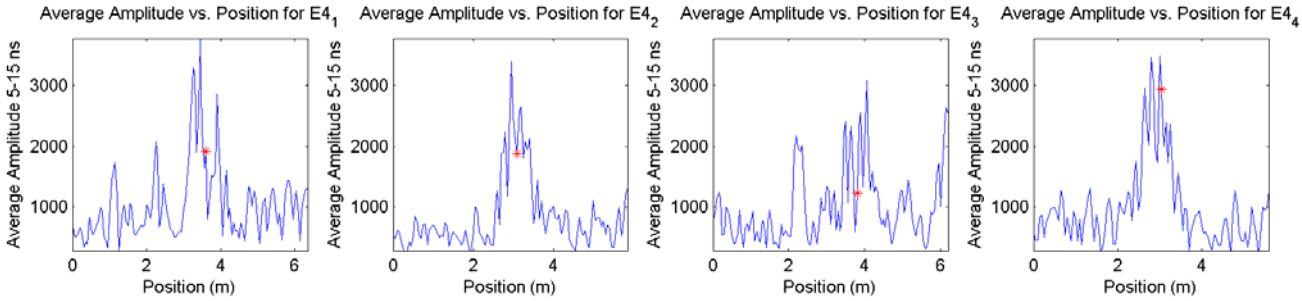

| | |
|---|---|
| Target Name | G6A1E5 |
| Item Description | 76-mm projectile (blue) |
| Depth (cm) | 30 |
| Dip | 45 |
| Azimuth | 320 |
| Easting (m) | 294348.0717 |
| Northing(m) | 3833329.961 |

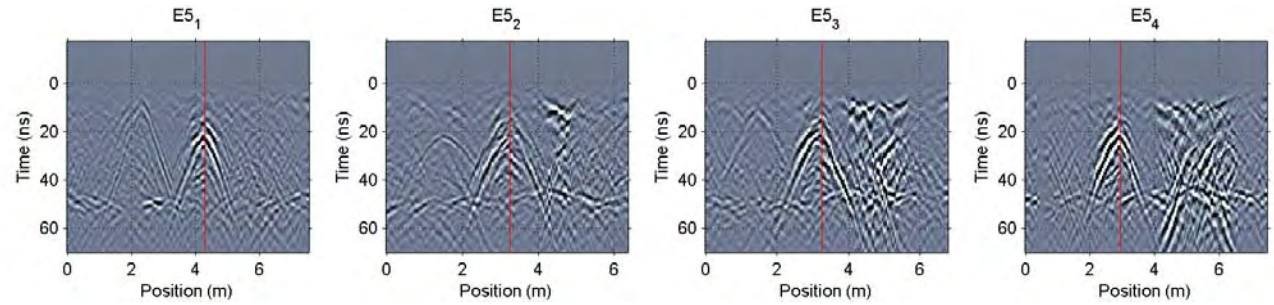


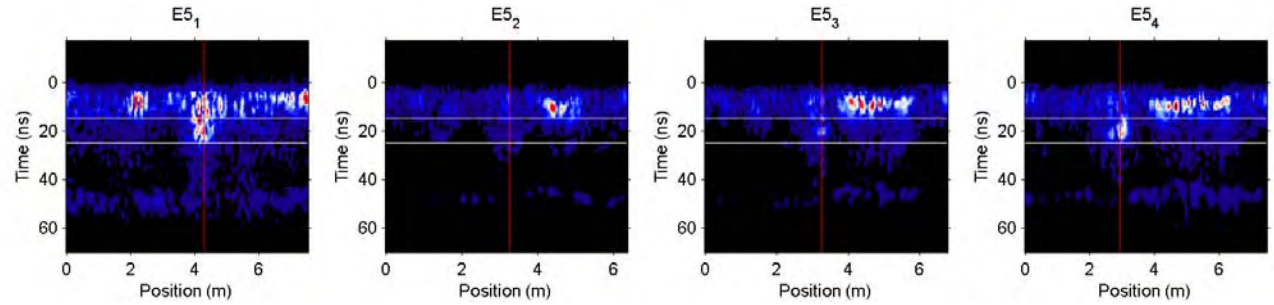


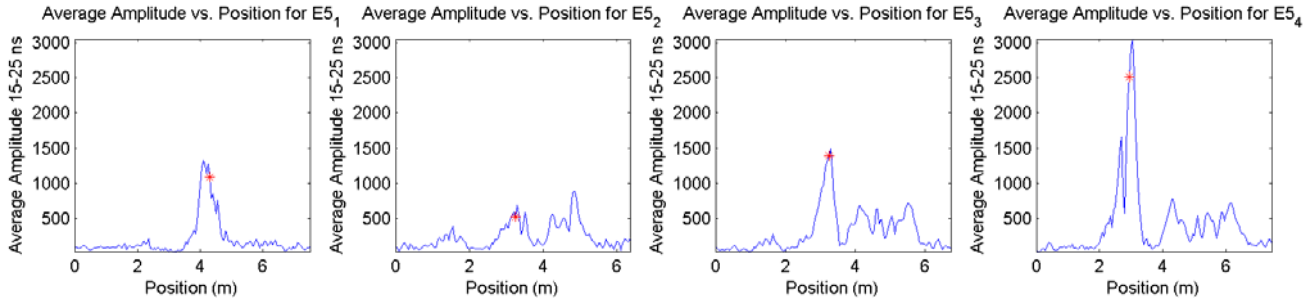

| | |
|---|---|
| Target Name | G6A1E6 |
| Item Description | 4.2-in. projectile (blue) |
| Depth (cm) | 50 |
| Dip | 90 |
| Azimuth | n/a |
| Easting (m) | 294367.0629 |
| Northing(m) | 3833293.036 |

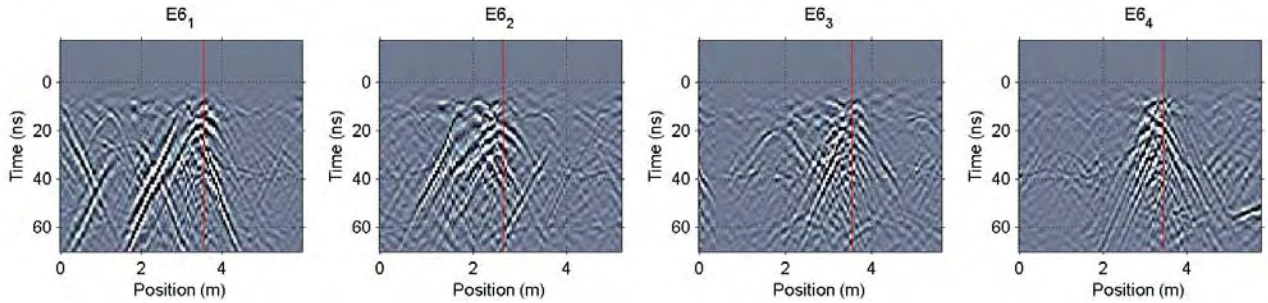


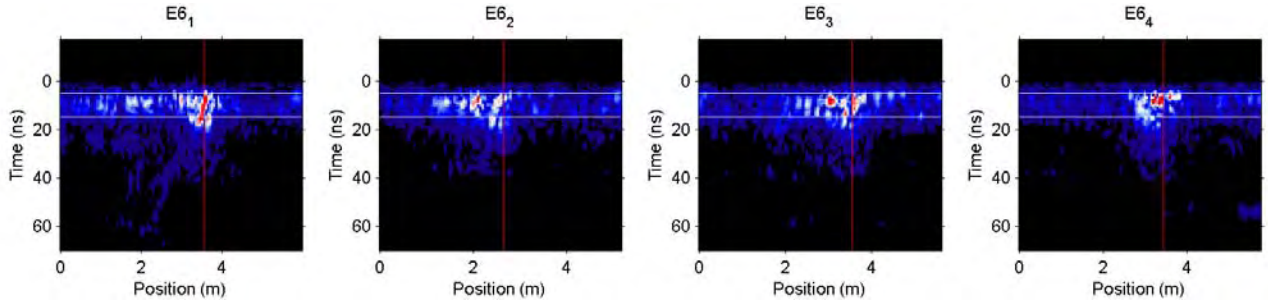


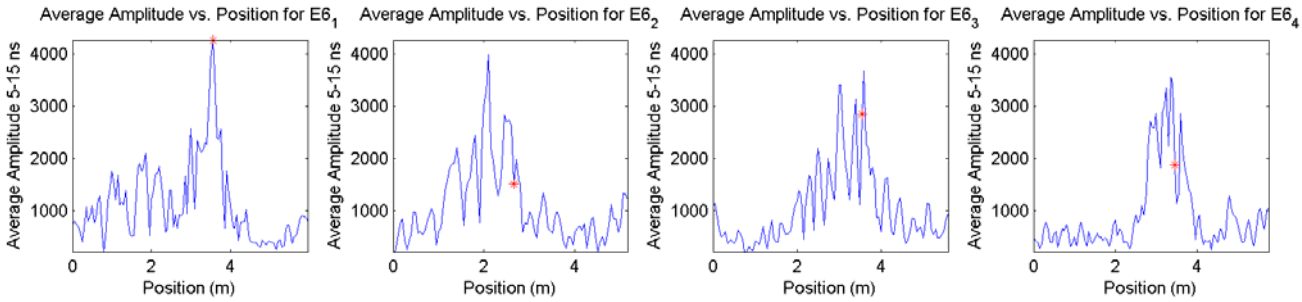

| | |
|---|---|
| Target Name | G6A1E7 |
| Item Description | 90-mm projectile (blue AP) |
| Depth (cm) | 30 |
| Dip | 90 |
| Azimuth | n/a |
| Easting (m) | 294364.0337 |
| Northing(m) | 3833302.94 |

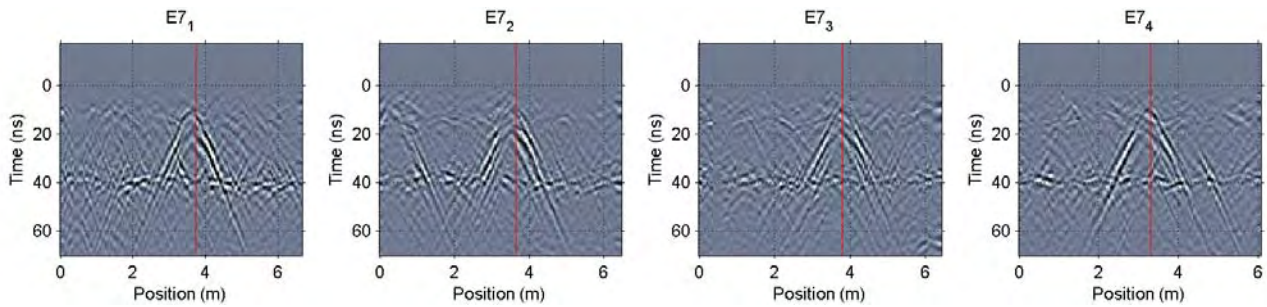


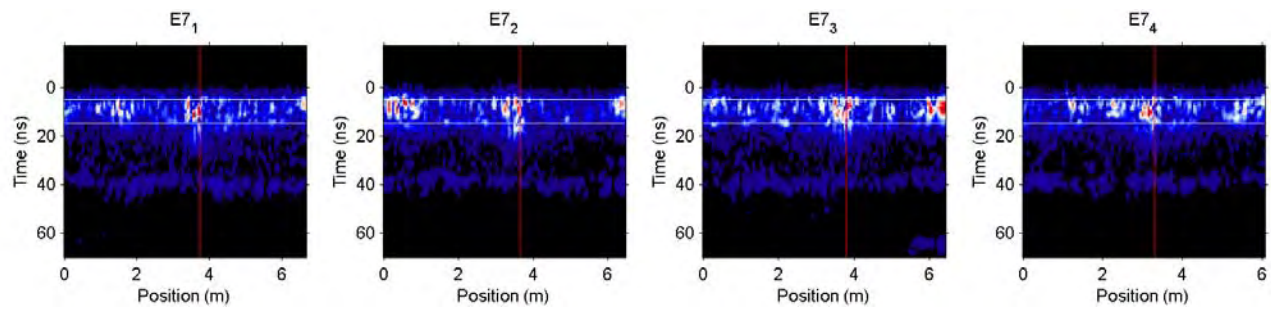


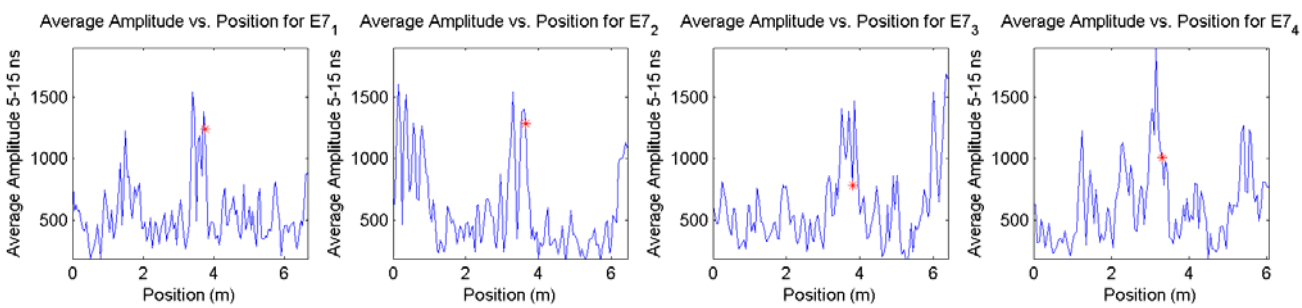

| | |
|---|---|
| Target Name | G6A1E8 |
| Item Description | 90-mm projectile (blue AP) |
| Depth (cm) | 60 |
| Dip | 45 |
| Azimuth | 120 |
| Easting (m) | 294361.8281 |
| Northing(m) | 3833311.877 |

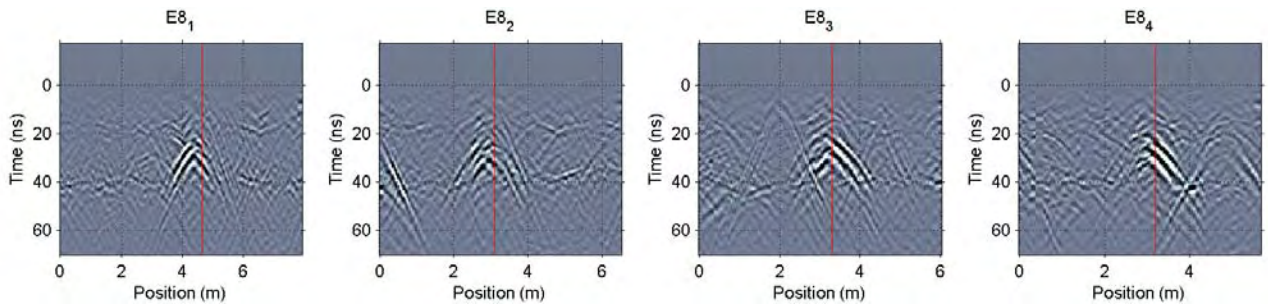


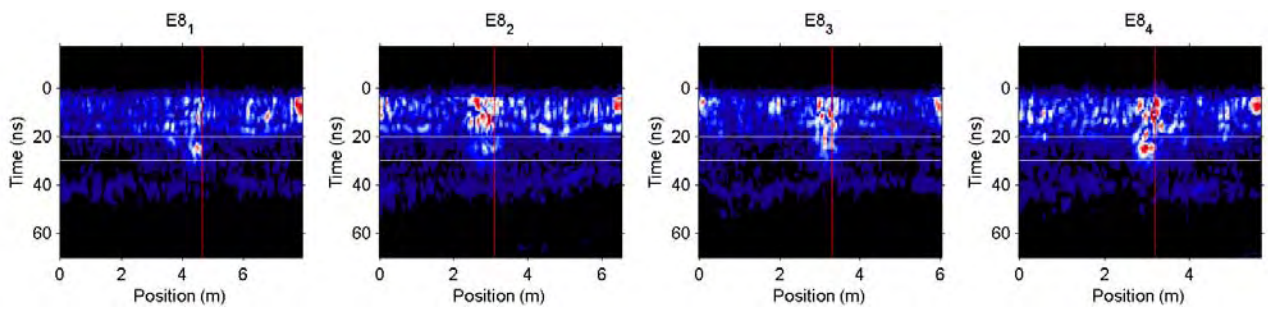


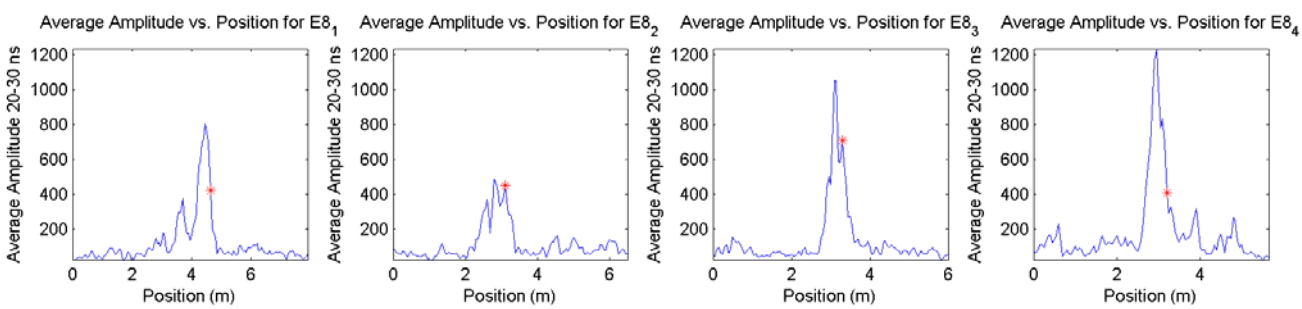

| | |
|---|---|
| Target Name | G6A1E9 |
| Item Description | 81-mm mortar (blue) |
| Depth (cm) | 30 |
| Dip | 90 |
| Azimuth | n/a |
| Easting (m) | 294359.3569 |
| Northing(m) | 3833321.797 |

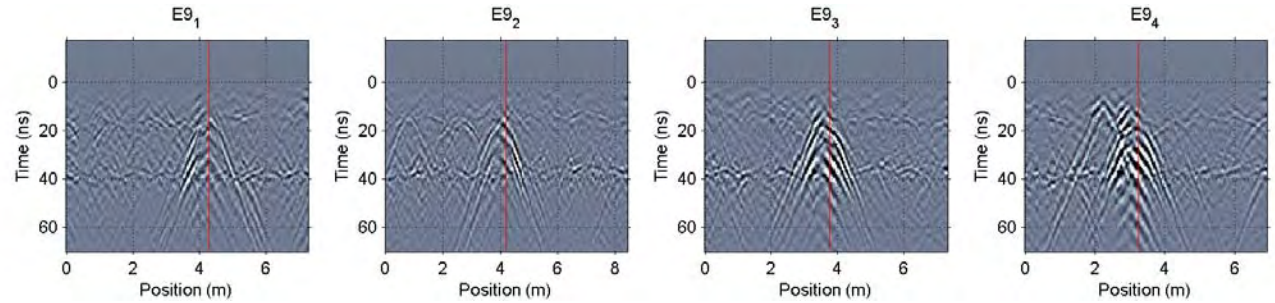


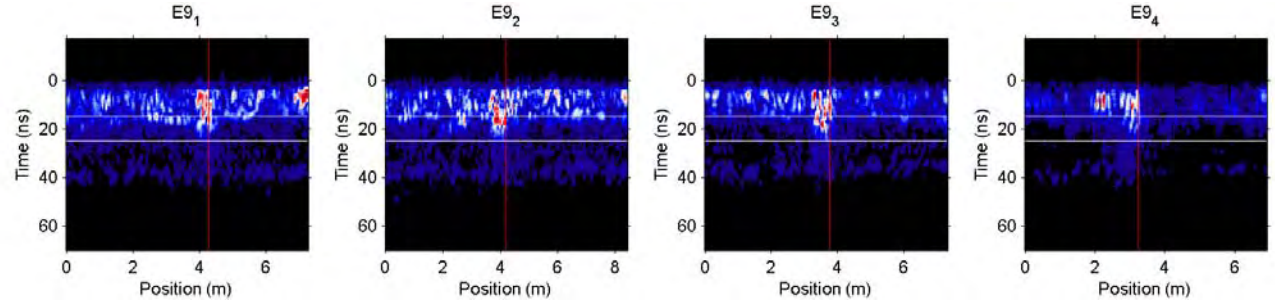


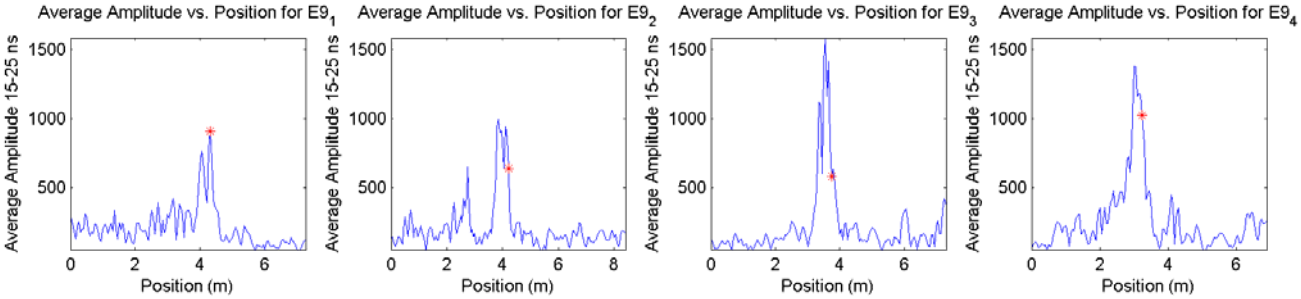

| | |
|---|---|
| Target Name | G6A1E10 |
| Item Description | 81-mm mortar (blue) |
| Depth (cm) | 60 |
| Dip | 45 |
| Azimuth | 120 |
| Easting (m) | 294356.6896 |
| Northing(m) | 3833332.278 |

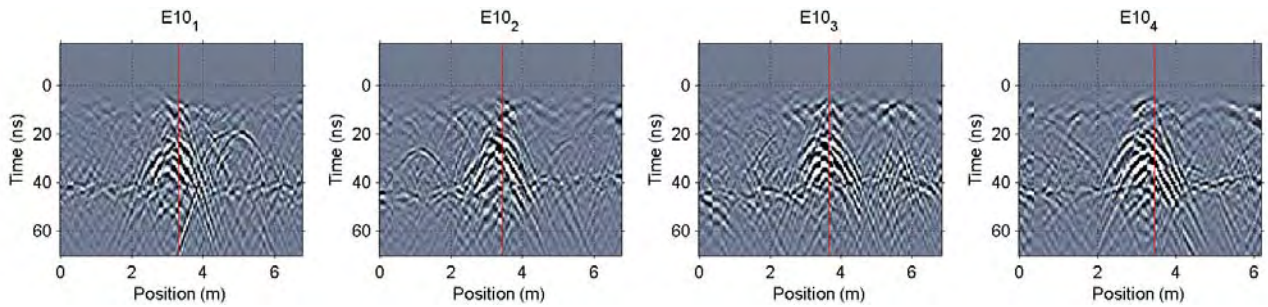


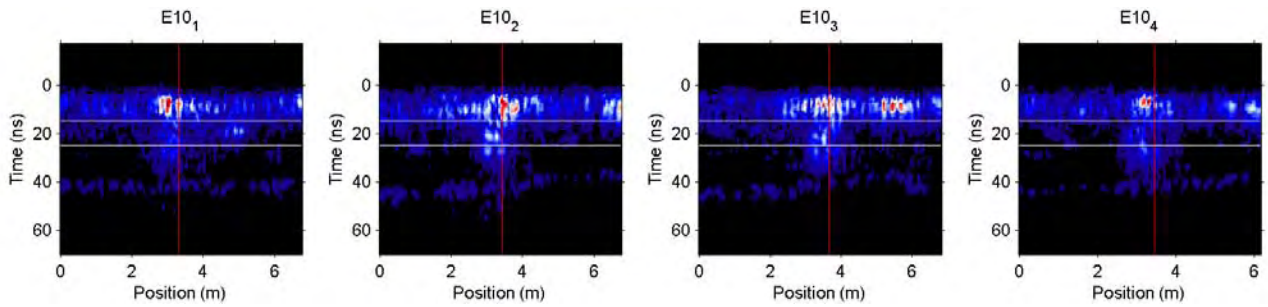


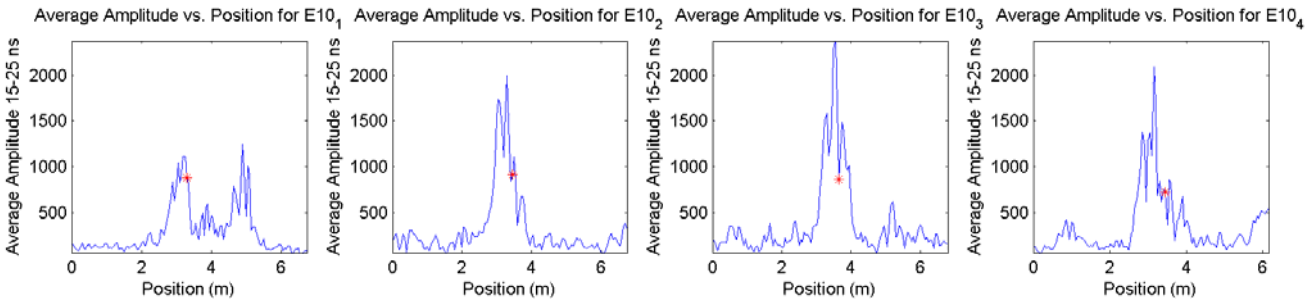

| | |
|---|---|
| Target Name | G6A1E11 |
| Item Description | 40-mm Projectile – Inert |
| Depth (cm) | 15 |
| Dip | 0 |
| Azimuth | 200 |
| Easting (m) | 294376.3381 |
| Northing(m) | 3833295.564 |

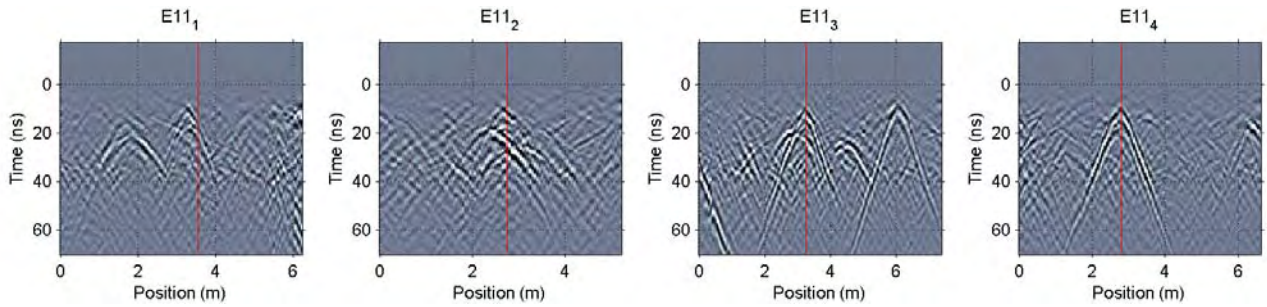


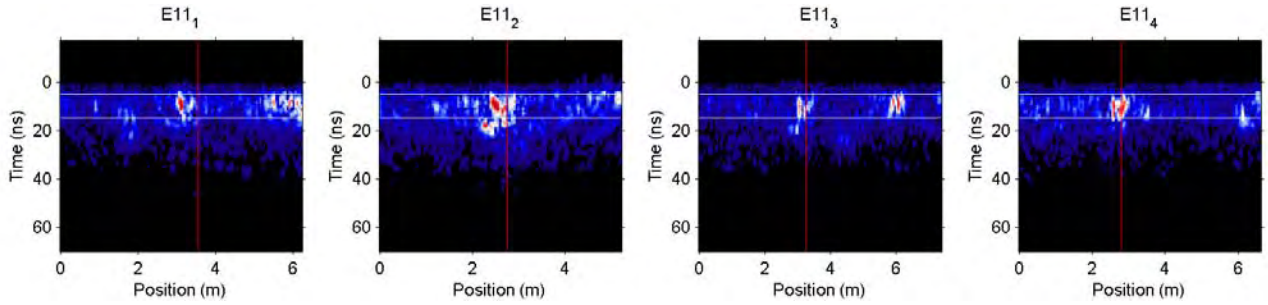


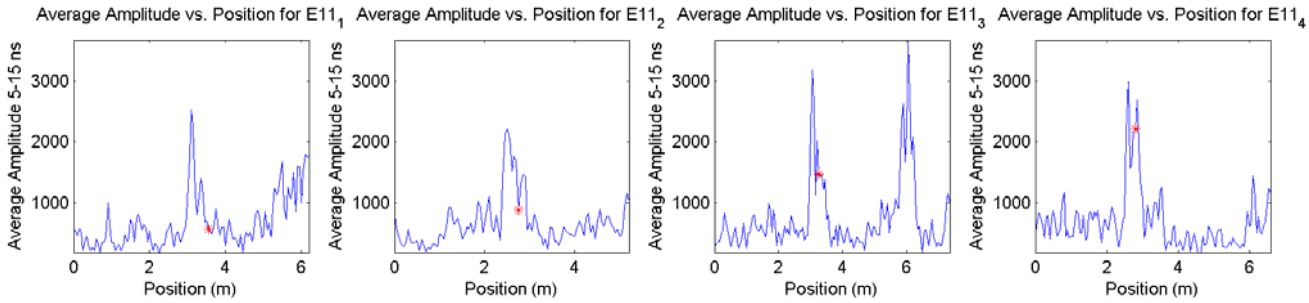

| | |
|---|---|
| Target Name | G6A1E12 |
| Item Description | F/40-mm Projectile – H.E.T. |
| Depth (cm) | 15 |
| Dip | 0 |
| Azimuth | 10 |
| Easting (m) | 294375.1408 |
| Northing(m) | 3833300.689 |

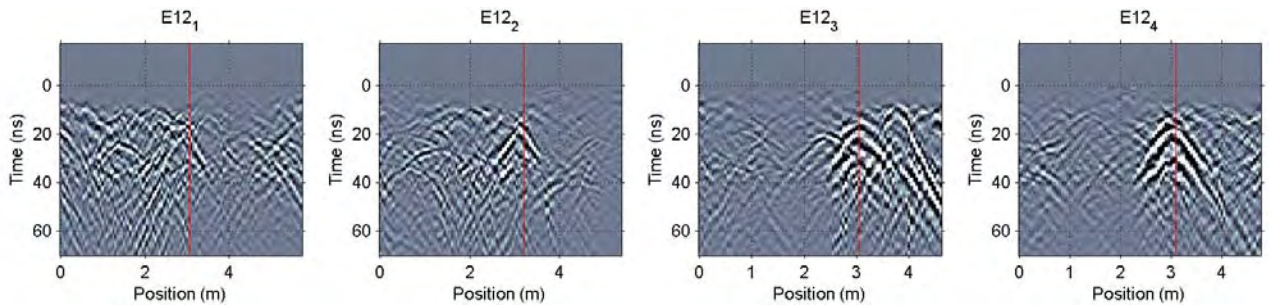


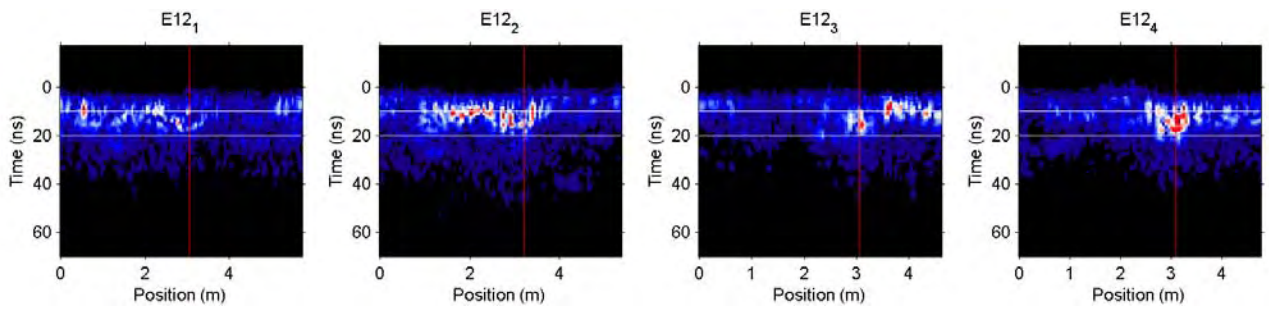


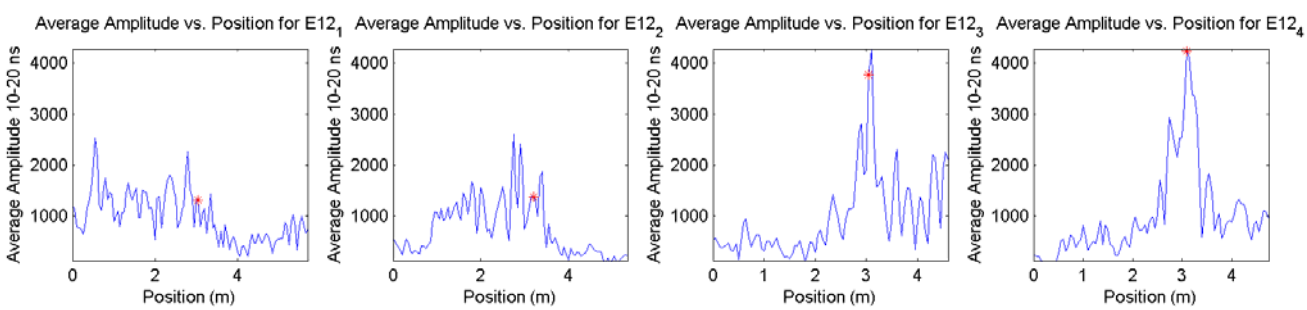

| | |
|---|---|
| Target Name | G6A1E13 |
| Item Description | MK118 – Rockeye |
| Depth (cm) | 15 |
| Dip | 0 |
| Azimuth | 40 |
| Easting (m) | 294374.3126 |
| Northing(m) | 3833305.529 |

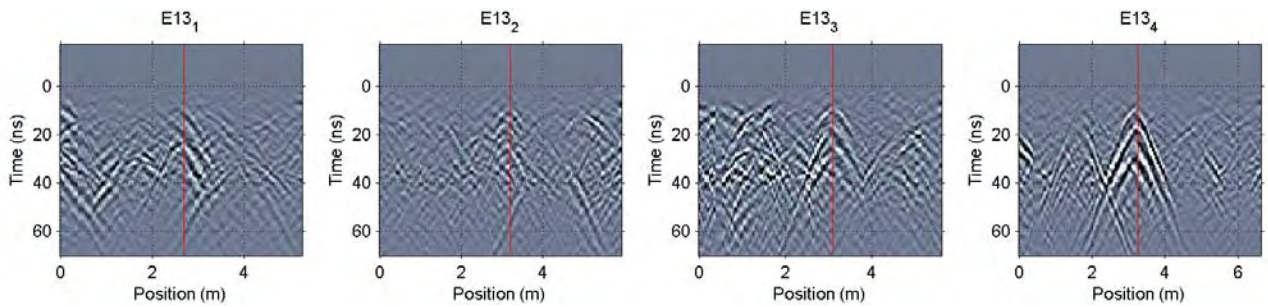


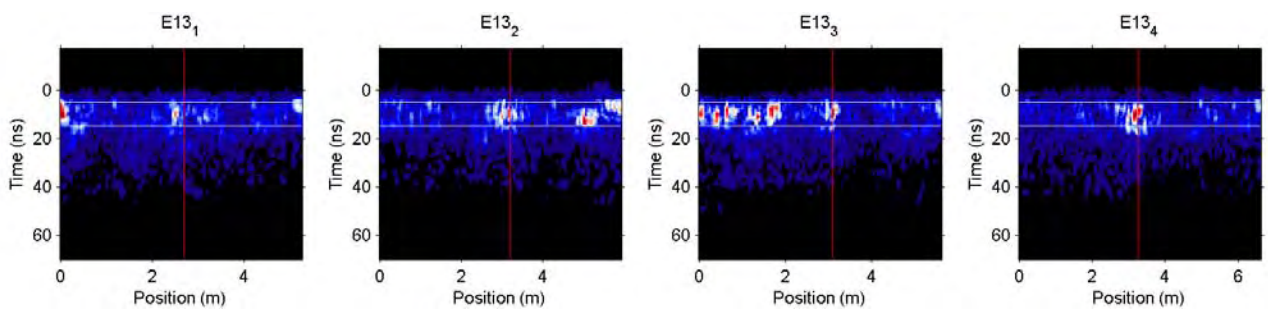


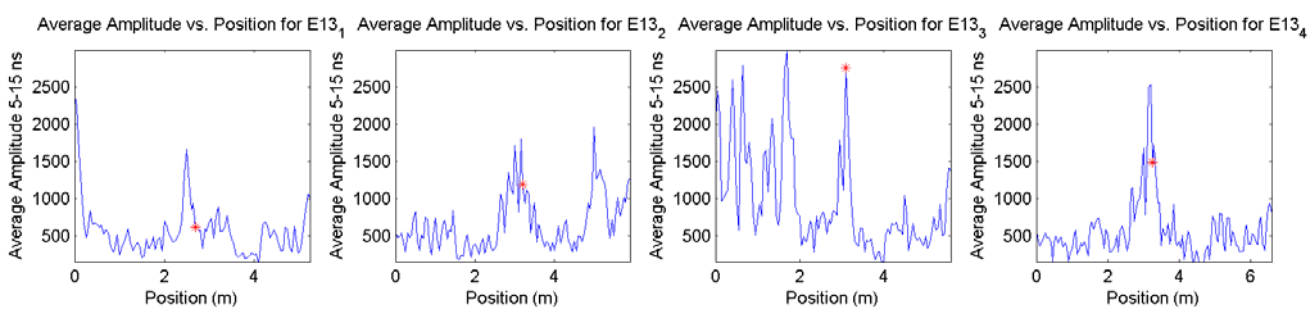

| | |
|---|---|
| Target Name | G6A1E14 |
| Item Description | Body Assembly Grenade Type PH F/M42 – Inert |
| Depth (cm) | 15 |
| Dip | 45 |
| Azimuth | 180 |
| Easting (m) | 294372.7496 |
| Northing(m) | 3833310.345 |

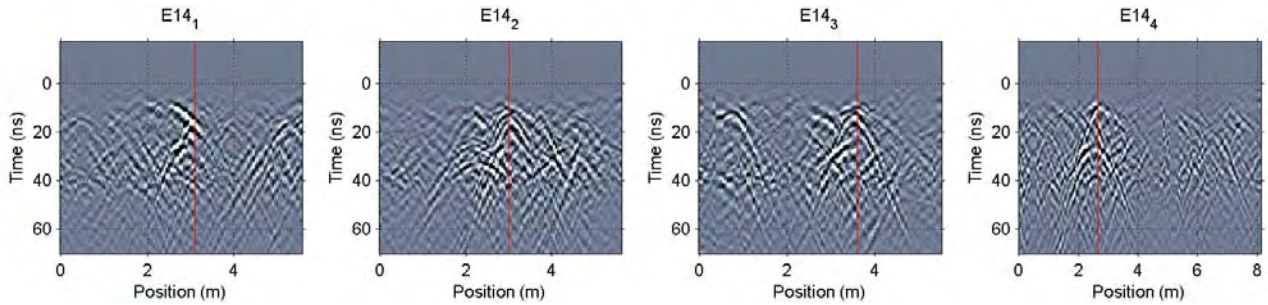


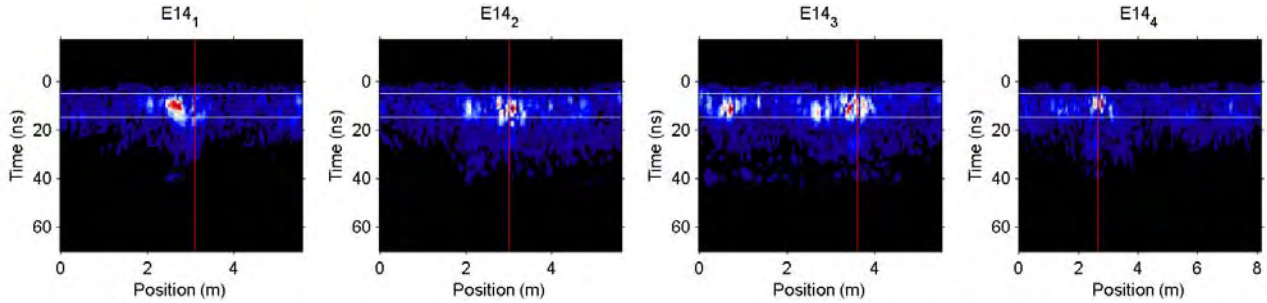


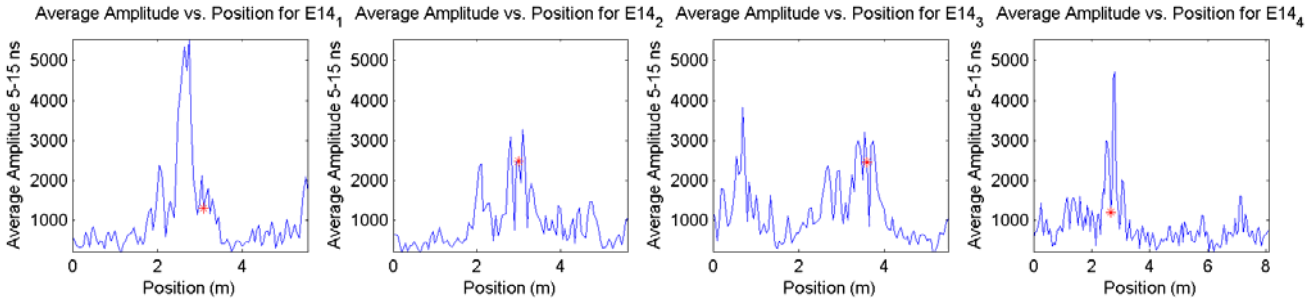

| | |
|---|---|
| Target Name | G6A1E15 |
| Item Description | Body 60-mm Inert Wax Filled |
| Depth (cm) | 25 |
| Dip | 45 |
| Azimuth | 0 |
| Easting (m) | 294372.0475 |
| Northing(m) | 3833315.293 |

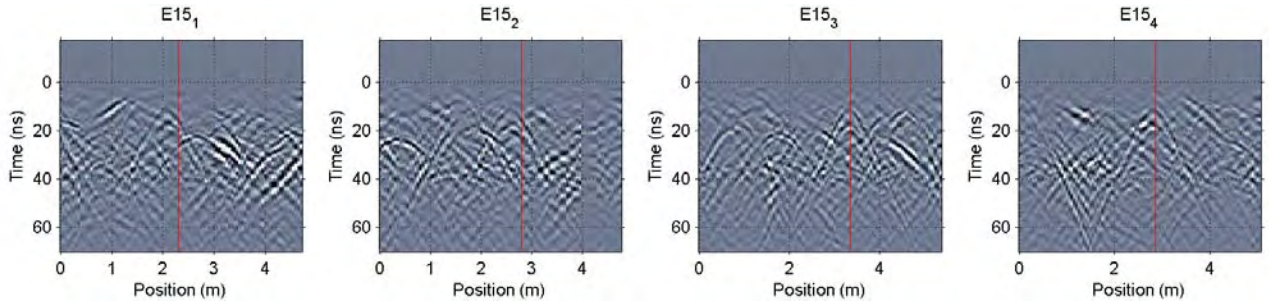


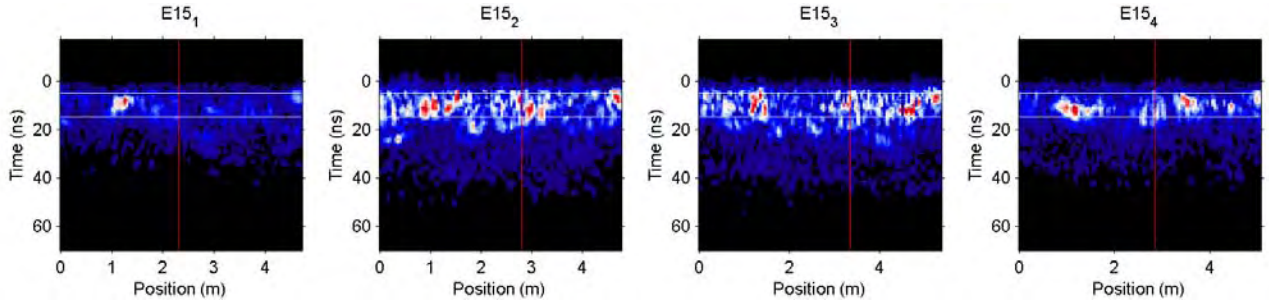


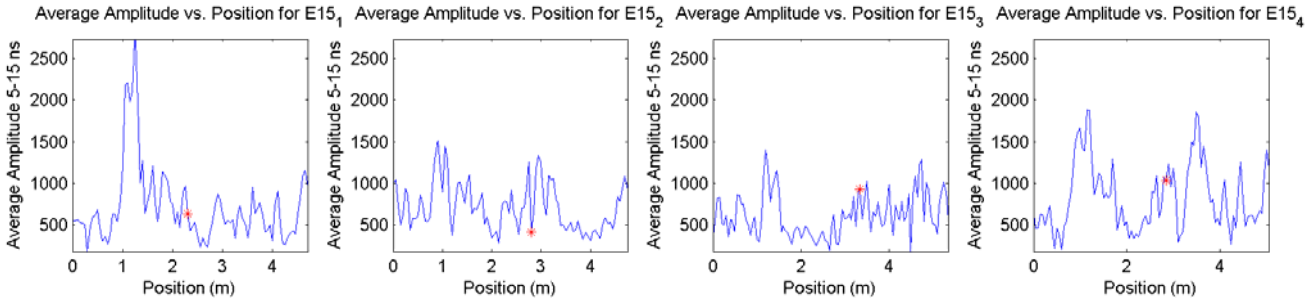

| | |
|---|---|
| Target Name | G6A1E16 |
| Item Description | 57mm Projectile – Inert |
| Depth (cm) | 25 |
| Dip | 45 |
| Azimuth | 270 |
| Easting (m) | 294371.0818 |
| Northing(m) | 3833320.146 |

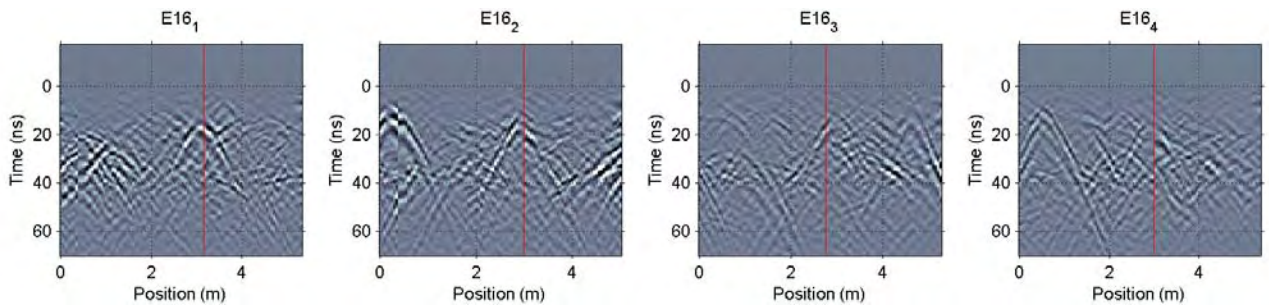


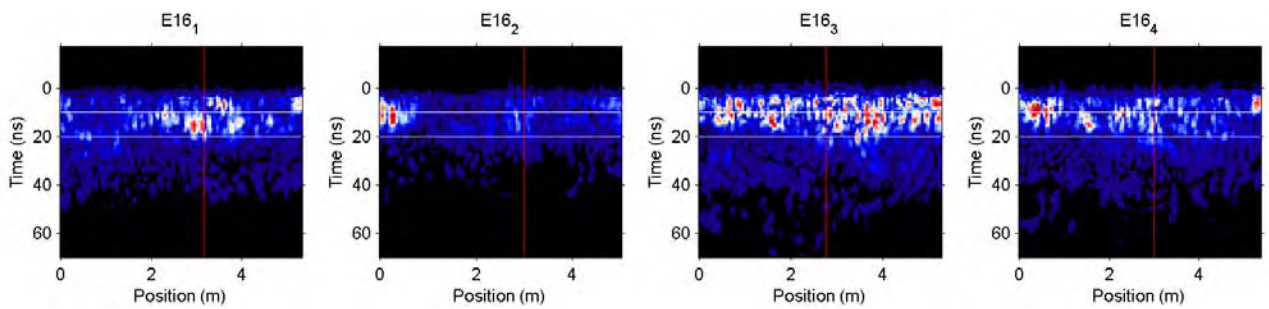


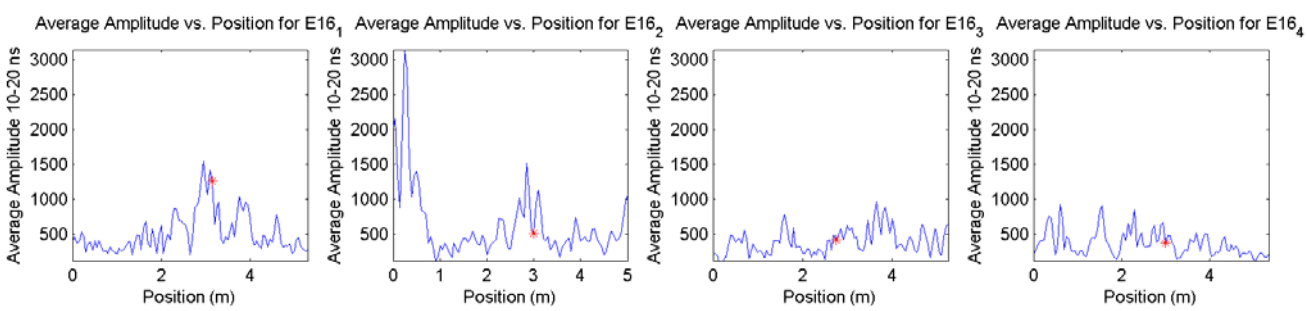

| | |
|---|---|
| Target Name | G6A1E17 |
| Item Description | Bomblet Dummy Representing BLU-26 |
| Depth (cm) | 15 |
| Dip | 0 |
| Azimuth | n/a |
| Easting (m) | 294369.9148 |
| Northing(m) | 3833325.051 |

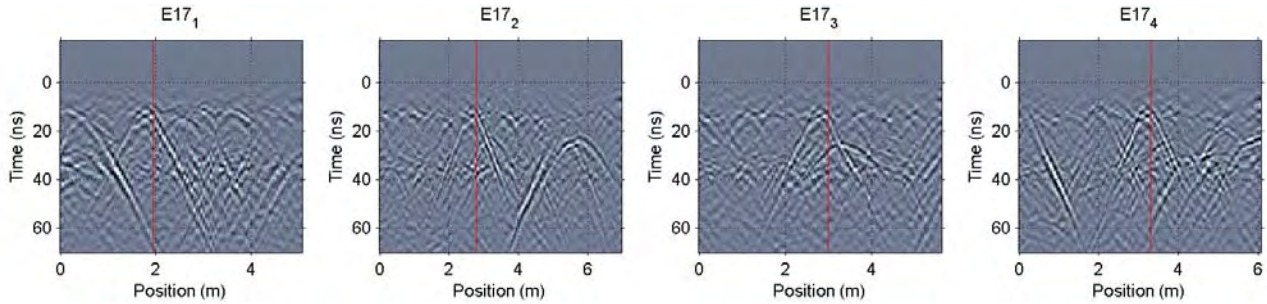


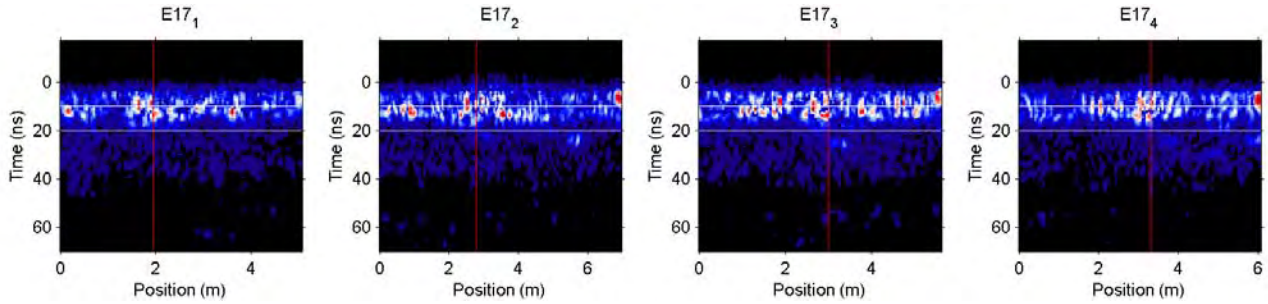


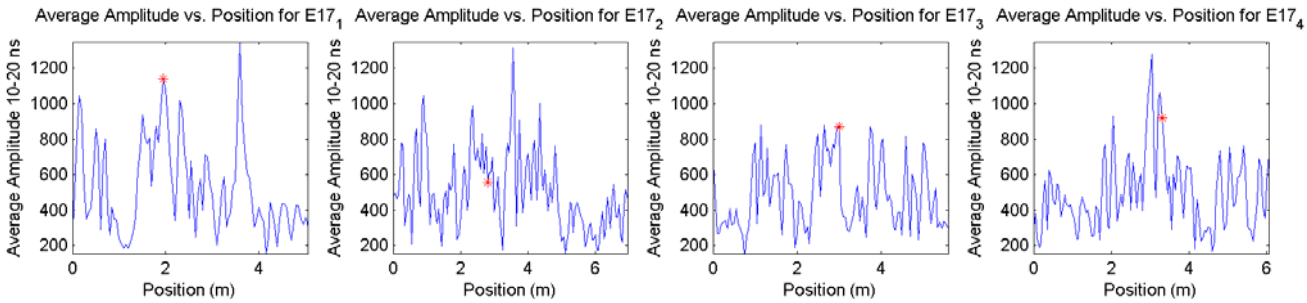

| | |
|---|---|
| Target Name | G6A1E18 |
| Item Description | Bomblet Dummy BDU-28/B |
| Depth (cm) | 15 |
| Dip | 0 |
| Azimuth | 45 |
| Easting (m) | 294369.2656 |
| Northing(m) | 3833329.844 |

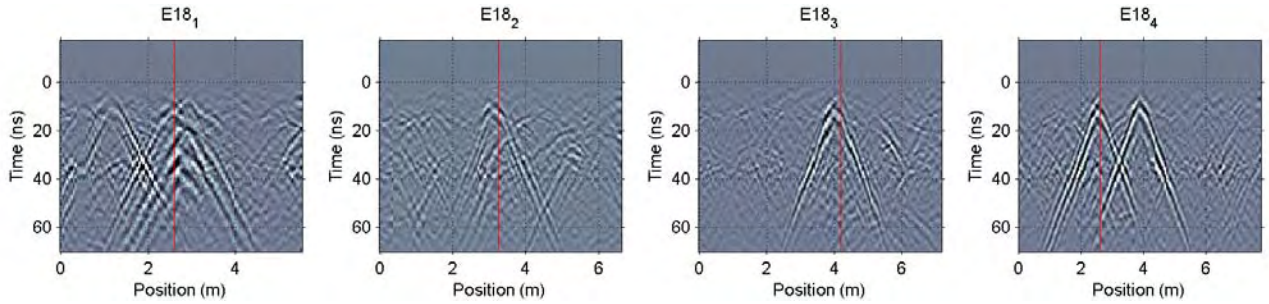


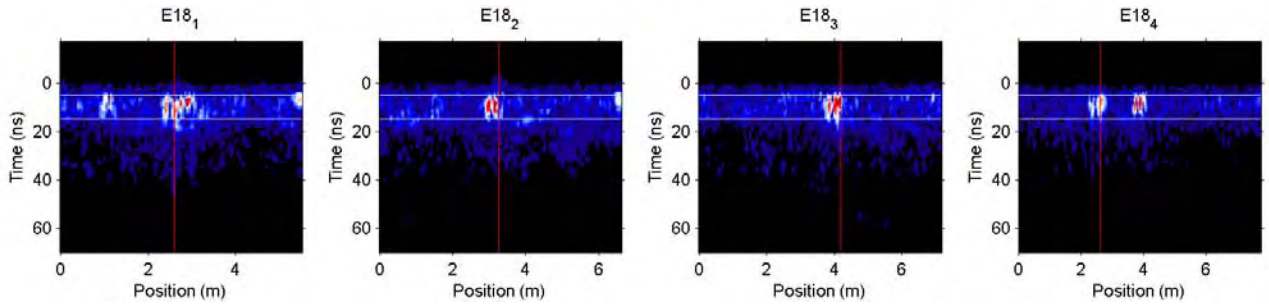


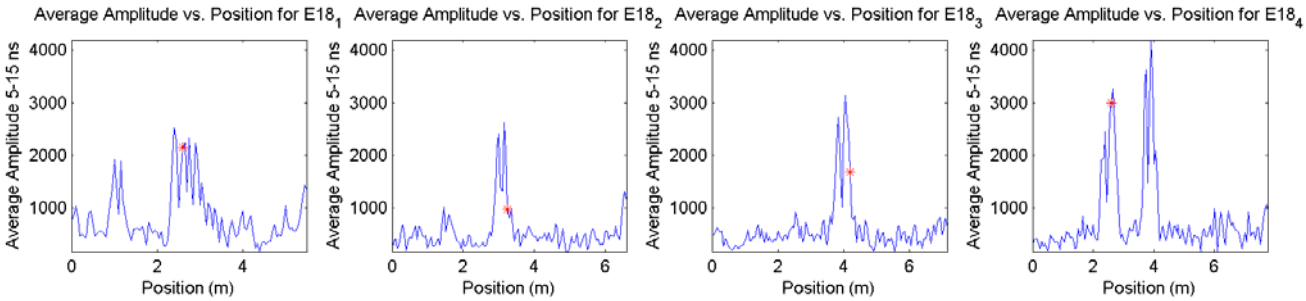

| | |
|---|---|
| Target Name | G6A2E19 |
| Item Description | 90-mm projectile (blue AP) |
| Depth (cm) | 30 |
| Dip | 0 |
| Azimuth | 180 |
| Easting (m) | 294397.9728 |
| Northing(m) | 3833338.043 |

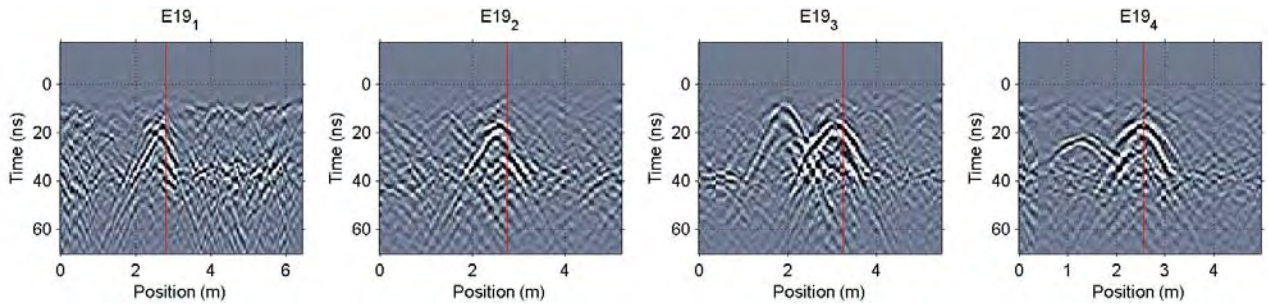


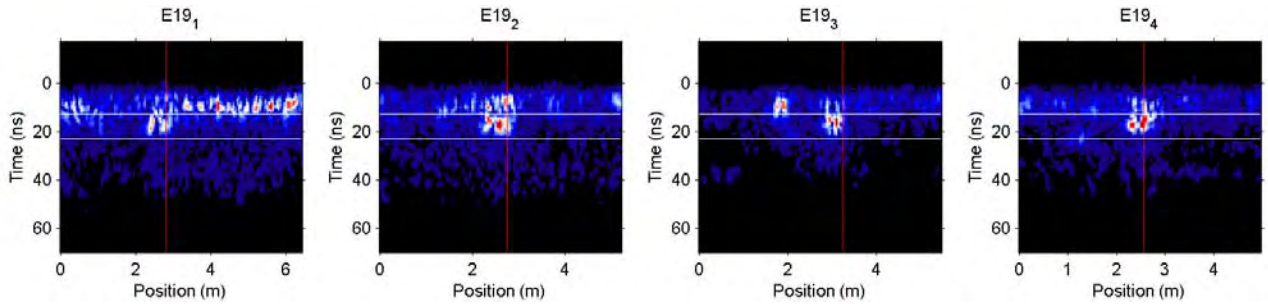


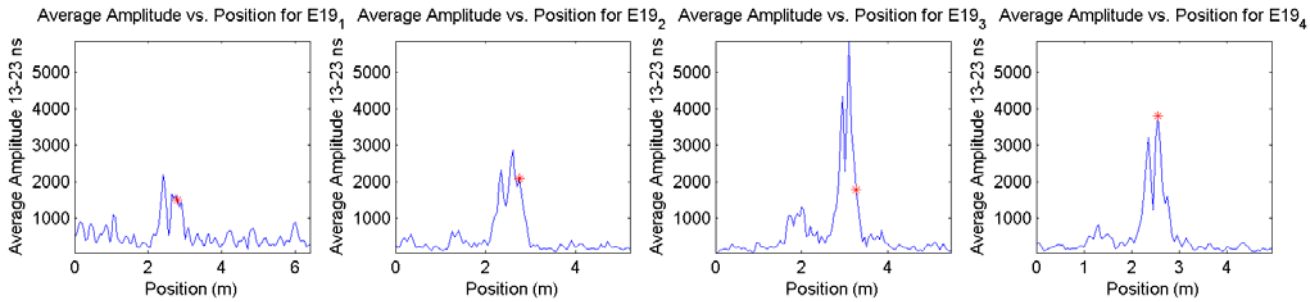

| | |
|---|---|
| Target Name | G6A2E20 |
| Item Description | 90-mm projectile (blue AP) |
| Depth (cm) | 30 |
| Dip | 90 |
| Azimuth | n/a |
| Easting (m) | 294417.7966 |
| Northing(m) | 3833314.137 |

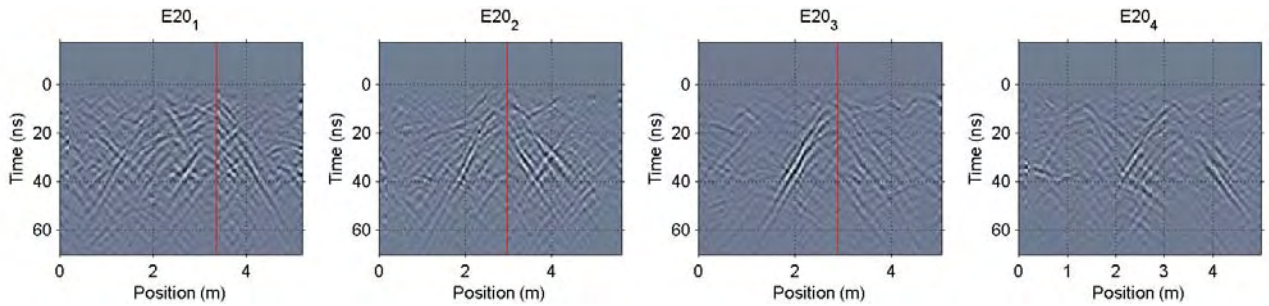


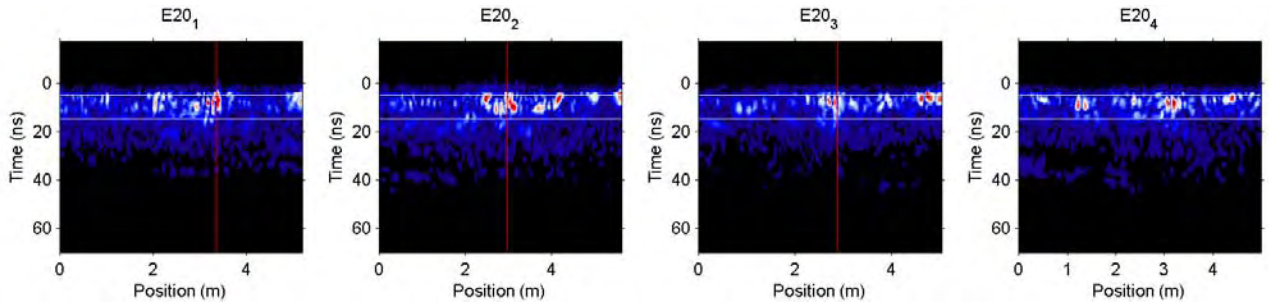


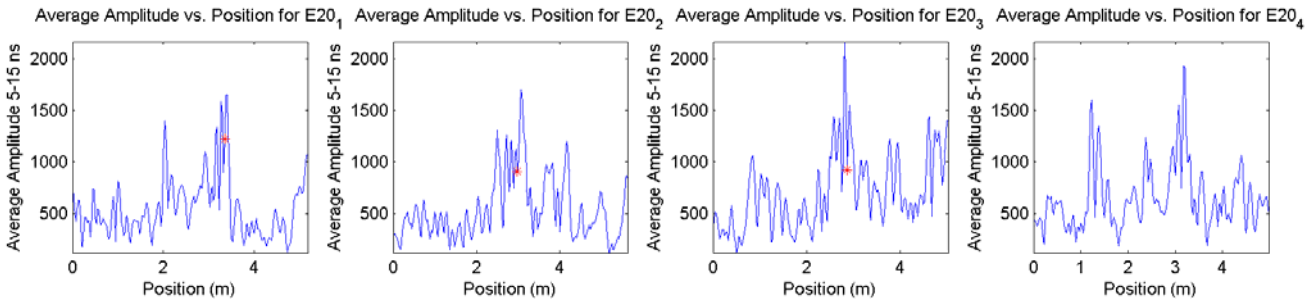

| | |
|---|---|
| Target Name | G6A2E21 |
| Item Description | 90-mm projectile (blue AP) |
| Depth (cm) | 60 |
| Dip | 45 |
| Azimuth | 235 |
| Easting (m) | 294423.6977 |
| Northing(m) | 3833315.238 |

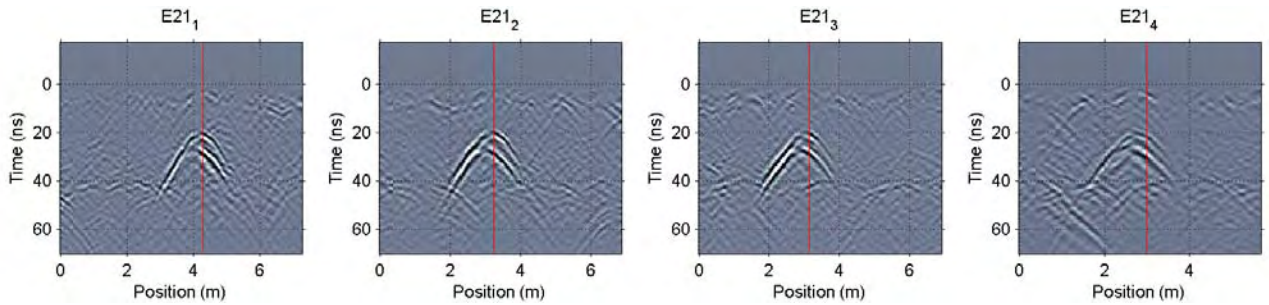


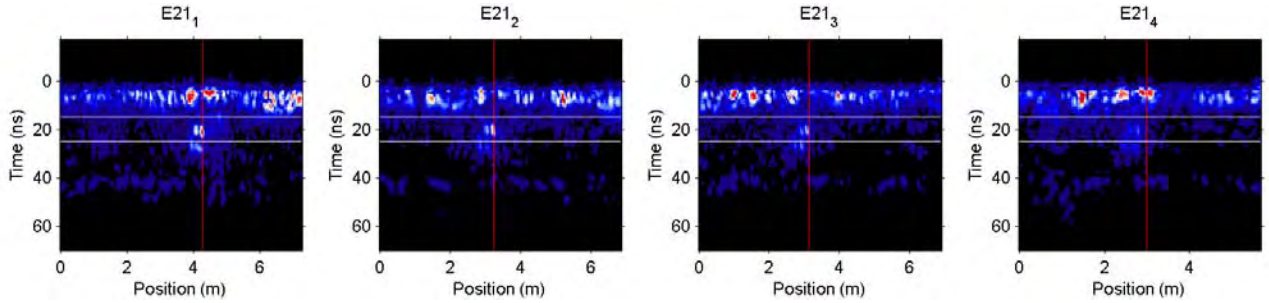


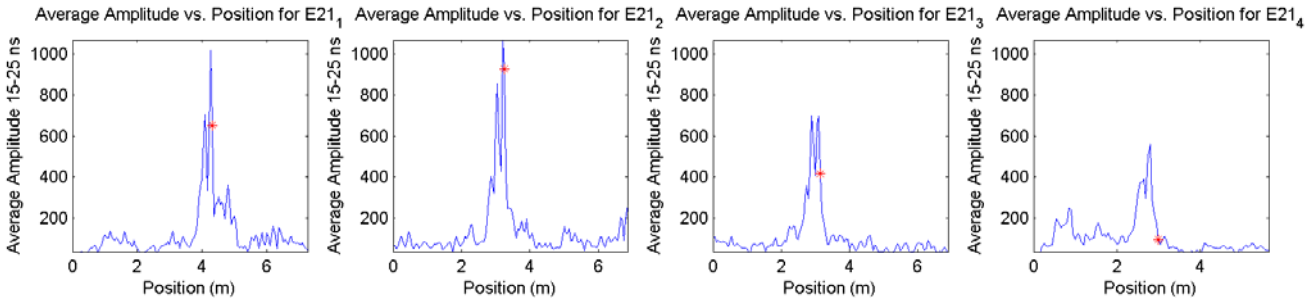

| | |
|---|---|
| Target Name | G6A2E22 |
| Item Description | 81-mm mortar (blue) |
| Depth (cm) | 30 |
| Dip | 0 |
| Azimuth | 95 |
| Easting (m) | 294424.995 |
| Northing(m) | 3833337.602 |

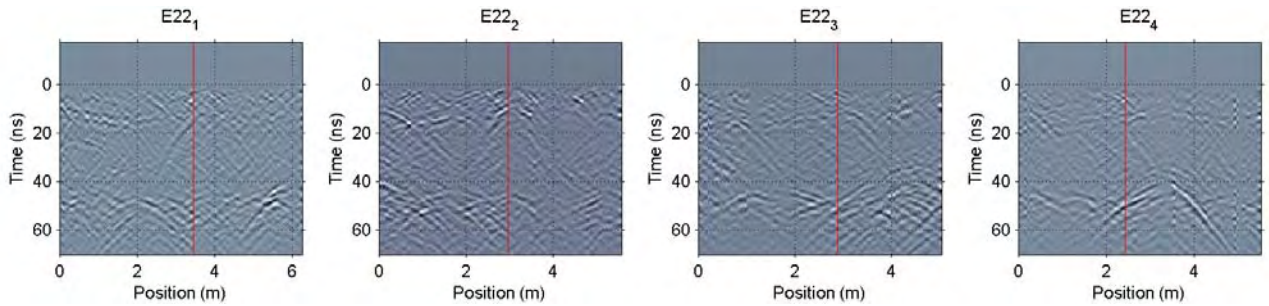


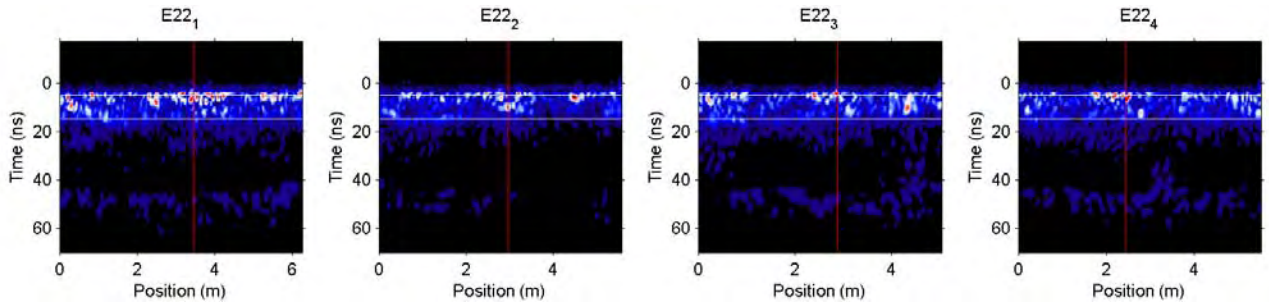


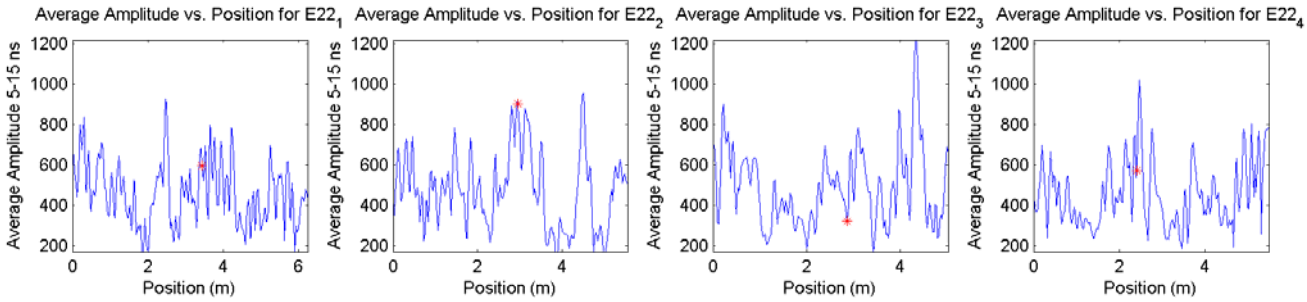

| | |
|---|---|
| Target Name | G6A2E23 |
| Item Description | 81-mm mortar (blue) |
| Depth (cm) | 30 |
| Dip | 90 |
| Azimuth | n/a |
| Easting (m) | 294431.6226 |
| Northing(m) | 3833326.895 |

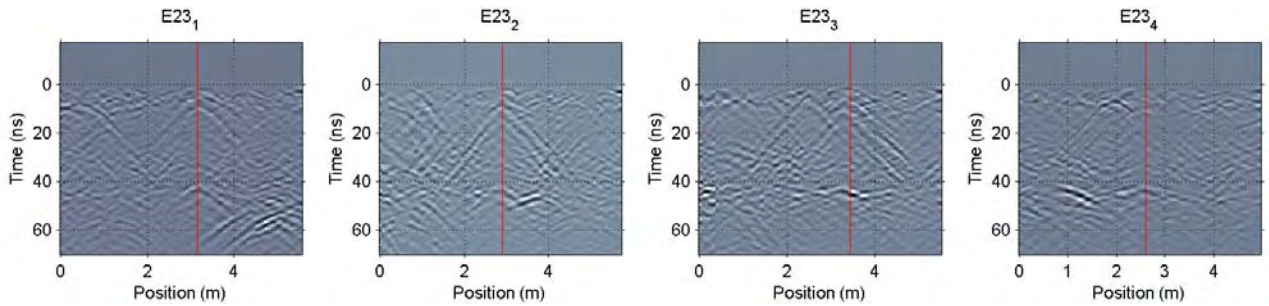


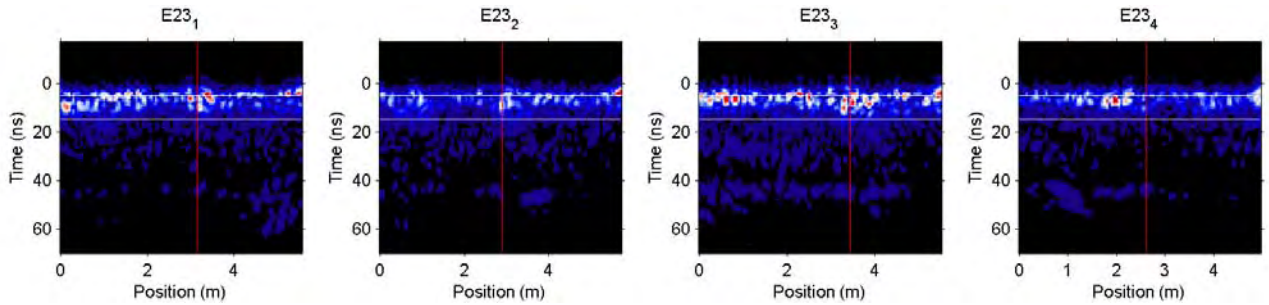


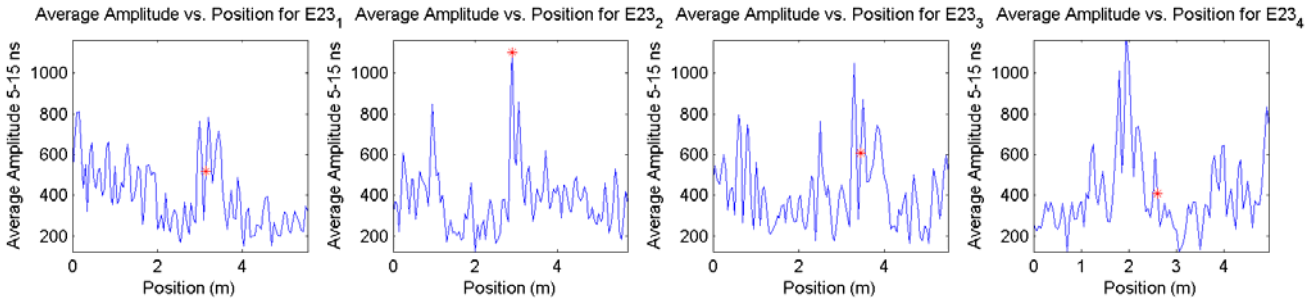

| | |
|---|---|
| Target Name | G6A2E24 |
| Item Description | 81-mm mortar (blue) |
| Depth (cm) | 60 |
| Dip | 0 |
| Azimuth | 70 |
| Easting (m) | 294425.5921 |
| Northing(m) | 3833345.856 |

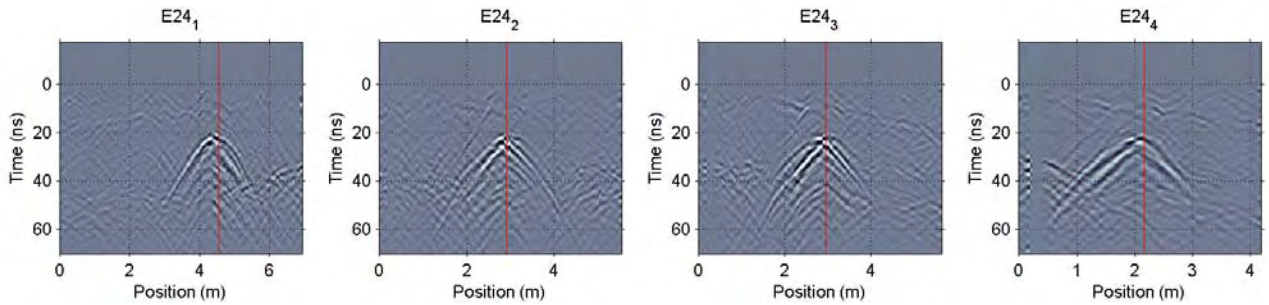


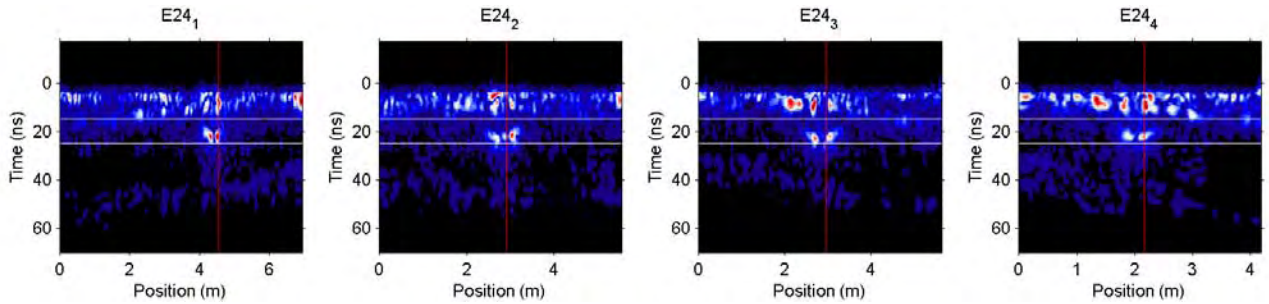


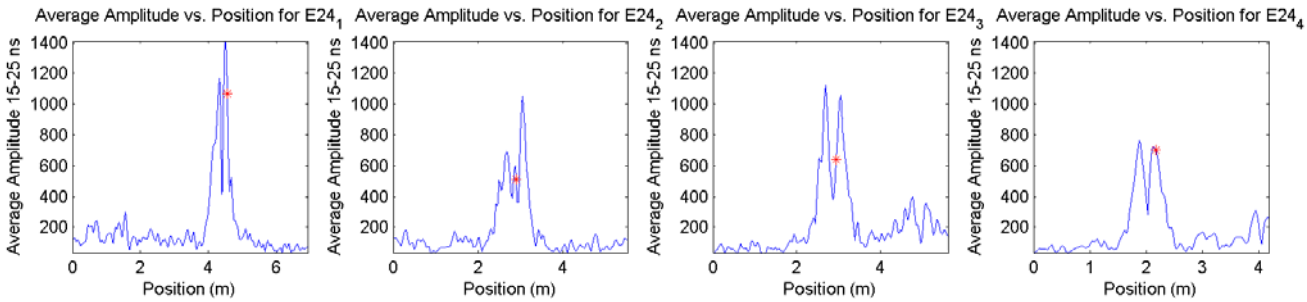

| | |
|---|---|
| Target Name | G6A2E25 |
| Item Description | 81-mm mortar (blue) |
| Depth (cm) | 60 |
| Dip | 45 |
| Azimuth | 270 |
| Easting (m) | 294398.5761 |
| Northing(m) | 3833325.178 |

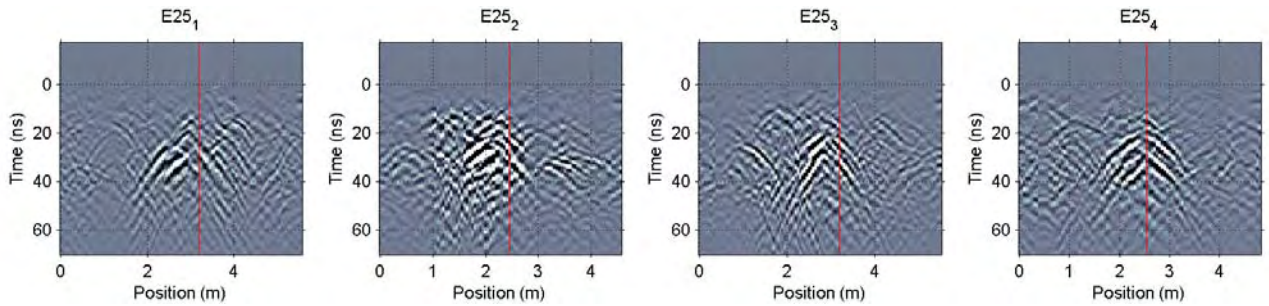


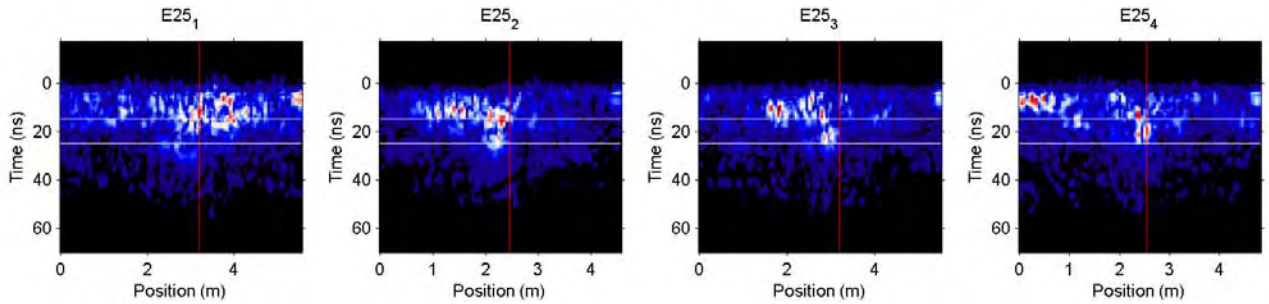


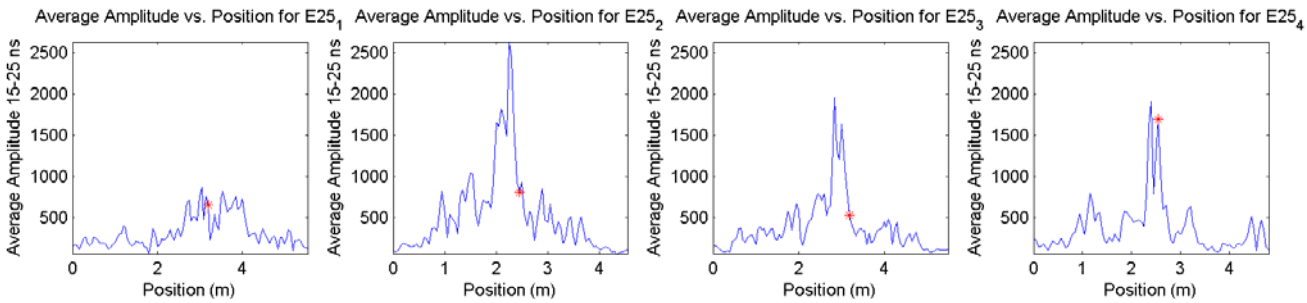

| | |
|---|---|
| Target Name | G6A2E26 |
| Item Description | GPR clutter (wood) |
| Depth (cm) | 26 |
| Dip | n/a (~horizontal) |
| Azimuth | 110 |
| Easting (m) | 294430.75 |
| Northing(m) | 3833310.607 |

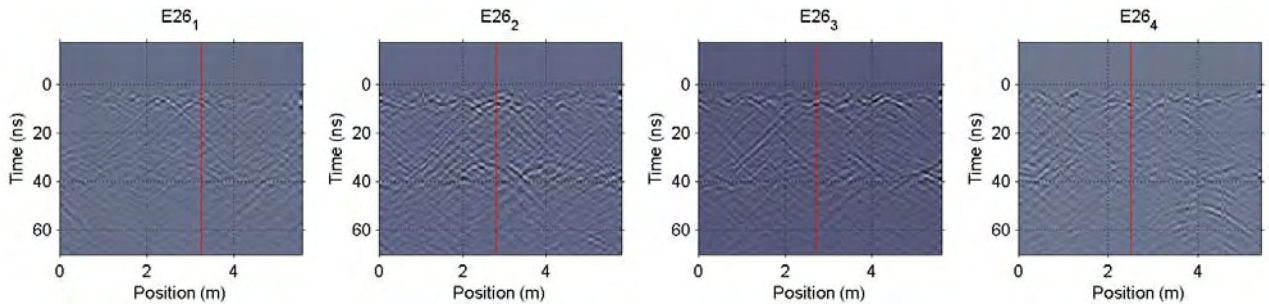


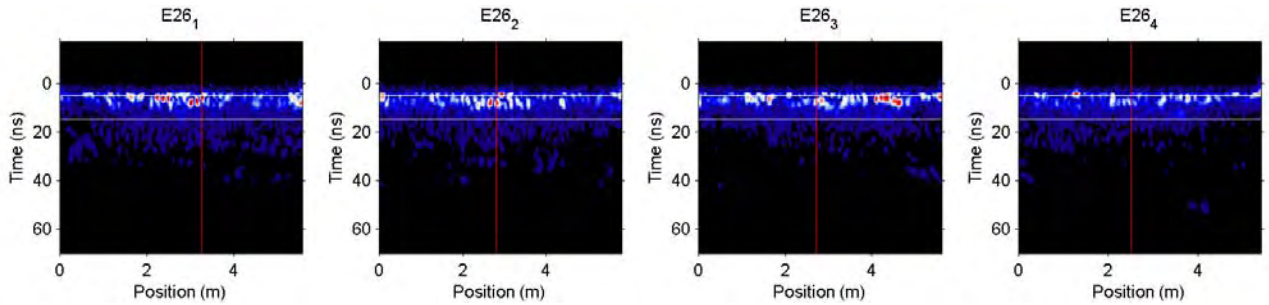


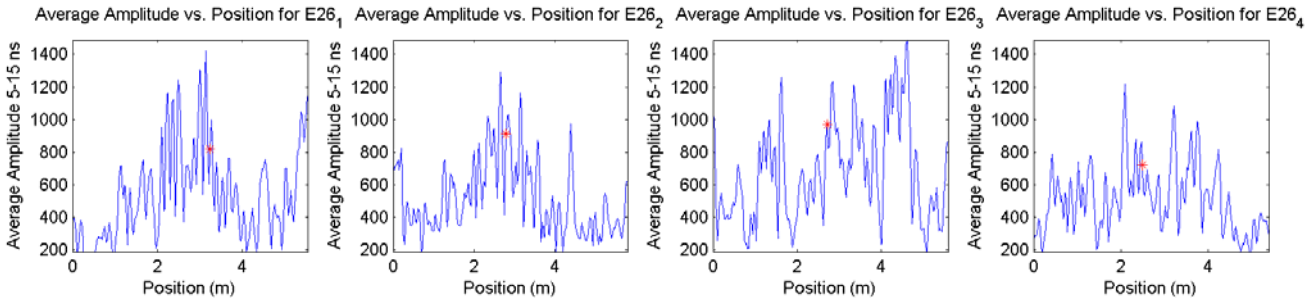

| | |
|---|---|
| Target Name | G6A2E27 |
| Item Description | GPR clutter (wood) |
| Depth (cm) | 20 |
| Dip | n/a (~horizontal) |
| Azimuth | 10 |
| Easting (m) | 294430.11 |
| Northing(m) | 3833313.685 |

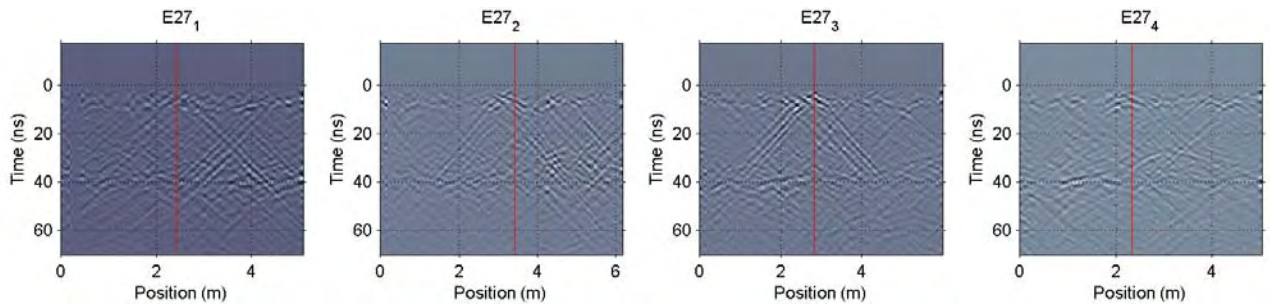


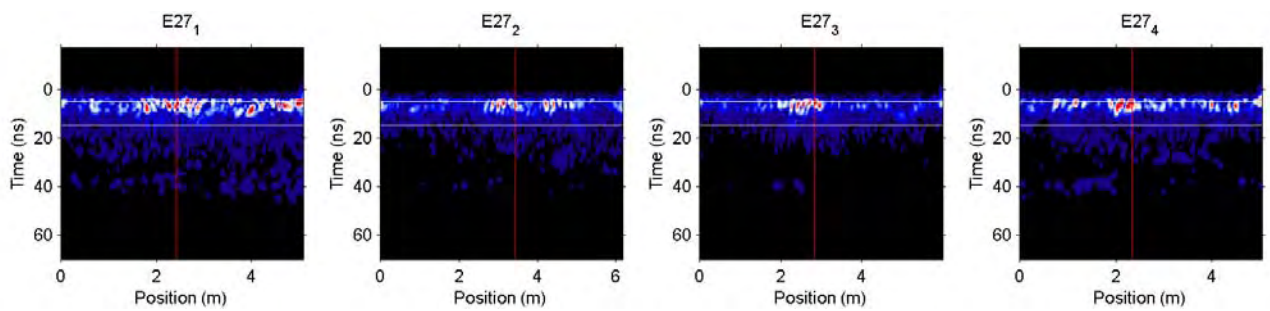


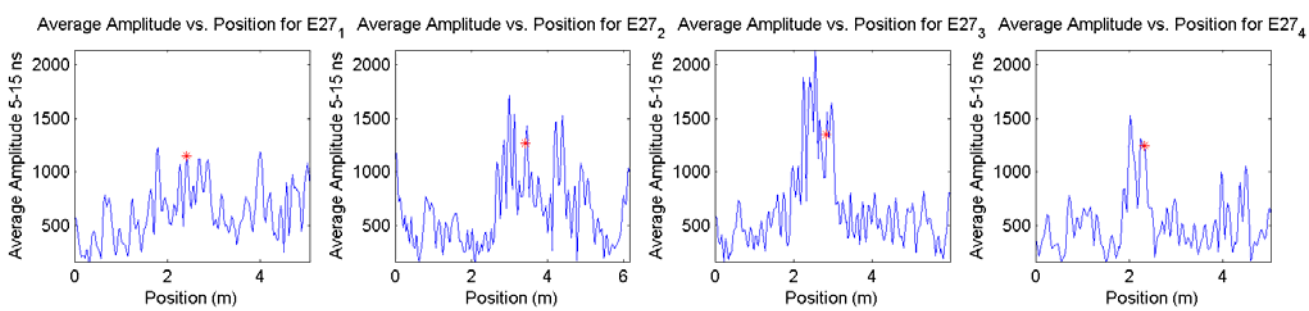

| | |
|---|---|
| Target Name | G6A2E28 |
| Item Description | GPR clutter (wood) |
| Depth (cm) | 10 |
| Dip | n/a (~horizontal) |
| Azimuth | 90 |
| Easting (m) | 294428.709 |
| Northing(m) | 3833318.302 |

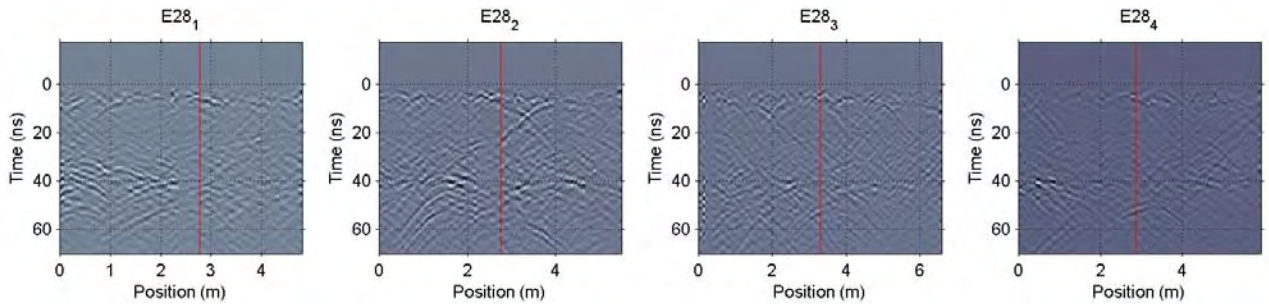


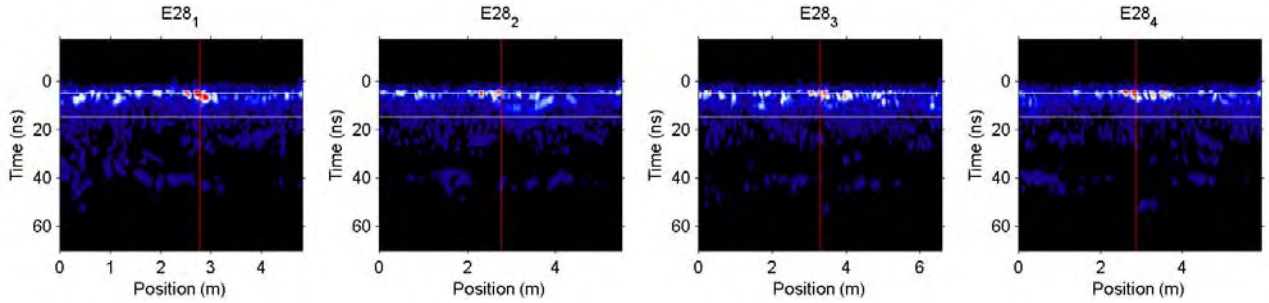


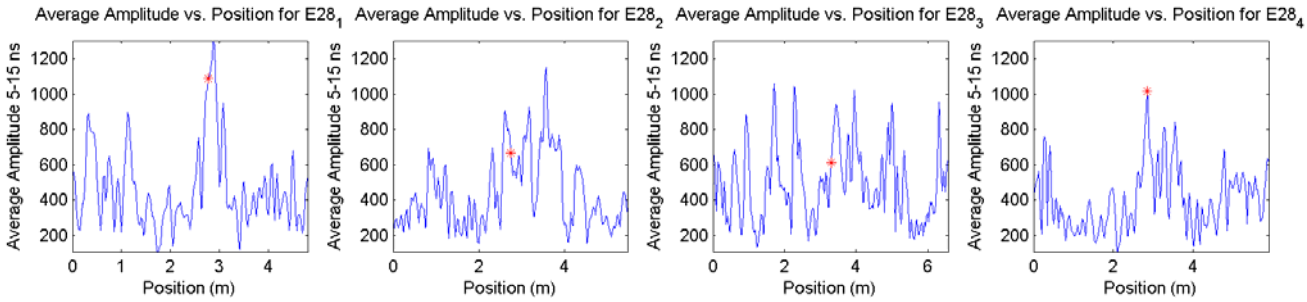

| | |
|---|---|
| Target Name | G6A2E29 |
| Item Description | GPR clutter (linear 3x foam tubing) |
| Depth (cm) | 18 |
| Dip | n/a (~horizontal) |
| Azimuth | 350 |
| Easting (m) | 294428.144 |
| Northing(m) | 3833321.451 |

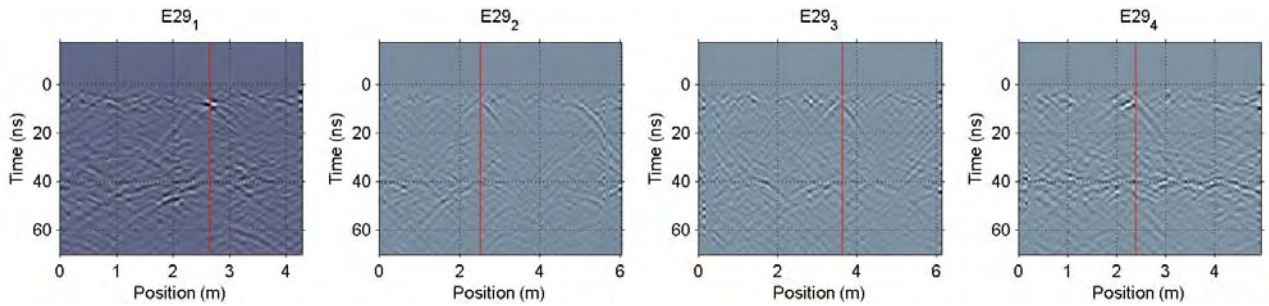


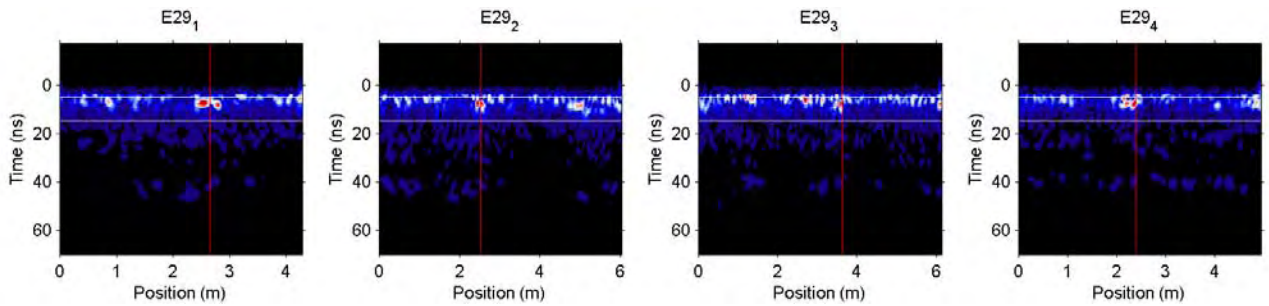


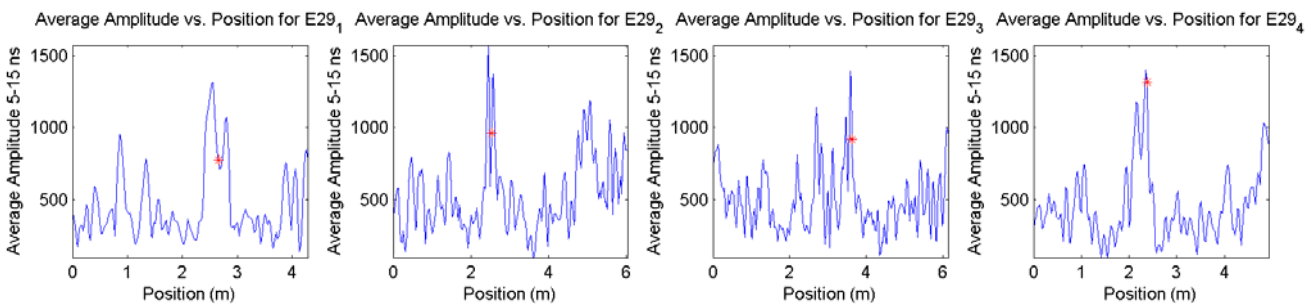

| | |
|---|---|
| Target Name | G6A2E30 |
| Item Description | GPR clutter (small styrofoam piece) |
| Depth (cm) | 8 |
| Dip | n/a (~horizontal) |
| Azimuth | 360 |
| Easting (m) | 294427.436 |
| Northing(m) | 3833323.782 |

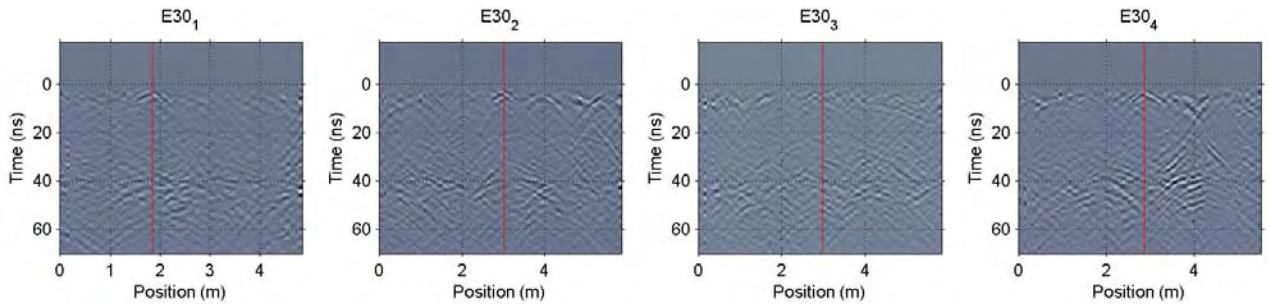


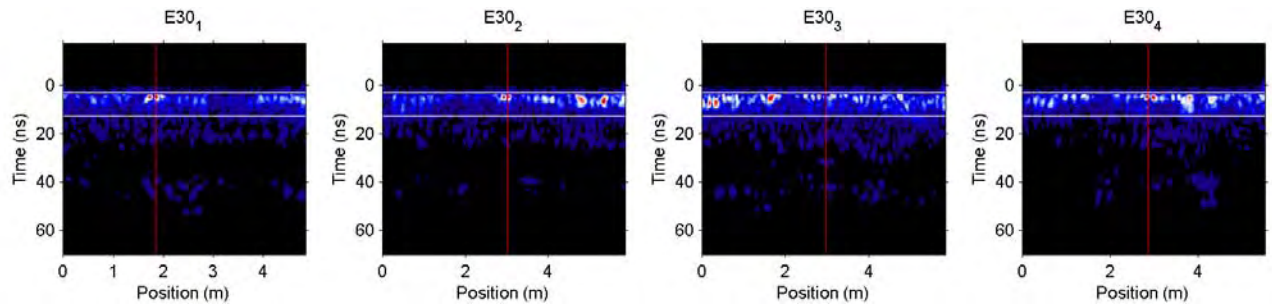


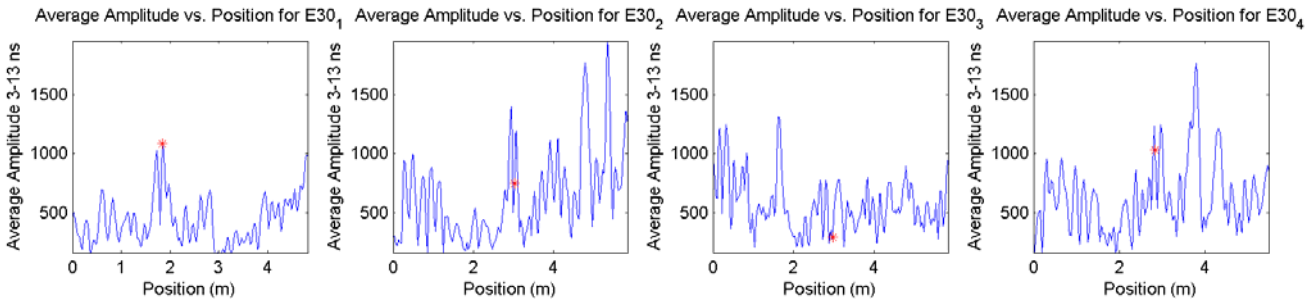

| | |
|---|---|
| Target Name | G6A2E31 |
| Item Description | GPR clutter (linear 3x foam tubing) |
| Depth (cm) | 28 |
| Dip | n/a (~horizontal) |
| Azimuth | 10 |
| Easting (m) | 294433.901 |
| Northing(m) | 3833316.349 |

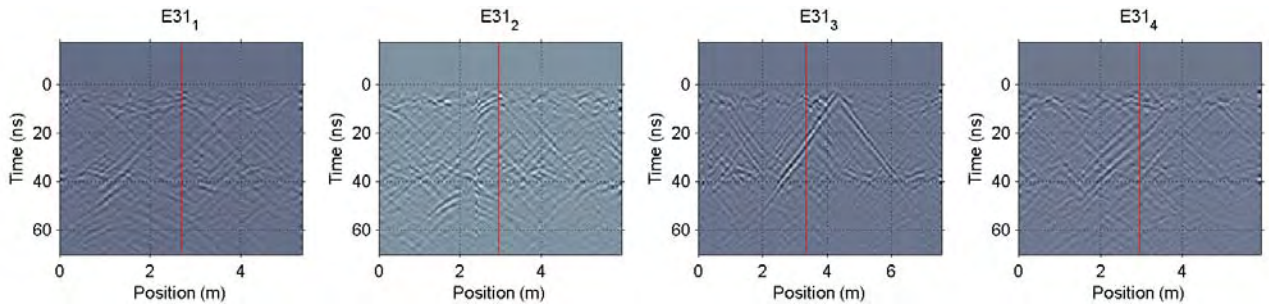


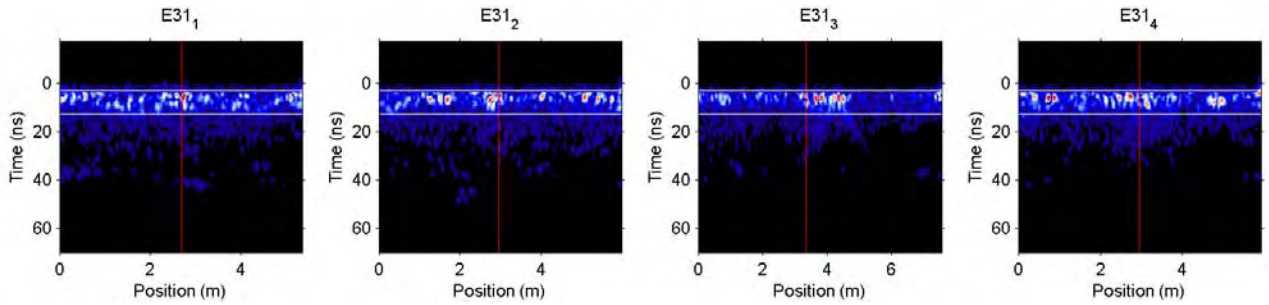


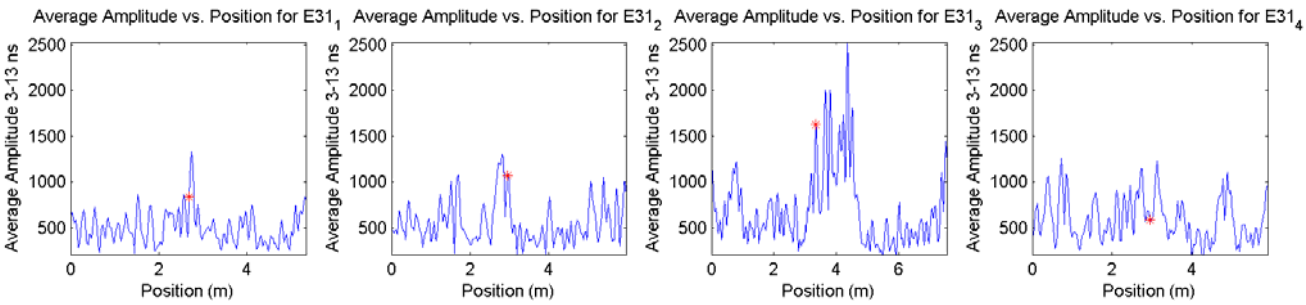

| | |
|---|---|
| Target Name | G6A2E32 |
| Item Description | GPR clutter (small styrofoam piece) |
| Depth (cm) | 7 |
| Dip | n/a (~horizontal) |
| Azimuth | 360 |
| Easting (m) | 294433.217 |
| Northing(m) | 3833320.842 |

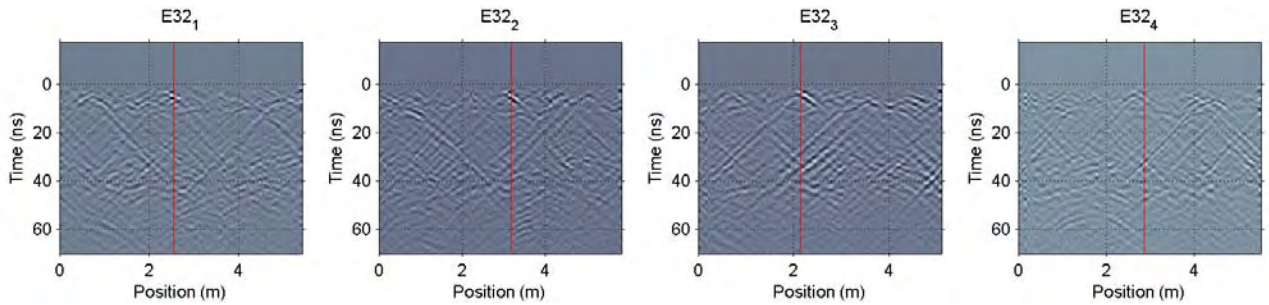


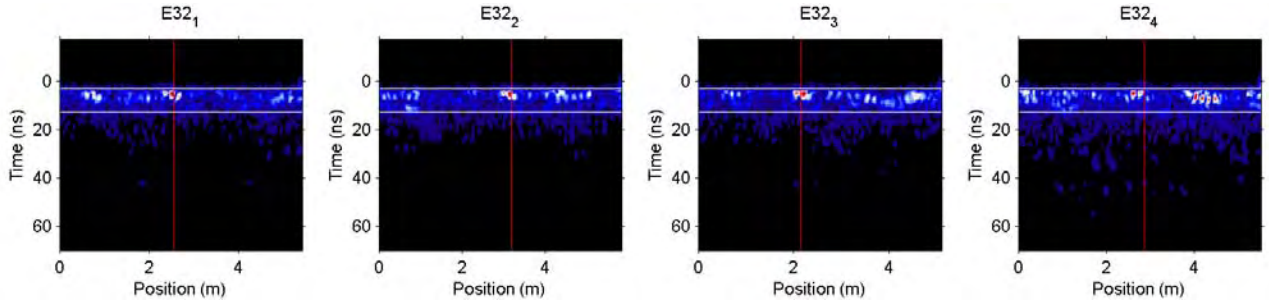


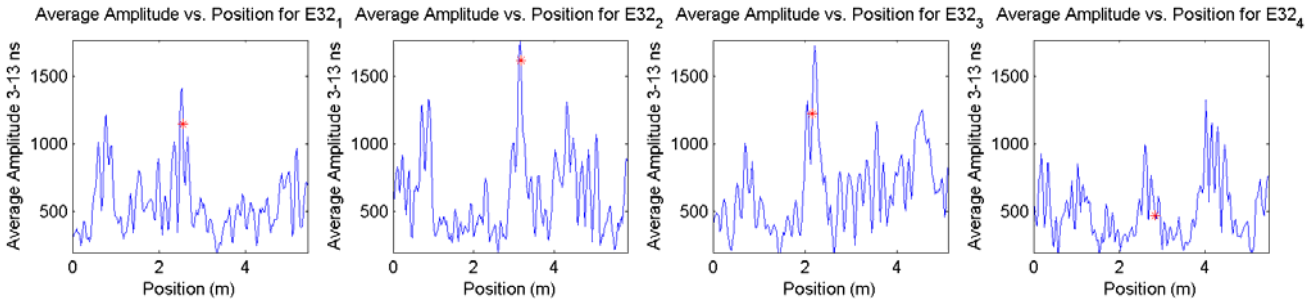

## D.2. 1000-MHz emplaced items

| | |
|---|---|
| Target Name | G6A1E13 |
| Item Description | MK118 – Rockeye |
| Depth (cm) | 15 |
| Dip | 0 |
| Azimuth | 40 |
| Easting (m) | 294374.3126 |
| Northing(m) | 3833305.529 |

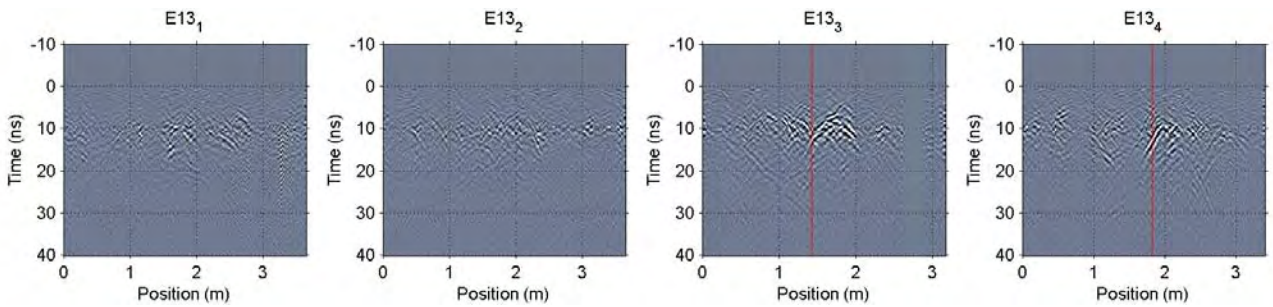


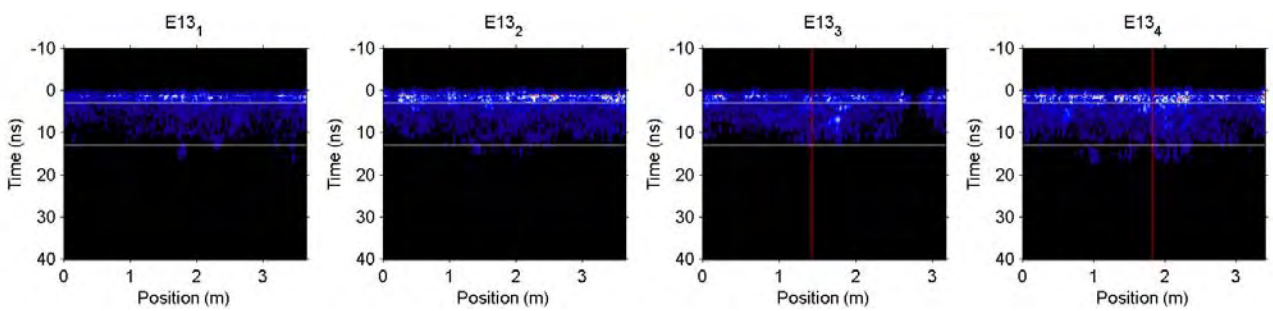


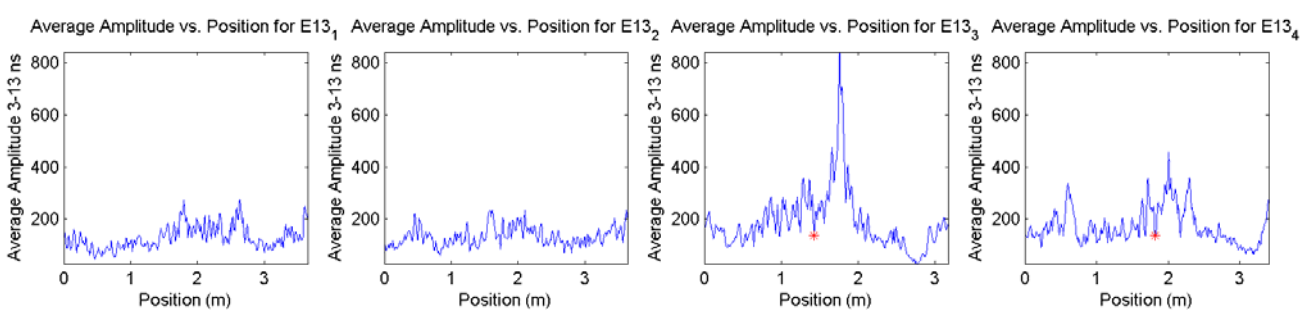

| | |
|---|---|
| Target Name | G6A1E14 |
| Item Description | Body Assembly Grenade Type PH F/M42 – Inert |
| Depth (cm) | 15 |
| Dip | 45 |
| Azimuth | 180 |
| Easting (m) | 294372.7496 |
| Northing(m) | 3833310.345 |

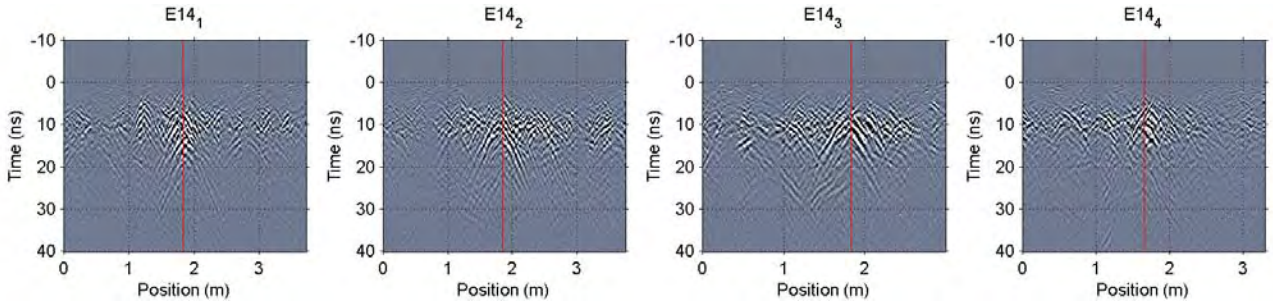


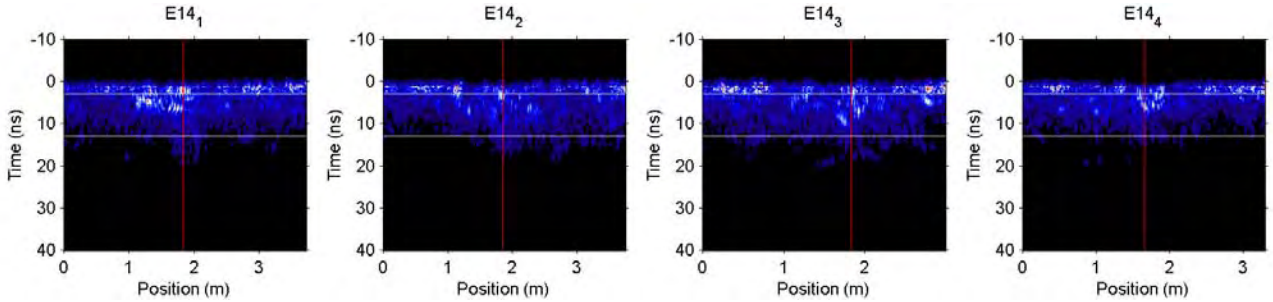


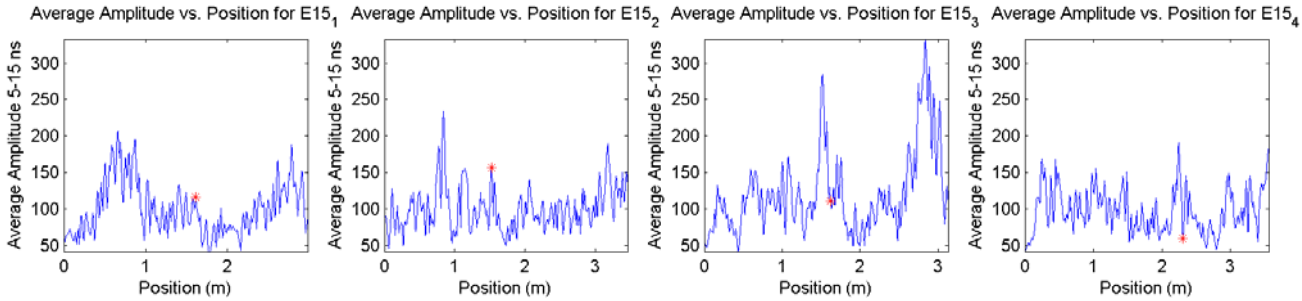

| | |
|---|---|
| Target Name | G6A1E15 |
| Item Description | Body 60mm Inert Wax Filled |
| Depth (cm) | 25 |
| Dip | 45 |
| Azimuth | 0 |
| Easting (m) | 294372.0475 |
| Northing(m) | 3833315.293 |

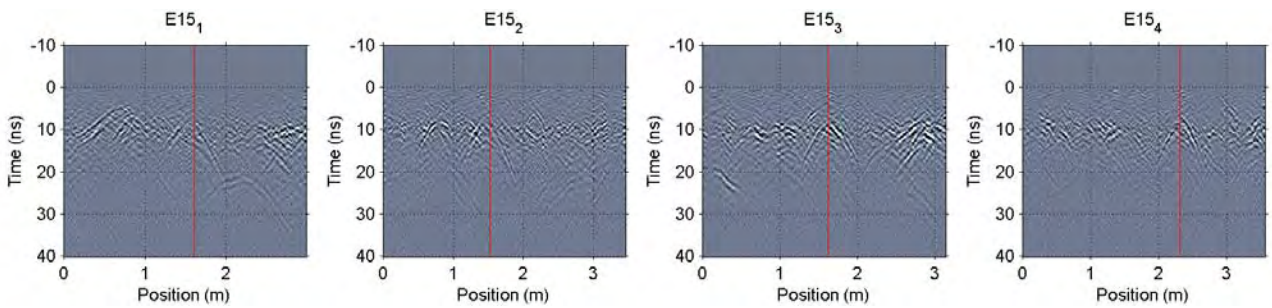


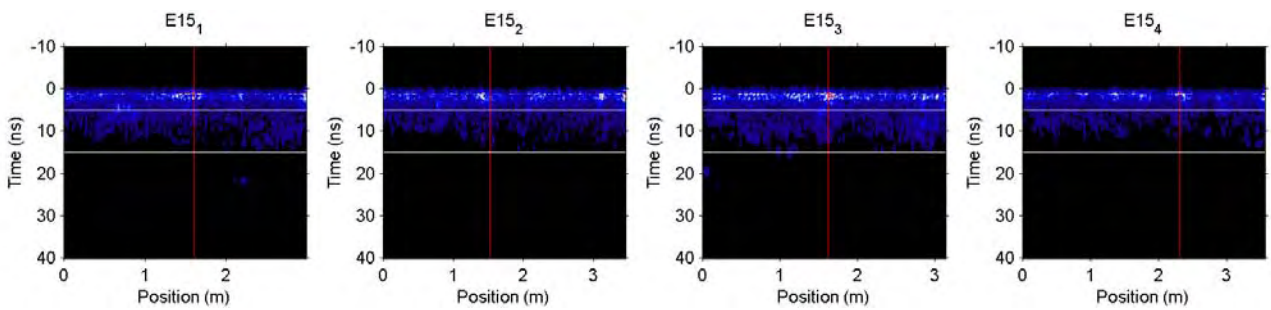


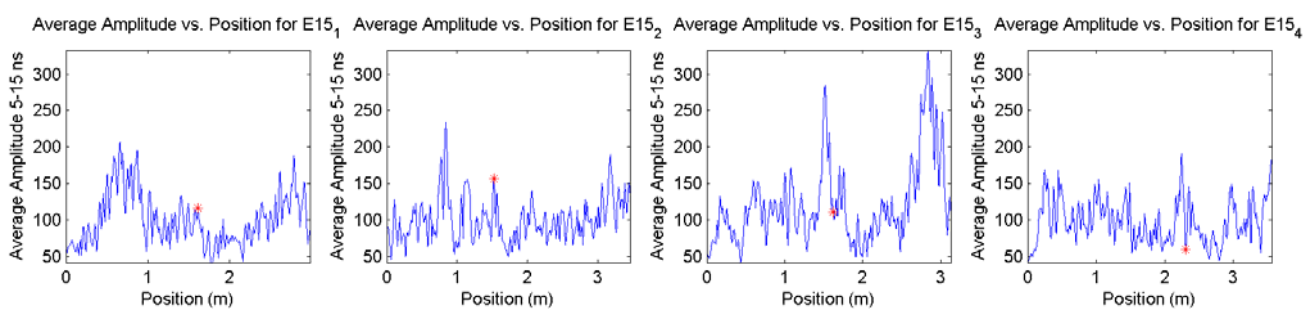

| | |
|---|---|
| Target Name | G6A1E16 |
| Item Description | 57mm Projectile – Inert |
| Depth (cm) | 25 |
| Dip | 45 |
| Azimuth | 270 |
| Easting (m) | 294371.0818 |
| Northing(m) | 3833320.146 |

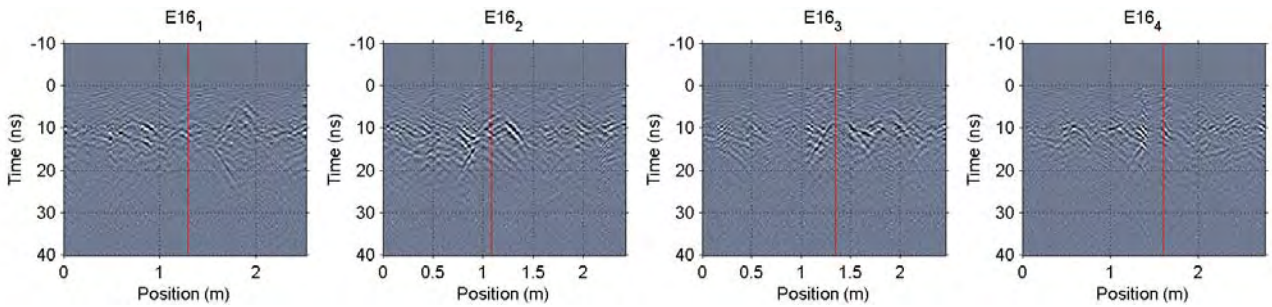


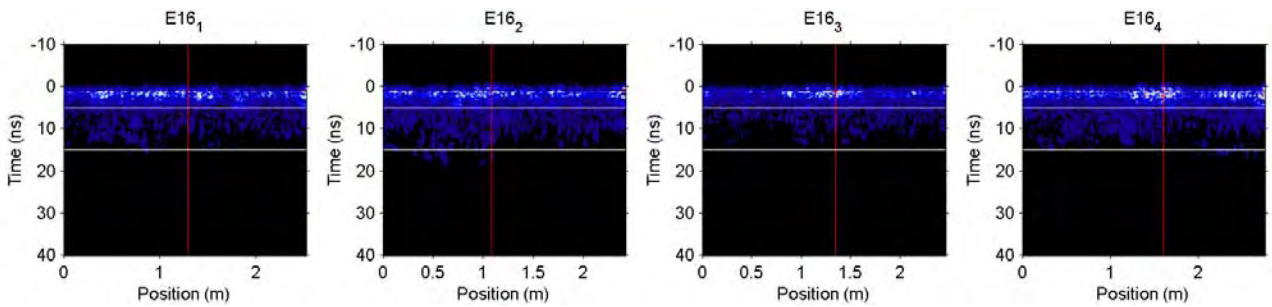


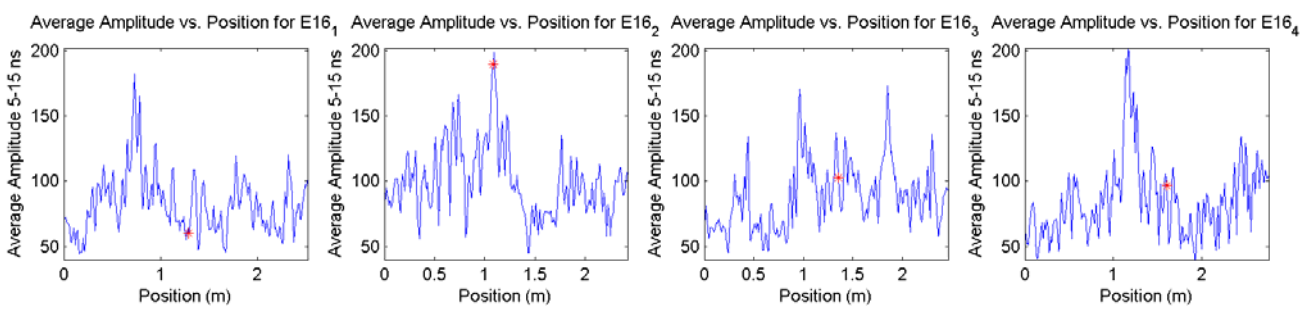

| | |
|---|---|
| Target Name | G6A1E17 |
| Item Description | Bomblet Dummy Representing BLU-26 |
| Depth (cm) | 15 |
| Dip | 0 |
| Azimuth | n/a |
| Easting (m) | 294369.9148 |
| Northing(m) | 3833325.051 |

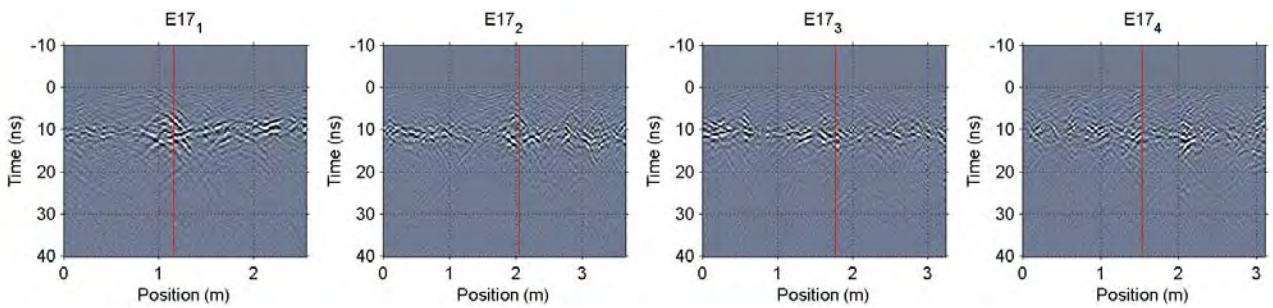


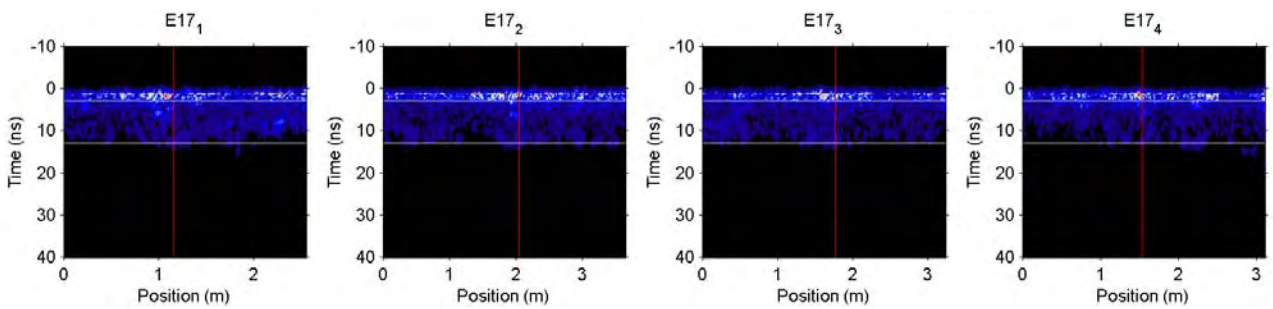


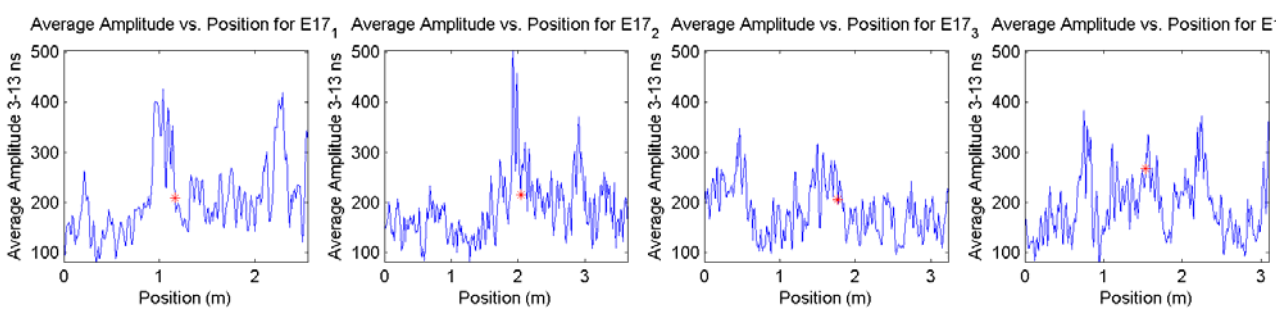

| | |
|---|---|
| Target Name | G6A1E18 |
| Item Description | Bomblet Dummy BDU-28/B |
| Depth (cm) | 15 |
| Dip | 0 |
| Azimuth | 45 |
| Easting (m) | 294369.2656 |
| Northing(m) | 3833329.844 |

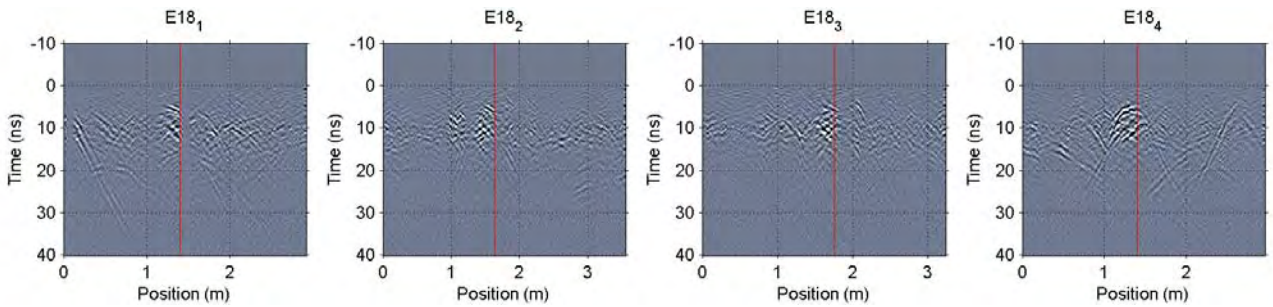


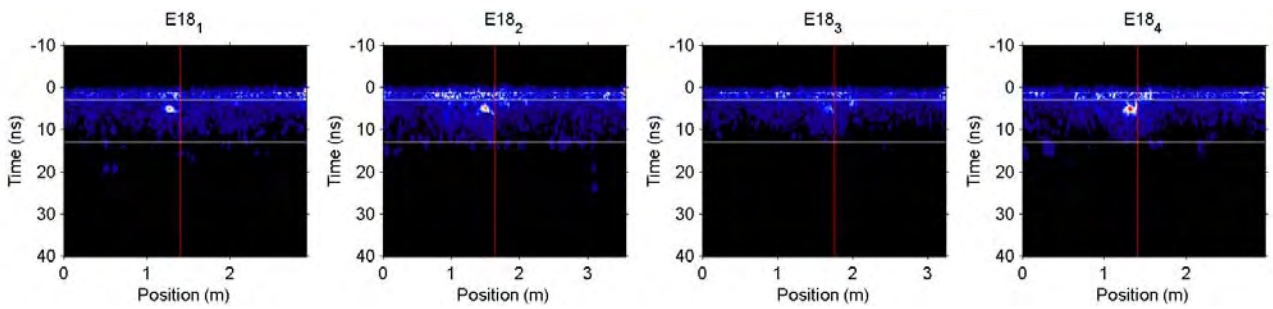


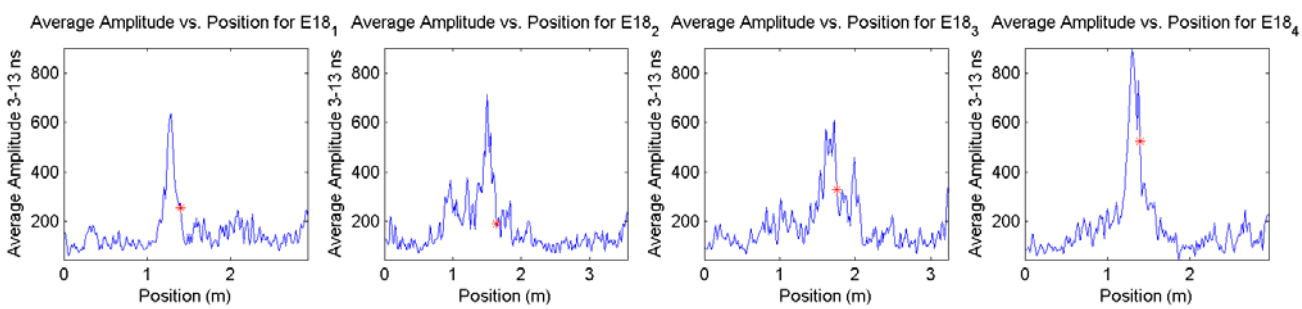

## D.3. 250 MHz UXO and practice rounds

| | |
|---|---|
| Target Name | G6B1_246 |
| Item Description | Possible Tow or Dragon |
| Depth (cm) | 12 |
| Distance From Pin (cm) | 5 |
| Easting (m) | 294393.97 |
| Northing(m) | 3833278.52 |

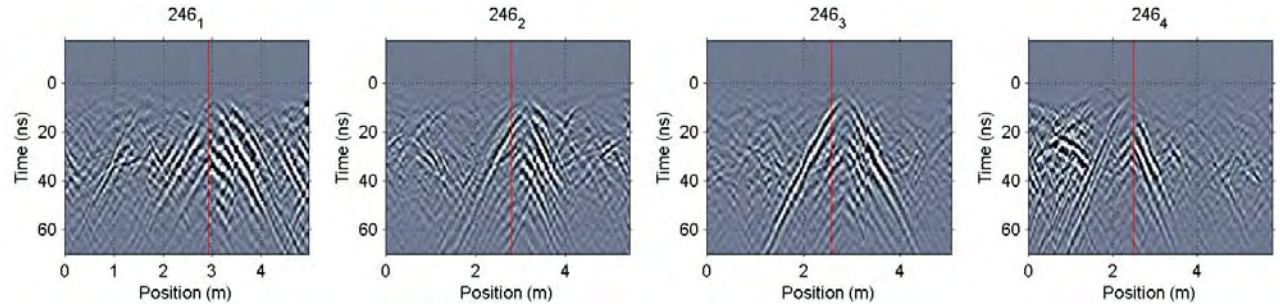


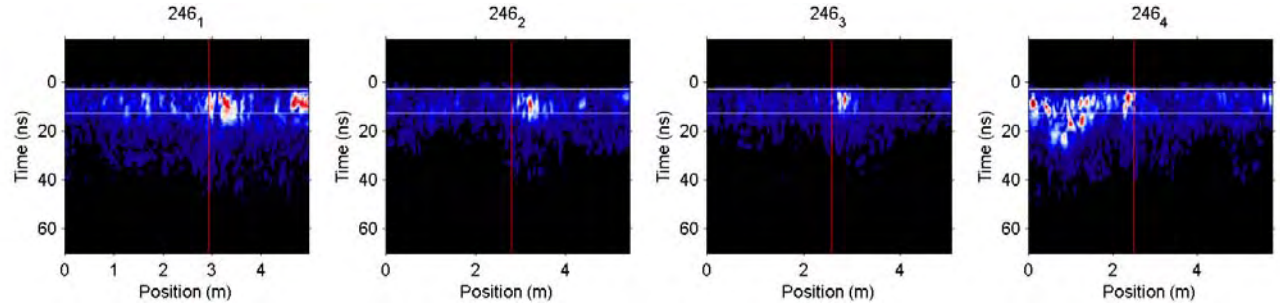


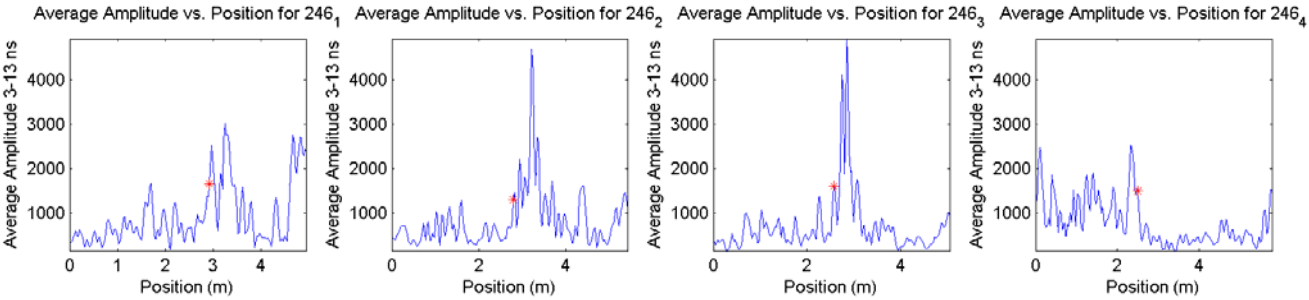

| | |
|---|---|
| Target Name | G6D2_6 |
| Item Description | 25 mm cartridge |
| Depth (cm) | 0 |
| Distance From Pin (cm) | 32 |
| Easting (m) | 294440.42 |
| Northing(m) | 3833178.38 |

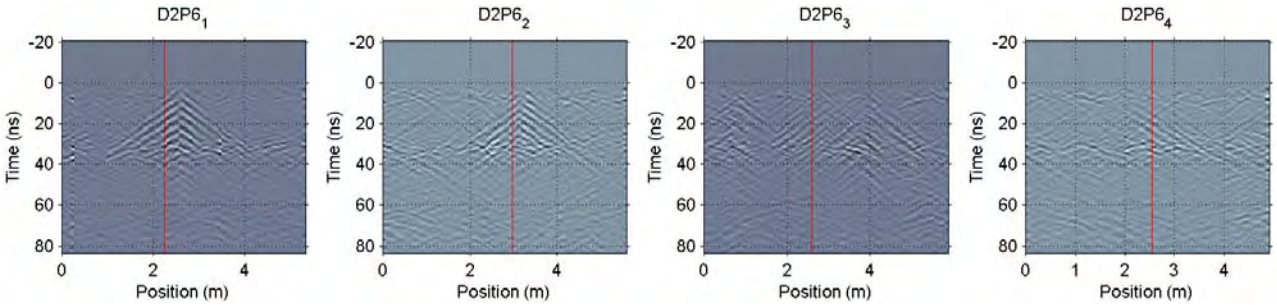


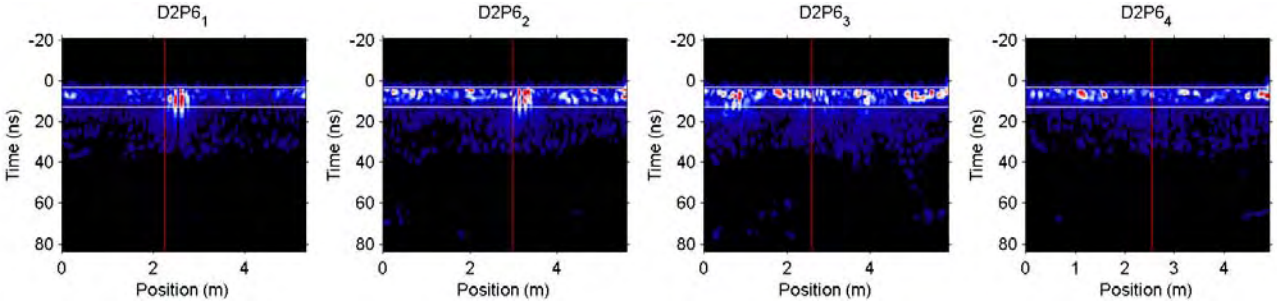


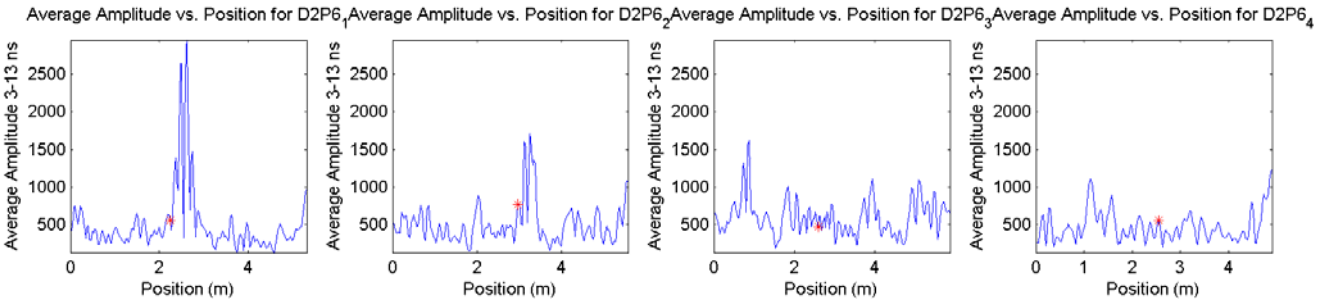

| | |
|---|---|
| Target Name | G6B1_351 |
| Item Description | 40 mm |
| Depth (cm) | 2 |
| Distance From Pin (cm) | 5 |
| Easting (m) | 294386.91 |
| Northing(m) | 3833242.57 |

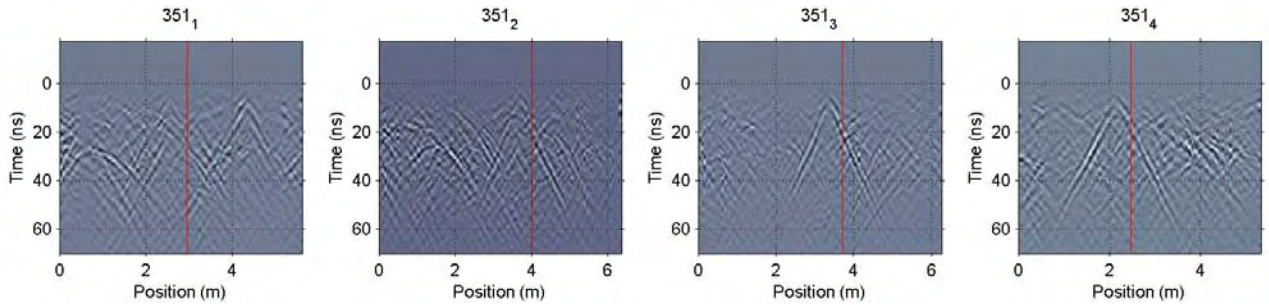


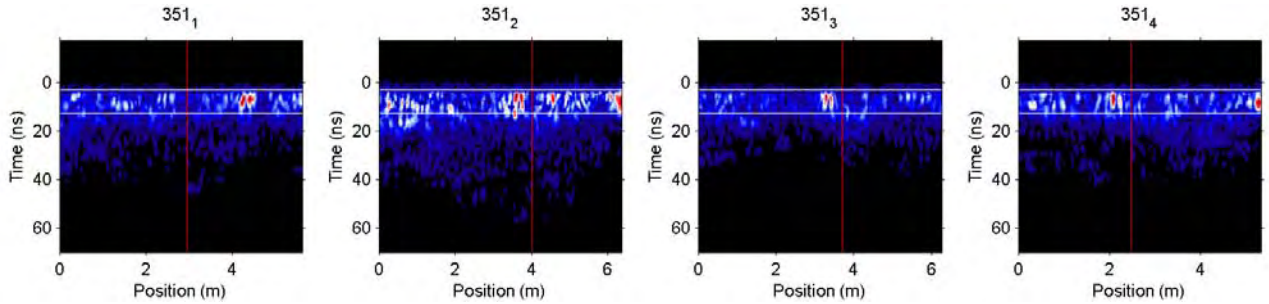


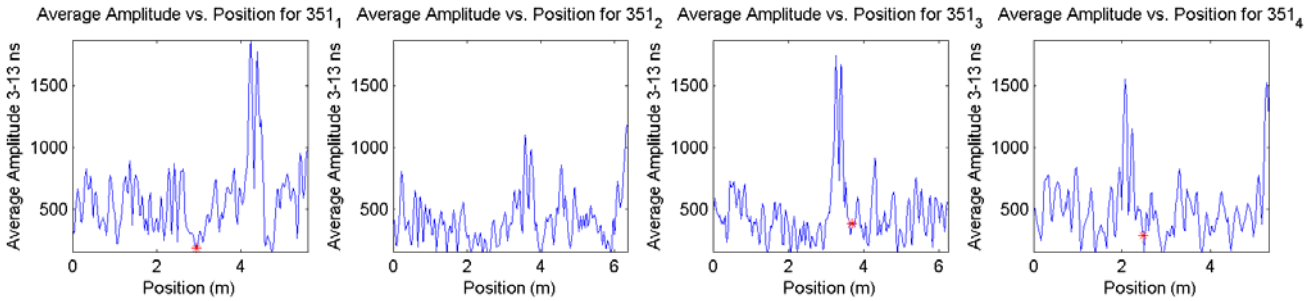

| | |
|---|---|
| Target Name | G6B1_379 |
| Item Description | 40 mm |
| Depth (cm) | 3 |
| Distance From Pin (cm) | 36 |
| Easting (m) | 294378.66 |
| Northing(m) | 3833245.83 |

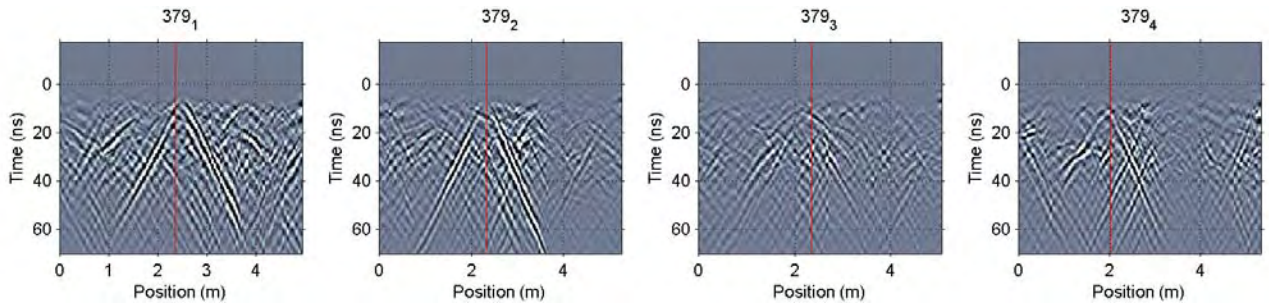


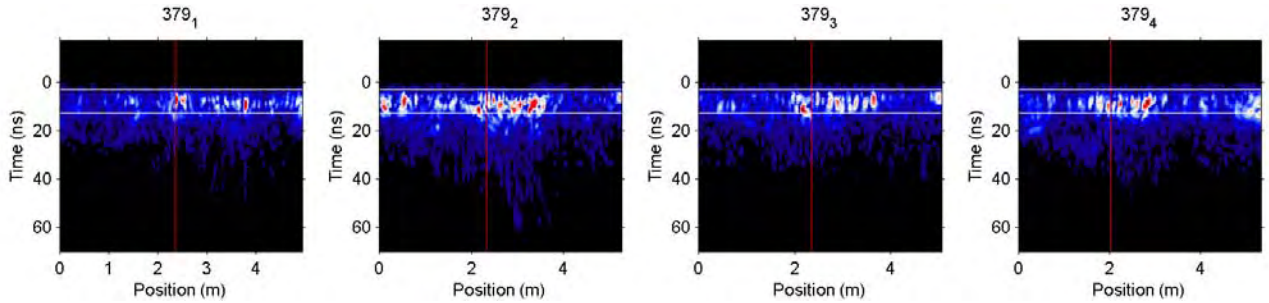


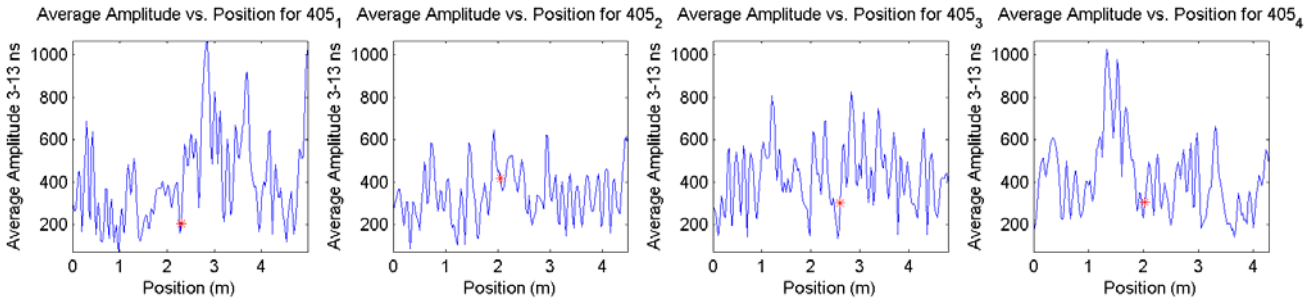

| | |
|---|---|
| Target Name | G6B2_405 |
| Item Description | 40 mm |
| Depth (cm) | 2 |
| Distance From Pin (cm) | 14 |
| Easting (m) | 294426.45 |
| Northing(m) | 3833280.62 |

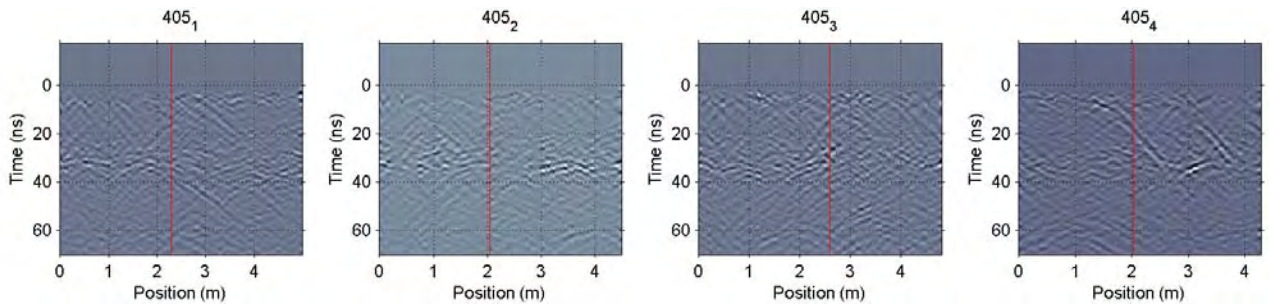


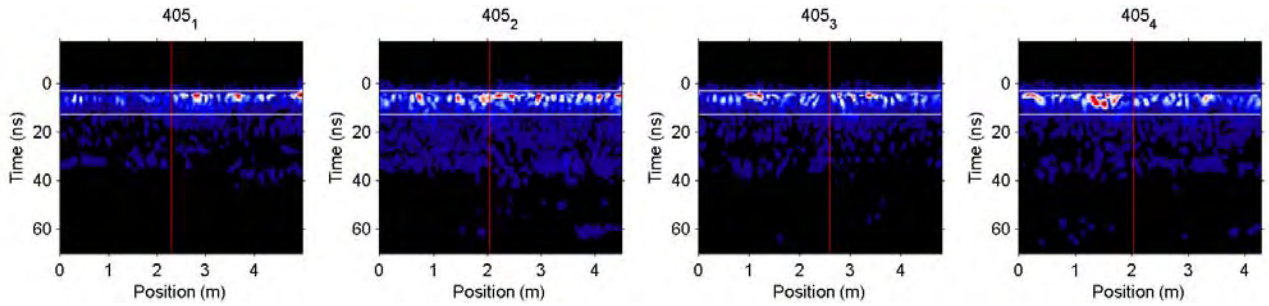


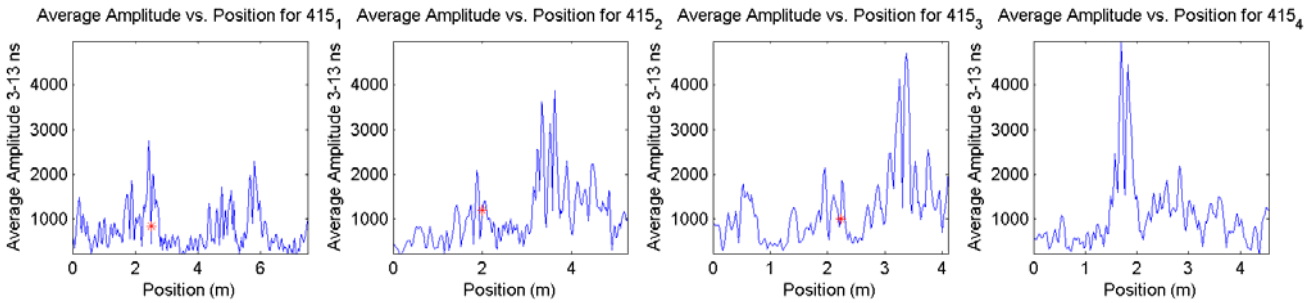

| | |
|---|---|
| Target Name | G6B1_415 |
| Item Description | 40 mm |
| Depth (cm) | 8 |
| Distance From Pin (cm) | 0 |
| Easting (m) | 294377.82 |
| Northing(m) | 3833244.59 |

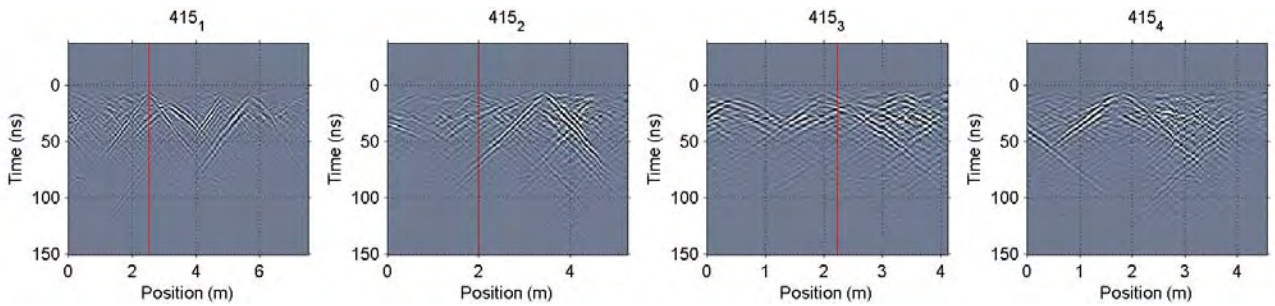


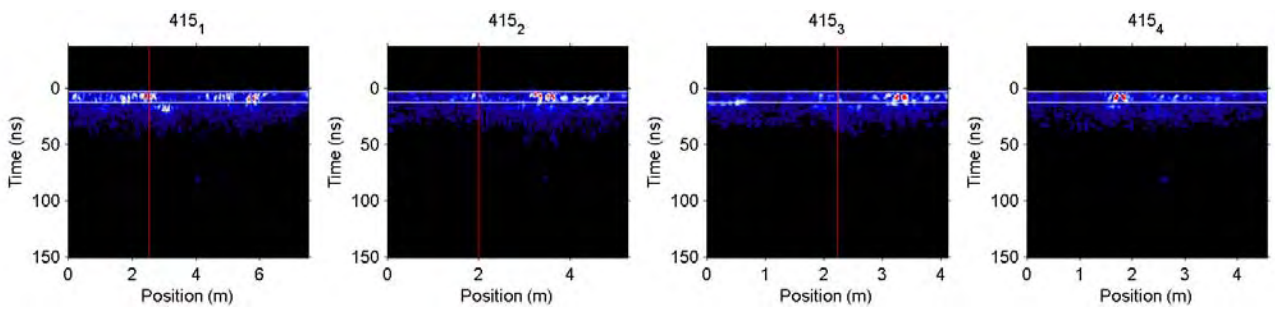


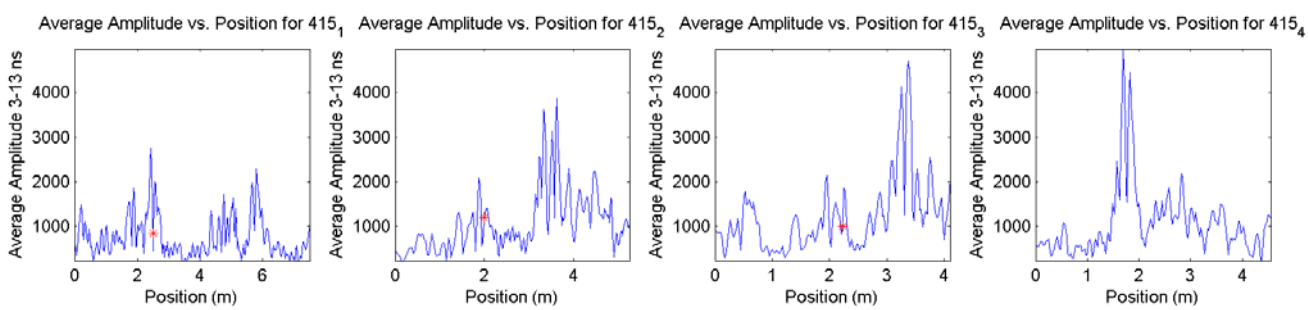

| | |
|---|---|
| Target Name | G6D1_7 |
| Item Description | 40 mm |
| Depth (cm) | 0 |
| Distance From Pin (cm) | 24 |
| Easting (m) | 294416.51 |
| Northing(m) | 3833181.32 |

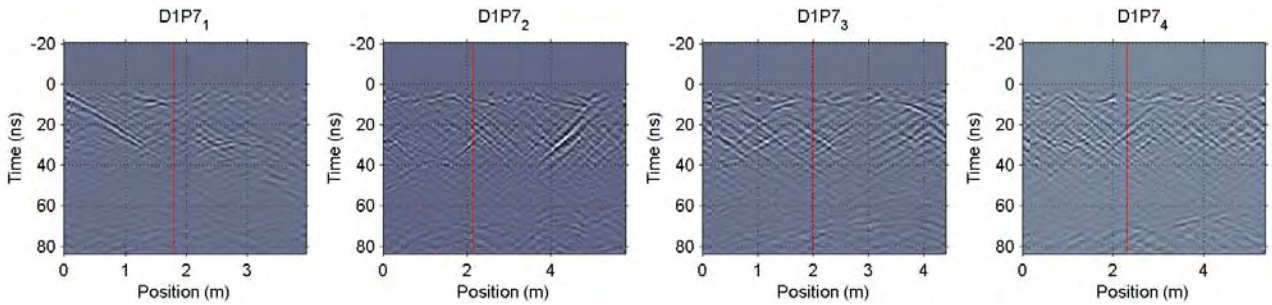


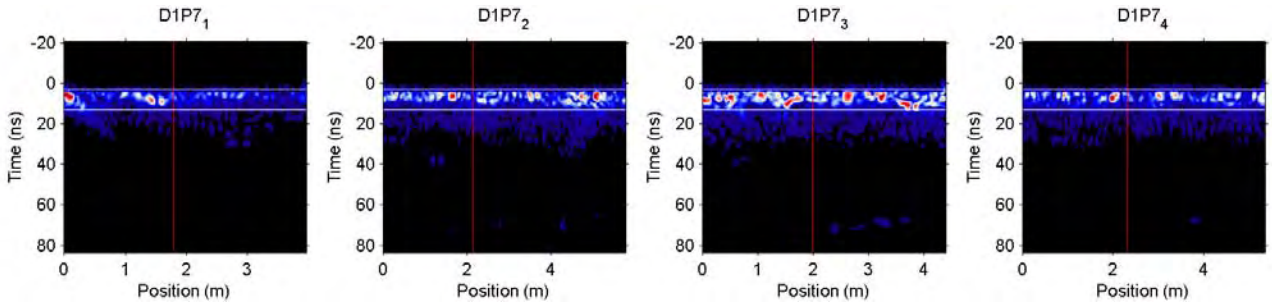


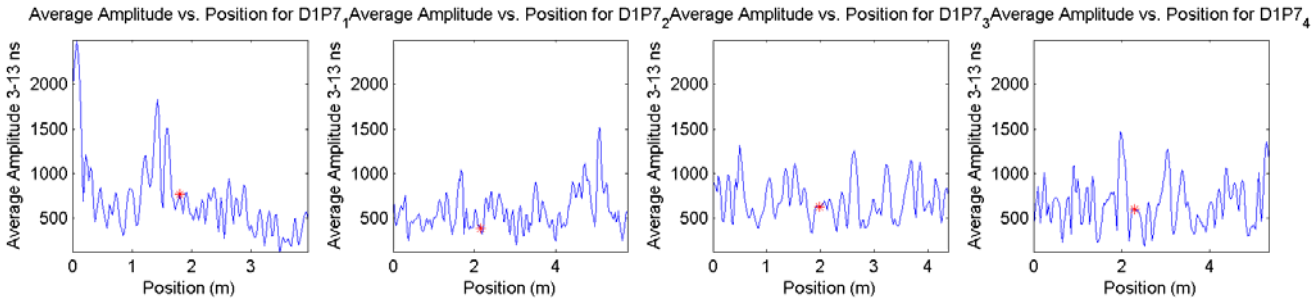

| | |
|---|---|
| Target Name | G6E1_2 |
| Item Description | 40 mm |
| Depth (cm) | 7 |
| Distance From Pin (cm) | 23 |
| Easting (m) | 294397.58 |
| Northing(m) | 3833110.95 |

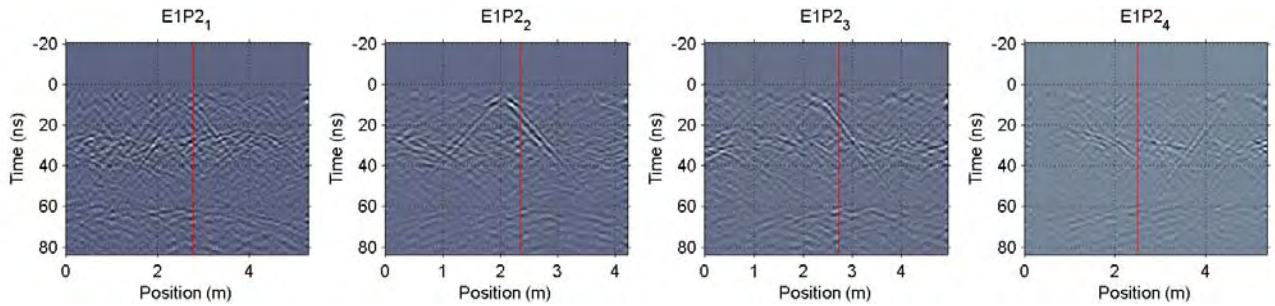


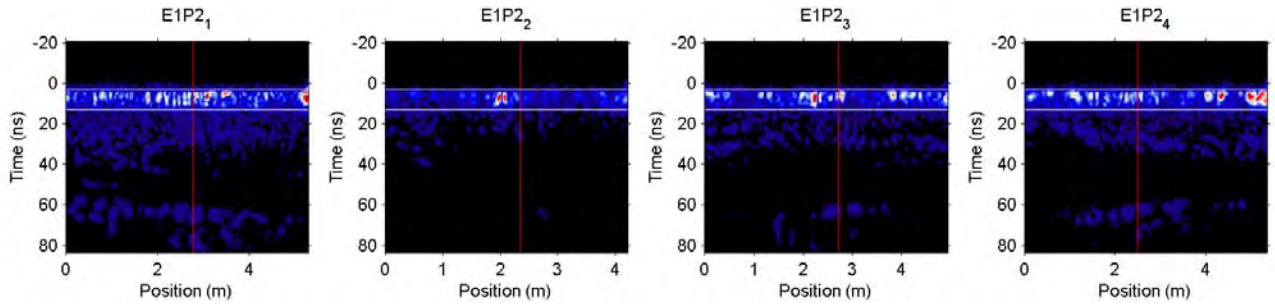


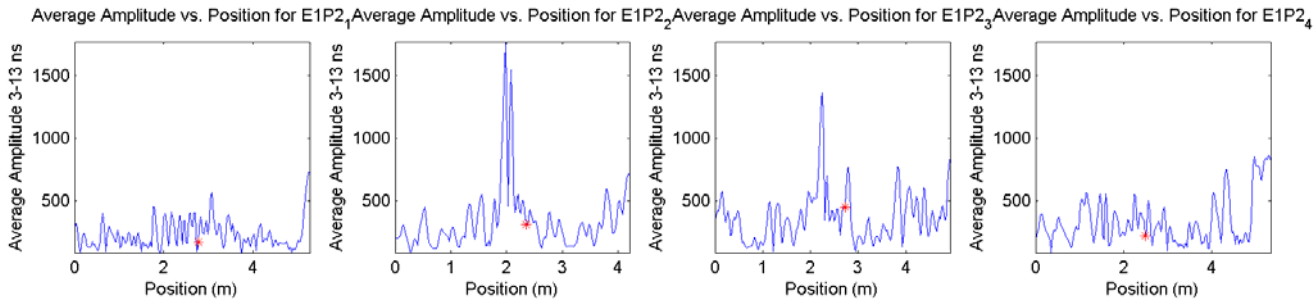

| | |
|---|---|
| Target Name | G6E1_3 |
| Item Description | 40 mm |
| Depth (cm) | 10 |
| Distance From Pin (cm) | 10 |
| Easting (m) | 294398.21 |
| Northing(m) | 3833110.09 |

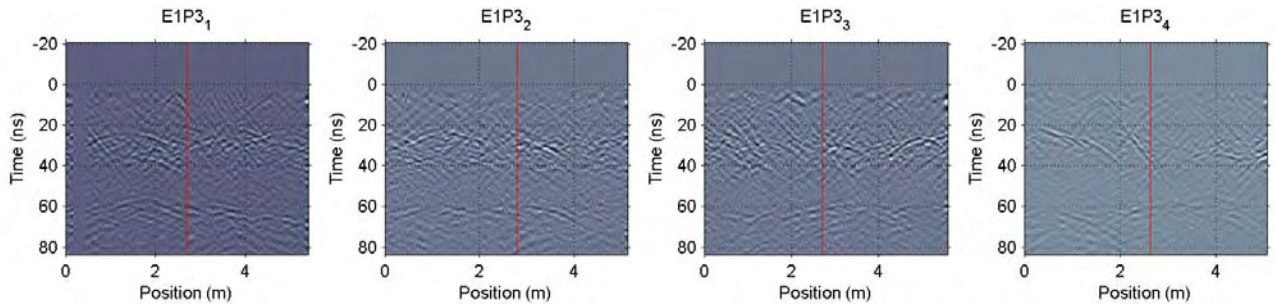


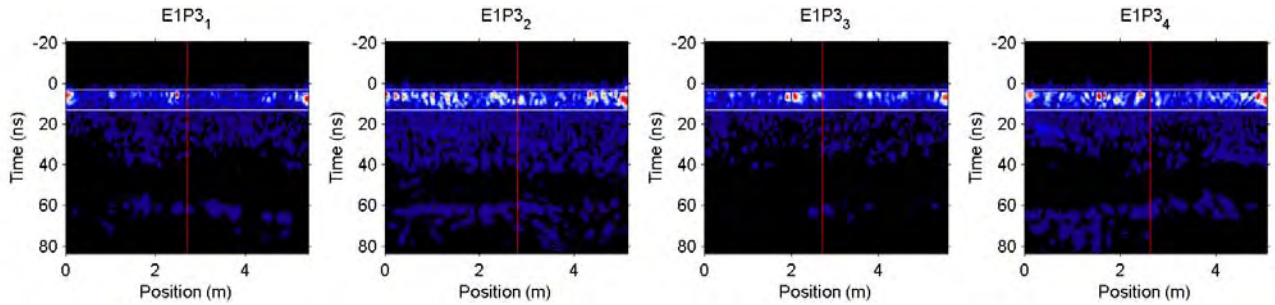


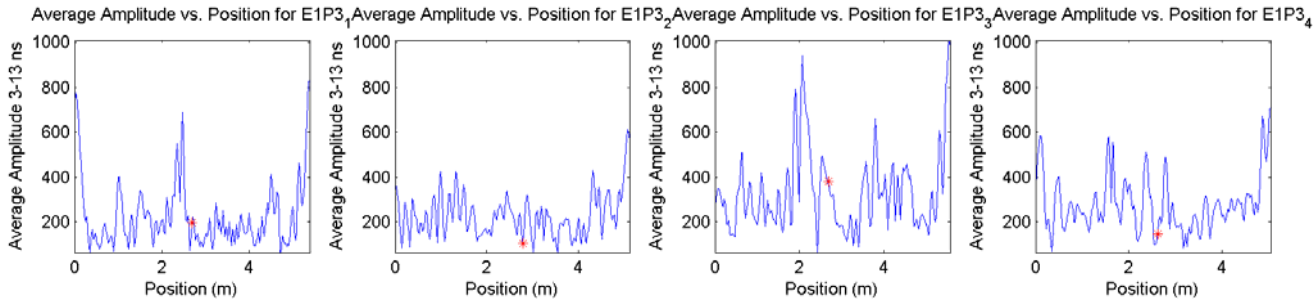

## D.4. 1000 MHz UXO and practice rounds

| | |
|---|---|
| Target Name | G6E2_2 |
| Item Description | 25-mm cartridge |
| Depth (cm) | 10 |
| Distance From Pin (cm) | 40 |
| Easting (m) | 294474.49 |
| Northing(m) | 3833115.68 |

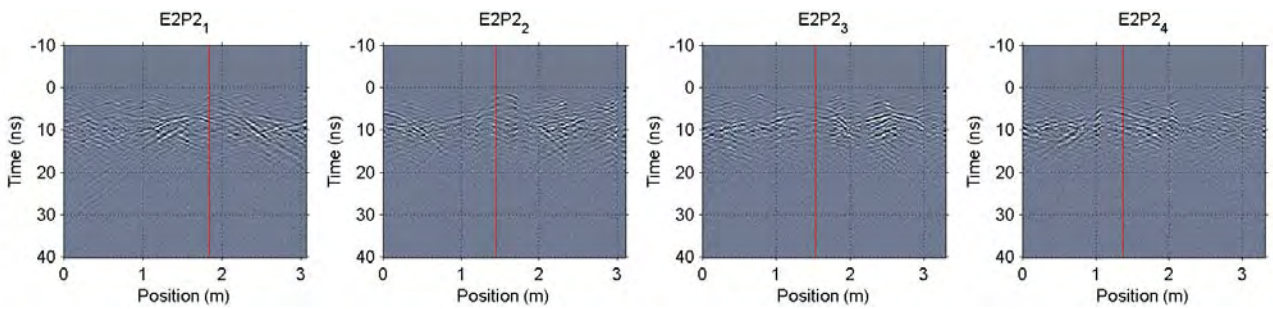


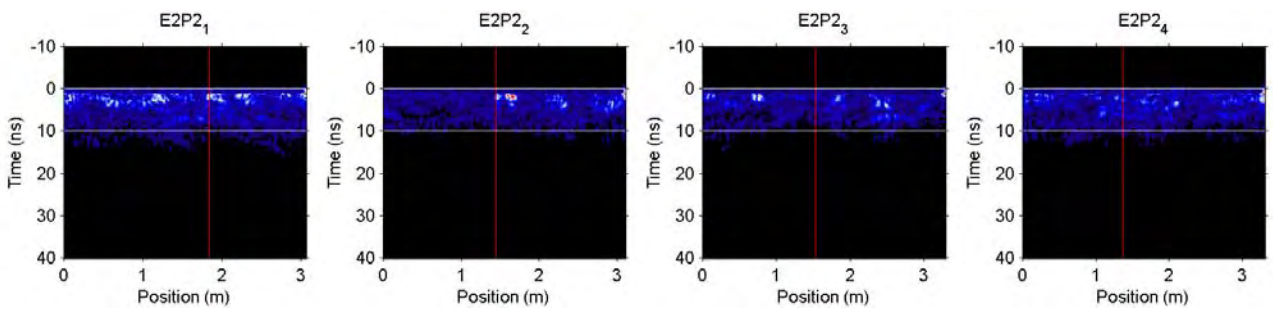


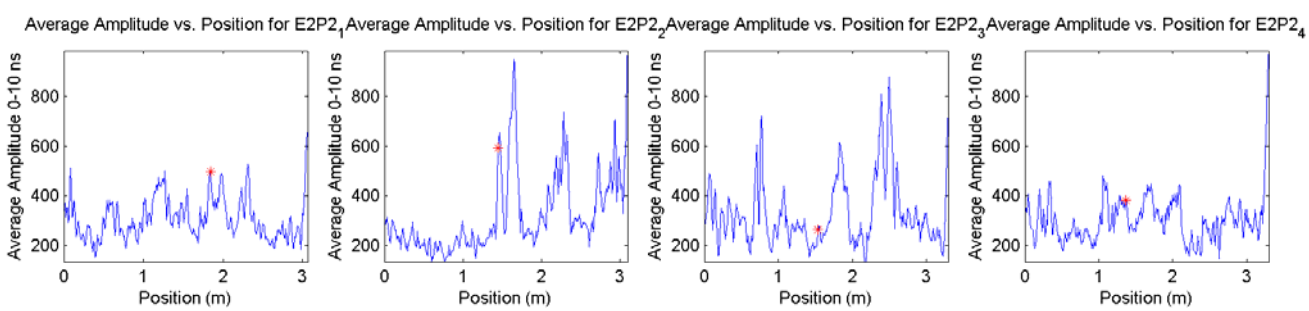

| | |
|---|---|
| Target Name | G6D2_6 |
| Item Description | 25-mm cartridge |
| Depth (cm) | 0 |
| Distance From Pin (cm) | 32 |
| Easting (m) | 294440.42 |
| Northing(m) | 3833178.38 |

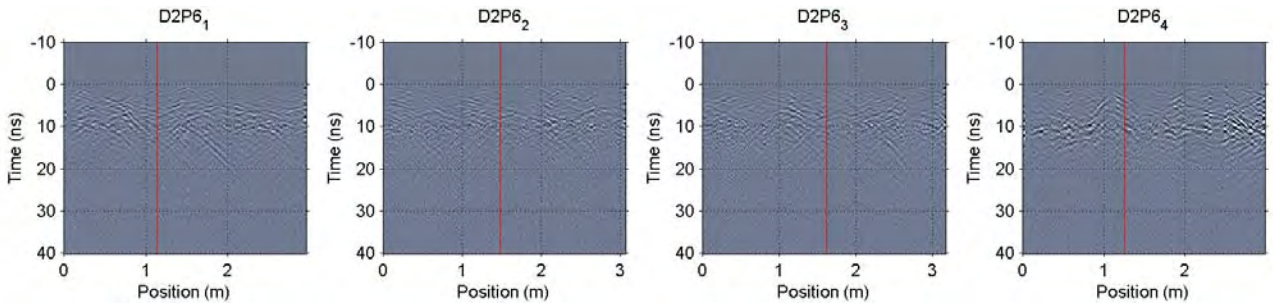


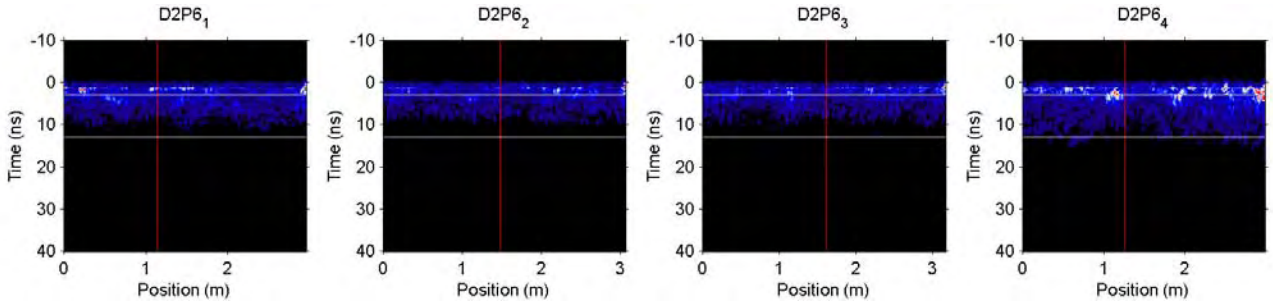


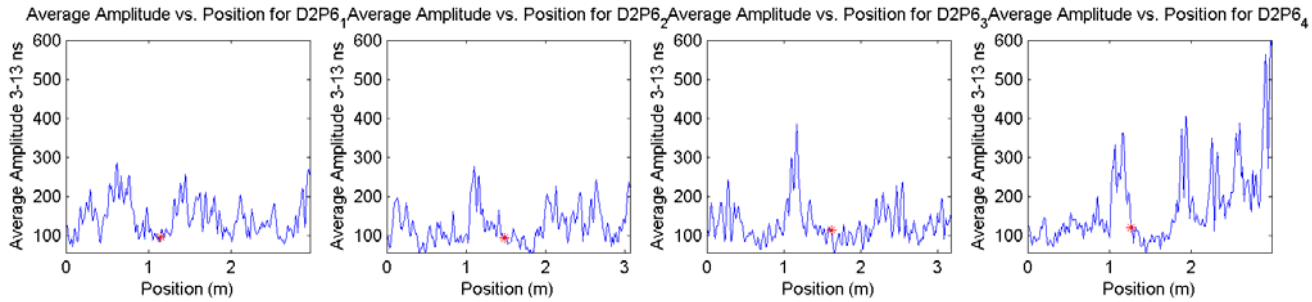

| | |
|---|---|
| Target Name | G6E1_2 |
| Item Description | 40 mm |
| Depth (cm) | 7 |
| Distance From Pin (cm) | 23 |
| Easting (m) | 294397.58 |
| Northing(m) | 3833110.95 |

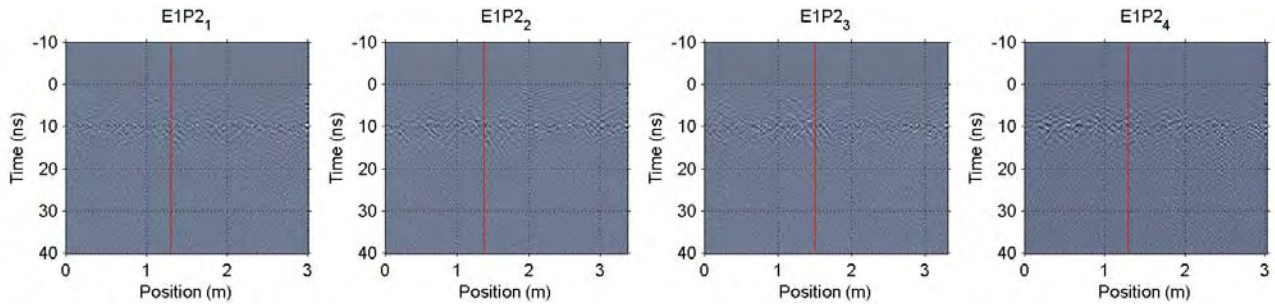


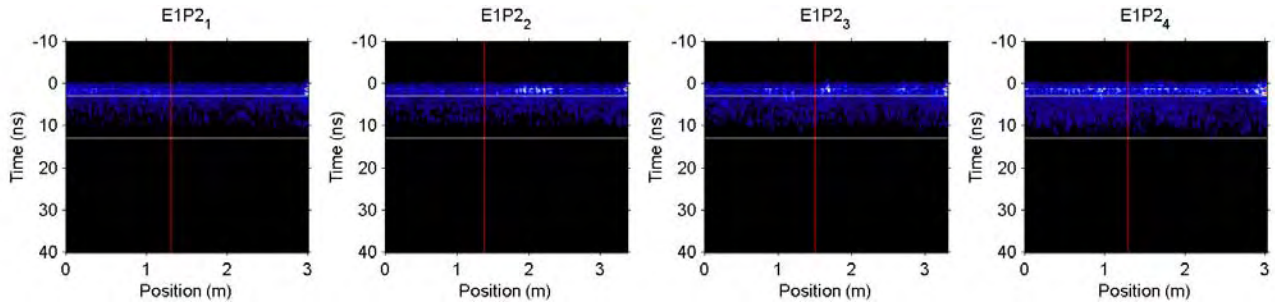


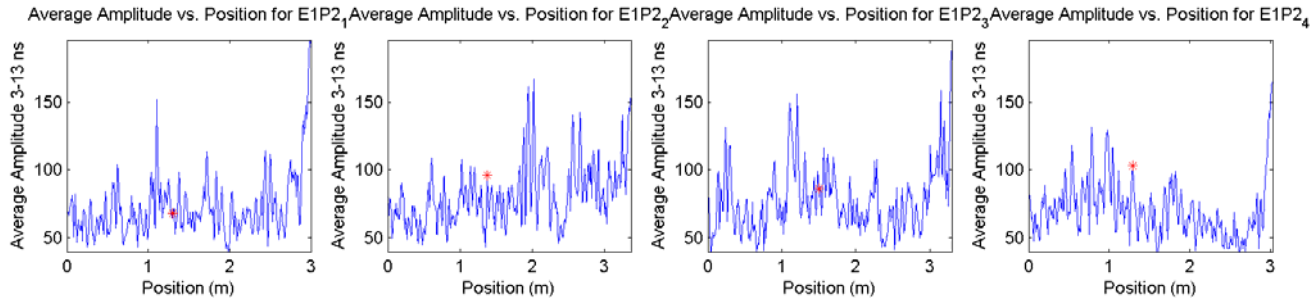

| | |
|---|---|
| Target Name | G6E1_3 |
| Item Description | 40 mm |
| Depth (cm) | 10 |
| Distance From Pin (cm) | 10 |
| Easting (m) | 294398.21 |
| Northing(m) | 3833110.09 |

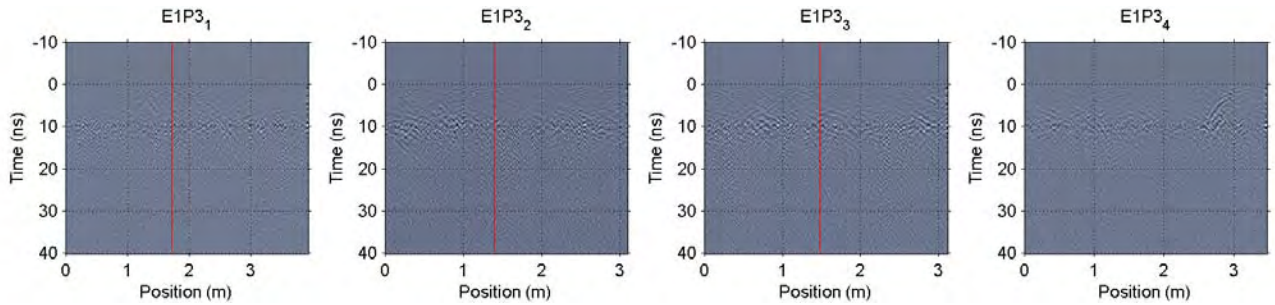


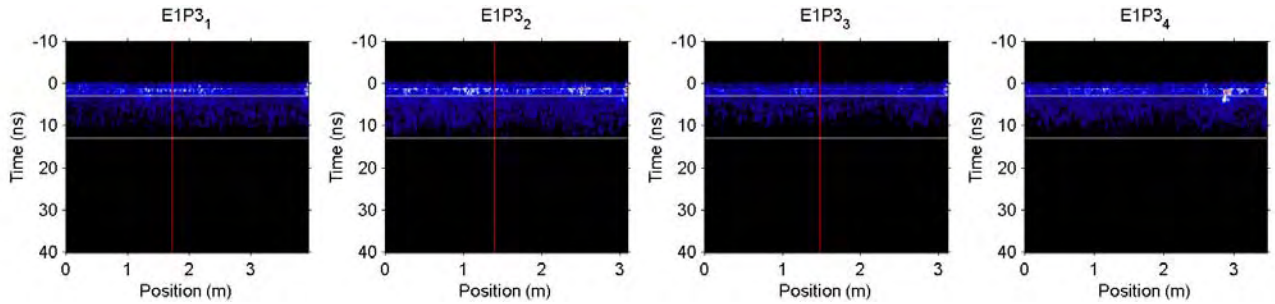


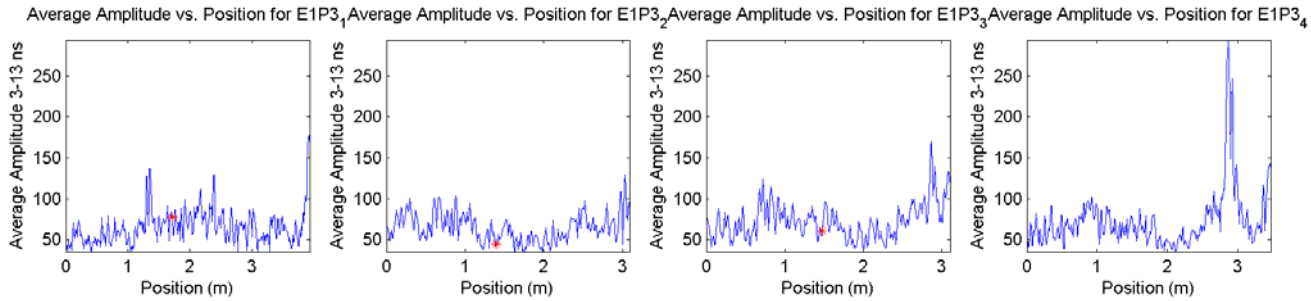

| | |
|---|---|
| Target Name | G6D1_7 |
| Item Description | 40 mm |
| Depth (cm) | 0 |
| Distance From Pin (cm) | 24 |
| Easting (m) | 294416.51 |
| Northing(m) | 3833181.32 |

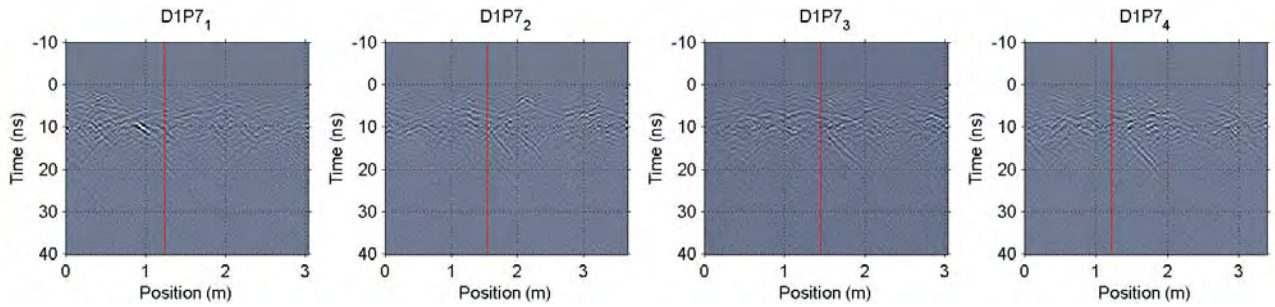


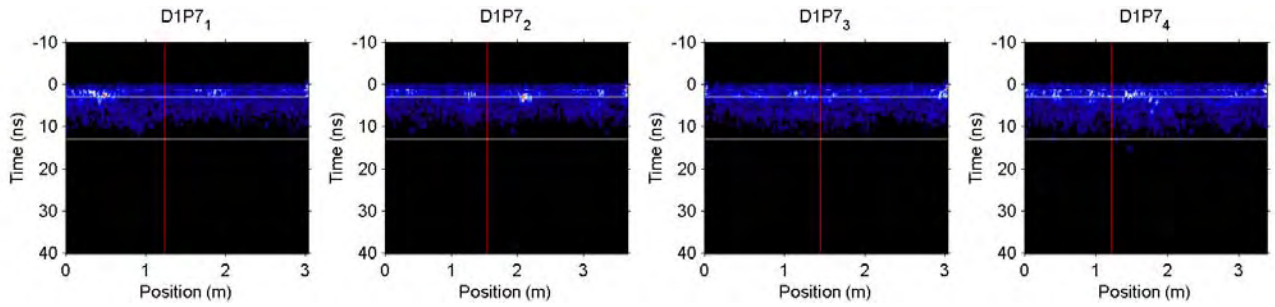


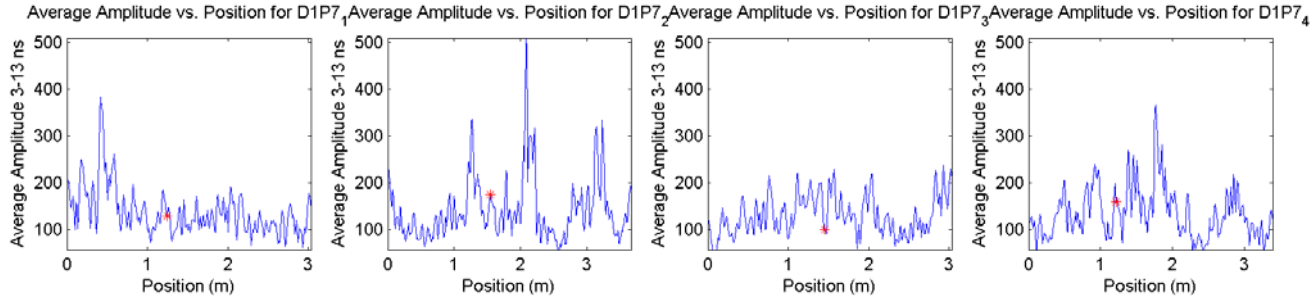

## D.5. 250 MHz adapters and end caps

| | |
|---|---|
| Target Name | G6B1_263 |
| Item Description | Adapter |
| Depth (cm) | 23 |
| Distance From Pin (cm) | 12 |
| Easting (m) | 294391.7 |
| Northing(m) | 3833250.36 |

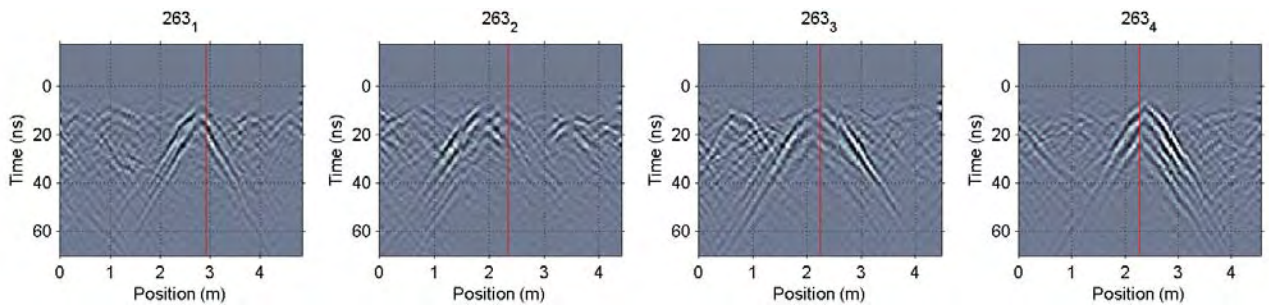


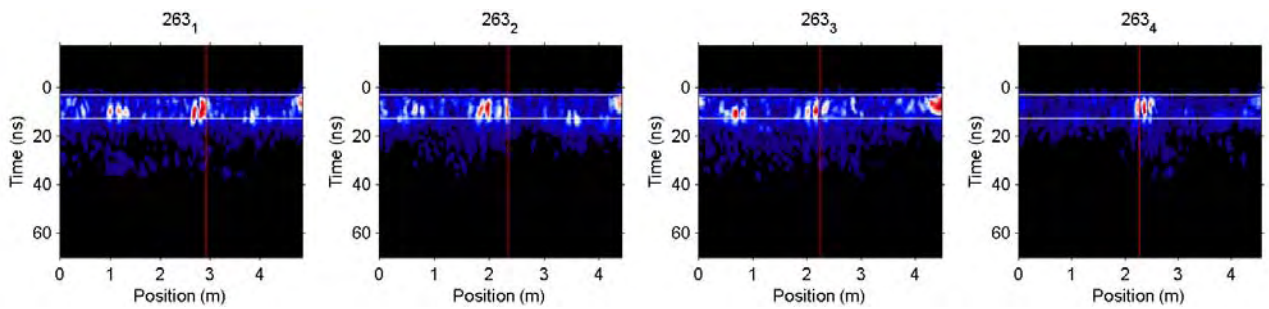


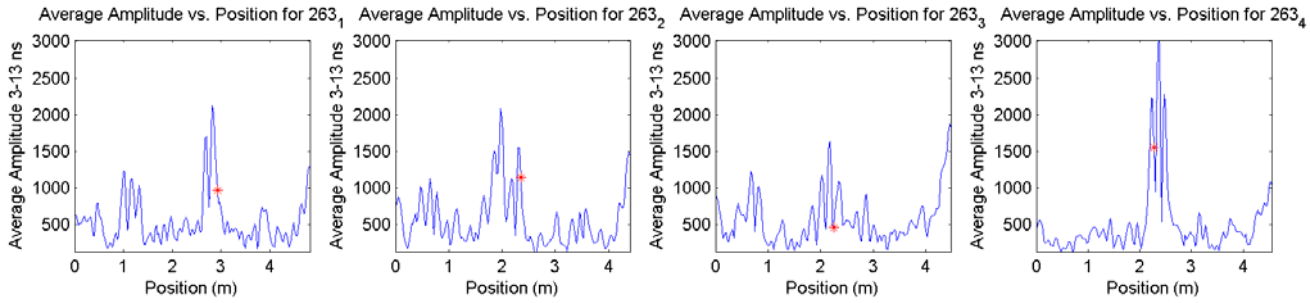

| | |
|---|---|
| Target Name | G6B1_265 |
| Item Description | Adapter |
| Depth (cm) | n/a |
| Distance From Pin (cm) | n/a |
| Easting (m) | 294392.91 |
| Northing(m) | 3833289.27 |

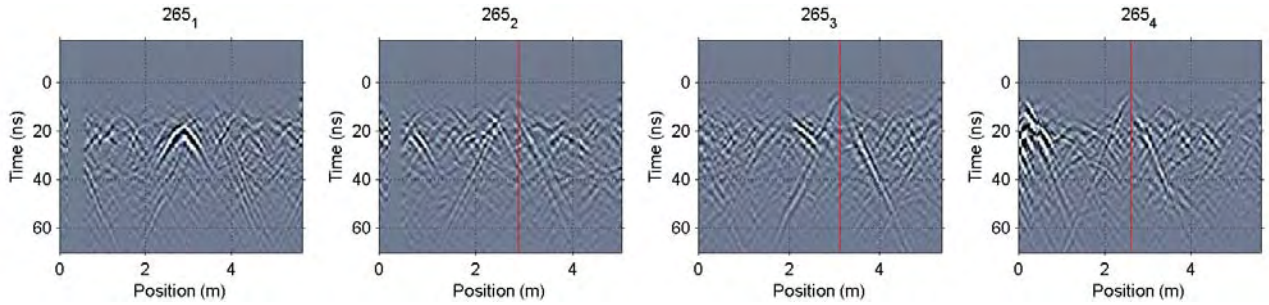


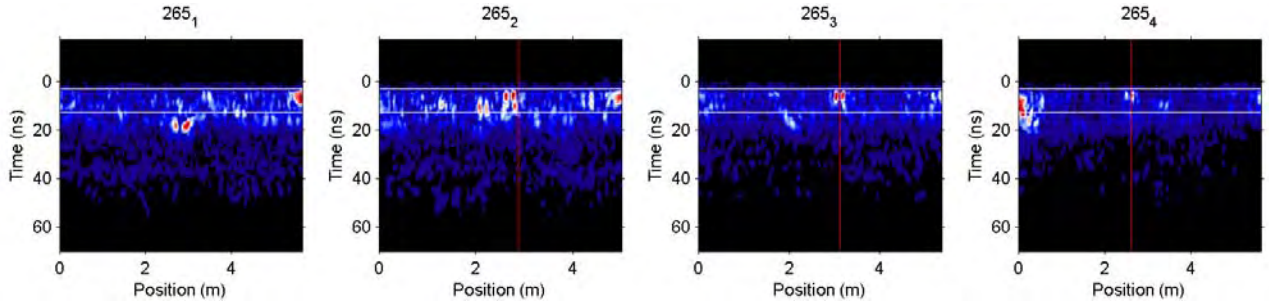


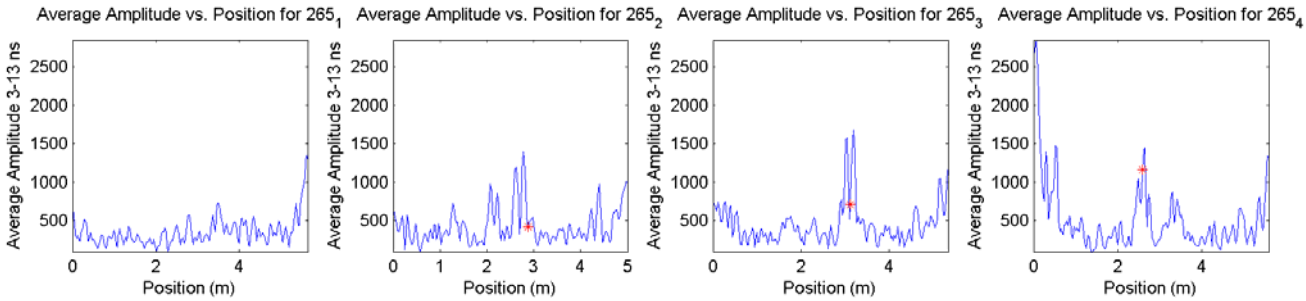

| | |
|---|---|
| Target Name | G6B1_273 |
| Item Description | Adapter |
| Depth (cm) | 14 |
| Distance From Pin (cm) | 12 |
| Easting (m) | 294392.71 |
| Northing(m) | 3833259.60 |

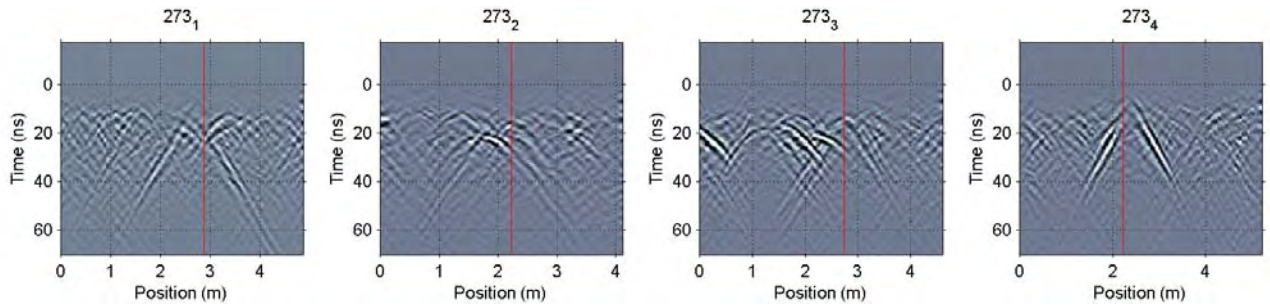


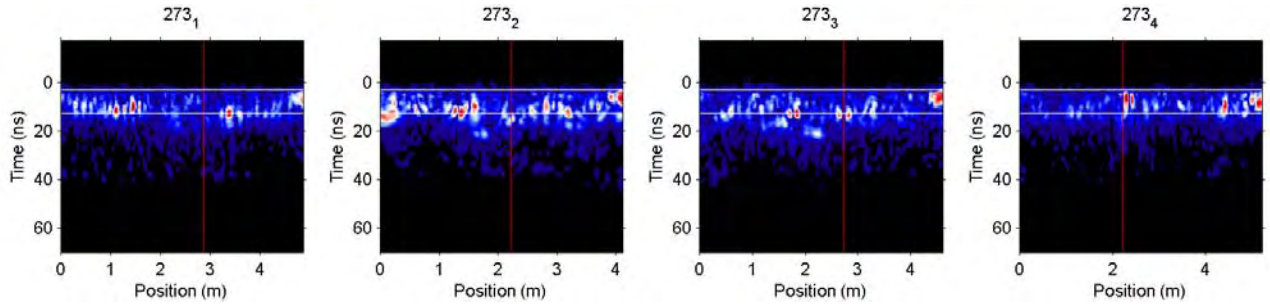


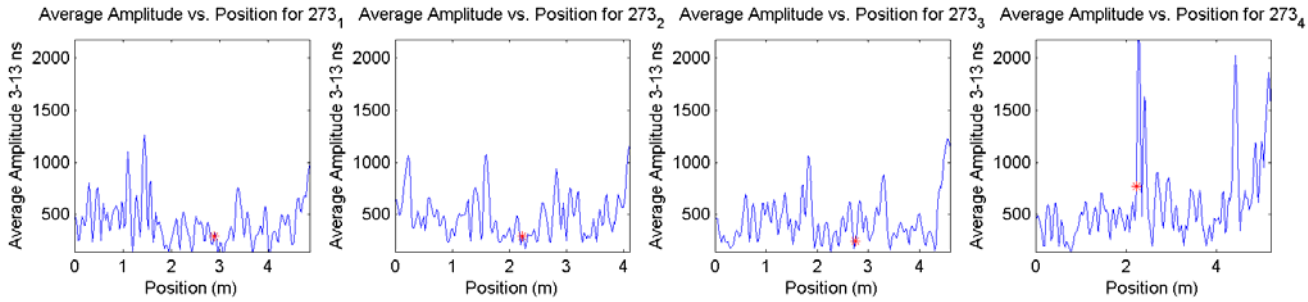

| | |
|---|---|
| Target Name | G6B1_280 |
| Item Description | Adapter |
| Depth (cm) | 8 |
| Distance From Pin (cm) | 15 |
| Easting (m) | 294370.30 |
| Northing(m) | 3833285.60 |

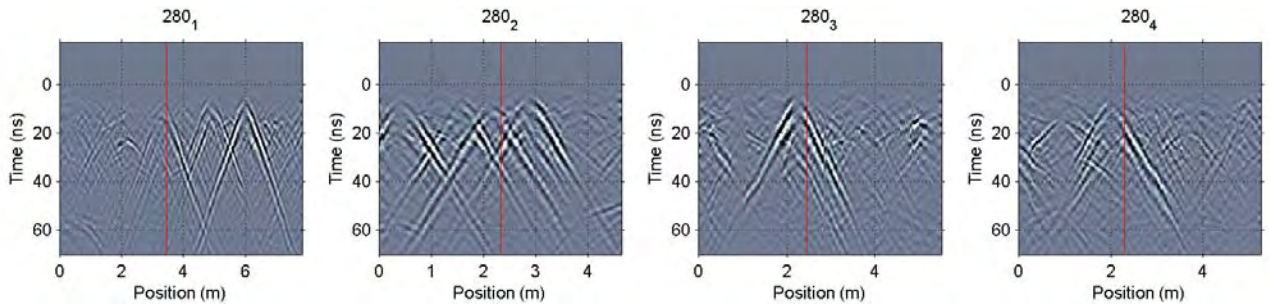


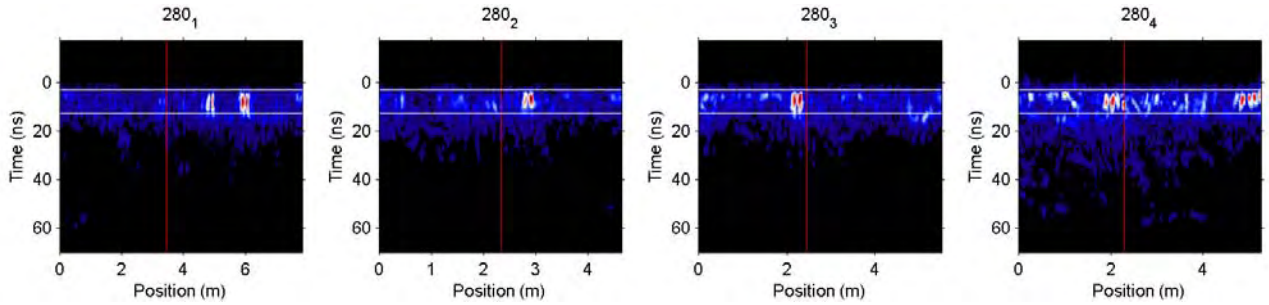


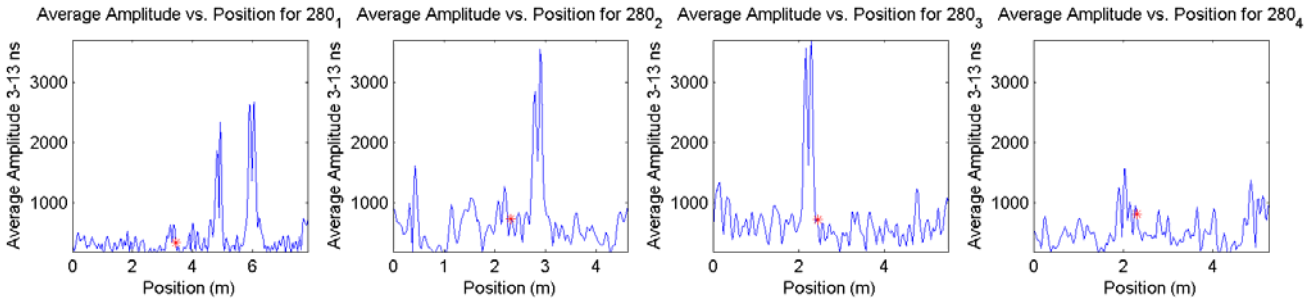

| | |
|---|---|
| Target Name | G6B1_281 |
| Item Description | Adapter |
| Depth (cm) | 0 |
| Distance From Pin (cm) | 36 |
| Easting (m) | 294402.38 |
| Northing(m) | 3833247.51 |

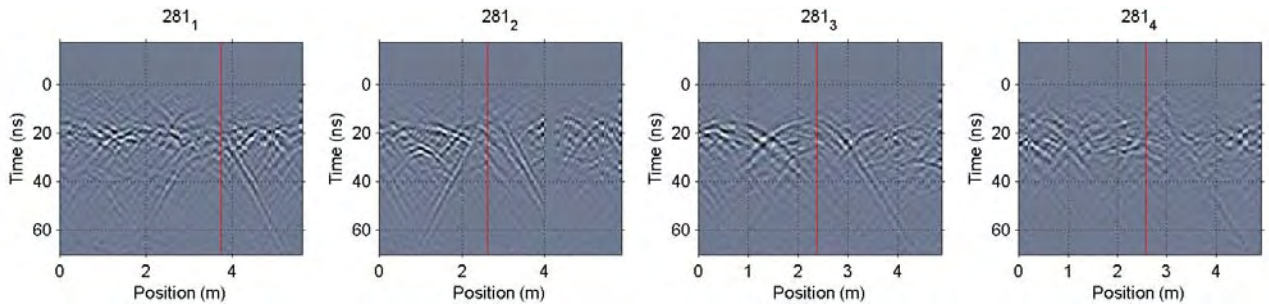


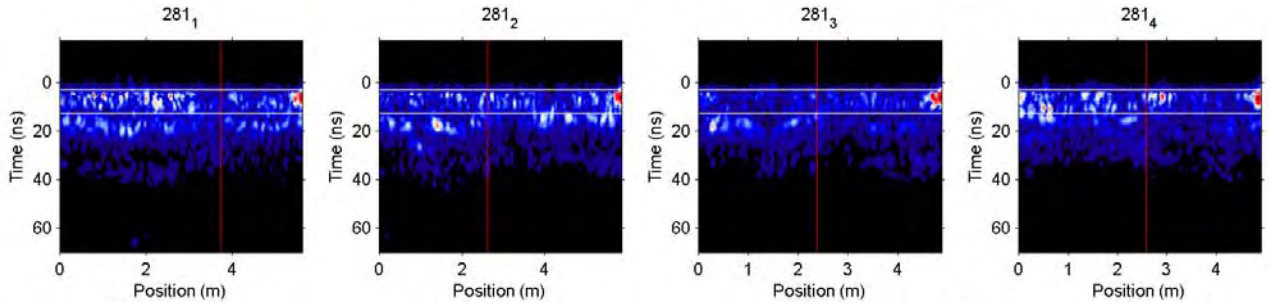


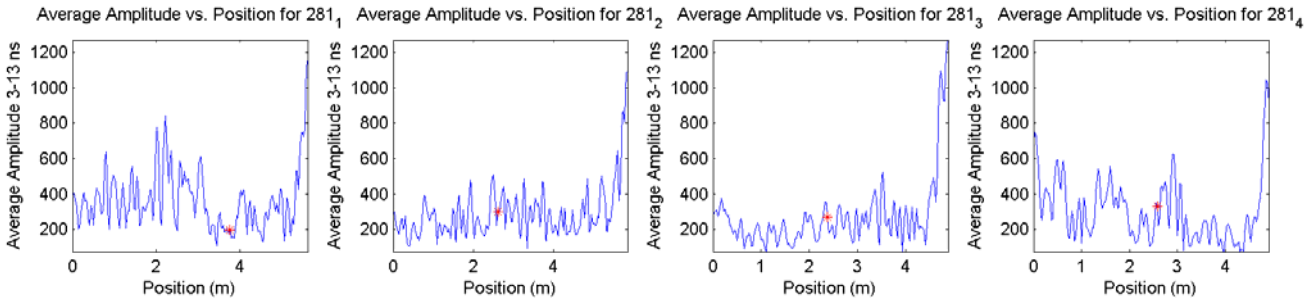

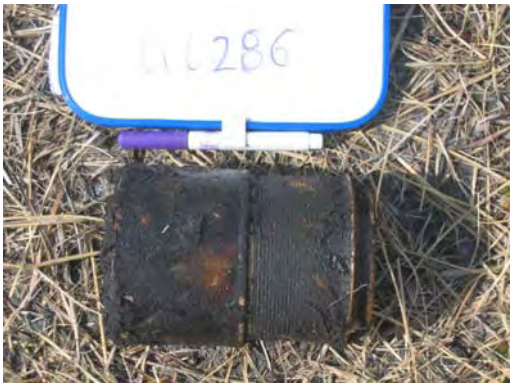

| | |
|---|---|
| Target Name | G6B1_286 |
| Item Description | Adapter |
| Depth (cm) | 16 |
| Distance From Pin (cm) | 0 |
| Easting (m) | 294370.01 |
| Northing(m) | 3833288.27 |

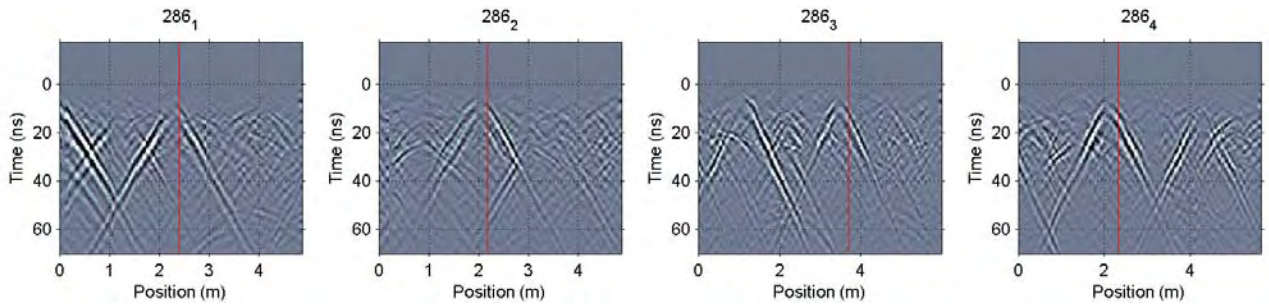


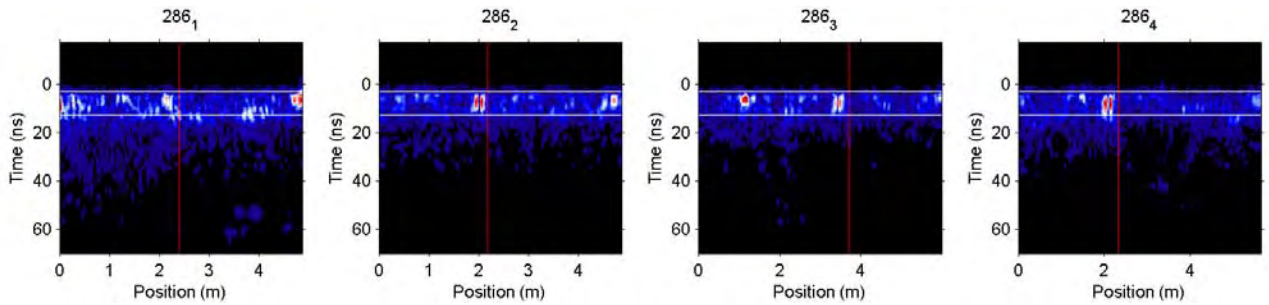


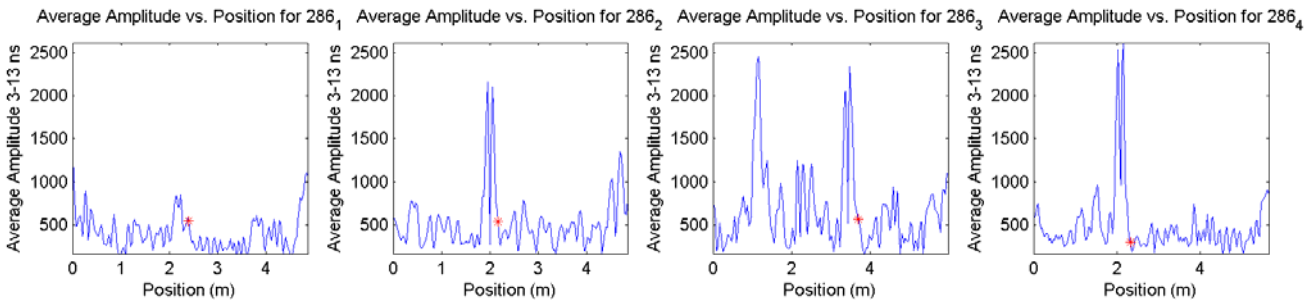

| | |
|---|---|
| Target Name | G6B1_290 |
| Item Description | Adapter |
| Depth (cm) | 7 |
| Distance From Pin (cm) | 25 |
| Easting (m) | 294397.64 |
| Northing(m) | 3833251.80 |

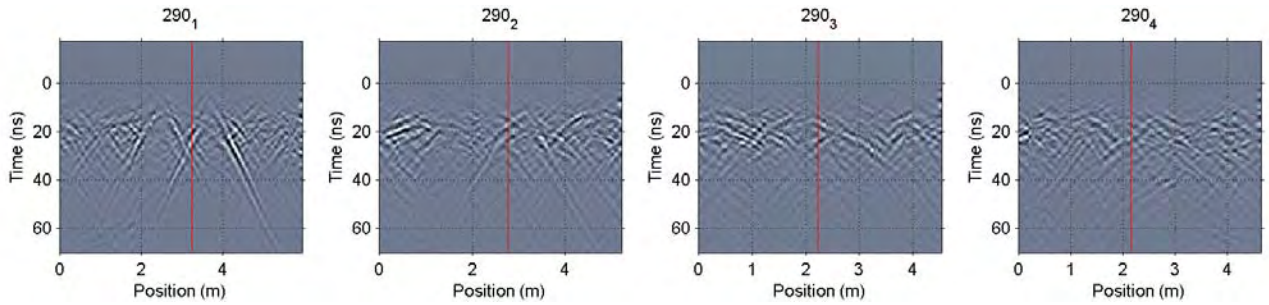


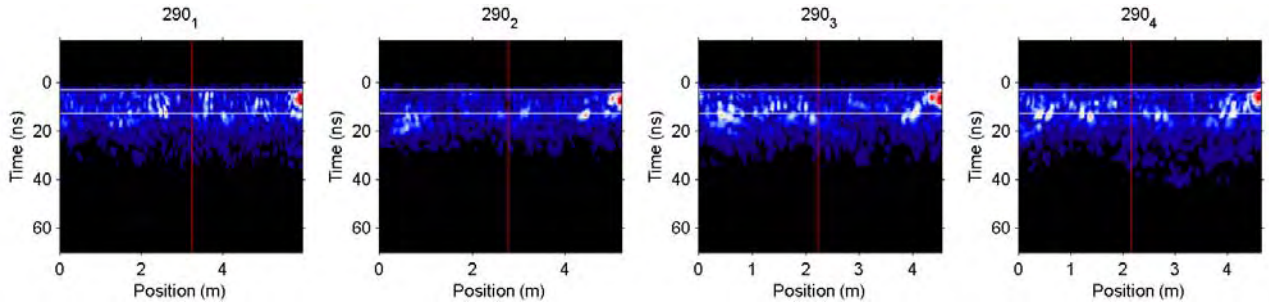


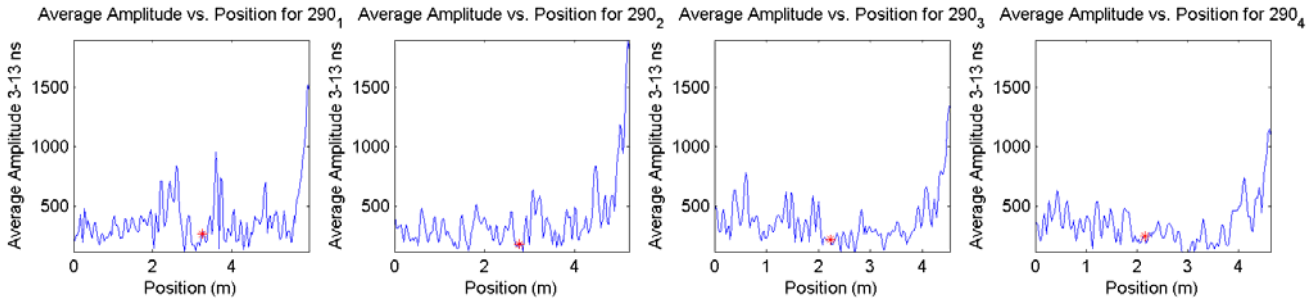

| | |
|---|---|
| Target Name | G6B1_292 |
| Item Description | Adapter |
| Depth (cm) | 13 |
| Distance From Pin (cm) | 15 |
| Easting (m) | 294406.79 |
| Northing(m) | 3833273.09 |

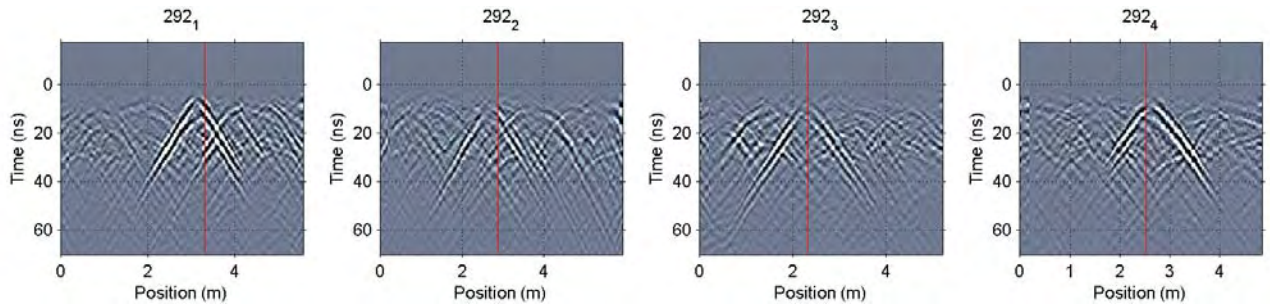


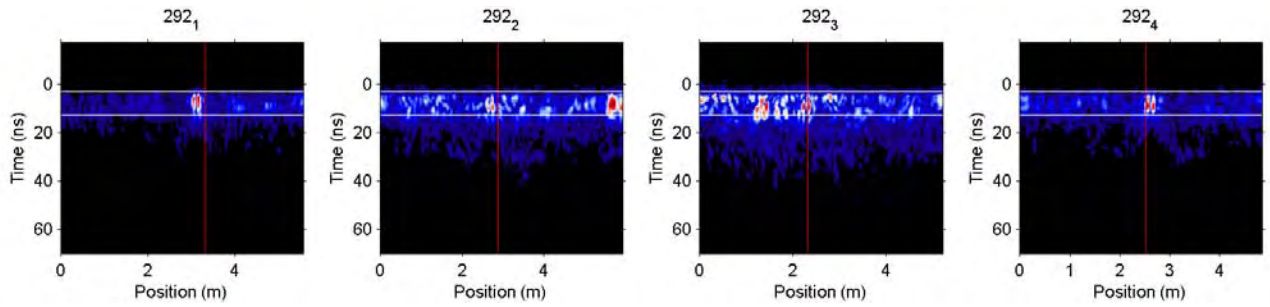


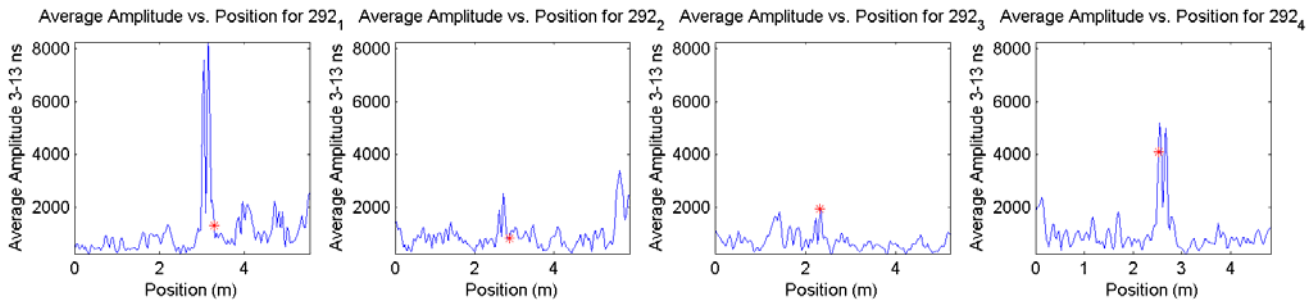

| | |
|---|---|
| Target Name | G6B1_294 |
| Item Description | Adapter |
| Depth (cm) | 8 |
| Distance From Pin (cm) | 12 |
| Easting (m) | 294391.57 |
| Northing(m) | 3833292.24 |

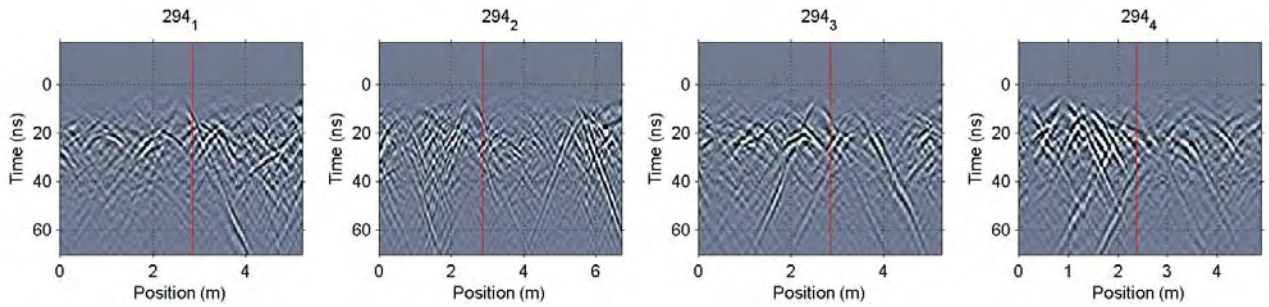


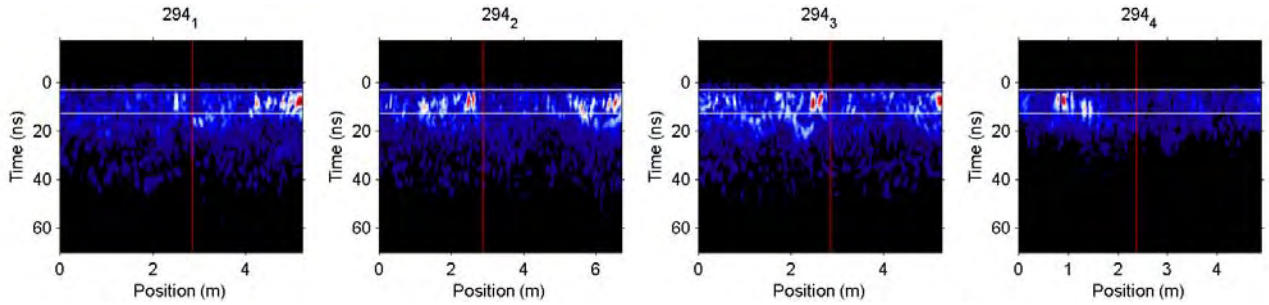


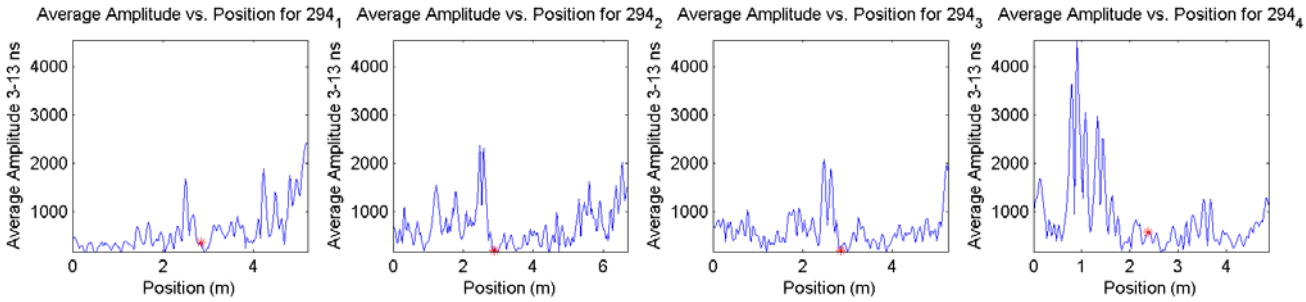

| | |
|---|---|
| Target Name | G6B1_295 |
| Item Description | Adapter |
| Depth (cm) | 6 |
| Distance From Pin (cm) | 5 |
| Easting (m) | 294387.42 |
| Northing(m) | 3833251.61 |

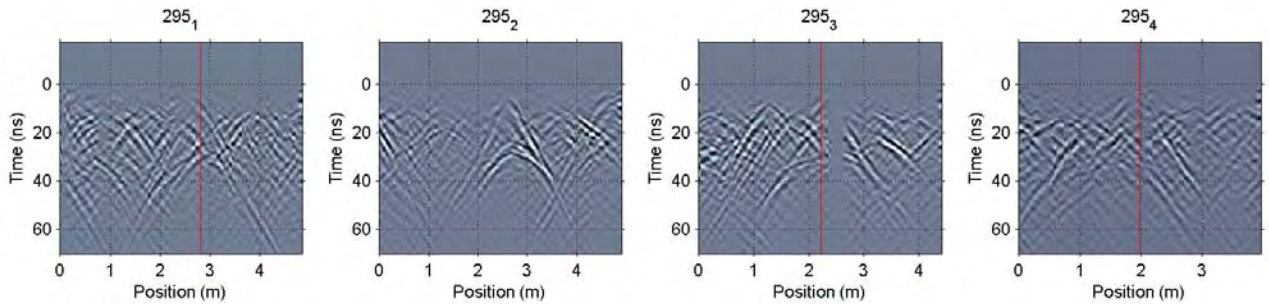


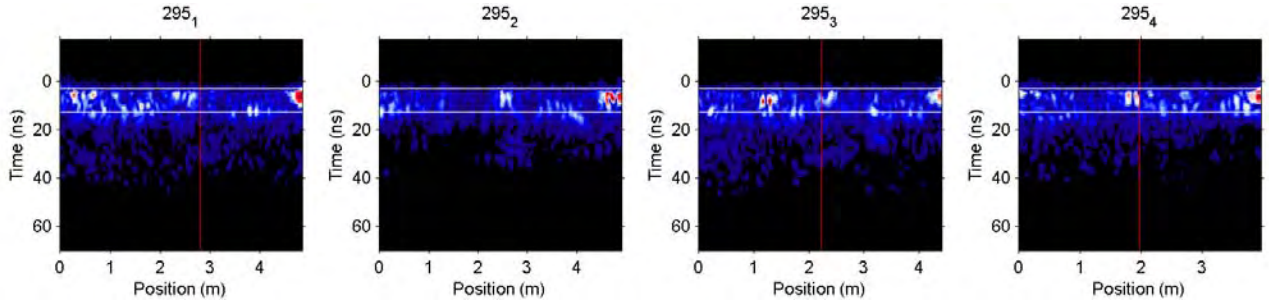


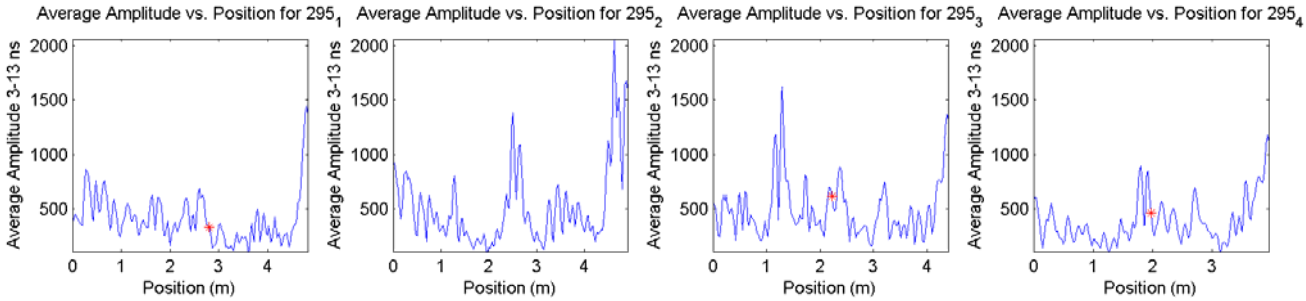

| | |
|---|---|
| Target Name | G6B1_300 |
| Item Description | Adapter |
| Depth (cm) | 8 |
| Distance From Pin (cm) | 15 |
| Easting (m) | 294399.24 |
| Northing(m) | 3833273.65 |

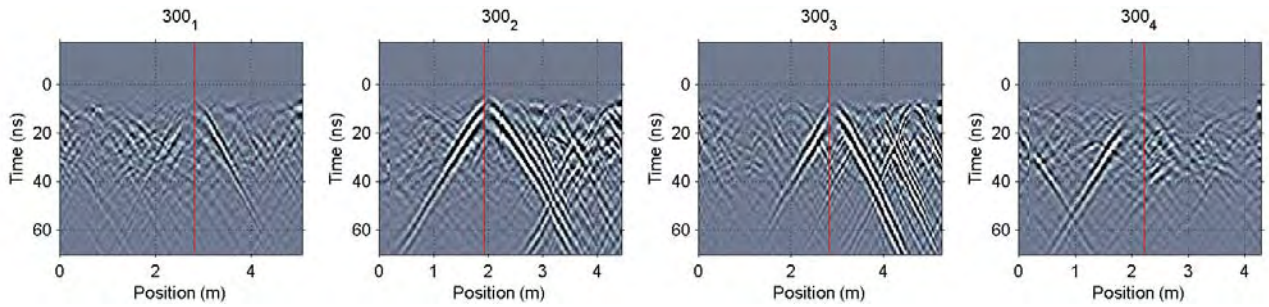


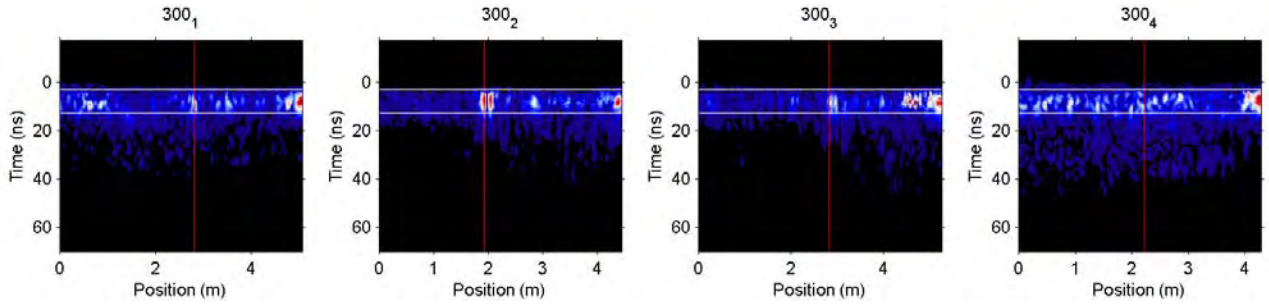


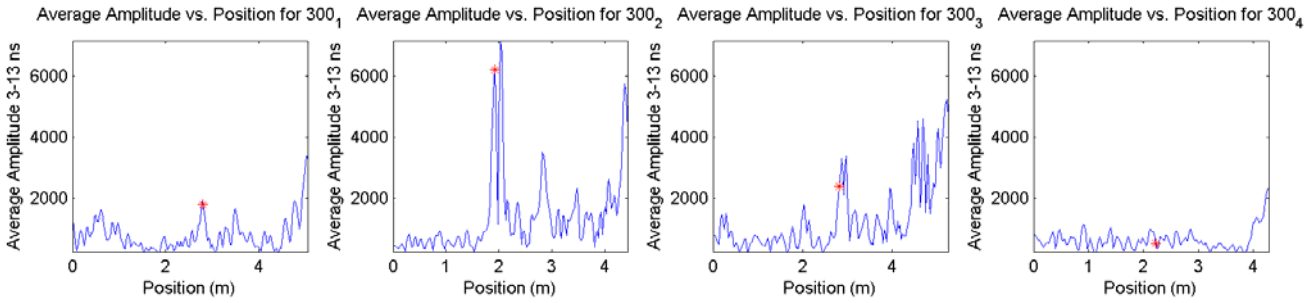

| | |
|---|---|
| Target Name | G6B1_303 |
| Item Description | Adapter |
| Depth (cm) | 10 |
| Distance From Pin (cm) | 30 |
| Easting (m) | 294394.44 |
| Northing(m) | 3833266.56 |

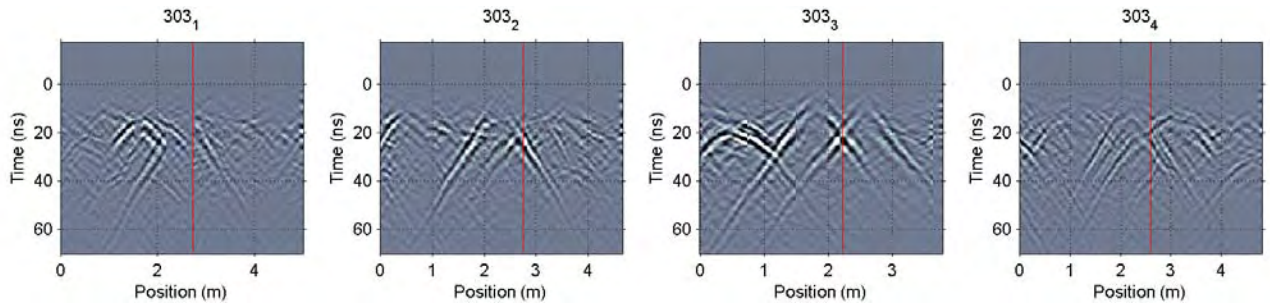


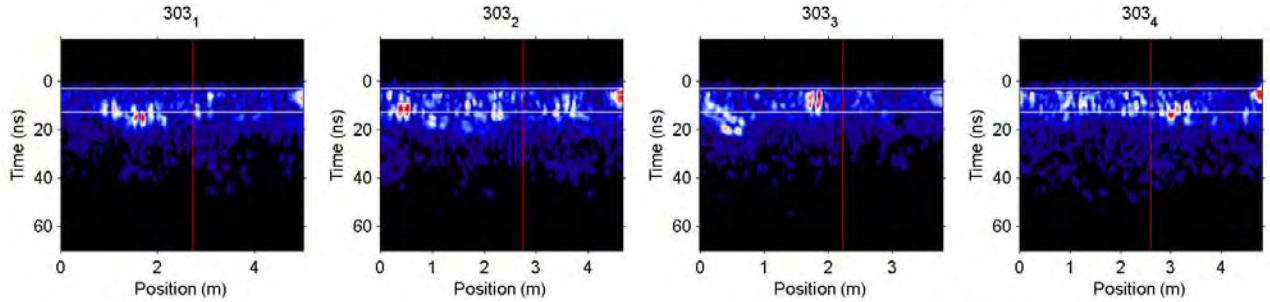


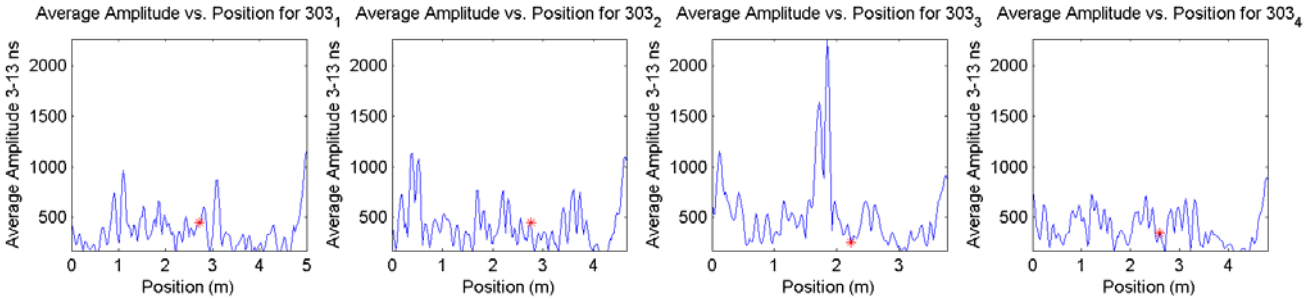

| | |
|---|---|
| Target Name | G6B1_311 |
| Item Description | Adapter |
| Depth (cm) | 8 |
| Distance From Pin (cm) | 12 |
| Easting (m) | 294393.20 |
| Northing(m) | 3833286.96 |

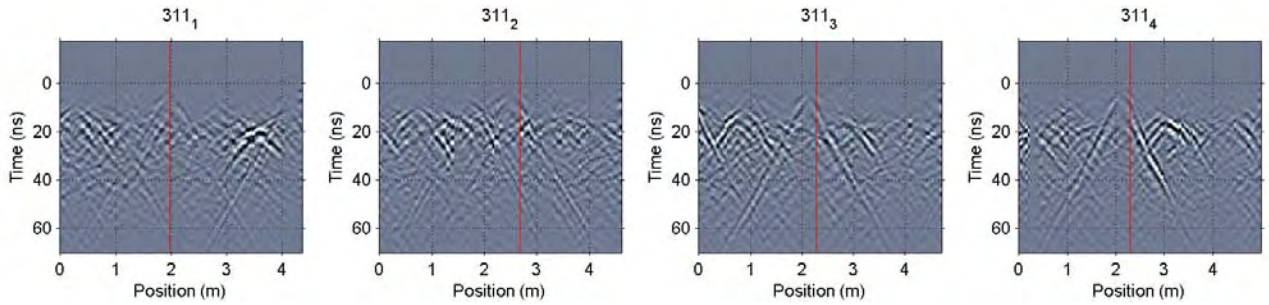


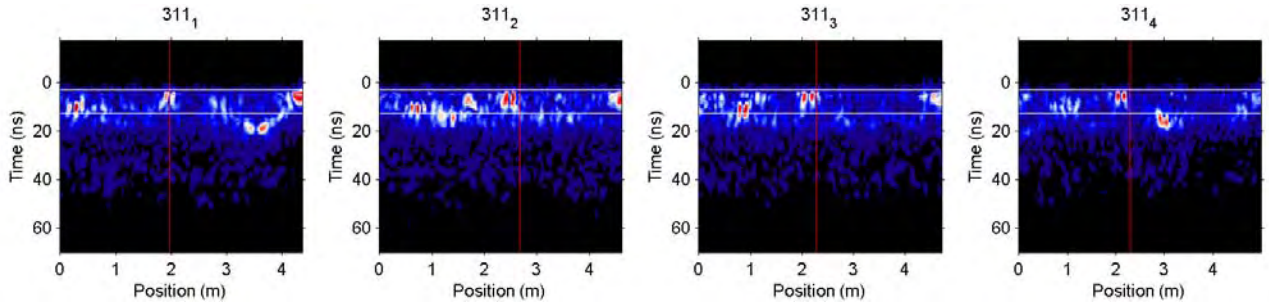


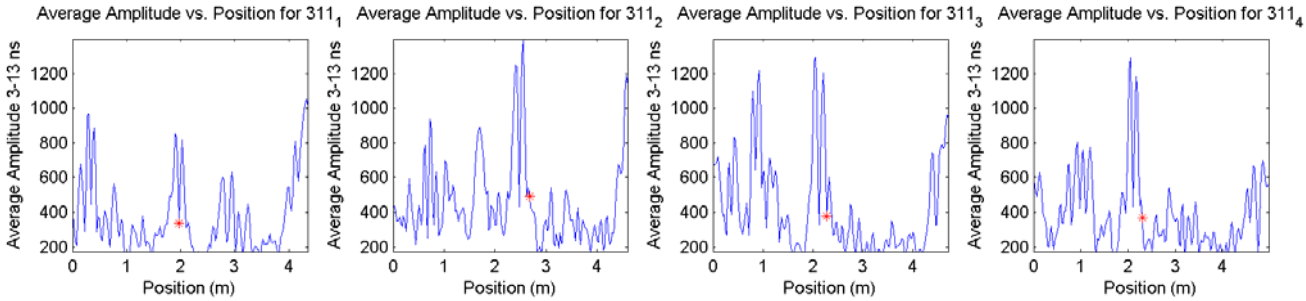

| | |
|---|---|
| Target Name | G6B1_314 |
| Item Description | Adapter |
| Depth (cm) | 10 |
| Distance From Pin (cm) | 24 |
| Easting (m) | 294386.73 |
| Northing(m) | 3833251.63 |

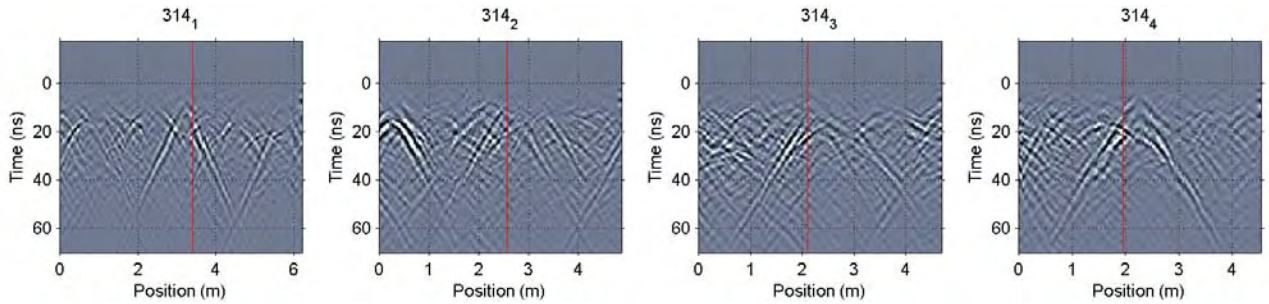


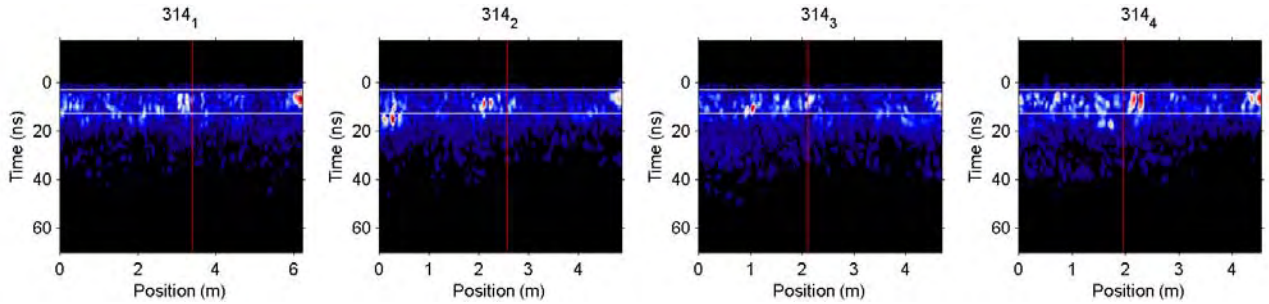


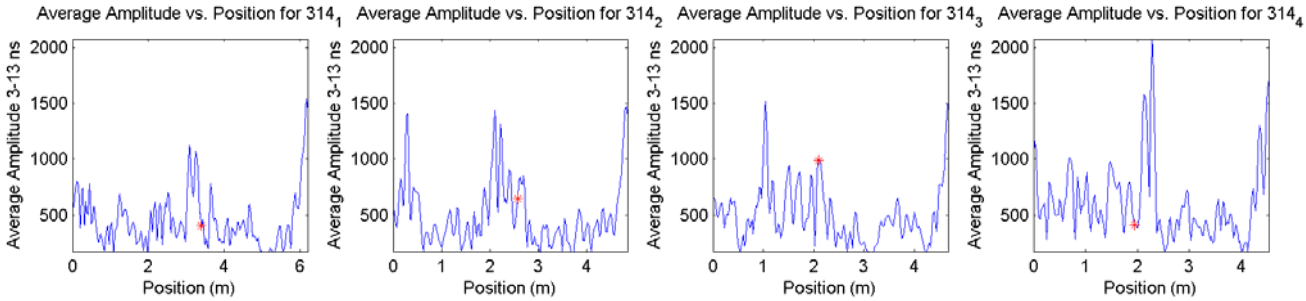

| | |
|---|---|
| Target Name | G6B1_319 |
| Item Description | Adapter |
| Depth (cm) | 0 |
| Distance From Pin (cm) | 30 |
| Easting (m) | 294396.60 |
| Northing(m) | 3833245.92 |

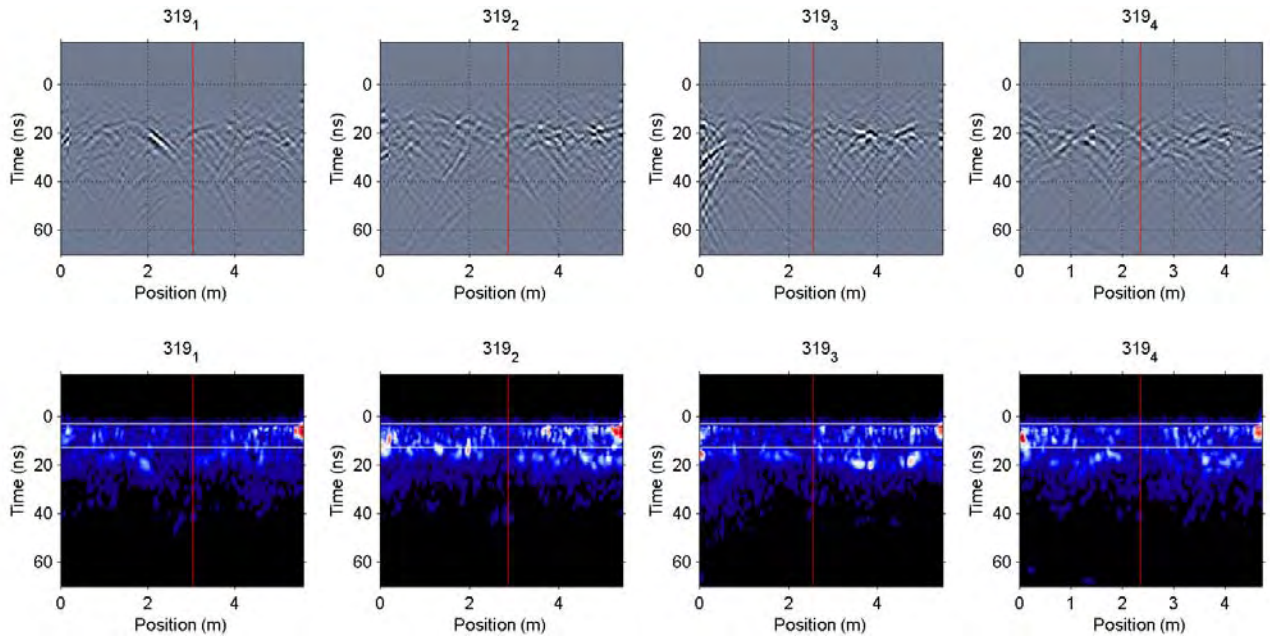


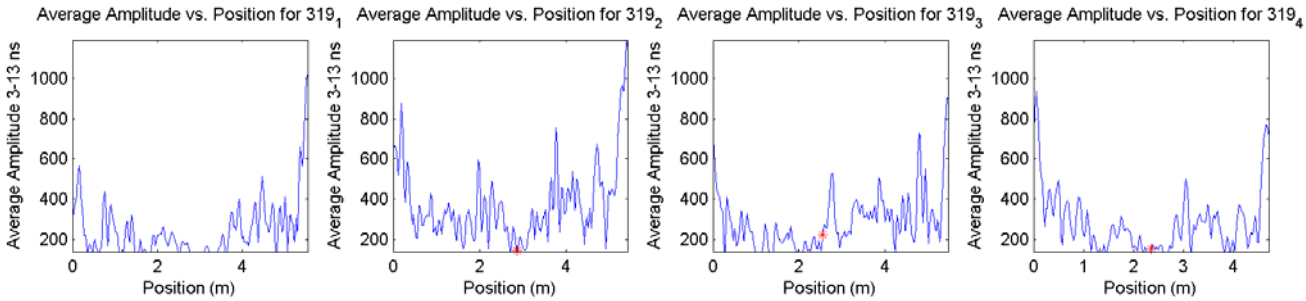

| | |
|---|---|
| Target Name | G6B1_321 |
| Item Description | Adapter |
| Depth (cm) | 18 |
| Distance From Pin (cm) | 13 |
| Easting (m) | 294396.89 |
| Northing(m) | 3833273.60 |

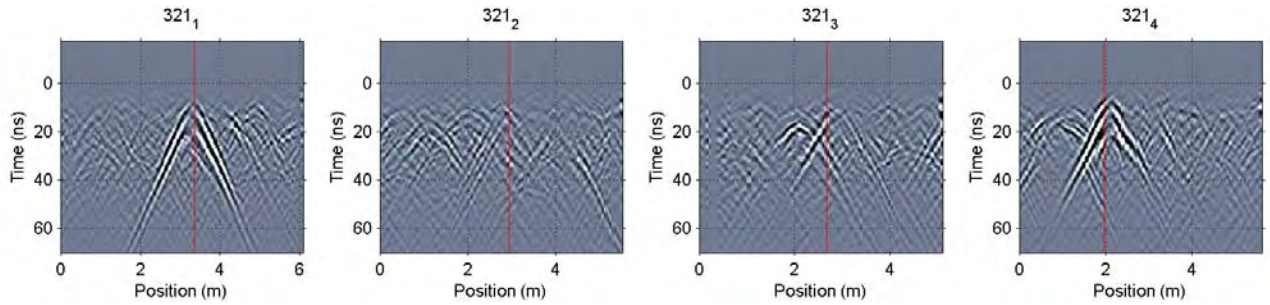


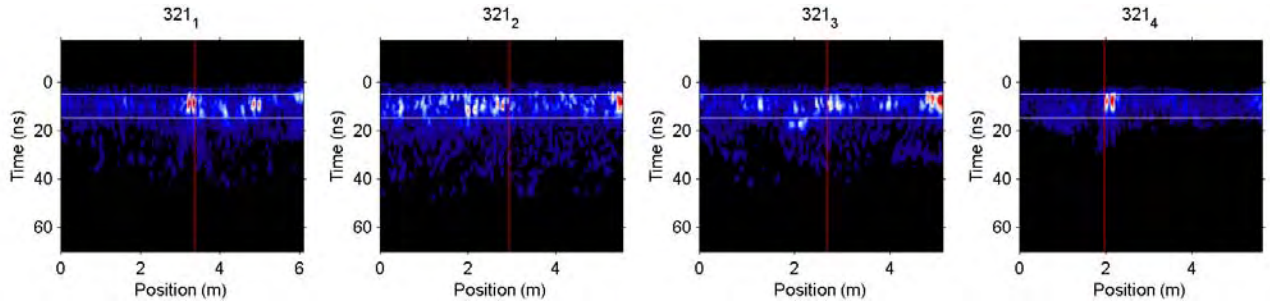


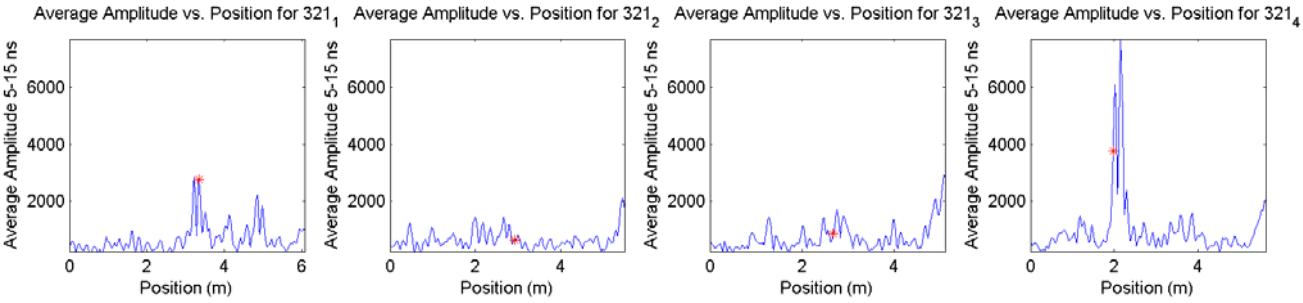

| | |
|---|---|
| Target Name | G6B1_322 |
| Item Description | Adapter |
| Depth (cm) | 5 |
| Distance From Pin (cm) | 2 |
| Easting (m) | 294400.59 |
| Northing(m) | 3833284.65 |

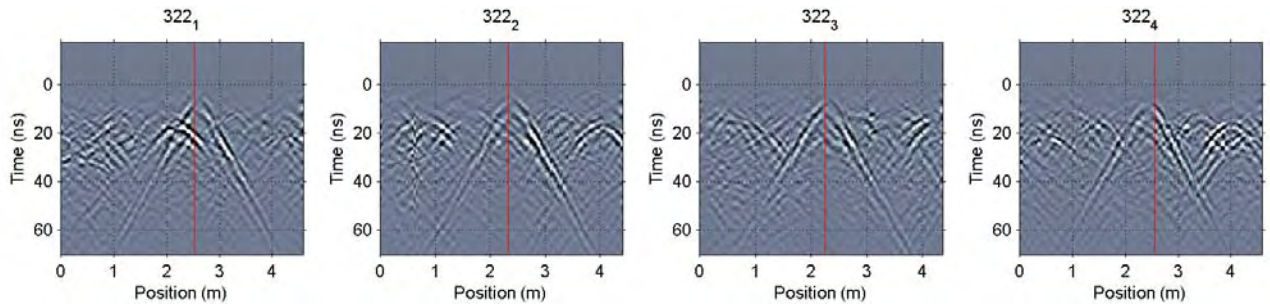


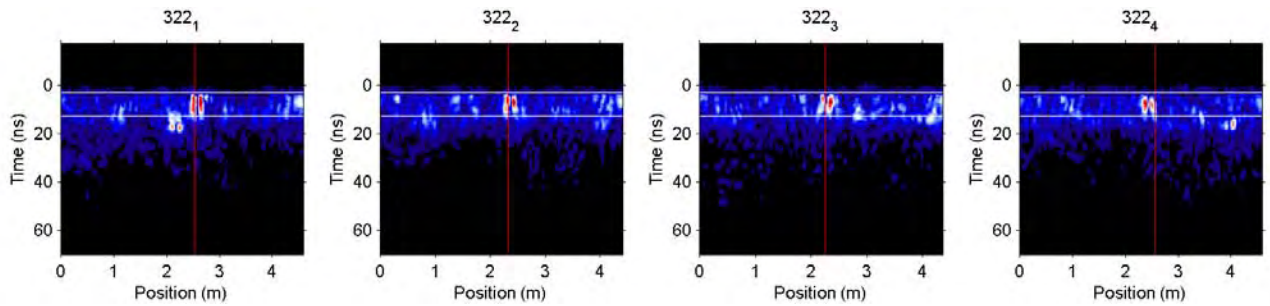


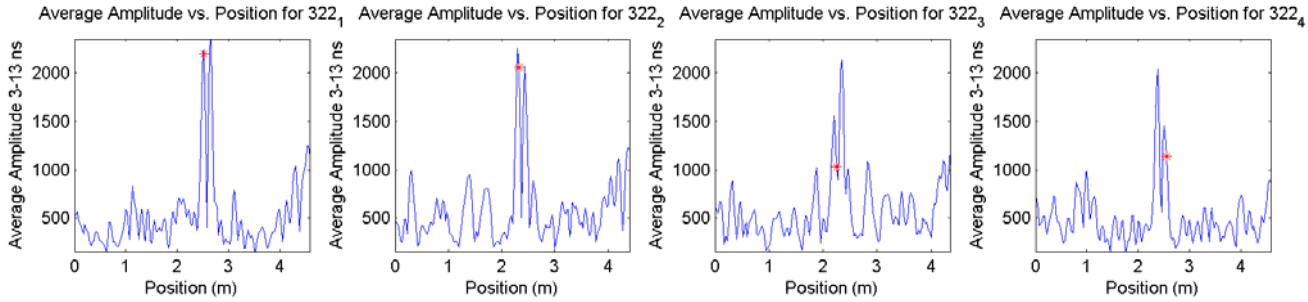

| | |
|---|---|
| Target Name | G6B1_325 |
| Item Description | Adapter |
| Depth (cm) | 13 |
| Distance From Pin (cm) | 0 |
| Easting (m) | 294392.85 |
| Northing(m) | 3833248.23 |

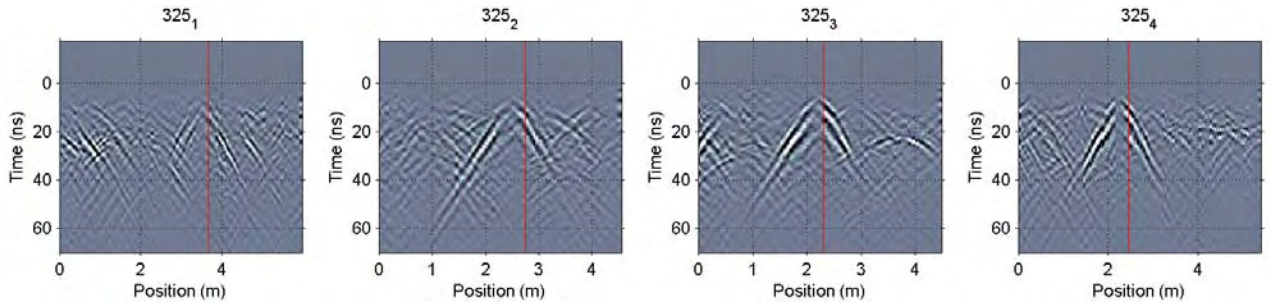


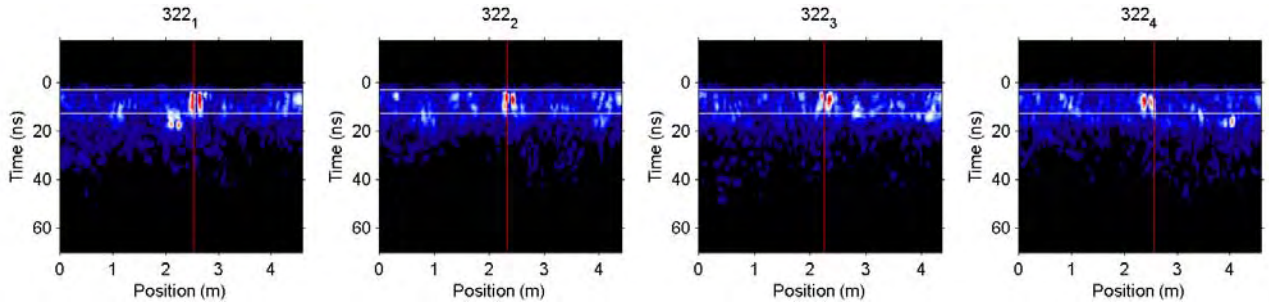


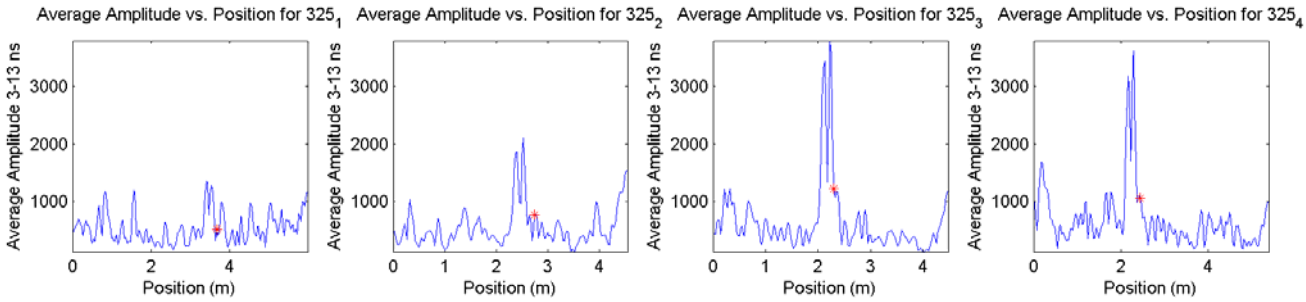

| | |
|---|---|
| Target Name | G6B1_326 |
| Item Description | Adapter |
| Depth (cm) | 0 |
| Distance From Pin (cm) | 6 |
| Easting (m) | 294389.46 |
| Northing(m) | 3833264.84 |

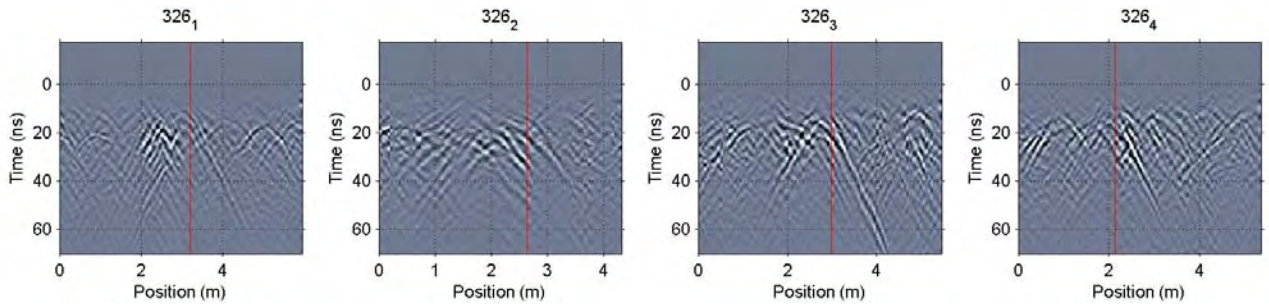


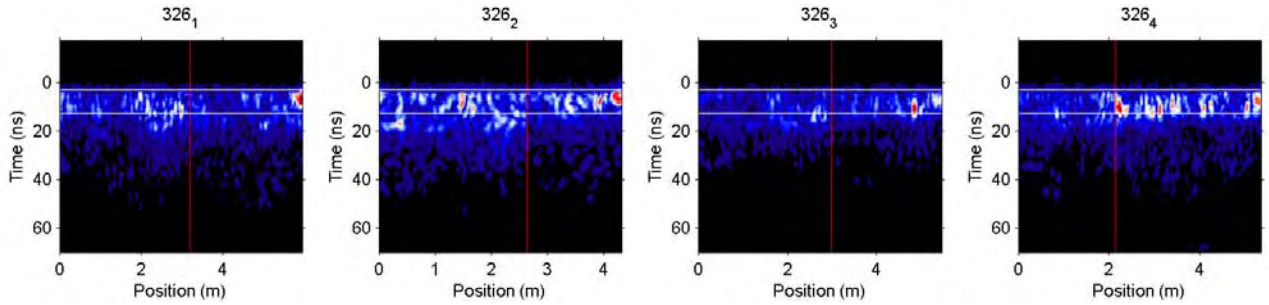


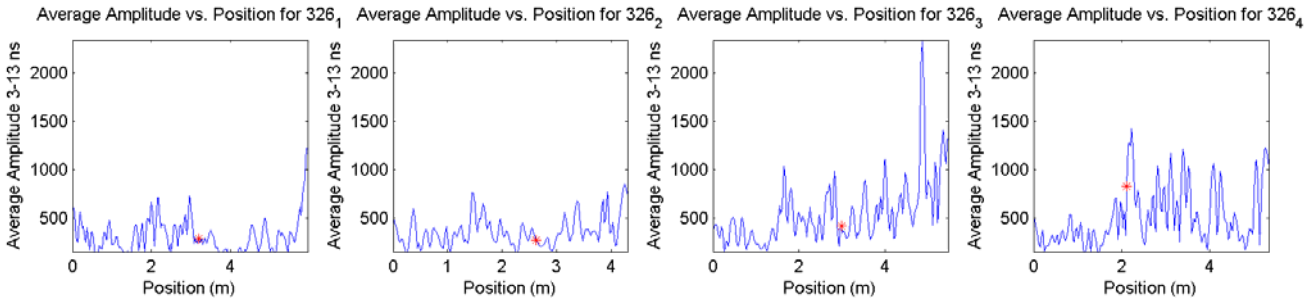

| | |
|---|---|
| Target Name | G6B1_332 |
| Item Description | Adapter |
| Depth (cm) | 14 |
| Distance From Pin (cm) | 3 |
| Easting (m) | 294386.98 |
| Northing(m) | 3833244.06 |

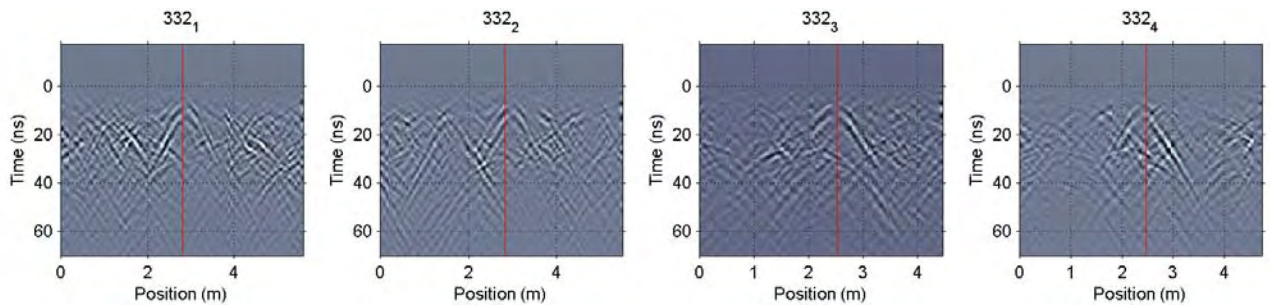


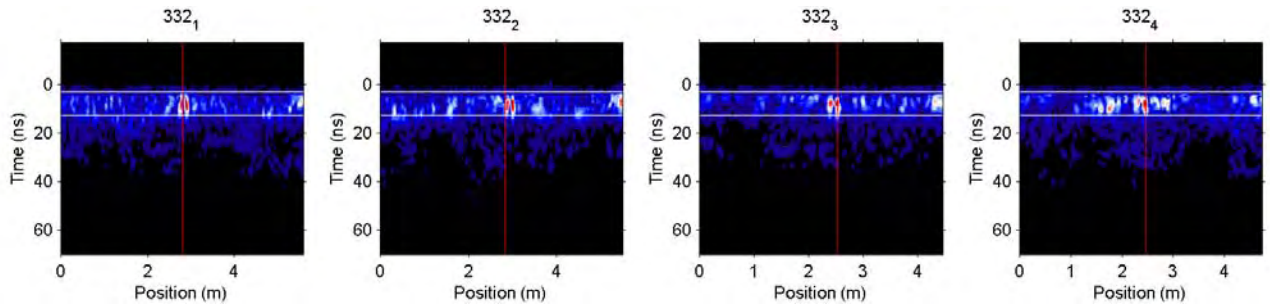


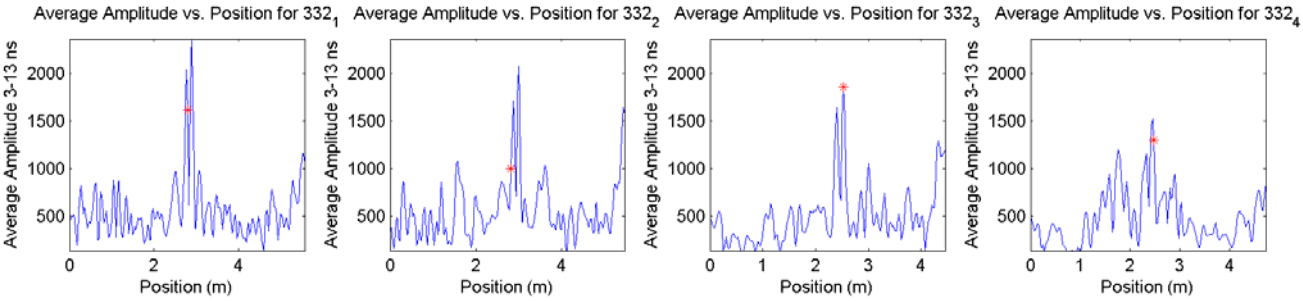

| | |
|---|---|
| Target Name | G6B1_340 |
| Item Description | Adapter |
| Depth (cm) | 10 |
| Distance From Pin (cm) | 10 |
| Easting (m) | 294396.24 |
| Northing(m) | 3833247.59 |

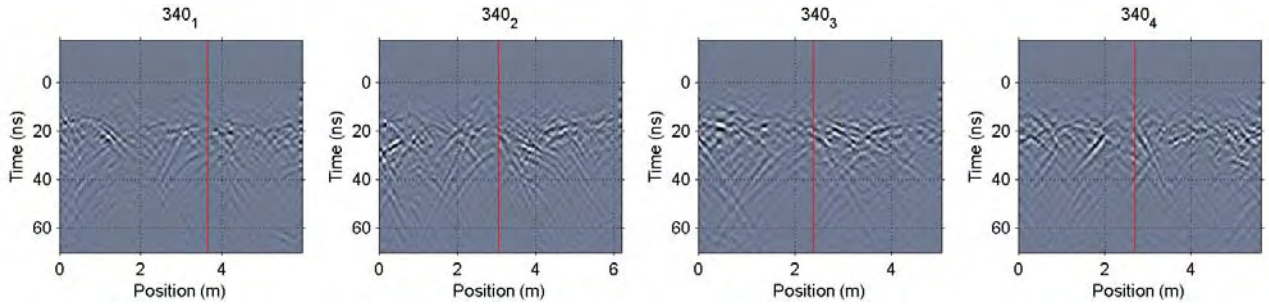


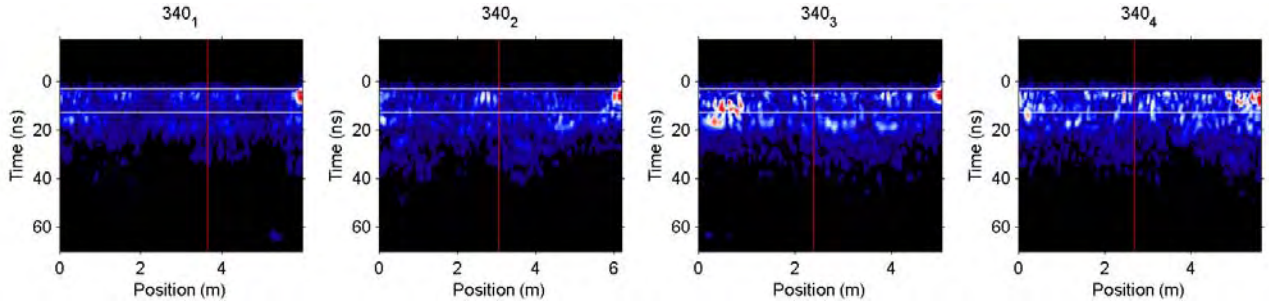


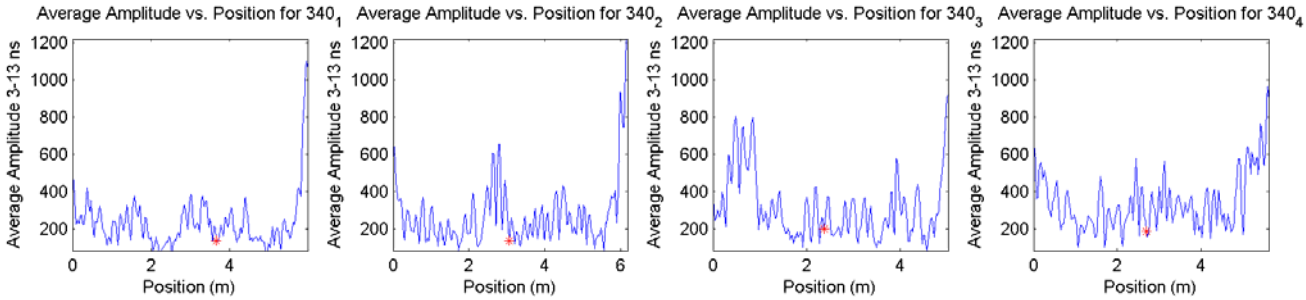

| | |
|---|---|
| Target Name | G6B1_342 |
| Item Description | Adapter |
| Depth (cm) | 23 |
| Distance From Pin (cm) | 12 |
| Easting (m) | 294391.7 |
| Northing(m) | 3833250.36 |

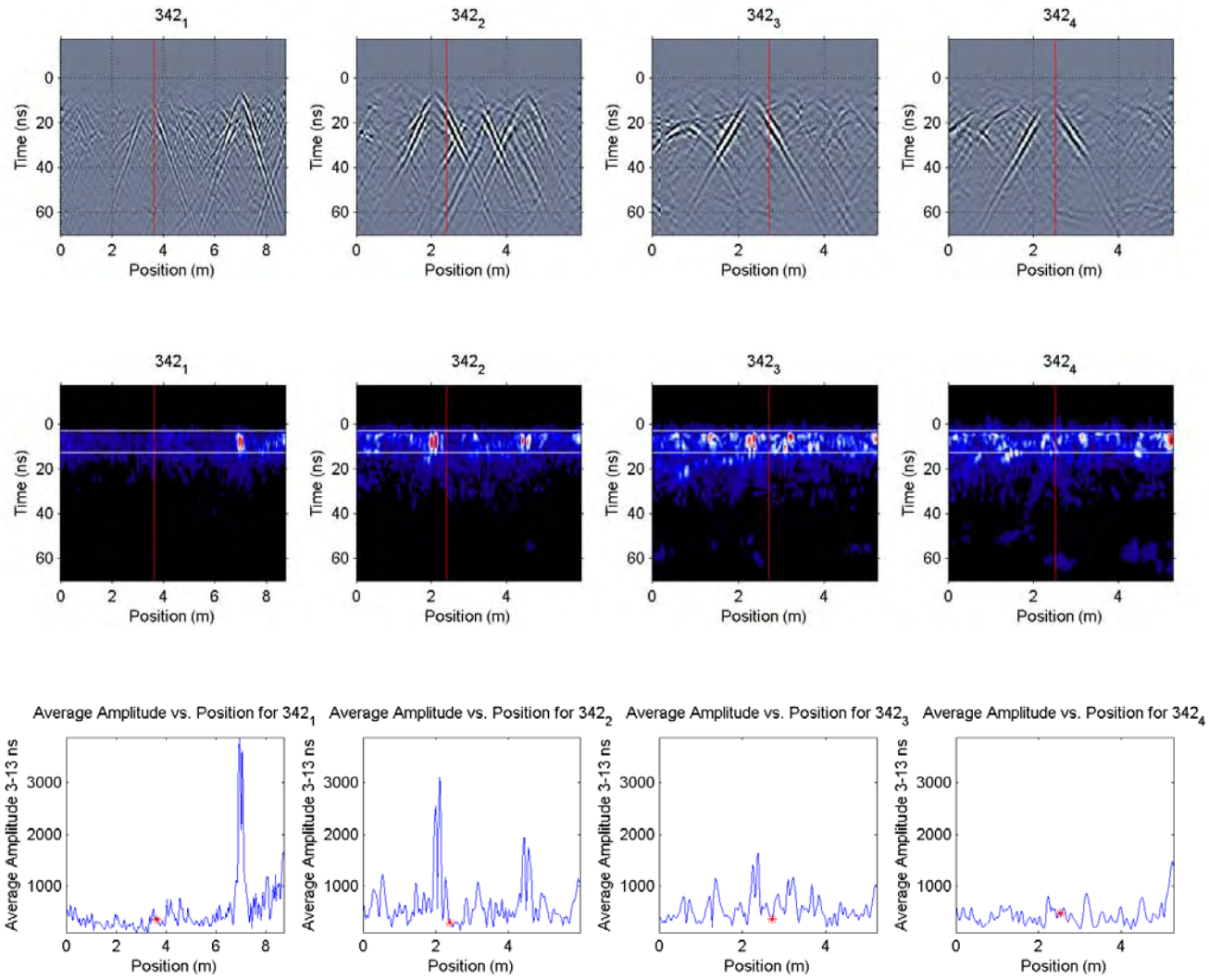

| | |
|---|---|
| Target Name | G6B1_343 |
| Item Description | Adapter |
| Depth (cm) | 27 |
| Distance From Pin (cm) | 20 |
| Easting (m) | 294377.05 |
| Northing(m) | 3833247.74 |

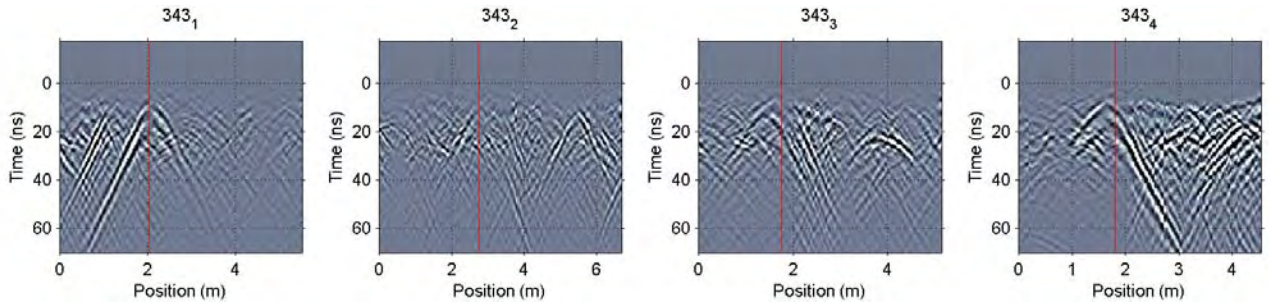


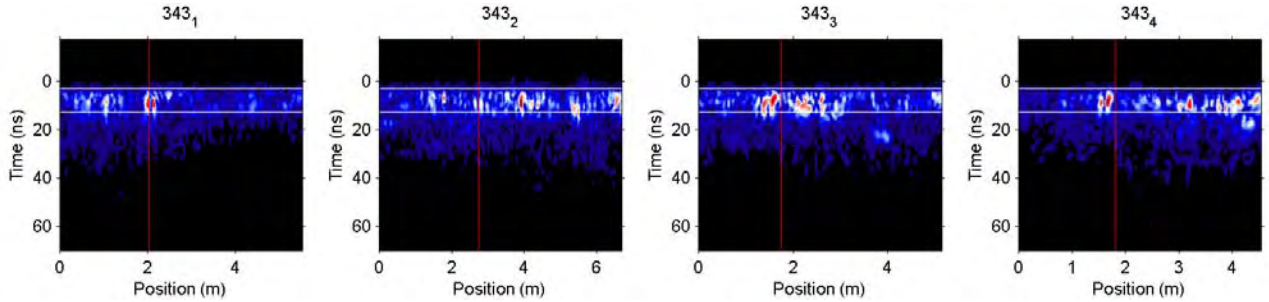


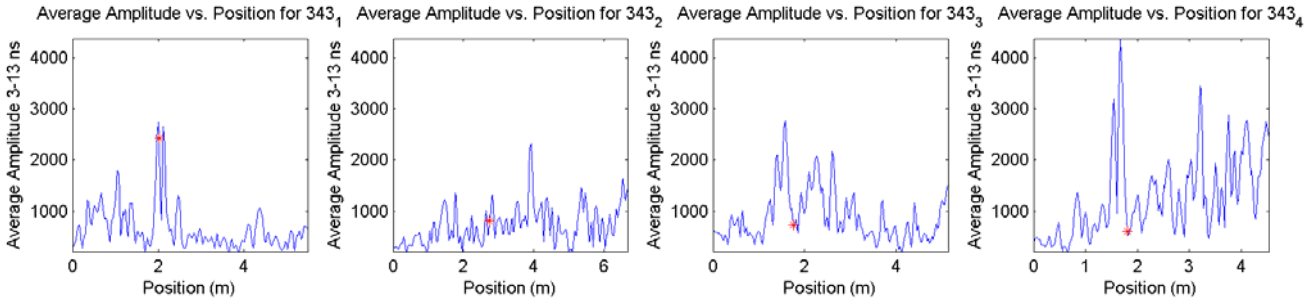

| | |
|---|---|
| Target Name | G6B1_349 |
| Item Description | Adapter |
| Depth (cm) | 25 |
| Distance From Pin (cm) | 15 |
| Easting (m) | 294387.84 |
| Northing(m) | 3833248.33 |

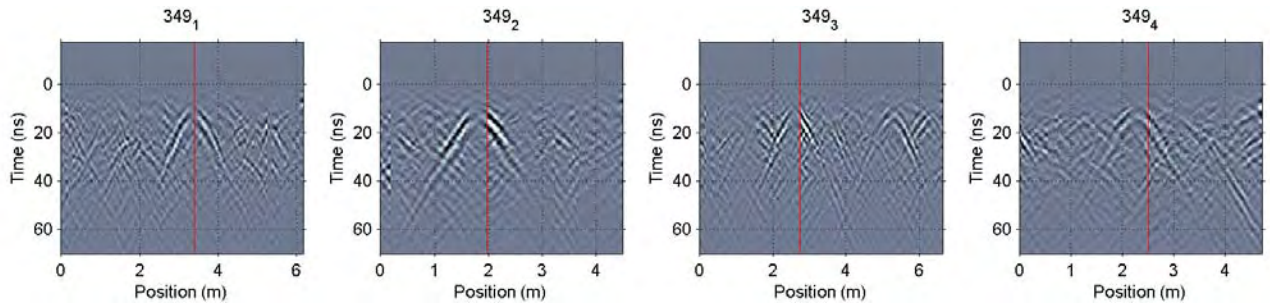


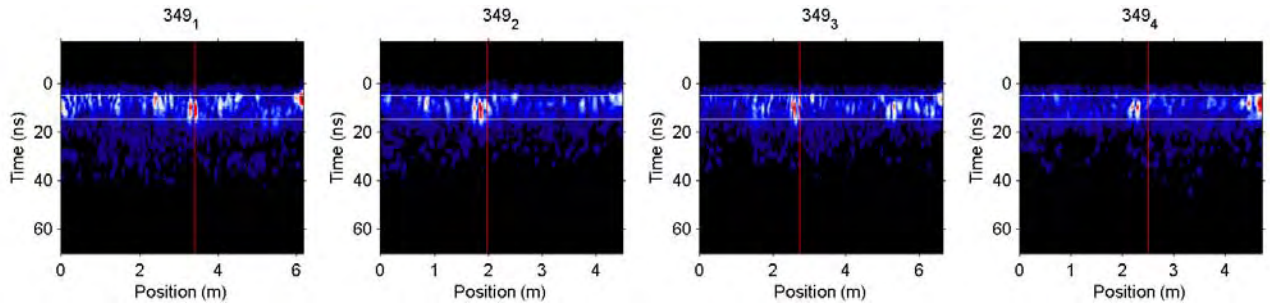


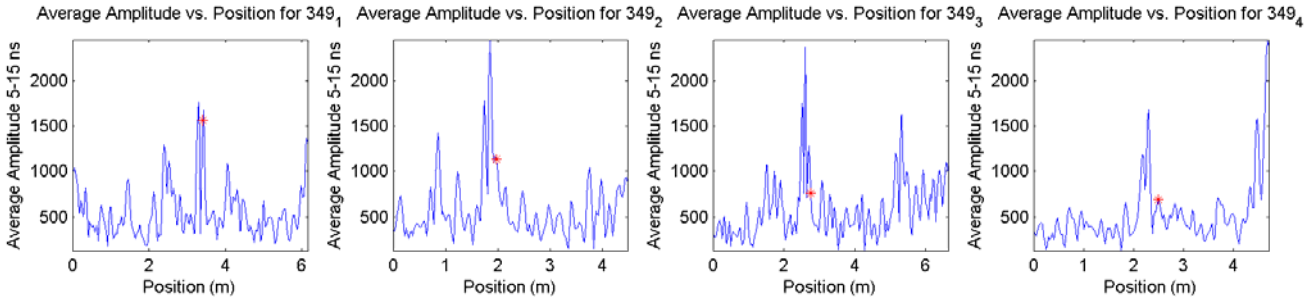

| | |
|---|---|
| Target Name | G6B2_298 |
| Item Description | Adapter |
| Depth (cm) | 10 |
| Distance From Pin (cm) | 30 |
| Easting (m) | 294456.31 |
| Northing(m) | 3833256.58 |

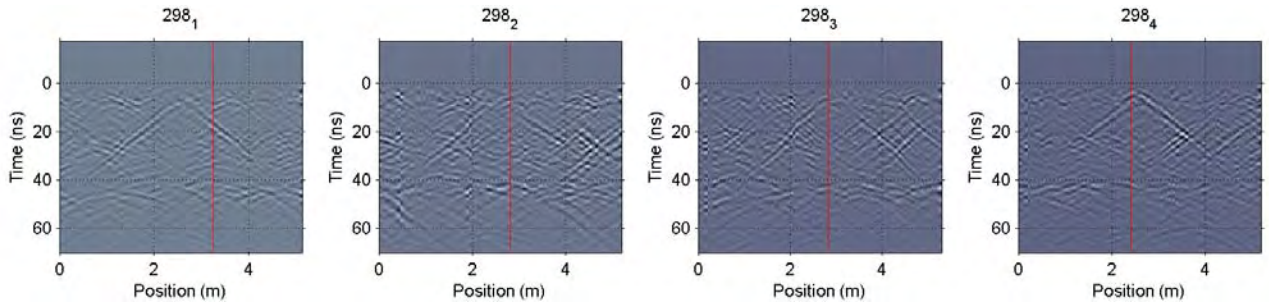


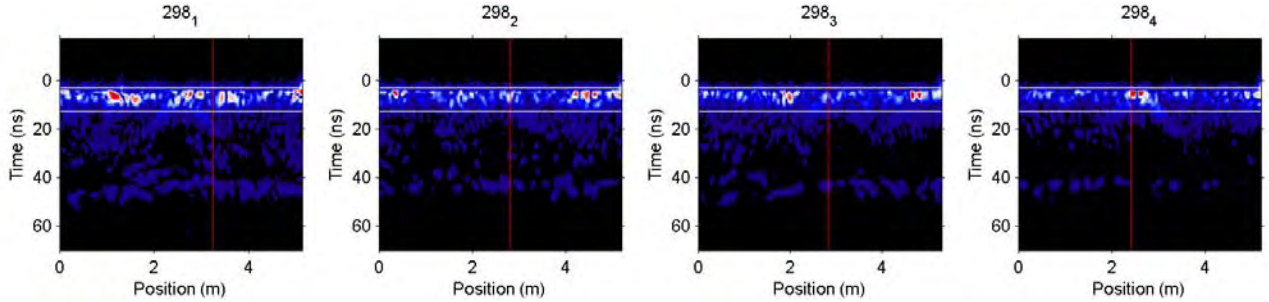


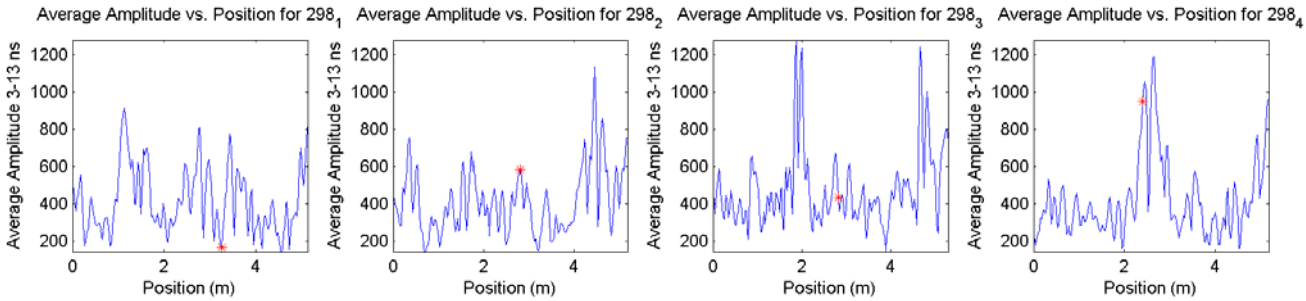

| | |
|---|---|
| Target Name | G6B2_320 |
| Item Description | Adapter |
| Depth (cm) | 10 |
| Distance From Pin (cm) | 30 |
| Easting (m) | 294456.85 |
| Northing(m) | 3833260.33 |

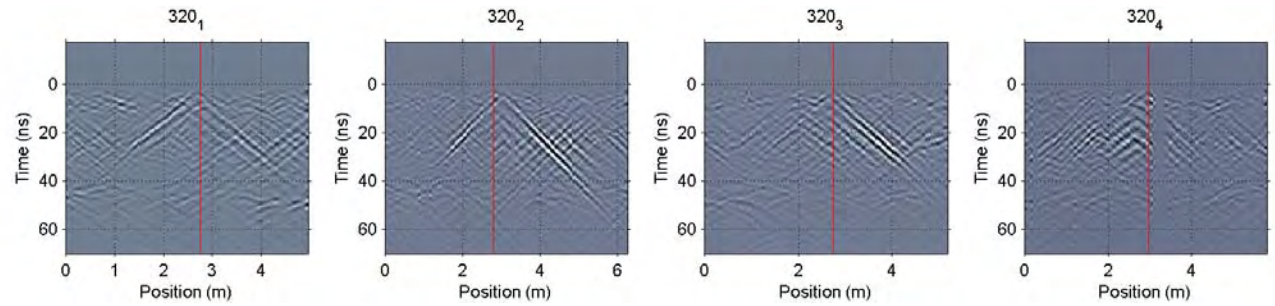


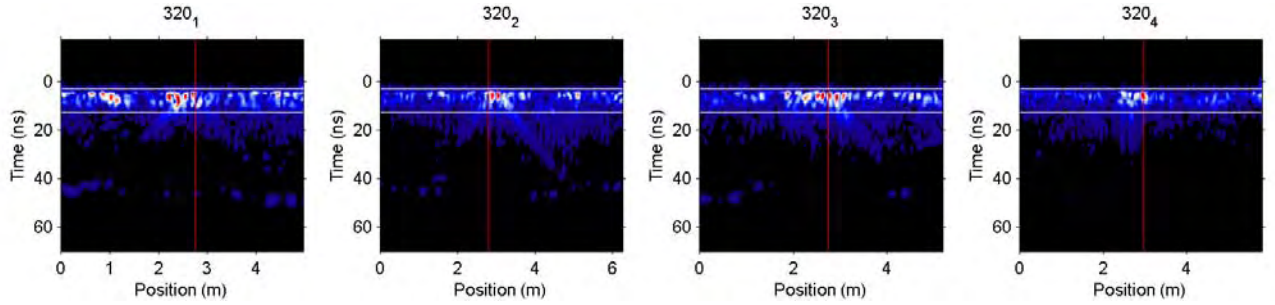


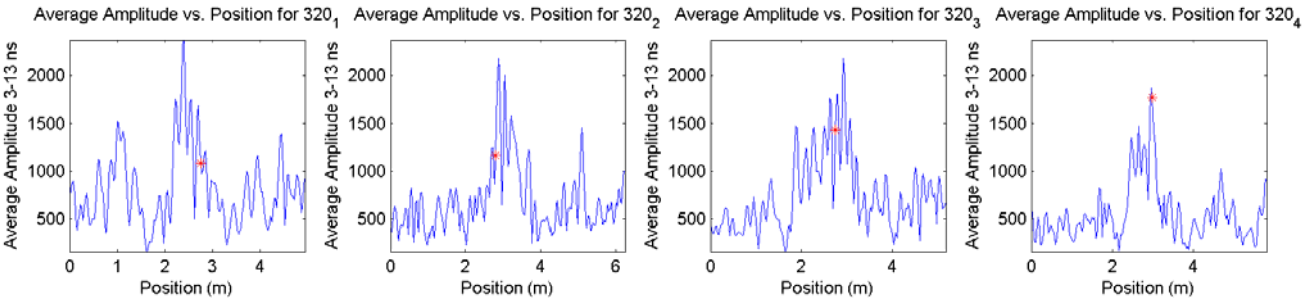

| | |
|---|---|
| Target Name | G6B2_418c |
| Item Description | Adapter |
| Depth (cm) | 0 |
| Distance From Pin (cm) | 70 |
| Easting (m) | 294424.42 |
| Northing(m) | 3833281.72 |

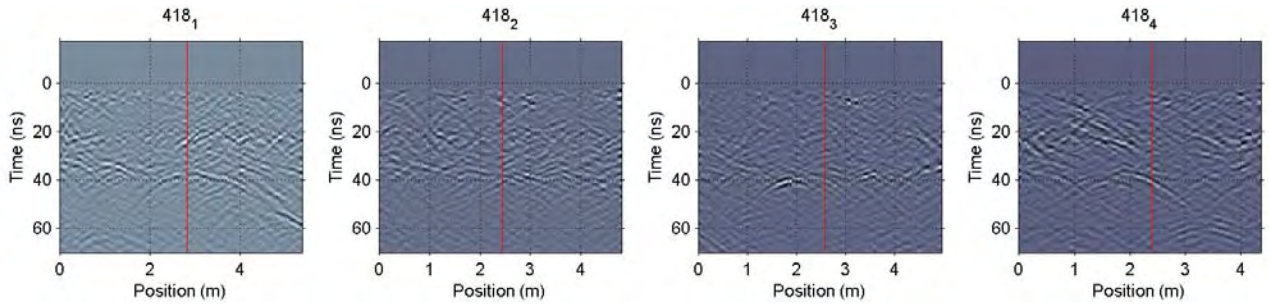


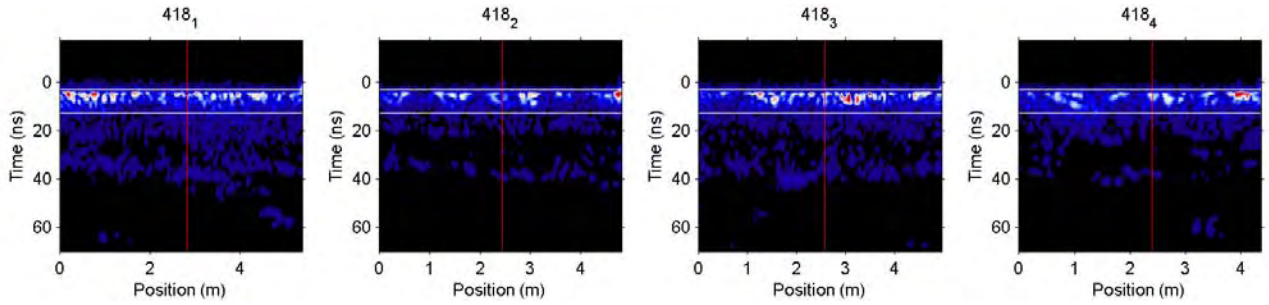


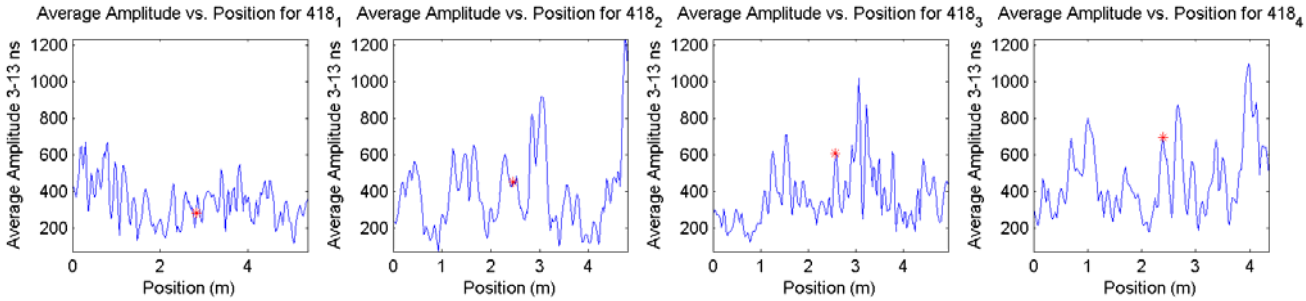

| | |
|---|---|
| Target Name | G6D1_3 |
| Item Description | Adapter |
| Depth (cm) | 0 |
| Distance From Pin (cm) | 5 |
| Easting (m) | 294413.70 |
| Northing(m) | 3833168.89 |

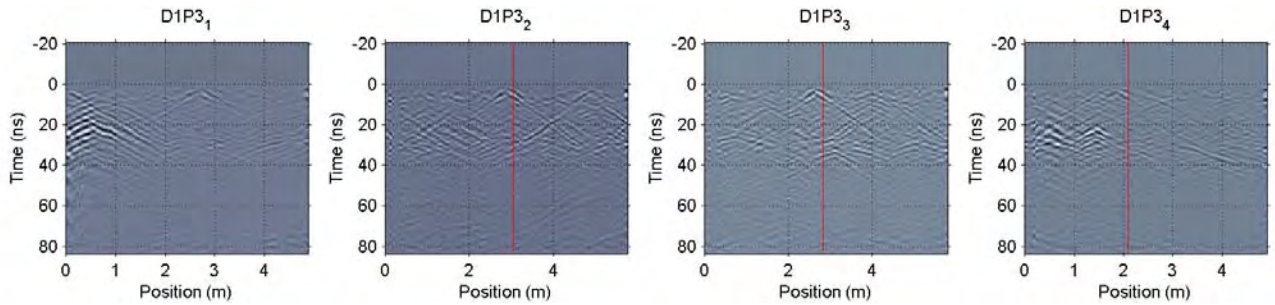


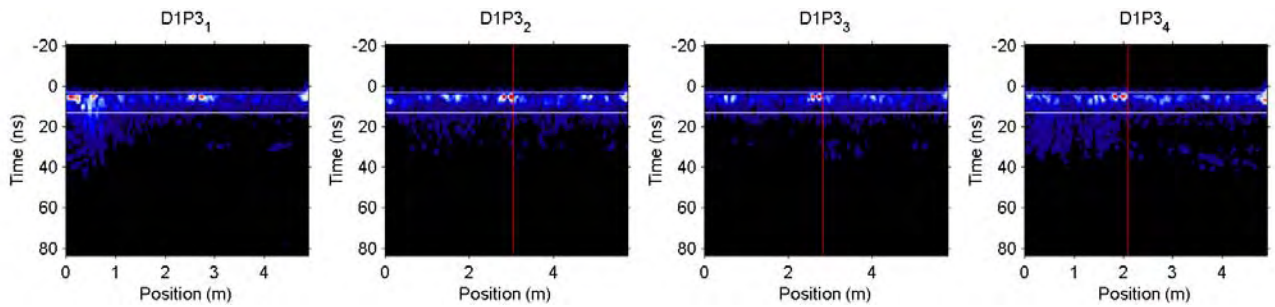


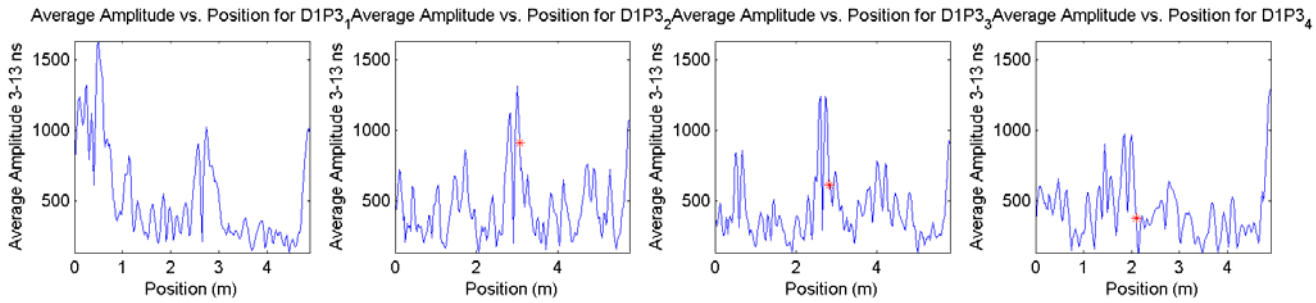

| | |
|---|---|
| Target Name | G6D1_4 |
| Item Description | Adapter |
| Depth (cm) | 0 |
| Distance From Pin (cm) | 0 |
| Easting (m) | 294410.91 |
| Northing(m) | 3833156.70 |

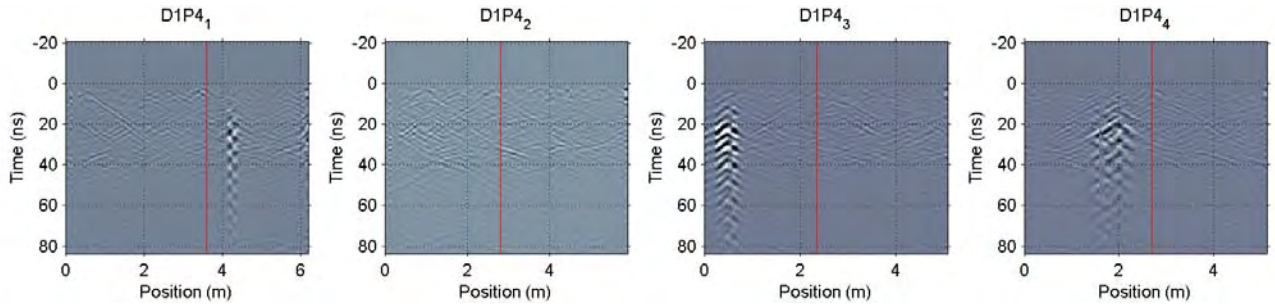


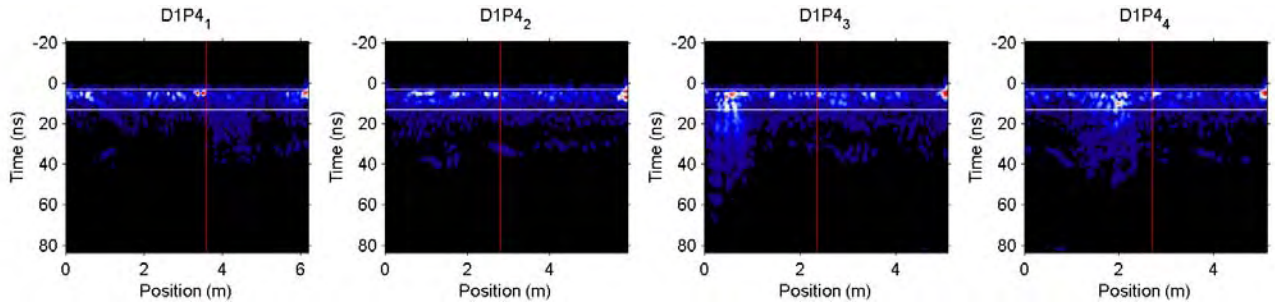


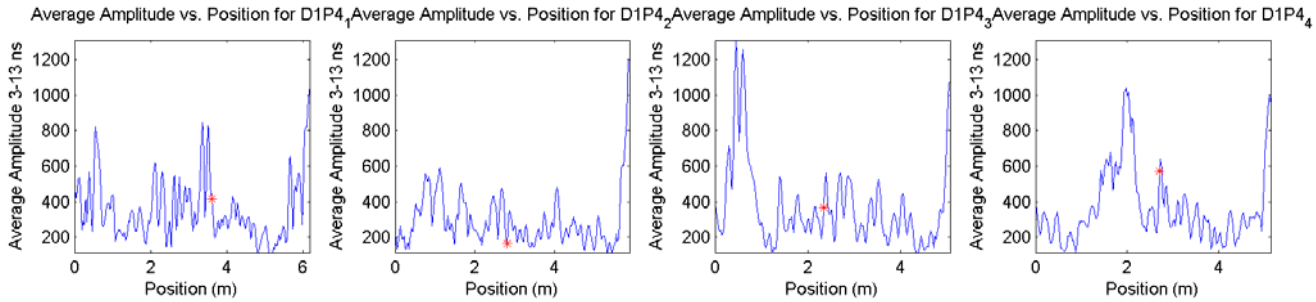

| | |
|---|---|
| Target Name | G6D2_1 |
| Item Description | Adapter |
| Depth (cm) | 7 |
| Distance From Pin (cm) | 0 |
| Easting (m) | 294431.67 |
| Northing(m) | 3833198.18 |

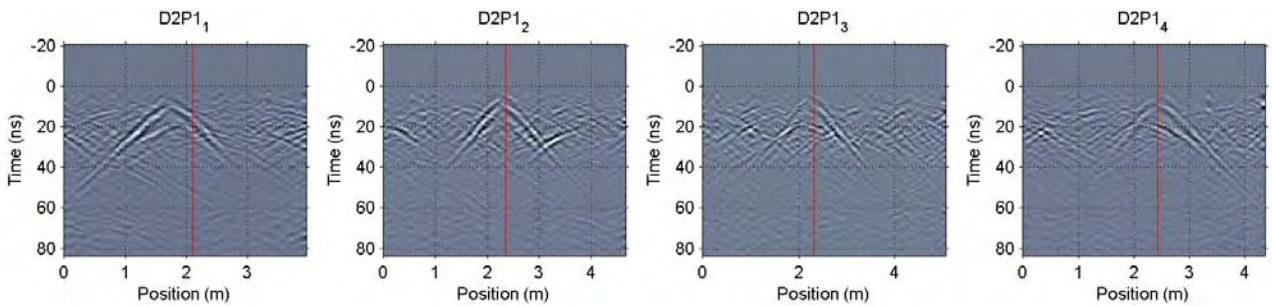


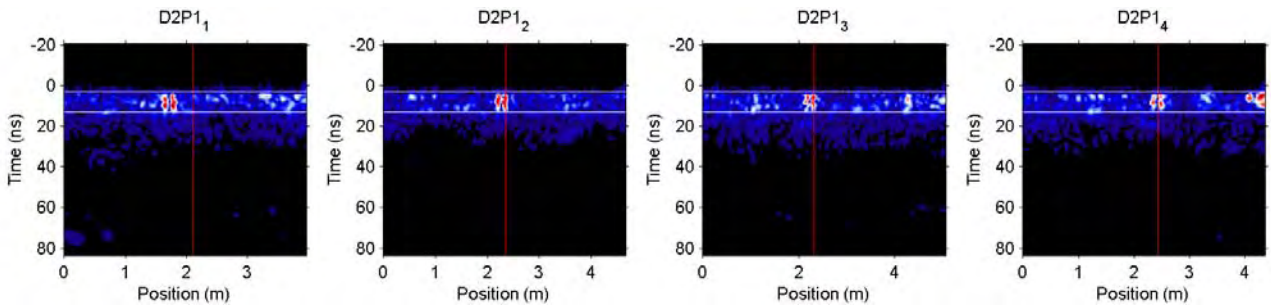


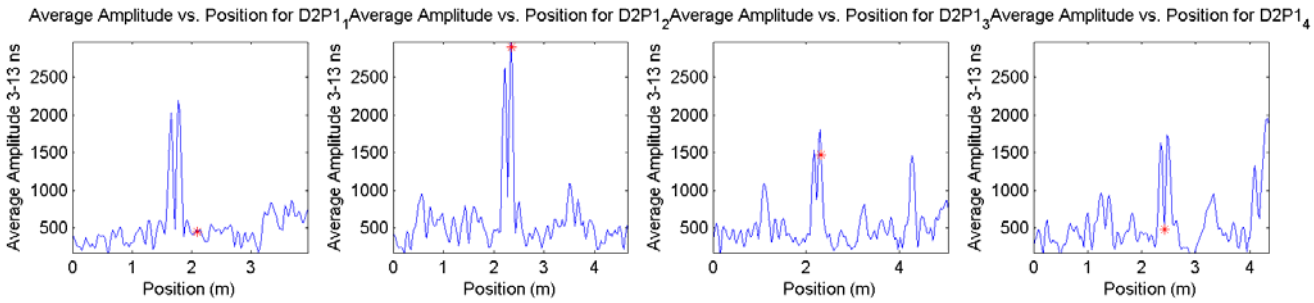

| | |
|---|---|
| Target Name | G6D2_5 |
| Item Description | Adapter |
| Depth (cm) | 2 |
| Distance From Pin (cm) | 5 |
| Easting (m) | 294449.01 |
| Northing(m) | 3833176.15 |

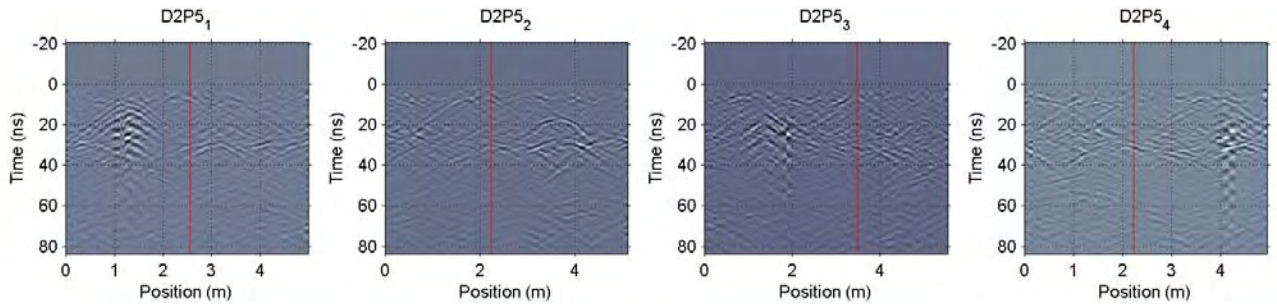


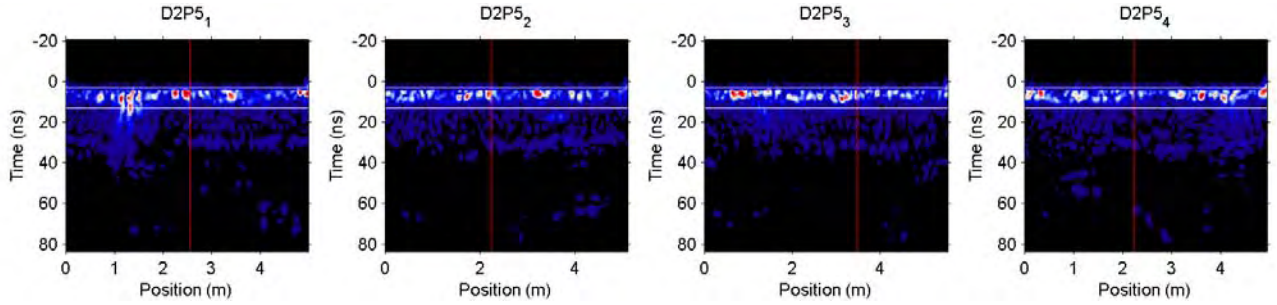


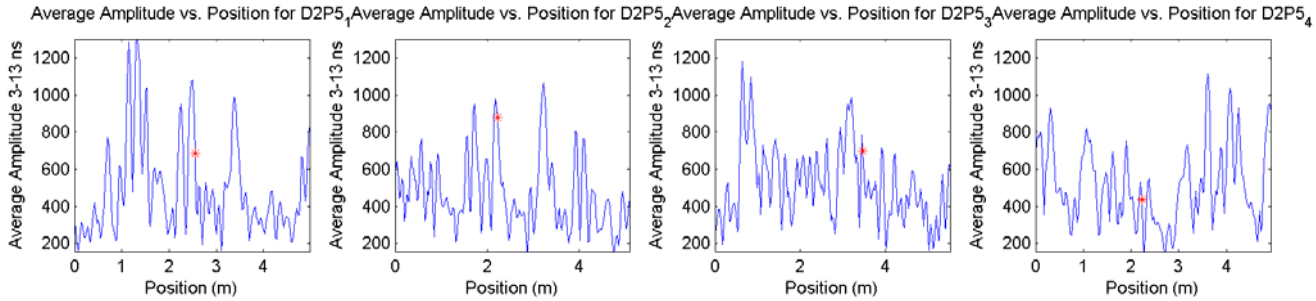

| | |
|---|---|
| Target Name | G6D2_7 |
| Item Description | Adapter |
| Depth (cm) | 0 |
| Distance From Pin (cm) | 6 |
| Easting (m) | 294449.01 |
| Northing(m) | 3833176.15 |

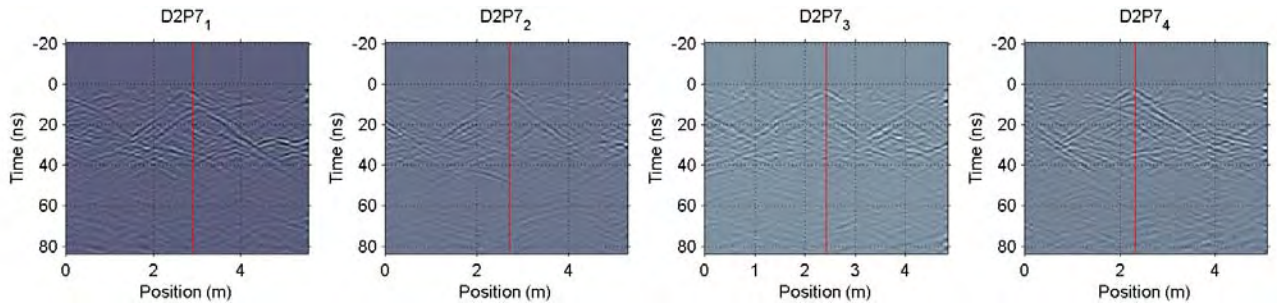


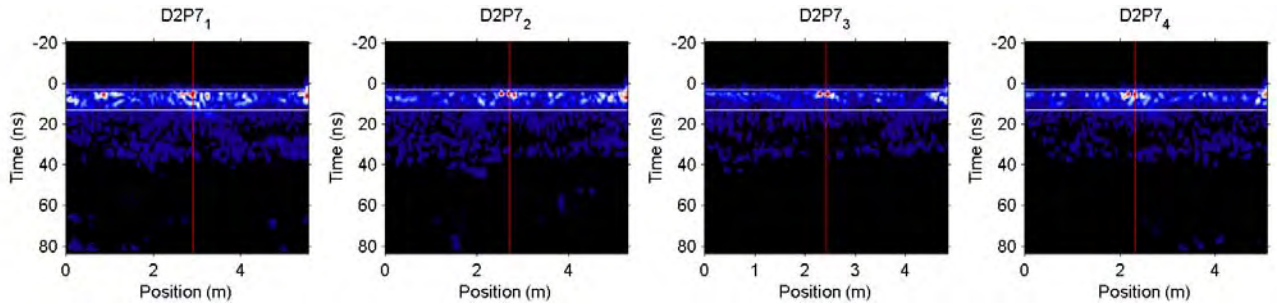


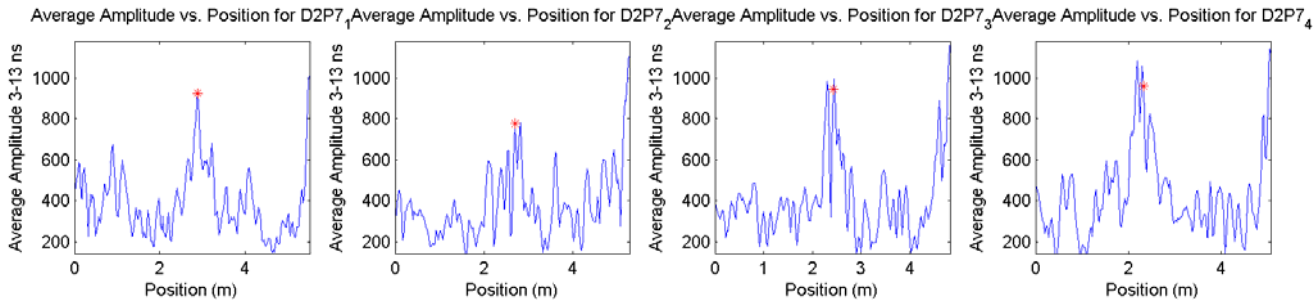

| | |
|---|---|
| Target Name | G6D2_8 |
| Item Description | Adapter |
| Depth (cm) | 8 |
| Distance From Pin (cm) | 0 |
| Easting (m) | 294447.89 |
| Northing(m) | 3833189.26 |

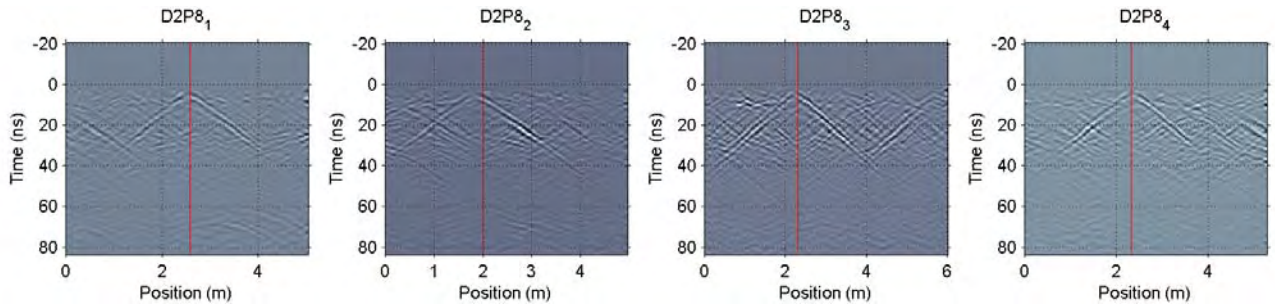


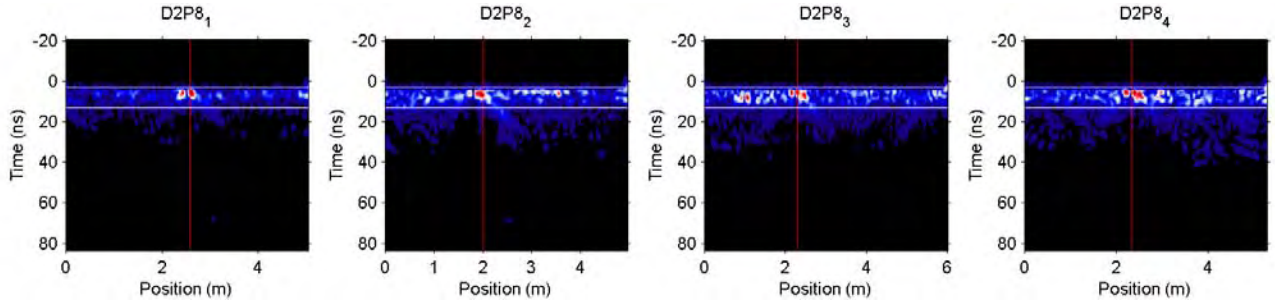


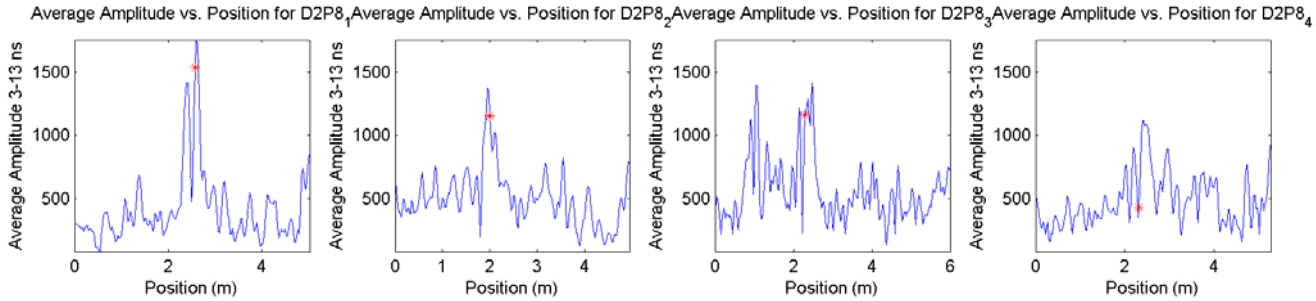

| | |
|---|---|
| Target Name | G6E1_4 |
| Item Description | Adapter |
| Depth (cm) | 4 |
| Distance From Pin (cm) | 0 |
| Easting (m) | 294427.27 |
| Northing(m) | 3833122.27 |

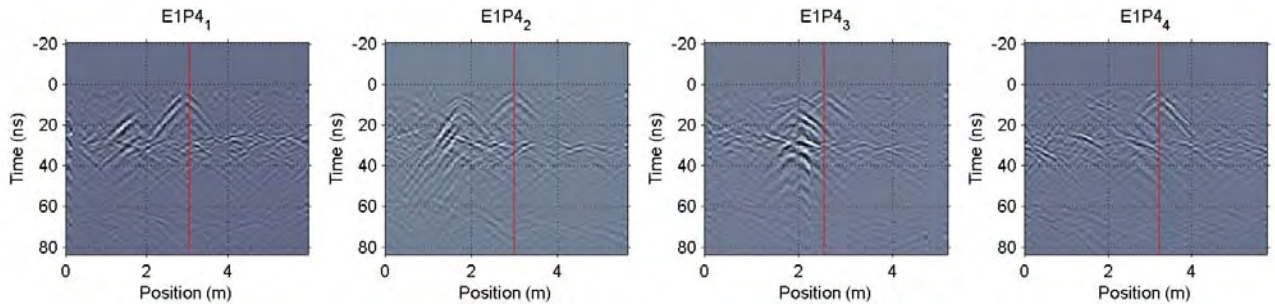


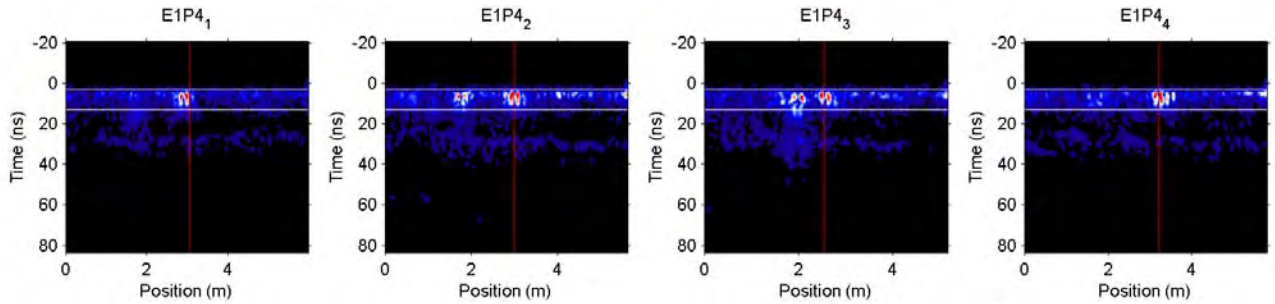


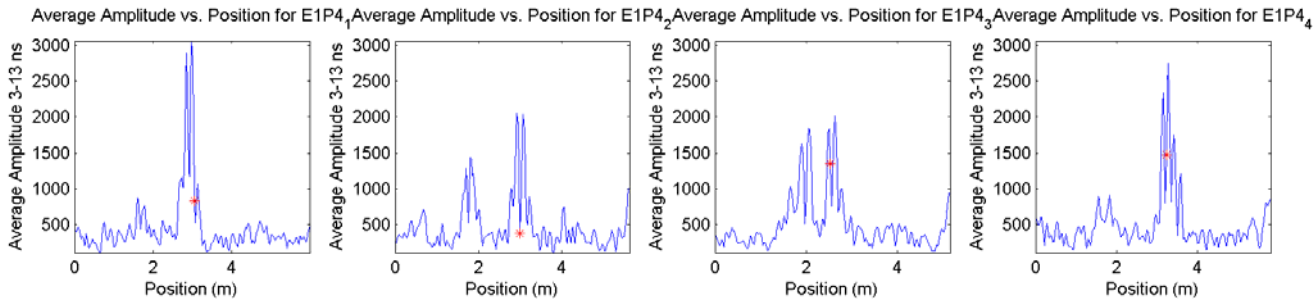

| | |
|---|---|
| Target Name | G6E1_8 |
| Item Description | Adapter |
| Depth (cm) | 2 |
| Distance From Pin (cm) | 7 |
| Easting (m) | 294397.41 |
| Northing(m) | 3833140.34 |

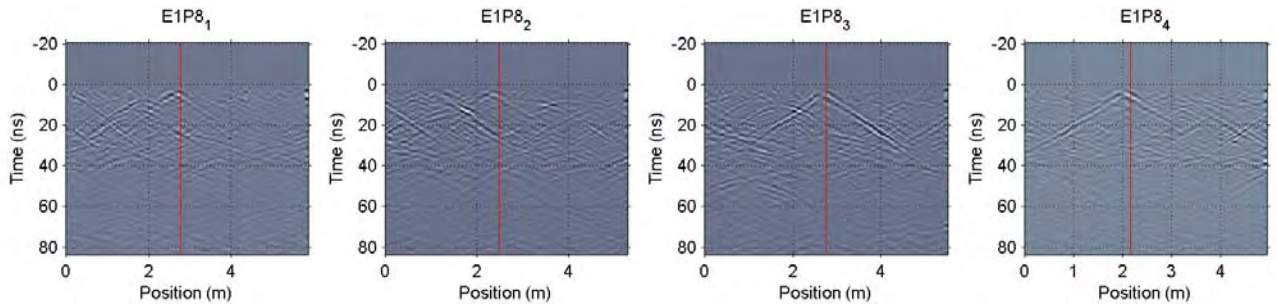


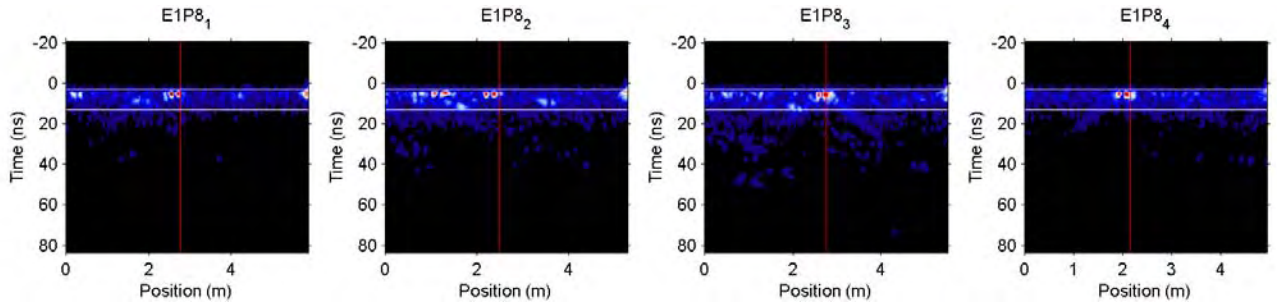


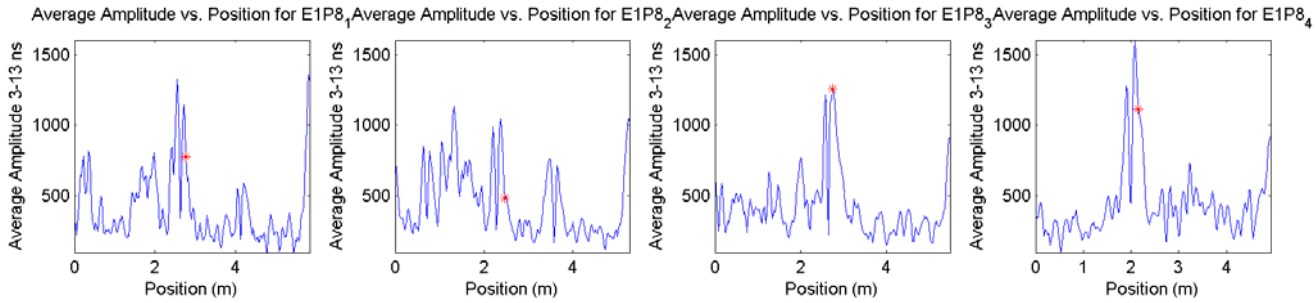

| | |
|---|---|
| Target Name | G6B1_336 |
| Item Description | Adapter end cap |
| Depth (cm) | 12 |
| Distance From Pin (cm) | 0 |
| Easting (m) | 294379.08 |
| Northing(m) | 3833240.31 |

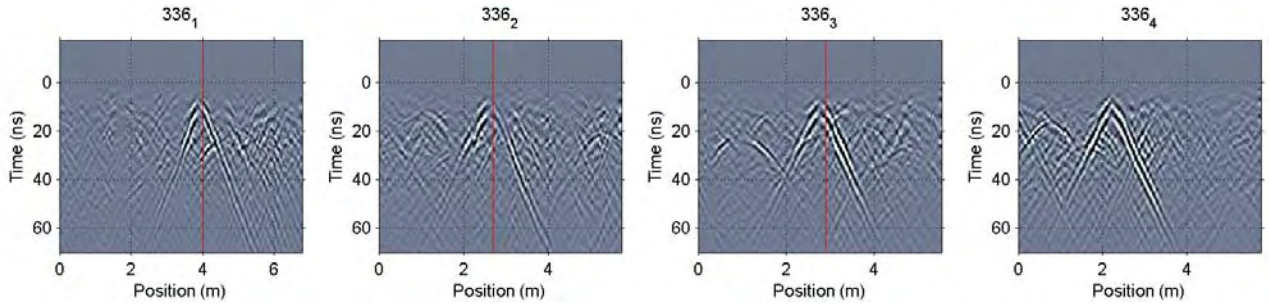


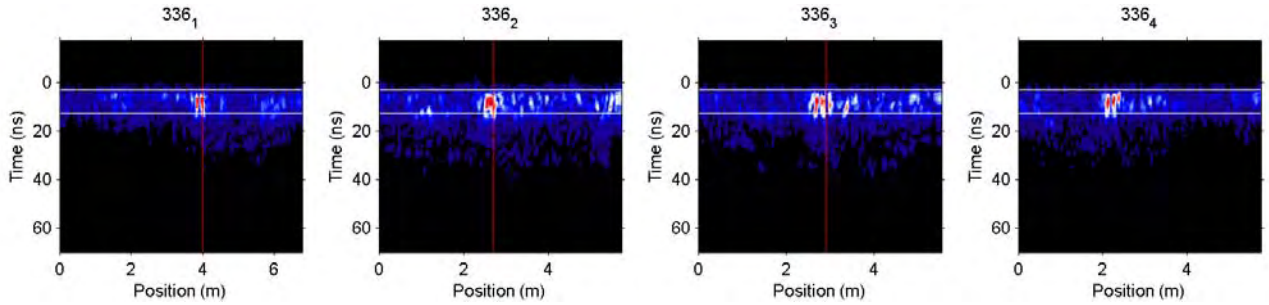


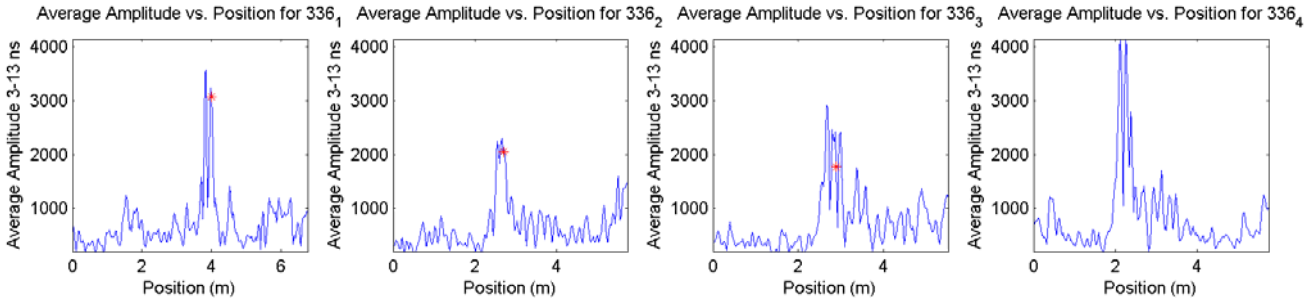

| | |
|---|---|
| Target Name | G6B2_346 |
| Item Description | Adapter end cap |
| Depth (cm) | 5 |
| Distance From Pin (cm) | 5 |
| Easting (m) | 294432.32 |
| Northing(m) | 3833260.90 |

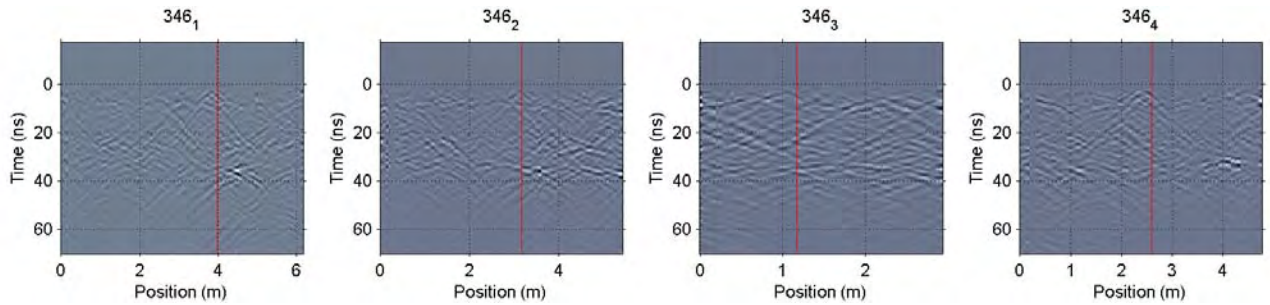


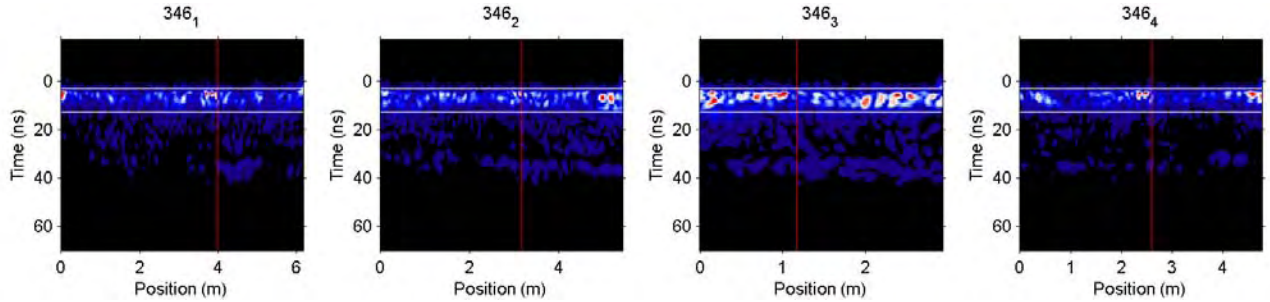


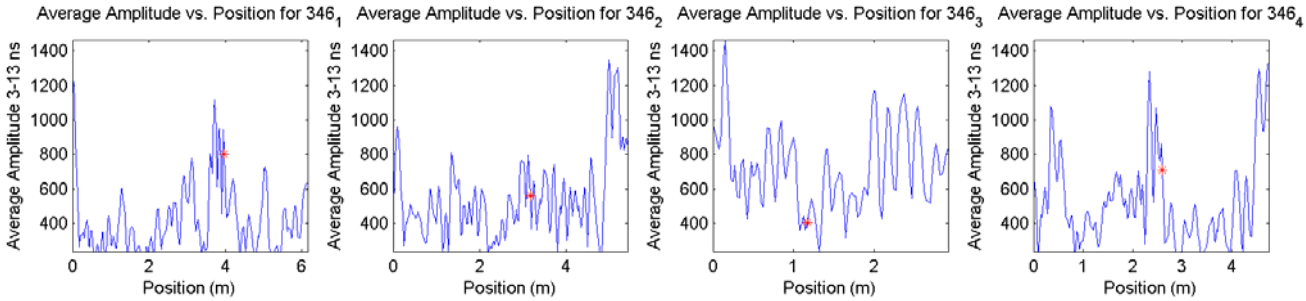

| | |
|---|---|
| Target Name | G6B1_354 |
| Item Description | Adapter end cap |
| Depth (cm) | 8 |
| Distance From Pin (cm) | 4 |
| Easting (m) | 294375.52 |
| Northing(m) | 3833239.30 |

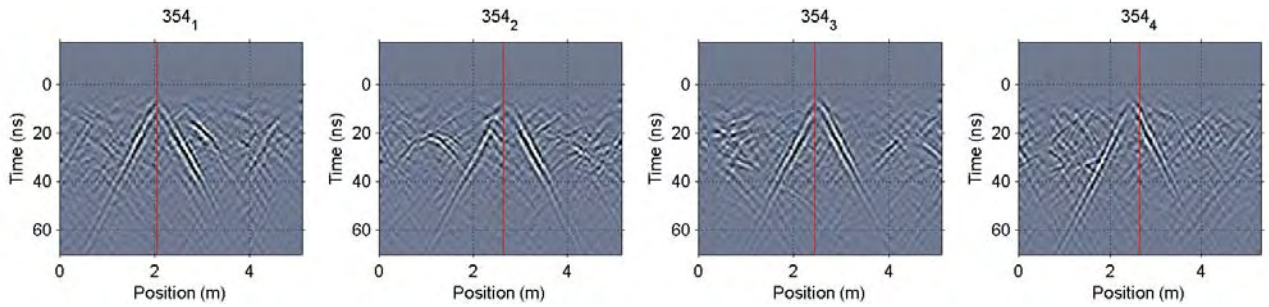


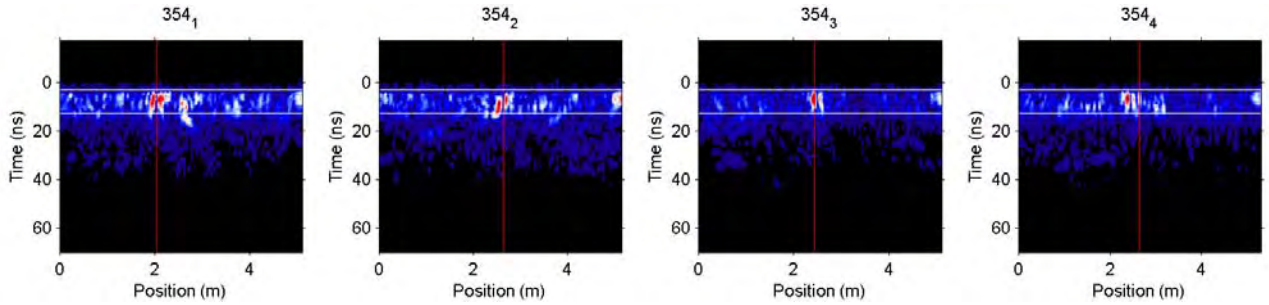


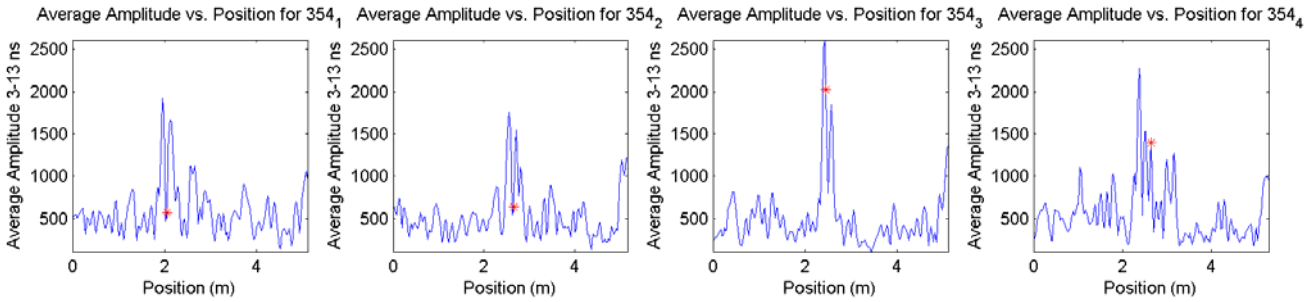

| | |
|---|---|
| Target Name | G6B1_360 |
| Item Description | Adapter end cap |
| Depth (cm) | 8 |
| Distance From Pin (cm) | 20 |
| Easting (m) | 294370.43 |
| Northing(m) | 3833241.46 |

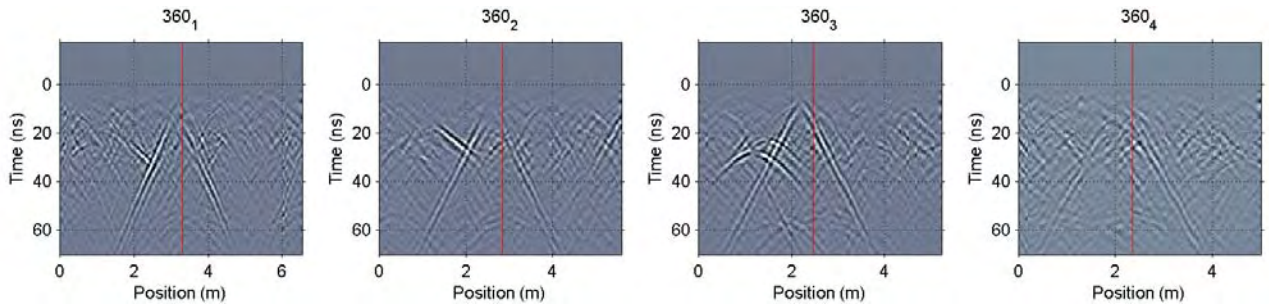


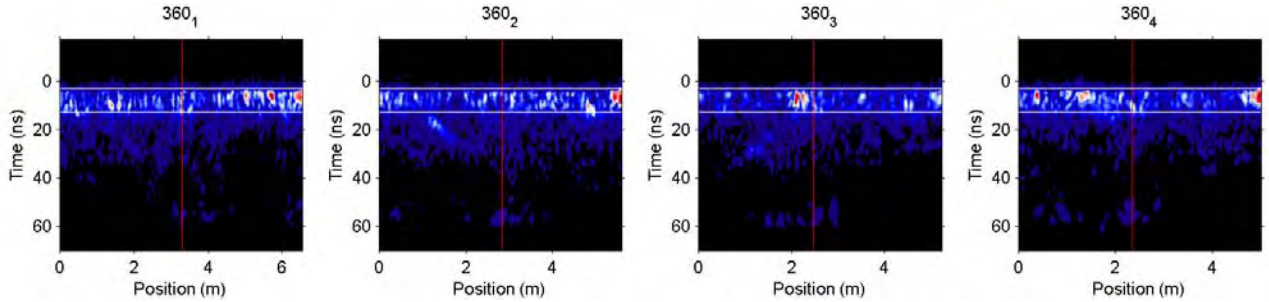


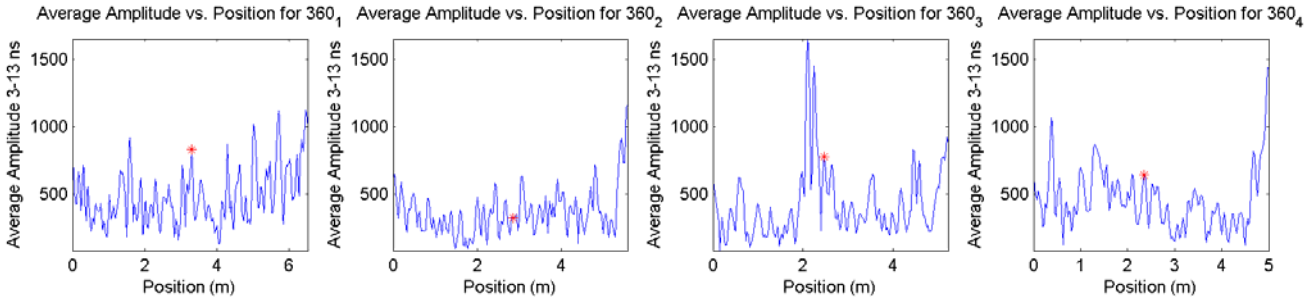

| | |
|---|---|
| Target Name | G6B1_369 |
| Item Description | Adapter end cap |
| Depth (cm) | 10 |
| Distance From Pin (cm) | 20 |
| Easting (m) | 294386.13 |
| Northing(m) | 3833246.54 |

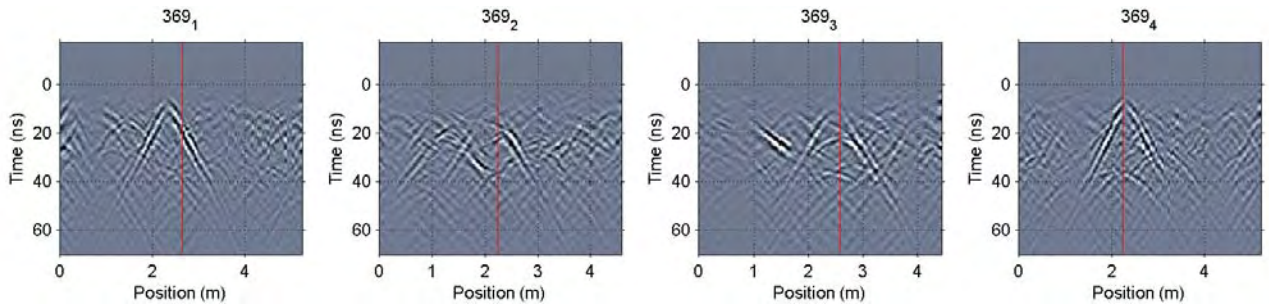


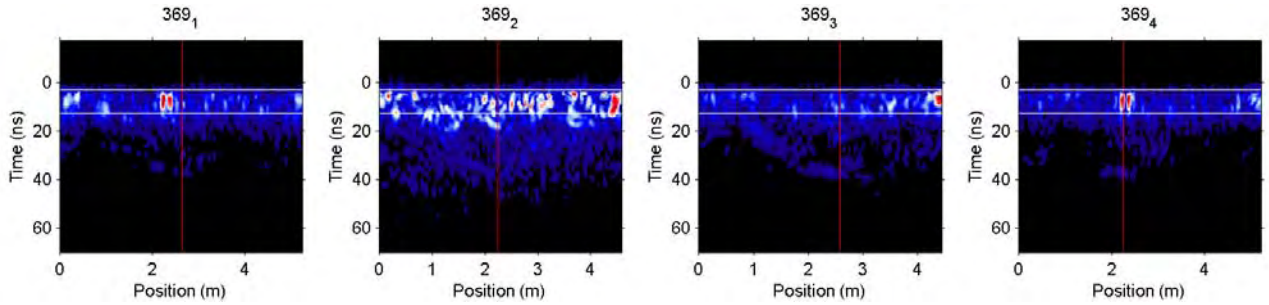


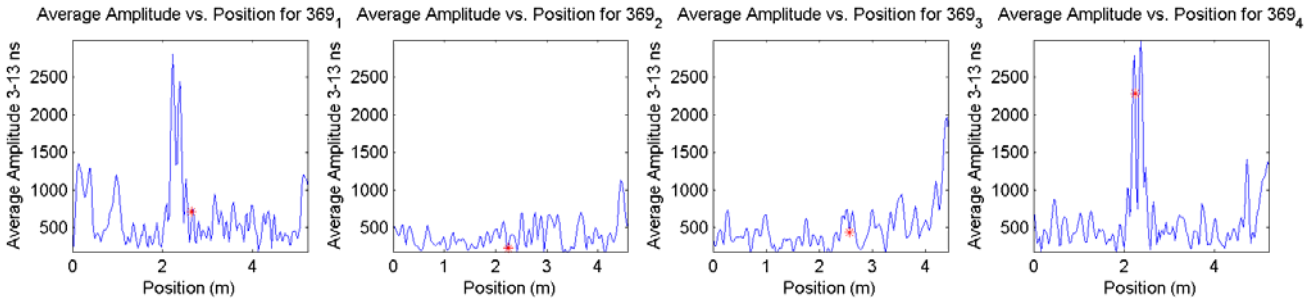

| | |
|---|---|
| Target Name | G6B2_374 |
| Item Description | Adapter end cap |
| Depth (cm) | 10 |
| Distance From Pin (cm) | 8 |
| Easting (m) | 294430.48 |
| Northing(m) | 3833257.00 |

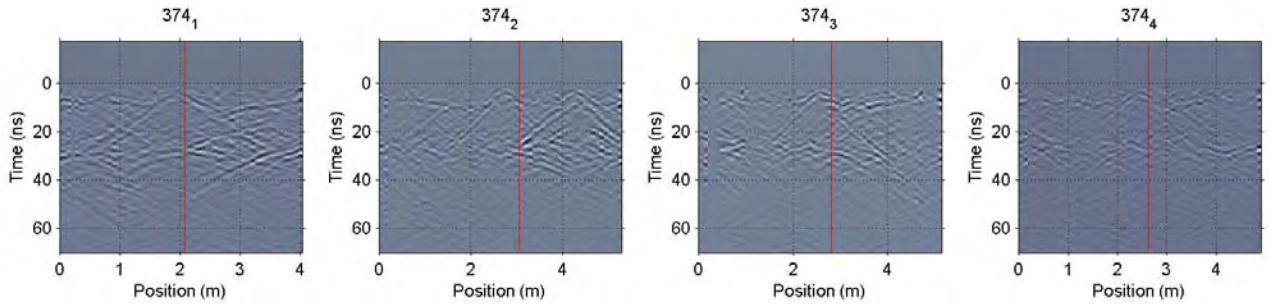


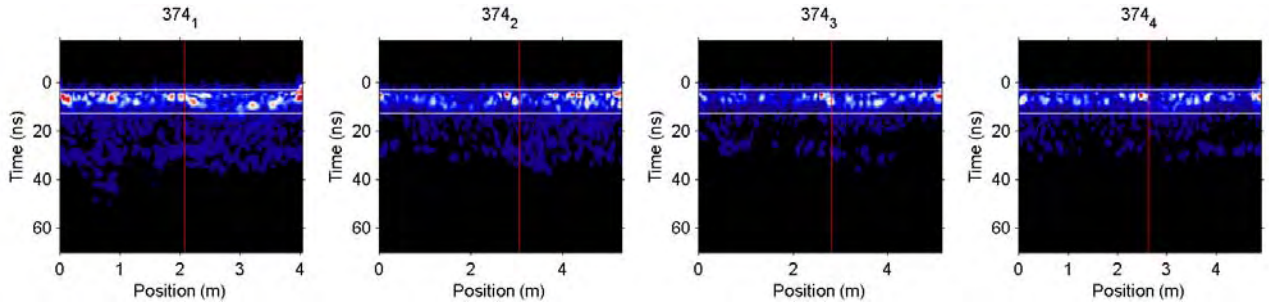


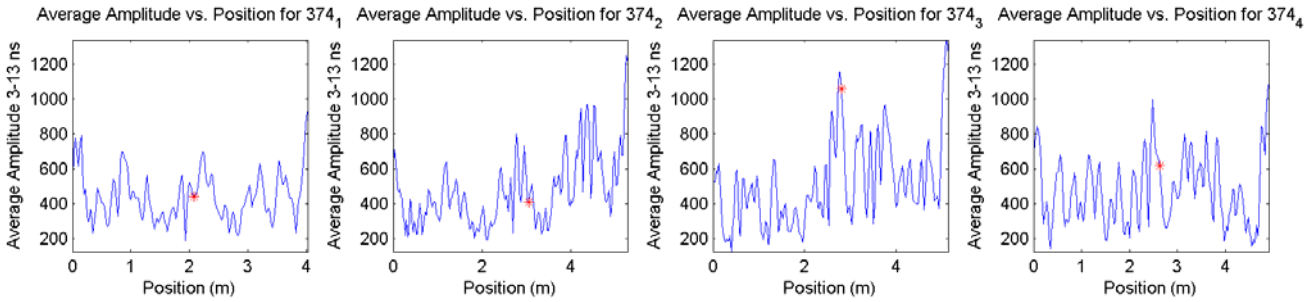

| | |
|---|---|
| Target Name | G6B1_376 |
| Item Description | Adapter end cap |
| Depth (cm) | 7 |
| Distance From Pin (cm) | 8 |
| Easting (m) | 294417.07 |
| Northing(m) | 3833289.28 |

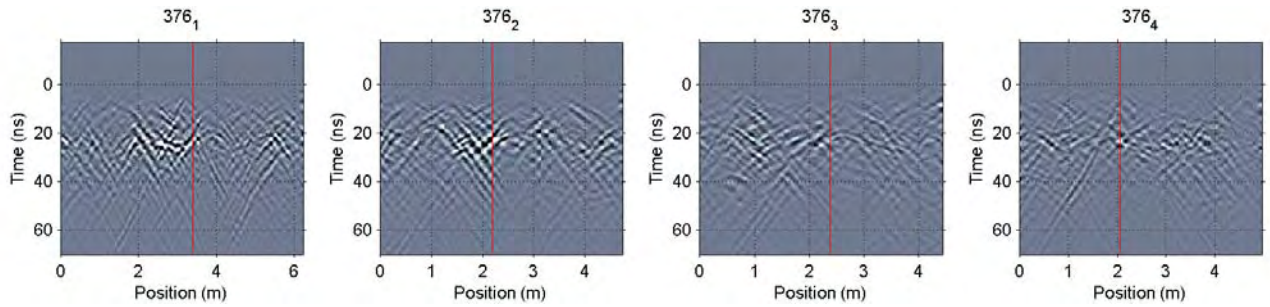


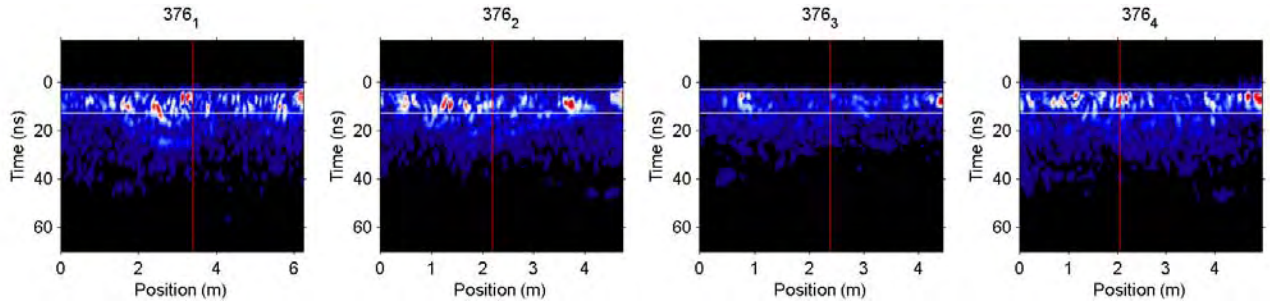


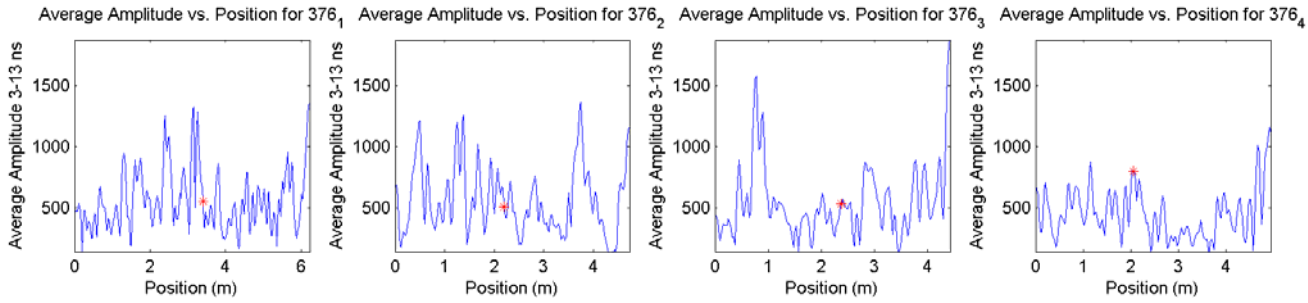

| | |
|---|---|
| Target Name | G6B1_381 |
| Item Description | Adapter end cap |
| Depth (cm) | 15 |
| Distance From Pin (cm) | 20 |
| Easting (m) | 294391.45 |
| Northing(m) | 3833267.67 |

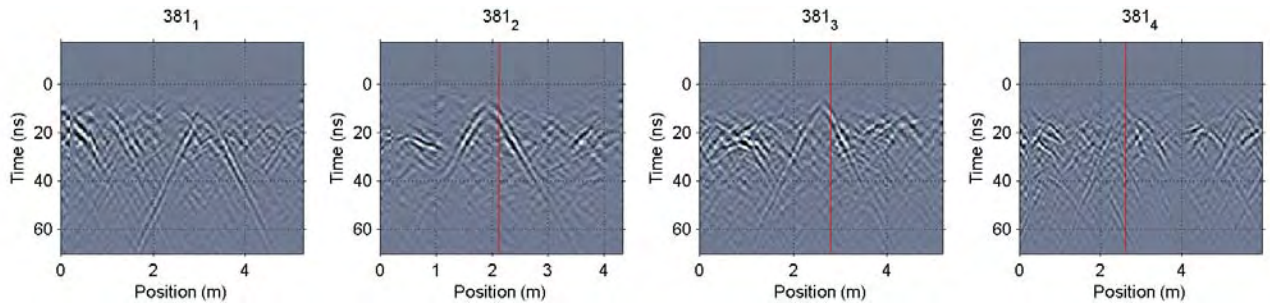


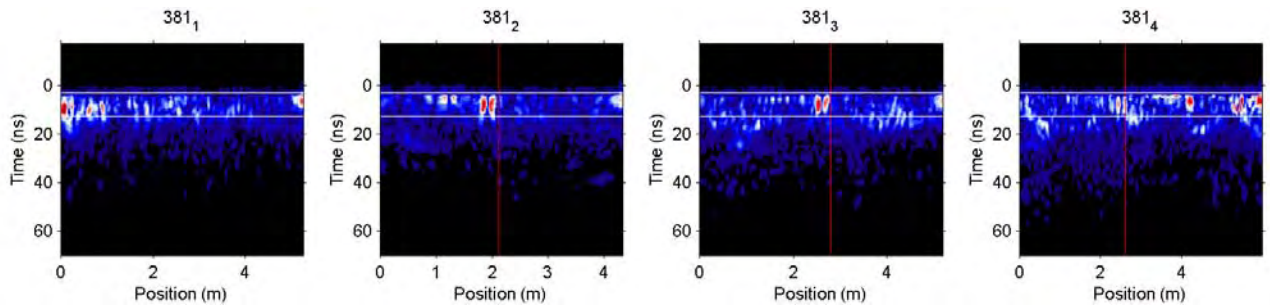


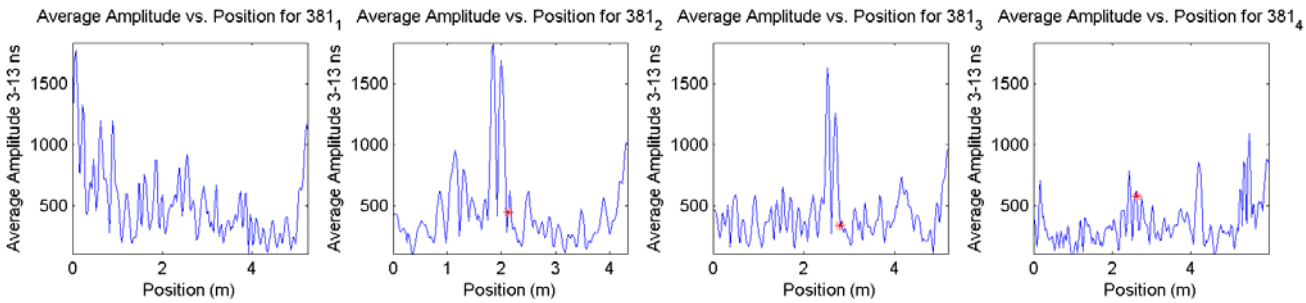

| | |
|---|---|
| Target Name | G6B1_392 |
| Item Description | Adapter end cap |
| Depth (cm) | 0 |
| Distance From Pin (cm) | 5 |
| Easting (m) | 294404.50 |
| Northing(m) | 3833261.63 |

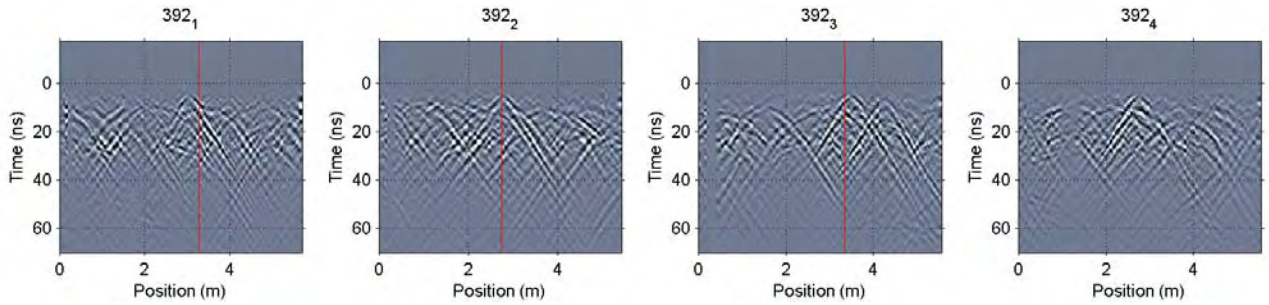


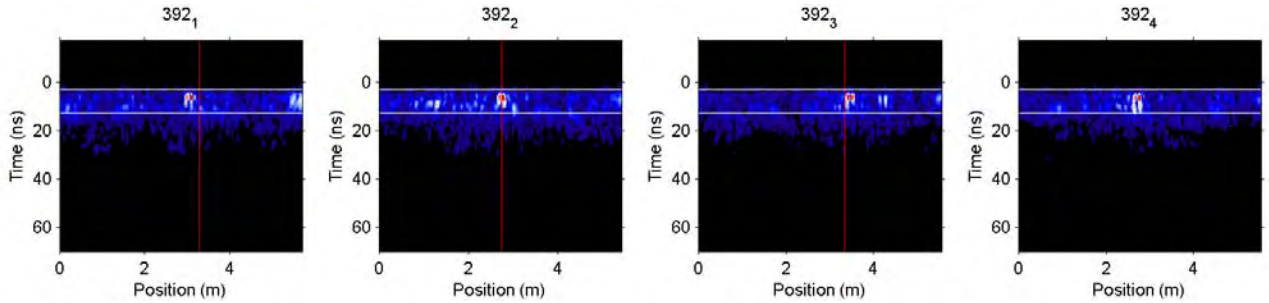


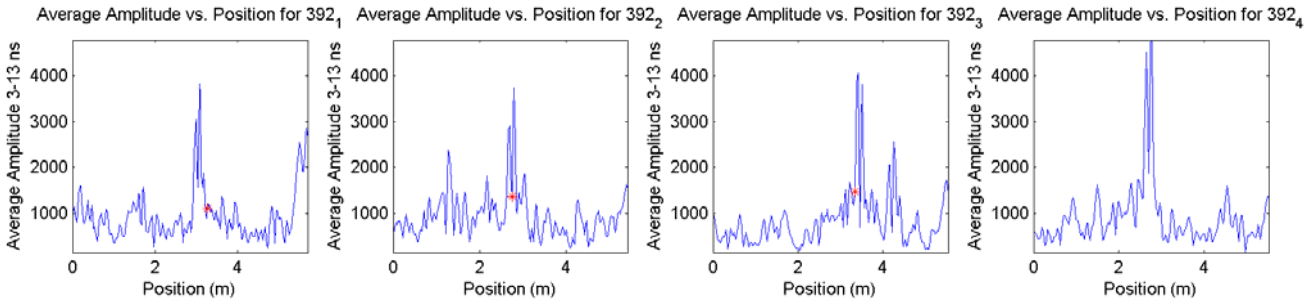

| | |
|---|---|
| Target Name | G6D2_3 |
| Item Description | Adapter end cap |
| Depth (cm) | 0 |
| Distance From Pin (cm) | 0 |
| Easting (m) | 294435.20 |
| Northing(m) | 3833158.13 |

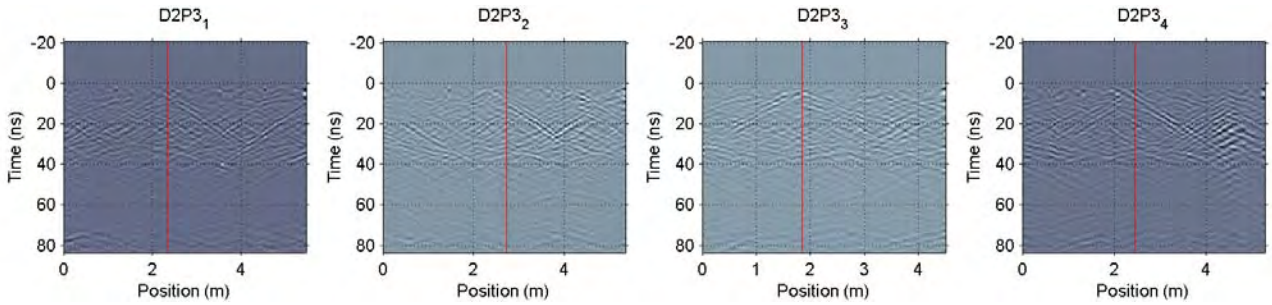


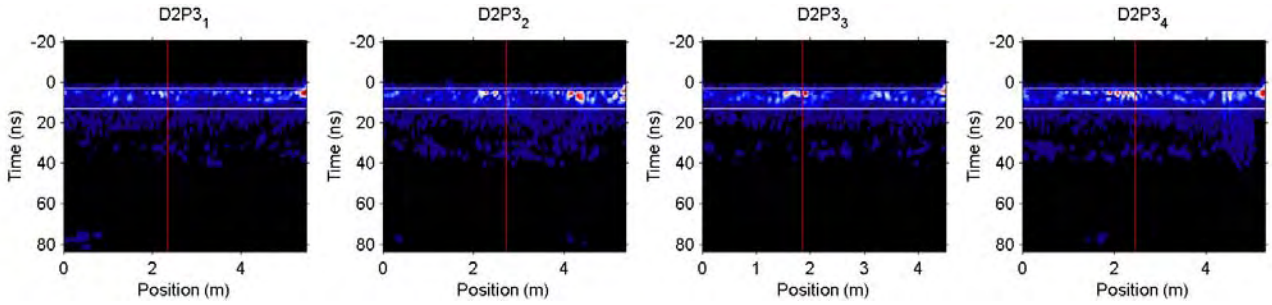


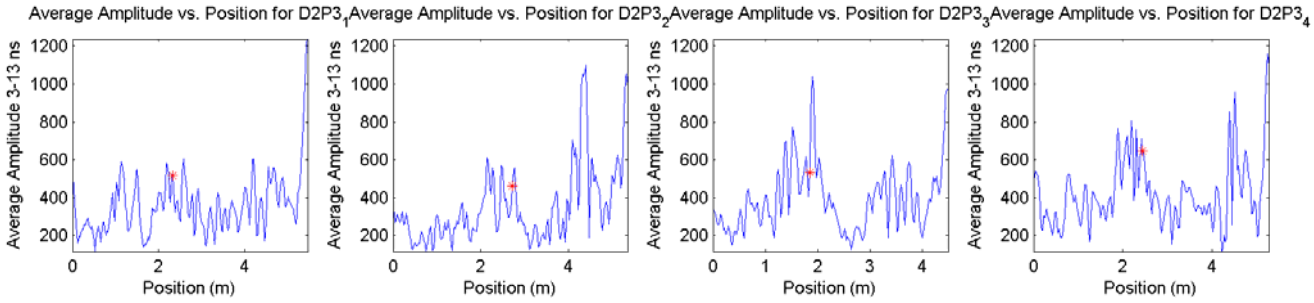

| | |
|---|---|
| Target Name | G6E1_6 |
| Item Description | Adapter end cap |
| Depth (cm) | 0 |
| Distance From Pin (cm) | 6 |
| Easting (m) | 294434.50 |
| Northing(m) | 3833119.80 |

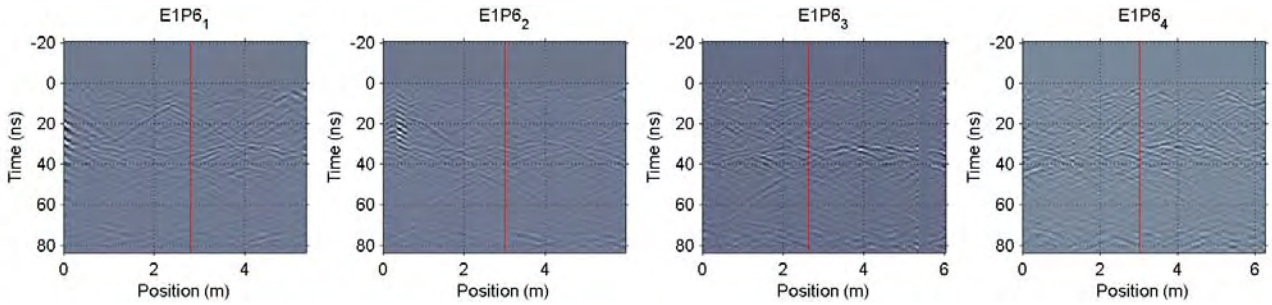


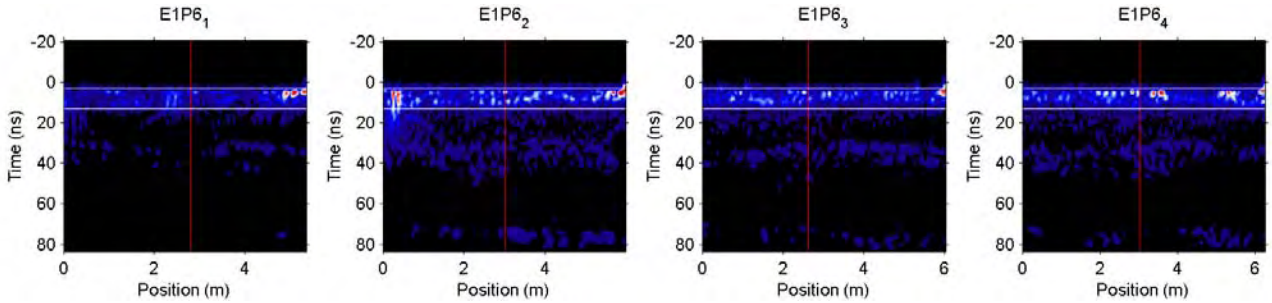


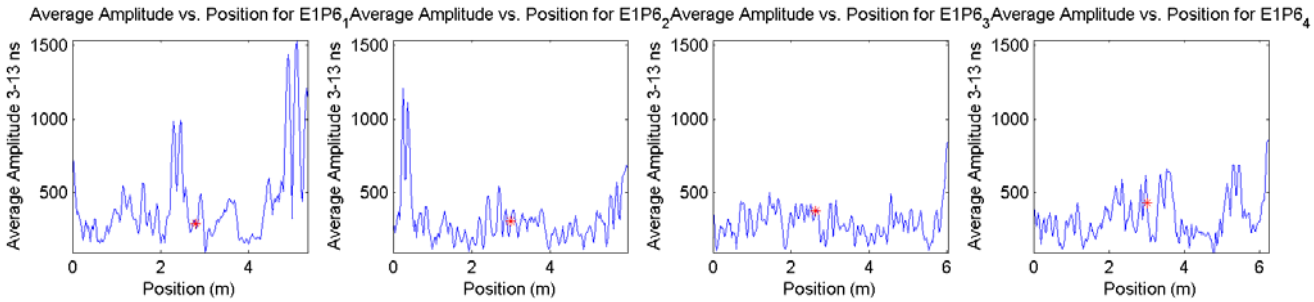

| | |
|---|---|
| Target Name | G6E2_3 |
| Item Description | Adapter end cap |
| Depth (cm) | 5 |
| Distance From Pin (cm) | 17 |
| Easting (m) | 294457.06 |
| Northing(m) | 3833144.91 |

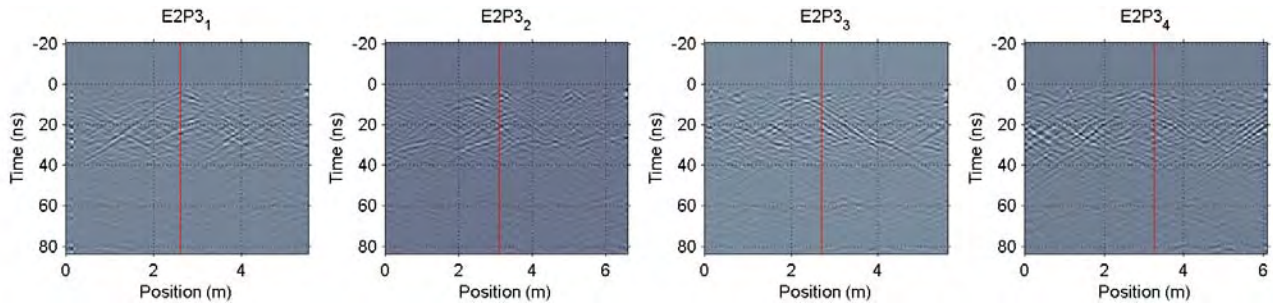


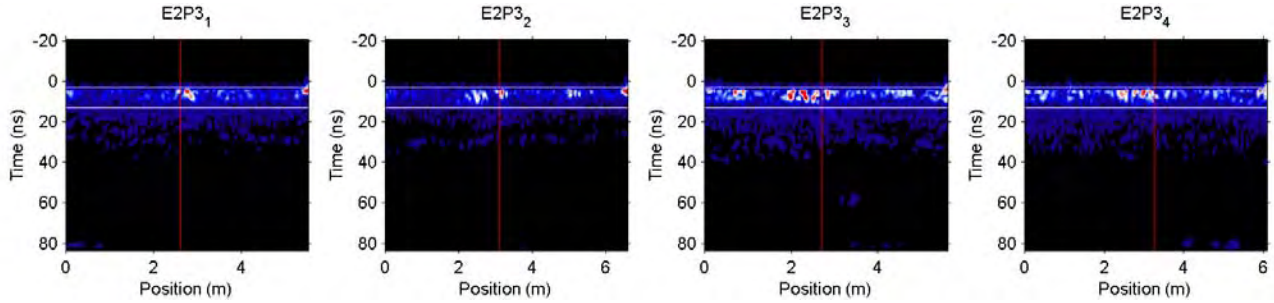


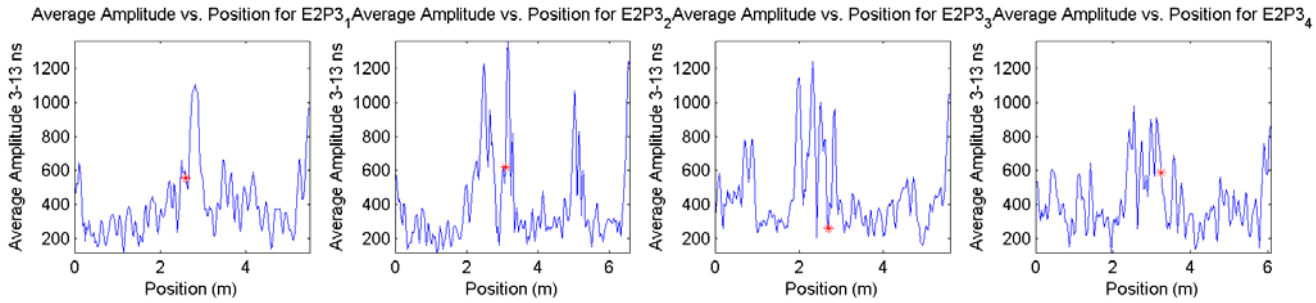

| | |
|---|---|
| Target Name | G6E2_6 |
| Item Description | Adapter end cap |
| Depth (cm) | 3 |
| Distance From Pin (cm) | 42 |
| Easting (m) | 294468.08 |
| Northing(m) | 3833123.88 |

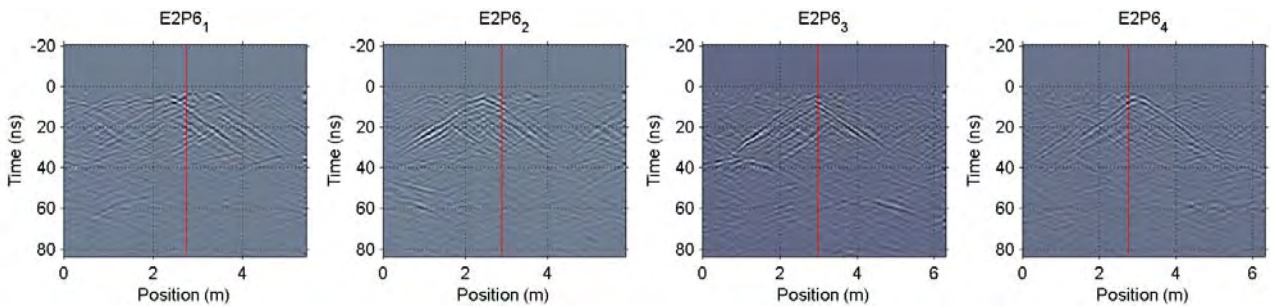


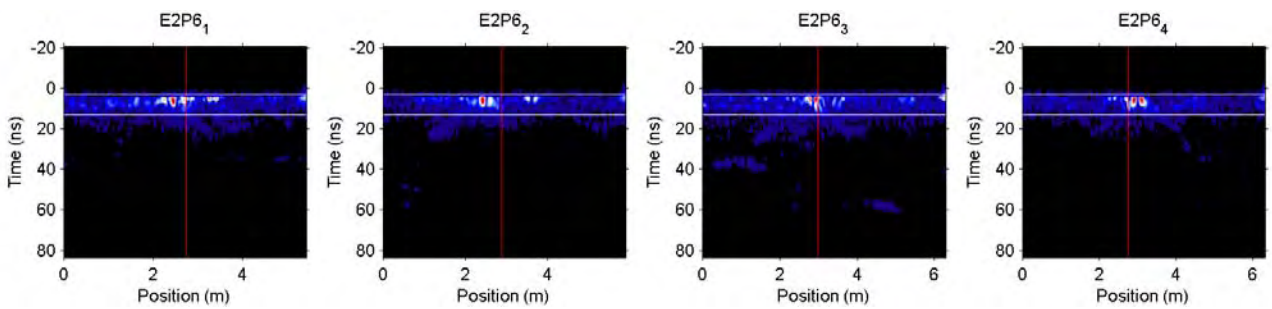


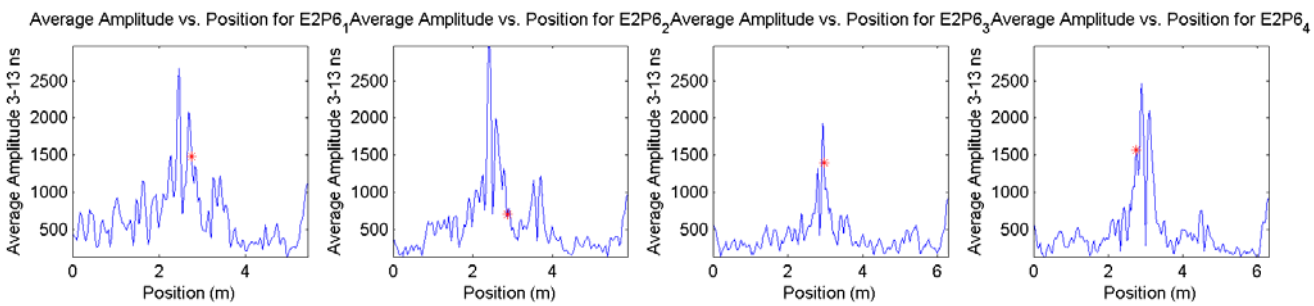

## D.6. 1000 MHz adapters and end caps

| | |
|---|---|
| Target Name | G6D1_3 |
| Item Description | Adapter |
| Depth (cm) | 0 |
| Distance From Pin (cm) | 5 |
| Easting (m) | 294413.70 |
| Northing(m) | 3833168.89 |

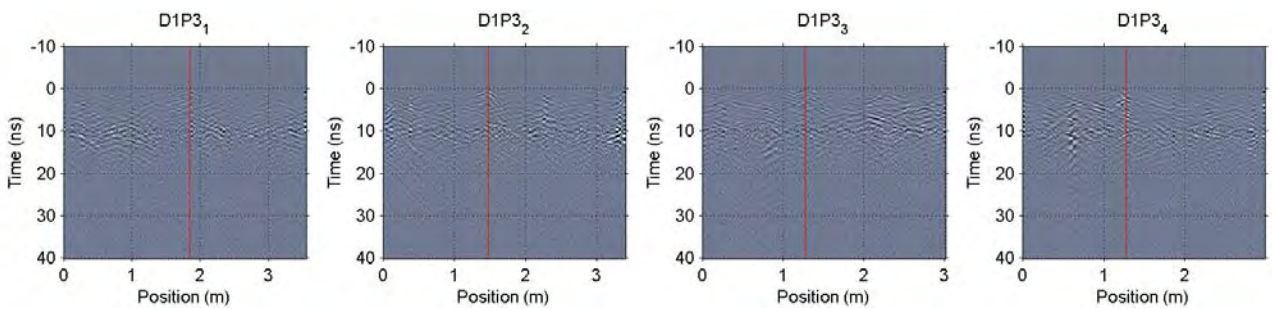


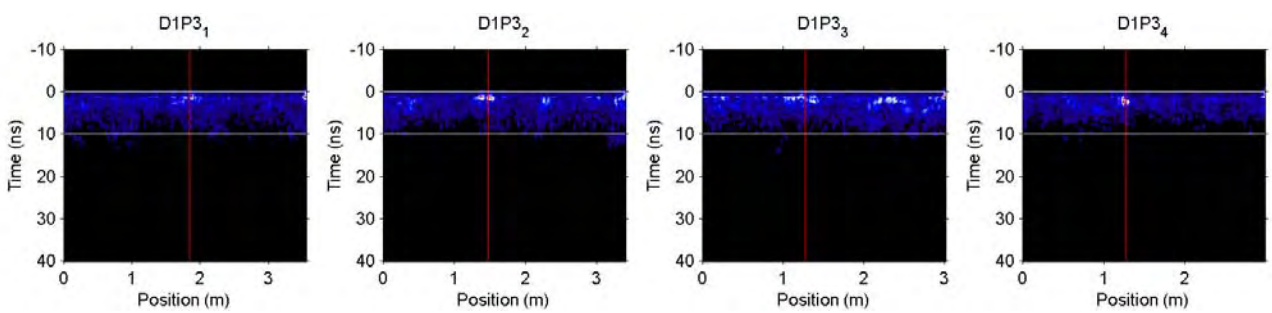


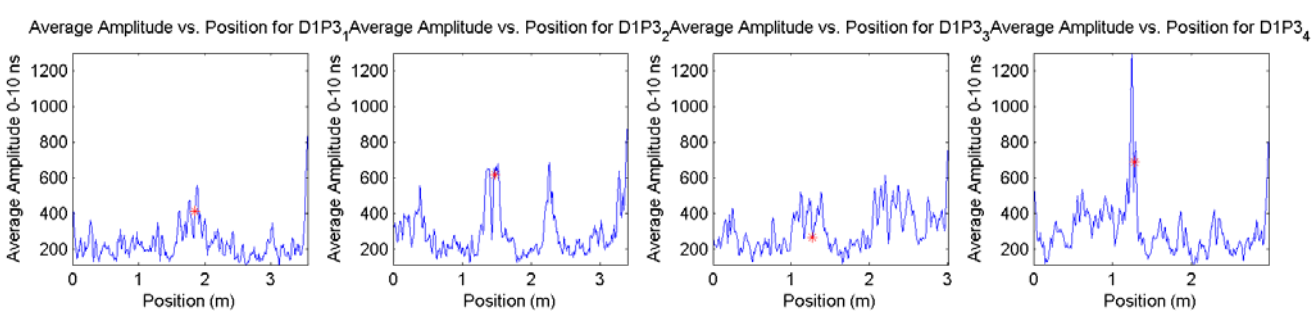

| | |
|---|---|
| Target Name | G6D1_4 |
| Item Description | Adapter |
| Depth (cm) | 0 |
| Distance From Pin (cm) | 0 |
| Easting (m) | 294410.91 |
| Northing(m) | 3833156.70 |

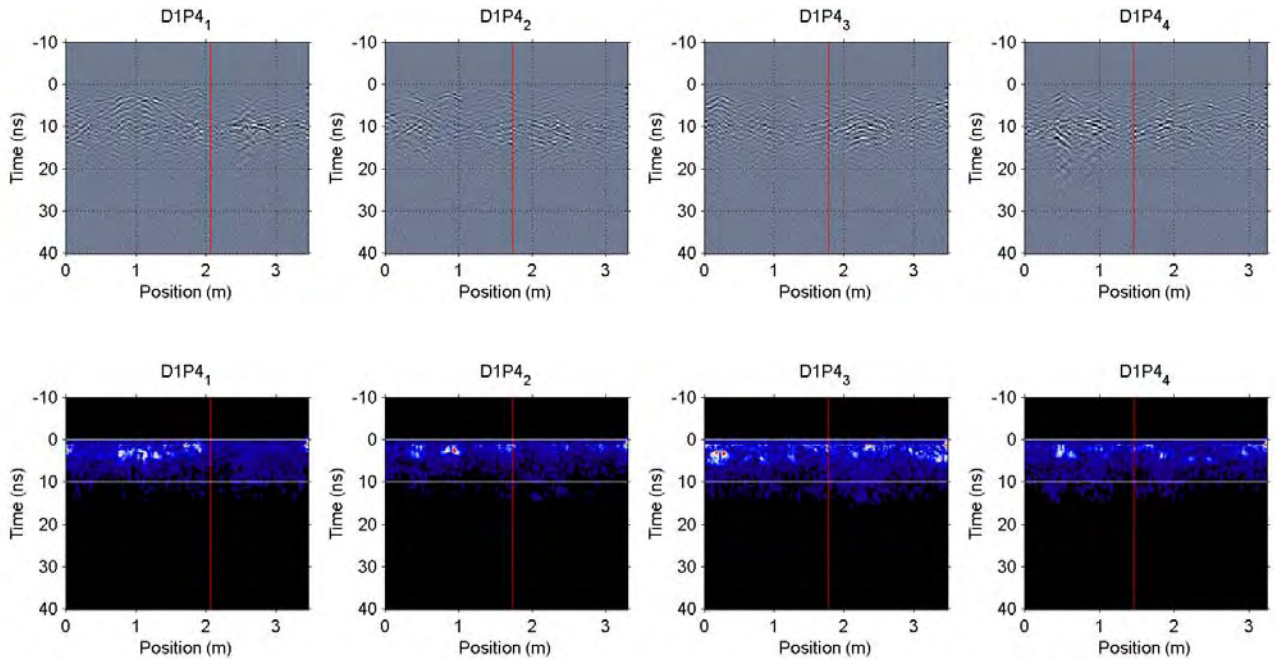


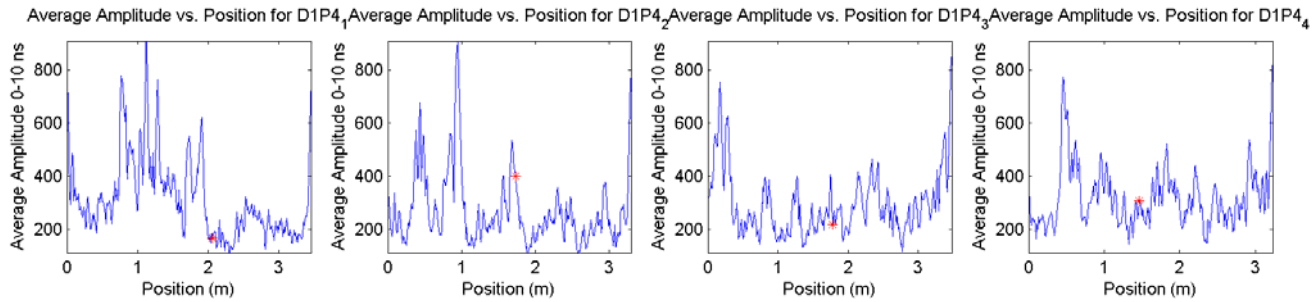

| | |
|---|---|
| Target Name | G6D2_1 |
| Item Description | Adapter |
| Depth (cm) | 7 |
| Distance From Pin (cm) | 0 |
| Easting (m) | 294431.67 |
| Northing(m) | 3833198.18 |

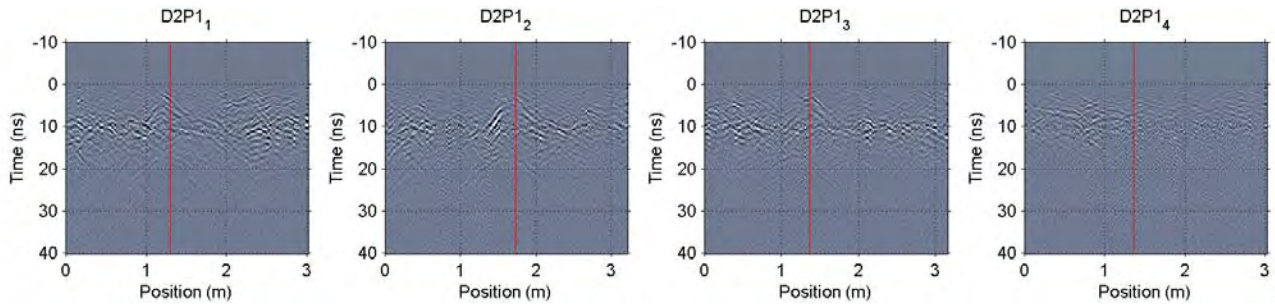


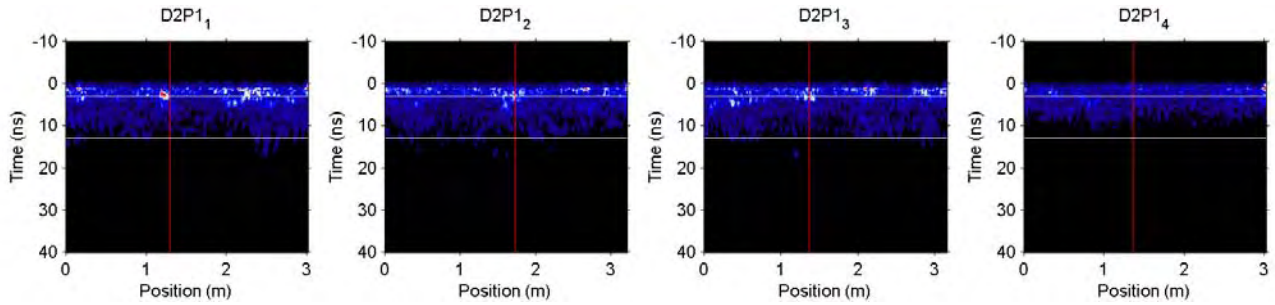


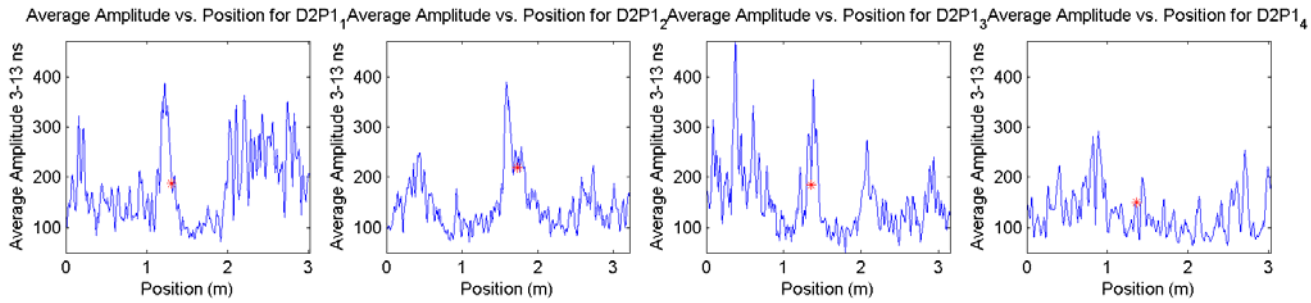

| | |
|---|---|
| Target Name | G6D2_5 |
| Item Description | Adapter |
| Depth (cm) | 2 |
| Distance From Pin (cm) | 5 |
| Easting (m) | 294449.01 |
| Northing(m) | 3833176.15 |

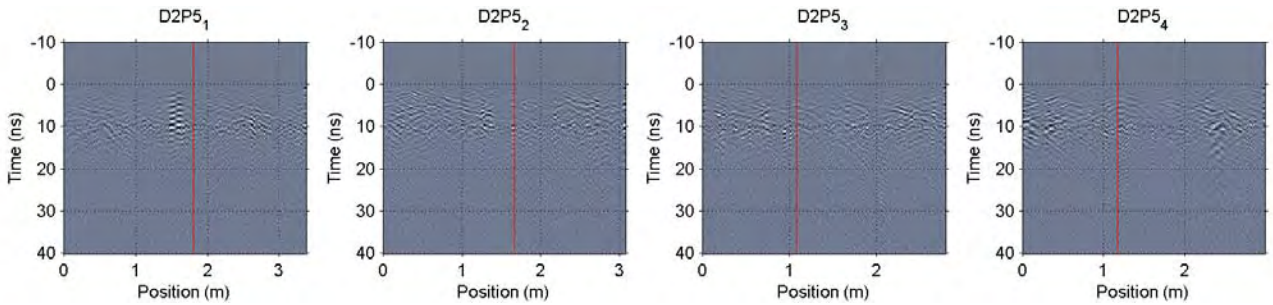


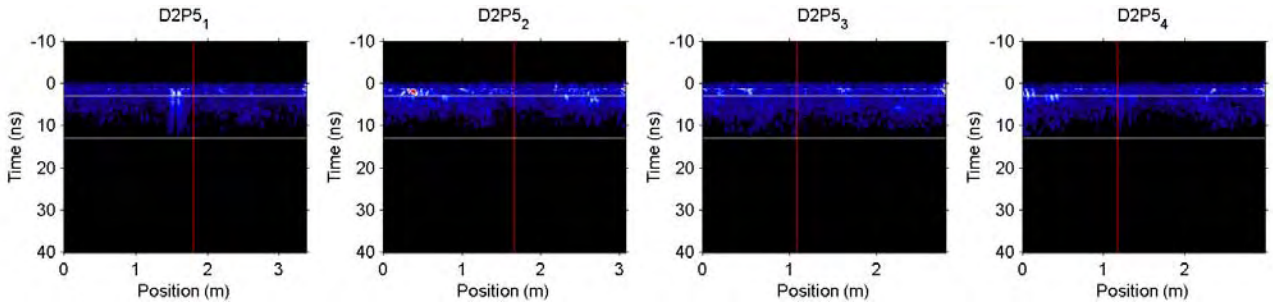


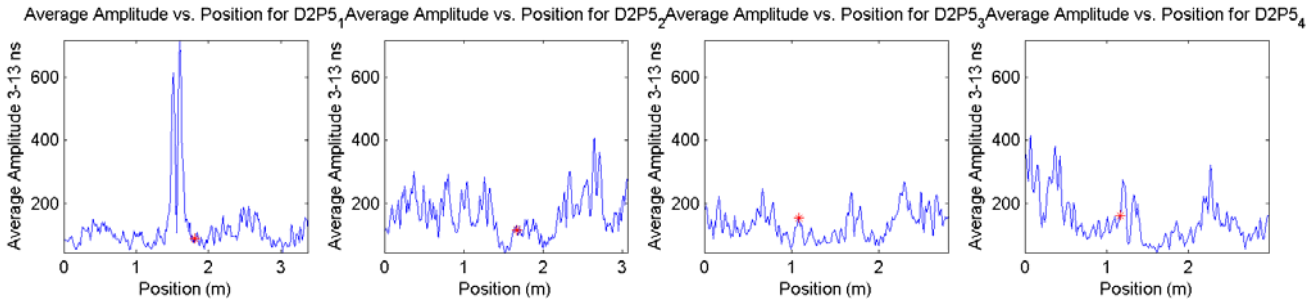

| | |
|---|---|
| Target Name | G6D2_7 |
| Item Description | Adapter |
| Depth (cm) | 0 |
| Distance From Pin (cm) | 6 |
| Easting (m) | 294448.96 |
| Northing(m) | 3833163.58 |

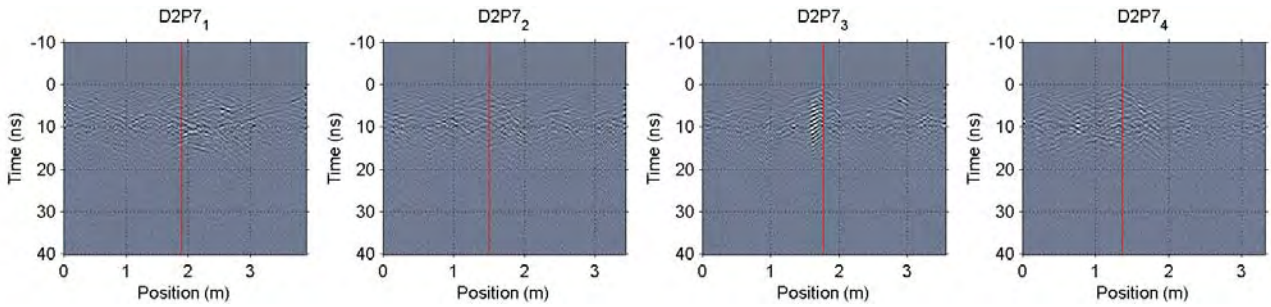


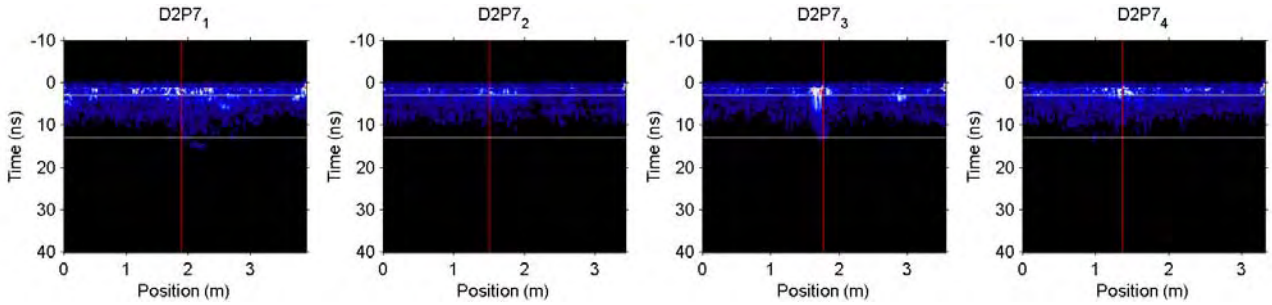


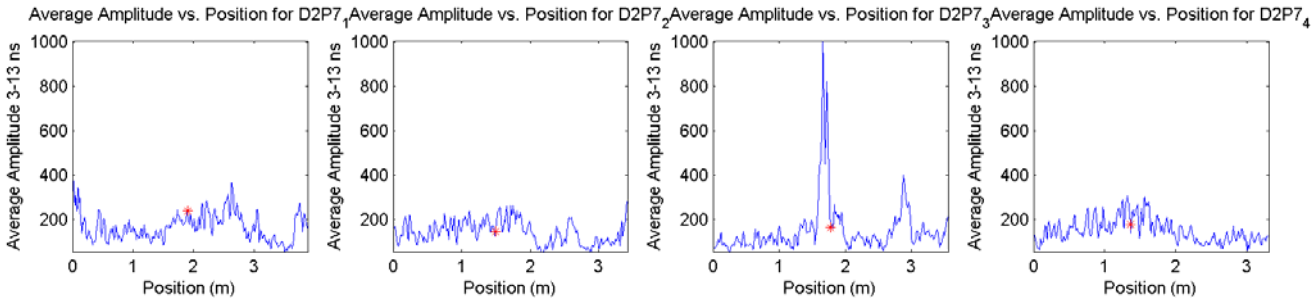

| | |
|---|---|
| Target Name | G6D2_8 |
| Item Description | Adapter |
| Depth (cm) | 8 |
| Distance From Pin (cm) | 0 |
| Easting (m) | 294447.89 |
| Northing(m) | 3833189.26 |

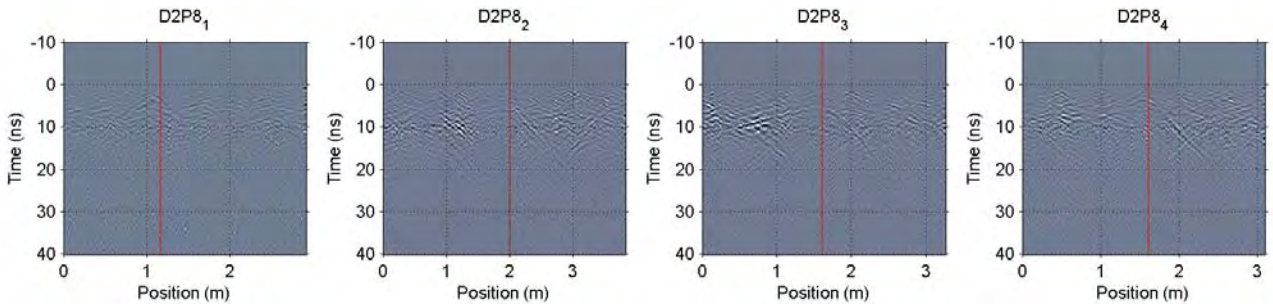


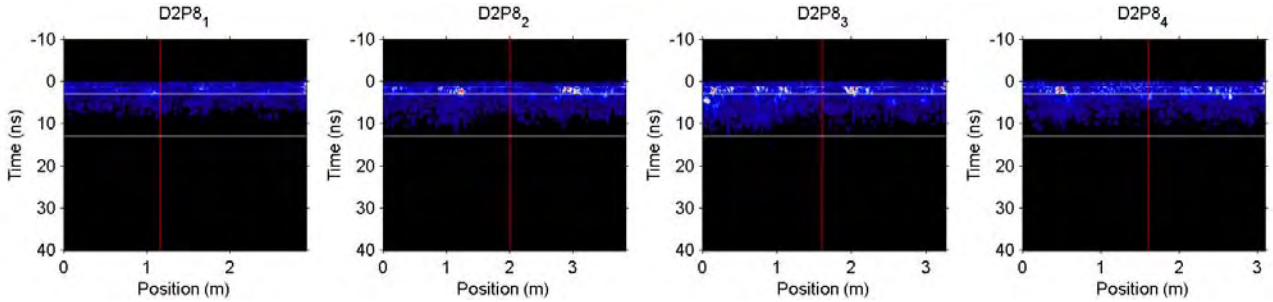


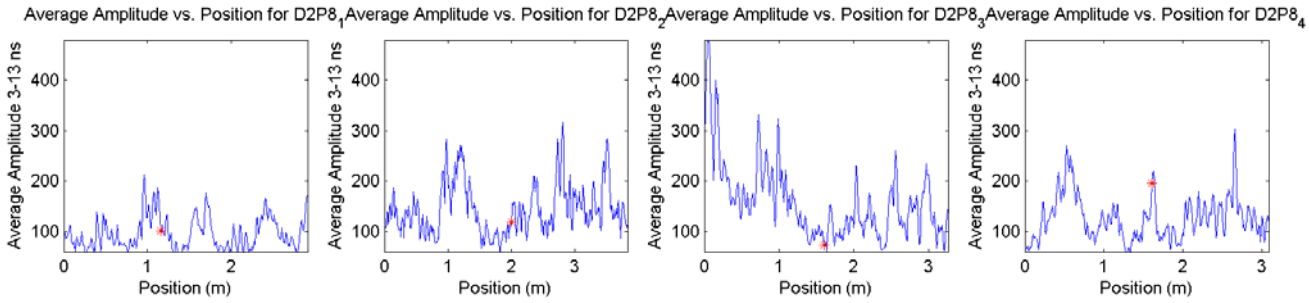

| | |
|---|---|
| Target Name | G6E1_8 |
| Item Description | Adapter |
| Depth (cm) | 2 |
| Distance From Pin (cm) | 7 |
| Easting (m) | 294397.41 |
| Northing(m) | 3833140.34 |

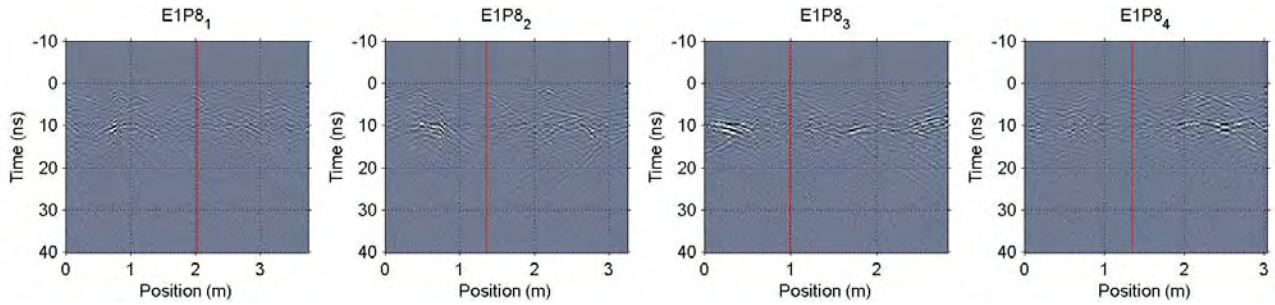


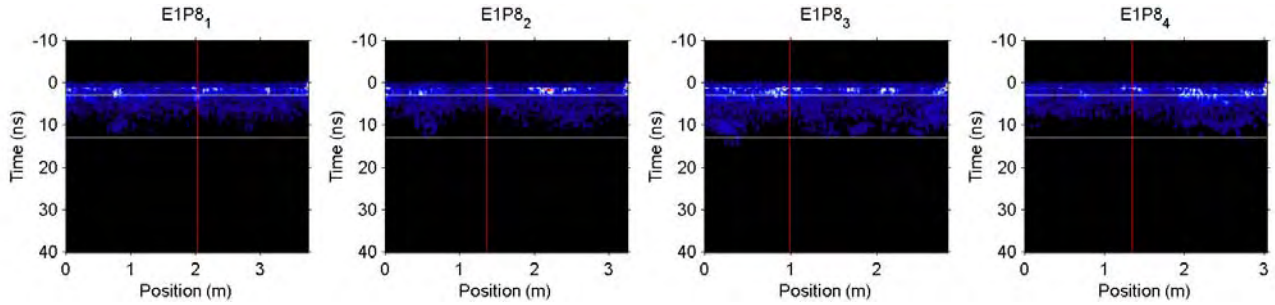


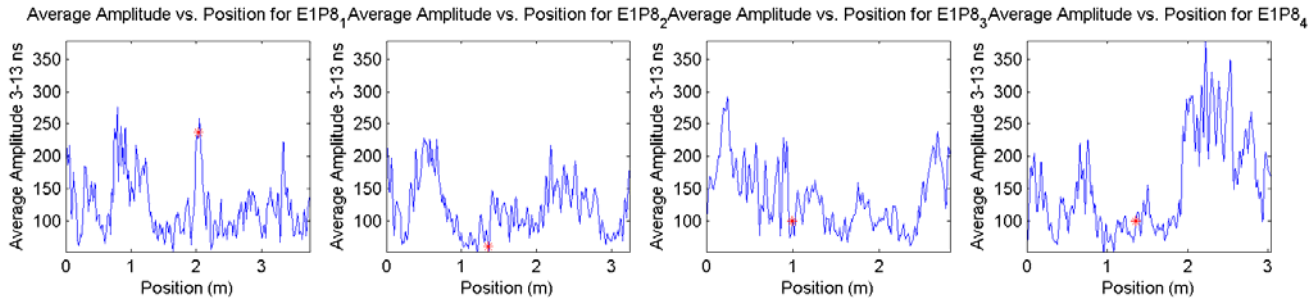

| | |
|---|---|
| Target Name | G6E1_4 |
| Item Description | Adapter |
| Depth (cm) | 4 |
| Distance From Pin (cm) | 0 |
| Easting (m) | 294427.27 |
| Northing(m) | 3833122.27 |

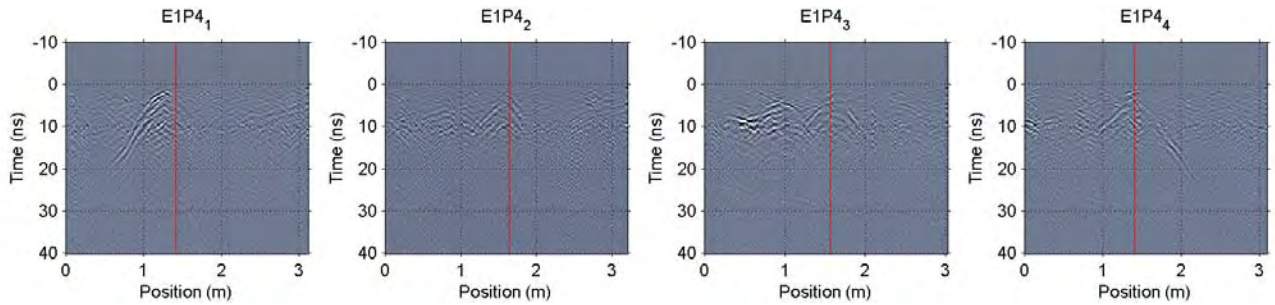


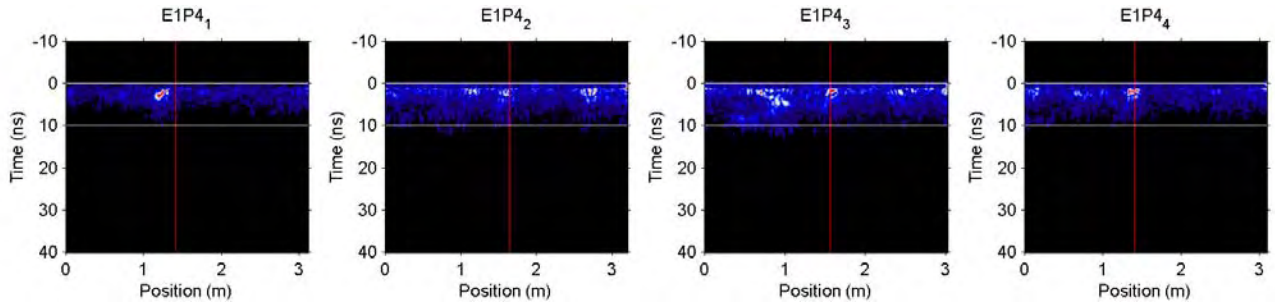


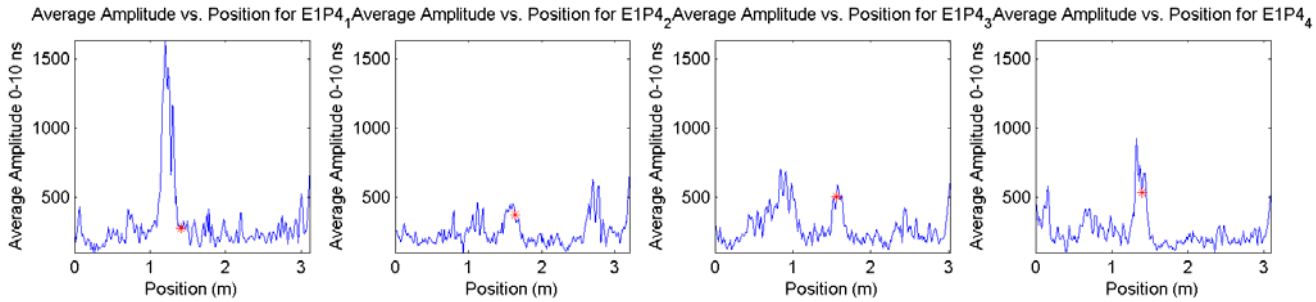

| | |
|---|---|
| Target Name | G6D2_P3 |
| Item Description | Adapter end cap |
| Depth (cm) | 0 |
| Distance From Pin (cm) | 0 |
| Easting (m) | 294435.20 |
| Northing(m) | 3833158.13 |

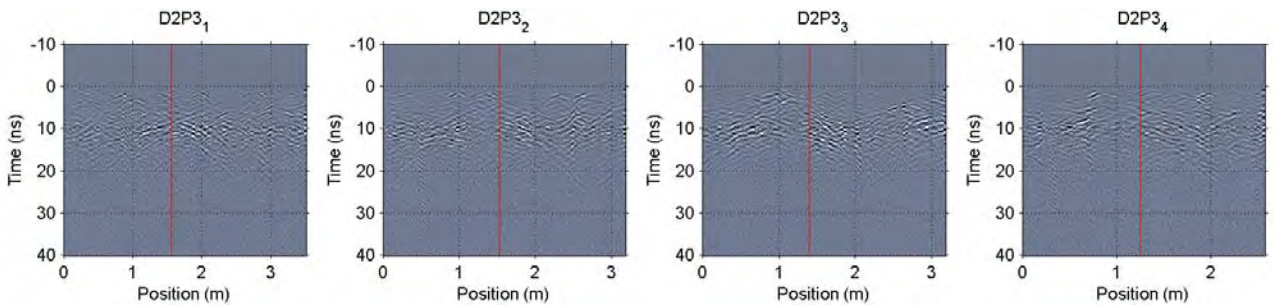


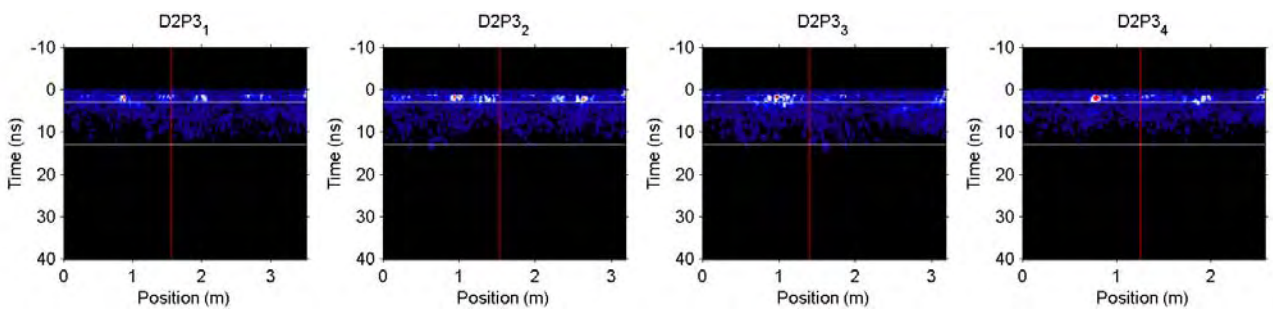


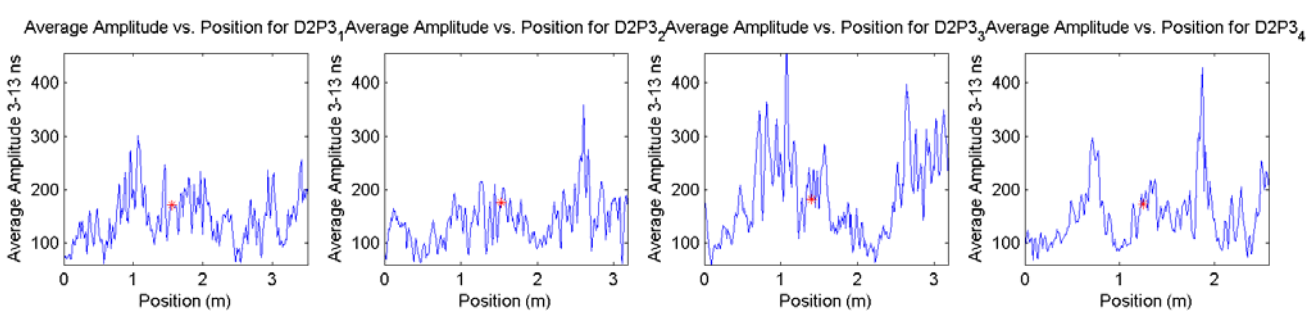

| | |
|---|---|
| Target Name | G6E1_P6 |
| Item Description | Adapter end cap |
| Depth (cm) | 0 |
| Distance From Pin (cm) | 6 |
| Easting (m) | 294434.50 |
| Northing(m) | 3833119.80 |

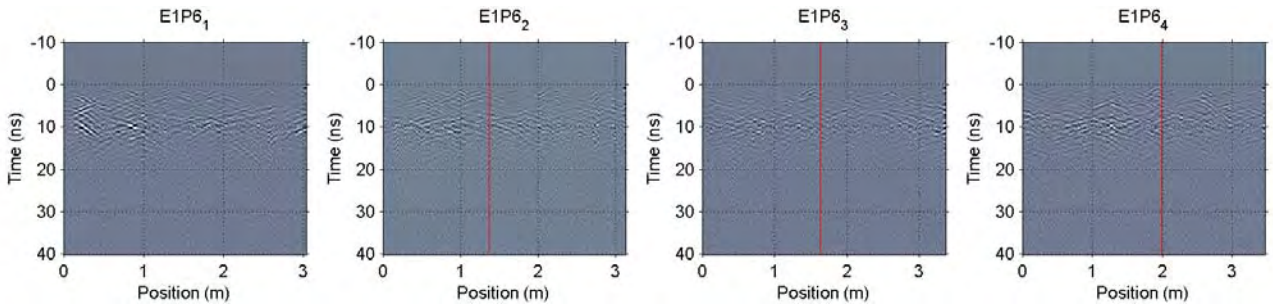


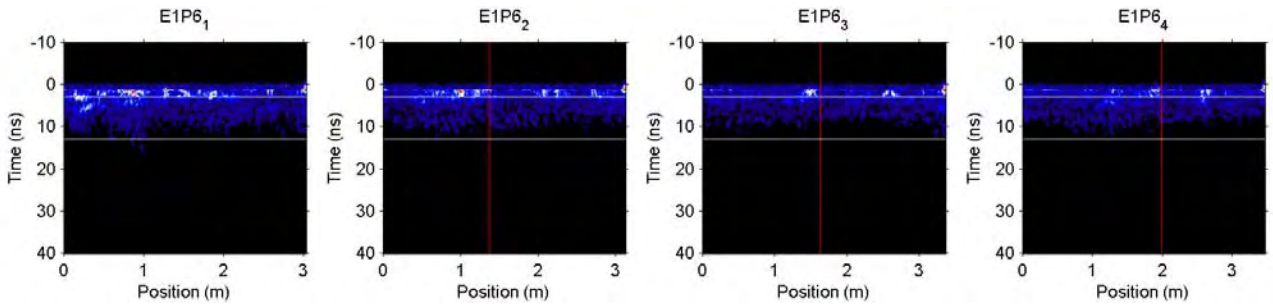


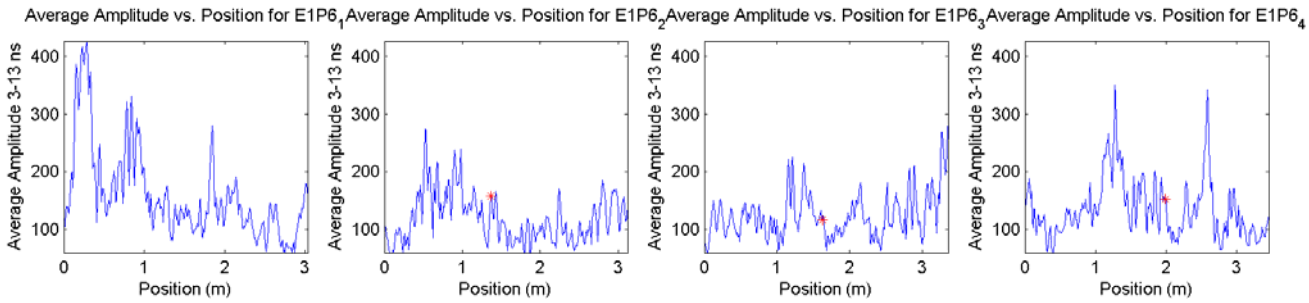

| | |
|---|---|
| Target Name | G6E2_P1 |
| Item Description | Adapter end cap |
| Depth (cm) | 15 |
| Distance From Pin (cm) | 14 |
| Easting (m) | 294473.65 |
| Northing(m) | 3833116.46 |

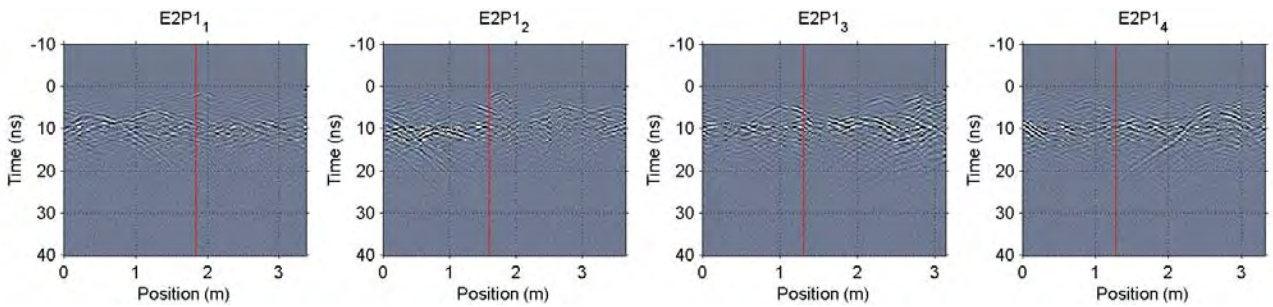


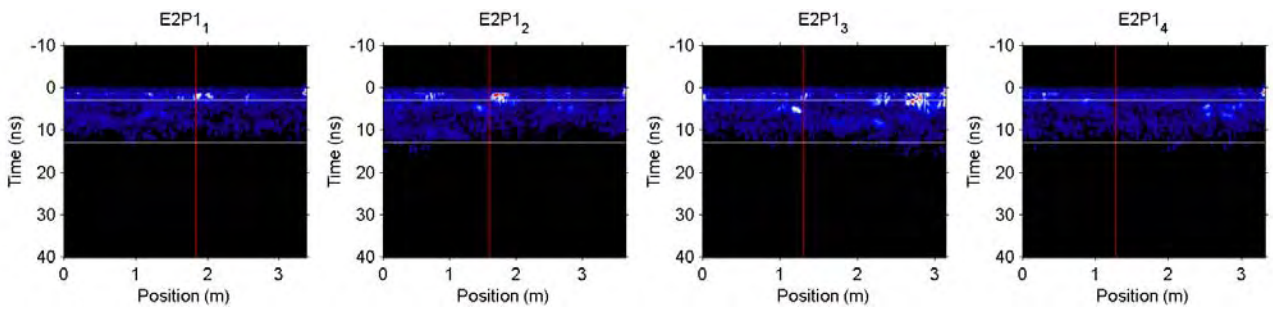


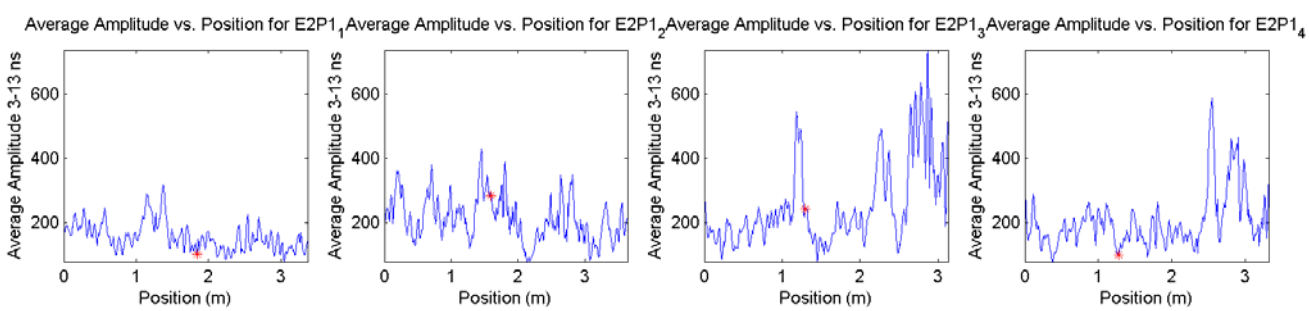

| | |
|---|---|
| Target Name | G6E2_P3 |
| Item Description | Adapter end cap |
| Depth (cm) | 5 |
| Distance From Pin (cm) | 17 |
| Easting (m) | 294457.06 |
| Northing(m) | 3833144.91 |

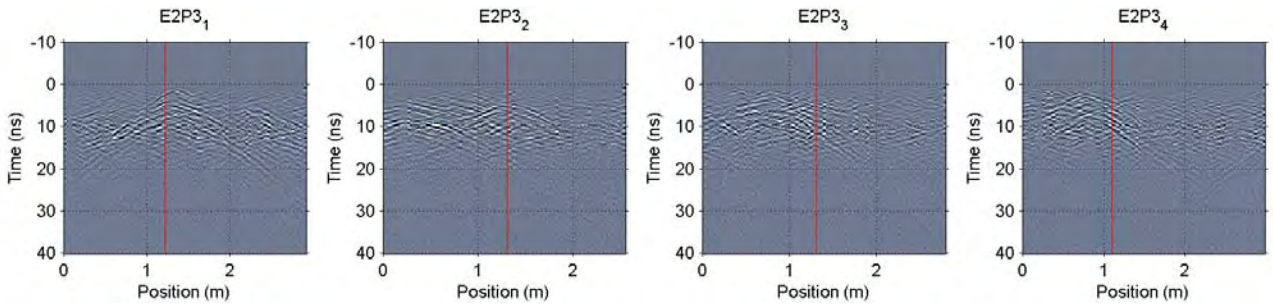


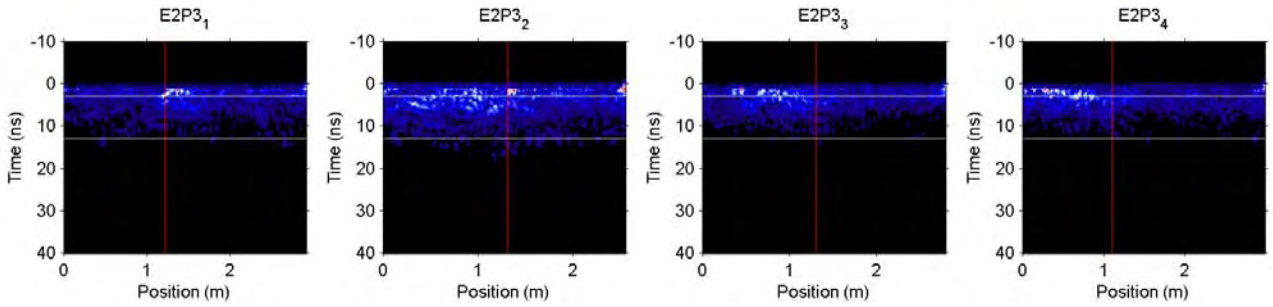


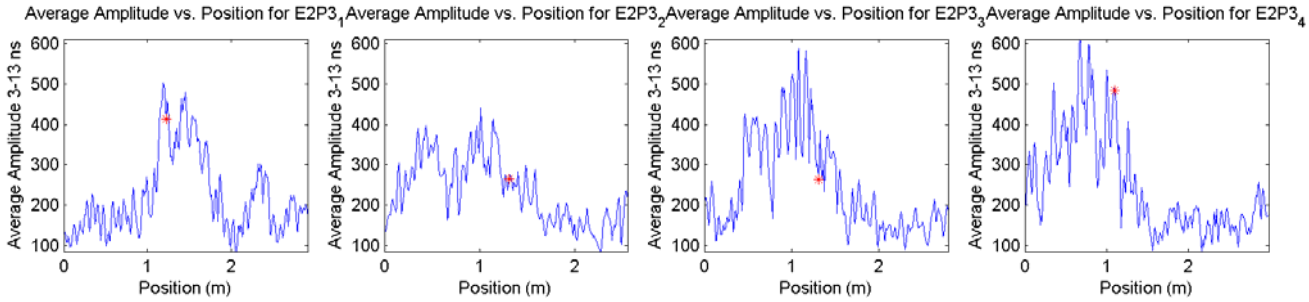

| | |
|---|---|
| Target Name | G6E2_P6 |
| Item Description | Adapter end cap |
| Depth (cm) | 3 |
| Distance From Pin (cm) | 42 |
| Easting (m) | 294468.08 |
| Northing(m) | 3833123.88 |

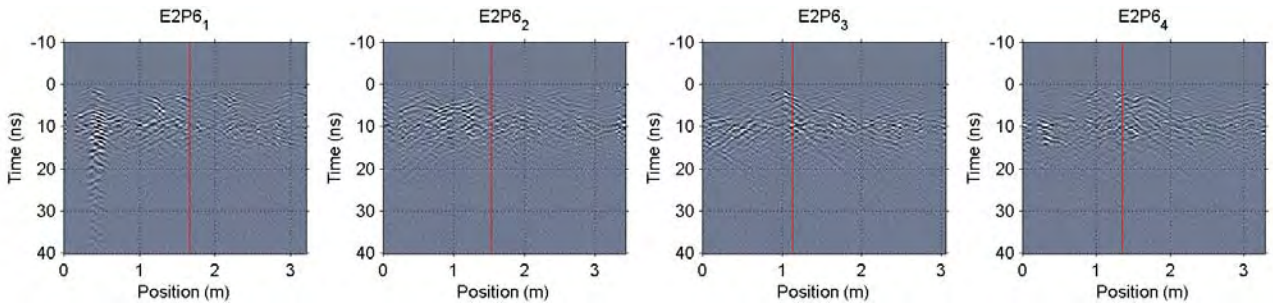


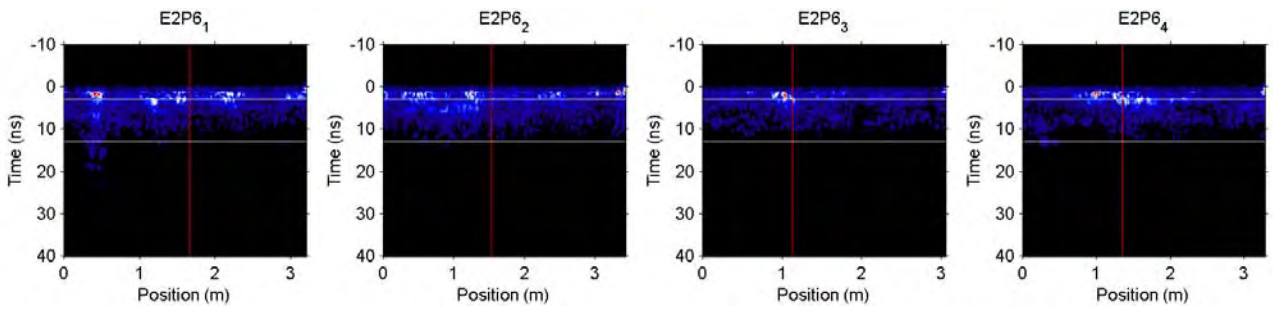


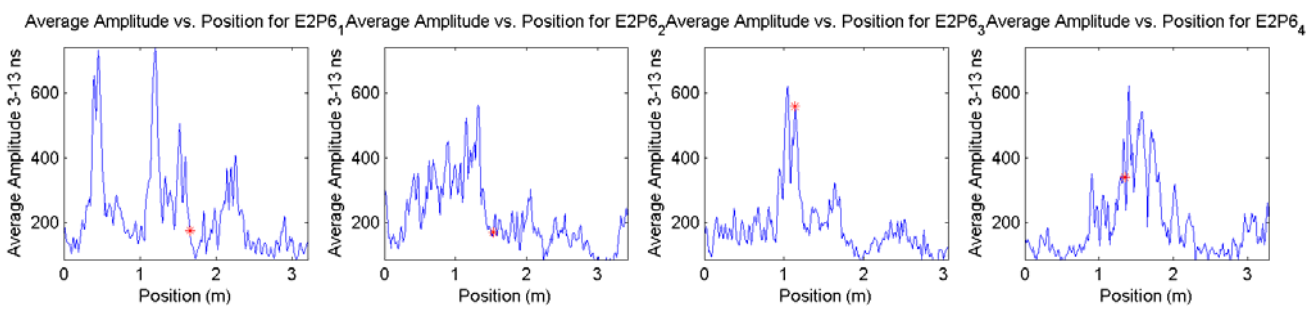

## D.7. 250 MHz large frag and scrap

| | |
|---|---|
| Target Name | G6B2_262 |
| Item Description | Metal plate |
| Depth (cm) | 20 |
| Distance From Pin (cm) | 12 |
| Easting (m) | 294436.68 |
| Northing(m) | 3833269.93 |

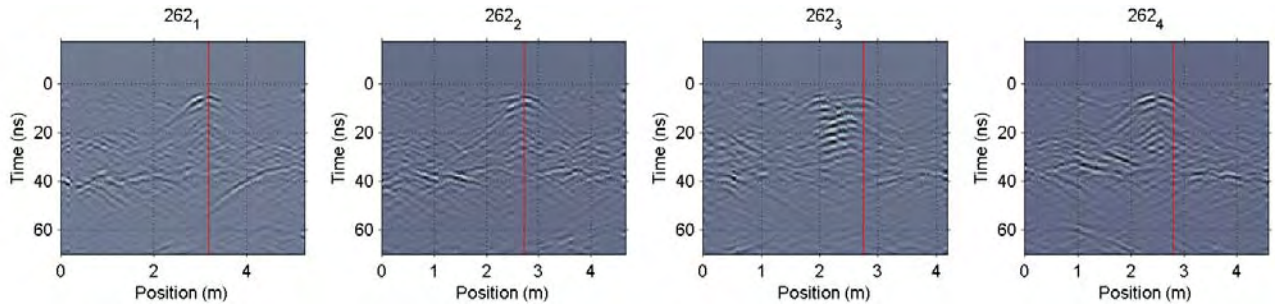


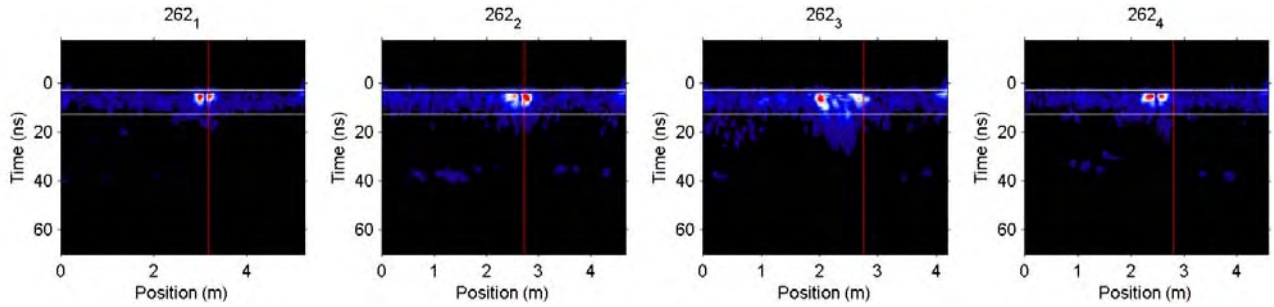


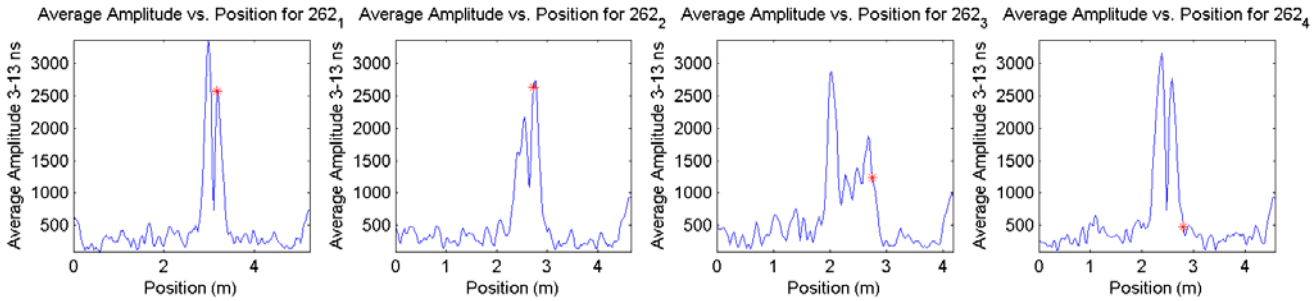

| | |
|---|---|
| Target Name | G6B2_274 |
| Item Description | Metal plate |
| Depth (cm) | 22 |
| Distance From Pin (cm) | 0 |
| Easting (m) | 294438.31 |
| Northing(m) | 3833272.45 |

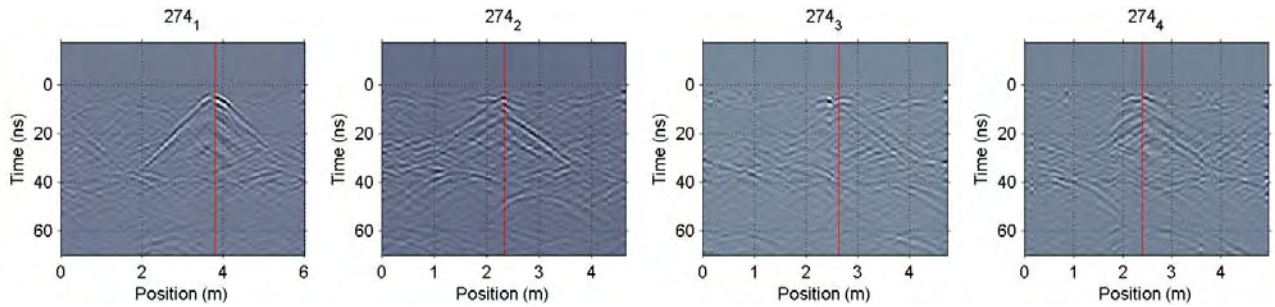


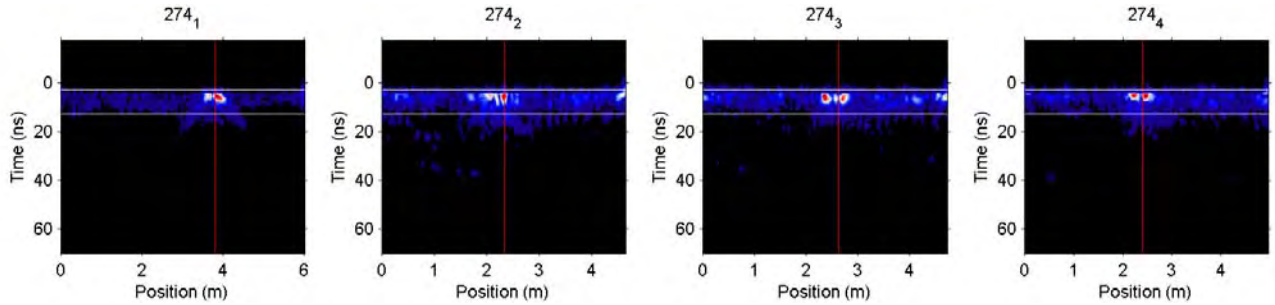


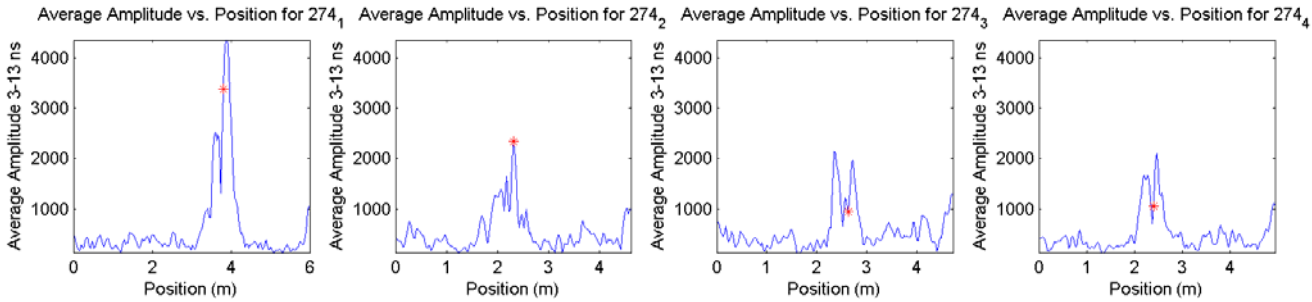

| | |
|---|---|
| Target Name | G6B1_410 |
| Item Description | Target parts |
| Depth (cm) | 6 |
| Distance From Pin (cm) | 36 |
| Easting (m) | 294407.51 |
| Northing(m) | 3833253.62 |

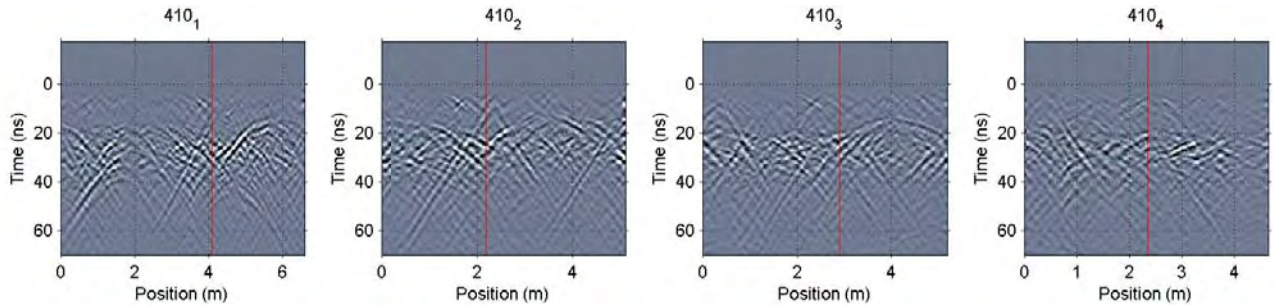


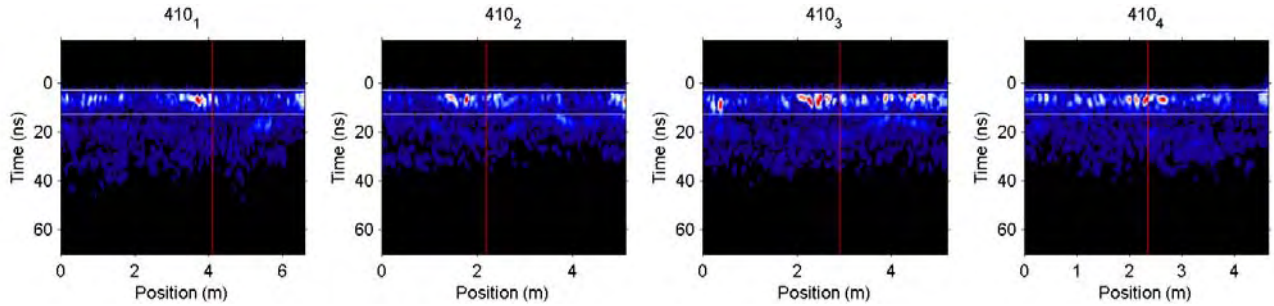


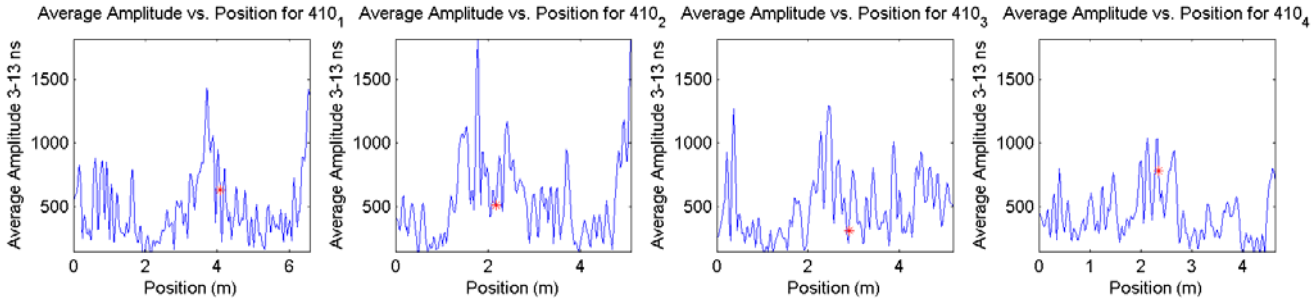

| | |
|---|---|
| Target Name | G6D1_5 |
| Item Description | Sabot half |
| Depth (cm) | 0 |
| Distance From Pin (cm) | 16 |
| Easting (m) | 294420.30 |
| Northing(m) | 3833176.71 |

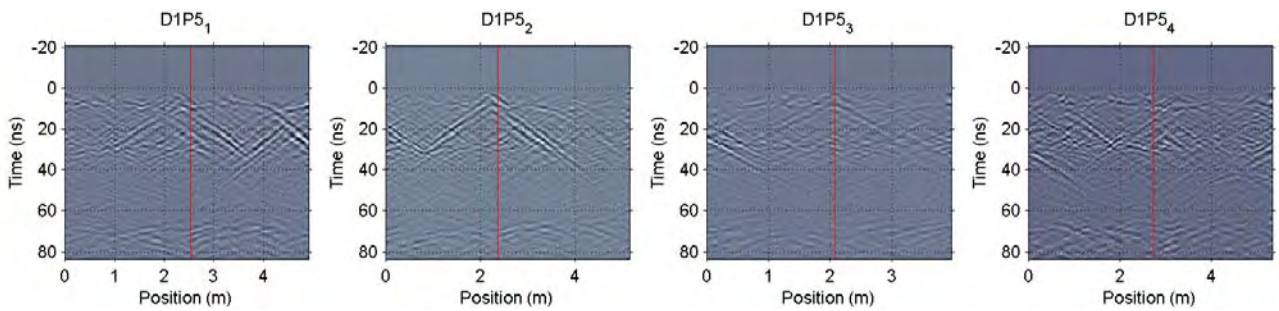


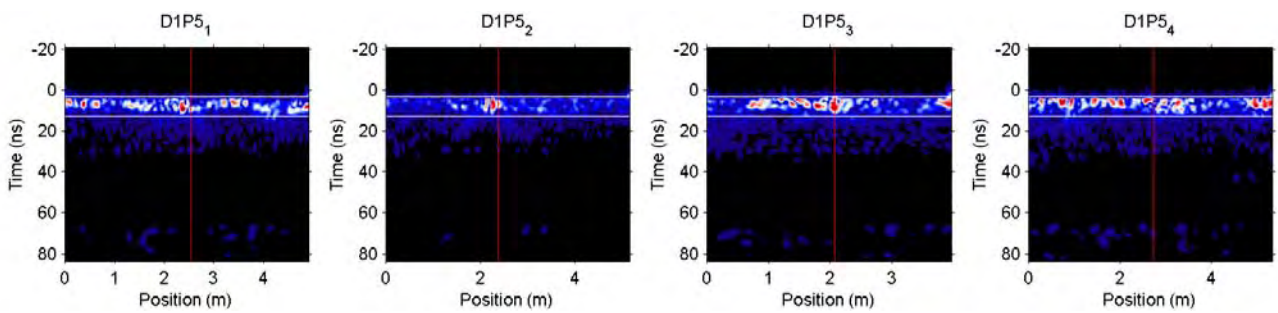


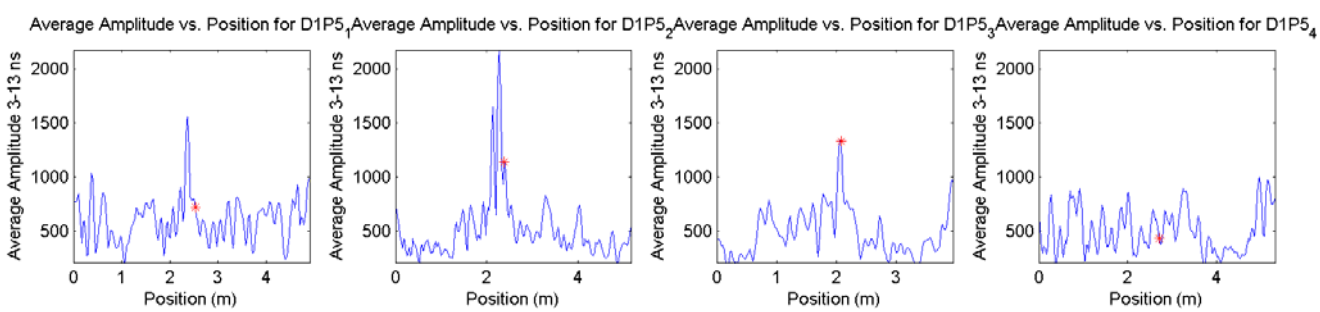

# REPORT DOCUMENTATION PAGE

*Form Approved*
*OMB No. 0704-0188*

Public reporting burden for this collection of information is estimated to average 1 hour per response, including the time for reviewing instructions, searching existing data sources, gathering and maintaining the data needed, and completing and reviewing this collection of information. Send comments regarding this burden estimate or any other aspect of this collection of information, including suggestions for reducing this burden to Department of Defense, Washington Headquarters Services, Directorate for Information Operations and Reports (0704-0188), 1215 Jefferson Davis Highway, Suite 1204, Arlington, VA 22202-4302. Respondents should be aware that notwithstanding any other provision of law, no person shall be subject to any penalty for failing to comply with a collection of information if it does not display a currently valid OMB control number. **PLEASE DO NOT RETURN YOUR FORM TO THE ABOVE ADDRESS.**

**1. REPORT DATE** *(DD-MM-YYYY)*
December 2008

**2. REPORT TYPE**
Report 7 of 9

**3. DATES COVERED** *(From - To)*

**4. TITLE AND SUBTITLE**
UXO Characterization: Comparing Cued Surveying to Standard Detection and Discrimination Approaches: Report 7 of 9 – Marine Corps Base Camp Lejeune: UXO Characterization Using Ground Penetrating Radar

**5a. CONTRACT NUMBER**
W912HZ-04-C-0039

**5b. GRANT NUMBER**

**5c. PROGRAM ELEMENT NUMBER**

**6. AUTHOR(S)**
Kevin Kingdon and Stephen D. Billings

**5d. PROJECT NUMBER**

**5e. TASK NUMBER**

**5f. WORK UNIT NUMBER**

**7. PERFORMING ORGANIZATION NAME(S) AND ADDRESS(ES)**
Sky Research, Inc.
445 Dead Indian Memorial Road
Ashland, OR 97520

**8. PERFORMING ORGANIZATION REPORT NUMBER**
ERDC/EL TR-08-38

**9. SPONSORING / MONITORING AGENCY NAME(S) AND ADDRESS(ES)**
Headquarters, U.S. Army Corps of Engineers
Washington, DC 20314-1000;
U.S. Army Engineer Research and Development Center
Environmental Laboratory
3909 Halls Ferry Road, Vicksburg, MS 39180-6199

**10. SPONSOR/MONITOR'S ACRONYM(S)**

**11. SPONSOR/MONITOR'S REPORT NUMBER(S)**

**12. DISTRIBUTION / AVAILABILITY STATEMENT**
Approved for public release; distribution is unlimited.

**13. SUPPLEMENTARY NOTES**

**14. ABSTRACT**

The detection and discrimination potential of GPR at the Marine Corps Base, Camp Lejeune are evaluated herein. Discrimination mode surveying data were collected over large areas by Witten Technologies CART imaging system and Applied Research Associates Nemesis Advanced Ordnance Detection. The Ohio State University multi-frequency, fully polarimetric system and a COTS GPR system were both deployed in a cued-interrogation surveying mode over previously identified targets. For all systems, saturated ground conditions at the time of the surveys resulted in significant attenuation of the GPR signal and degraded detection and characterization performance. The COTS GPR system provided accurate depths to targets and confirmed the presence of multi-object scenarios. While the inferred depths can be used to constrain inversions of EM data, detailed target information such as material properties, lengths, and aspect ratios are not attainable with a time domain (impulse), single-polarization COTS GPR system. A cued-interrogation approach incorporating OSU's fully polarimetric GPR system allowed for a more sophisticated classification of targets. An estimated linear factor could be calculated based on late time responses of the polarized data allowing targets to be classified as UXO-like or non-UXO.

**15. SUBJECT TERMS**
EMI sensors
Frequency-domain electromagnetic induction (FEM)
Ground penetrating radar
Time-domain electromagnetic induction (TEM)
Total-field magnetics
Unexploded ordnance (UXO)
UXO discrimination

| **16. SECURITY CLASSIFICATION OF:** | | | **17. LIMITATION OF ABSTRACT** | **18. NUMBER OF PAGES** | **19a. NAME OF RESPONSIBLE PERSON** |
|---|---|---|---|---|---|
| **a. REPORT** | **b. ABSTRACT** | **c. THIS PAGE** | | | **19b. TELEPHONE NUMBER** *(include area code)* |
| UNCLASSIFIED | UNCLASSIFIED | UNCLASSIFIED | | 330 | |

**Standard Form 298 (Rev. 8-98)**
**Prescribed by ANSI Std. 239.18**